INSTITUTE OF THEORETICAL PHYSICS, WARSAW UNIVERSITY, WARSAW
INSTITUTE OF EXPERIMENTAL PHYSICS, WARSAW UNIVERSITY, WARSAW

PROCEEDINGS OF THE IX WARSAW SYMPOSIUM ON ELEMENTARY PARTICLE PHYSICS

KAZIMIERZ, POLAND, MAY 25 – 31, 1986

WARSZAWA 1986

INSTITUTE OF THEORETICAL PHYSICS, WARSAW UNIVERSITY, WARSAW
INSTITUTE OF EXPERIMENTAL PHYSICS, WARSAW UNIVERSITY, WARSAW

PROCEEDINGS

OF THE IX WARSAW SYMPOSIUM

ON ELEMENTARY PARTICLE PHYSICS

KAZIMIERZ, POLAND, MAY 25 - 31, 1986

Edited by Z. AJDUK

WARSZAWA 1986

O r g a n i z i n g C o m m i t t e e

H. ABRAMOWICZ S. POKORSKI

Z. AJDUK R. SOSNOWSKI

G. BIALKOWSKI A. WRÓBLEWSKI

D. KIEŁCZEWSKA J. ZAKRZEWSKI

f r o m

INSTITUTE OF THEORETICAL PHYSICS, WARSAW UNIVERSITY, WARSAW

INSTITUTE OF EXPERIMENTAL PHYSICS, WARSAW UNIVERSITY, WARSAW

INSTITUTE FOR NUCLEAR STUDIES, WARSAW

This is the ninth volume in the series of Proceedings:

1. Proceedings of the I International Symposium on Hadron Structure and Multiparticle Production, Kazimierz, 1977;
2. Proceedings of the II International Symposium on Hadron Structure and Multiparticle Production, Kazimierz, 1979;
3. Proceedings of the III Warsaw Symposium on Elementary Particle Physics, Jodłowy Dwór, 1980 (appeared in the journal "Nukleonika", 26, 147, 1095(1981));
4. Proceedings of the IV Warsaw Symposium on Elementary Particle Physics, Kazimierz, 1981;
5. Proceedings of the V Warsaw Symposium on Elementary Particle Physics, Kazimierz, 1982;
6. Proceedings of the VI Warsaw Symposium on Elementary Particle Physics, Kazimierz, 1983;
7. Proceedings of the VII Warsaw Symposium on Elementary Particle Physics, Kazimierz, 1984;
8. Proceedings of the VIII Warsaw Symposium on Elementary Particle Physics, Kazimierz, 1985.

LIST OF PARTICIPANTS

1.H.Abramowicz	- Warsaw	26.H.Hänni	- CERN Geneva
2.Z.Ajduk	- Warsaw	27.T.Haupt	- Cracow
3.B.Badełek	- Warsaw	28.T.Hofmokl	- Warsaw
4.J.Bartelski	- Warsaw	29.H.Høgaasen	- Oslo
5.H.Białkowska	- Warsaw	30.W.Hollik	- Hamburg
6.J.Bieńkowska	- Warsaw	31.B.Humpert	- CERN Geneva
7.J.Bogdanowicz	- Warsaw	32.R.Jaffe	- MIT Cambridge
8.R.Budzyński	- Warsaw	33.J.Jasiak	- Warsaw
9.V.Chernyak	- Novosibirsk	34.P.Jetzer	- Geneva
10.J.Ciborowski	- Warsaw	35.J.Karpiuk	- Warsaw
11.A.Czechowski	- Warsaw	36.J.Kempa	- Łódź
12.W.Dębaki	- Warsaw	37.D.Kiełczewska	- Warsaw
13.K.Doroba	- Warsaw	38.A.Kiselev	- Protvino
14.S.Dubnička	- Bratislava	39.D.Kisielewska	- Cracow
15.Z.Dziembowski	- Warsaw	40.B.Klima	- Hamburg
16.T.Dżurak	- Warsaw	41.J.Kowalski-Glikman	- Warsaw/Amsterdam
17.J.Gajewski	- Warsaw	42.M.Krawczyk	- Warsaw
18.C.Geich-Gimbel	- Bonn	43.P.Krawczyk	- Warsaw
19.R.Geiges	- Heidelberg	44.J.Królikowski	- Warsaw
20.P.Ghez	- Annecy	45.E.Kryś	- Łódź
21.M.Giler	- Łódź	46.Z.Lalak	- Warsaw
22.R.Gokieli	- Warsaw	47.W.Langguth	- Karlsruhe
23.P.Górnicki	- Warsaw	48.A.Leike	- Leipzig
24.P.Grafström	- CERN Geneva	49.A.Lipniacka	- Warsaw
25.C.Guyot	- Saclay		

50.B.Löhr - Hamburg
51.M.Lokajíček - Prague
52.M.Łapucha - Warsaw
53.M.Majewski - Łódź
54.R.Mańka - Katowice
55.L.Mankiewicz - Warsaw
56.K.Meissner - Warsaw
57.J.Nassalski - Warsaw
58.A.Okopińska - Białystok
59.M.Olechowski - Warsaw
60.G.Parrour - Orsay
61.J.Pawełczyk - Warsaw
62.M.Pawlak - Warsaw
63.U.Pirogov - Protvino
64.G.Pócsik - Budapest
65.B.Poensgen - Hamburg
66.S.Pokorski - Warsaw
67.D.Prorok - Wrocław
68.T.Radożycki - Warsaw
69.P.Renton - Oxford
70.T.Riemann - JINR Dubna
71.E.Rondio - Białystok
72.M.Roos - Helsinki
73.J.Rożynek - Warsaw
74.N.Ryskulov - Novosibirsk
75.D.Saxon - Didcot
76.M.Sawicki - Warsaw
77.M.Schaeffer - Strasbourg
78.D.Schütte - Bonn
79.V.Šimák - Prague
80.T.Sloan - CERN Geneva
81.R.Sosnowski - Warsaw
82.M.Spaliński - Warsaw
83.C.Spiering - Zeuthen
84.M.Staszel - Warsaw
85.R.Szwed - Warsaw
86.A.Szymacha - Warsaw
87.L.Szymanowski - Warsaw
88.P.Szymański - Warsaw
89.K.Tanaka - Columbus
90.S.Tkaczyk - Warsaw
91.R.Turlay - Saclay
92.A.Turski - Warsaw
93.J.Wdowczyk - Łódź
94.R.Wischnewski - Zeuthen
95.E.De Wolf - Antwerp
96.J.Wosiek - Cracow
97.A.Wróblewski - Warsaw
98.T.Wybig - Łódź
99.K.Zabłocki - Warsaw
100.J.Zakrzewski - Warsaw
101.W.Zieliński - Cracow
102.M.Zrałek - Katowice
103.A.Żarnecki - Warsaw

CONTENTS *

---

* We list here the names of the speakers only.

A complete list of the authors is given in the text of the talk.

INTERACTIONS WITH NUCLEI. COSMIC RAYS

Chairman: M. Schaeffer

e^+e^- INTERACTIONS

Chairman: M. Roos

ELECTROWEAK INTERACTIONS

Chairmen: G. Pocsik, R. Jaffe

SUPERSYMMETRY AND SUPERSTRINGS

Chairman: D. Schütte

* * *

PHYSICS RESULTS AT THE CERN $\bar{p}p$ COLLIDER

(UA1 and UA2 experiments)

presented by G. Parrour

Université Paris – Sud, L.A.L.
Centre Orsay, 91405 ORSAY, France

INTRODUCTION

It turns out to be a challenge trying to summarize within an one hour talk the results from UA1 and UA2 experiments obtained with the $\bar{p}p$ facility at CERN.

Hopefully main topics about the high – p_T jet physics will be covered with talks given in this conference by P. Ghez (UA1) and H. Hänni (UA2). So I shall stress on the physics with leptons preceded by an introduction about identification criteria in both experiments.

1. PERFORMANCES OF EACH APPARATUS

Detailed descriptions of both UA1 and UA2 apparatus were given in various publications [1]. To summarize :

a. In UA1 there is a complete acceptance in θ view (beam plane) and a hole in ϕ view (transverse to the beams). This rejects events with electrons or jets within $\pm 15°$ with respect to the vertical axis. The calorimeter granularity is poor in ϕ (gondola).
There is a magnetic field perpendicular to the beam for charge measurements in all the detector volume.
UA1 apparatus is able to detect muons.

b. In UA2 a hole in θ view prevents detection for angles $\theta < 20°$ or $\theta > 160°$ with respect to the proton beam A partial magnetic field – in a region defined by $20° < \theta < 40°$ and $140° < \theta < 160°$ – allows charge identification in forward–backward direction only.
The calorimeter granularity ($\Delta\phi \times \Delta\theta = 10° \times 15°$) is good and allows special triggers. In UA2 there is no muon signature.

1.1 Jet identification

First of all it is worth pointing out the following obvious assertion : a good granularity allows simplier algorithms.

In UA1 "energy vectors" are defined from electromagnetic and hadronic calorimeters. Using ϕ, η (rapidity) variables, they must cluster within a cone defined by an half–aperture $\Delta R = \sqrt{\Delta\eta^2 + \Delta\phi^2} < 1$ around the maximum.

In UA2 a "cluster" is defined by a set of adjacent cells with $E_{TOT} > 400$ MeV.

In both experiments this needs a lot of energy corrections for the non linearity of calorimeters, various detection probabilities (for π^0,$\pi^\pm$, jets) and the energy lost by the choice of the algorithm.

1.2 Electron identification

At the collider the main background for electrons results from jets containing π^0's. From these π^0's one can get a photon conversion or/and a $\pi^\pm$ with a converted π^0 superimposed. To get an idea of such occurences one can notice that at $p_T \simeq 40$ GeV/c, the ratio e/jet is about 10^{-3}.

Both experiments use similar criteria to define a track as an "electron" :

a. First in both cases such a track has few hadronic leakage in hadronic calorimeter (for example 1% in UA2 in this analysis).

b. The longitudinal developpement of the e.m. shower is over four samples in UA1, and taking advantage of the good calorimeter granularity, in UA2 the lateral size of the e.m. shower has to be small.

c. Concerning the quality of the track, a good matching is required between energy and momentum in UA1 and in UA2 in the magnetic field regions. Moreover in UA2 one looks for a good matching in the preshower detector ($1{,}5\ \chi^0$ after the vertex detector) between the charged track and the apex of the e.m. shower.

d. Owing to the non identification of the electrons in jets, energy isolation criteria are applied in a cone of an half−aperture equal to 40° in UA1 and to 15° in UA2.

1.3 Neutrino identification

From the decay $W \rightarrow e\nu$ a non−interacting high p_T neutrino is expected in the final state.

The neutrino identification is based on the determination of the missing transverse momentum $\vec{P}_T$, identified as the neutrino transverse momentum $\vec{P}_T{}^{\nu}$.

a. In UA1 $\vec{P}_T{}^{\nu}$ is calculated from $\vec{P}_T{}^{\nu} = -\vec{P}_T{}^{e} - \Sigma\, \vec{P}_T{}^{i}$ where $||\vec{P}_T{}^{i}|| = E^i$ the energy in the i^{th} cell of the calorimeter and $\vec{P}_T{}^{i}$ directed from the vertex to the impact point in the cell. The sum is carried over all cells.

Due to imperfect calorimetry in the two azimuthal sectors at ± 15° with respect to the vertical axis, ν's in these sectors are eliminated. After these rejections the $p_T{}^{\nu}$ resolution becomes almost gaussian.

b. In UA2 there is no particule detection at $\theta < 20°$ or $\theta > 160°$. In the two forward backward regions $20° < \theta < 40°$ and $140° < \theta < 160°$ there is a partial detection because of incomplete azimuthal coverage (toriod coils) and lack of hadronic calorimetry. This produces non−gaussian tails in $P_T{}^{miss}$ resolution. (The probability of losing one jet in a 2−jet event varies between 10% for P_T = 15 GeV/c and 2% for P_T = 40 GeV/c)

$\vec{P}_T{}^{\nu}$ is calculated from $\vec{P}_T{}^{\nu} = -\vec{P}_T{}^{e} - \Sigma\vec{P}_T{}^{j} - \lambda\vec{P}_T$

The sum is for $\|\vec{P}_T^{\,j}\| > 3$ GeV/c, and $\vec{P}_T$ is the total transverse momentum for particles which do not belong to jets. The λ factor is an empirical correction taking into account the non-linearity response of the calorimeter to low-energy particles (the λ value is determined by $\langle \vec{P}_T^{\,\nu} \rangle = \vec{0}$ for the sample of $Z \to e^+e^-$ in UA2).

2. SAMPLES FOR ANALYSIS

2.1 Final $W \to e\nu$ sample

The figure 1 displays the distributions of events containing at least one electron with $P_T^e > 15$ GeV/c in a (P_T^e, P_T^{ν}) plane for respectively UA1 and UA2.

In high P_T^e regions ($P_T^e \geq 25$ GeV/c), signals from $W \to e\nu$ ($P_T^{\nu} \simeq P_T^e$) and $Z \to e^+e^-$ ($P_T^{\nu} \simeq 0$) are visible above the background.

Figure 2 gives the projections for both experiments on the P_T^{ν} axis (data from the end of 85 are not included). From these projections it turns out that the rejection power of a cut on P_T^{ν} against the background is larger in UA1 than in UA2. In UA1 events with $P_T^{\nu} > 15$ GeV/c exhibit the caracteristic Jacobian structure expected from the $W \to e\nu$ decay.

In UA2 the separation is not so easy due to the non-gaussian tail of the P_T^{ν} distribution.

The final cuts are the following :

UA1 $P_T^e > 15$ GeV/c, $P_T^{\nu} > 15$ GeV/c. This corresponds to a total number of 314 (172 + 142 from the 1985 data) candidats after rejection of ν's and e's in azimuthal vertical direction (holes defined in part I).

UA2 $P_T^e > 25$ GeV/c, $P_T^{\nu} > 15$ GeV/c and, on top of that, a topological cut defined by "no jet within $\Delta\phi = 60°$ back to the electron". This corresponds to a total number of 216 candidats. The figure 3, gives the inclusive P_T^e distribution from UA2 analysis including the last 85 data.

The background

The main sources of background are :

a. QCD background, jets look like $e\nu$.

b. $Z^0 \to e^- + e^+$ where one particle is unseen.

c. $W \to \tau\nu_\tau$ with either the leptonic decay of the τ ($\tau \to e\nu_e\nu_\tau$) or the semileptonic τ decays ($\tau \to \nu_\tau\pi^0$ + hadrons).

In UA1 the hadronic background is estimated from the shape of the P_T^{ν} resolution.

In UA2 the topological cut mentioned above is applied to minimize the background from misidentified hadrons with a jet at opposite direction. To do this one defines $\rho_{opp} = -\vec{P}_T^{\,e} \cdot \Sigma \vec{P}_T^{\,j} / |\vec{P}_T^{\,e}|^2$, sum is over all reconstructed jets with $P_T^{\,j} > 3$ GeV/c and $(\vec{P}_T^{\,j}, \vec{P}_T^{\,e}) > 120°$.

The cut is $\rho_{opp} < .2$ (most of $W \to e\nu$ decays are events with large P_T umbalance $\rho_{opp} \simeq 0$, whereas for misidentified high p_T hadrons $\rho_{opp} \simeq 1$).

Background contributions are listed in table I. The figure 4 gives the resulting $P_T^{\,e}$ distributions.

Table I

	UA1	UA2
$P_T^{\,e}$ threshold (GeV/c)	15 GeV/c	25 GeV/c
Number of events	172	214
Hadronic background	5.3 ± 1.9	11.6 ± 2.4
$Z^0 \to e+e$ (undetected)		9. ± 1.1
$W \to \tau\nu_\tau(\tau \to e\nu_\tau\nu_e)$	9.1 ± 0.5	3.3 ± 0.3
$W \to \tau\nu_\tau$ ($\tau \to \nu_\tau\pi^0$ + hadrons)	2.7 ± 0.4	
$W \to e\nu$ Signal	155 ± 13	190 ± 15

* For UA1 this analysis does not include the 1985 data.

Cross sections

For UA1, the last 1985 data are not used for the cross-sections given in table II. The first quoted errors are statistic, then systematic. These last ones come mainly from uncertainties on total luminosity (±15% in UA1 and ±8% in UA2 which takes advantage of the total cross-section measured by UA4 in the same intersection).

Table II

$\sqrt{s}$ (GeV)	UA1	UA2
546	(.55 ± 0.08 ± 0.09)nb	(0.50 ± 0.09 ± 0.05)nb
630	(.63 ± 0.05 ± 0.09)nb	(0.53 ± 0.06 ± 0.05)nb
$R = \frac{(\sigma B)_{630}}{(\sigma B)_{540}}$	1.15 ± 0.17	1.06 ± 0.23

(Theoretical prediction 1.20)

2.2 $Z \rightarrow e^+e^-$ event samples

The electron identification efficiency is about 75% in both experiments. So, to minimize an important lost of events ($\simeq$ 50%) when applying all electron criteria, it is required that first both energy clusters are compatible with an electron from calorimeter information alone ($E_T > 8$ GeV) and moreover, one track at least satisfy the full electron identification criteria.

The resulting distributions for the invariant masse m_{ee} are shown in figure 5. A well-separated peak around $m_{ee} = 90$ GeV/c^2 appears in each distribution. The low-mass continum decreases rapidly and becomes negligeable for m_{ee} masses larger than 50 GeV/c^2. It is due mainly to QCD 2-jet events and a contribution of the Drell-Yan process.

3. ANALYSIS

3.1 Angular distribution of the electron in $W \rightarrow e\nu$ decay

At the CERN $\bar{p}p$ collider energies, W is produced mainly from valence quarks and antiquarks. As a consequence of the V/A coupling, the helicity of quarks (antiquarks) is -1 ($+1$) and the W is almost fully polarized along the $\bar{p}$ beam (the contribution of sea quarks becomes important at higher energies and the resulting W polarization is reduced) [2].

From very simple helicity arguments one predicts then : antileptons are manily emitted along the W ($\bar{p}$) direction (and the reverse for the leptons). The resulting angular distribution is given by

$$d\sigma/d\cos\theta^* \propto (1+\cos\theta^*)^2 \text{ where } \theta^* \text{ is the } e^+(e^-)$$

angle in the W rest frame measured with respect to a direction parallel (antiparallel) to the W polarization. (It is worth noticing this axis coincides with the $\bar{p}(p)$ beam in case of a null transverse momentum for the W : $P_T^W = 0$; for $P_T^W \neq 0$ initial parton directions being unknown, θ^* is defined by the Collins-Soper convention [3]).

In figure 6 the $\cos\theta^*$ distribution from UA1, corrected for the acceptance, agrees very well with the expected $(1+\cos\theta^*)^2$ form.

In UA2 the absence of magnetic field over most of the solid angle allows a charge-average $\cos\theta^*$ measurement only.

In figure 7 the UA2 experimental data agree well with the expected $(1+\cos^2\theta^*)$ form of the distribution in this case.

Spin from $<\cos\theta^*>$. Obviously if $J = 0$ $<\cos\theta^*> = 0$.

For arbitrary spin J, one expects [4] :

$$<\cos\theta^* > = <\lambda> <\mu>/J(J+1)$$

where $<\mu>$ is the global helicity of the production vertex (ud) and $<\lambda>$ is the global helicity of the decay vertex ($e\nu$).

For a V−A coupling $<\mu> = <\lambda> = -1$. From this,

$$<\cos\theta^* > = .5 \text{ for } J = 1$$
$$\text{and } |<\cos\theta^* >| \leq 1/6 \text{ for } J > 1$$

UA1 published [5], $<\cos\theta^* > = 0.43 \pm 0.07$ in agreement with $J = 1$ for the W boson.

One can notice that such measurements do not provide a way to distinguish between V−A and V+A couplings (in fact in V+A, $<\mu> = <\lambda> = +1$). A way to do this would be to measure the lepton helicity.

3.2 Longitudinal momentum of the W and the quark distributions

This analysis was done by UA1. No new result including 85 data is available for the time being. To summarize the UA1 analysis, the Feynman variable $x_W = 2P_L{}^W/\sqrt{s}$ ($P_L{}^W$ longitudinal momentum of the W) is expressed with the fractionnal momenta x_p and $x_{\bar{p}}$ of the interacting partons contained in the p and $\bar{p}$ beams : $x_W = x_p - x_{\bar{p}}$.

The m_W mass is expressed with these variables too : $m_W{}^2/s = x_p x_{\bar{p}}$. From these two equations and using events with unambiguous determination of the charge, UA1 gives the fractionnal momentum of a u and $\bar{d}$ in case of W^+ or a d and $\bar{u}$ in case of W^-. Figures 8a and 8b show the exprimental distributions of u and d quarks which agree fairly good with the parametrization of Eichten et al [6].

3.3 Transverse momentum of the W

The W transverse momentum $\vec{P}_T{}^W$ is obtained from :

$$\vec{P}_T{}^W = \vec{P}_T{}^e + \vec{P}_T{}^\nu$$

Figure 9 gives the $P_T{}^W$ distribution for UA1 and UA2 including the 85 data. Curves are QCD predictions from reference [7].

UA1 $\sin^2\theta_W = 0.214^{+.004}_{-.005} \pm 0.015$ (4) (the 1985 data not included)

UA2 $\sin^2\theta_W = 0.232 \pm 0.004 \pm 0.008$ (5) (preliminary result including the 1985 data).

The quoted errors are respectively statistical and systematical. These last ones are mainly due to uncertainties on mass scale from uncertainties on calorimeter calibrations.

As a comparison these results agree well with an average of the low energy data

$$\sin^2\theta_W = 0.220 \pm 0.008 \qquad [10]$$

A very recent result [11] published by the CDHS experiment

$$\sin^2\theta_W = 0.227 \pm 0.005 \pm 0.003 \pm 0.013\ (m_c - 1.5\ \mathrm{GeV}/c^2) \qquad (6)$$

is also in a very good agreement with the previous figures (the very last uncertainty here reflects the contribution of the quark−c mass in this determination).

As it was shown elsewhere [12] the need for the radiative corrections in the Standard Model from the two results (4) and (5) cannot be proved for the time being. But, as it is underlined in the Ref. [11], without radiative corrections result (6) and results (4) and (5) are in very poor agreement.

By using (1) one assumes that the ρ parameter defined as $\rho = m_W^2/m_Z^2 \cos\theta^2_W$ (7), is equal to 1.

To test this, equations (2) and (7) are combined to get :

$$\rho = m_W^2/(m_Z^2(1 - B^2/m_W^2))$$

where $B^2 = A^2/(1-\Delta r)$.

The results are :

$$\text{UA1}\ \rho = 1.028 \pm 0.037 \pm 0.019$$
$$\text{UA2}\ \rho = 0.996 \pm 0.033 \pm 0.009$$

This two results agree with each other and with the low energy average value

$$\rho = 1.02 \pm 0.02 \qquad [9]$$

All these figures are compatible with $\rho = 1$. which corresponds to the minimal Standard Model with only one Higgs boson (one isodoublet of complex Higgs fields).

4. RESULTS OF PHYSICS WITH MUONS

All these results are from the UA1 experiment where muons can be detected.

4.1 Inclusive muon spectrum and W mass

The analysis requires an high $-p_T$ isolated track in the muon detector ($P_T^{\mu} > 15$ GeV/c) and a large missing transverse momentum ($E_T^{\nu} > 15$ GeV). This gives a sample of 82 events including the 1985 data. The P_T^{μ} distribution is shown in figure 12 where it is compared with the spectrum expected from $W \rightarrow \mu\nu$ decay for $m_W = 83$ GeV/c^2.

From this one calculates the partial cross $-$ section for W production followed by $W \rightarrow \mu\nu$ decay which turns out to be compatible with the $\mu - e$ universality. The results are summarized in the following table [13].

Table III

Cross $-$ sections for $W^{\pm} \rightarrow \mu^{\pm}\nu$

$\sqrt{s}$ (GeV)	Theory (nbarn)	σ.B($W \rightarrow \mu\nu$)1983	(nbarn)1984
546	0.39 ± 0.10	$0.56 \pm 0.18 \pm 0.12$	
630	0.47 ± 0.10		$0.61 \pm 0.11 \pm 0.12$
Ratio	1.20	1.09 ± 0.40	

W mass determination from the μ sample. From the 1984 data, after tight cuts in the central detector and μ chambers, the UA1 experiment uses the 22 remaining events to get :

$$m_W = 81.6 \pm {}^{4.6}_{4.5} \pm {}^{9.0}_{8.1}$$

in quite good agreement with the W mass values determined from the inclusive electron analysis ($W \rightarrow e\nu$ decay). The corresponding transverse distribution is shown in figure 13, the curve is an expectation from $m_W = 83$ GeV/c^2.

4.2 Dimuon production

The following analysis does not include the 1985 data.

The figure 14 shows the $m_{\mu\mu}$ distribution with $P_T^{\mu} > 3$ GeV/c and $m_{\mu\mu} > 6$ GeV/c^2. On can notice a rapidly falling continuum for the low mass values which is well separated from events with masses around 90 GeV/c^2, the Z^0 mass region.

Dashed events in the UA2 distribution contain at least one jet with $E_T > 5$ GeV. The corresponding information including 85 data is not yet available for UA1, but the percentage of such events (using data up to 84) is 38% and 28% for UA1 and UA2 respectively.

3.4 W mass determination

To determine the W mass value, both experiments define a transverse mass $m_T^2 = 2P_T^e P_T^\nu (1 - \cos\Delta\phi)$ with $m_T \leq m_W$ and $\Delta\phi = (\vec{P}_T^e, \vec{P}_T^\nu)$.

A Monte Carlo generate different m_T distributions for various m_W values. The W−mass is then determined by a maximum of likelihood.

The advantage of this is that unlike P_T^e and P_T^ν, m_T is rather insensitive to the transverse momentum of the W.

From UA1 one gets only very a preliminary experimental m_T spectrum shown in figure 10 without any adjustement. UA2 gives the transverse mass distribution in figure 10b including 85 data as a preliminary result.

The results for the time being are

UA1 $m_W = 83.5^{+1.1}_{-1.0} \pm 2.7$ GeV/c² (without 85 data)
UA2 $m_W = 80.3 \pm 0.8 \pm 1.3$ GeV/c² (preliminary including all data)

(The systematic errors reflect the uncertainty on the absolute energy scale of the calorimeters). A fit to the m_T distribution with the W width Γ_W as a free parameter provides a way to get an upper limit on Γ_W.

(The following figures are not revised with 85 data) :

UA1 $\Gamma_W < 0.5$ GeV/c²
UA2 $\Gamma_W < 7$ GeV/c² (90% C.L.)

3.5 Z mass determination

The m_{ee} distribution given in figure 5 is adjusted in high−mass regions by a maximum likelihood fit of a Breit−Wigner folded with the experimental mass resolution.

a. From UA1 there are no new fit available for the time being, the result including the 1984 data is :

$$M_Z = 93.0 \pm 1.4 \pm 3.0 \text{ GeV/c}^2$$

In figure 11a the m_{ee} distribution in the Z^0 region from the 1985 data is given as a preliminary result. It includes 17 new $Z^0 \to e^+e^-$ events.

b. From UA2 a new analysis including 85 data is available, the corresponding m_{ee} distribution in the Z^0 region is given in figure 11b. It contains 30 $Z^0 \to e^+e^-$ events (with $m_{ee} > 70$ GeV/c^2) including 14 new events from the 1985 data.

As a preliminary result, the measured mass is

$$M_Z = 91.5 \pm 0.9 \pm 1.5 \text{ GeV/c}^2$$

3.6 The Z width and the number of neutrino species

In the frame work of the Standard Model, the value of the Z width is related to the number of fermion doublets for which the decay $Z \to f\bar{f}$ is kinematically allowed.

This point of view was carried out by the two experiments [8] and allowed to put an upper limit on ΔN_ν the number of new neutrino species. No new analysis has been done yet with the 1985 data in both experiments. I just recall the relevant conclusions.

With 90% of confidence level this upper limit is $\Delta N_\nu < 7$ from UA1 and $\Delta N_\nu < 2.6$ (± 1.7) from UA2 (here the quoted error reflects the theoritical uncertainties).

3.7 Comparison with the standard model

To compare the results about the W and Z mass with the Standard Model predictions one uses the weak mixing angle defined as [9]

$$\sin^2\theta_W = 1 - (m_W/m_Z)^2 \qquad (1)$$

This leads to

$$M_W = A^2/[(1-\Delta r)\sin^2\theta_W] \qquad (2)$$

$$M_Z = 4A^2/[(1-\Delta r)\sin^2 2\theta_W] \qquad (3)$$

where $A = \sqrt{(\pi\alpha/\sqrt{2}\,G_F)} = 37.2810 \pm 0.0003)$ GeV/c^2 and Δr is the one-loop radiative corrections computed to be [9] $\Delta r = 0.0696 \pm 0.0020$ for a top quark mass $m_t = 36$ GeV/c^2 and assuming the mass of the Higgs boson equal to the Z mass.

From (2) and (3) and using the W mass and the Z mass, one determines $\sin^2\theta_W$:

UA1 $\sin^2\theta_W = 0.214^{+.004}_{-.005} \pm 0.015$ (4) (the 1985 data not included)

UA2 $\sin^2\theta_W = 0.232 \pm 0.004 \pm 0.008$ (5) (preliminary result including the 1985 data).

The quoted errors are respectively statistical and systematical. These last ones are mainly due to uncertainties on mass scale from uncertainties on calorimeter calibrations.

As a comparison these results agree well with an average of the low energy data

$$\sin^2\theta_W = 0.220 \pm 0.008 \qquad [10]$$

A very recent result [11] published by the CDHS experiment

$$\sin^2\theta_W = 0.227 \pm 0.005 \pm 0.003 \pm 0.013\ (m_c - 1.5\ \mathrm{GeV}/c^2) \qquad (6)$$

is also in a very good agreement with the previous figures (the very last uncertainty here reflects the contribution of the quark−c mass in this determination).

As it was shown elsewhere [12] the need for the radiative corrections in the Standard Model from the two results (4) and (5) cannot be proved for the time being. But, as it is underlined in the Ref. [11], without radiative corrections result (6) and results (4) and (5) are in very poor agreement.

By using (1) one assumes that the ρ parameter defined as $\rho = m_W^2/m_Z^2 \cos\theta^2_W$ (7), is equal to 1.

To test this, equations (2) and (7) are combined to get :

$$\rho = m_W^2/[m_Z^2(1 - B^2/m_W^2)]$$

where $B^2 = A^2/(1-\Delta r)$.

The results are :

$$\text{UA1}\ \rho = 1.028 \pm 0.037 \pm 0.019$$
$$\text{UA2}\ \rho = 0.996 \pm 0.033 \pm 0.009$$

This two results agree with each other and with the low energy average value

$$\rho = 1.02 \pm 0.02 \qquad [9]$$

All these figures are compatible with $\rho = 1$. which corresponds to the minimal Standard Model with only one Higgs boson (one isodoublet of complex Higgs fields).

4. RESULTS OF PHYSICS WITH MUONS

All these results are from the UA1 experiment where muons can be detected.

4.1 Inclusive muon spectrum and W mass

The analysis requires an high $-p_T$ isolated track in the muon detector ($P_T^{\mu} > 15$ GeV/c) and a large missing transverse momentum ($E_T^{\nu} > 15$ GeV). This gives a sample of 82 events including the 1985 data. The P_T^{μ} distribution is shown in figure 12 where it is compared with the spectrum expected from $W \to \mu\nu$ decay for $m_W = 83$ GeV/c^2.

From this one calculates the partial cross $-$ section for W production followed by $W \to \mu\nu$ decay which turns out to be compatible with the $\mu - e$ universality. The results are summarized in the following table [13].

Table III

Cross $-$ sections for $W^{\pm} \to \mu^{\pm}\nu$

$\sqrt{s}$ (GeV)	Theory (nbarn)	$\sigma.B(W \to \mu\nu)$1983	(nbarn)1984
546	0.39 ± 0.10	$0.56 \pm 0.18 \pm 0.12$	
630	0.47 ± 0.10		$0.61 \pm 0.11 \pm 0.12$
Ratio	1.20	1.09 ± 0.40	

W mass determination from the μ sample. From the 1984 data, after tight cuts in the central detector and μ chambers, the UA1 experiment uses the 22 remaining events to get :

$$m_W = 81.6 \pm {}^{4.6}_{4.5} \pm {}^{9.0}_{8.1}$$

in quite good agreement with the W mass values determined from the inclusive electron analysis ($W \to e\nu$ decay). The corresponding transverse distribution is shown in figure 13, the curve is an expectation from $m_W = 83$ GeV/c^2.

4.2 Dimuon production

The following analysis does not include the 1985 data.

The figure 14 shows the $m_{\mu\mu}$ distribution with $P_T^{\mu} > 3$ GeV/c and $m_{\mu\mu} > 6$ GeV/c^2. On can notice a rapidly falling continuum for the low mass values which is well separated from events with masses around 90 GeV/c^2, the Z^0 mass region.

4.2.1 $Z^0 \rightarrow \mu^+\mu^-$

The selection criteria are $P_T^{\mu} > 15$ GeV/c for the first track and the event must containt a second minimum ionising track with $P_T > 15$ GeV/c. Including the 1985 data, this leaves 20 events (5 at $\sqrt{s} = 546$ GeV, and 15 (6+9 in 1985) at $\sqrt{s} = 630$ GeV) with invariant masses greater than 60 GeV/c^2.

A best fit of a Breit−Wigner gives : $m_W = 88.8^{5.5}_{4.6}$ GeV/c^2 (excluding the 1985 data for the time being).

From the 1984 data UA1 gives a partial cross section for $Z^0 \rightarrow \mu^+\mu^-$

$$\sigma B(Z^0 \rightarrow \mu^+\mu^-) = 63 \pm 26 \pm 12 \text{ pb}$$

This agrees with the theoretical prediction based on the $\mu - e$ universality [6,13].

4.2.2 Low mass dimuons

No new analysis including the 1985 data is available for the time being so I recall briefly the results already mentionned elsewhere [14].

In the sample containing dimuons with $P_T^{\mu} > 3$ GeV/c and $m_{\mu\mu} > 6$ GeV/c^2 (figure 14) there are 212 events with $m_{\mu\mu}$ lower than 60 GeV/c^2, namely 150 $\mu^+\mu^-$ and 62 $\mu^+\mu^+$ or $\mu^-\mu^-$ pairs.

Each of these two categories is splitted into isolated and non−isolated pairs according an isolation criteria defined as following :

Around the vector momentum of each muon, a cone having half−aperture $R = \sqrt{(\Delta\eta^2 + \Delta\phi^2)} = 0.7$ is constructed.

The total transverse energy ΣE_T carried by all other particles in this cone is measured. For each dimuon event the isolation parameter S is defined as

$$S = [\Sigma E_T^1]^2 + [\Sigma E_T^2]^2$$

where the two cones are taken into account.

Most of muons from $W \rightarrow \mu\nu$ or $Z \rightarrow \mu^+\mu^-$ decays satisfy the condition $\Sigma E_T < 3$ GeV. So $S < 9$ GeV^2 is choosed to defined the class of isolated dimuons, and remaining dimuons belong to the non−isolated dimuon class.

The figure 15 shows the S distribution of the dimuons events.

In the figure 15a there are 44 dimuons events with opposite sign peaking below $S = 9$, whilst the corresponding distribution in figure 15b for the same sign dimuons is flat. In fact one has :

$$\text{dimuons with opposite sign } 150 = 44(S < 9) + 106(S > 9)$$

dimuons with same sign 62 = 7(S < 9) + 55(S > 9)

1. Muon pairs with opposite sign are expected from three main sources :

   i. The decay of the upsilon $\Upsilon \rightarrow \mu^+\mu^-$. This accounts for 9.7 ± 3.3 isolated dimuons.

   ii. The Drell−Yan process $\bar{p}p \rightarrow \gamma^* \rightarrow \mu^+\mu^-$ is estimated to 20.4 ± 5.2 isolated dimuons.

   iii. QCD production of pairs of heavy quarks ($b\bar{b}$, $c\bar{c}$) followed by semi−leptonic decays ($b \rightarrow c\mu\nu$) of both quarks. This contributes for both isolated and non−isolated dimuons. A flat distribution in S is expected for this last source as one can check in figure 15a after substraction of the two first contributions.

2. Muon pairs with same sign.
   The first possible source is the production of $b\bar{b}$ pairs where $\mu^-(\mu^+)$ is produced from a semileptonic decay of the $b(\bar{b})$ quark and the other $\mu^-(\mu^+)$ is produced from a semileptonic decay of the $\bar{c}(c)$ quark which results from the hadronic decay of the $\bar{b}(b)$ quark. For example $b \rightarrow c\mu^-\bar{\nu}$ and $\bar{b} \rightarrow \bar{c} \rightarrow \bar{s}\mu^-\bar{\nu}$

An other possible interesting source is the $B^0-\bar{B}^0$ oscillation (The B^0 is a neutral meson containing a $\bar{b}$−quark). In this case for example a μ^- is produced from a b quark whilst the other quark $\bar{b}$ first fragments into a $\bar{B}^0$ meson which turns into B^0 meson state (analog to $K^0-\bar{K}^0$ transition) and produces a μ^- again. Obviously $\mu^+\mu^-$ pair is produced following the same scheme starting from a $\bar{b}$ direct decay and a b which first fragments into B^0.

These two sources give both isolated and non−isolated same sign dimuons. This is reflected by the flatness of the S−distribution in figure 15b.

The published measure related to the low mass dimuons is the ratio :

$$R = [N(\mu^+\mu^+) + N(\mu^-\mu^-)]/N(\mu^+\mu^-)$$

calculated from the non isolated pairs only, R = 0.45 ± 0.10. This corresponds to a lower limit R > 0.30 with 90% of confidence level.

The estimation of the last contribution, $B^0-\bar{B}^0$, depends strongly on the used Monte−Carlo Model (EUROJET).

So the UA1 experiment needs a lot of tests to prove the real contribution of this source in the previous R value.

5. ISOLATED PHOTONS [15]

The isolated photons are mainly analysed by the UA2 experiment taking advantage of a good granularity for the calorimeter and of the apex determination for electromagnetic showers in the preshower part in front of the calorimeter.

The main contributions are estimated from the following graphs.

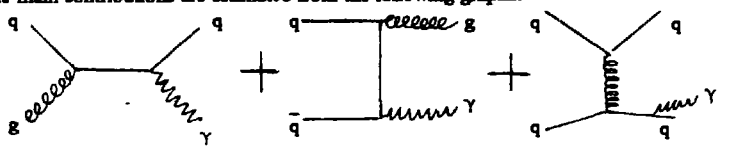

Compton 50% annihilation 25% bremstrahlong 25%

The inclusive spectrum of the transverse momentum of γ's is shown on figure 16. This distribution is compared with the theoretical second order QCD prediction [16]. The main relevant conclusions are about the ratio γ/jet and the ratio γ/π^0.

Concerning the ratio γ/jet, a complete lowest order calculation [17,18] predicts $\sigma(\gamma)/\sigma(\text{jet}) = 4.2\ 10^{-4}$ for 30 GeV < P_T^γ < 50 GeV. In this range, the ratio of the measured direct photon cross-section to the measured jet cross-section is

$$\sigma_\gamma/\sigma_{jet} = 2.9 \pm 0.9 \pm 1.2(\text{syst.})\ 10^{-4}$$

in good agreement with the theoretical estimation.

The ratio $\sigma(\gamma)/\sigma(\pi^0)$ of the single photon cross-section to the inclusive π^0 one increases from 0.06 at P_T = 15 GeV/c to 0.25 at P_T = 35 GeV/c.

A crude comparison with the ISR results for this ratio gives $<\gamma/\pi^0>_{p\bar{p}} \simeq 0.1$ and $<\gamma/\pi^0>_{ISR} \simeq 0.05$.

In fact one has to be very careful about this factor of two. The mean value of x_T for both experiment is different $<x_T>_\gamma^{p\bar{p}} \simeq 0.5 <x_T>_\gamma^{ISR}$, and scaling violations for both the structure functions $F(x,Q^2)$ and the fragmentation functions $D(z,Q^2)$ have to be taken into account.

CONCLUSION (present and future)

In this talk clearly some points developped in previous reports such as unexplained events or even top quark search have disappeared. At present time, with a large increase in the statistics, one accepts the idea that large statistical fluctuations in standard physics could account for those peculiar events. Concerning the top search in the UA2 experiment the present apparatus does not allow extracting significant signal from the background despite the rejection factor reached ($\simeq 10^6$). In the UA1 experiment, after 3 electrons candidats and 3 muons candidats published in 1983 and 6 electrons candidats in 1984 (no muon analysis published in 1984), one does not get more confirmation up to now. In fact to account for observed $e\nu$ + two jets production (which is believed a way to reach the top quark from $W \to bt$, with $t \to be\nu$, and $b(\bar{b}) \to$ jets) the UA1 experiment needs an important QCD $t\bar{t}$ production which weaks a lot the whole analysis. Moreover all this needs a counter part with μ production. In 1985, the micro-vertex did not work so at present time one has to wait for ACOL.

The future with ACOL

The two experiments renamed UA1' and UA2' expect working with a luminosity $\mathcal{L} \leq 4\ 10^{30}\ cm^{-2}\ s^{-1}$ which corresponds, over three data taking periods, to a total luminosity of $\int \mathcal{L} dt \simeq 10\ pb^{-1}$ in each experiment. With such a luminosity, the field of physics would be

1. $W \to e\nu$ and $Z \to ee$ with respectively 4000 decays and 400 decays.

2. Top search

3. $W \to$ jet + jet

4. Search for Susy particles (from $Z \to ee$, determination of $\tilde{m}_q, \tilde{m}_\gamma, \ldots$).

For each items the foreseen problems and competitions are :

1. The Z mass M_Z will be measured within ± 50 MeV at SLC moreover one needs the best calorimeter calibration (better than 1% is a challenge), and at Fermilab the total available energy is $\sqrt{s} = 1.6$ TeV that means a factor of three in the W cross section production (but along with this, the two jet cross-section is increased by a factor of ten, so this will need a better rejection factor against the background in fact.).

2. If the top mass is $30\ GeV/c^2 < m_T < 50\ GeV/c^2$, one predicts a low ratio for the decay $W \to tb$ (30 - 60 events/exp.) and moreover it will be a clear competition with Fermilab.

3. Concerning the W decay into two jets, the granularity of calorimeters mainly in UA2' prevents competition at first glance but it turns out to be very difficult anyway.

4. Concerning the discovery of SUSY particles, Fermilab with a total energy $\sqrt{s}$ = 1.6 TeV, is clearly in better position in principle.

ACKNOWLEDGEMENTS

I am grateful to M.N. Minard, S.J. Wimpenny and P. Ghez from the UA1 experiment for their help in preparing this report. It a pleasure for me to thank the Organisation Committee of the Kazimierz Conference mainly J.A. Zakrzewski for his invitation, the Scientific Secretary Z. Ajduk for his efficient help and all our collegues for their warm welcome in Poland.

References

[1] UA2 collaboration, P. Bagnaia et al., Z. Phys. C – Particles and Fields 24 (1984) 1.

[2] See for example G. Altarelli, proceedings of the International Europhysics Conference on High–Energy Physics, BARI, Italy, July 1985, p. 729.

[3] J.C. Collins and D.E. Soper, Nucl. Phys. B193 (1981) 381; B194 (1982) 4445; B197 (1982) 446.

[4] M. Jacob, Nuovo Cimento 9 (1958) 826.

[5] G. Arnison et al. Nuovo Cimento Lett. 44 (1985) 1.

[6] E. Eichten et al. Rev. Mod. Phys. 56 (1984) 579.

[7] G. Altarelli et al., Nucl. Phys. B246 (1984) 12;
G. Altarelli, R.K. Ellis and G. Martinelli, Z. Phys. C27 (1985) 617.

[8] See for example, L. DiLella, Proceedings of the International Europhysics Conference on High–Energy Physics, BARI, Italy, July 1985, p. 761.

[9] W.J. Marciano and A. Sirlin, Phys. Rev. D29 (1984) 945.

[10] W.J. Marciano and A. Sirlin, Nucl. Phys. B189 (1981) 442.

[11] H. Habramowicz et al., CERN–EP/86–33, March 1986, submitted to Phys. Rev. Letters.

[12] For example, UA2 Collaboration, J.A. Appel et al., Z. Phys. C30 (1986) 1–22.

[13] S. Wimpenny, XXI_{th} Rencontre de Moriond – Les Arcs, France, March 1986.

[14] See for example, E. Radermacher, Proceedings of the International Europhysics Conference, BARI, Italy, July 1985.

[15] UA2 Collaboration, CERN–EP/86–64, submitted to Phys. Letters.

[16] P. Aurenche et R. Baier, Private Communication.

[17] D.W. Duke and J.F. Owens, Phys. Rev. D30 (1984) 49.

[18] R. Baier et al., Z. Phys. C2 (1979) 265.

Figure Captions

1. Scatter plots of transverse momenta P_T^e versus P_T^ν (events with $P_T^e < 15$ GeV/c).

2. P_T^ν distributions from the scatter plots in Fig. 1.

3. From UA2, inclusive spectrum P_T^e (preliminary).

4. Resulting P_T^e distributions after final cuts.

5. Invariant mass distributions m_{ee}, for events with two electrons.

6. From UA1, the $\cos\vartheta^*$ distribution for the electron in $W \to e\nu$.

7. The $\cos\theta^*$ distribution in UA2 (without charge signature).

8. From UA1, fractional momentum distributions
   a) for u quark
   b) for d quark.

9. Transverse momentum distribution of W, P_T^W
   a) from UA1
   b) from UA2.

10. Transverse mass distribution m_T of the W ($W \rightarrow e\nu$)
    a) from UA1 (very preliminary)
    b) from UA2.

11. Invariant mass distribution m_{ee} in the Z^0 region
    a) from UA1
    b) from UA2.

12. From UA1, the P_T^μ distribution of the muon transverse momentum in the decay $W \rightarrow \mu\nu$.

13. Transverse mass distribution of the W ($W \rightarrow \mu\nu$).

14. Invariant mass distribution of the two muons observed in UA1.

15. "S – distribution" for the dimuon events
    a) opposite sign dimuons
    b) same sign dimuons.

16. From UA2, the inclusive spectrum of the photon transverse momentum (isolated photon events), P_T^γ at $\sqrt{s} = 630$ GeV and rapidity $\eta \simeq 0$.

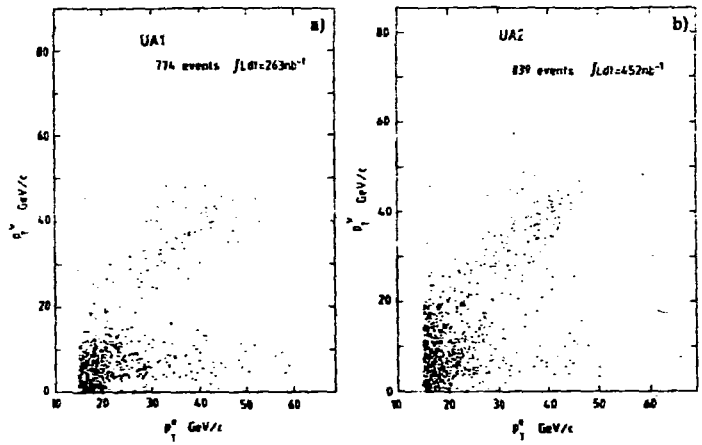

Fig. 1

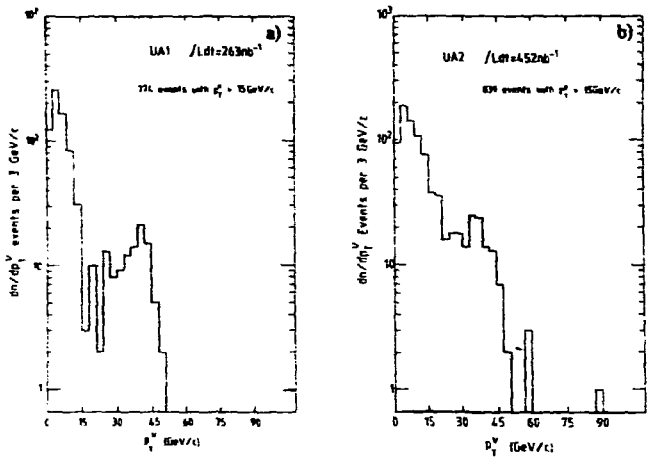

Fig. 2

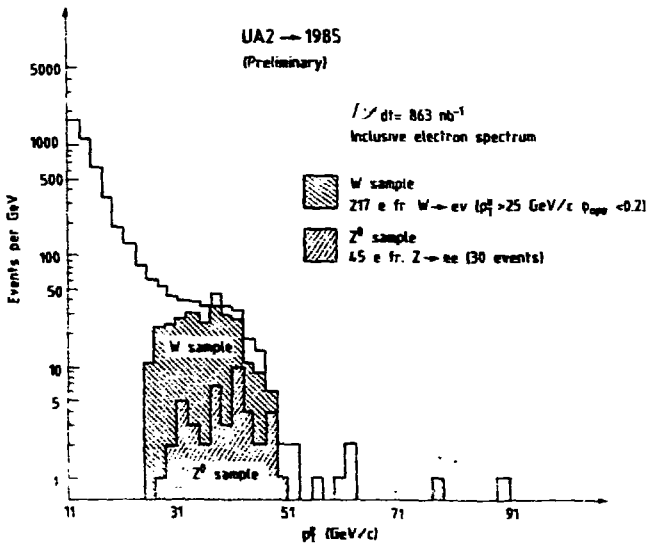

Fig. 3

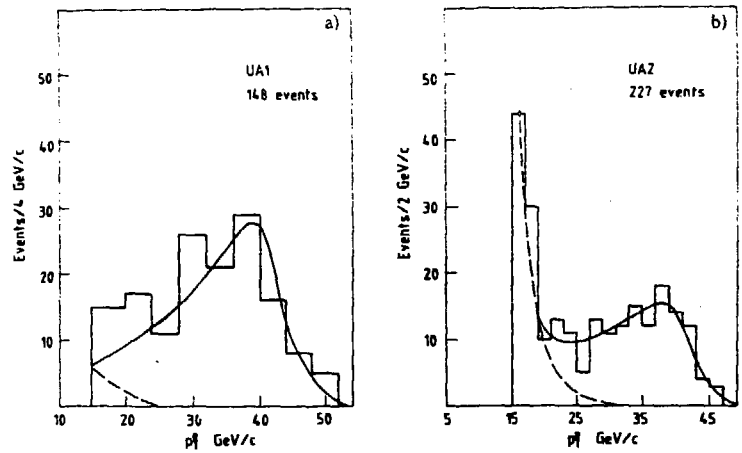
a)
UA1
148 events
Events/4 GeV/c
p⊥ GeV/c
b)
UA2
227 events
Events/2 GeV/c
p⊥ GeV/c

Fig. 4

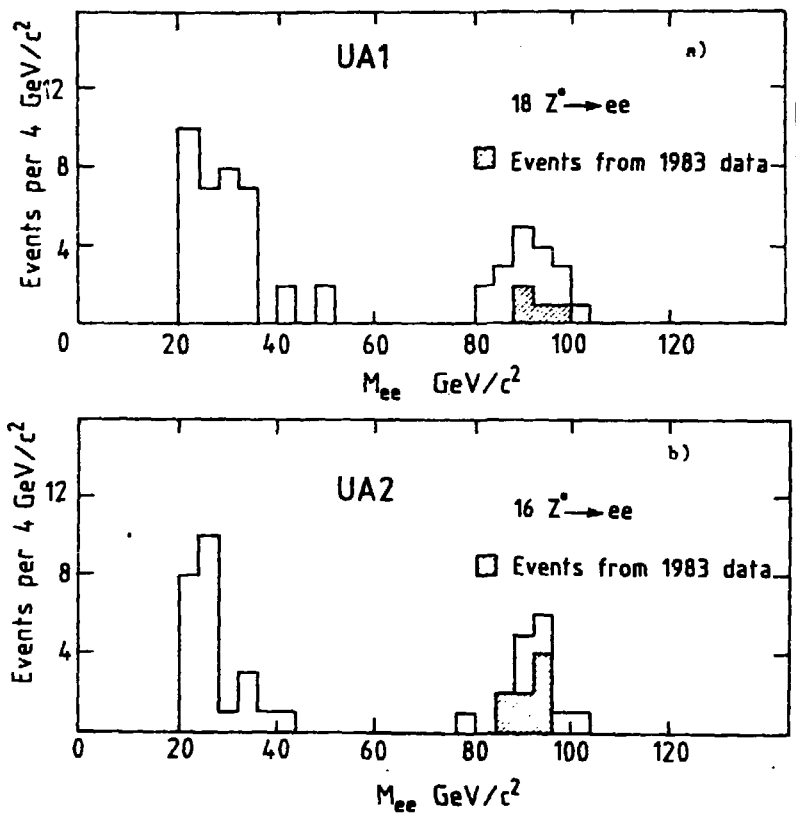
UA1
a)
18 Z°→ee
Events from 1983 data
Events per 4 GeV/c²
M_ee GeV/c²
UA2
b)
16 Z°→ee
Events from 1983 data
Events per 4 GeV/c²
M_ee GeV/c²

Fig. 5

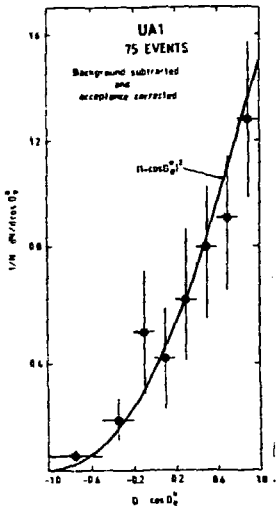

Fig. 6

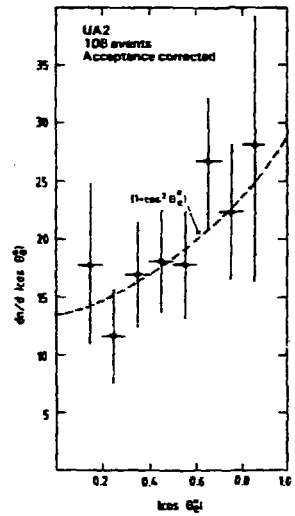

Fig. 7

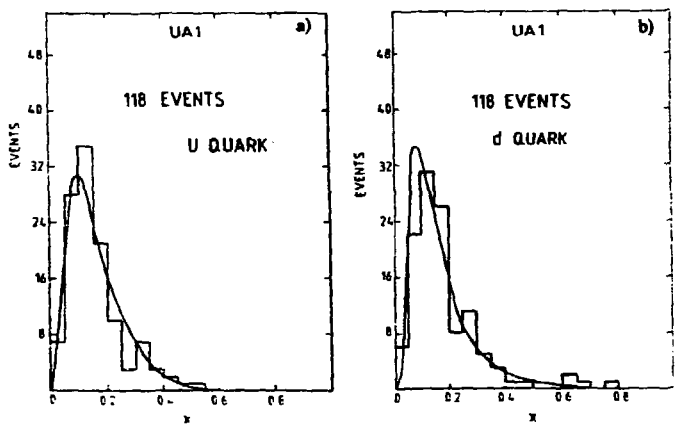

Fig. 8

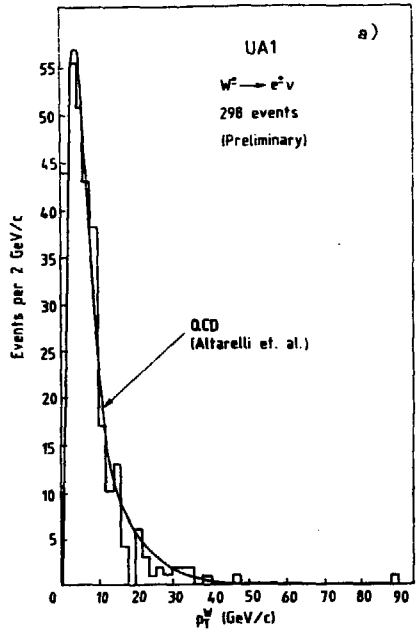
a)
UA1
$W^{\pm} \rightarrow e^{\pm}\nu$
298 events
(Preliminary)
QCD
(Altarelli et. al.)
Events per 2 GeV/c
p_T^W (GeV/c)

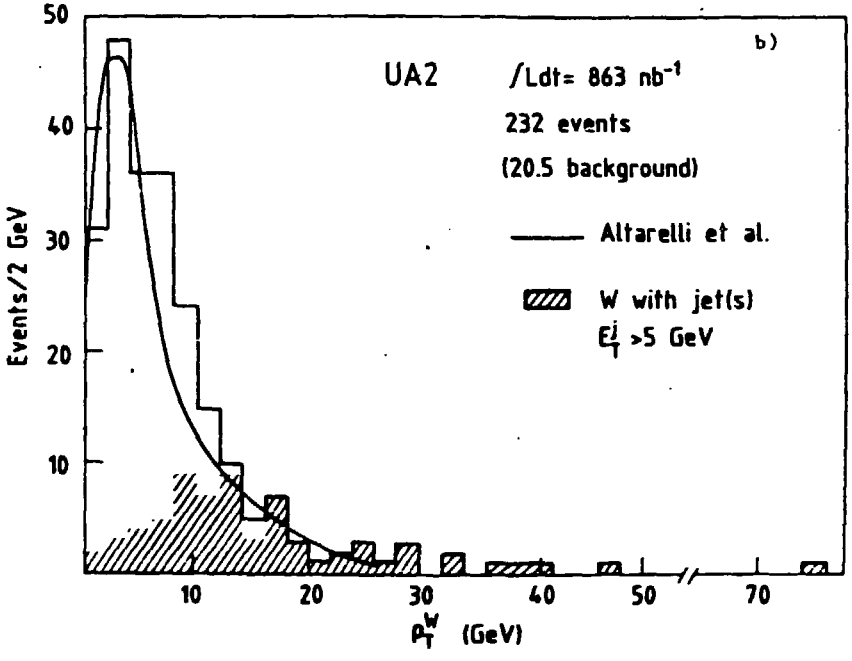
b)
UA2
/Ldt= 863 nb^{-1}
232 events
(20.5 background)
Altarelli et al.
W with jet(s)
E_T^j >5 GeV
Events/2 GeV
p_T^W (GeV)

Fig. 9

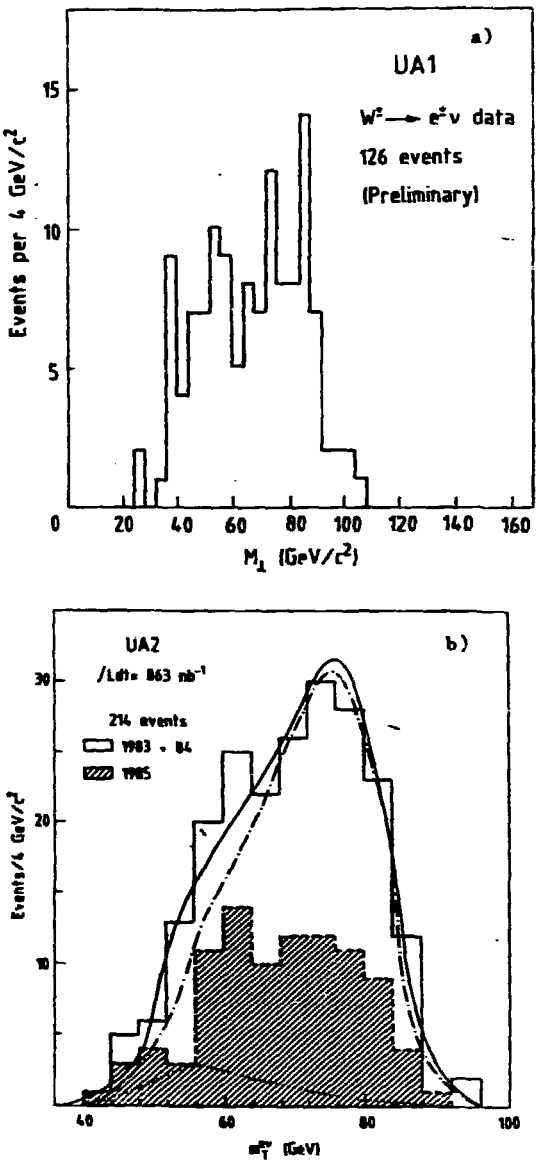
a)
UA1
W± → e±ν data
126 events
(Preliminary)
Events per 4 GeV/c²
M_T (GeV/c²)
b)
UA2
214 events
1983 + 84
1985
Events/4 GeV/c²
(GeV)

Fig. 10

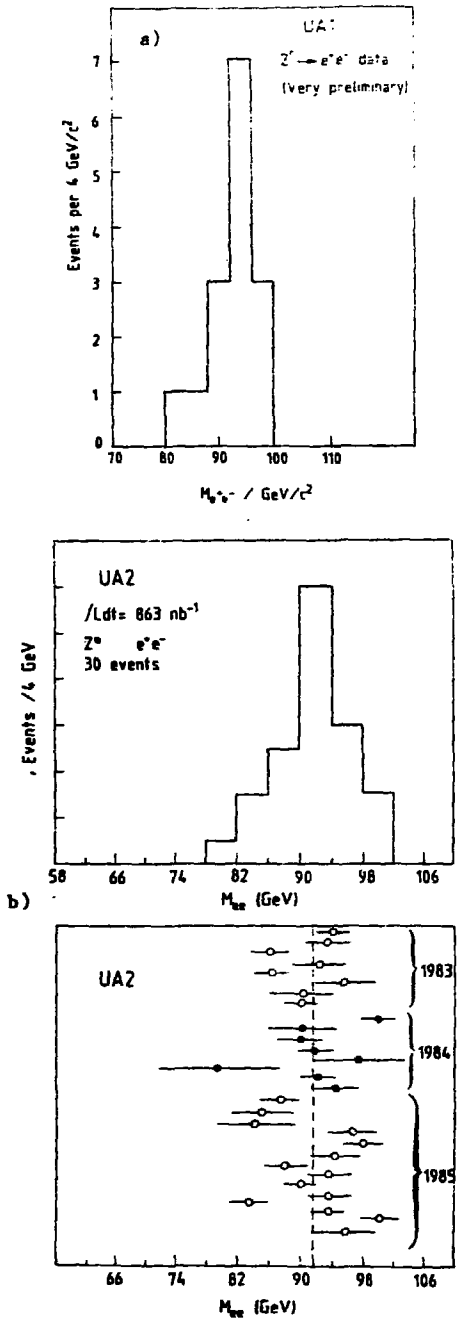
a)
UA1
Z' → e⁺e⁻ data
(very preliminary)
Events per 4 GeV/c²
M e⁺e⁻ / GeV/c²
b)
UA2
/Ldt= 863 nb⁻¹
Z° e⁺e⁻
30 events
Events /4 GeV
M ee (GeV)
UA2
1983
1984
1985
M ee (GeV)

Fig. 11

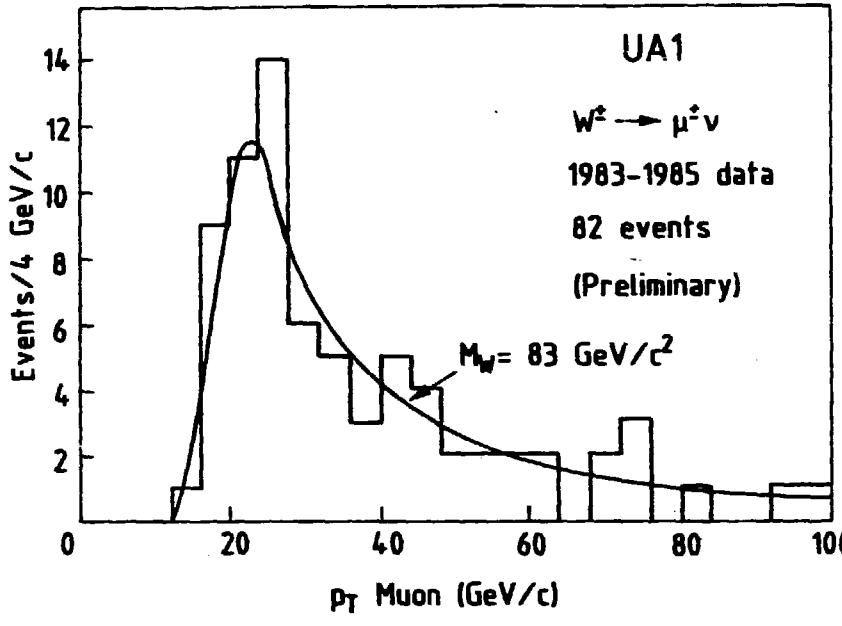
UA1
W± → μ±ν
1983-1985 data
82 events
(Preliminary)
M_W = 83 GeV/c²
Events/4 GeV/c
p_T Muon (GeV/c)
0
20
40
60
80
100
2
4
6
8
10
12
14

Fig. 12

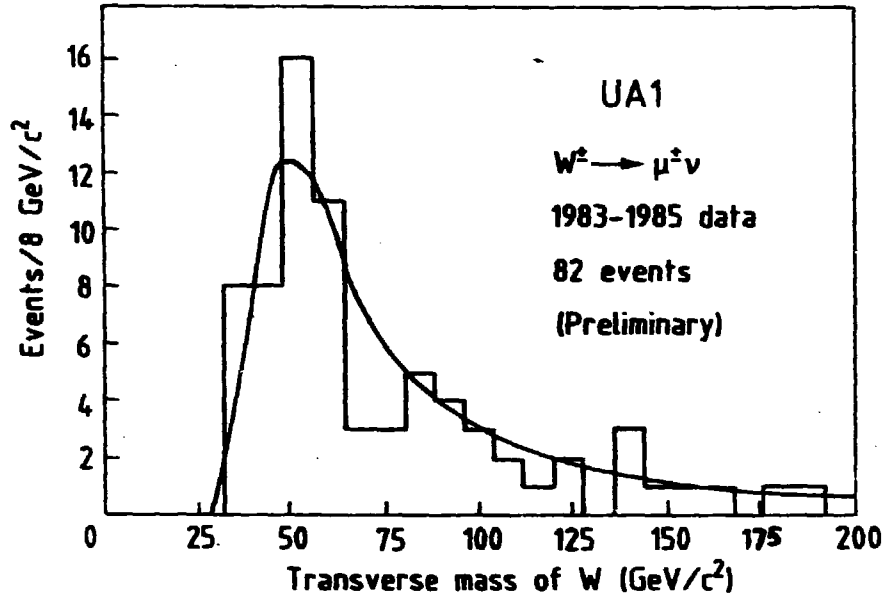
UA1
W± → μ±ν
1983-1985 data
82 events
(Preliminary)
Events/8 GeV/c²
Transverse mass of W (GeV/c²)
0
25
50
75
100
125
150
175
200
2
4
6
8
10
12
14
16

Fig. 13

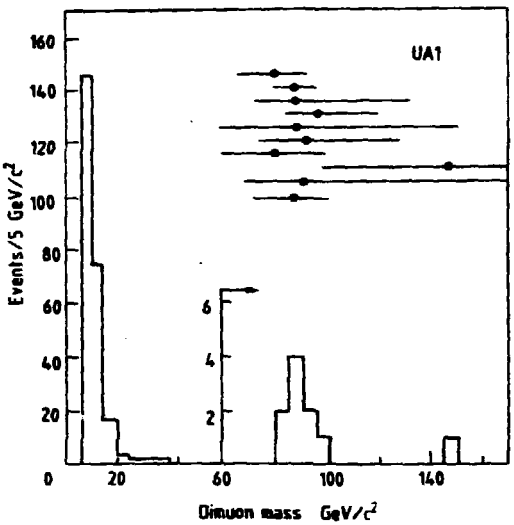

Fig. 14

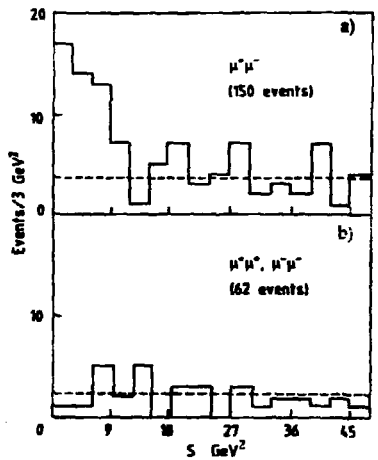

Fig. 15

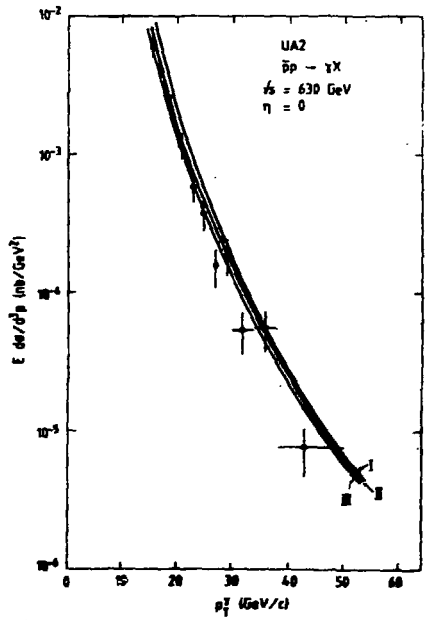

Fig. 16

A STUDY OF MULTI-JET EVENTS AT THE CERN $\bar{p}p$ COLLIDER

The UA2 Collaboration

Bern – CERN – Copenhagen (NBI) – Heidelberg – Orsay(LAL) – Pavia – Perugia – Pisa – Saclay (CEN) Collaboration

presented by H. Hänni
CERN
Geneva, Switzerland

ABSTRACT

Within the UA2 collaboration a study has been made of events containing three hard jets in the final state. The angular distributions of the three jets show evidence for gluon bremsstrahlung, in good agreement with a QCD model to leading order in the strong coupling constant α_s. The yield of three-jet events relative to that of two-jet events provides a measure of the strong coupling constant : $\alpha_s K_3/K_2 = 0.23 \pm 0.01 \pm 0.04$, where K_2 and K_3 represent the contributions arising from higher order corrections in α_s to the two- and three-jet exclusive cross-sections. A preliminary study has also been performed on events containing four jets in the final state. The observed features of these events agree well with a recent leading order QCD calculation, indicating a strong deviation from phase space behavior. These results are not consistent with the presence of a large contribution from multi-parton scattering, in which more than one hard scattering takes place among the nucleon constituents.

1. Introduction

Since its start in 1981 the CERN $\bar{p}p$ Collider has proven to be an excellent laboratory to produce and examine hard collisons between partons (quarks and gluons). These collisions have been extensively studied and their properties have been successfully compared with the predictions of perturbative quantum chromodynamics (QCD). This is made possible by the presence of hadron jets which can be isolated from the other collision products and identified with the outgoing partons. In particular, most features of two-jet final states are well described by the leading term in the perturbative expansion of the parton-parton cross-section in powers of the strong coupling constant α_s. In the present report the studies are extended to three-jet and four-jet final states which are proportional to higher powers of α_s. We discuss the observation [1,2] of such states and present a detailed study [3] of their measured properties.

The study is divided into two areas of investigation: First, we examine the three-jet events and – in order to test the underlying dynamics – compare several distributions with those obtained from Monte Carlo calculations based on a QCD model or on pure phase space. These comparisons confirm the qualitative features expected of QCD, in particular, a Rutherford-like angular dependence for the scattering angle of the leading jet and a bremsstrahlung spectrum for the energy and angle of the softest jet. This agreement encourages us to perform more quantitative tests of QCD. To do so, we measure the cross-section for the production of three-jet events relative to that for two-jet events. This ratio provides a measurement of the strong coupling constant α_s, in the sense that it yields a numerical value for the expression $\alpha_s K_3/K_2$, where K_2 and K_3 represent the contributions arising from higher order corrections in α_s to the two- and three-jet exclusive cross-sections.

Second, we present a preliminary study of four-jet events. Again, the features of these events are compared with a QCD model and with phase space with the goal of testing perturbative QCD to order α_s^4. The event shapes are found to agree well with the QCD model, and a measurement of α_s, using the ratio of the four-jet cross–section to the three-jet cross-section, is in progress. In additon, several authors have predicted a second mechanism for producing four-jet events, in which more than one hard parton scattering takes place in a single collision [4]. A simple model for this so-called multi-parton mechanism has been used to search for the presence of such events. The preliminary conclusion is that the observed

events are consistent with leading order QCD, and there is no evidence for the multi−parton process in the current data sample.

2. The Data

The data for the present study have been obtained using the UA2 central calorimeter [5] which covers the pseudo-rapidity region $-1 \leq \eta \leq +1$ over the whole azimuthal range. Its granularity (240 cells, each covering 15° in azimuth and 10° in polar angle) is well matched to the jet structure of hard collision final states at Collider energies. The trigger is obtained from a coincidence between a minimum bias signal, ensuring the occurrence of a non-diffractive $\bar{p}p$ collision, and the requirement that ΣE_T, the total transverse energy measured in the 240 calorimeter cells, exceeds 60 GeV. The data were collected at $\sqrt{s}$ = 630 GeV and correspond to a total integrated luminosity of 310 nb^{-1} from 1984 and an additional luminosity of 440 nb^{-1} from 1985.

In each event, energy clusters are constructed using a refined algorithm optimized for the study of multi-jet final states [3]. We have studied the angular resolving power associated with this refined algorithm by superimposing jets obtained from two different two-jet events. The fraction of such events for which the clustering algorithm finds two clusters is a measure of the resolving power. It is found to have a distribution with an approximately energy−independent cut-off at 30° ± 10° (Figure 1).

Once the clusters have been defined, we proceed to select a sample of events which arise primarily from hard scattering processes. This topic has been studied previously by UA2 in an analysis of the emergence of the hard scattering contribution to two-jet final states [6]. This analysis was based on a simple two component model for hadron collisions. The soft component is characterized by a fairly uniform distribution of energy among a large number of low energy clusters, and dominates at low total transverse energy. The hard component consists of two high transverse energy jets accompanied by an underlying event of low transverse energy secondaries, and dominates at high total transverse energy. The results of this study are summarized in Figure 2, which shows the inclusive cross-section and the fraction of hard scattering events as a function of two transverse energy variables: the total transverse energy (ΣE_T) and the leading jet transverse energy ($\hat{E}_T = E_T^1 + E_T^2$). This figure suggests that the contamination from the soft component decreases much more rapidly if we require a large transverse energy in the leading jets ($\hat{E}_T$).

In each event, the clusters are sorted in order of decreasing transverse energy and labeled 1, 2, 3, etc. In addition, we calculate the transverse momentum P_T of the jet system as the vector sum of the transverse momenta of the leading clusters. The events are then required to satisfy the follwing conditons:

$$E_T^1 + E_T^2 + ... + E_T^n > 70 \text{ GeV}, \quad (1a)$$

$$E_T^i > 10 \text{ GeV}, \quad E_T^{n+1} < 10 \text{ GeV}, \quad (1b)$$

$$|\eta_i| < 0.80, \quad i = 1...n. \quad (1c)$$

$$P_T < 20 \text{ GeV} \quad (1d)$$

The first condition ensures that the configuration of the leading jets is unbiased by the trigger threshold, and reduces the contamination from the soft collisions discussed above. The second condition retains events in which the leading clusters are likely to be associated with the hard collision rather than with spectator fragments. The third condition defines a fiducial volume in which the jet energy measurements are reliable. The fourth condition eliminates events with large missing momentum. Using these criteria, we define the two, three, and four jet samples which will be used in the subsequent analysis.

3. The QCD Model

The present study relies on comparisons between experimental distributions associated with the multi-jet sample and the corresponding QCD predictions. It is therefore useful to describe the QCD model and its implementation in a Monte Carlo simulation.

To leading order in α_s, the cross-section for producing n final state partons with a total invariant mass $\sqrt{\hat{s}}$ is expressed in terms of elementary subprocesses in which two incident partons, i and j, carrying fractions x_i and x_j of their nucleon parent momentum, interact :

$$\sigma_n^{LO} = ([\alpha_s]^n/\hat{s}) \int \Sigma_{ij} F_i(x_i) F_j(x_j) Q_n^{ij} \Phi_n (dx_i/x_i) (dx_j/x_j) \quad (2)$$

where Φ_n is the n-body phase-space factor and $x_i x_j s = \hat{s}$.

Explicit expressions for the contribution Q_n^{ij} of each elementary subprocess are available in the literature for n = 2 [7], n = 3 [8], and n = 4 [9]. In Equation (2), they are weighted according to the structure functions $F_i(x)$ which describe the parton content of the incident nucleons.

As a result of the bremsstrahlung nature of the gluon radiation spectrum, Q_n^{ij} diverges when the mass of any two partons, one from the final state and one from either the initial or final state, approaches zero. These divergences are cancelled by non-leading contributions to the topological cross-sections. Since we are working with leading order calculations, we will only consider final states in which the initial and final state partons are well separated in phase-space.

We implement this requirement in our model by defining cut-offs to ensure that the parton configuration in the final state is free of these divergences : we only consider partons having a transverse momentum in excess of 8 GeV and parton pairs having a separation in excess of 20°. With these cut-offs, the ratio K_n between the topological cross-section σ_n and its leading order approximation σ_n^{LO} can, in principle, be computed, although the necessary calculations have not yet been performed. Lacking a precise calculation of K_n we shall have to compare the multi-jet data to expressions proportional to $K_n \alpha_s^n$, which means that the ratio of cross-sections is sensitive to the quantity $\alpha_s K_3/K_2$, instead of simply α_s.

The quark and antiquark structure functions, $Q(x)$ and $\bar{Q}(x)$, are taken from low q^2 neutrino data [10] evolved to the q^2-range of the present experiment. The gluon structure function is taken to be

$$G(x) = F(x)/K - 4/9\,[Q(x) + \bar{Q}(x)] \qquad (3)$$

where $F(x)$ is the effective structure function obtained from the two-jet data of the UA2 experiment [11]. In this evaluation, we assume that the inclusive K-factor takes the value $K = 2$. In addition, both the structure functions and the strong coupling constant α_s are functions of q^2. We choose to identify $\sqrt{q^2}$ with the largest transverse momentum among the final state partons.

In order to convert the final state partons of Equation (2) into observable hadrons, we use a fragmentation method based on the Field-Feynman algorithm [12], modified to reproduce the cluster radius distribution observed in the present experiment [1]. We have checked that this method of fragmentation, when used in conjunction with the clustering algorithm described previously, produces extra clusters in less than 2% of the events for cluster transverse energies in excess of 15 GeV. This empirically demonstrates that in our model the radiation of hard partons can be separated from the soft fragmentation process, and ensures that the jets in the final state arise from the hard-scattering matrix element and not from the fragmentation model.

The acceptance of the UA2 detector and the details of the energy response of the central calorimeter are simulated in a Monte Carlo program which reproduces the experimental details of relevance [1]. The underlying event, associated with spectator particles, is simulated by superimposing actual minimum bias events onto the jets produced by the hard collision.

4. The Three – Jet Sample and a Comparison with the QCD Model

In this section we study the event configurations for a three-jet sample selected from the 1984 data sample of 310 nb^{-1} according to criteria (1). After boosting to the center of mass of the jet system, the leading jets are arranged in order of decreasing p_i^*. The three-jet system can be described in terms of six variables, three defining the orientation of the plane containing the three-jet system in space, and three defining the configuration of the jets within this plane. In order to emphasize those features peculiar to QCD, the distributions of several variables will be compared with the predictions of the model described in the previous section, as well as with a phase space model obtained by setting the Q_n^{ij} in Equation (2) equal to one.

We first examine the distribution of $\cos\theta^*$, the angle of the scattering plane relative to the beam direction. This distribution, normalized to one at $\cos\theta^* = 0$ and corrected for the limited UA2 acceptance, is shown in Figure 3. The figure also contains the corrected distribution for two-jet events [11]. The shapes are very similar, and are characteristic of vector gluon exchange. The curve in Figure 3 shows the parton level calculation of the cross-section for the $gg \rightarrow ggg$ sub-process, computed using Equation (2) and the transverse momentum and angular separation cut-offs described in the preceding section. The curves for the other sub-processes are not significantly different, and the overall agreement with QCD is very good.

We next discuss the internal configuration of the three-jet system, independent of its orientation. The qualitative features can be seen in a Dalitz plot, constructed by defining scaled variables using the two-body masses m_{ij} :

$$x_{ij} = m_{ij}^2 / \hat{s} \qquad (4)$$

Figure 4 shows the distribution of x_{12} versus x_{23}. If the events were distributed according to a phase space density, the population would be uniform across the plot (ignoring acceptance effects). Instead, there is an increased density in the region of small x_{23} (corresponding to final state bremsstrahlung of a soft third jet) compared to that of large x_{23} (corresponding to equal sharing of energy among the three jets). The absence of events near $x_{12} = 1$ and $x_{23} = 0$ is a result of the event selection criteria (1) and of the two-jet angular resolving power. The projections of the Dalitz plot are also shown. They are compared with the QCD model (solid histogram) and the phase space model (dashed curve). The QCD model agrees well with the data, and there is a large excess of events above the phase space curve in the region of small x_{23}.

In the preceding analysis we used selection criteria which allowed us to display the dominant features of the three-jet data sample. In particular, loose cuts were used on the jet transverse momenta and on the opening angle of jet pairs (Figure 1) to study the effect of bremsstrahlung. In this way, we have shown that the QCD model gives a good description of the shapes of the three-jet distributions. We now pursue a more quantitative comparison with the QCD model. To this end, we measure the quantity $\alpha_s K_3/K_2$ by adjusting α_s in the QCD model until the theoretical value of the ratio between the three-jet cross-section and the two-jet cross-section (R_{QCD}) is equal to its experimental value, R_{exp}.

There are several sources of systematic error associated with this measurement which can be reduced by applying stricter event selection criteria. We want to avoid those regions of phase space where either two of the partons are separated by a small angle, or one of the partons is soft. For this reason, we redefine the two-jet and three-jet data samples using two additional criteria :

i. the standard clustering algorithm is followed by an additional step in which secondary cluster pairs, having an opening angle smaller than 50° and a transverse energy in excess of 5 GeV, are merged into a single cluster (Figure 1).

ii. the 10 GeV threshold used in (1b) is replaced by a 15 GeV threshold to further reduce the contamination from spectator particles.

The new selection criteria retain 14635 two-jet and 2596 three-jet events. The experimental value R_{exp} is simply calculated as the ratio between these two numbers. This procedure gives a value $R_{exp} = 0.177 \pm 0.004$.

The selection criteria applied to the data samples are also applied to the Monte Carlo event samples. The value of R_{QCD} is then the ratio between two cross-sections, σ_3^{QCD} and σ_2^{QCD}. Due to the limited acceptance and resolving power of the UA2 detector, some n-jet final states will be observed as m-jet events, m < n. This requires us to include in σ_3^{QCD} both events from σ_3^{LO} and from σ_4^{LO} which have three and only three jets obeying the selection criteria. Similarly, σ_2^{QCD} contains events generated from σ_2^{LO} and σ_3^{LO} which have two and only two jets obeying the selection criteria. At the time of this analysis, the full QCD calculation of σ_4^{LO} was not yet complete. An approximate estimate of σ_4^{LO} was obtained by taking Equation (2) for n = 3, and adding the bremsstrahlung of a single gluon. The estimate was then normalized to the total number of observed four-jet events. The relative contributions to σ_3^{QCD} from σ_4^{LO} and to σ_2^{QCD} from σ_3^{LO} are respectively 21% and 16%. Higher order contributions, such as from σ_5^{LO} to σ_3^{QCD} and from σ_4^{LO} to σ_2^{QCD} are ignored.

By varying α_s in the QCD model, we find that the value of the strong coupling constant that makes R_{QCD} equal to R_{exp} is

$$\alpha_s K_3/K_2 = 0.23 \pm 0.01. \qquad (5a)$$

The effects of the dependence of α_s on q^2 are displayed in Figure 5, which shows the values of $\alpha_s K_3/K_2$ in different bins of the multi-jet mass M. The q^2-range covered by the data sample is from ~600 to 10,000 GeV^2, with the average q^2~1700 GeV^2. The curve in Figure 5, obtained by computing α_s for an average q^2 calculated for each mass bin in the figure, shows the expected ±7% variation of α_s over this mass range. The data are in agreement with the curve, but show no significant deviation from a constant value.

Several sources of systematic uncertainties affect our evaluation of the strong coupling constant. We now consider each of these in turn and evaluate their contributions to the error on $\alpha_s K_3/K_2$.

i. Fragmentation effects: In the high energy range of the present experiment, there is virtually no ambiguity in distinguishing between two-jet and three-jet configurations. Instead, the main consequence of using different fragmentation functions is to modify the fraction of the original parton energy which is collected in the corresponding calorimeter cluster. This affects the three-jet sample, which often contains a relatively soft third jet, more than the two-jet sample. Changes in the fragmentation model produce variations of α_s which do not exceed $(\Delta\alpha_s/\alpha_s) \simeq \pm$ 10%.

ii. Underlying event: The spectator scattering contribution is simulated by superimposing a minimum bias event onto each generated hard collision. However, we know [1] that the value of $\hat{E}_T$ is, on average, twice as high for hard collisions as for minimum bias events. Part of the difference can be accounted for by particles directly associated with the hard collision. Nevertheless, we have studied the effect of doubling the transverse energy carried by the underlying event. From this study we evaluate an uncerteinty on α_s, $(\Delta\alpha_s/\alpha_s) = \pm 10\%$.

iii. Structure functions: Uncertainties in the structure functions may affect the α_s measurement to the extent that the quark to gluon ratio may be modified. Because of the higher colour charge of gluons, a relative increase of the gluon content results in a larger value of R_{QCD}, and consequently in a lower value of α_s. Changes in the quark to gluon ratio result in an uncertainty $(\Delta\alpha_s/\alpha_s) = \pm 7\%$.

iv. Higher order contributions: The contribution to R_{QCD} from σ_4^{LO} is important, of the order of 21%. As mentioned earlier, σ_4^{LO} was computed without the benefit of the full QCD calculation. We estimate an uncertainty of $\pm$ 40% on the absolute scale of σ_4^{LO} which appears in the α_s measurement as an error $(\Delta\alpha_s/\alpha_s) = \pm 8\%$.

v. Energy response: Uncertainties in the energy response of the UA2 central calorimeter partially cancel since they affect both the two-jet and the three-jet samples. They introduce an uncertainty on the α_s measurement of $(\Delta\alpha_s/\alpha_s) = \pm 3\%$.

vi. Event selection: The measurement of α_s should not depend on the criteria used to select the jet samples, as long as these selection criteria are compatible with the cut-offs used in the QCD model. After varying the selection, we infer an upper limit $(\Delta\alpha_s/\alpha_s) < 4\%$ on the uncertainty resulting from this source.

After this summary of the individual uncertainties, we can compute the total systematic error. Some effects are accounted for in several of the systematic uncertainties described above. We conservatively ignore this double counting and retain as a global systematic uncertainty the number obtained by adding all individual contributions, i) to vi), in quadrature. The result is

$$\alpha_s\, K_3/K_2 = 0.23 \pm 0.01 \pm 0.04 \qquad (5b)$$

where the second error represents the systematic uncertainty.

Finally, we note that our choice of q^2 in the scaling violation factors is somewhat arbitrary. A different choice of q^2 will not affect α_s, but only modifies the QCD scale Λ, as long as the two-jet and three-jet samples are treated equally. However, it is possible to choose q^2 definitions which alter the average q^2 of the two-jet sample with respect to that of the three-jet sample. We have considered a concrete example by replacing our choice, $\sqrt{q^2} = \text{Max}\,(p_T^i)$, by $\sqrt{q^2} = \langle p_T^i \rangle$, thereby reducing the three-jet $\langle q^2 \rangle$ with respect to the two-jet $\langle q^2 \rangle$. The result is to increase only the value of α_s that appears in the calculation of σ_3^{LO}, typically by 8%, and hence to increase the value of R_{QCD}. As a consequence, the measured value of α_s K_3/K_2 decreases by 25%.

5. A Study of Four-Jet Events

In this section, we describe an analysis of four-jet events selected from a combined data sample of 750 nb^{-1}. The selection is made according to criteria (1), with an additional step in the clustering algorithm in which secondary clusters with an opening angle smaller than 30° are merged into a single cluster. This reduces the sensitivity to fragmentation effects while still retaining good angular resolution, and results in a sample of 2219 events. A typical high ΣE_T event from this sample is shown in Figure 6, with four clearly resolved jets in the final state. If we apply the stricter cuts, used in the previous section for the α_s measurement, we arrive at a much smaller sample of 255 events.

For this analysis, we again boost to the center of mass of the jet system and arrange the jets in order of decreasing p_i^*. The four jet system can be described in terms of nine variables: three describing the orientation of the jet system and six describing the internal configuration of the jets. This large number of variables make the description of this final state rather complex. The jets do not lie in a plane, nor can they be described by simple Dalitz plots. A natural set of variables are the six x_{ij} defined in Equation (4), or equivalently the space angles between the jets in the center of mass, $\cos \omega_{ij}^*$. Only five of these variables are independent – the sixth degree of freedom corresponds to the total mass of the jet system.

As for the three-jet analysis, comparisons will be made between the data, a parton level QCD model based on recent calculations by Kunszt and Sterling [9], and a phase space model obtained by setting Q_n^{ij}

in Equation (2) equal to one. At this preliminary stage of the analysis, we will only study the shapes of the distributions – questions of normalization will be avoided by setting the area of the distributions to one.

To examine the qualitative features of the events, we first look at the sphericity calculated from the jet momenta in the center of mass. The distribution is shown in Figure 7, and it is apparent that the observed event shape agrees well with the QCD model, and is significantly less spherical than phase space. A more detailed understanding of the features of four-jet events can be obtained by examining the space angles defined previously. Figure 8 shows the distribution of $\cos \omega_{23}^{*}$. The data shows a significant enhancement above the phase space model in the region of small angular separation, indicating the presence of bremsstrahlung. This enhancement agrees very well with the QCD model. A similar, less dramatic, enhancement can also be observed in the distribution of $\cos \omega_{14}^{*}$.

Several authors have predicted an additional source of four-jet events [4]. This is the multi-parton mechanism, in which multiple hard parton collisions take place in a single hadron collision. This mechanism, which is suppressed by extra powers of $\hat{s}$, becomes important for small values of the parton momentum fraction, where the density of partons in the nucleon becomes very large. The simplest form of this process, in which two independent pairs of partons interact, can be described as follows:

$$\sigma_{mp} \sim \int G(x_1,x_2)\, G(x_3,x_4)\, d\hat{\sigma}_{12}\, d\hat{\sigma}_{34} \qquad (6)$$

where the G are double structure functions and the $d\hat{\sigma}$ are the cross-sections for the two parton sub-processes. In order to search for evidence of multi-parton interactions, we have constructed a simple model in which the double structure functions take the form:

$$G(x_1,x_2) \sim F(x_1)\, F(x_2) \qquad (7)$$

We simulate the effects of soft gluon radiation from the initial state partons by giving each jet-jet system a Gaussian P_T kick. The magnitude of this kick has been adjusted to agree with the measured two-jet data [11]. Using this model, one can then look for deviations from the leading order QCD prediction, choosing variables which should be sensitive to a multi-parton contribution.

The most characteristic feature of multi-parton events should be the appearance of pair-wise correlations among the jets. To search for these correlations, we choose to look at transverse variables in the lab frame, since they are relatively insensitive to center of mass motion. A simple variable of this kind is the difference between the azimuthal angle of the leading jet, and the azimuthal angles of the other jets in the event. This variable, called ϕ_{lead}, is sensitive to the presence of a second jet opposite to the leading jet. The distribution of this variable, with three entries per event, is shown in Figure 9a. The data agree well with the QCD model, and show no sign of the narrow peak that is expected for the multi-parton process. An alternate variable is the P_T unbalance in the event, defined by the expression:

$$P_T\,(\mathrm{unb})^2 = 2 \min\,(\vec{P}_T^{\,1} + \vec{P}_T^{\,i})^2 \qquad (8)$$

where i is chosen to minimize the unbalanced P_T. This variable should take on small values for the multi-parton process since there will be a second jet balancing the P_T of the leading jet. The observed distribution is shown in Figure 9b, and agrees well with the QCD model. Again, there is no sign of the enhancement expected at small P_T unbalance from the multi-parton mechanism.

A slightly more sophisticated approach involves finding the pairing of the four jets which minimizes the P_T sum for pairs of jets:

$$\min\,(|\vec{P}_T^{\,i} + \vec{P}_T^{\,j}| + |\vec{P}_T^{\,k} + \vec{P}_T^{\,l}|) \qquad (9)$$

Once the jets have been paired, it is possible to calculate the difference in azimuthal angle between the jets in each pair. The resulting distributions are shown in Figure 10, where $\phi(1)$ is always the difference for the higher E_T pair. The pairing process itself introduces some correlations, but there is no evidence for the narrow peak expected in $\phi(2)$ from the multi-parton interaction. Once again, the observed events are consistent with the leading order QCD calculation.

Two preliminary conclusions emerge from this discussion. The first is that the observed four-jet distributions agree well with a leading order QCD calculation, and differ significantly from four-body phase space. The second is that there is no evidence for the additional contribution from the higher twist multi-parton processes. These studies of four-jet events are being extended to include a more quantitative test of the QCD model using the ratio of the four-jet to three-jet cross-sections, as well as an attempt to find multi-parton interactions at lower ΣE_T.

REFERENCES

1. UA2, P. Bagnaia et al., Z. Phys. **C20** (1983) 117.

2. UA1, G. Arnison et al., Phys. Lett. **158B** (1985) 494.

3. UA2, J. A. Appel et al., Z. Phys. **C30** (1986) 341.

4. N. Paver and D. Treleani, Nuovo Cimento **70A** (1982) 215 ;
   B. Humpert, Phys. Lett. **131B** (1983) 461 ;
   N. Paver and D. Treleani, Phys. Lett. **146B** (1984) 252 ;
   B. Humpert and R. Odorico, Phys. Lett. **154B** (1985) 211 ;
   U. Amettler, N. Paver and D. Treleani, Trieste preprint IC/85/118 (1985).

5. A. Beer et al., Nucl. Instr. Meth. **224** (1984) 360.

6. UA2, J. A. Appel et al., Phys. Lett. **165B** (1985) 441 ;
   V. Vercesi, Proceedings of this conference.

7. B.L. Combridge, L. Kripfganz and J. Ranft, Phys. Lett. **70B** (1977) 234;
   R. Cutler and D. Sivers, Phys. Rev. **D17** (1978) 196.

8. Z. Kunszt and E. Pietarinen, Nucl. Phys. **B164** (1980) 45 ;
   T. Gottschalk and D. Sivers, Phys. Rev. **D21** (1980) 102 ;
   F.A. Berends et al., Phys. Lett. **118B** (1981) 124.

9. Z. Kunszt and W. J. Sterling, Four Jet Production at Hadron Colliders, CERN – TH 4351/86 (1986), and references contained therein.

10. CDHS, H. Abramowicz et al., Z. Phys. **C12** (1982) 289, **C13** (1982) 199, **C17** (1983) 283, and private communication from F. Eisele. We have studied the effect of using other structure functions, and found that our conclusions were insensitive to this choice after evolution to the q^2-range of the present experiment. See e.g. CHARM, F. Bergsma et al., Phys. Lett. **153B** (1985) 111.

11. UA2, P. Bagnaia et al., Phys. Lett. **144B** (1984) 283.

12. R.D. Field and R.P. Feynman, Nucl. Phys. **B136** (1978) 1.

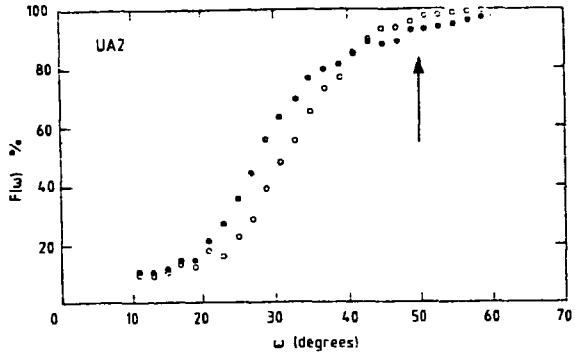

Figure 1

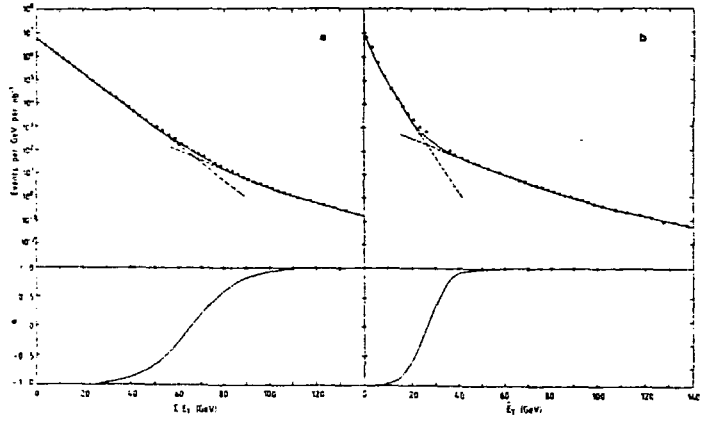

Figure 2

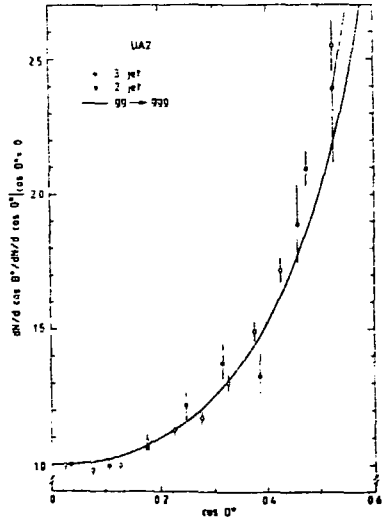

Figure 3

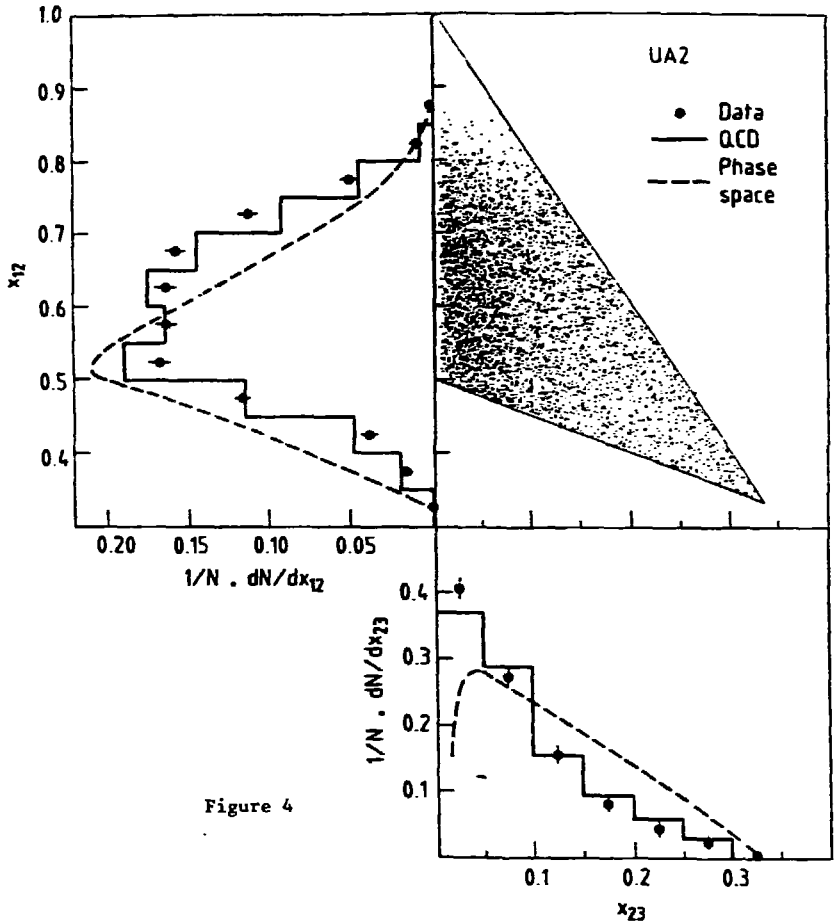

Figure 4

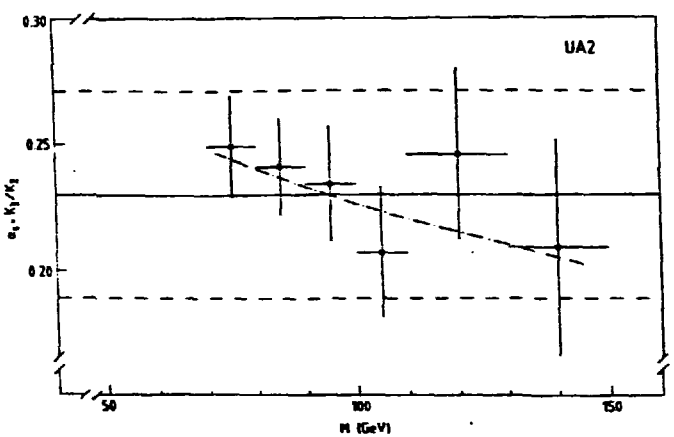

Figure 5

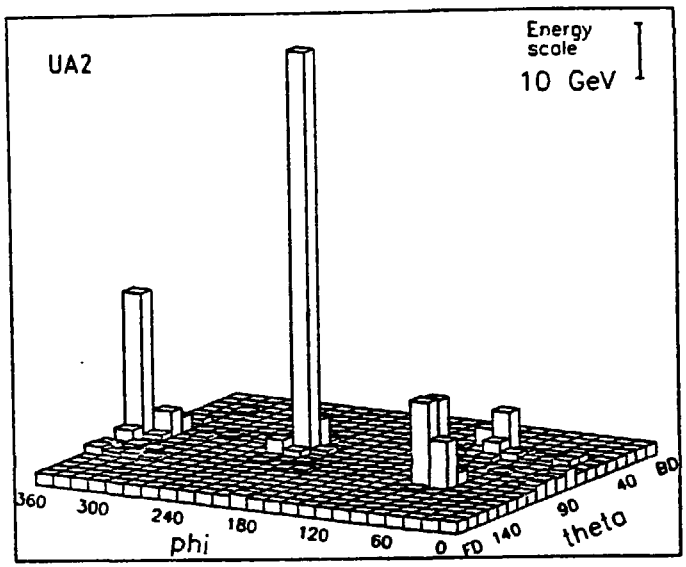

Figure 6

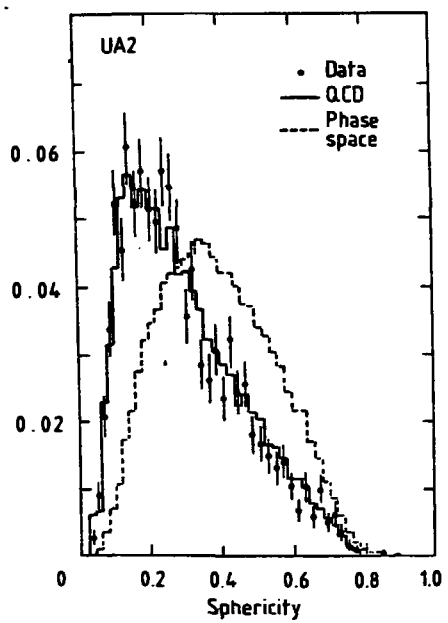

Figure 7

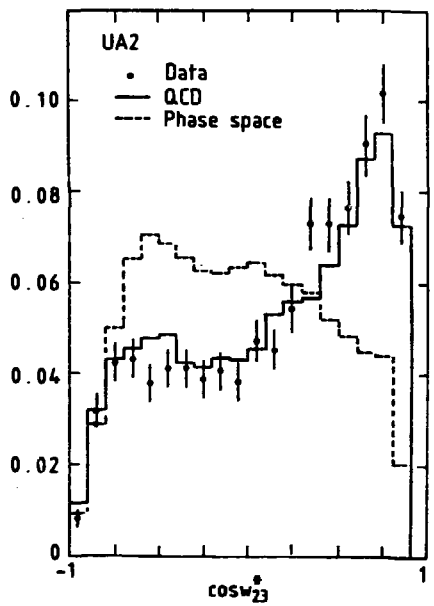

Figure 8

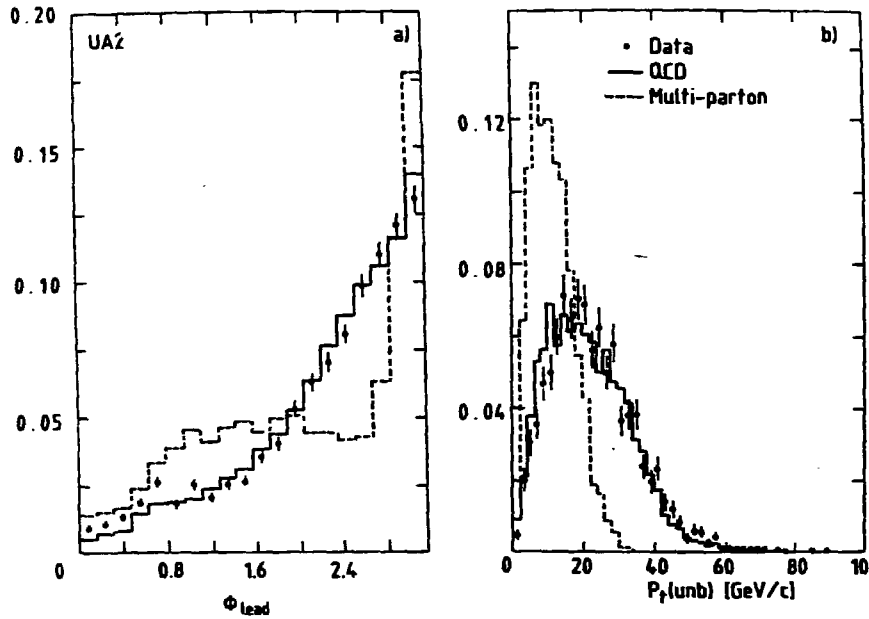

Figure 9

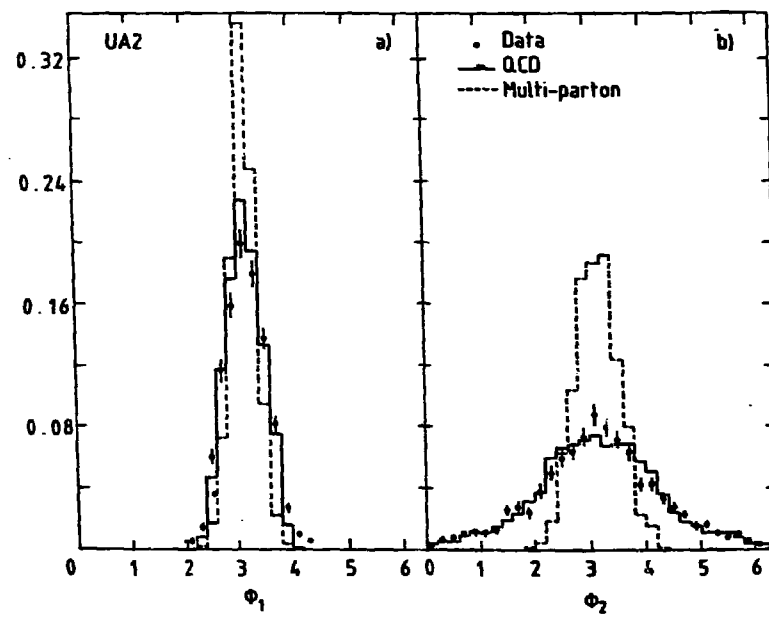

Figure 10

FRAGMENTATION OF JETS IN UA1

UA1 COLLABORATION
Aachen-Amsterdam(NIKHEF)-Annecy(LAPP)-Birmingham-CERN-
Harvard-Helsinki-Kiel-Queen Mary College,London-Padua-
Paris(Coll.de France)-Riverside-Rome-Rutherford Appleton Lab.-
Saclay(CEN)-Victoria-Vienna-Wisconsin Collaboration-

presented by Philippe GHEZ
L.A.P.P., Annecy-Le-Vieux,France

ABSTRACT

We present the final results [1] of an analysis of jet fragmentation using two-jet events recorded by UA1 at the CERN $p\bar{p}$ Collider. The fragmentation of collider jets is shown to be softer than the fragmentation of jets obtained at lower energies. We also describe a method to statistically separate quark and gluon jets. Using this method, we show evidences for a different fragmentation between quark and gluon jets. This difference is in good agreement with fragmentation models based on QCD.

INTRODUCTION

The extensive production of events containing jets [2] has been one of the dominant features of the physics at the CERN SPS $p\bar{p}$ Collider. In such a context the UA1 experiment has recorded a large amount of events with high transverse momentum (p_T) jets. Most of these jets are gluon jets therefore the first part of the analysis will be the study of the fragmentation properties of high p_T gluon jets. With the help of the very large acceptance of the UA1 detector we have also recorded jets at large pseudo rapidity (η). In this case, jets are more preferentially quark jets and the second part of the analysis will show the differences of fragmentation between quark and gluon jets.

The data are coming from a run period in 1983 at $\sqrt{s} = 546$ GeV with an integrated luminosity of 118 nb^{-1}. Jets are selected by a single jet hardware trigger with three different thresholds (15,20,25 GeV/c) on the jet p_T [3]. The offline selections require a clean two-jet topology where one of the two jets at least is in a good region of acceptance both for the calorimeters (jet energy/momentum measurement) and for the central detector (charged track momentum measurement). We avoid most of the trigger biases by using in the analysis only those jets which were not responsible of the hardware trigger ("away jets"). Finally, if a third jet is present in the event, the event is accepted only if this third jet does not affect the 2-body kinematics calculations. It implies that it is a low p_T, well separated third jet.
At the end of this selection, 10.007 jets remain for the analysis.

INCLUSIVE JET RESULTS

Figure 1 shows the fragmentation function :

$$D(Z) = \frac{1}{N_{jet}} \frac{dN_{ch}}{dZ} \quad \text{with} \quad Z = \frac{P_{\ell}(\text{track})}{P(\text{jet})}$$

of all the accepted jets (statistical errors only).
This result is obtained after the application of several corrections on the jet or the charged tracks :

- the background tracks are removed,
- the geometrical regions of inefficiencies are taken into account,
- the jet energy/momentum is corrected,
- the smearing of the distribution due to measurement errors is corrected.

Finally, this correction procedure was checked using a full simulation of Monte-Carlo events [4] and found to be satisfactory.
Figure 1 also compares our results to the fragmentation function of lower p_T jets obtained in e^+e^- collisions [5] and pp collisions [6]. A significantly softer fragmentation function is observed for collider jets compared to lower energy jets.
Figure 2 shows our data including statistical and systematic errors. Also a comparison to a recent model of jet fragmentation [7] including QCD evolution of parton showers and Lund string hodronization, is performed. The agreement between model and data is satisfactory.

The correlation between the longitudinal and the transverse momentum of the fragments (with respect to the jet axis) is shown on Figure 3. This correlation is still visible ("seagull effect") in the case of collider jets. Also we observe an averall increase of $\langle p_t \rangle$ at collider energy compared to e^+e^- jets [5] and ISR data [6]. For example, for $Z > 0.1$, one obtains an average value $\langle p_t \rangle$ of :

$$\langle p_t \rangle = 0.85 \pm 0.02 \text{ (stat.)} \pm 0.08 \text{ (sys.)}$$

which is two times larger than one would have obtained with lower-energy jets.

The jet charged multiplicity N_{ch} is obtained by integrating over $D(Z)$. But in the low Z region ($Z < 0.05$) the background contamination is so important that the fraction of multiplicity contained at low Z has been evaluated by the following method :
We assume that the rapidity distribution (w.r.t. the jet axis) shows a plateau and we extrapolate this plateau at low rapidity ($Z = 0$). The result, where the charged multiplicity is studied in function of the two-jet mass, is given below :

m_{jj} (GeV)	N_{ch}
60 - 80	12.2 ± 0.2
80 - 100	12.0 ± 0.5
100 - 120	12.1 ± 1.0
120 - 160	12.4 ± 1.2

This result is in good agreement with the one obtained by the UA2 Collaboration [8].

To summarize this inclusive analysis, we will say that the overall behaviour of Collider jets compared to lower-energy data is :

- a softer longitudinal fragmentation together with an increase of the internal transverse momentum,
- a larger charged multiplicity.

These features are compatible both with a change in the nature of the parton initiating the jet (gluon at the collider, quark at lower energy) and with a change in the energy scale (higher energy at the collider compared to Patra/ISR data). Therefore we need to analyse separately the two contributions.

FRAGMENTATION OF QUARK AND GLUON JETS

In order to statistically separate quark and gluon jets, we exploit the differences existing between gluon and quark structure functions ; since we have selected clean two-jet events, we can calculate all the relevant kinematical quantities of the two-parton scattering process and particularly :

- $x_1(x_2)$ the $p(\bar{p})$ momentum fraction carried by the incoming partons,
- $\hat{s}$ the c.m.s. energy squared,
- θ^* the c.m.s. scattering angle.

One sub-process cross section is proportionnal to :

$$F_a(x_1,Q^2) \times F_b(x_2,Q^2) \times M^2(\hat{s},\theta^*)$$

where F are the structure functions and M^2 is the relevant QCD metrix element. By normalizing each sub-process cross section to the total jet cross section and by summing the relevant sub-processes, one can obtain the probability for each jet to be a gluon (or a quark). Having defined Q^2 and limited the Q^2 variations (Q^2 = 1600 - 2600 GeV^2) we have split our sample in a "quark" and a "gluon" enriched sub sample where the mean probability for a jet to ba a gluon was known and constant. We have then measured the fragmentation properties of jets of each sub sample and extracted the fragmentation properties of "pure" quark and gluon jets.

Figure 4 shows the ratio of the fragmentation function of gluon and quark jets. The prediction of [7] is also plotted. The quark jet have a harder fragmentation than the gluon jets and this difference looks in good agreement with the model.

A same kind of study does not show within the errors, any difference between the internal transverse momentum of quark and gluon jets. The distribution of charged tracks $[(1/N_{jet})(1/\Delta R)(dN_{ch}/d\Delta R)]$ as a function of $\Delta R = \sqrt{[\phi(jet) - \phi(track)]^2 + [\eta(jet) - (\eta(track)]^2}$ around the jet axis is shown on Figure 5 for quark and gluon jets. This distribution, measuring the opening of the jet, shows a difference between quark and gluon jets : gluon jets are wider than quark jets. This effect compensates the difference in the fragmentation functions and then the internal transverse momentum is approximatively identical for quark and gluon jets.

The method used to separate quark and gluon jets can be extended to separate u and $\bar{u}$ quark flavours. Using several possible definitions of the jet charge (see [9]), we have measured the average charge of jets enriched in gluon, u and $\bar{u}$ quarks. Within errors, all tested definitions give the same numerical values ; for example, with $Q(jet) = \sum_I Q_i \, Z_i^{1/3}$, where i runs over all associated charged tracks, one gets :

sample	<Q(jet)>
∿ 62 % gluon	- 0.03 ± 0.01
68 % u quark	+ 0.15 ± 0.03
68 % $\bar{u}$ quark	- 0.15 ± 0.03

As expected, we do observe a neutral charge for jets enriched in gluon whereas the charge of jets enriched in quark is non zero.

Finally, after having measured the differences between quark and gluon jets at fixed Q^2, we have fixed the proportion of quark and gluon jets and studied the fragmentation properties, of this sample for various Q^2 bins. We find that the scaling violation effects are more important than the gluon/quark differences, both for the fragmentation function and for the internal transverse momentum. Figure 6 gives a summary of the two effects : we have plotted the fragmentation function per bin of Z for our quark and gluon sample in function of Q^2 (where $Q^2 = m_{jj}^2$). We have also plotted the results of TASSO [5]. One can see that most of the changes of D(Z) compared to low energy data are due to the Q^2 change and not to the quark/gluon differences.

Moreover, the extrapolation at high Q^2 of the TASSO data seems to be in good agreement with our quark data. This leads us to the conclusion that if the differences in the fragmentation between quark and gluon jets are visible, most of the saftening of the fragmentation observed in our inclusive sample, compared to low-energy data, is due to the large increase ($\sim$ 10) of the Q^2 scale.

ACKNOWLEDGEMENTS

It is a pleasure to thank A.Wróblewski and Z.Ajduk for organizing such a nice conference. I want to thank also all my colleagues of UA1 who have made this analysis possible.

REFERENCES

[1] G.Arnison et al. (UA1 Collaboration), CERN-EP/86-55 (1986).

[2] M.Banner et al. (UA2 Collaboration), Phys. Lett. 118B (1982) 203.
G.Arnison at al. (UA1 Collaboration), Phys. Lett. 123B (1983) 115.

[3] G.Arnison et al. (UA1 Collaboration), Phys. Lett. 132B (1983) 223.

[4] F.Paige and S.D.Protopopescu, ISAJET, BNL 31987 (1982).

[5] R.Althoff at al. (TASSO Collaboration), Z.Phys. C22 (1984) 307.

[6] T.Akesson et al. (AFS Collaboration), Z.Phys. C30 (1986) 27.

[7] P.Ghez and G.Ingelmann, in preparation.

[8] P.Bagnaia et al. (UA2 Collaboration), Phys. Lett. 144B (1984) 291,
Z.Phys. C20 (1983) 117.

[9] R.D.Field and R.P.Feynman, Nucl. Phys. B136 (1978) 1.

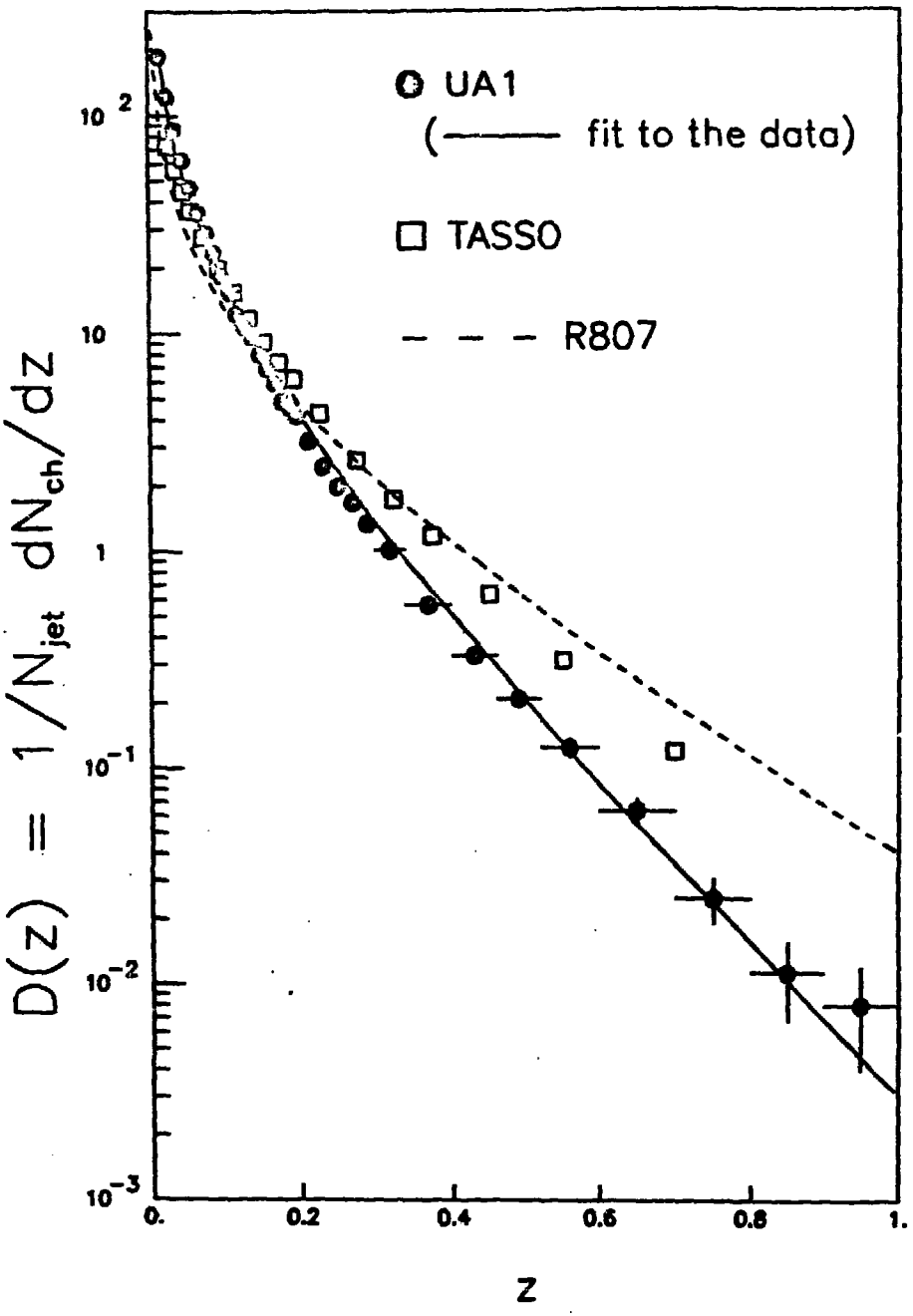
UA1
(——— fit to the data)
TASSO
– – – R807
$D(z) \equiv 1/N_{jet}\ dN_{ch}/dz$
10^2
10
1
10^{-1}
10^{-2}
10^{-3}
0.
0.2
0.4
0.6
0.8
1.
z

Fig.1

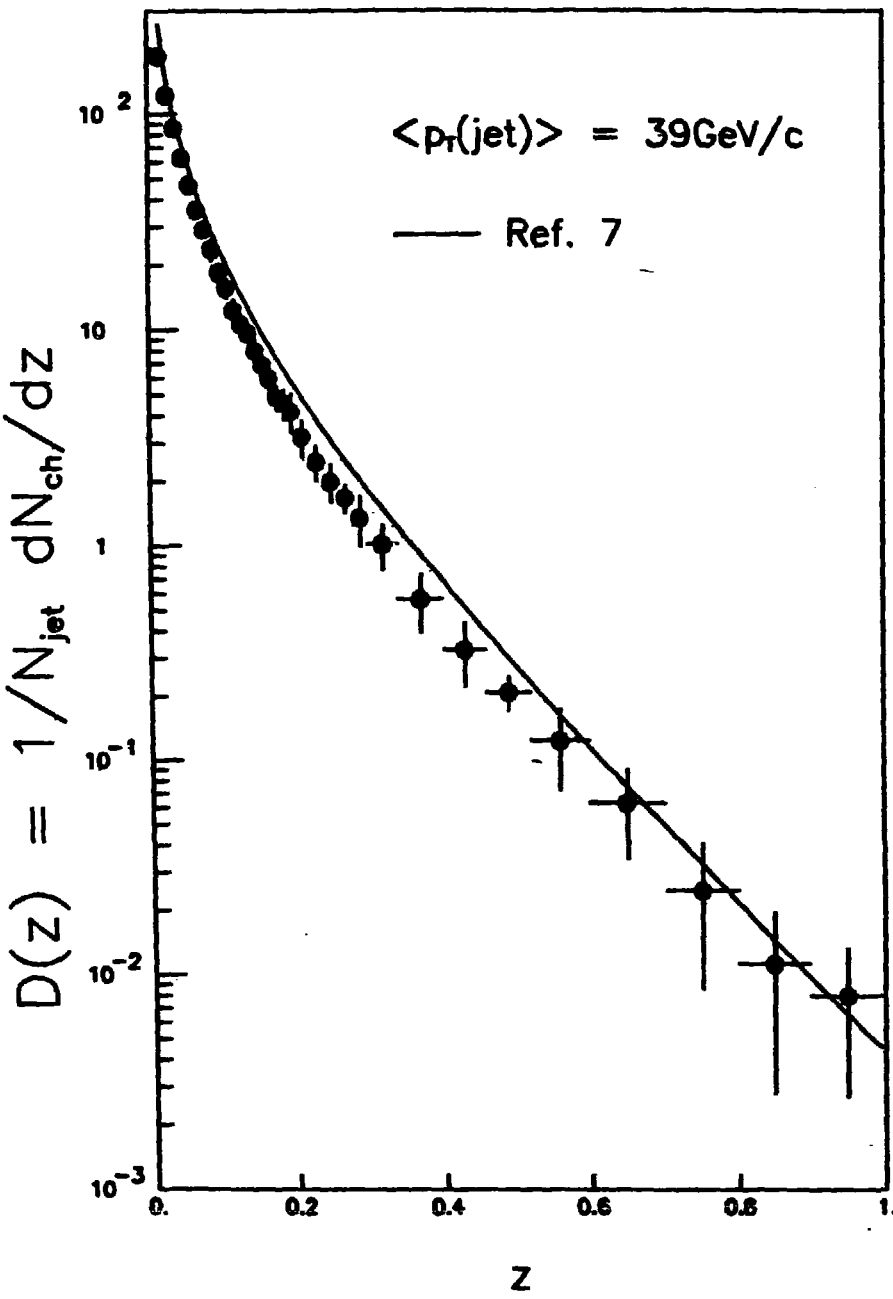
$\langle p_T(jet)\rangle$ = 39GeV/c
Ref. 7
$D(z) \equiv 1/N_{jet}\ dN_{ch}/dz$
10^2
10
1
10^{-1}
10^{-2}
10^{-3}
0.
0.2
0.4
0.6
0.8
1.
z

Fig.2

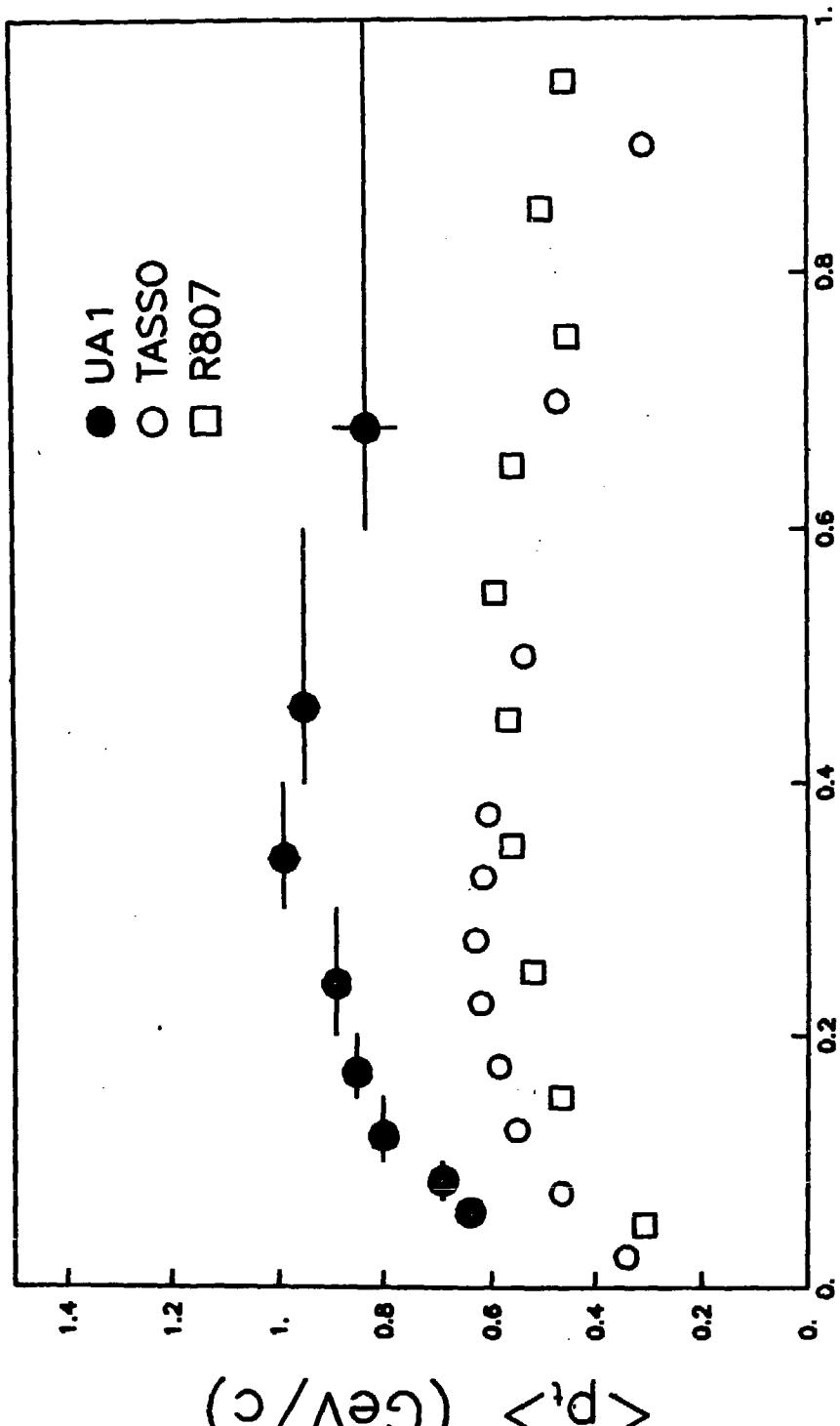

Fig.3

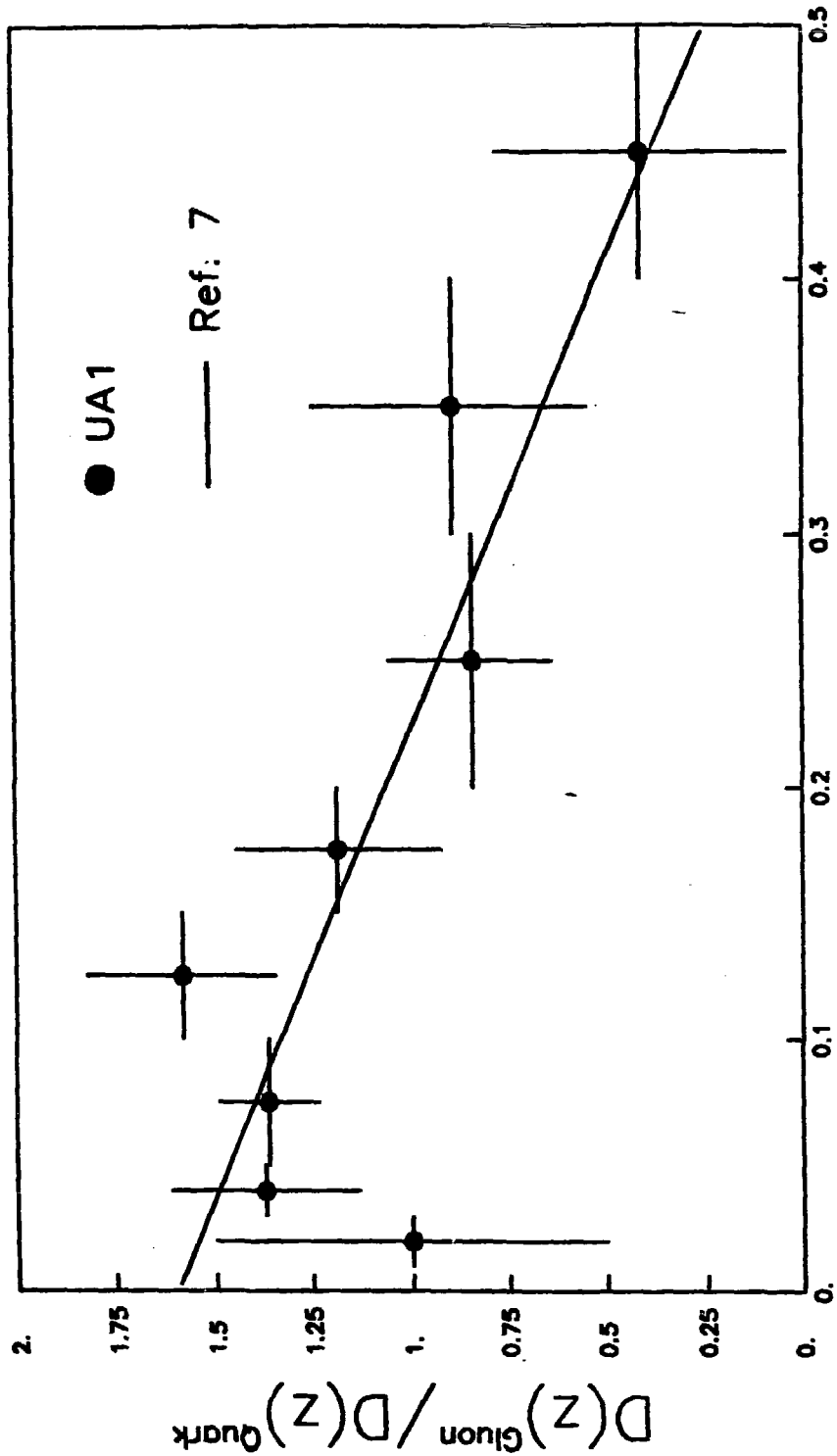
UA1
Ref: 7
$D(Z)_{Gluon}/D(Z)_{Quark}$
Z
2.
1.75
1.5
1.25
1.
0.75
0.5
0.25
0.
0.1
0.2
0.3
0.4
0.5

Fig.4

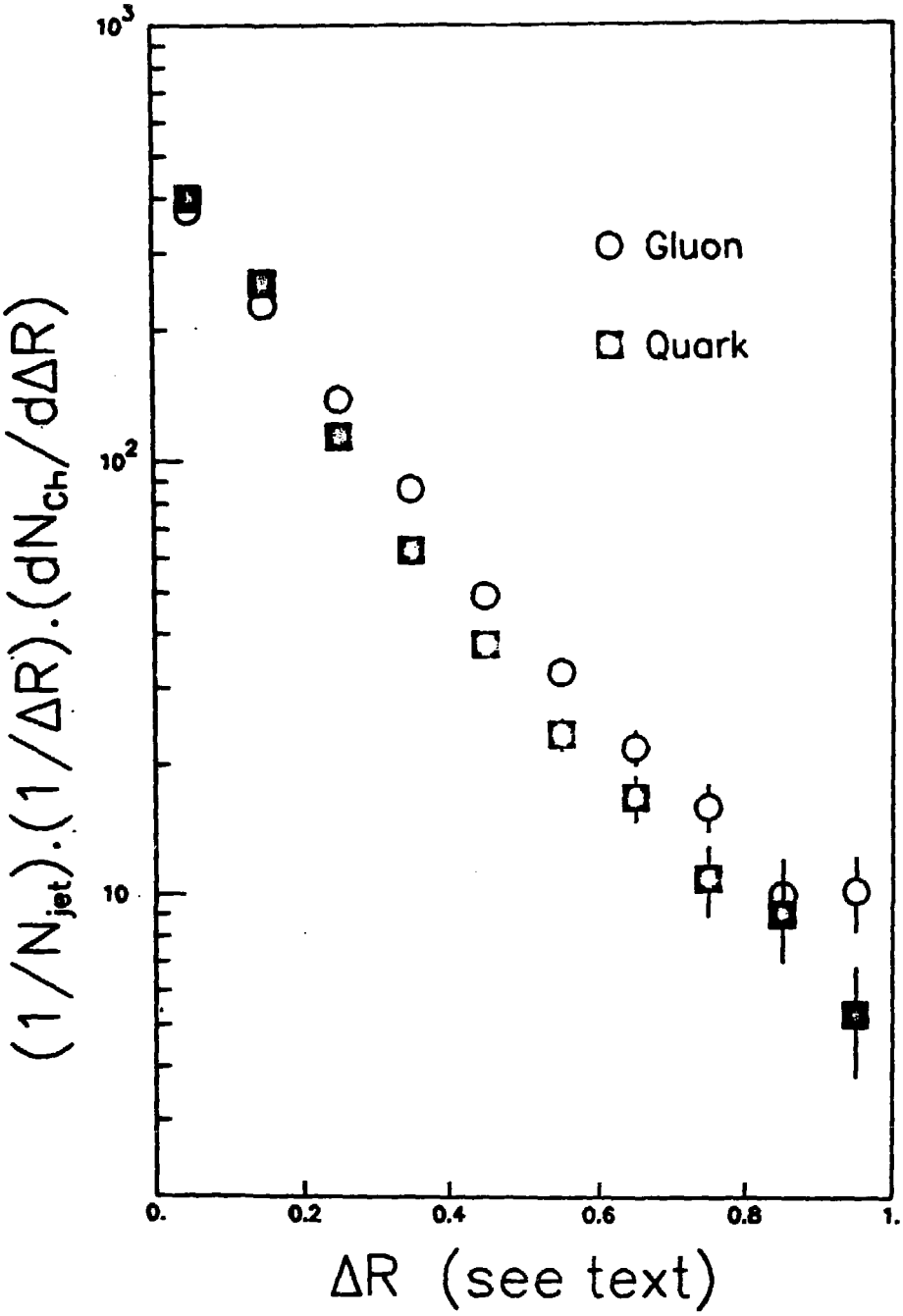
10^3
10^2
10
$(1/N_{jet}).(1/\Delta R).(dN_{ch}/d\Delta R)$
Gluon
Quark
0.
0.2
0.4
0.6
0.8
1.
ΔR (see text)

Fig.5

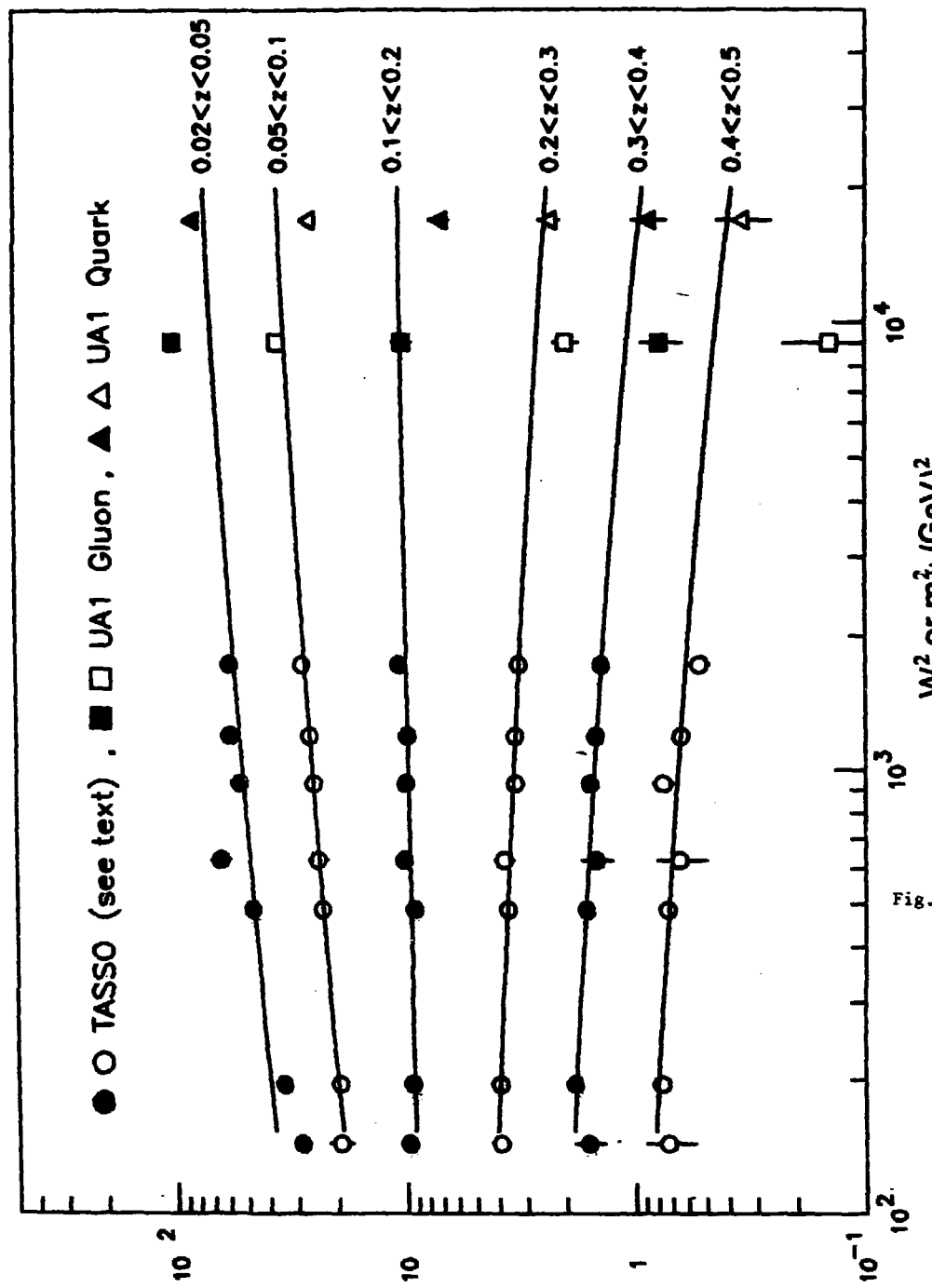
● ○ TASSO (see text) , ■ □ UA1 Gluon , ▲ △ UA1 Quark
0.02<z<0.05
0.05<z<0.1
0.1<z<0.2
0.2<z<0.3
0.3<z<0.4
0.4<z<0.5
D(z) = 1/N_jet dN_ch/dz
W² or m²_jj (GeV)²

Fig.6

SUPERCLUSTERS IN MULTIPLICITY DISTRIBUTIONS ?

V.Šimák[1], M.Šumbera[2] and I.Zborovský [2]

Abstract

We have analysed multiplicity distributions of charged hadrons produced in $pp/p\bar{p}$ and μ^+p, e^+e^-, νp, $\bar{\nu}p$ interactions using the concept of superclusters. It was found that the multiplicity distributions can be expressed in terms of two parameters $\langle \nu_0 \rangle$ and β which are approximately energy independent. Relation between $\langle \nu_0 \rangle$, β, $\langle N \rangle$, D generalizes the relation $D \sim \langle N \rangle$ from KNO energy region towards higher energies.

1) Institute of Physics, Czech. Acad. Sci., Prague, Czechoslovakia

2) Nuclear Physics Institute , Czech.Acad. Sci., Řež near Prague, Czechoslovakia

Recent experimental information /1,2/ concerning multiplicity distributions for the non single-diffractive part of the $p\bar{p}$ inelastic interactions at $\sqrt{s}$ = 200,546 and 900 GeV has considerably changed our understanding of asymptotic behavior of multiparticle production. KNO scaling/3/, after its approximate (and surprisingly early) onset at $10 \leqslant \sqrt{s} \leqslant 60$ GeV, is now badly broken. Its early occurence seems to be accidental/4/ and "KNO-asymptotia", if it exists, must start at much higher energies.

Scaling violation is conveniently described by the following combination of first two moments of multiplicity distribution P(N) :

$$k^{-1} = \frac{D^2 - \langle N \rangle}{\langle N \rangle^2} \qquad (1)$$

KNO predicts that asymptotically $D/\langle N \rangle$ = const.(s) and (1) implies that $k^{-1} \longrightarrow$ const.(s). Contrary to this pp and $p\bar{p}$ non single-diffractive (NSD) data seem to indicate that $k \cdot \ln(s/s_0)$ = const.(s) /4/.

This new empirical regularity is usually discussed in the framework of negative bi-nomial (NB) distribution

$$P(N, \langle N \rangle, k) = \binom{N+k-1}{k-1} \left(\frac{\langle N \rangle / k}{1 + \langle N \rangle / k}\right) \left(1 + \langle N \rangle / k\right)^{-k} \qquad (2)$$

which describes multiplicities of charged secondaries for NSD component of $p\bar{p}$ reaction at 200,546 and 900 GeV and pp reactions above 10 GeV /2,4/. Its phenomenological strength is based on the property that it allows two different decompositions into one parametric distributions: 1) P(N) is summ of k Bose-Einstein (or geometrical) distributions. 2) P(N) is a coumpound Poisson distribution. Interpretations based on first decomposition/5/ struggle with too many

emission cells at lower energies and their noninteger number at $Sp\bar{p}S$ collider[4], while those based on the second one [6,7] should explain an origin of Poisson distributed superclusters[8], their charge composition[9,10] etc.

The second approach substitutes early KNO by a new asymptotic behavior for high-energy multiparticle production: the average number of (Poisson distributed) superclusters

$$\langle \nu \rangle = k \ln(1 + \langle N \rangle / k) \qquad (3)$$

after a slow increase for CM energies between 10 and 50 GeV levels on above ISR energies at $\langle \nu \rangle = 8$ (Fig.1). The task of answering the questions why the onset of a new asymptotics regime takes place just in the region the former (KNO) breaks down and why the average number of superclusters is 8 has been removed by inclusion of neutral particles[7,9] (Fig.1).

For fixed total multiplicity of secondary particles $N_T = N + N_0$ the multiplicity of charged N and neutral N_0 particles is distributed according to the binomial distribution

$$P(N, N_0) = \frac{N_T!}{N!\, N_0!}\, \beta^N (1-\beta)^{N_0} \qquad (4)$$

Then the following relations between first two moments of total and charged multiplicity hold

$$\langle N \rangle = \beta \langle N_T \rangle, \quad D^2 = \beta^2 \cdot D_T^2 + \beta(1-\beta)\langle N_T \rangle \qquad (5)$$

From (5) and (1) one obtains $k = k_T$, i.e. k is an invariant under bi-nomial randomization. The form invariance of NB distribution under this randomization[11,12] guarantees that $P(N_T)$ is also given by eq.(2) with corresponding change in parameters given by (5) and the average number of superclusters is

$$\langle \nu_T \rangle = k_T \cdot \ln(1 + \langle N_T \rangle / k_T) = k \cdot \ln(1 + \beta^{-1} \cdot k^{-1} \cdot \langle N \rangle) \qquad (6)$$

Figure 1. shows a comparison between $\langle \nu \rangle$ and $\langle \nu_T \rangle$[7,9] for $\beta = 2/3$. Asymptoticaly $\langle \nu_T \rangle$ should coincide with $\langle \nu \rangle$.

Rapid increase of the average number of particles inside one supercluster $\langle n_T \rangle = \langle N_T \rangle / \langle \nu_T \rangle$ (Fig.1) supresses the probability of supercluster decaying into final state consisting of neutral partiles only.

As an alternative of binomial randomization scheme (4) one can assume that the superclusters have on average equal number of +, - and neutral particles[10]. In this case the number of superclusters remains the same.

A common deffect of both approaches seems to be that neither can explain why are the superclusters produced independently of each other. Their distribution according to a Poisson distribution[13] (i.e. without any correlations) implies that superclusters are strictly neutral and not only so on the average.

To built in exact charge conservation we allow charged particles to be produced in +- pairs only[14]. Additional condition to eq.(2) $P(2N+1)=0$ describing the multiplicity distribution of charged particles is no longer needed and multiplicity of +- pairs is given by (2) with the new parameters:

$$\langle N_{pairs} \rangle = \langle N \rangle / 2, \quad D_{pairs} = D/2, \quad k^{-1}_{pairs} = k^{-1} - \langle N \rangle^{-1} \tag{7}$$

To include neutral particles we reinterpret the basic NB distribution as applying to clusters rather than the actual observed hadrons[12]. Each cluster than contains one +- pair with probability β. Expresion for average number of neutral superclusters follows from (1),(5) - (7) :

$$\langle \nu_0 \rangle = k_{pairs} \ln\left(1 + \beta^{-1} k^{-1}_{pairs} \langle N_{pairs} \rangle\right) = k \frac{\langle N \rangle}{\langle N \rangle - k} \ln\left(1 + \frac{\langle N \rangle - k}{2\beta k}\right) \tag{8a}$$

$$= \frac{\langle N \rangle}{D^2/\langle N \rangle - 2} \ln\left(1 + \frac{D^2/\langle N \rangle - 2}{2\beta}\right) \tag{8b}$$

$$\langle \nu_0 \rangle \underset{\langle N \rangle \gg k}{\approx} \langle \nu \rangle - k \ln 2\beta \tag{8c}$$

Let us stress that parameter β in (8) need not be equal to the ratio $\langle N\rangle/\langle N_T\rangle$ as the number of neutral hadrons inside a cluster is not specified within this model.

In Fig.2 $\langle\bar{\nu}_o\rangle$ as a function of energy for NSD pp and $p\bar{p}$ data[15] and β = 1/2, 2/3 and 0.9 is plotted. Assuming $\langle\bar{\nu}_o\rangle$ to be a constant within the whole energy range ($6.8 \lesssim \sqrt{s} \lesssim 900$ GeV) we have found the best fit for $\beta = 0.67 \pm 0.01$ and $\langle\bar{\nu}_o\rangle = 7.7 \pm 0.2$. From (8c) follows that asymptotically $\langle\bar{\nu}\rangle \longrightarrow \langle\bar{\nu}_o\rangle$. Thus the proper choice of β improves constancy of $\langle\bar{\nu}_o\rangle$ at lower energies.

The NB distribution is defined for $k \gtrsim 0$, however $\langle\bar{\nu}\rangle$ and $\langle\bar{\nu}_o\rangle$ can be calculated also for $k^{-1} > -\langle N\rangle^{-1}$ and $k^{-1} > (1-2\beta)/\langle N\rangle$ respectively. This is ilustrated by Fig.3 for $\bar{\nu}p$, $\bar{p}p$[16], μ^+p[17] and e^+e^-[18] data. Again a proper choice of β guarantees an approximate constancy of $\langle\bar{\nu}_o\rangle$ over the whole energy region.

It is possible that the supercluster is only a convenient concept describing a corresponding regrouping of final state particles and not a real physical object.

Thanks to the independence of $\langle\bar{\nu}_o\rangle$ and β on energy D and $\langle N\rangle$ are correlated by eq.(8b) which at lower energies recovers the linear relation between them[19].

For all studied processes k^{-1} is an increasing function of energy (for pp[4], e^+e^-[20]). So at high enough energies a description of multiplicity distributions within the framework of NB should be possible. Using eq.(8) and extrapolated values of the fits $k^{-1} = a \ln(s/s_o)$ we predict the average multiplicities of charged particles at high energies (Fig.4).

A smooth transition of k^{-1} from negative to positive values indicates that NB is only a limiting case of some more general distribution defined for all k. For this we suggest a confluent hypergeometric distribution

$$P(N) = \frac{P(0)}{N!}\prod_{j=0}^{N-1} g(j), \qquad g(j) = \frac{a + bj}{1 + cj} \tag{9}$$

This distribution for $c = 0$ coincides with the NB distribution /6/ while for $k^{-1} < 0$ $b \simeq 0$ and it is again a distribution depending on two parameters only.

REFERENCES

/1/ UA5 Collab., G.J.Alner et al.,Phys.Lett.138B(1984) 304.

/2/ UA5 Collab., G.J.Alner et al., Phys.Lett.167B(1986)476.

/3/ Z.Koba, H.B.Nielsen and P.Olesen, Nucl.Phys.B40(1972)317.

/4/ UA5 Collab., G.J.Alner et al.,Phys.Lett. 160B(1985)199.

/5/ A.Giovannini, Nuovo Cimento 15A(1973)543.
P.Carruthers and C.C.Shih, Phys.Lett. 127B(1983)242.
S.Mrówczyński, Z.Phys.C27(1985)131.

/6/ A.Giovannini and L.Van Hove, Z.Phys.C30(1986)391.

/7/ V.Šimák and M.Šumbera, Czech.J.Phys.B, in press.

/8/ J.G.Rushbrooke, Proc.of Int. Europhysics Conf. on H.E.P.85, Bari, July 18-24, 1985, p.837

/9/ K.Fiałkowski, Phys.Lett. 169B(1986)436.

/10/ L. Van Hove, private communication.

/11/ L.N.Chang and N.P.Chang, Phys.Rev. D9(1974)660.

/12/ P.Carruthers and C.C.Shih, Phys.Lett. 165B(1985)209.

/13/ D.Levy , Nucl.Phys. B59 (1973)583.

/14/ T.T.Chou and C.N.Yang, Phys.Lett. 167B(1986)453.

/15/ For pp at $\sqrt{s}$ = 6.8 GeV we used J.Benecke et al.,Nucl.Phys. B76(1977)29, for $11.5 \lesssim \sqrt{s} \lesssim 62.3$GeV those quoted in /4/. $p\bar{p}$ data are from /1/ and /2/.

/16/ M.Grässler et al., Nucl.Phys.B223(1983)269.

/17/ BMC Collab.,M.Arneodo et al., Nucl.Phys. B258(1985)249.

/18/ TASSO Collab., M.Althoff et al., Z.Phys.C22(1984)307.

/19/ A.Wróblewski, Acta Phys.Pol. B4(1974)857.

/20/ C.K.Chew and Y.K.Lim, Phys.163B(1985)257.

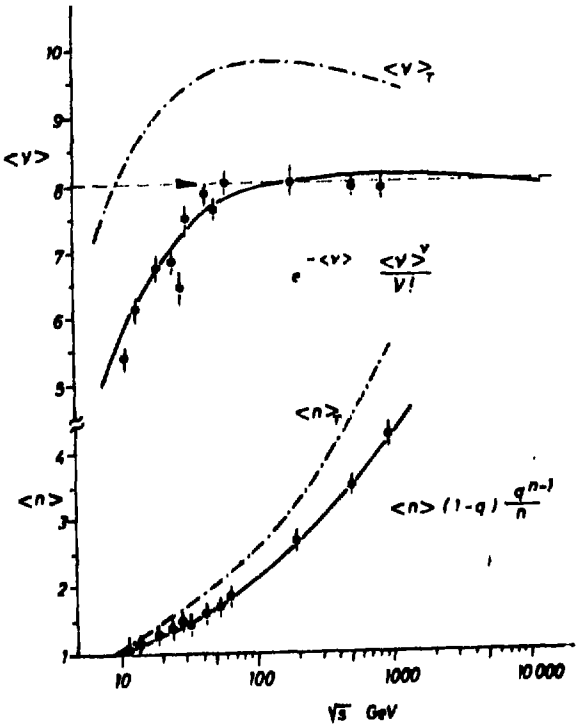

Fig. 1

Average number of superclusters $\langle \nu \rangle$ (eq. (2)) and average number of particles inside one supercluster $\langle n \rangle$. The dot-dashed lines represent $\langle \nu_\tau \rangle$ and $\langle n_\tau \rangle$ assuming $N_\tau = 3\langle N \rangle/2$

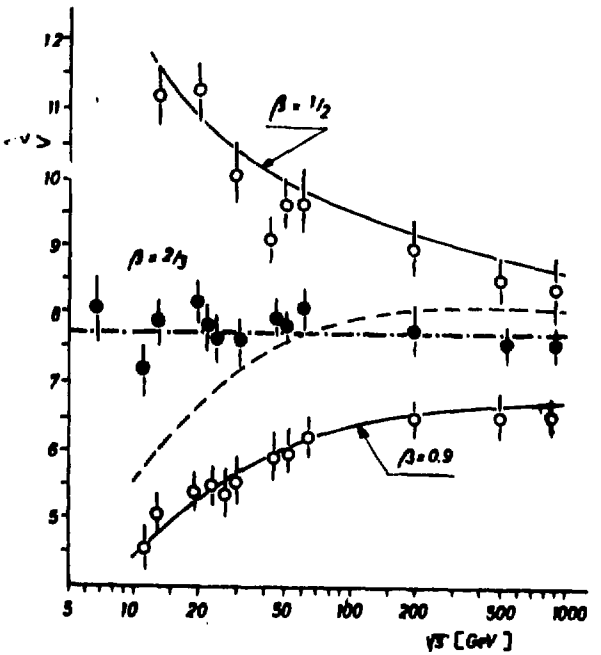

Fig. 2

Average number of neutral superclusters $\langle \nu_0 \rangle$ (eq. (8a)) for various β. The dashed line corresponds to $\langle \nu \rangle$ from Fig. 1.

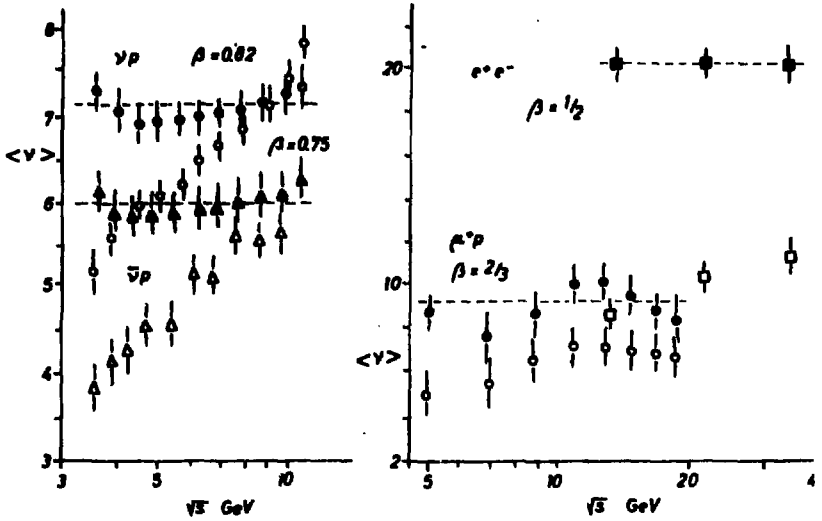

Fig. 3

The $\langle \nu_e \rangle$ and $\langle \nu \rangle$ (full and empty symbols, respectively) for ν p (circles) and $\bar{\nu}$ p (triangles); e^+e^- (squares) and μ^+p (circles)

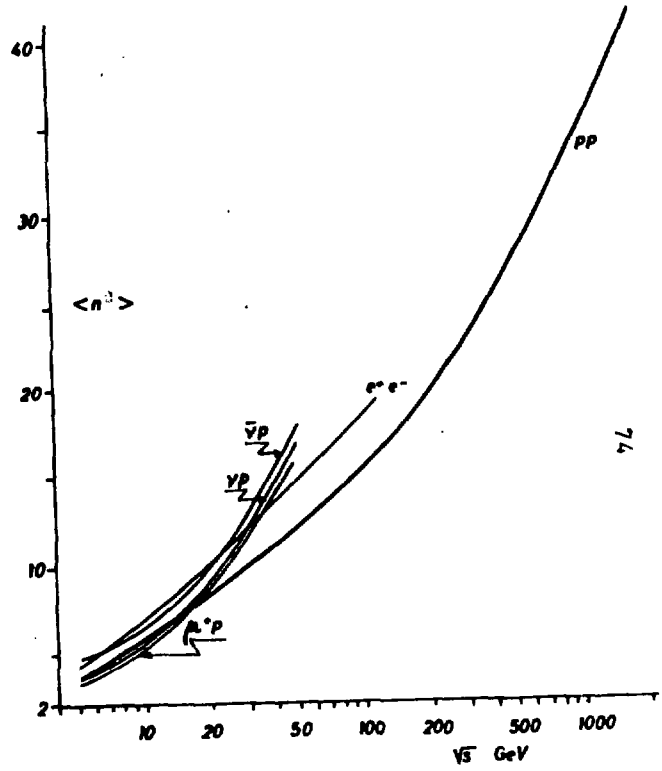

Fig. 4

Predictions for average charged multiplicity extrapolated from lower energies using eq.(8) and $k^{-1} = a \ln(s/s_0)$.

MOMENTUM-TRANSFER DEPENDENCE OF THE PHASE OF ELASTIC AMPLITUDE IN HIGH-ENERGY HADRON SCATTERING

V. Kundrát, M. Lokajíček
Institute of Physics, CSAV, Prague, Czechoslovakia

D. Krupa
Institute of Physics, SAV, Bratislava, Czechoslovakia

The interpretation of the high-energy scattering of light nuclei is based usually on the Glauber method, which starts from the knowledge of nucleon-nucleon elastic-scattering amplitude at a corresponding energy. This amplitude is taken always as purely imaginary since it is commonly assumed that at least in the region of smaller $|t|$ the influence of the phase can be fully neglected. It has been found, however, recently /1/ that a substantially better agreement with experimental data for light-nuclei scattering can be reached if a strong t-dependence of the phase of nucleon-nucleon amplidute is assumed.

It was shown in /2/ several years ago that the phase t-dependence plays also a very significant role if the probability distribution of scattering events in the impact-parameter plane is studied. The peripheral behaviour of the elastic scattering is obtained only if the phase increases rather strongly with $|t|$ in the region of small values.

The neglection of the phase t-dependence is equivalent to the assumption that the imaginary part of amplitude is dominant, which is being reasoned by some theoretical arguments regarded as valid at asymptotic energies /3/. The equality of particle-particle and antiparticle-particle differential cross sections follows from these arguments, too. However, the experimental data concerning the pp and $\bar{p}p$ scattering /4/ show that the given arguments can be applied at available energies to the region of very small momentum transfers, only. And thus, there is not any convincing argument for the dominant imaginary part in interpreting contemporary experimental data, either.

Contrary to this fact a majority of papers is still based on the assumption of the dominant imaginary part. That leads unavoidably to a central behaviour of elastic scattering in impact-parameter plane and to a relatively large transparency of hadrons in head-on collisions /5/, which should be still regarded as a puzzle (see e.g. /6/). Therefore, one is fully entitled to conclude that the central distribution /7/ of elastic nucleon-nucleon scattering can be hardly justified. Another reason can be found in a close similarity of all diffractive collisions and in the common assumption that diffractive production processes are peripheral /8/.

There is, of course, a certain difference between the t-dependences considered in /1/ and /2/. A simple linear increase of phase with $|t|$ was assumed in /1/ while a more complicated dependence was derived in /2/. The peripherality of hadron scattering requires the phase to increase for small $|t|$ but a maximum value should be reached at $t \simeq -0.3$ GeV^2.

As to the experimental data the amplitude phase can play an important role in the description of interference between Coulomb and hadronic scattering of charged hadrons. In papers /9,10/ (see also /11/) the momentum-transfer distributions were fitted with the help of the following parametrization of the total amplitude

$$F(s,t) = \frac{\alpha s}{t} f^2(t)\, e^{i\alpha\phi} + \frac{\sigma_{tot}}{4\pi} p\sqrt{s}\,(\rho + i)\, e^{Bt/2} \qquad (1)$$

with

$$f^2(t) = \left(\frac{0.71}{0.71 - t}\right)^2 , \qquad \alpha\phi = -\alpha\left[\ln(-Bt/2) + \gamma\right] ; \qquad (2)$$

$\sqrt{s}$ is the total CMS energy, α - the fine-structure constant, f^2 - the conventional dipole form factor, $\alpha\phi$ - the total West-Yennie phase /12/ of the Coulomb amplitude and $\gamma = 0.577$ is the Euler constant. And futher, σ_{tot} is the total hadronic cross section, p - the CMS momentum of one colliding particle, B - the diffractive slope of hadronic interaction and ρ - the ratio of the real and imaginary parts of the hadronic amplitude in the forward direction.

Three assumptions are involved in the derivation of formula (1): (i) spin effects are neglected; (ii) characteristic exponential dependence of the module of hadronic amplitude in the interference region is assumed; (iii) the same t-dependence of the real and imaginary parts of hadronic amplitude is supposed.

The first two assumptions should be regarded as fully justified. The first one is supported by the fact that different mutually independent methods for measuring the total cross sections give nearly the same values lying within the experimental errors /13/. The other one then by the fact that the corresponding exponential dependence has been found in the case of high-energy elastic np scattering also for $|t| < 10^{-2}$ GeV^2 /14/. The third assumption is equivalent to neglecting any t-dependence of the phase, and therefore, there are not any reasonable arguments for it.

It would be possible, in principle, to abandon the third assumption by introducing a complex quantity instead of West-Yenni $\alpha\phi$-phase. There are not, however, any ideas how to parametrize such a phase. Thus, the approach proposed recently by Cahn /15/ and based on the eikonal approximation provides a much suitable starting point. The following form has been derived for the total amplitude in this case /15/

$$F(s,t) \sim \frac{\alpha s}{t} + F^N(s,t)\left\{1 - i\alpha \int_{-\infty}^{0} dt' \ln\frac{t'}{t} \frac{d}{dt'}\left[f^2(t') \frac{F^N(s,t')}{F^N(s,0)}\right]\right\} . \quad (3)$$

The hadronic amplitude can be written as

$$F^N(s,t) \sim e^{Bt/2 - i\delta(t)} \quad (4)$$

where the phase will be parametrized in the following manner

$$\delta(t) = \delta_0 + \delta_1 \left|\frac{t}{t_0}\right|^{\alpha} e^{\gamma t} + \delta_2 \left|\frac{t}{t_0}\right|^{\lambda} , \; t_0 = 1\,\text{GeV}^2 . \quad (5)$$

This parametrization is based on the results of /2/ and allows the peripheral as well as central behaviours of the elastic scattering in the impact-parameter plane. For $\delta(t) = \delta_0 = \text{const}$ the amplitude (3) reduces in the principle to the amplitude (1) used in all previous analyses.

The new formula can be now fitted to the experimental data obtained for differential cross sections being defined by

$$\frac{d\sigma}{dt} = \frac{\pi}{sp^2} |F(s,t)|^2 . \quad (6)$$

p_{lab} [GeV/c]	Fit I				Fit II			
	σ_{tot} [mb]	B [GeV^{-2}]	ρ	χ^2/DF	σ_{tot} [mb]	B [GeV^{-2}]	ρ	χ^2
100	38.43	11.78	-.096	81.15/69	38.49	11.74	-.090	81.44
150	38.73	12.03	-.038	74.61/64	38.73	11.86	-.040	75.14
250	39.26	12.03	-.043	43.70/60	39.29	11.94	-.039	43.72
300	39.47	12.16	-.035	63.18/56	39.53	12.08	-.035	62.89
1063	41.88	13.10	0.056	59.70/53	41.93	13.10	0.061	51.84
1487	42.38	13.11	0.075	45.51/37	42.36	13.10	0.082	43.06
2081	43.49	13.14	0.086	30.58/30	43.82	13.20	0.089	28.70

Tab. 1: The results for both the types of fits

We have applied it to elastic pp scattering at different energies. For p_{lab} = 100 - 300 GeV/c the data from /16/ have been used; they concern momentum-transfer interval $-t \in (0.02, 0.04)$ GeV^2 covering the interference regions. The other data taken from /17/ are for ISR energies $\sqrt{s}$ = 44 - 63 GeV and momentum-transfer interval $-t \in (0.001, 0.04)$ GeV^2. Some preliminary results have been given in /18/.

Two types of more detailed fits have been performed at all energies. In the first case (labelled as I) we have chosen $f_1 = f_2 = 0$ while in the other case (labelled as II) all parameters defining the phase t-dependence in Eq. (5) have been allowed to change; however, a series of constraints has been applied in order to obtain a peripheral distribution in impact-parameter plane. In all cases we have started from the values of σ_{tot} and B determined with the help of other independent approaches; only small deviations (in the limits of given experimental arrors) have been allowed for these parameters.

The numerical values of the parameters σ_{tot}, B and $\rho = \mathrm{tg}\, f_0$ for both the types of fits are given in Tab. 1; the χ^2-values obtained in individual cases under the same conditions are shown, too. For the fit I the normal central behaviour in impact-parameter plane is obtained. The free parameters for fit II have been modified in such a way so as the peripheral behaviour be obtained.

Some examples of the distributions in impact-parameter plane are given in Fig. 1; the corresponding t-dependences of the phase are shown in Fig. 2.

One must conclude from the values given in Tab. 1 that for fit I the ful agreement with results obtained in /16,17/ has been obtained in all cases. As to fit II there exist only very small deviations from the values of the fit I. Also the χ^2 values are in both the cases practically the same. Thus the analysis of experimental interference data cannot decide between the two different possibilities. The preference should be given to the peripheral interpretation due to logical reasons. Perhaps more convincing arguments will be obtained if our results are combined with more detailed analyses of light-nuclei scattering.

1/ Franco V.,Yin Y.: Phys. Rev. Lett. 55 (1985), 1059

2/ Kundrát V.,Lokajíček M.Jr.,Lokajíček M.: Czech. J. Phys. B 31 (1981), 1334

3/ Van Hove L.: Phys. Lett. 7 (1963), 76

4/ Breakstone A. et al.: Phys. Rev. Lett. 54 (1985), 2180

5/ Henzi R.,Valin P.: Phys. Lett. 149B (1984), 239; Z. Phys. C - Part. and Fields 27 (1985), 351

6/ Giacomelli G.,Jacob M.: Phys. Rep. 55 (1979), 1

7/ Mietinnen H.I.: Proc. of the IXth Rencontre de Moriond, Meribel les Allues, Vol. 1 (ed. J.Tran Tranh Van), Orsay 1974

8/ Giovannini et al.: Rivista Nuovo Cim. 2 (1971), 1

9/ Amaldi U. et al.: Phys. Lett. 66B (1977), 390

10/ Amos N. et al.: Nucl. Phys. B 262 (1985), 689

11/ Block M.M.,Cahn R.N.: Rev. Mod. Phys. 57 (1985), 563

12/ West G.B.,Yenni D.R.: Phys. Rev. 172 (1968), 1413

13/ Martin A.: Journal de Phys. Coll. C 2 (1985), C2-727

14/ Arefiev A. et al.: Nucl. Phys. B 232 (1984), 365

15/ Cahn R.: Z. Phys. C - Part. and Fields 15 (1982), 253

16/ Burq J.P. et al.: Nucl. Phys. B 217 (1983), 285

17/ Bystricky J. et al.: in Landolt-Börnstein: Numerical Data and Functional Relationships in Science (ed.H.Schopper),Springer 1980

18/ Kundrát V.,Lokajíček M.,Krupa D.: in "Elastic and Diffractive Scattering at the Collider and Beyond" (ed. B.Nicolescu, J.Tran Tranh Van), Singapore 1986 (Proc. of the First Workshop, Blois, France, 3-6 June 1985), p. 301

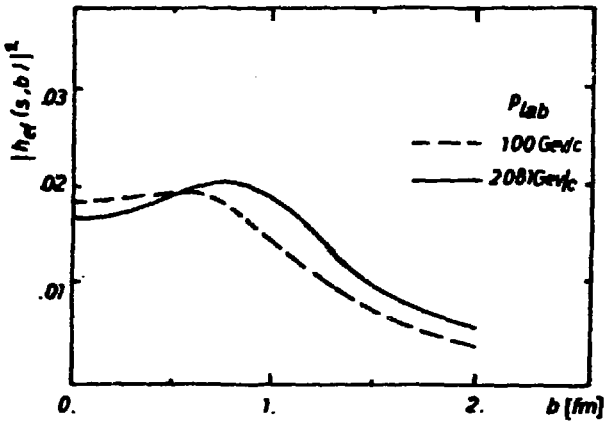

Fig. 1: Examples of peripheral distributions obtained for fit II

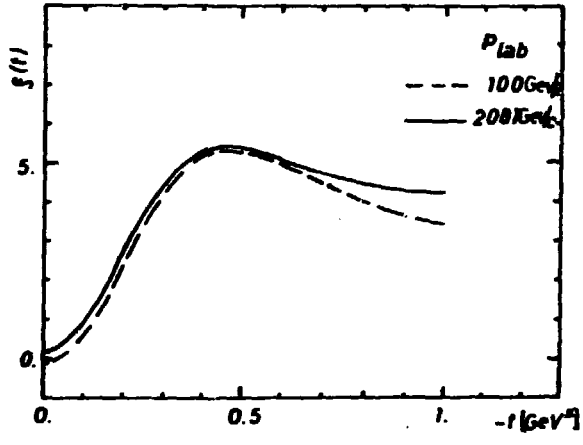

Fig. 2: Examples of phase t-dependence obtained for fit II

RAPIDITY DEPENDENCE OF MULTIPLICITY DISTRIBUTIONS
in
NON-DIFFRACTIVE π^+p AND pp INTERACTIONS AT 250 GeV/c

NA22 Collaboration

Aachen[1]- Berlin (Zeuthen)[2]- Brussels/Antwerpen[3]- Helsinki[4]- Krakow[5]- Moscow[6]- Nijmegen[7]- Rio de Janeiro[8]- Serpukhov[9]- Warsaw[10]- Yerevan[11]

Presented by E. De Wolf[3,*]

ABSTRACT. Multiplicity distributions of all charged and of negative particles for non (single)-diffractive events in π^+p and pp interactions at 250 GeV/c ($\sqrt{s}$ = 22 GeV) are presented for various central rapidity intervals. The data are all well described by the negative binomial distribution. The π^+p and pp data are different for full phase space, but similar in the central region. In the central region, the relation $k_{CH} \approx (1/2)k_-$ holds for charged and negative multiplicities. This contradicts the interpretation in terms of (partial) stimulated emission.

1. INTRODUCTION

Measurements of charged particle multiplicity distributions in hadron physics has been a popular subject of study for more than 30 years.

With bubble chambers and other "visual" detectors,the multiplicity distributions of all charged or negative particles are relatively easy to measure. Systematic uncertainties are usually small and quite well understood. Over the years, a large data-base on multiplicity distributions in hadron-hadron collisions has been collected.

[1] III. Physikalisches Institut B, RWTH, Aachen, Fed. Rep. Germany

[2] Institut für Hochenergiephysik der Akademie der Wissenschaften der DDR, Berlin-Zeuthen, German Dem. Rep.

[3] Inter-University Institute for High Energies, Brussels, and Dept. of Physics, Universitaire Instelling Antwerpen, Belgium

[4] University of Helsinki, Helsinki, Finland

[5] Institute of Physics and Nuclear Techniques of the Academy of Mining and Metallurgy and Institute of Nuclear Physics, Krakow, Poland, partially supported by grants from CPBP 01.06 and 01.09

[6] Moscow State University, Moscow, USSR

[7] University of Nijmegen and NIKHEF-H, Nijmegen, The Netherlands

[8] Centro Brasileiro de Pesquisas Fisicas, Rio de Janeiro, Brasil

[9] Institute for High Energy Physics, Serpukhov, USSR

[10] University of Warsaw and Institute of Nuclear Problems, Warsaw, Poland

[11] Institute of Physics, Erevan, USSR

[*] Research Associate of the National Science Foundation, Belgium

More recently, multiplicity data have also become available for lepton–hadron interactions and e^+e^- annihilations.

Given the large collection of data, it is not surprising that much effort went into the qnest for empirical regularities.

In the vast litterature on the subject, few of the well-known (and less-known) discrete and continuous probability distributions found in Treatises on Probability and Statistics, were not tested against the data. Fits were made to Poisson, Bose-Einstein and gaussian distributions, and to combinations and convolutions thereof.

Although many of these comparisons have not withstood the time and the advent of new data at ever increasing energies, such activity has often contributed to a better understanding of the problem at hand.

Important milestones in the quest of regularities were, among others, i) the observation by Wróblewski–Malhotra[1] of a linear relationship among the average multiplicity and dispersion of charged multiplicity distributions , ii) the prediction of asymptotic scaling by Koba, Nielsen and Olesen[2], originally derived from Feynman-scaling[3].

Although KNO-scaling was found to be only approximate in the PS–ISR energy range, the strong scaling violations observed by UA5[4] in non (single)-diffractive interactions, still came as a surprise.

Immediately afterwards, the same group proposed a new multiplicity law[5], dependent on two energy dependent parameters—$\overline{n}$ and k—: the negative binomial probability distribution (NB). It is also kwown as the generalized Bose–Einstein distribution (for integer k). It becomes a Poisson distribution for $k \to \infty$, and a simple Bose–Einstein (geometric) distribution for $k = 1$. Such distributions have applications in many areas of science.

2. EXPERIMENTAL RESULTS

The negative binomial (NB) distribution is defined as

$$P_n(\overline{n}, k) = \frac{(n+k-1)!}{n!(k-1)!} \left(\frac{\frac{\overline{n}}{k}}{1+\frac{\overline{n}}{k}}\right)^n (1+\frac{\overline{n}}{k})^{-k},$$

where P_n is the probability for an event with n (charged or negative) particles. The two parameters $\overline{n}$ (the average) and k are related to the dispersion D by

$$\frac{D^2}{\overline{n}^2} = \frac{1}{k} + \frac{1}{\overline{n}}.$$

For $p\bar{p}$ collisions at $\sqrt{s} = 540$ GeV, not only the full phase space charged particle multiplicity distribution appears to be of this type, but also the distribution in various

central pseudo-rapidity intervals[5]. The parameter k is smaller in the central region than for full phase space, corresponding to a broader distribution in the central region. A similar analysis has been carried out for e^+e^- annihilations at $\sqrt{s} = 29$ GeV/c[6]. In all intervals of rapidity (measured with respect to the thrust axis), the multiplicity distribution follows a negative binomial. The distributions are much narrower, however, than for hadronic collisions.

As recently demonstrated[7], there are at least two classes of mechanisms which can lead to the NB distribution: stimulated emission[8,9] and cascading[10,11].

Here we report on a study of the rapidity dependence of the multiplicity distribution for π^+p and pp collisions at $\sqrt{s} = 22$ GeV/c, and present data on charged and on negative particle multiplicities. This leads to a distinction between stimulated emission and cascade models. Preliminary results have been presented earlier[12].

The experiment (NA22) has been performed at CERN in the European Hybrid Spectrometer (EHS) equipped with the Rapid Cycling Bubble Chamber (RCBC) and exposed to a 250 GeV/c tagged positive meson enriched beam. A minimum bias interaction trigger was used. The experimental set-up and the trigger conditions are described in [13].

Events were accepted when topology and charge balance were correct and all tracks properly reconstructed. These events are weighted according to the measured topological cross section[13]. The "non (single)–diffractive" sample is defined by excluding events with $n_{CH} \leq 6$ which have one or more positive particle(s) with Feynman-x $|x| > 0.88$. The sample consists of 6832 π^+p and 2477 pp events.

The multiplicity distribution P_n is studied for different cuts in the c.m. rapidity y. The errors given are statistical only, except for the case of full phase space. The systematic uncertainties arise from trigger and reconstruction biases, incomplete particle identification and imperfect exclusion of (single-) diffractive events. They are estimated to be $\approx 5\%$.

The multiplicity distribution of all charged and of negative particles for full phase space and in selected rapidity intervals $|y| < y_C$ are fitted to the NB distribution. Fig. 1a-b shows the statistically more significant π^+p data in KNO form, together with the corresponding best fit. Note that each successive distribution is shifted down by a factor of ten. In addition, the full phase space distribution is multiplied by 0.5 for proper normalization. The quality of the fits is good, both for the π^+p and pp data.

The values of the fitted parameters $\bar{n}$ and k are shown in Fig. 2 as a function of y_C. As observed earlier[13] for inelastic events, the full phase space π^+p data have smaller width and higher average multiplicity than the pp data. For the full all-charged non (single)–diffractive multiplicity distribution we find $\bar{n}_{CH} = 9.21 \pm 0.05 \pm 0.1$ and $\bar{n}_{CH} = 8.76 \pm 0.06 \pm 0.1$; $k_{CH} = 17.3 \pm 1.1 \pm 1.0$ and $k_{CH} = 12.4 \pm 0.8 \pm 1.5$, for π^+p and pp interactions, respectively. The first error is statistical, the second systematic.

However, in the central region, the π^+p and pp data are similar, both for $\overline{n}$ and k. Fig. 2 clearly shows that the difference for the full phase space is due to the fragmentation region, an interesting but not totally surprising result.

For a given y-interval, the k-values are larger for π^+p and pp interactions at $\sqrt{s} = 22$ GeV than for $p\bar{p}$ at 540 GeV[5], but lower than for e^+e^- at the comparable energy of 29 GeV[6], shown in Fig. 3.

Comparing the negative to the all charged multiplicity distribution, we also observe from Fig. 2 that $k_{CH} \approx (1/2)k_-$ in the central region. If the NB distribution is interpreted in terms of partial stimulated emission[7], one would expect $k_{CH} \approx 2k_-$, in strong contradiction to our observation.

REFERENCES

[1] A. Wróblewski: Acta Phys. Pol. B4 (1973) 857

[2] Z. Koba, H.B. Nielsen, P. Olesen: Nucl. Phys. B40 (1972) 317

[3] R.P. Feynman: Phys. Rev. Lett. 23 (1969) 1415

[4] UA5 Coll., K. Alpgård et al.: Phys. Lett. 121B (1983) 109; G. Alner et al.: Phys. Lett. 138B (1984) 199

[5] UA5 Coll., G. Alner et al.: Phys. Lett. 160B (1985) 199 and 167B (1986) 476

[6] M. Derrick et al.: Phys. Lett. 168B (1986) 299

[7] A. Giovannini, L. Van Hove, Z. Phys. C30 (1986) 391

[8] A. Giovannini: Nuovo Cim. 15A (1973) 543; W. Knox: Phys. Rev. D10 (1974) 65

[9] P. Carruthers, G.C. Shih: Phys. Lett. 127B (1983) 242

[10] A. Giovannini: Nucl. Phys. B161 (1979) 429

[11] C.S. Lam: *Generalized KNO scaling and the Branching Model*, XXIst Rencontre de Moriond, 1986

[12] F. Meyers: *Rapidity Dependence of Multiplicities in Non-Diffractive π^+p and pp Collisions at 250 GeV/c*, XXIth Rencontre de Moriond, 1986

[13] NA22 Coll. M. Adamus et al.: *Cross sections and charged multiplicity distributions for K^+p, π^+p and pp Interactions at 250 GeV/c*, Nijmegen preprint HEN262A (1986) subm. to Z. Phys. C

FIGURE CAPTIONS

Fig. 1 Charged (a) and negative (b) multiplicity distributions for π^+p data at 250 GeV/c in central rapidity intervals. Errors are statistical only, except for 2 and 4 prongs in the full phase space distribution. Histograms show best fits to the negative binomial distribution.

Fig. 2 Fit values of the $\overline{n}$ and k parameters verus the size of the rapidity interval $Y_{GAP} = 2y_C$, for the charged and negative multiplicities of the π^+p and pp data at 250 GeV/c. Except for full phase space, errors are statistical.

Fig. 3 Fitted values of k as a function of rapidity span for two-jet data in e^+e^- annihilations at 29 GeV[6].

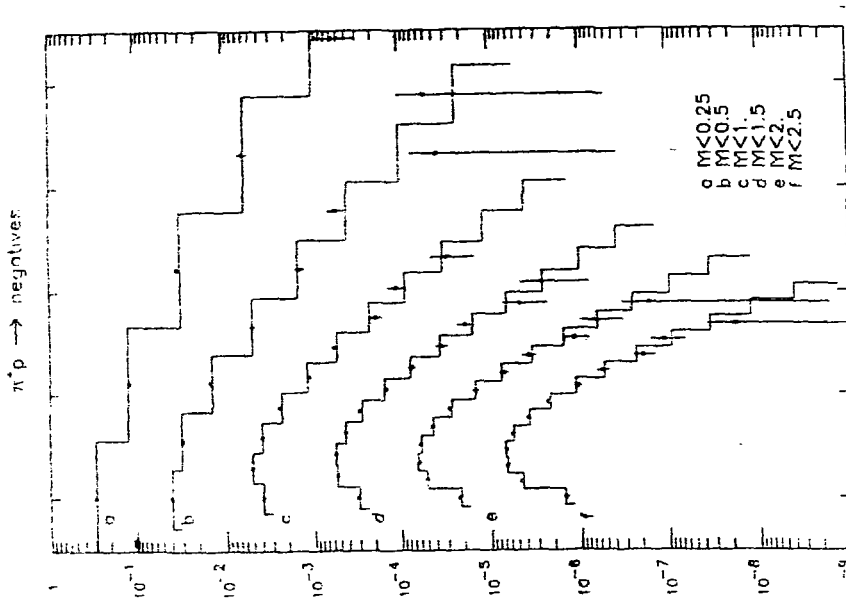
$\pi^+ p \longrightarrow$ negatives
a M<0.25
b M<0.5
c M<1.
d M<1.5
e M<2.
f M<2.5
$z = n/\bar{n}$

Fig. 1b

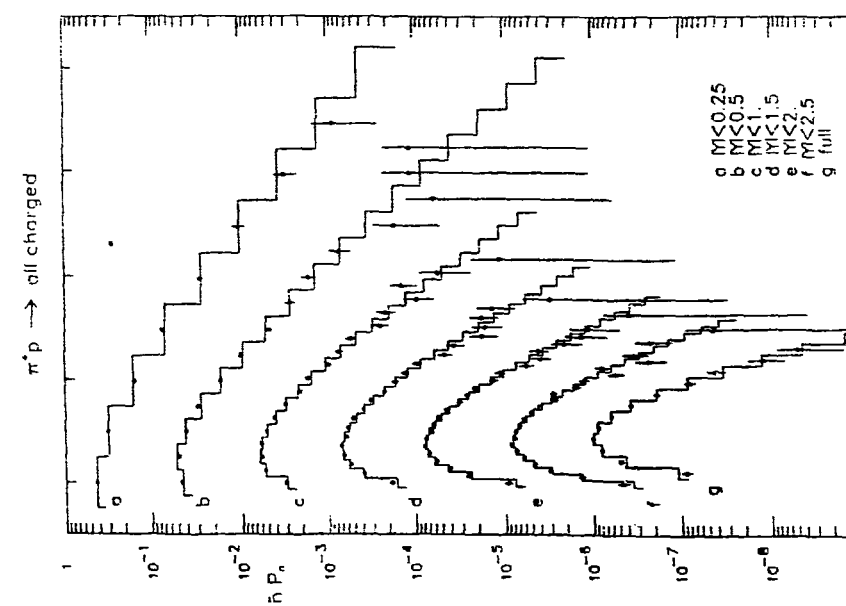
$\pi^+ p \longrightarrow$ all charged
a M<0.25
b M<0.5
c M<1.
d M<1.5
e M<2.
f M<2.5
g full
$\bar{n} P_n$
$z = n/\bar{n}$

Fig. 1a

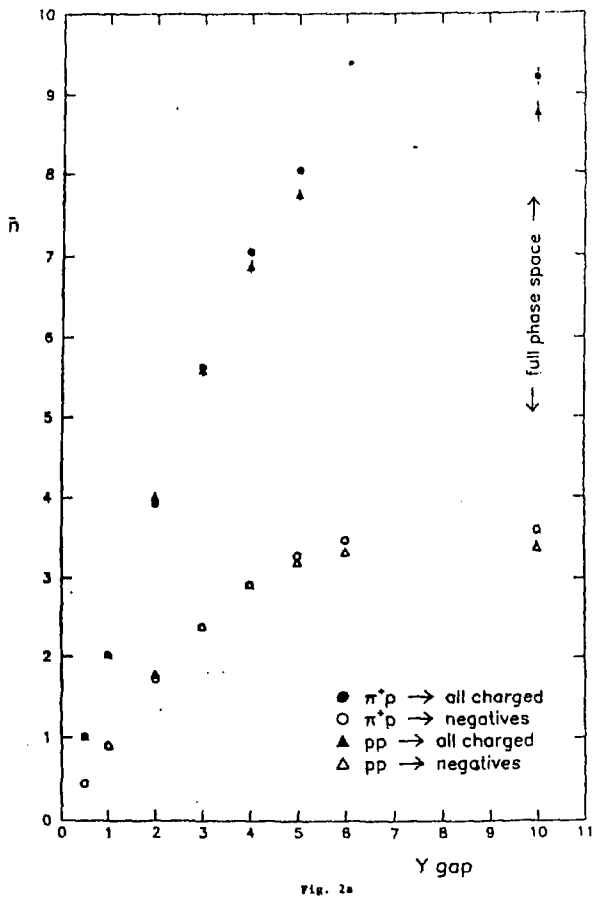
n̄
Y gap
full phase space
π⁺p → all charged
π⁺p → negatives
pp → all charged
pp → negatives

Fig. 2a

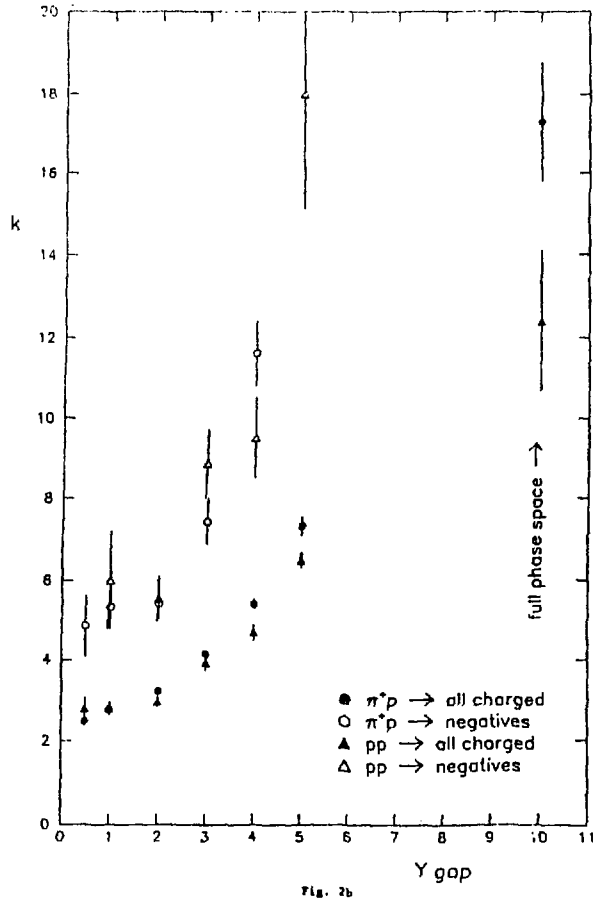
k
Y gap
full phase space
π⁺p → all charged
π⁺p → negatives
pp → all charged
pp → negatives

Fig. 2b

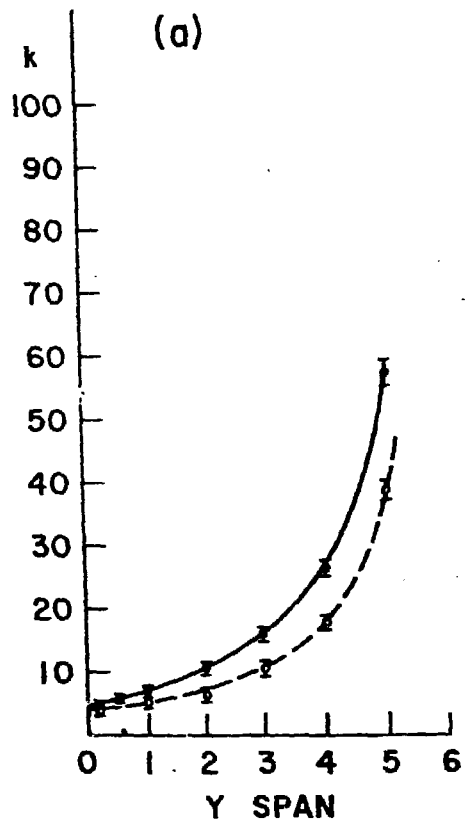

Fig. 3

DIFFRACTION DISSOCIATION

IN π^+/K^+p INTERACTIONS AT 250 GeV/c

NA22 Collaboration

Aachen - Antwerp/Brussels - Berlin(Zeuthen) - Cracow - Helsinki - Moscow - Nijmegen - Serpukhov - Warsaw - Yerevan

presented by
R. Wischnewski
Institut fuer Hochenergiephysik, Zeuthen, GDR

Abstract:

Preliminary results on single diffraction dissociation in π^+/K^+p interactions at 250 GeV/c are presented. The cross sections obtained for meson diffraction are 2.23 ± 0.27 mb for π^+p and 1.68 ± 0.24 mb for K^+p. For proton diffraction we derived 1.78 ± 0.26 mb for π^+p and 1.30 ± 0.20 mb for K^+p. To study the hadronization of diffractive systems, the dependence of the average charged multiplicity on the diffractive mass is given and compared to e^+e^- data.

1. INTRODUCTION

Diffraction dissociation represents an important component of particle production in hadron-hadron interactions at high energies and has been interpreted within the framework of the Regge theory in terms of pomeron exchange /1/. Recently evidence has been found for single-quark-pomeron interactions in proton diffraction at the ISR /2/ supporting modern approaches to understand the dynamics of diffraction at the parton level. On the other hand the hadronization properties of diffractively excited systems have been studied /3,4/ and interesting similarities to e^+e^--interactions were observed.

We present preliminary results on single beam and target diffraction dissociation in π^+/K^+p interactions at 250 GeV/c, the highest energy so far reached for positive meson-hadron collisions.

After discussion of the experimental data the beam and target diffraction cross sections are extracted. We confront these cross sections to data from other experiments and compare the dependence of the average charged multiplicity on the diffactively produced mass to e^+e^- data.

2.EXPERIMENTAL DATA

The experiment has been performed in the European Hybrid Spectrometer (EHS) with the Rapid Cycling Bubble Chamber (RCBC) as a vertex detector exposed to a tagged meson enriched beam of 250 GeV/c at the CERN SPS. Details on the experimental set-up and the minimum bias interaction trigger are described elsewhere /5/.
The present study is based on about 11% of the total amount of 600 k pictures taken in two running periods. All completely measureable events (~90%) were passed through the geometry program GEOHYB resulting in 12356 π^+p and 4748 K^+p collisions on a DST. Additional event qualitiy criteria have been applied:
(i) a well measured and reconstructed beam,
(ii) a completely reconstructed topology and charge balance,
(iii) a momentum measurement of $\Delta p/p<25\%$ for all secondary tracks and reliable fits for spectrometer tracks.
Exclusion of elastic events was done on the basis of a cut in missing transverse and missing longitudinal momentum. We end up with 6589 π^+p and 2541 K^+p interactions representing a sensitivity of 0.32 and 0.14 events/ μb, respectively. For proton identification the mass dependent fits in GEOHYB have been used because ionisation scan results were not yet available. For the fastest positive track the mass of the beam particle was adopted, all other tracks are interpreted as pions.

3.BEAM AND TARGET DIFFRACTION DISSOCIATION

The extraction of the diffractive signal has been done in different experiments using rather different methods. Since the EHS-Spectrometer offers excellent momentum resolution over the whole momentum range we look for the characteristic quasi-elastic target and beam diffractive signal in the Feynman-x distributions of the forward and backward leading particles, as done in refs./6,7/.
First we discuss beam diffraction. Figures 1a)-e) present for p events the distributions of Feynman-x, $x_F = 2p_L^*/\sqrt{s}$, of the slowest positively charged hadron, h^+(slowest), for different topologies (raw data not corrected for trigger inefficiencies). The leading proton signal is clearly visible for the 2- and 4-prongs. For the higher topologies the signal to background ratio can be increased by restricting the x_F values of all other charged particles to the region $x_F > -0.05$ (see hatched histograms in fig.1). A hemisphere cut at this value leaves the leading proton signal almost unchanged. Enhancements are observed for 6- and 8-prongs, while no clear signal for $n_{ch} \geq 10$ is seen at the present level of statistics.
We interpret the leading signals as beam diffraction according to the reaction

$$h^+ + p \rightarrow p + X \qquad (1)$$

where h^+ stands for π^+ or K^+ and X denotes the diffractively produced system.
The diffractive cross sections are obtained from the $x_F(h^+\text{slowest})$ - distributions for each multiplicity separately by counting events above a smooth handdrawn background (see fig.1) in the region $x_F(h^+\text{slowest}) < x_F^{cut}$. For $n_{ch} \geq 6$ the hemisphere cut in addition has been used. The x_F^{cut}-values vary from -0.95 to -0.75 for 2- to 8-prongs as indicated in fig.1. Table 1 contains for π^+p and K^+p the resulting number of diffractive events

together with the diffractive trigger efficiencies (obtained from MC-simulations) and the cross sections for $n_{ch} \leq 8$. The errors quoted take into account statistical as well as systematic uncertainties.
We obtained an overall beam single diffraction cross section of 2.23 ± 0.27 mb for π^+p and 1.68 ± 0.24 mb for K^+p interactions for $n_{ch} \leq 8$.
For the following analysis we define the beam diffractive event sample by the same cuts in $x_F(h^+\text{slowest})$ as used for calculating the cross sections. In addition we require the slowest particle h^+(slowest) to be identified as a proton. The non-diffractive background in this sample amounts to 12 - 30 % for 2- to 8-prongs (see fig.1).
The distributions of the effective mass squared M_x^2 for the π^+p diffractive sample calculated as missing mass squared recoiling against the leading proton are shown in fig.2 for topologies up to 8-prongs and also for $\geq$10-prongs (not corrected for trigger efficiencies). The events with a multiplicitiy $n_{ch} \geq 10$ are included here and later in the multiplicity analysis. As can be seen low multiplicities are dominiated by the quasi-elastic peak typical for low mass diffractive processes. With growing multiplicity the M_x^2-distribution gets flatter not showing a distinct low mass enhancement. Such a behaviour has also been found in π^-p interactions at 147 GeV/c /7/ and at 205 GeV/c /8/.

The extraction of the target diffraction signal is done similar to the case of beam diffraction. Feynman-x cuts applied to the forward leading particle range from 0.95 to 0.75 for 2- to 8-prongs, the hemisphere cut for $n_{ch} \geq 6$ is 0.1. The topological cross sections are given in table 2. We obtained an overall target single diffraction dissociation cross section of 1.78 ± 0.26 mb for π^+p and 1.30 ± 0.20 mb for K^+p.

4.COMPARISON OF CROSS SECTIONS AND AVERAGE CHARGED MULTIPLICITIES

A comparision of the total single diffractive cross sections derived in sect.3 with values determined by two other methods is presented in table 3. The first method consists in fitting the topological charged multiplicity distribution measured by this experiment for multiplicities $\geq$10 with a negative binomial and counting the excess of events when extrapolating the fitted curve to multiplicities <8 /9/. The second one is a model parametrization of toplogical cross sections suggested by Goulianos /1,10/. The agreement of both the total diffactive cross sections and the multiplicity distribution can be regarded as quite satisfactory within the errors. Nevertheless, the first method seems to overestimate the low multiplicity cross sections. Diffraction cross sections for different hadrons can be related assuming factorization /1/. As a consequence the cross sections of a hadron dissociating on different targets scale as the corresponding elastic cross sections while those of different hadrons dissociating on the same target scale as the corresponding total cross sections. The relevant relations for our analysis are

$$\frac{\sigma(K^+ p \to K^+_{sd})}{\sigma(\pi^+ p \to \pi^+_{sd})} = \frac{\sigma_{tot}(K^+p)}{\sigma_{tot}(\pi^+p)} \qquad (2)$$

and

$$\frac{\sigma(p \xrightarrow{K^+} p_b)}{\sigma(p \xrightarrow{\pi^+} p_b)} = \frac{\sigma_{el}(K^+p)}{\sigma_{el}(\pi^+p)} \qquad (3)$$

The left hand side of eq.(3) gives 0.75 ± 0.14 to be compared with 0.84 ± 0.01 for the right hand side. For eq.(4) the values to be compared are 0.73 ± 0.16 and 0.79 ± 0.04. The agreement is satisfactory within the errors.
Next we discuss the energy dependence of the cross sections. Comparing our K^+p data with available data at lower energies /11,12/ we notice a rise of (0.74 ± 0.28) mb for the beam and of (0.38 ± 0.23) mb for the proton diffraction in the energy range from 32 to 250 GeV/c. The contribution from the 2- and 4-prongs to this rise is about 45 % in the case of beam and about 20 % in the case of proton diffraction. Due to lack of data no such comparison can be carried out for π^+p.
To confront our results with single diffraction data for other meson-proton and (anti)proton-proton collisions we present in fig.3 a compilation of one vertex proton single diffraction cross sections from $\sqrt{s} \sim 6$ GeV up to $Sp\bar{p}S$ collider energies. In this plot the meson $h^\pm$ induced proton diffractive cross sections $\sigma(p \xrightarrow{h^\pm} p_b)$ are scaled up to the one vertex proton diffraction cross section $\hat{\sigma}(p \xrightarrow{p} p_b)$ according to the factorization hypothesis by

$$\hat{\sigma}(p \xrightarrow{p} p_b) = \frac{\sigma_{el}(pp)}{\sigma_{el}(h^\pm p)} \sigma(p \xrightarrow{h^\pm} p_b) \qquad (3a)$$

while the pp data are reduced by a factor of 0.5. The data are taken from refs. /6,7,11,13-16/. For ISR /13/ and UA4 /14/ the high mass cross sections ($M_x^2/s < 0.1$) are chosen since our data include diffractive contributions from even a slightly higher M_x^2/s region. The UA5 results at 200 and 900 GeV/c are given only for $M_x^2/s < 0.05$ /15/ (according to the ISR and UA4 data this lower mass cut leads to a reduction of the cross sections by 0.3 - 0.6 mb).
Within the caution necessary when comparing the cross sections obtained with rather different methods we find our values not to be inconsistent with a slight increase of diffractive cross sections in the energy range considered.

To study hadronization properties we give in fig.4 the dependence of the average charged multiplicity of the diffractive particle system $\langle n_{ch} \rangle$ on its mass M_x for meson and proton diffraction. Systematic uncertainties are estimated to be 0.5 units . With the present statistics no difference between π^+p and K^+p data is observed. Plotting $\langle n_{ch} \rangle$ versus the available energy $E_A = M_x - m_h$ (not shown) where h refers to π^+, K^+ or p we find agreement between the meson and proton diffraction curves as obtained already at lower energies /4/. The multiplicity dependence in our experiment also agrees with π^- diffraction data at 205 GeV/c /3/.
A comparison of hadronization properties of quark-antiquark systems produced in e^+e^- annihilation and in meson diffraction is suggested in ref./3/. Assuming jet universality similarities should be found. As a first step we compare in fig.5 the average charged multiplicity from π^+-diffraction with those from hadron production in e^+e^- interactions at appropriate energies $\sqrt{s} = M_x$ /17/ (our multiplicities have been scaled up since e^+e^- data contain π^0 from K^0_S - decays /16,17/). A resonable correspondence is found for masses $M_x \geq 2.5$ GeV. The discrepancy at lower masses can be attributed to a low multiplicity cut-off in the Adone-data.

5. SUMMARY

We obtained the following preliminary results:

(i) The single meson diffraction cross sections for topologies up to $n_{ch} = 8$ are 2.23 ± 0.27 mb for $\pi^+ p$ and 1.68 ± 0.24 mb for $K^+ p$. The corresponding values for proton diffraction are 1.78 ± 0.26 mb in $\pi^+ p$ and 1.30 ± 0.20 mb $K^+ p$ collisions.

(ii) Factorization of the diffractive vertex is found to hold at our energy. Our cross section values scaled up to one vertex single proton diffraction are not inconsistent with a slight increase of diffractive cross sections in the energy range from $\sqrt{s} \sim 6$ GeV up to collider energies.

(iii) Within the present accuracy of the data the dependence of the average charged multiplicity of the meson diffractive system on its mass is found to be compatible with hadronic multiplicities in e^+e^- annihilation.

Acknowledgements

It is a great pleasure to thank all people who contributed to preparation and running the EHS as well as scanning and measuring the films.

References

/ 1/ K. Goulianos, Phys. Rep. 101 (1983) 169
/ 2/ A.M. Smith et al., Phys. Lett. 163B (1985) 267
/ 3/ S.P. Misra et al., PRL 45 (1980) 322
/ 4/ R.L. Cool et al., PRL 48 (1982) 1451
/ 5/ M. Adamus et al., Nijmegen preprint HEN 262 (1986) to be published in Z. Phys. C
/ 6/ R. Goettgens et al., Z. Phys. C19 (1983) 283
/ 7/ D. Brick et al., Phys. Rev. D21 (1980) 1726
/ 8/ F.C. Winkelman et al., Phys. Rev. Lett. 32 (1974) 121
/ 9/ F. Meiers, private communication
/10/ P.v. Hal, private communication
/11/ J. Saudraix et al., Z. Phys. C5 (1980) 105
/12/ E.A. de Wolf et al., Nucl. Phys. B246 (1984) 431
/13/ J.C.M. Armitage et al., Nucl. Phys. B194 (1982) 365
/14/ V. Palladino, CERN/EP-154, contribution to the Workshop on Elastic and Diffractive Scattering, 3-6 june 1985, Chateau de Blois, France
/15/ Ch. Geich-Gimbel, these proceedings
/16/ A. Wroblewski, Proceedings of the XIV International Symposium on Multiparticle Dynamics, 22-27 june 1983, Lake Tahoe, p. 573 and references therein
/17/ G. Wolf, DESY 81-086

Table 1: Cross sections for single beam diffraction

	π^+p			K^+p		
prongs	events	ε *)	σ, μb	events	ε *)	σ, μb
2	194	0.80	485 ± 130	85	0.80	441 ± 128
4	267	0.62	996 ± 190	89	0.62	742 ± 166
6	191	0.95	547 ± 104	55	0.90	355 ± 89
8	67	0.95	205 ± 90	20	0.95	138 ± 66
total			2233 ± 268			1676 ± 237

Table 2: Cross sections for single target diffraction

	π^+p			K^+p		
prongs	events	ε *)	σ, μb	events	ε *)	σ, μb
2	144	0.48	600 ± 164	49	0.48	434 ± 134
4	171	0.57	694 ± 157	62	0.57	563 ± 122
6	72	0.55	356 ± 111	20	0.55	211 ± 71
8	39	0.85	133 ± 60	12	0.85	93 ± 55
total			1783 ± 260			1301 ± 202

*) Trigger efficiencies for diffractive events

Table 3: Comparison of different methods in deriving total single diffractive cross sections σ, μb

	π^+p			K^+p		
prongs	this work	negative binom.	Goulianos param.	this work	negative binom.	Goulianos param.
2	1085 ± 209	1100	893	875 ± 185	1060	797
4	1690 ± 246	1900	1581	1305 ± 206	1700	1296
6	903 ± 152	750	821	566 ± 144	680	619
8	338 ± 108	120	313	231 ± 86	170	238
10			142			110
total	4016 ± 373	3870	3750	2977 ± 312	3610	3060

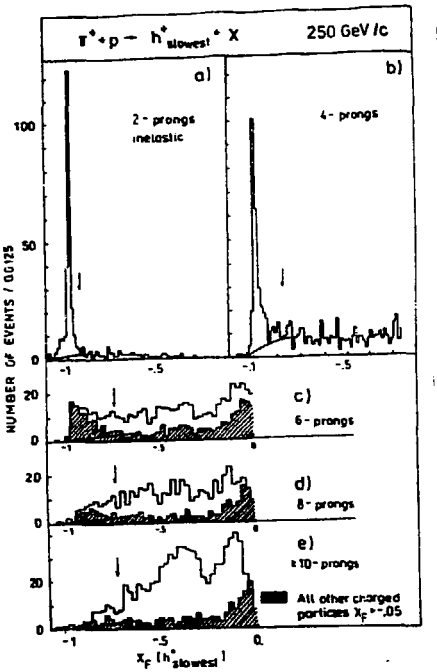

Fig. 1: X_F- distribution of the slowest positive hadron, h^+slowest, for inelastic 2- to ≥10-prongs (shaded area = events with all other charged particles at $x_F > -.05$; full curve = estimated non-diffractive background; arrows = x_F- cuts for diffractive selection

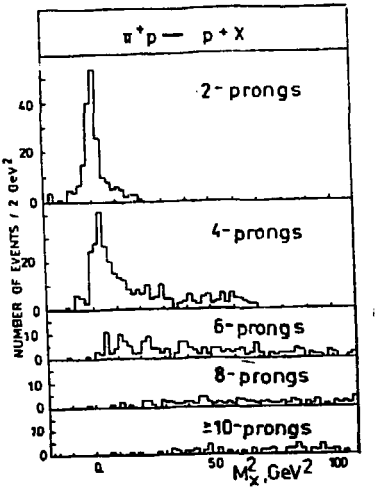

Fig. 2 The distribution of the missing mass squared to the proton, M_X^2, for the selected π^+ diffraction sample.

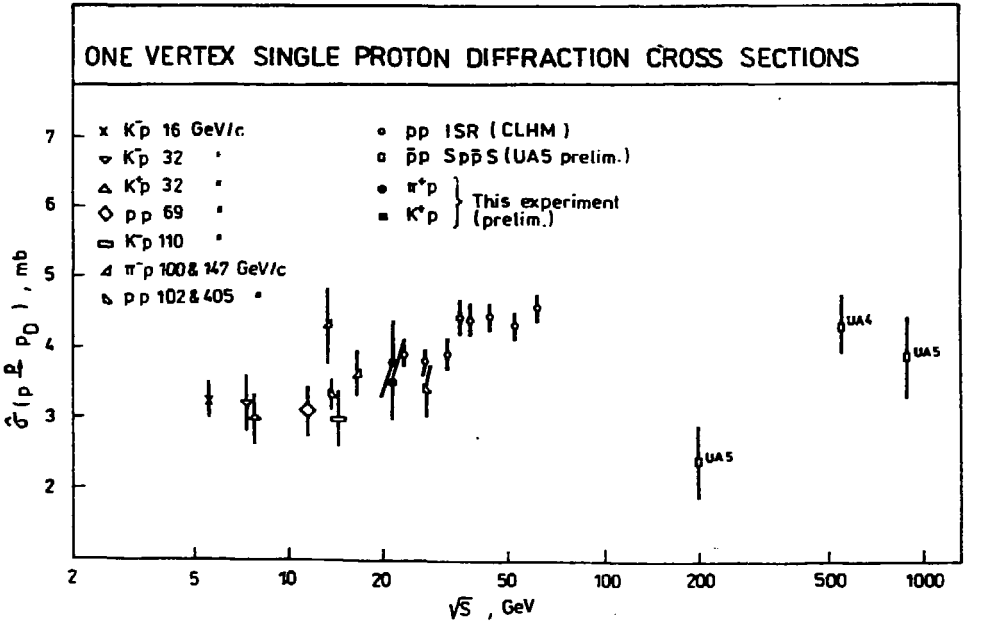

Fig. 3: Compilation of one vertex proton single diffractive cross sections $\hat{\sigma}$ ($p \to p_D$) up to collider energies. Meson-proton data are scaled acc. to eq.(3a) (see text for details).

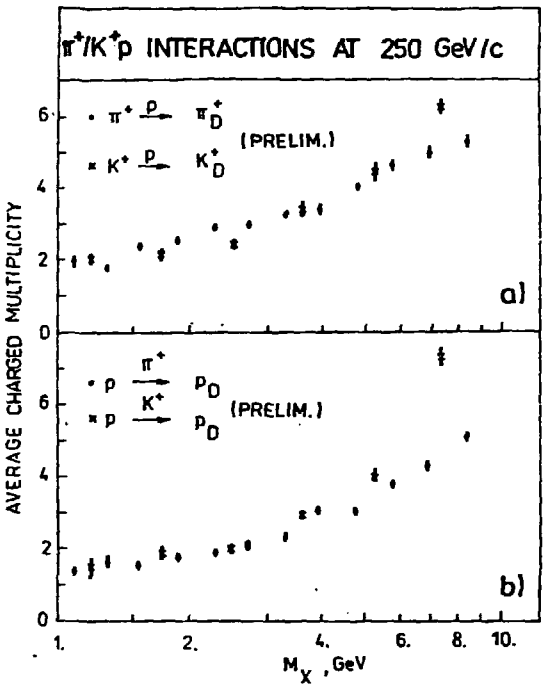

Fig. 4: The average charged multiplicity of the diffractive (a) meson- and (b) proton - system as a function of its mass M_X.

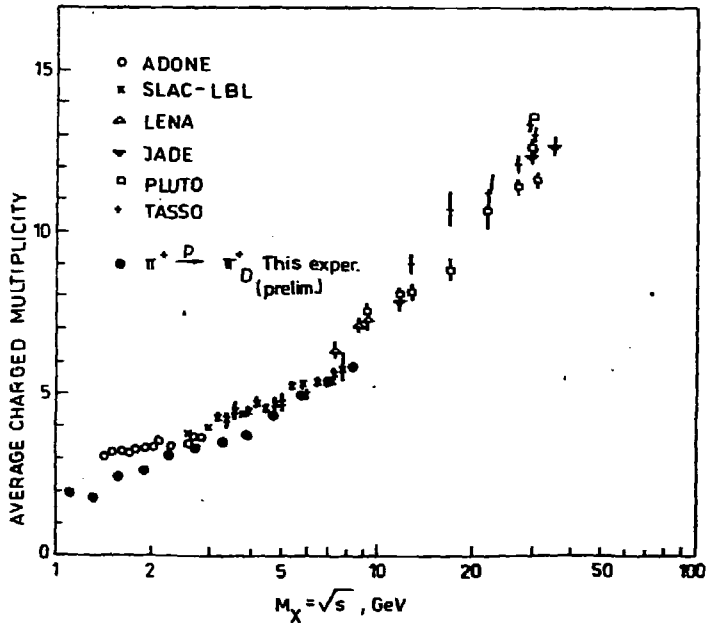

Fig. 5: Comparison of the average charged multiplicity of the diffractive π^+ system in π^+p interactions as a function of its mass M_X with e^+e^- data at $\sqrt{s} = M_X$.

APPLICATION OF MANY-BODY THEORY TO PROBLEMS OF GAUGE FIELD THEORIES*

B. Faber, H. Nguyen and D. Schütte
Institut für Theoretische Kernphysik der Universität Bonn
Nussallee 14-16, D-5300 Bonn, F.R. Germany

Summary:
A new proposal for the calculation of the spectrum of gauge field theories is discussed. The basic principles are the application of non-perturbative many-body techniques to the cutoff field-theoretical Hamiltonian and a check of the continuum limit. Simple many-body approximations (Bogoliubov and Brueckner-approach) fail to yield correct scaling. Possible extensions are discussed.

Introduction

The motivation for the investigation which shall describe in the following, is threefold:
(i) The calculation of the QCD spectrum by lattice gauge theory - though undoubtedly the presently most advanced non-perturbative method - reveals the structure of hadrons only in a limited way - in fact one is left with the feeling that the computer knew more about the dynamics of the gauge fields during the Monte-Carlo run than we do afterwards[1].
(ii) This makes it desirable to develop alternative techniques which - if successful - throw more light the way how quarks and gluons combine to form a hadron. Since any field-theoretical problem is a many-body problem (in fact, the vacuum problem is very similar to nuclear matter), we propose to apply non-perturbative many-body techniques to the field-theoretical Hamiltonian[2]. We hope that the experience with many-body theory in other domains of physics (especially in nuclear physics) might give some guidance to this admittedly rather daring attempt.

(iii) There is an increasing host of "QCD inspired" quark models (MIT-, cloudy-, little-, Warsaw-, big-bag; constituent, soliton, chiral soliton, etc.) trying to compute hadron properties phenomenologically. The conceptual relation of these models to QCD might be given through such a canonical formulation of the quantum field theory[3].

It is the purpose of this talk to give a general survey on the many-body approach to gauge field theories which we are pursueing at the moment in Bonn. Technical details will be left out and will be referred to in the literature. The talk is organized as follows: in sect. 2 we shall discuss renormalization, covariance and the construction of the gauge field Hamiltonian. In sect. 3 we describe the prescription for our regularisation and the many-body techniques we tried up to now in order to approximate vacuum and glueball states. Results will be presented in sect. 4 and an outlook on possible generalizations will be discussed in sect. 5.

2. Basic principles

We shall first discuss the basic principles for our procedures. In order to have a definite example, we consider the case of a SU(n) Yang-Mills field theory (without quarks). Canonical quantization yields a Hamiltonian[4]

$$H(\vec{A},\vec{E})$$

depending on the canonically conjugate fields $\vec{A}$ and $\vec{E}$ ($A_j, E_j \in$ Lie SU(n), j=1...3)

2.1 Renormalization

This Hamiltonian, describing interacting gluons, will be pathological in the Fockspace yielding the well-known infinities of any non-trivial field theory. The standard way to deal with this problem is renormalization which can be summarized in the following way:

(i) Introduce a regularization of H by a cutoff (M,Ω) (momentum, volume-cutoff) yielding H(g,M,Ω) (g = unrenormalized coupling constant). For fixed M, the "thermodynamical" limit Ω→∞ is well defined[2].
(ii) Introduce a "running coupling constant" g(M). If g(M) is suitably chosen, observables computed with

$$H(g(M),M,\Omega)$$

should have a smooth limit for M→∞. (H is derived from a renormalizable field theory!)
(iii) For large M, g(M) fulfilling the condition (ii) should be the universal function

$$(1)\quad g(M) = g_0^2/(1+ag_0^2\ln(M/M_0)); \quad a = 22/16\pi^2 \text{ for SU(3)}; \quad g_0 = g(M_0).$$

The standard example of such a renormalization is the lattice QCD in the Kogut-Süsskind formulation[1,5], our special prescriptions will be given in sect. 3.

2.2 Covariance

An important question is how, in principle, Poinaré invariance can be restored within such a procedure: of course, invariance is broken through the introduction of the cutoff M (we take Ω→∞ for these considerations, restoring translation and rotation invariance, but boost invariance keeps to be violated). Thus the "cutoff generators" of the Poincaré group

$P^\mu(g(M),M)$ (Hamiltonian, momentum)

$L^{\mu\nu}(g(M),M)$ (angular momentum, boost generators)

will not fulfil the correct commutation relations. (As they do, in any chosen gauge, at least formally for M→∞[6]).

However, if one considers some finite set of energy-eigenstates $\Psi_\alpha(M)$ (α = momentum, spin, mass and other quantum numbers) it is plausible that for large enough M the action of the operators $P^\mu, L^{\mu\nu}$ becomes consistent with the Poincaré algebra up to an arbitrary small deviation and yields then the well-known formulas for the irreducible representations of the Poincaré group characterized by mass and spin. Within lattice calculation, such checks have been untertaken with encouraging success[7].

2.3 The Yang-Mills Hamiltonian

For a gauge field theory, the construction of H(g,M,Q) via Noether's theorem is made more difficult by the fact that the independent variables of the theory are equivalence classes (orbits) of gauge fields where two fields have to be identified if they can be related by a gauge transformation.

The standard way to deal with this problem is the introduction of a gauge fixing condition (choice of representatives). Because of compatibility with rotation and translation invariance, the most convenient condition is (starting from the temporal gauge $A_0=0$)[4]

$$\vec{\nabla}\vec{A} = 0 \tag{2}$$

This yields the Coulomb gauge Hamiltonian

$$H = \frac{1}{2}\int d^3x \mathrm{tr}(E^2+B^2) + V_c(A,E) + V_{Fad}(A) \tag{3}$$

containing a Coulomb interaction $V_c(A,E)$ - similar to Dirac-Schwinger QCD, but of arbitrary order in A - and a Faddeev-Popov term $F_{Fad}(A)$ which guarantees that the spectrum of H is independent from the choice of the gauge[4]. Details of this Hamiltonian are described in ref. 2.

It should be noted that the transversality condition (2) does not fix the representative: independent representatives (in sense of gauge transformations) are given by those transversal gauge potentials A which lie inside the Gribov horizon[8]. However,

this restriction to the amplitude of A appears to be automatically fulfilled within our calculational scheme because V_c and V_{Fad} are singular at the Gribov horizon which forces the carrier of wave functionals $\Psi(A)$ to lie inside this boundary. This property of the Coulomb gauge Hamiltonian was first observed by Cutkosky[9].

3. Many-body techniques

3.1 Regularization

For the purpose of applying our many-body techniques, it is convenient to define a regularization of H in the following way:

Introduce cutoff field operators $A_{\Omega,M}, E_{\Omega,M}$ by an expansion into a plane wave basis with finite volume Ω (yielding discrete momenta $\vec{k} = 2\pi\Omega^{-1/3}(n_1,n_2,n_3)$, n_j integer) and by limiting this expansion by a momentum cutoff M ($|\vec{k}|<M$). This yields:

$$\vec{A}_{M,\Omega} = \sum_k \frac{1}{\sqrt{2\Omega|k|}} \vec{e}(k,r) a_{kr} + h.c.$$

$$\vec{E}_{M,\Omega} = -i\sum \sqrt{\frac{|k|}{2\Omega}} \vec{e}(k,r) a_{kr} + h.c. \qquad (4)$$

Here, a^+_{kr}, a_{kr} are creation and annihilation operators obeying the standard commutation relations, $\vec{e}(k,r)$ (r = 1,2) are polarization vectors with different helizity guaranteering transversality[2], colour indices are suppressed.
Inserting these expressions for $\vec{A}_{M,\Omega}$, $\vec{E}_{M,\Omega}$ into (3) yields the cutoff Hamiltonian

$$H(g,M,\Omega) = H(a^+,a) .$$

The eigenvalue problem of $H(a^+,a)$ in now a well-defined many-body problem where standard techniques may be applied.

The "thermodynamical" limit $\Omega \to \infty$ is easily taken in the expression for any observable by replacing

$$(5) \qquad \frac{1}{\Omega} \sum_{k} \to \frac{1}{(2\pi)^3} \int d^3k$$

We mention that this definition of the cutoff is not the only possibility. Cutkosky[3,9] has investigated an alternative by introducing the volume cutoff through a compactification of R^3 by S^3 and using expansions in terms of hyperspherical functions on S^3 instead of plane waves.

3.2 Exp S-techniques

General many-body theory - which is also applicable to the particle number non-conserving bosonic Hamiltonian $H(g,\Omega,M) = H(a^+,a)$ - shows that the ground state Ψ (= physical vacuum state) has the structure

$$\Psi = e^S |0\rangle$$

where $|0\rangle$ is the bare vacuum obeying $a_{kr}|0\rangle = 0$ and S is a function only of the creation operators which can be expanded in terms of polynomials S_n of order 2,3,4,...

$$(6) \qquad S = S_2(a^+a^+) + S_3(a^+a^+a^+) + \ldots$$

(For the Yang-Mills theory, $S_1(a^+)$ is missing becsuse all operators S_n must be colour singletts).

The general procedure of standard many-body theory is now to define an approximation to Ψ by the following prescriptions:

(i) Truncate the expansion (6) with few terms. Keeping S_2 only would be a Bogoliubov approximation, including S_2 and S_3 we call YM-Brueckner theory in analogy to the nuclear matter approach.

(ii) Compute the expectation value

$$E(S) = \langle \Psi H \Psi \rangle / \langle \Psi \Psi \rangle$$

within a cluster expansion the order of which is adjusted to the order of the truncation of (6).

The cluster expansion is defined in analogy to the Mayer expansion of the classical grand partition function or to the hypernetted chain expansion of the Yastrow approximation for the ground state of Liquid He^4 [10]. It is obtained by introducing a linked diagram expansion for E(S) and by classifying these diagrams into reducible and irreducible clusters (like in the case of the Mayer expansion). The approximation is then given by summing up all diagrams which do not contain any irreducible cluster of some minimal order.

Within YM-Brueckner theory, diagrams containing irreducible three- (and more) body clusters (yielding irreducible nine- (and higher) dimensional integrals) are neglected. Details of this procedure are described in refs. 2,11.

(iii) The expansion coefficients defining the operators $S_2, S_3 \ldots$ are to be determined by applying the Ritz-variational principle to the (approximate) ground state energy expectation value E(S).

4. Results within the YM-Brueckner approach

We have performed numerical calculations for the ground state and analogously for glueball states within the YM-Brueckner theory. The results can be characterized as follows:

(i) An important vacuum structure function is the (on-shell) gluon propagator

$$\lambda_k = \frac{1}{\sqrt{(2\pi)^3}} \int e^{i\vec{k}(\vec{x}-\vec{y})} \langle \Psi | \mathrm{tr} \vec{A}(\vec{x}) \vec{A}(\vec{y}) \Psi \rangle / \langle \Psi | \Psi \rangle$$

Of course, we have $\lambda_k = 1/|k|$ for the free case ($\Psi = |0>$). Gribov[8] conjectures that this function goes to zero (instead of ∞) for small k yielding in this way a suppression of small momenta (large distances), a (rather weak) signal of confinement.

Our variational approach gives such a structure for λ_k[11]. The reason can be traced back to the singularity of H at the Gribov horizon. Similar results were obtained by Cutkosky[9].

(ii) A more direct indication of confinement would be the occurrance of a $1/k^4$-singularity of the Coulomb (longitudinal gluon-) propagator (the function σ_k/k^2 in ref. 2). Gribov conjectured that this happens if Ψ is dominated by configurations very near to the horizon.

This structure is not confirmed within our approach, in fact it is just the variational principle which - within the YM-Brueckner approximation - prevents the occurrance of such a singularity of the longitudinal gluon propagator. Thus the YM-Brückner-approximation does not yield confinement between static quarks.

(iii) A computation of the glueball masses within the same approximation (we have considered the quantum numbers 0^{++},0^{-+} 2^{++}) and a study of the continuum limit of these quantities (which is much easier performed than in lattice calculations) reveals that this missing of confinement is not inconsistent: fixing g(3 MeV) = 1 from lattice results and inserting g(M) from eq. (1), we do not obtain scaling, i.e. independence of the glueball masses $\varepsilon(M)$ from M. We rather find for large M

$$\varepsilon(M) = 0.5\ M$$

Thus we conclude that the YM-Brueckner approach though a rather natural generalization of the standard many-body techniques fails to approximate the low mass spectrum of H, taking g(M) from (1) yields high lying states which go to infinity for $M \to \infty$.

5. Outlook on possible generalizations

There exist several routes for the improvement of our YM--Brueckner scheme.

A first source of error could be the cluster expansion for our expectation value. This we have checked numerically and we found that this technique yields good approximations (higher orders yield only correction ≈ 1%).

Thus apparently the truncation of the ansatz (6) with only 2 terms must be bad. Apparently, the small -k behaviour of Ψ must be improved. From the alternative Hamiltonian approach, the Kogut-Susskind formulation which is at present pursued by Furmanski and Kalowa[1], one may guess that "loop-like" states should be important. Our proposal, therefore, is that the ansatz for S might be essentially improved by allowing string-like integral equations for S where the kernel must be determined from the variational principle. (S would then contain polynomials of arbitrary order in a^+).

Another strategy could be a variation of the gauge fixing condition $\vec{\nabla}\vec{A} = 0$. It is clear that the structure of the eigenstates depends on the choice of the gauge, and it might be that a given approximation is good in one gauge, but bad in another gauge. Especially non-linear gauge-fixing conditions $F(\vec{\nabla}\vec{A},\vec{A}^2)=0$ could provide a non-trivial freedom to improve on our approximation.

Summarizing we conclude that there seems to exist no simple way to approximate the solution of non-abelian gauge theories by many-body techniques. The two main attempts, discussed at present, seem to have both advantages and disadvantages:

The "loop-space expansion"[1] has the advantage of having built in confinement in the strong coupling limit - but the reality, which has to be computed, is weak coupling and it is still open whether one will be able to tackle the complexities of the problem in this limit. Our fixed gauge approach has the advantage that the abelian case is always trivially correct, that the large volume limit can be taken and that the calculation of the continuum limit might be simpler, but a guess of the correct ansatz for eigenfunction seems to be difficult. It has to be decided by the future which approach will be finally successful.

+Supported by the Deutsche Forschungsgemeinschaft

References

1) W. Furmanski and A. Kalowa, Yang-Mills-vacuum, an attempt of lattice loop calculus, preprint CALT 68-1330
2) D. Schütte, Phys.Rev. D 31, 810 (1985)
3) R.E. Cutkosky, Phys.Rev. Letters 51 (1983) 538
4) N.H. Christ and T.D. Lee, Phys.Rev. D22, 939 (1980)
5) J. Kogut and L. Süsskind, Phys.Rev. D11, 395 (1975)
6) H. Cheng and E.C. Tsai, Canonical Quantization of Non-Abelian Gauge Theories, MIT-preprint 1985
7) G. Schierholz, private communication
8) V.N. Gribov, Nucl.Phys. B139, 1 (1978)
9) R.E. Cutkosky, Phys.Rev. D30 (1984) 447
10) See, e.g., S. Rosati and S. Fantoni, in The Many-Body Problem, Lecture Notes in Physics No. 138, edited by R. Guardiolo and J. Ros (Springer, Berlin, 1981), p. 1
11) B. Faber, H. Nguyen and D. Schütte, The Structure of the Yang-Mills Field Theory in the Frame of Many-Body Approximations, to be published in Phys. Rev. D

THE GLUON CONDENSATION IN THE PURE GAUGE THEORY

R. Mańka

Silesian University , Katowice , Poland

The effective mass gauge theory is constructed. The gluon condensation in this theory is examined.

The variational method [1] constructed on the Bogolubov inequality [2] and on the canonical quantization approach [3] to the pure gauge theory is presented . It allows to obtain the effective potential for SU(n) gauge theory which gives the first-order phase transition . The transverse gluon masses and the phase transition temperature is established .

The Lagrangian density for SU(n) , the pure gauge field , is equal to

$$\mathcal{L} = -\frac{1}{4}F^a_{\mu\nu}F^{a\mu\nu} - \partial_\mu B^a A^{a\mu} + \frac{1}{2}\xi B^a B^a - i\partial^\mu \bar{c}_a \nabla^{ab}_\mu c_b \quad , \tag{1a}$$

with

$$F^a_{\mu\nu} = \partial_\mu A^a_\nu - \partial_\nu A^a_\mu + g f_{abc} A^b_\mu A^c_\nu \quad , \tag{1b}$$

and

$$\nabla^{ab}_\mu = \delta^{ab}\partial_\mu - g f_{abc} A^c_\mu \quad . \tag{1c}$$

The Lagrangian (1) is invariant under the BRS [4] transformation which defines the physical subspace $\mathcal{H}_{ph}$ in the state space $\mathcal{H}$ with indefinite metric . In general , only transverse gluons belong to the $\mathcal{H}_{ph}$.

The variational method is based on the Bogolubov inequality for the free energy :

$$F \leqslant F_1 = F_0 + \langle H - H_0 \rangle_0 \quad , \tag{2a}$$

where

$$F_0 = -k_B T \cdot Tr_{\mathcal{H}_{ph}} \left(e^{-\beta H_0} \right) \quad , \tag{2b}$$

and $\langle H - H_0 \rangle_0$ is calculated with respect to the trial system / H_0 /. Only the physical states / two transverse gluons / should be taken into consideration during evaluations of the traces .

The trial system Lagrangian is postulated as

$$\mathcal{L}_0 = -\frac{1}{4} G^a_{\mu\nu} G^{a\mu\nu} - \partial_\mu \bar{B}^a \bar{A}^{a\mu} + \frac{1}{2} m^2 \bar{A}^a_{\mu T} \bar{A}^{a\mu}_T - i \partial_\mu \bar{c}^a \gamma^\mu c^a \quad , \tag{3a}$$

with

$$G^a_{\mu\nu} = \partial_\mu \bar{A}^a_\nu - \partial_\nu \bar{A}^a_\mu \quad . \tag{3b}$$

$\bar{A}^a_{\mu T}$ means that only the transverse gluons build the potentials . $\mathcal{L}_0$ is also BRS invariant what does not change the physical subspace $\mathcal{H}_{ph}$. Unfortunately , assumption that all gluons have the same mass m , violates the BRS symmetry . The transverse gluon mass m will be treated as the variational parameter . We assume that

$$A^a_\mu = \bar{A}^a_\mu + \alpha^a_\mu \quad , \tag{4}$$

where α^a_μ is the classical gauge field , what corresponds to the gluon condensation .

The free energy F_1 (2) may be interpreted as the energy of the classical gluon condensate

$$F_1 = \int d^3x \, \mathcal{H}_{eff} \quad , \tag{5a}$$

$$\mathcal{H}_{eff} = \alpha^{o,i} f^{a,oi} - \mathcal{L}_{eff} \quad , \tag{5b}$$

which effective Lagrangian is equal to

$$\mathcal{L}_{eff} = -\frac{1}{4} f^a_{\mu\nu} f^{a\mu\nu} + \frac{1}{2} M^{bd}_{\mu\nu} \alpha^{b\mu} \alpha^{d\nu} , \qquad (5c)$$

where $f^a_{\mu\nu}$ is the same as (1b) for the classical field α^a_μ. The gluon mass tensor $M^{bd}_{\mu\nu}$ is equal to

$$M^{ad}_{\mu\nu} = -g^2 f_{abc} f_{abd} \left(\langle \bar{A}^b_\varsigma \bar{A}^{b\varsigma} \rangle_0 g_{\mu\nu} - \langle \bar{A}^b_\mu \bar{A}^b_\nu \rangle_0 \right) . \qquad (5d)$$

The tensor mass means that transverse massive gluons propagate in the different way then these massless unphysical ones. The gluon mass may be determined from the experimentaly known value of

$$S = \frac{g^4}{4\pi^2} \langle F^a_{\mu\nu} F^{a\mu\nu} \rangle \approx -\frac{3n g^4}{16 N \pi^2} \langle \bar{A}^+_\mu \bar{A}^{+\mu} \rangle^2_0 , \qquad (6a)$$

which is equal to [5]

$$S = -(360 \pm 20\ MeV)^4 \qquad (6b)$$

/ $N=n^2-1$ for SU(n) gauge theory /. It allows us to calculate the gluon mass. If we assume that all gluons have the same mass m, what violates the BRS symmetry, then

$$\langle \bar{A}^b_\mu \bar{A}^d_\nu \rangle_0 = \frac{1}{4N} \delta^{bd} g_{\mu\nu} \langle \bar{A}^+_\varsigma \bar{A}^{+\varsigma} \rangle_0 , \qquad (7)$$

what gives us

$$m = \sqrt[4]{-\frac{3n g^2}{N} S} = 657\ MeV \pm 37\ MeV . \qquad (8)$$

More accurate calculations should include into account only the transverse gluons. This gives us

$$m = \sqrt[4]{-\frac{2n g^2}{N} S} = 594 \pm 33\ \ MeV. \qquad (9)$$

On the other hand the gluon mass may be calculated from the variational method . Taking into consideration the fact that only the transverse gluons could condensate , this gives us

$$\alpha_\mu^a = (0, -\varrho^a, -\varrho^a, 0) . \qquad (10)$$

The variational equation

$$\frac{\delta F_1}{\delta m^2} = 0 \qquad \text{gives} \qquad m^2 = \frac{n}{N} g^2 \varrho^2 \qquad (11)$$

where $\varrho^2 = \sum_a \varrho^a \varrho^a$.

The gluon mass is the function of the gluons condensate α_μ^a / or ϱ^a /. All further calculations lead to infinities , so the appropriate renormalization procedure is used . After that , and after introducing the convenient dimensionless values x , t

$$\varrho = \varrho_0 x \ , \qquad (12a)$$

with $T = T_1 t$, (12b)

$$\varrho_0 = \sqrt{\frac{N}{n}} \frac{\Lambda}{g} e^{\frac{11}{6}} \quad , T_1 = \frac{\Lambda}{\pi} e^{\frac{11}{6}} , \qquad (12c,d)$$

where Λ is the renormalization constant , we get

$$F_1 \sim U(x) = \frac{1}{4} x^4 \left\{ \ln x^2 - \frac{1}{2} \right\} + \frac{1}{2} t^2 x^2 . \qquad (13)$$

The potential U(x) is a typical one , leading to the discontinous phase transition / Fig. 1 / . It has a deeper minimum than U=0 for t=0 at $x_0 = 1$. Then the gluon mass is equal to

$$m = \Lambda e^{\frac{11}{6}} . \qquad (14)$$

It allows us to establish from (9) the renormalisation constant value

$$\Lambda = 95 \pm 5 \ \text{MeV} . \qquad (15)$$

The nontrivial minimum has the value $U=0$ at the phase transition point $x_c = \sqrt{e^{-1}}$ for the temperature $t_c = 1/\sqrt{2}$. Above this temperature there is still another local minimum till $t = 1$. The order parameter, being the shift describing the boson condensation leaps at $t = t_c$.

Knowing Λ we can calculate the phase transition temperature

$$T_c = T_1 t_c = 134 \pm 7 \ \text{MeV} , \qquad (16)$$

and the overheating temperature T_1

$$T_1 = 189 \pm 11 \ \text{MeV} . \qquad (17)$$

Above this temperature, certainly, the gluon condensate vanish. $T_1 \approx 200$ MeV on the lattice [6]. The fact that transverse gluons gain mass is analogous to the plasmon creation in QED.

References

1. R.Menka ,Annals of Phys. /N.Y./ 169 , in press
2. R.P.Feynman , Statistical Mechanics / Benjamin, New York , 1972 /
3. T.Kugo , I.Ojima , Prog.Theor.Phys.Suppl. 66 , / 1979 / , 1
4. C.Becchi , A.Rouet , R.Stora , Commun.Math.Phys. 42 , / 1975 / , 127
5. L.J.Reinders , H.R.Rubinstein , CERN preprint TH.3912 , / 1984 /
6. G.Martinelli , preprint LNF-84/58 P , / 1984 /

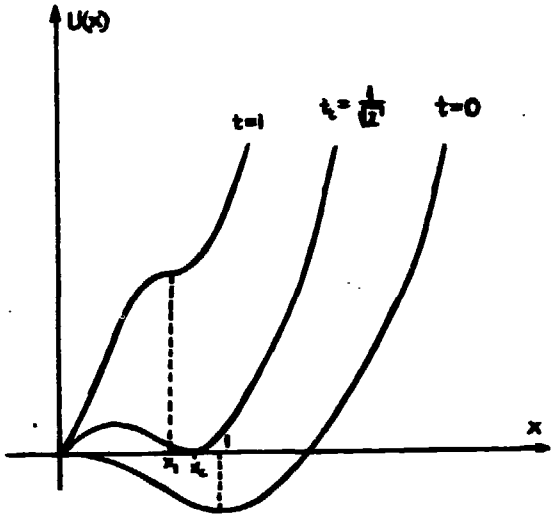

Fig. 1 . Dimensionless free energy for different temperatures .

RELATIVISTIC MODEL FOR THE LIGHT MESON DISTRIBUTION AMPLITUDES

Zbigniew Dziembowski
Institute of Theoretical Physics, Warsaw University
PL-00-681 Warszawa, Poland

Lech Mankiewicz
Nicolaus Copernicus Astronomical Centre of Polish Academy
of Sciences, PL-00-716 Warszawa, Poland

Presented by L. Mankiewicz

ABSTRACT

We calculate the spin - 0 and spin - 1 distribution amplitudes in a simple relativistic meson - wave - function model. With the basic concepts of the constituent quark model formulated within the light - cone approach we are able to reproduce the essential features of the Chernyak - Zhitnitsky amplitudes for the pion and ϱ as they are obtained from the QCD sum rules techniques.

One of the most interesting areas of application of Quantum Chromodynamics (QCD) are large momentum transfer exclusive reactions. These includes e.g. electromagnetic formfactors of bound state mesons and baryons as well as nuclei at large momentum transfer Q^2. A key result, which enables one to apply the perturbative QCD analysis to such reactions is the so called factorization theorem (#1-#2): at large momentum transfer the corresponding amplitudes factorize in form of a convolution of a hard amplitude T_H which is computable perturbatively and a process - independent "distribution amplitude" $\phi_{H_i}(x,Q)$ which contains all of the bound state non - perturbative dynamics of each of the inteacting hadrons:

$$\mathcal{M} = \int_0^1 T_H(x_j, Q) \prod_{H_i} \phi_{H_i}(x_i, Q)[dx] \quad (1)$$

Here T_H is the probability amplitude to scatter quarks with fractional momentum $0 \leq x_i \leq 1$ from the incident to final hadron directions. It is computable in the power series of strong

---

#1. G. P. Lepage and S. J. Brodsky, Phys. Rev. D22 , 2175 (1980).
#2. S. J. Brodsky, T. Huang and G. P. Lepage, in Quarks and Nuclear Forces, edited by D. Fries and B. Zeitnitz, Springer Tracks in Modern Physics, Vol. 100 (Springer - Verlag, New York, 1982).

coupling α_s taken at the scale $\sim Q^2$:

$$T_H(x,Q) = \frac{\alpha_s(Q^2)}{\pi} t^1(x,Q) + \ldots \qquad (2)$$

and it is the perturbative QCD part of the calculations. ϕ_{H_i} is the probability amplitude to find quarks in the wavefunction of hadron H_i colinear up to scale Q. In principle it contains all our (un)knowlegde about soft bound state dynamics. The measure $[dx] = \prod_i dx_i\, \delta(1 - \sum_k x_k)$ forces the longitudinal momentum conservation. The key to derivation of this factorization is the use of the Fock basis $\{\psi^n(x_i, k_i^\perp, \lambda_i)\}$ defined at equal $\tau = t + z$, rather than more familiar equal t Fock basis. Here λ_i are helicities and $x_i = (k_i^0 + k_i^3)/(p^0 + p^3)$ and $k_i^\perp$ ($\sum x_i = 1$, $\sum k_i^\perp = 0$) are the relative momentum coordinates of the constituents. The general decomposition of the bound state vector (say pion) in QCD reads (#2):

$$|\pi\rangle = |q\bar{q}\rangle\, \psi_\pi^{(2)} + |q\bar{q}g\rangle\, \psi_\pi^{(3)} + \ldots \qquad (3)$$

However, in the physical gauge like e.g. $A^+ = 0$ only minimal, or valence Fock states dominate the hard scattering, higher states being suppresed by additional powers of hard propagators in T_H .

From now on we shall focus our attention on the light - meson distribution amplitudes. Recently, Chernyak and Zhitnitsky (#3 - #4) have used the QCD sum rules method, combined with some general properties of ϕ_H (normalization and boundary conditions) to establish a model for the pion and ρ distribution amplitudes. Suprisingly, they have found large spin effects (i.e. the pion distribution amplitude is much different than the ρ one, which itself differs for different helicity states), as well as the large asymmetry between quarks. In the pion a large part of the total momentum is carried by one quark. Finally, the quarks are highly relativistic. All distributions are broad and very different from the nonrelativistic δ - function form, as well as they differ significantly from the so - called asymptotic form $\phi_{as}(x) = 4\, x_1 x_2$. It should be stressed that despite of the fact that various objections could in principle be raised against the application of the QCD sum rules method for detemination of the hadronic wave function, Chernyak - Zhitnitsky distribution amplitudes are responsible for succesfull description of the wide range of available experimental data - for a reviev see Ref. 4.

In an attempt to explain an unusual features of light - meson distribution amplitudes we proposed a simple relativistic model of meson light - cone wave function (#2). We use the basic concepts of the constituent quark model (#5) formulated within the light - cone

---

#3. V. L. Chernyak and A. R. Zhitnitsky, Nucl. Phys. B201 , 492 (1982); B204 , 477 (1982).
#4. V. L. Chernyak and A. R. Zhitnitsky, Phys. Rep. 112 , 175 (1982).
#5. N. Isgur, in the New Aspects of Subnuclear Physics, edited by A. Zichichi (Plenum, New York, 1980), p. 107.

approach: (i) meson states are dominated by the valence $q\bar{q}$ configuration with typical constituent masses of about 300 MeV. (ii) Quark - antiquark pair is a system with substantial relativistic internal motion. (iii) The π and ρ have standard spin - parity assigments.

To distinguish between the π and ρ meson we need the wave functions of definite angular momentum - J. These can be easily constructed within the equal - t approach. On the contrary, we are faced with difficulties for the case of light - cone wave function. Here the problem is related to the dynamical character of the angular momentum operator in the light - cone dynamics (#6). Obviously, we need some approximation to deal with the problem, i.e., (i) we assume that the ground state mesons are described by the harmonic oscillator model wave functions. These equal - t wave functions are known to give reasonable first approximation description of the static properties (#5). (ii) In order to deal with the problem of angular momentum we follow to some extend the mock - hadron method by Isgur (#7). Namely, we assume that our pseudoscalar and vector mesons are a collection of quarks with the wave function (i) but with all binding turn off and a mock - meson mass equal to the mean total energy of free quarks. Although this assumption is untenable, we use it as a guide to asses a significance of the relativistic kinemtics. For free spin 1/2 constituents the one particle instant (T) and light - cone (LC) states are related by the familiar Melosh transformation (#8). (iii) Now we can make use of an ansatz, due to Brodsky and Lepage (#2), relating harmonic oscillator instant wave functions and corresponding light - cone wave functions, while the spin structure may be related by Melosh transformation, as discussed above. As a result we obtain a model for the Lorentz - invariant light - cone wave function of definite (free) angular momentum:

$$\Psi_{J\Lambda}(k_j^{\perp}, x_j, \lambda) \sim N \exp -\frac{1}{8\beta^2} \sum_{i=1}^{2} \left(\frac{k^{\perp 2} + m^2}{x}\right)_i C_{J\Lambda}^{(LC)} / \sqrt{x_1 x_2} \qquad (4)$$

The light - cone Clebsch - Gordan coefficients can be expressed by the following invariants:

#6. H. Leutwyler and J. Stern, Ann. Phys. 112, 94 (1978).
#7. N. Isgur, Acta Phys. Polon. B8 , 1081 (1977), C. Hayne and N. Isgur, Phys. Rev. D25 , 1944 (1982).
#8. L. A. Kondratyuk and M. V. Terentyev, Yad. Fiz. 31 , 1087 (1980). Sov. J. Nucl. Phys. 31, 561 (1980).

$$C_0^{(LC)}(\lambda_1,\lambda_2) = \bar{u}_{\lambda_1}\left(m_H\gamma_5 + \hat{p}\gamma_5\right)v_{\lambda_2}$$

$$C_{1\Lambda}^{(LC)}(\lambda_1,\lambda_2) = \bar{u}_{\lambda_1}\left(m_H\hat{\epsilon}_\Lambda + \tfrac{1}{2}[\hat{p}_1\hat{e}_\Lambda]\right)v_{\lambda_2} \qquad (5)$$

where u_λ, v_λ and ϵ_Λ^μ are the light - cone spinors and polarization vectors of Ref. 1, respectively.

We are aware of the fact that the mock - hadron prescription is by no means unique. For example, if one turns off the interaction in the spin wave function (5), assuming $p = k_1 + k_2$, then

$$C_0^{(LC)} = 2(m_1+m_2)\,\bar{u}_{\lambda_1}\gamma_5 v_{\lambda_2}$$

$$C_{1\Lambda}^{(LC)} = 2(m_1+m_2)\,\bar{u}_{\lambda_1}\hat{e}_\Lambda v_{\lambda_2} \qquad (6)$$

But as it has beee shown in Ref. 9 these spin wave functions lead to the distribution amplitudes which are close to the asymptotic ones. (iv) Our quarks have typical constituent masses. To be specific, we use the value $m_u = m_d = 300$ MeV. The Gaussian parameter β is related to the mean transverse momentum in the meson $\beta^2 \sim \langle k^{\perp 2}\rangle$. We allow it to vary in a wide range of values around 350 MeV, which is consistent with various estimations (#4 - #10) . As explained e.g. in Ref. 5 harmonic oscillator wave functions are valid in a scheme without short-range hyperfine interactions. Therefore it is reasonable to assume that the and masses are equal and both approximated by the spin averaged value $m_H = (1/4m_\rho + 3/4m_\rho)_{exp}$.

Since the specification of the wave function is completed, we can evaluate the distribution amplitude. It is defined (#1) to be the probability amplitude to find quarks in the $L_z=0$ projection of the wave function collinear up to scale Q:

$$\phi_{J\Lambda}(x,Q) = \int^{Q}[d^2k^\perp]\,\Psi_{J\Lambda}^{L_z=0}(x,k^\perp,\lambda) \qquad (7)$$

Because of the presence of the Gaussian damping factor in our wave function, we can perform the integration up to infinity. With the value of β quoted above it corresponds to the scale $Q \simeq 500 - 600$ MeV. It is interesting to note that with our seemingly naive model of the wave function (4) we are able to reproduce the most essential features of the pion and ρ distribution amplitudes. In particular, the rich structure of the spin-0 amplitude is illustrated in Fig. 1 which shows the normalized amplitude (6) for two values of β along with that evaluated with QCD sum rules , viz. $\phi_\pi \sim \xi^2(1-\xi^2)$ (#4). On the other hand, the ρ case is

---

#9. A. S. Bagdasaryan et al., Yad. Fiz. 42,440 (1985).
#10. S. J. Brodsky, T. Huang and G. P. Lepage, SLAC-PUB-2580.

more obscure. Although we do observe helicity

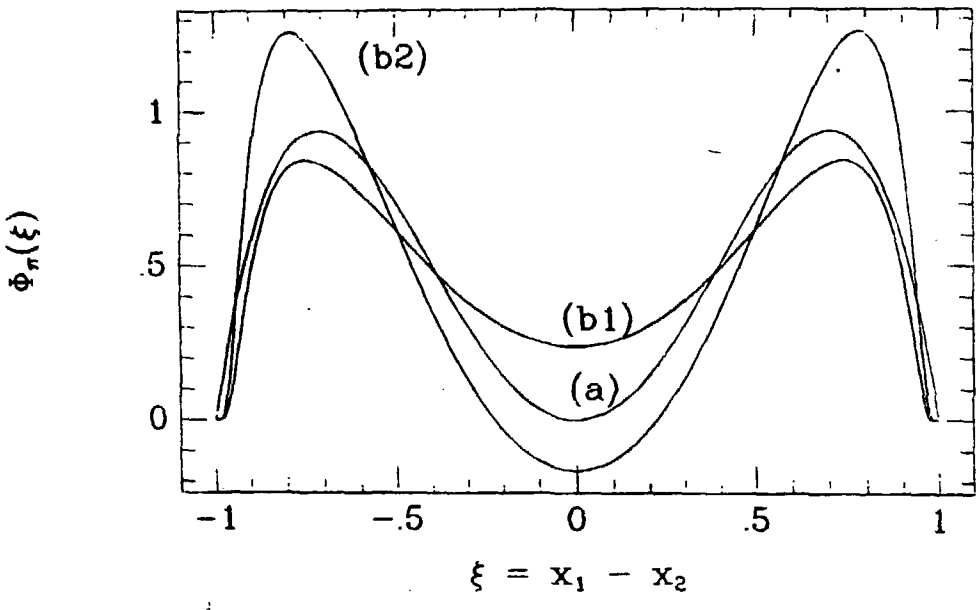

Fig. 1: The normalized π distribution ampliude. Curve (a) is the result from QCD sum rules (Ref. 4). Curves (b1) and (b2) result in our model for β = 430 MeV and β = 460 MeV, respectively.

dependence in our distribution amplitudes, numericaly they prove to be much smaller than those found via QCD sum rules. As a consequence, our ρ meson distribution amplitudes looks more like the asymptotic form. Note that the recent reanalysis of QCD sum rules in Ref. 11 finds that moments of the ρ distribution amplitude are much smaller than that of the pion. This result leads to the conclusion that ϕ_ρ should be close to the asymptotic form. It is clear that our model favors the result of Ref. 11.

#11. X. D. Xiang, X. N. Wang and T. Huang, Beijing Institute of Theoretical Physics Preprint BIHEP-TH-84-29 (1984). T. Huang, X. D. Xiang and X. N. Wang, Chinese Phys. Lett. 2, 67 (1985).

Finally, this agreement, even if semiquantative, must be treated with some causion. It is rather an indication of a role playing by the relativistic effects in the bound state wave function . Assuming that the inacuracy inherent to the method of Ref. 4 and 11 has not misled us, the difference between the distributions given by our model and those obtained from QCD sum rules can be related to the quark dynamics and all the rest of it may be understood with the insight of the relativistic kinematics and fundamentals of the quark model.

Acknowledgments

We are grateful to Professor V. L. Chernyak for calling our attention to the work of Ref. 9 and to S. Tatur for useful discussions. This work is supported in part by the Research Program CPBP - 01.03.

PRECISION MEASUREMENT OF $\sin^2\theta_W$ FROM SEMILEPTONIC NEUTRINO SCATTERING

The
CDHS - collaboration
presented by
Rainer Geiges
Inst. for High Energy Physics Univ. of Heidelberg
Federal Rep. of Germany

During 1984 the CDHS collaboration has preformed the last experiment. It was dedicated to a precise measurement of the Weinberg angle $\sin^2\theta_W$ in ν_μ-neutrino nucleon scattering. There are three reasons to measure $\sin^2\theta_W$ with high precision. First, it is a fundamental parameter in the standard model [1], therefore it is selfevident to measure it as precise as possible. Second, $\sin^2\theta_W$ determined in different processes is subject to different radiative corrections. A comparison of those different experiments will test the renormalizability of the theory [2,3]. Third, models of Grand Unification [4] may predict a value of $\sin^2\theta_W$, which has to be verified by experiments.

Despite the exellent work which is done at the CERN $\bar{p}$-p collider [6,7] the neutrino nucleon scattering still offers the most precise way to determine $\sin^2\theta_W$. In this brief report main emphasis is put on the important features of the experiment which had a big influence on the precision of the result.

The CDHS neutrino detector was exposed to the 160GeV/c narrow band neutrino beam (NBB). In a NBB the neutrinos originate from decays of sign and momentum selected kaons and pions. The NBB spectrum is easy calculable, which is necessary for the Monte Carlo simulation of the experiment. The setup of the beam line was optimized to obtain a maximal flux of secondary hadrons per incident proton.

In the NBB there exists a background of wide band beam (WBB) neutrinos. These WBB-neutrinos originate from hadron decays taking

place upstream of the decay tunnel. Their energy spectrum is unknown. In order to measure this background a dump was installed in front of the decay tunnel. For about 25% of the data taking the dump was put into the hadron beam and only WBB-neutrinos were measured in the detector. The events observed in this "dump-in" runnig condition were subtracted from all data after flux normalization. In the previous experiment this WBB background caused the largest systematic uncertainty [8], with this direct measurement the systematic error on the ratio R_ν of the neutral to charged current cross section of neutrinos could be reduced to 0.1% which makes it unimportant.

The upgraded CDHS neutrino detector consisted out of 21 magnetized iron toroids instrumented as iron-scintillator sandwich calorimeter [9]. The 21 modules were interspaced with drift chambers for the muon track measurement. In order to avoid any bias between NC and CC events the event selection was based on calorimetric and topological information only. No reference to the muon momentum reconstruction from the drift chamber hit pattern was made. Every neutrino event candidate was characterized by three measured quantities: First the longitudinal and lateral shower vertex position, second the shower energy E_s, from the pulseheight recorded in the first 1.5m of iron after the vertex (the shower box), third the eventlenght, defined as the distance in iron between the first and last scintillator hit belonging to the event.

All neutrino event candidates had to match the following selection criteria:

1) The lateral shower vertex had to lay inside a radius of 1.3m around the detector axis, excluding a $20*20$ cm^2 area around the central hole for the magnet coil. This insured full transverse shower containment and high final state muon acceptance. The muon acceptance was further increased by a toroidal magnetic field which focussed the muons to the centre of the apparatus.
2) The longitudinal vertex position was restricted to the space between the middle of module 3 and the middle of module 10. The first two modules served as a veto counter against muons penetrating the iron and earth shielding in front of the

detector and producing in-time overlays with real events.

3) The hadron energy of each event was requested to be larger than 10 GeV. For NC events the hadron energy was equal to the visible energy E_v in the shower box. For CC events the muon pulseheight contributed to the measured E_v and had to be subtracted. This muon pulse height was equivalent to typically 3 GeV of hadronic energy and was measured from isolated muon tracks to a precision of ±5%. This uncertainty in the E_v cut for CC events caused a systematic error of 0.3% on R_ν.

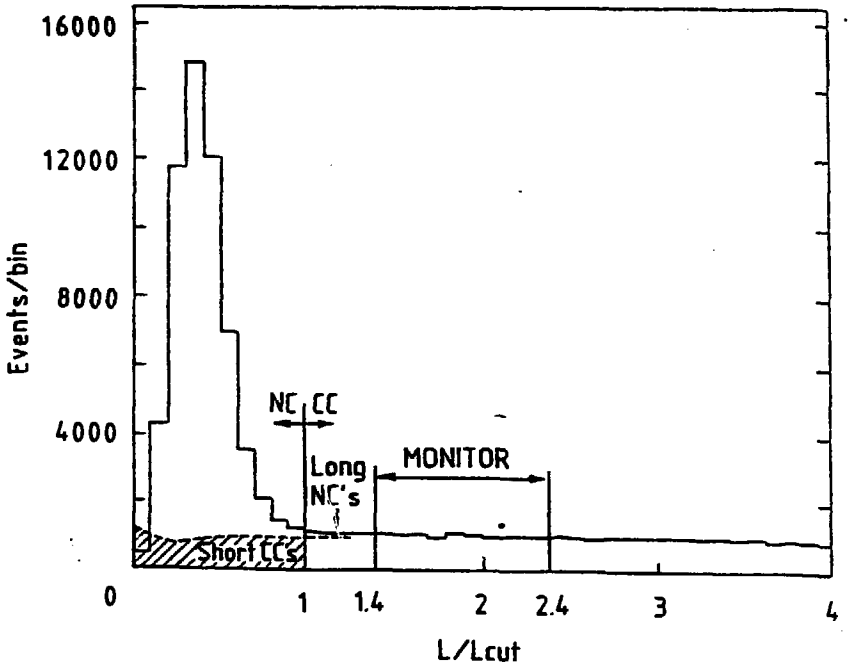

Fig.1 Distribution of the eventlength L, in units of the cut-off L_{cut} (see text), for neutrino events with E_v > 10 GeV. The background from cosmic rays and WBB has been subtracted already. The dashed line shows the Monte Carlo prediction of the muon length in CC events, normalized to the monitor region.

The events matching the selection criteria were classified as NC or CC candidates according to their eventlenght as shown in fig. 1. The lenght was measured in multiples of a cut-off lenght defined by $L_{cut} = 75 + 35 \cdot \ln E_e\,(GeV)$, in cm of iron, which provides an optimal separation of NC and CC events.

From fig. 1 it is evident, that the raw number of NC and CC is subject to several corrections to obtain the genuine event numbers (Table 1).

Cosmic-ray events were subtracted using data taken between the beam spill. The WBB background measured in "dump-in" running conditions was subtracted after normaliztion to the same hadron flux as for normal data taking.

For a small fraction of short events a migration beyond L_{cut} may occure. This happened mostly due to secondary muons from hadron decay in the shower or due to a lenghtening of the shower by noise. The amount of this "Long Shower" correction was estimated by Monte Carlo calculations, by visual inspection of events and from hadron test beam data.

The largest correction is the determination of the number of short CC events in the NC region. These are mainly CC events with muons of such small momentum, that it ranges out within the shower. Only 7% of the short CC events have a muon produced under large scattering angle, where the muon is leaving the detector at the side.

The number of short CC events is determined by Monte Carlo simulation of the muon length distribution. No simulation of the hadronic shower is needed. The Monte Carlo length distribution is normalized to a monitor region defined as $1.4 < L/L_{cut} < 2.4$ (see fig. 1). This procedure is equivalent to an extrapolation of the CC y distribution ($y = 1 - E_e/E_\nu$) and is much less sensitive to physics assumptions than the normalization to the whole CC sample would be. Uncertainties in the knowledge of the y distribution, primarily from the longitudinal structure function, induce an error of 0.7% on the value of the correction. Because of the normalization to the monitor region the correction is insensitive to errors in the momentum, the divergence, the π/K composition of the parent beam, the muon energy loss and the hadron energy calibration. However, it is sensitive to a bias in the length measurement. This was estimated to be less than $\pm 1{,}5$cm, corresponding to an error of $\pm 1\%$ on the correction.

Table 1

Event numbers and corrections of NC and CC events with $E_\nu > 10$ GeV

	NC	CC	Change of NC/CC and systematic error (%)
Candidates	60936	137853	±0.3
Cosmic rays	-1120	-9	-1.8±0.1
WBB background	-2920	-5187	-1.2±0.1
Long Shower	+159	-158	+0.5±0.2
Short CC	-9642	+9526	-22.5±0.35
K_{e3} correction	-3016	+2488	-8.0±0.2
Corr. event numbers	44397	144513	±0.65

In the neutrino beam there is a small admixture of electron neutrinos from K_{e3} decays. The CC events of these ν_e's appear as NC candidates since the electromagnetic shower from the final state electron is hidden in the hadronic cascade. The total number of CC ν_e events is determinded from the Monte Carlo simulation normalized to the number of fully reconstructed CC ν_μ from Kaon decay. The CC ν_e events are subtracted from the NC sample and those with $E_\nu > 10$ Gev are added to the CC sample.

Having done all these corrections we compute the NC to CC cross section ratio for neutrino interactions in iron to be:

$$R_\nu = 0.3072 \pm 0.0025(\text{stat.}) \pm 0.0020(\text{syst.}).$$

For an isoscalar target consisting out of u,$\bar{u}$,d and $\bar{d}$ quarks only and without quark mixing $\sin^2\theta_W$ can be determined from the following formula [3]:

$$R_\nu = 1/2 - \sin^2\theta_W + 5/9 \sin^4\theta_W (1+r),$$

where r denotes the ratio of the CC $\bar{\nu}$ to CC ν cross section integrated over the same neutrino spectrum and with the same E_h cut off. We have measured this ratio to be $r = 0.39 \pm 0.01$.

In order to use the above formula the experimental result has to be corrected for the non-isoscalarity of the target, the presence of s and c quarks and antiquarks in the nucleon and the charm quark excitation. The corrections were done by using a quark parton model of the nucleon. Corrections due to higher twist effects are claimed to be small for events with $E_h > 10$ GeV and are therefore neglected [3,10]. Radiative corrections are calcuated in the on-shell renormalization scheme according to ref 11. The largest uncertainty of the model comes from the choice of the charm quark mass m_c, which affects the threshold suppression of charm production in the CC events [12]. Therefore we give the result on $\sin^2\theta_W$ as a function of m_c:

$$\sin^2\theta_W = 0.225\pm0.005(\text{exp.})\pm0.003(\text{theo.})+0.013(m_c - 1.5\text{GeV})$$

The experimental error is the statistical and the systematic error on R_ν and r added in quadrature. The theoretical error does not include the uncertainty on m_c, choosing $m_c = 1.5 \pm 0.3$ GeV/c^2 it increases to ±0.005.

This value of $\sin^2\theta_W$ is compatible with earlier results obtained by this group [5,8]. It is also compatible with recent results from other semileptonic neutrino experiments [13,14,15,16] and with recent determinations of $\sin^2\theta_W$ from the W mass [6,7]. The good agreement between the values of $\sin^2\theta_W$ obtained from neutrino scattering and from the W mass holds only if electroweak radiative corrections are applied. Without these corrections the values of $\sin^2\theta_W = 0.207\pm0.008$ from the W mass and $\sin^2\theta_W = 0.236\pm0.007$ from this experiment differ by more than two standard deviations. But to really test the weak part of the radiative corrections more precise values are needed.

ACKNOWLEDGEMENTS

It is a pleasure to thank all collaborators who contributed to the successful performance of this experiment. I would like to thank all organizers of the Symposium for the stimulating meeting.

REFERENCES

[1] S. L. Glashow, Nucl. Phys. 22 (1961) 579;
A. Salam, Proc. 8th Nobel Symposium, Aspenäsgarden, 1968 (Almquist and Wiksell, Stockholm, 1968), p.367;
S. Weinberg, Phys. Rev. Lett. 19 (1967) 1264;
Phys. Rev. D5 (1972) 1412.
[2] W. J. Marciano and A. Sirlin, Phys. Rev. D29 (1984) 945.
[3] C. H. Llewellyn Smith, Nucl. Phys. B228 (1983) 205.
[4] See, for example, P. Langacker, Phys. Rep. 72 (1981) 185.
[5] M. Holder et al., Phys. Lett. 71B (1977) 222, and 72B (1977) 254.
[6] G. Arnison et al., Phys. Lett. 166B (1986) 484.
[7] J. A. Appel et al., preprint CERN-EP/85-166 (1985).
[8] H. Abramowicz et al., Z. Phys. C28 (1985) 51.
[9] M. Holder et al. Nucl. Instrum. Methods 148 (1978) 235.
[10] S. Fajfer and R. J. Oakes, Proc. Int. Europhysics Conf. on High-Energy Physics, Bari, 1985 (Eur. Phys. Soc., Geneva, 1985) p.190;
P. Castorina and P. J. Mulders, Phys. Rev. D31 (1985) 2753.
[11] A. Sirlin, Phys. Rev. D22 (1980) 97;
R. G. Stuart, preprint CERN-TH 4342/85 (1985).
[12] R. M. Barnett, Phys. Rev. D14 (1976) 70;
H. Georgi and H.D. Politzer, Phys. Rev. D14 (1976) 1829.
[13] P. G. Reutens et al. Phys. Lett. 152B (1985) 404.
[14] M. Jonker et al., Phys. Lett. B99 (1981) 265.
[15] D. Bogart er al., Phys. Rev. Lett. 55 (1985) 1969.
[16] R. Pain, Proc. Int. Europhysics Conf. on High-Energy Physics, Bari, (1985) (Eur. Phys. Soc., Geneva, 1985) p. 249.

RECENT RESULTS IN DEEP INELASTIC SCATTERING

T. Sloan

CERN
Geneva, Switzerland
(On leave of absence from the University of Lancaster)

ABSTRACT

Recent results on deep inelastic charged lepton and neutrino scattering are reviewed.

1. INTRODUCTION

In this paper, developments in the field of deep inelastic scattering are discussed. Three areas, where recent data has been presented, will be covered.

1. Exclusive or elastic ρ^0, ϕ and J/ψ production in deep inelastic muon production is described i.e. the process $\mu N \to \mu VN$, where V is a vector meson and N is a nucleon. The data indicate that at high Q^2 the vector dominance behaviour of the photon dies away and the photon becomes a pure electromagnetic probe, even for the production of vector mesons.

2. Tests of the quark parton model of the nucleon and QCD from deep inelastic neutrino and muon scattering are described.

3. Data on the differences between the structure functions of the nucleon bound in nuclei and those in free nucleons are reviewed.

Figure 1 shows the lowest order diagram for deep inelastic scattering by neutrinos or charged leptons ($e^{\pm}$,$\mu^{\pm}$). Corrections for higher order diagrams are required and such radiative corrections can be routinely made[1]. The data are analysed in terms of the variables ν, the energy in the laboratory frame and Q^2, the negative four momentum squared transferred to the virtual boson probe. The Bjorken scaling variables $x=Q^2/2M\nu$ and $y=\nu/E$, where E is the energy of the incident lepton and M is the nucleon mass, are used. The variable wavelength of the virtual probe which decreases like $1/Q^2$ at fixed x allows the structure of the nucleon to be investigated in deep inelastic scattering.

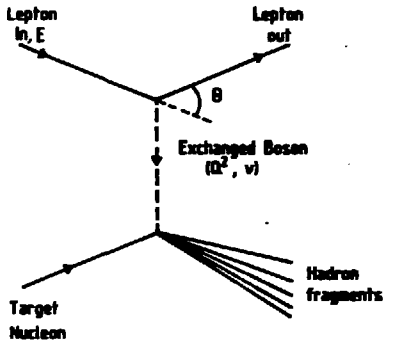

Lepton in	Lepton out	Interaction	Exchanged Boson
$\mu^{\pm}$ / $e^{\pm}$	$\mu^{\pm}$ / $e^{\pm}$	Electromagnetic	Photon
ν_μ	μ^-	Weak Charged current	W^+
$\bar{\nu}_\mu$	μ^+		W^-
ν_μ	ν_μ	Weak Neutral current	Z^0
$\bar{\nu}_\mu$	$\bar{\nu}_\mu$		

$Q^2 = 4EE' \sin^2 \theta/2$

$\nu = E-E'$

Fig. 1
The lowest order Feynman graph for deep inelastic lepton-nucleon scattering

2. THE PROPERTIES OF THE PHOTON (IN CHARGED LEPTON SCATTERING)

High energy real photons ($Q^2=0$) have much larger cross sections for the production of hadrons than would be expected from a pure electromagnetic interaction. The exclusive production of pion pairs

is found to be dominated by ρ^0 production. This observation led to the formulation of the vector meson dominance model to explain such behaviour[2]. Recently data has been presented by the EMC on elastic ρ^0 production at high Q^2 in muon scattering from targets of hydrogen[3] and ammonia[4] (mainly nitrogen) and also for elastic ϕ production.

To select exclusive events containing a single hadron pair, the total energy of the pair was required to be greater than $0.92\ \nu$[3,4]. Figure 2 shows the invariant mass distributions of the hadrons treated as either K^+K^- or $\pi^+\pi^-$ pairs. Clear peaks are seen at the ρ^0 and ϕ masses in the $\pi^+\pi^-$ and K^+K^- distributions, respectively.

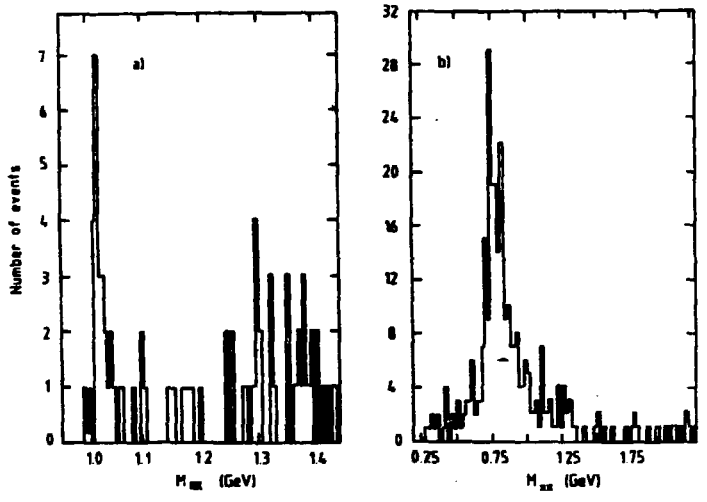

Fig. 2
Invariant mass spectra of oppositely charged pairs of hadrons of total energy larger than 0.92 ν, treated as a) K^+K^- pairs b) $\pi^+\pi^-$ pairs.

The mass spectra shown in fig. 2 were corrected for the acceptance and a fit of a Breit-Wigner distribution and a smooth background

function performed. The number of elastic ρ^0 and ϕ mesons were found from this fit to be 538±40 and 94±24, respectively. From these yields the ratio of the cross sections at a mean value of Q^2=7.5 GeV^2, is

$$\frac{\sigma(\gamma^* p \to \rho p)}{\sigma(\gamma^* p \to \phi p)} = \frac{9}{1.6 \pm 0.4} \quad . \qquad (1)$$

The observed ratio is consistent with the value of 9:2 expected from SU(3) flavour symmetry (i.e. from the quark charges). However, it is inconsistent with the value of 9:(0.62±0.02) measured in real photon production (Q^2=0) at similar incident photon energies[5].

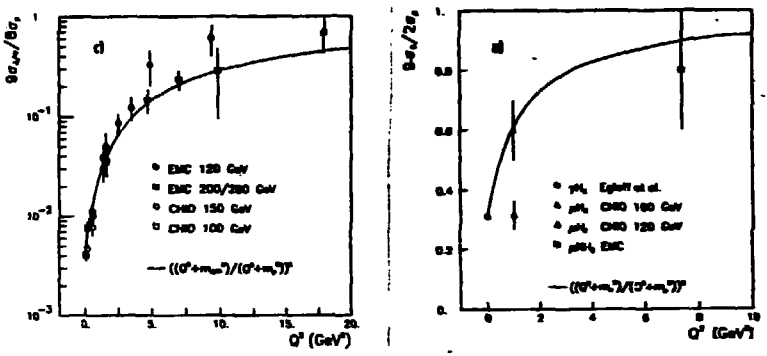

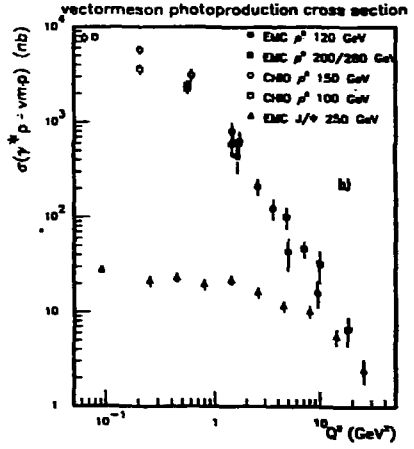

Fig. 3

a) The ratio $9\sigma(\phi)/2\sigma(\rho)$

b) The cross sections for elastic ρ^0[3,6] and J/ψ[7] production.

c) The ratio $9\sigma(J/\psi)/8\sigma(\rho)$ as a function of Q^2

The smooth curves represent the model described in the text

Figure 3(a) shows this result together with previous measurements[5,6] of the ratio of the cross sections for elastic ρ^0 to elastic ϕ production as a function of Q^2. Figure 3(b) shows the cross sections for elastic ρ^0 photoproduction on hydrogen[3,6] and elastic J/ψ photoproduction on iron[7] as a function of Q^2. It can be seen that these cross sections become almost equal at high Q^2. Figure 3(c) shows the data in fig. 3(b) presented as a ratio of the cross sections. The smooth curves in figs. 3(a) and 3(c) show the predictions of the following simple model. Firstly, it is assumed that in the limit of large Q^2 ($Q^2 >> m_i^2$, where m_i is the mass of the vector meson i) the ratio $\sigma_\rho : \sigma_i$ approaches the value expected from flavour symmetry i.e. 9:2 (9:8) for ϕ(J/ψ). Secondly, in the intermediate Q^2 range it is assumed that the cross section follows the propagator form $1/(1+Q^2/m_i^2)^2$, a behaviour which is well established for the Q^2 dependence of the ρ^0 and J/ψ cross sections[2,3,7]. With these assumptions the ratio of the cross sections will vary as

$$R = \frac{\sigma_i}{\sigma_\rho} = \frac{c_i}{9} \frac{(m_\rho^2+Q^2)^2}{(m_i^2+Q^2)^2} \qquad (2)$$

with c_i=2 for ϕ and 8 for J/ψ. The curves agree well with the data in both figs. 3a) and c) indicating that the mechanisms for the photoproduction of elastic vector mesons ρ^0, ϕ, and J/ψ are similar. The differences in the production cross-sections are determined by the different meson masses which are related to the quark masses. The photon gluon fusion model[8] gives a reasonable representation of the J/ψ data although an arbitrary normalisation factor is required in the elastic region to account for non-perturbative effects[9]. This indicates that elastic ρ^0 and ϕ production at high Q^2 could also be described by a similar mechanism.

Figure 4 shows the dependence of the yields for elastic ρ^0 production from the ammonia target as function of $t' = |t - t_{min}|$ where t is the four momentum transfer between the photon and the ρ^0 meson and t_{min} is the kinematic minimum value. The peaks at small values of t'

correspond to coherent production from the nitrogen in the target smeared by experimental resolution. The lines show fits of the form $e^{-bt'}$ to the data for $t'>0.2$ GeV^2 excluding the coherent region. The slopes of the fitted lines decrease as Q^2 increases and at high Q^2 the slopes are characteristic of a hard scattering process. This is consistent with the behaviour described in[3] and the measured values of the slopes at each Q^2 agree with the hydrogen data[3]. Furthermore, as in the hydrogen data for $t'>0.2$ GeV^2 the polarisation of the ρ^o was found to vary like $\cos^2\theta$ indicating that the ρ^o is produced in a dominantly helicity zero state.

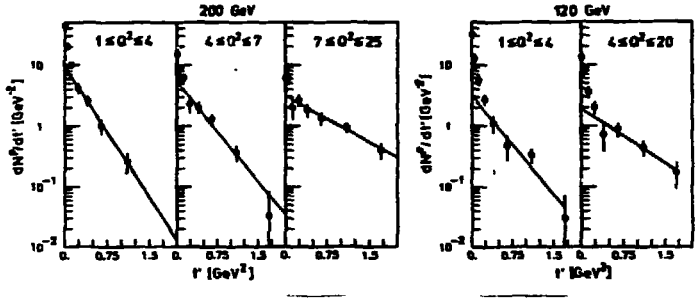

Fig. 4

The event yields as a function of $t'=|t-t_{min}|$ in different Q^2 bins

The straight line fits in fig. 4 were extrapolated under the coherent peak in order to estimate the ratio of the coherent, σ_{coh}, to incoherent, σ_{inc}, cross sections neglecting the effects of quasi-elastic suppression at small t'. Figure 5 shows the ratio of $\sigma_{coh}/\sigma_{inc}$ for elastic ρ^o production from nitrogen as a function of Q^2. The points at $Q^2=0$ were obtained by performing similar extrapolations using photoproduction data from carbon and copper targets[10,11]. The smooth curve in fig. 5 shows the expected kinematic effect due to the increase of $t_{min}=(Q^2+m_\rho^2/2\nu)^2$ with Q^2. The data fall much faster with Q^2 than expected from such kinematic effects.

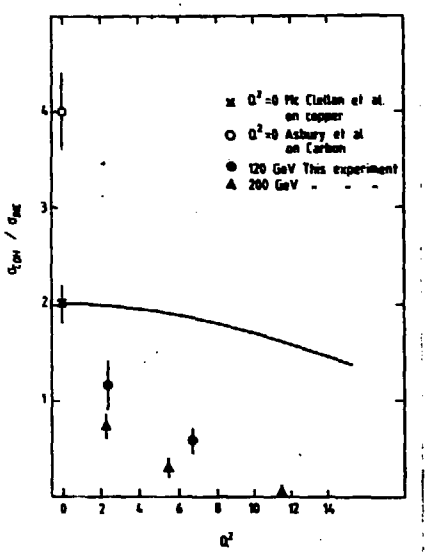

Fig. 5
The ratio of the total coherent to incoherent cross sections as a function of Q^2. The smooth curve shows the expected decrease due to the increase of t_{min} with Q^2.

The decrease of the coherent part of the cross section with Q^2 may be understood as follows. In[3] it was shown that elastic ρ^o mesons at high Q^2 are produced dominantly in a helicity 0 state from mainly transverse photons. In the forward direction the spin flip of the ρ^o implies that the proton spin flips to conserve angular momentum. Such spin flip amplitudes will not contribute to coherent production as the nuclear state must change. The observed coherent signal at larger Q^2 is due to the residual non spin flip (diffractive) amplitude which decreases approximately as $1/Q^2$. This indicates that the residual diffractive amplitude which is presumably due to the vector meson dominance properties of the photon is a higher twist mechanism. Thus at high Q^2, even in elastic vector meson photoproduction, the photon behaves as an electromagnetic probe and the vector meson dominance properties die away.

3. INCLUSIVE DEEP INELASTIC SCATTERING

In deep inelastic scattering the inclusive differential cross sections are measured. From the lowest order Feynman graph for the process (fig. 1) the measured differential cross sections are related to the structure functions[12] of the target nucleon as follows:-

a) Charged lepton (pure vector interaction)

$$\frac{d^2\sigma^{\mu N}}{dxdy} = \frac{4\pi\alpha^2}{Q^4} 2ME \left[F_2^{\mu N}(x,Q^2)(1-y-\frac{Mxy}{2E}) + 2xF_1^{\mu N}(x,Q^2)\frac{y^2}{2}\right] \quad (3)$$

b) Charged current neutrino interactions (V-A)

$$\frac{d^2\sigma^{(-)\nu N}}{dxdy} = \frac{G^2ME}{\pi}\left[F_2^{(-)\nu N}(x,Q^2)(1-y-\frac{Mxy}{2E})+2xF_1^{(-)\nu N}\frac{y^2}{2} \pm xF_2^{(-)\nu N}(x,Q^2)(1-\frac{y}{2})\right] \quad (4)$$

Here α is the electromagnetic coupling constant and G is the Fermi weak coupling constant measured in muon and nuclear β decays.

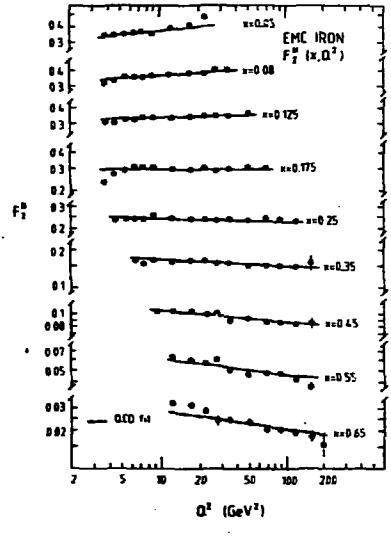

Fig. 6
The nucleon structure function F_2^N in iron The smooth curve is a QCD fit.

Figure 6 shows a sample of the recent structure function data[13]. It can be seen that the structure functions $F_2^{\mu N}$ are approximately independent of Q^2 at fixed values of x i.e. the absorption probability of the virtual photon probe is independent of the wavelength of the probe. Such behaviour indicates that the nucleon contains point-like structures i.e. quarks. The observed independence of the structure functions with a length scale is termed scaling. The small deviations from scaling are expected from QCD. The smooth curves in fig. 6 show the predictions of leading order QCD taking the mass scale parameter Λ=90 MeV. The agreement of the smooth curves with the data shows that QCD gives a reasonable representation of the data over the whole kinematic range.

4. TESTS OF THE QUARK PARTON MODEL AND QCD

The structure functions measured in neutrino and muon scattering in principal are not the same. However, if these particles scatter off the same constituents of the nucleon (the quarks) the structure functions are related to the quark distribution functions[12] as follows

$$
\begin{aligned}
F_2^{\mu p} &= e_u^2 x(u+\bar{u}) + e_d^2 x(d+\bar{d}) + \tfrac{4}{9} x(c+\bar{c}) + \tfrac{1}{9} x(s+\bar{s}) \\
F_2^{\mu n} &= e_d^2 x(u+\bar{u}) + e_u^2 x(d+\bar{d}) + \tfrac{4}{9} x(c+\bar{c}) + \tfrac{1}{9} x(s+\bar{s}) \\
F_2^{\mu N} &= \tfrac{1}{2}(F_2^{\mu p}+F_2^{\mu n}) = \frac{e_u^2+e_d^2}{2} x\,[u+\bar{u}+d+\bar{d}] + \tfrac{4}{9} x\,(c+\bar{c}) + \tfrac{1}{9} x\,(s+\bar{s}) \\
F_2^{\nu p} &= 2x[d+\bar{u}+s] \qquad F_2^{\nu n} = 2x[u+\bar{d}+\bar{s}] \\
F_2^{\nu N} &= \tfrac{1}{2}(F_2^{\nu p}+F_2^{\nu n}) = \textstyle\sum_f x(q_f+\bar{q}_f) \\
xF_3^{\nu N} &= \tfrac{1}{2}(xF_3^{\nu p}+xF_3^{\nu n}) = \textstyle\sum_f x(q_f-\bar{q}_f) = \sum_v xq_v
\end{aligned}
\qquad (5)
$$

Here f denotes any quark flavour, v denotes a valence quark, u,d,c,s, ($\bar{u}$,$\bar{d}$,$\bar{c}$,$\bar{s}$) the momentum distributions of the quarks (antiquarks) in the appropriate target (n=neutron, p=proton, N=nucleon i.e. the average of the proton and neutron), q denotes any quark distribution and the charges on the u and d flavoured quarks are e_u and e_d. The charm and strange quarks in equations 5 are assumed to have charges 2/3 and 1/3, respectively.

The quark distribution functions are a function of x and Q^2. However, as can be seen from fig. 6 the Q^2 dependence induced by QCD is rather weak. To avoid such effects in the following the neutrino and muon data are averaged over approximately the same ranges of Q^2.

a) The Gross-Llewellyn Smith Sum Rule[14] is given by

$$\int_0^1 \frac{xF_3^{\nu N}}{x}dx = \int_0^1 \sum_v q_v(x)dx \left(1-\frac{\alpha_s}{\pi}\right) \qquad (6)$$

where α_s = the strong coupling constant of QCD. In deducing this the sea quark distribution is assumed to be symmetric. The integral on the left hand side represents the total number of valence quarks in the nucleon. The world average value of the integral is 2.81±0.10[15]. Correcting for the small QCD radiative correction term[16], assuming α_s=0.2, gives the total number of valence quarks to be 3.0±0.1.

b) The Adler Sum Rule[17] is written

$$\int_0^1 \frac{F_2^{\nu n}-F_2^{\nu p}}{x} = \int_0^1 (u_v-d_v)dx \qquad (7)$$

assuming that the sea distributions in the neutron and proton are the same and that the quark seas are symmetric. The integral averaged over Q^2 has been measured to be 1.07±0.20[18]. Thus the difference in the number of valence quarks in the proton is 1.07±0.20.

From these observations the neutrino data are compatible with 3 valence quarks of which there are 2 of u flavour and one d flavour in the proton.

The quark charges can be measured by comparing the structure functions obtained from muon and neutrino experiments. Figure 7 shows the values of 5/18 $F_2^{\nu N}/F_2^{\mu N}$ [19]) on iron obtained from comparing data from the CDHSW[19]) and CCFRR[20]) neutrino experiments with the EMC muon data[13]).

From equations (5) it can be seen that

$$\frac{F_2^{\mu N}}{F_2^{\nu N}} = \frac{e_u^2+e_d^2}{2}(1-\delta) \qquad (8)$$

where δ is a small correction factor for charm and strange quarks. The data in fig. 7 show that this ratio is independent of x within the errors even though the structure functions change by more than an order of magnitude over this range. The mean value is compatible with unity within the normalisation uncertainties on the experiments. From the data in fig. 7 the mean value of the ratio of the muon and neutrino structure functions is

$$\left\langle \frac{F_2^{\mu N}}{F_2^{\nu N}} \right\rangle = 0.29 \pm .02 \qquad (9)$$

making the small corrections for the strange[15]) and charmed quark seas[21]) (-6% at x=.03 and decreasing as x increases).

In muon scattering it follows from equations (5) that

$$\int_0^1 \frac{F_2^{\mu p}-F_2^{\mu n}}{x}dx = \frac{e_u^2-e_d^2}{2} \qquad (10)$$

assuming that there are two u and one d valence quarks in the proton and that the quark seas are identical in the proton and neutron. The value of the integral has been measured to be 0.25 ± 0.12[22]).

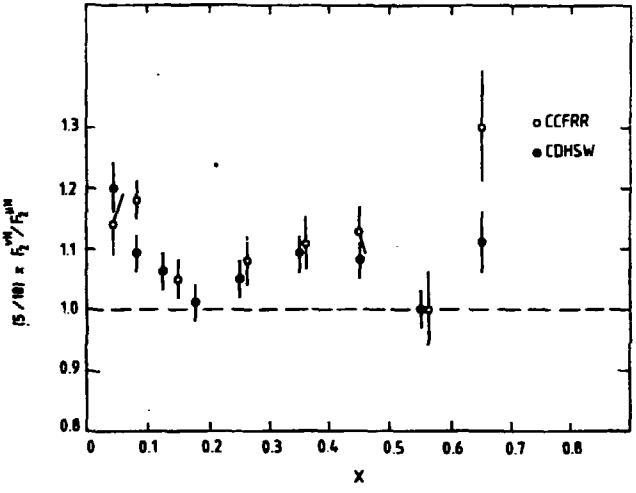

Fig. 7
The charge weighted ratio of the structure functions measured in neutrino and muon scattering experiments[19] from iron.

Using the measured values in equations 8 and 10 gives

$$|e_u| = 0.64 \pm .05 \text{ and } |e_d| = 0.41 \pm .08. \qquad (11)$$

Thus the absolute values of the structure functions measured in muon and neutrino scattering are compatible with the quark structure of the nucleon and show that the quarks have fractional charges.

However, all is not perfect in such comparisons. Figures 8 show similar comparisons to those in fig. 7 for neutrino data from the WA21 collaboration using a hydrogen[15] and the WA25 collaboration[18] using a deuterium target and muon data on the same targets[22,23]. The smooth curve shows the calculated change in the ratio caused by a systematic shift of ~1% in the same direction on the measurement of the incident neutrino energy. This energy is difficult to measure in these experiments and it is estimated by the same technique in both

experiments. The trend of the ratios is reasonably represented by the smooth curves. Thus such systematic shifts can explain the data in figs. 8 rather than a deviation from the quark parton model.

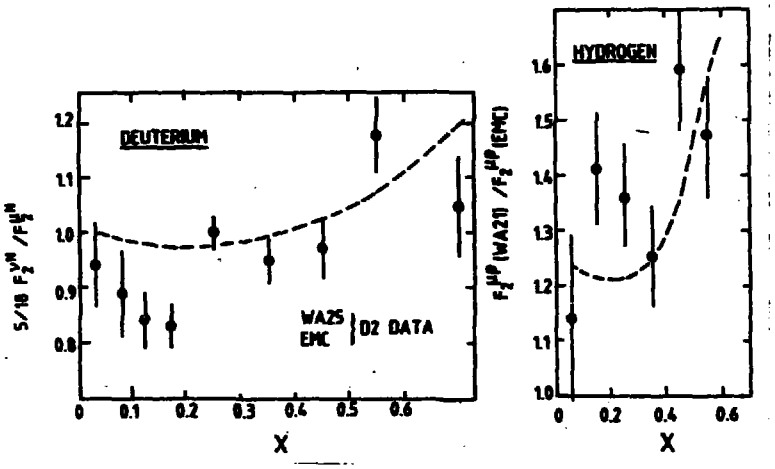

Fig. 8
Comparison of the structure function F_2 measured in a) D_2 b) H_2. In b) $F_2^{\mu p}$ was calculated from the quark distribution functions measured by WA21[15]. The dashed curves show the effect of a ~1% systematic decrease in the measured incident neutrino energy together with a normalisation shift of 25% in b).

6. TESTS OF QCD

Figure 9 shows the measurements of the strong coupling constant, α_s, in leading order as a function of Q^2 from many different techniques[24] neglecting higher order corrections[25].

It can be seen that many different techniques give similar values of α_s within the errors. This shows that QCD provides a good description of a wide variety of processes. However, the errors are too large to ascertain if α_s runs. Thus the available data shows that QCD gives an adequate description of the strong interaction when it can be

applied in the perturbative region although it is not yet proven that the coupling constant changes with the energy scale.

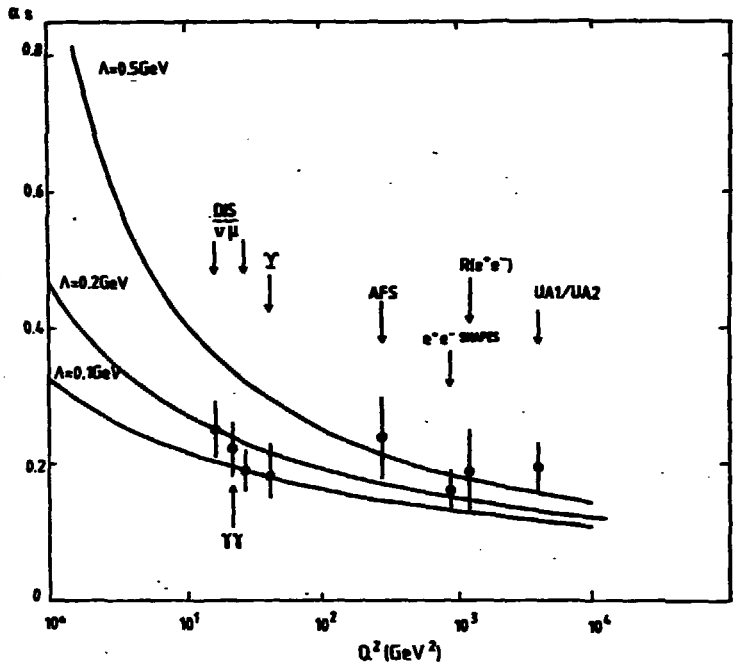

Fig. 9
The strong coupling constant, α_s, in leading order, as a function of Q^2, measured from different techniques. The smooth curves show the expected behaviour

7. NUCLEAR EFFECTS

Results have been presented by the EMC[26] which showed that the nucleon structure function measured on bound nucleons in iron is different from that measured on quasi-free nucleons in deuterium. The effect was subsequently confirmed by data from SLAC[27,28] and by the

BCDMS collaboration at CERN[29]. This indicates that the quark and by implication the gluon distributions in a bound nucleon, are different from those of the quasi-free nucleons in deuterium. Many theoretical models have been proposed to explain these effects reviews of which are given in [30].

The original EMC data[26] were obtained from separate measurements of the absolute values of the nucleon structure function F_2 with iron and deuterium targets. These measurements were taken under different experimental conditions (beam energy, beam intensity, target length and trigger) and at different times. In consequence, the systematic errors on the F_2^N ratios were rather large. Figure 10 shows the original measurements where the error bars are statistical only. The shaded band shows the range of the systematic error on the slope. The systematic errors on each data point are similar in magnitude to those indicated by the shaded band. In addition to these systematic errors there is a further normalisation uncertainty of 7% common to

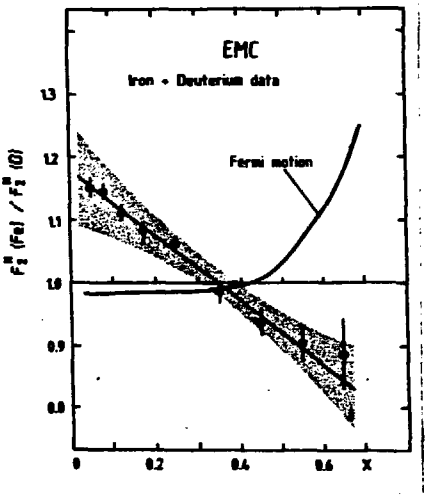

Fig. 10
The original EMC data[26] on the ratio of the nucleon structure functions F_2 measured in iron and deuterium

all the ratios. The data from SLAC[27,28] and the BCDMS collaboration[29] indicate that the ratio of $F_2^N(Fe)/F_2^N(D)$ tends to fall at the lowest values of x whereas the original EMC data (fig. 10) indicated a continuous rise. However, the different measurements are not incompatible within the systematic errors on the data. Figure 11 shows the measured ratios from neutrino experiments [31]. No single

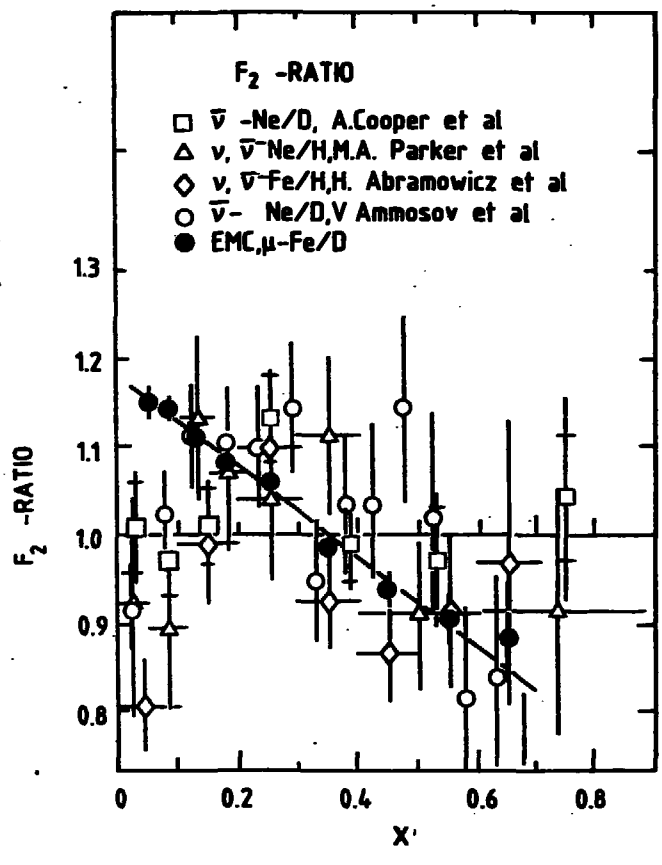

Fig. 11

The nucleon structure function ratios from neutrino experiments[31]

neutrino experiment is statistically precise enough to verify the effect. However, the trend of the data is similar to that from the charged lepton experiments.

In order to decrease the systematic errors, new data has been taken by both the EMC and BCDMS collaborations[32] in experiments designed to measure the ratios of the nucleon structure functions from nuclear and deuterium targets. The EMC data were taken as a parasitic measurement on the polarised target experiment with thin targets of either copper, carbon or deuterium and the polarised target in the beam simultaneously. The geometry of the nuclear targets was identical and they were interchanged at intervals of a few hours in order to average out the effects of time dependent inefficiencies in the spectrometer and the beam intensity monitoring apparatus. In this way the systematic errors were better controlled. The BCDMS experiment used two targets in the beam simultaneously to minimise the systematic uncertainties.

In the EMC experiment events were only accepted with $Q^2>3$ GeV^2, the angle of the scattered muon $\theta>0.01$ radians, energy of the scattered muon $E_\mu'>30$ GeV, $\nu>25$ GeV and $y=\nu/E<0.85$ where E is the incident muon energy. These cuts avoid regions of small or rapidly varying acceptance and where radiative corrections are large.

Radiative corrections, to obtain the single photon exchange contribution to deep inelastic scattering, were calculated using the procedures described in[13,23]. The corrections for coherent radiative events were calculated taking the form factors for copper and carbon from[33]. The suppression of the quasi-elastic radiative events was calculated according to the Fermi gas model of the nucleus given in[34]. The absolute radiative corrections for each target separately decreased from 19% at x=0.05 on copper through zero at x~0.35 and continued to decrease to ~5% at x=0.65. However, the corrections to the ratios are always less than 4% in the range of the data presented.

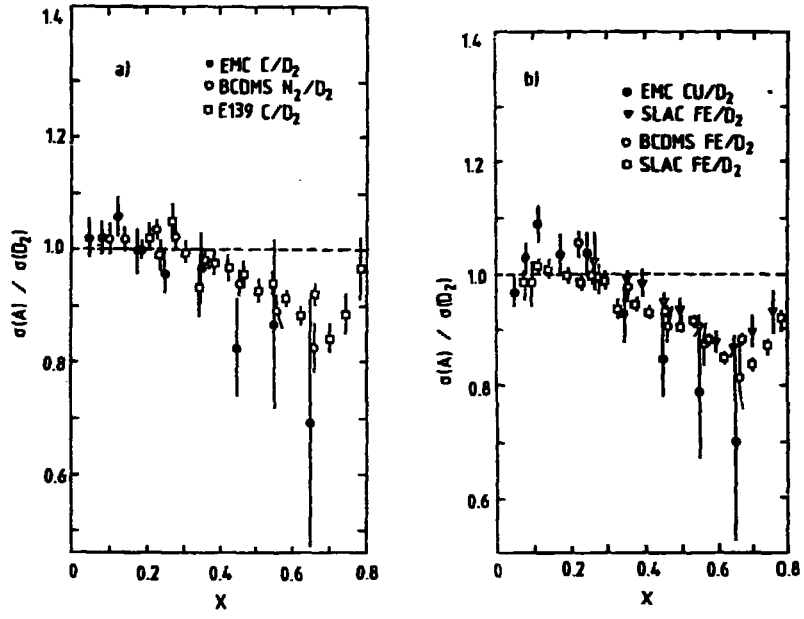

Fig. 12
The ratios of the structure function F_2 measured in a) carbon, b) copper to deuterium

Figures 12 show the ratios of the event yields of copper to deuterium and carbon to deuterium as a function of x after applying the radiative corrections. The error bars are statistical only, the systematic errors which represent a normalisation uncertainty are ~5% and are currently being studied. Assuming that R, the ratio of the photo-absorption cross sections for longitudinally and transversely polarised photons is independent of the nuclear target, these are the ratios of the structure functions F_2^N(Nucleus)/F_2^N(Deuterium). Within the systematic and statistical uncertainties of the measured ratios, the data in figs. 12 are compatible with those in fig. 10 and with the previous measurements of the nuclear effects on the structure

functions but at $x<0.1$ the ratios tend to decrease rather than show a continuous increase as x decreases[26].

Figures 12 also shows the recent structure function ratios from carbon, iron or copper and deuterium as a function of x from other experiments[27,28,29,32]. There is good agreement between the different experiments. This indicates that the effect is not strongly Q^2 dependent as the data from each experiment cover different Q^2 ranges. The data show that the quark distributions for a bound nucleon are softened for $x>0.3$. This behaviour can be explained by bag models and rescaling models for the effect. In the region $0.1<x<0.2$ the ratios tend to be greater than unity indicating antishadowing. At smaller values of x ($x<0.1$) the trend of the ratio is to decrease indicating the onset of shadowing. Such behaviour at large values of Q^2 was predicted by[35]. The observed decrease at small x indicates that the pion content of the nucleus is probably small and it is obscured by the effects of shadowing.

8. CONCLUSIONS

Over the past year deep inelastic scattering experiments have continued and some of the new results have been reviewed. The data discussed show that

1. The vector meson dominance behaviour of the photon decreases approximately as $1/Q^2$, indicating that such behaviour is a higher twist mechanism. At higher values of Q^2 the photon becomes a pure electromagnetic probe.
2. The quark parton model of the nucleon and QCD, the currently favoured theory of the strong interaction, have been successfully tested.
3. New data have become available which confirm the observation that the structure functions for a nucleon bound in a nucleus are different from those for free nucleons. These

data indicate that there is an interplay between quark and gluon degrees of freedom in the nucleus and the nuclear medium.

References

1. Ho, L.W. and Tsai, Y.S., Rev. Mod. Phys. 41 205 (1969). de Rujula, A., et al., Nucl. Phys. B259 189 (1985).
2. For a review see, Bauer, T., Spital, R.D., Yennie, D.R., Pipkin, F.M., Rev. Mod. Phys., 50 Vol. 2 261 (1978).
3. EMC, Aubert, J.J., et al., Phys. Lett. 161B 203 (1985).
4. Mönig, K., Diplom Thesis, Univ. of Wuppertal, WuD 86-10 (1986).
5. Egloff, R.M., et al., Phys. Rev. Lett. 43 657 (1979).
6. CHIO, Schambroom, W.D., et al., Phys. Rev. D26 1 (1982).
7. EMC, Aubert, J.J., et al., Nucl. Phys. B213 1 (1983).
8. Berger, E. and Jones, D., Phys. Rev. D23 1521 (1981).
9. Baier, R. and Rückl, R., Nucl. Phys. B218 289 (1983).
10. McClellan, G., et al., Phys. Rev. Lett. 22 377 (1969).
11. Asbury, J.G., et al., Phys. Rev. Lett. 19 865 (1967).
12. Close, F.E., An Introduction to Quarks and Partons (Academic Press).
13. EMC, Aubert, J.J., et al., Nucl. Phys. B272 158 (1986).
14. Gross, D. and Lewellyn Smith, C.H., Nucl. Phys. B14 1144 (1969).
15. Sculli, F.J., Rapporteur's talk at the International Symposium on Lepton and Photon Interactions, Kyoto (1985).
16. Altarelli, G., Phys. Rep. 81 1 (1981).
17. Adler, S.L., Phys. Rev. 143 1144 (1966).
18. WA25, Allasia, D., et al., Z. Phys. C. Part and Fields 28 321 (1985).
19. Feltesse, J., Rapporteur's talk Proc. of the International Europhysics Conference on High Energy Physics, Bari (1985).
20. CCFRR, MacFarlane, D.B., et al., Z. Phys. Part. and Fields C26 1 (1984).
21. EMC, Aubert, J.J., et al., Nucl. Phys. B213 31 (1983).

22. EMC, Aubert, J.J., et al., Phys. Lett 123B 123 (1983).
23. EMC, Aubert, J.J., et al., Nucl. Phys. B259 189 (1985).
24. Duke, D. and Roberts, R.H., Phys. Rep. 120 275 (1985).
25. Sloan, T., EMC/86/9 (to be published in Nature).
26. EMC, Aubert, J.J., et al., Phys. Lett. 123B 275 (1983).
27. Bodek, A., et al., Phys. Rev. Lett. 50 1431 (1983).
Bodek, A., et al., Phys. Rev. Lett. 51 534 (1983).
28. Arnold, R.G., et al., Phys. Rev. Lett. 52 722 (1984).
29. BCDMS, Bari, G., et al., Phys. Lett. 163B 282 (1985).
30. Wachtmann, O., Proc. 11th Int. Conf. on Neutrino Physics and Astrophysics, Nordkirchen near Dortmund, 1984, p. 405;
Nikolaev, N.N., Oxford University preprint TP 58/84 (1984);
Llewellyn Smith, C.H., Proc. PANIC (Heidelberg) 1984, eds. Povh, B. and Putlitz, zu G., Nucl. Phys. A434 35c (1985);
Krzywicki, A., Proc. 11th Europhysics Conf. "Nuclear Physics with Electromagnetic Probes", Paris 1985, eds Gerard, A. and Semour, C., Nucl. Phys. A446 135c (1985);
Dias de Deus, J., Proc. Int. Conf. on High Energy Physics, Bari 1985, eds. Nitti L. and Preparata, G., p. 571.
31. Parker, M.A., et al., Nucl. Phys. B232 1 (1984).
Cooper, A.M., et al., Phys. Lett. 141B 327 (1984).
Ammosov, V.V., et al., PISMA v ZHETF 39 327 (1984).
Abramowicz, H., et al., Z. Phys. C25 29 (1984).
32. Teichert, K.M., Proceedings of this conference.
33. Carbon charge distribution: Bailey, J., et al., Nucl. Phys. B151 367 (1979).
Copper charge distribution: Atomic and Nuclear Data Tables 14 479 (1974).
34. de Forrest, T., Jr. and Walecka, J.D., Adv. in Phys. 15 1 (1966).
35. Nicholaev, N.N. and Zacharov, V.I., Phys. Lett. 55B 397 (1975).

HADRON PRODUCTION IN LEPTON-NUCLEON SCATTERING

Peter B. Renton

Nuclear Physics Laboratory
Oxford OX1 3RH
England

1. Introduction

This review is concerned with the properties of hadronic final states in deep inelastic lepton nucleon scattering, with an emphasis on recent, and often new, results. The main underlying physics motivation in these, and in similar studies on e^+e^- →hadrons and on jet production from hadron colliders, is to advance our understanding of Quantum Chromodynamics. Although the gross features expected from QCD, namely the production of hadron jets produced by the fragmentation of energetic partons, have been beautifully confirmed in e^+e^- and high energy $p\bar{p}$ collisions, precision tests have proven difficult. This arises, in part, from uncertainty in defining, at the hadron level, quantities for which there are reliable asymptotic QCD predictions. At the parton level, there are generally large contributions from higher order graphs in regions of phase space where one of the gluons is relatively soft, or two partons have relatively small effective mass (ie $(p_i + p_j)^2$ small).

In QED these problems can be handled by defining 'measurable' quantities which sum up the effects of soft and colinear photons. This procedure cannot be directly applied to QCD, of course, since the partons are not detected. The long-distance high order properties of the theory (ie the fragmentation of partons to hadrons) mean that the properties of the hadrons cannot be directly related to those of the underlying partons. While lattice QCD provides a future hope in the solution of these difficulties, the most common approach is to make simplifying assumptions or to use QCD motivated fragmentation models. These models are based on the quark parton model (QPM), so it is important to test the basic assumptions of the QPM, as well as the various additional assumptions made in the fragmentation models.

Fig.1 shows the basic lowest order diagram. This involves the exchange of a virtual γ^*, for μN scattering, and a $W^{\pm}$, for $\nu/\bar{\nu}$ charged current interactions. The data is generally corrected for higher order electromagnetic processes to correspond to this lowest order diagram. The kinematic quantities used to describe the events are the square of the exchanged four-momentum $q^2 = -Q^2$, the energy transferred by the virtual boson in the lab. system $\nu = E_\ell - E_{\ell'}$ and the Bjorken scaling variables $x_{BJ} = Q^2/2M\nu$ and $y = \nu/E_\ell$, where M is the nucleon mass. The centre of mass (cms) energy W of the outgoing hadronic system (or the γ^*-nucleon system) is uniquely determined for given values of x_{BJ} and Q^2, since

$$W^2 = M^2 + Q^2(1/x_{BJ} - 1). \tag{1}$$

The bulk of the experimental results are on the inclusive properties of the final state hadrons. Their momenta can be conveniently resolved along (p_L) and transverse to (p_T) the virtual boson direction. In the hadronic cms the Feynman variable x_F and the rapidity y^* are used and are defined as

$$x_F = \frac{2p_L}{W} \quad ; \quad y^* = \frac{1}{2}\log\left(\frac{E+p_L}{E-p_L}\right) \tag{2}$$

In the lab. system $z = E_{had}/\nu$ is frequently used. Note that for $x_F \gtrsim 0.2$ and for high values of W, $x_F \approx z$. In the QPM, z (or x_F) represents the fraction of the energy of the struck quark carried by the hadron.

In the QPM, x_{BJ} is the fraction of the nucleon's momentum carried by the struck quark in a frame in which the nucleon has a momentum large enough that masses and momenta transverse to the virtual boson direction can be neglected. In $\nu(\bar{\nu})$ nucleon interactions the main valence quark transition is $W^+d \to u$ ($W^-u \to d$), so that the fragmentation products in the current (forward) region are mainly those of a $u(d)$ quark.

In μp scattering valence quark interactions occur off both u and d quarks, but in the ratio 4:1 (from the squares of the quark charges). Since the proton is uud and the d quark distribution is suppressed at large x_{BJ}, most of the interactions are off u quarks at large x_{BJ}. At small x_{BJ} ($\lesssim 0.15$ for $Q^2 \sim 10$ GeV^2) there is also a large contribution from sea-quark interactions. The main final states at the parton level are given in Table 1. A similar list can be written down for scattering off neutrons. Lepton scattering thus provides an ideal laboratory for the study of the fragmentation of light quarks and various diquark combinations.

The QCD $O(\alpha_s)$ corrections to the QPM process are shown in fig.2. These configurations will, at sufficiently high energies, lead to 3-jet final states. The soft gluon limit of these diagrams is also expected to influence the properties of the final state hadrons. The asymptotic requirements needed for the validity of leading order QCD are not met in practice, so that sizeable non-perturbative effects are expected. For example, the struck quark can have a transverse momentum, k_T, arising from its confinement in the nucleon. From the uncertainty principle one expects $k_T \sim 1/R_N \sim 0.3$ GeV, and this has the effect of rotating the parton configuration with respect to the virtual boson (fig.3).

What happens in between the production of energetic partons in the interaction and the emergence of hadrons in the laboratory can only be approximated by models. The energetic struck quark can go off-shell ($\sim Q^2$) and it is expected, in most models, that the fragmentation process occurs over a distance of several fermis. Much of the analysis work on the properties of the final state hadrons is thus in the testing of models. Four main models have been tested in lepton-nucleon scattering

i) Independent jet model of Field and Feynman [1]. As an energetic parton leaves the interaction region, $q - \bar{q}$ pairs are formed in the resulting colour field. The $q - \bar{q}$ pairs are suitably combined to form mesons. Baryons can be added by producing $(qq)-(\bar{q}\bar{q})$ pairs, either directly or indirectly. Jets are treated separately, with consequent problems in joining them together and maintaining relativistic invariance.

ii) Lund string model [2]. In this model the colour field is represented as a string stretched between the q (colour 3) and qq pair (colour $\bar{3}$). The string subsequently breaks up and fragments to hadrons. A gluon is represented as a 'kink' in the string. This model is found to reproduce many aspects of lepton-nucleon final states, but contains a rather large number of parameters.

iii) QCD Branching models eg. Webber model [3]. In this model the off-shell quark loses energy by the branching processes ($q \to q + g$, $g \to q + \bar{q}$, $g \to g + g$ etc.), calculated in the leading log approximation and including the effects of soft gluon interference, until colourless clusters of partons of low mass ($\lesssim 1$ GeV) are formed. These clusters are then hadronised, using phase space formulae, to the known hadrons.

iv) Firestring model [4]. In this model the ideas of QCD, in particular dynamical gluons, are not used. The hadrons are produced by the decay of one or more firestrings, formed by interactions of the virtual bosons with the quarks and anti-quarks. A confrontation with the data is described in [5].

On the experimental side, the $\nu/\bar{\nu}$ data come from the FNAL 15' and CERN BEBC bubble chambers; filled with either H_2, D_2 or Ne. A typical charged current event sample from one of these exposures has about 10K evetns, $< E_\nu > \sim 50$ GeV (but with a long tail to high energies) and W up to about 12 GeV. Charged particles can be identified by ionisation, but only for $p_{lab} \lesssim 1$ GeV. Neutral decays (K°, Λ) are identified by kinematics. The muon data come from three phases of the European

Muon Collaboration (EMC) programme. In the first and third phases (NA2 1978/80 and NA2' 1984/5), only hadrons which were forward going in the cms were detected. Data samples with $E_\mu = 120$, 200 and 280 GeV have been collected from these phases. Long targets of H_2 and D_2 were used for the NA2 phase, giving consequently high statistics ($\sim$ 500K events). In the NA2' phase, hadrons from a polarised target (mainly NH_3) and from some additional parisitic targets of D_2, He, C, Cu and Sn (to study A dependent effects), have been used. The NA9 phase (1981/3) has $\sim 4\pi$ acceptance for charged hadrons and good particle identification (in contrast to the NA2 set up). Using differential Cherenkov and time of flight counters about 50% of the charged final state hadrons are identified. The beam energy used was 280 GeV and the event samples consist of about 25K on H_2 and 20K on D_2, with $< Q^2 > \sim 20$ GeV^2 and $4 < W < 20$ GeV.

A general review of hadron properties in $\ell - N$ scattering can be found in [6] and some more recent results are covered in [5].

2. Point-like nature of the virtual boson probe

It is generally assumed that, at high enough Q^2, the virtual γ^* (or $W^\pm$) behaves as a point-like probe of the q and $\bar{q}$ constituents of the nucleon. However, the analysis of the interactions of real photons ($Q^2 = 0$) on nucleons and of low energy electroproduction ($Q^2 \lesssim 1$ GeV^2), has led to the following picture of the photon. Fluctuations from the γ (real or virtual) to a $q\bar{q}$ pair can occur, the time of which is limited by the uncertainty principle. This $q\bar{q}$ pair will carry the quantum numbers of the photon and can thus behave as a virtual vector meson (ρ, ω, ϕ, J/ψ etc). The vector meson-nucleon cross section is large, so that the probability that the virtual meson interacts is high, and these interactions account for the bulk of the total $\gamma(\gamma^*) - N$ cross section. This picture is called the vector meson dominance model (VDM) and predicts that the final states will be generally diffractive in nature (ie the momentum transferred to the nucleon will be small).

The diagram in the VDM for the exclusive reaction $\mu N \to \mu N \rho^\circ$ is shown in fig.4. The γ^* converts into a virtual ρ°, which scatters diffractively (ie with small t) off the nucleon (eg by Pomeron exchange). The γ^* can be polarised either transversely (helicity $\lambda = \pm 1$) or longitudinally (helicity $\lambda = 0$). The helicity of the final state ρ° can be measured from the distribution of the angle (θ) made by the π with respect to the ρ° direction, in the ρ° cms. In general we have, integrating over azimuthal angles,

$$W(\cos\theta) = \frac{3}{4}\left[(1-r)\sin^2\theta + 2r\cos^2\theta\right] \qquad (3)$$

where $r = 0$ corresponds to a transverse $\rho^\circ(\lambda = \pm 1)$ and $r = 1$ to a longitudinal $\rho^\circ(\lambda = 0)$, giving a $\sin^2\theta$ or $\cos^2\theta$ angular distribution respectively.

Measurement of the ratio of the longitudinal to transverse virtual photon cross sections for this process gives, for $Q^2 = 2$ GeV^2, $R = \sigma_L/\sigma_T = -0.38 \pm 0.14(\text{stat})^{+0.9}_{-0.4}(\text{syst})$ [7]. Hence the photons are mainly transverse. Fig.5a shows the results of some measurements of r as a function of Q^2. It can be seen that r changes from $r \sim 0(\lambda = \pm 1)$ at $Q^2 = 0$ (which corresponds to the ρ° helicity being equal to that of the γ^* i.e. s-channel helicity conservation) to $r = 1(\lambda = 0)$ for $Q^2 \gtrsim 5$ GeV^2. It is interesting to note that inclusive ρ°'s in $\bar{\nu}$Ne scattering favour $\lambda \sim 0$ [5].

The t dependence (see fig.4) of elastic ρ° production can be parameterised by

$$\frac{d\sigma}{dt} \sim e^{-b|t|} \quad , \qquad |t| \sim p_T^2 \qquad (4)$$

In the VDM $b \approx (R_\rho^2 + R_N^2)/2$, where R_ρ and R_N are the ρ° and N radii. From the uncertainty principle, the lifetime of the virtual ρ° is

$$\Delta\tau \sim \frac{1}{\Delta E} = \frac{1}{\nu - \sqrt{\nu^2 - Q^2 - m_\rho^2}} \simeq \frac{2\nu}{Q^2 + m_\rho^2} \tag{5}$$

In the ρ° cms $R_\rho \approx 2m_\rho/(Q^2 + m_\rho^2)$, which is much less than 1 fm for $Q^2 > 1$ GeV^2. Hence, at large Q^2, $b \to R_N^2/2 \sim 4$ GeV^{-2}. Fig.5b shows some data on the values of b as a function of Q^2. The slope is steep ($b \sim 8$) at $Q^2 \lesssim 1$ GeV^2 but becomes progressively broader (ie harder p_T distribution) as Q^2 grows. Thus for $Q^2 \gtrsim 5$ GeV^2 the elastic ρ° channel has the characteristics of a hard scattering process and not that of a diffractive hadron process.

The $W^\pm$ probe can also dissociate into virtual mesons. The coherent production of a single π^- in the process $\bar{\nu}_\mu Ne \to \mu^+\pi^- Ne$ has been studied by the WA59 Collaboration [8] to look for such effects. This process can occur by a $W^- \to \rho^-$ transition, together with the exchange of an ω° in the t-channel (ie vector interaction) or by $W^- \to A_1^-(\pi^-)$ and a Pomeron exchange in the t-channel (ie axial vector interaction). The vector term has a cross section $\sigma(Q^2 \to 0) \to 0$, from CVC. The $W^- \to \pi^-$ transition arises from PCAC ($\partial_\mu A^\mu = f_\pi \phi_\pi$), but is predicted to give a small contribution. The main term is thus the A_1 contribution, which using PCAC and VDM can be written

$$d\sigma \sim G^2 f_\pi^2 \frac{d\sigma^{\pi N_s \to \pi N_s}}{dt} \left(\frac{m_A^2}{m_A^2 + Q^2}\right)^2 \times \begin{pmatrix}\text{kinematic}\\ \text{term}\end{pmatrix} \tag{6}$$

Experimentally it is found that

$$\frac{\sigma(\bar{\nu}_\mu + Ne \to \mu^+\pi^- Ne)}{\sigma_{\text{tot}}} = (0.9 \pm 0.1)\% \tag{7}$$

Fitting the data to equation 6, a plausible value of $M_A (= 1.35 \pm 0.18$ GeV) is found. Further, the model gives a reasonable fit to the dependence of the cross section on the various kinematic distributions.

It is also of interest to investigate whether a deuterium target, which is normally treated as a loosely bound system of p and n (and thus elementary), has additional structure. It has been suggested that the deuteron may be composed, for some fraction G of the time, of $\Delta(1236)\,\Delta(1236)$. From isospin symmetry, the states $\Delta^{++}\Delta^-$ and $\Delta^+\Delta^\circ$ should be equally probable. If an interaction occurs on the Δ^-, then the spectator Δ^{++} should leave an experimentally measurable signal from its $p\pi^+$ deacy. A study of the interactions of ν_μ and $\bar{\nu}_\mu$ in D_2 should then lead to a signal in ν_μ, but not in $\bar{\nu}_\mu$ (since the $\bar{\nu}_\mu$ does not interact with the valence quarks of $\Delta^- = ddd$). A search in these reactions has been made for a Δ^{++} signature [9]. No signal was found and an upper limit $G < 0.4\%$ at the 90% c.l. is given.

3. Tests of the Quark Parton Model

Much of our knowledge of the strong and electroweak properties of quarks has been extracted from the data assuming the QPM. It is thus important to test, wherever possible, the underlying assumptions of the QPM. The normalised cross section for the production of a hadron h in deep inelastic scattering is given, in the QPM, by

$$\frac{1}{\sigma_{\nu\nu}} \frac{d\sigma^h}{dz}(x,z) = \frac{1}{N_\mu} \frac{dN^h}{dz} = \frac{\sum_q e_q^2 x q(x) D_q^h(z)}{\sum_q e_q^2 x q(x)} \tag{8}$$

where the sum is over all q and $\bar{q}$ contributing to the cross section and D_q^h is the fragmentation function for quark q to fragment to hadron h. The denominator is equal to the structure function $F_2(x)$ and, for H_2 and D_2 targets, has the form

$$F_2^{H_2}(x) = \frac{4}{9}xu_v(x) + \frac{1}{9}xd_v(x) + sea \tag{9}$$

$$F_2^{D_2}(x) = \frac{5}{9}[xu_v(x) + xd_v(x)] + sea \tag{10}$$

where the valence quark distributions refer to the proton.

Assuming that $D_u^{\pi^+} = D_{\bar{d}}^{\pi^-}$, $D_u^{\pi^-} = D_{\bar{d}}^{\pi^+}$ (from isospin) and also $D_u^{K^-} = D_{\bar{d}}^{K^+}$, $D_u^p = 2D_{\bar{d}}^p$ etc., then

$$\sum(x,z) = \frac{1}{N_\mu}\left[\frac{dN^{h^+}}{dx} + \frac{dN^{h^-}}{dx}\right] \approx D_u^{h^+}(z) + D_u^{h^-}(z) \tag{11}$$

where the approximation is expected to be good to a few percent. That is, $\sum$ should not depend on x, nor on the target, so that $\sum_{\mu p} = \sum_{\mu d}$. Some data on $\sum$ from high energy μp and μd interactions [10] is shown in fig.6, and it can be seen that the prediction is consistent with the data.

If we take the difference between h^+ and h^-, namely

$$\Delta^h(x,z) = \frac{1}{N_\mu}\left[\frac{dN^{h^+}}{dx} - \frac{dN^{h^-}}{dx}\right] \tag{12}$$

the effects of sea-quarks cancel. For example,

$$\Delta^\pi(x,z) = \frac{1}{F_2(x)}\left[\frac{4}{9}xu_v(x) - \frac{1}{9}xd_v(x)\right]\left[D_u^{\pi^+}(z) - D_u^{\pi^-}(z)\right] \tag{13}$$

Thus Δ can be factorised into x and z dependent parts. Similar equations can be written down for Δ^K and Δ^P. By measuring Δ^π, Δ^K and Δ^P in μp and μd interactions the structure functions $u_v(x)$ and $d_v(x)$ can be extracted. This has been done using identified $\pi^\pm$, $K^\pm$ p and $\bar{p}$ hadrons, with $x_F > 0$, by the EMC NA9 Collaboration. The quark distribution $u_v(x)$, extracted in this way, is compared in fig.7 to that determined by fitting functional forms to the EMC H_2 and D_2 structure functions [11]. Attention should be drawn to the remarkable similarity of the results, rather than to the possible small differences at small x. Note that the extraction of $u_v(x)$ from the structure functions is sensitive, at small x, to the parameterisation assumed for the sea.

Using the μd data from the EMC NA2 experiment, the fragmentation functions $D_u^{\pi^+}$ and $D_u^{\pi^-}$ have been extracted [12]. Since the above tests of the QPM have proven satisfactory, this can be done with some degree of confidence. The data is restricted to $x_{BJ} > 0.15$, so that the corrections for sea-quark contributions are small. The resulting fragmentation functions can be parameterised (for $z > 0.1$) by

$$zD_u^{\pi^+} = 0.7(1-z)^{1.75}, \quad zD_u^{\pi^-} = \frac{(1-z)}{(1+z)}zD_u^{\pi^+} \tag{14}$$

The difference $D_L^{\pi^+}(z) = D_u^{\pi^+}(z) - D_u^{\pi^-}(z)$ gives the fragmentation function of a u-quark to a leading π^+; that is to a π^+ formed by a u-quark picking up a $\bar{d}$ quark directly (or from the decay of a resonance eg ρ^+). Contributions further down the fragmentation cancel. Fig.8 shows the measured distribution of $D_L^{\pi^+}(z)$, and it can

be seen that small values of z are favoured. This is in contrast to heavy (c,b) quark fragmentation, where $< z_L > \gtrsim 0.5$. The momentum fraction $zD_L^{\pi^+}$ carried by the leading π is roughly constant up to $z = 0.5$, and then drops rapidly.

4. Fragmentation to Identified Hadrons

Detailed measurements on the fragmentation properties of identified hadrons are an important ingredient in our attempts to understand the hard to soft fragmentation process. Data, from μp scattering, now exist on $\pi^{\pm}$, π^c, $K^{\pm}$, K^o, p, $\bar{p}$, Λ $\bar{\Lambda}$ and on the ρ, ω, ϕ, K^*, f, Δ^{++} and J/ψ resonances. Obvious questions to be answered are what are relative production rates of vector and tensor particles relative to pseudoscalar particles and what is the mechanism by which baryons are produced.

The Lund model (with the ratio of $s\bar{s}$ to $u\bar{u}$ pairs set to $\gamma_s/\gamma_u = 0.3$, the ratio of $(qq) - (\bar{q}\bar{q})$ pairs to $q - \bar{q}$ pairs set to $\gamma_{qq}/\gamma_q = 0.075$ and with the ratio $V/PS = 1$) can be used as a guide to the data. The Lund model adequately reproduces the observed proton distribution, but overestimates Δ^{++} production by a factor of about two [5]. SU(6) symmetry for the proton target is assumed in the model, however this could be violated, for example, by the presence of a $(ud)_{I=S=0}$ diquark state.

Fig.9 shows the normalised x_F distributions for ρ^o, K^{*o} and $\bar{K}^{*o}$ mesons from the μp EMC NA9 experiment. The ρ^o production in the central region falls below the Lund model curve. The $K^*(892)$ production is, however, reasonably well reproduced, including the excess of K^{*o} over $\bar{K}^{*o}$ in the backward hemisphere. This can be understood, because the K^{*o} can be produced more easily with a Λ^o.

A comparison of the z distributions of non-strange vector mesons is shown in fig.10. The inelastic data ($z < 1$) on ρ^o, ω^c and ϕ come from the NA9 experiment. The elastic ρ^o point (at $z = 1$) is from the NA2 phase of the experiment [7], and has $< Q^2 >= 17$ GeV^2 (which is similar to that of the inelastic data). The ratio of elastic ϕ to elastic ρ^o production has been determined, using data obtained from the NA2′ polarised target (mainly NH_3), to be $(1.6 \pm 0.4)/9$, with $< Q^2 > \sim 7.5$ GeV^2. This ratio is considerable larger than that measured for real photons ($\sim 0.6/9$) or that for low energy electroproduction and approaches the value $\phi/\rho = 2/9$, expected from SU(3). The elastic ϕ point in fig.10 is obtained by scaling the elastic ρ^o point by the measured ϕ/ρ ratio. The J/ψ data is from the NA2 phase of the experiment (using an iron target) and is normalised to 8/9 of the ρ^o elastic (ie the SU(3) prediction). Possible mechanisms for the fragmentation of light and heavy quarks to vector mesons are shown in fig.11. The mechanism of fig.11a would lead to a rapidly falling fragmentation function with increasing z (as observed for ρ^o and ω). The photon gluon fusion diagram (fig.11b), which reproduces most aspects of J/ψ production, gives a fragmentation function which increases as $z \to 1$ (ie as the final state gluon radiated becomes softer). The $\phi(s\bar{s})$ data falls less rapidly than that for ρ^o and ω, indicating perhaps that both mechanisms may contribute.

The production mechanism of tensor mesons is also of interest. Fig.12 shows a comparison of the normalised x_F distribution of the $f(1270)$ meson (identified as a peak in the $\pi\pi$ mass spectrum), compared to the distributions of ρ^o and protons. Unlike the ρ^c meson, the f shows no peak in the central region and the shape of the distribution is more similar to the proton than to the ρ^o. Factors which could contribute to the suppression of the f in the central region are its high mass and high spin (if indeed the peak is the $J^P = 2^+ f$ meson).

5. Direct Photon Production

The observation of direct photons (ie not from the decay of π^c, ω, η etc.) in hadronic final states is potentially of great interest in understanding the behaviour of

quarks in the fragmentation process. In a recent analysis of the EMC NA2 200 GeV μp data, such a direct photon signal has been observed. Using a lead-glass detector, signals compatible with having arisen from a single photon (with $E_\gamma > 5$ GeV) were extracted. Fig.13 shows the z-distribution of the observed photons, together with the yields expected from QED processes on the ingoing and outgoing muons and from the decays of π°, ω, η etc. The latter curve was calculated using the Lund model, which was carefully tuned to fit the observed π° spectra in the same experiment. For $z_\gamma \lesssim 0.4$, the photon data is larger than the sum of these contributions. The difference, which is attributable to direct photon production, is also shown in fig.13. The total observed yield after acceptance correction is $N_\gamma(z_\gamma > 0.05)/N_\mu = 0.15 \pm 0.01(\text{stat.}) \pm 0.06(\text{syst.})$.

A possible source of the direct photons is the QED Compton process. This corresponds to the graphs shown in figs.2a and b, with the gluon replaced by a photon. A calculation of this process [13] leads to the photon fragmentation function

$$D_q^\gamma(z) = \frac{\alpha}{2\pi} e_q^2 \frac{1+(1-z)^2}{z} \ln \frac{Q^2}{m_q^2} \qquad (15)$$

For $m_q = 3$ MeV (ie a current quark mass) and $< Q^2 > \sim 10\ \text{GeV}^2$, this gives $N_\gamma/N_\gamma = 0.023$; somewhat less than the observed yield.

The differential distributions of the direct photons, as a function of z_γ and p_T^2 (wrt the virtual photon) are shown in figs.14a and b respectively. Also shown are the expectations from the QED Compton model for $m_q = 3$ MeV and $m_q = 300$ MeV. It can be seen that the data is much larger than the prediction at small $z(\lesssim 0.2)$. The p_T^2 distribution is also underestimated. Note that the p_T^2 distribution of the direct photons is much softer than those of π° mesons.

6. Transverse Momenta

Momenta transverse to the virtual photon direction are sensitive to the magnitude of the various potential underlying sources. In the large p_T region, perturbative QCD should dominate, leading to production of events with two forward jets. At the other extreme, soft hadronisation processes will dominate for $< p_T^2 > \lesssim (0.4\ \text{GeV})^2$; this is the domain of fragmentation models. From the form of the leading log QCD formulae, significant production of soft gluons is expected at the parton level. These gluons may be too soft to form a separate jet, but may well influence the final state hadrons. In the Lund model, the transverse momenta of the soft gluons are summed over one unit of rapidity and given to the final state hadrons. The recoil is taken up by the struck quark. In this scheme the p_T of the leading $h^\pm$ is compensated in the central region. Another source of transverse momentum is the intrinsic k_T of the struck quark, which leads essentially to a rotation of the jet axes wrt the γ^* axis. In this case the p_T of the leading $h^\pm$ will be compensated in the backward (target fragmentation) region.

Fig.15 shows a plot of $< p_T^2 >$ against x_F, for all charged hadrons, from the μp NA9 experiment. Also shown are various curves computed using the Lund model. It can be seen that the inclusion of both hard and soft gluon radiation, together with a value $< k_T^2 > \sim (0.4\ \text{GeV})^2$, are needed to reproduce the data. An estimate of the value of $< k_T^2 >$ has been made using $< P_T >$, where $P_T = |\Sigma \mathbf{p}_T|$ is the modulus of the sum of the $\mathbf{p}_T$ vectors of the backward going hadrons. It is found that $< k_T^2 >$ is correlated to the parameter σ_q, which controls the width of the transverse momentum distribution for fragmentation. The parameter σ_q is found from a study of $< \delta_q >$, where $\delta_q = |\mathbf{p}_{T_1} - \mathbf{p}_{T_2}|$ is the absolute value of the difference between the transverse momentum vectors of hadrons having opposite charge and within 1 unit of rapidity.

Comparison of the measured values of $< P_T >$ and $< \delta_q >$ with those computed by Monte Carlo with different settings of $< k_T^2 >$ and σ_q gives

$$< k_T^2 > = \left[0.29^{+.05}_{-.06}(\text{stat})^{+.14}_{-.18}(\text{syst})\ \text{GeV}\right]^2$$
$$\sigma_q = 0.410 \pm 0.002 \pm 0.020\ \text{GeV} \qquad (16)$$

The values $< k_T^2 >= (0.44\ \text{GeV})^2$ and $\sigma_q = 0.44$ GeV are used in the curves labelled standard Lund in figs.15, 16 and 17. The transverse momentum balancing the leading particle in the forward direction (defined as $x_F > 0.5$) is shown in figs.16a and b as a function of y^*. The data is the same in both cases. Figs.16c and d show the p_T balancing a trigger particle in the backward direction ($-0.5 < x_F < -0.2$). The conclusion concerning the Lund model (figs.16a and c) is the same as that for the plot of $< p_T^2 >$ v. x_F. In figs.16b and d two variants of the independent jet model are shown, corresponding to the energy-momentum conservation schemes of Hoyer *et al* and Ali *et al*. The independent jet model, the parameters of which were tuned to fit the data as well as possible, fails to reproduce the behaviour of the p_T compensation.

An obvious question to be asked is whether there is any direct evidence for hard QCD 3-jet processes and to what extent such final states can be distinguished from higher order effects or from the effects of soft gluons. A search for events with three well separated jet has shown that their production rate is small (< 1%). However, evidence for hard QCD effects is found from a study of $\sum(p_T^{in})^2$ in the event plane (defined as the plane minimising $\sum(p_T^{out})^2$ for events with ≥ 4 forward charged hadrons). From fig.17 it can be seen that a long tail, compatible with planar events, is found and that this is well reproduced by hard QCD (with $\alpha_s(Q^2 = 20\ \text{GeV}^2) \sim 0.25$). The inclusion or exclusion of soft gluons does not substantially change the prediction.

QCD studies of the energy flow of the energy flow of final state hadrons are difficult to interpret because of their dependence on the fragmentation models. An interesting variable in this context is that proposed by Ochs and Stodolsky [14], namely

$$\lambda = \frac{x_F}{p_T} = \frac{2\cot\theta}{W} \qquad (17)$$

where θ is the angle made by a hadron with the virtual photon. Defining $d\epsilon = dE/E_{jet}$, where E is the hadron energy, then in cascade models, the energy flow $d\epsilon/d\lambda$ is predicted to be independent to E_{jet}. Fig.18 shows the ratios of the distributions of $d\epsilon/d\lambda$, as a function of λ, for various intervals of W. The denominator is in all cases $4 < W < 8$ GeV. It can be seen that the data is consistent with scaling in the backward direction but that there is an increase of $d\epsilon/d\lambda$ in the forward direction. This increase grows with increasing W. The independent jet model, with QCD included and $\Lambda = 300$ MeV, falls well below this increase. Increasing Λ would make the model incompatible with the data in the backward hemisphere. The Lund model with QCD adequately reproduces the data.

In e^+e^- annihilation, the QCD cluster model of Webber successfully accounts for many aspects of the data. The model predicts that, at the parton level,

$$x\frac{d\sigma}{dx}\ \text{v.}\log\left(\frac{1}{x}\right) \xrightarrow{\text{large } W^2} \text{gaussian with max. at } \frac{1}{4}\log\left(\frac{W^2}{W_0^2}\right) \qquad (18)$$

where $x = 2p/W$. The position of the maximum versus $\ln W^2$ should thus be linear, with a slope of 1/4. For the hadrons, this prediction may be modified by the effects of hadronisation.

The distributions of $x d\sigma/dx$, as a function of $1/x$, have been investigated for identified $\pi^{\pm}$, $K^{\pm}$, K° and ρ, all with $x_F > 0$, from the EMC (NA9) μp experiment. The distributions are indeed gaussian in shape and the positions of the maxima, as a function of W^2, are shown in fig.19. Also shown are some e^+e^- data from TASSO and the predictions of the Webber and Lund models. The Webber model is that for e^+e^-, modified to include the appropriate quark distribution functions for deep inelastic scattering. The Lund model serves as a control. Note that it is only the slopes of the distributions which should be compared with the theory. The slopes are summarised in table 2. It can be seen that for the heavier hadrons (K, p), the hadronisation in the Webber model does not significantly change the slope from the parton value of 0.25. The data are consistent with the Webber model, which contains the effects of soft gluon interference, and also with the Lund model, which does not.

7. Lepto-production off nuclear targets

The study of hadrons produced in a dense nuclear environment has two main aims. Firstly, by interfering with the process of hadronisation one may learn something about it. Secondly the flavour content of the leading hadrons can be used as a tool to study the quark distributions in nuclei. Such studies provide, therefore, a rather unique tool. Charged hadron data, in the forward direction, has been collected off deuterium, copper and other nuclear targets (He, C, Sn) in the NA2′ experiment. The copper nucleus has a radius of $\sim$ 5fm, which is large compared to the mean interaction length of a pion in nuclear matter $\ell_\pi \sim$ 2.4fm). Thus a pion created at the centre of the nucleus has about a 90% change of interacting. One common idea in many models of hadronisation is that the struck quark will travel a finite distance before fragmenting (formation length). Thus, if the hadronisation occurs outside the nucleus, there will be no attenuation of the hadrons, provided the parent partons traverse nuclear matter without interacting (theoretically there is some belief that this may be so). If the distance over which a hadron is formed is related to the hadron size ($\sim$ 1fm) then, in the lab system, this will be Lorentz boosted to larger distances. Hence fragmentation effects may depend on the velocity of the quark in the lab system and hence on ν.

Fig.20 shows some measurements of the ratios of the z distributions, for Cu and D_2 targets, for different regions of ν. The data were obtained using 120 and 200 GeV beam energies. The D_2 target, for the purposes of the comparison with Cu, can be considered as a free proton and neutron (at least to a good approximation). In addition to the statistical errors shown in fig.20 there is an overall systematic uncertainty of $\pm 10\%$. Fig.21 shows the ratio of $< p_T^2 >$ for Cu to D_2, for different regions of ν. Secondary interaction effects in the nucleus are expected to broaden the jet. Figs.20 and 21 show that the jet properties in Cu and D_2 are rather similar. Any nuclear effects are rather small ($\lesssim 20\%$), and are not a strong function of either z (in the range $z \geq 0.05$) or ν (in the range 30 to 200 GeV). This implies that the hadronisation process occurs mainly outside the nucleus. These results confirm a previous study made using the NA2 set-up [15]. An experiment at SLAC, exploring much lower ν values ($\sim$ 10 GeV), found considerable attenuation of hadrons in heavy nuclei [16]. These results, when combined with the EMC data at high ν, indicate that the formation length increases with ν. The long formation length for jet formation, together with the short ($\lesssim$ 1fm) longitudinal dimension found for the Bose-Einstein interference effects for like-sign pions [17], may indicate a space-time ordering of the hadron momenta. A reduction in the size of both the statistical and systematic errors, and the analysis of more nuclei, is expected from the more recent EMC data.

8. Summary and Conclusions

The region $Q^2 \gtrsim 5$ GeV^2 and $W \gtrsim 10$ GeV can be considered as the domain of deep inelastic scattering. Here the virtual γ^* ($W^{\pm *}$) behaves as a point-like probe and the assumptions of the QPM are satisfied to within the current precision of the data. Detailed measurements now exist for the fragmentation functions of vector mesons and the results are compatible with the production by a chain-like fragmentation mechanism for light quarks and from photon-gluon fusion for heavy quarks. The $f(1270)$ has a production spectrum in x_F more similar to the proton than to the ρ^0 meson. Preliminary results on the extraction of direct photons now exist and the measured cross section is higher than that expected from the Compton QED process.

In the domain of models, the independent jet model fails to reproduce the p_T correlations between the forward and backward jets and the behaviour of the scaled energy flow with W. The Webber model has not been fully formulated for deep inelastic scattering but, where tested, is consistent with the data. The Lund string model is compatible with many aspects of the data, provided that hard QCD and soft gluon effects are included and that a value $< k_T^2 > \sim (0.4 \text{ GeV})^2$ is used for the intrinsic k_T of the struck quark.

The hadronic jets formed in collisions on Cu and D_2 nuclei are rather similar, indicating that the fragmentation of fast hadrons occurs mainly outside the nucleus. Possible differencies are $\sim 10\%$, but will need further studies in order to establish them firmly.

Table 1

Main reactions at the parton level for deep inelastic lepton-proton scattering at $Q^2 \sim 10$ GeV^2.

Interaction		Forward	Backward
νp	valence	u	uu
	sea	$\bar{d}_s$	$uud\bar{u}_s$
$\bar{\nu} p$	valence	$\bar{d}$	$\bar{u}\bar{d}$
	sea	$\bar{u}_s$	$\bar{u}\bar{d}\bar{d}_s$
μp	valence	$\frac{4}{9}u + \frac{1}{9}d$	$\frac{4}{9}ud + \frac{1}{9}uu$
	sea	$\frac{4}{9}(u_s + \bar{u}_s) + \frac{1}{9}(d_s + \bar{d}_s)$	$\frac{4}{9}uud(\bar{u}_s + u_s) + \frac{1}{9}uud(\bar{d}_s + d_s)$

Table 2

Slope	$\pi^\pm$	$K^\pm$	K^0	P
data	$.42 \pm .01 \pm .02$	$.29 \pm .06 \pm .09$	$.36 \pm .12 \pm .10$	$.21 \pm .05 \pm .06$
Lund model	.38	.43	.35	.23
Webber model	.32	.26	.24	.25

Acknowledgements

I would like to thank the organisers of the symposium and all my Polish colleagues for their warm hospitality. I thank also my colleagues in the EMC for their help.

References

[1] Field R.D. and Feynman R.P., *Phys. Rev.* D15, 2590 (1977).
[2] Anderson B. *et al*, *Phys. Rep.* 97, 31 (1983).
[3] Webber B.R., *Nucl. Phys.* B238, 492 (1984).
[4] Preparata G. *et al*, BARI/GT 83/10, 84/06 and refs. therein.
[5] Renton P., Proceedings of the XVI Symposium on Multi-particle Dynamics, Kiryat Anavim, Israel (1985) p.17.
[6] Renton P. and Williams W.S.C., *Ann. Rev. Nucl. Sci.* 31, 193 (1981).
[7] Aubert J.J. *et al* (EMC), *Phys. Lett.* 161B, 203 (1985).
[8] Marage P. *et al* (WA59), *Z. Phys.* C31, 191 (1986).
[9] Tenner A.G., NIKHEF-H/86-7. (1986)
[10] Aubert J.J. *et al* (EMC), *Z. Phys.* C31, 175 (1986).
[11] Gibson V., Proceedings of the International Europhysics Conference on High Energy Physics, Bari, July 1985, p.561.
[12] Aubert J.J. *et al* (EMC), *Phys. Lett.* 160B, 417 (1985).
[13] Ingelman G., private communication.
[14] Ochs W. and Stodolski, *Phys. Lett.* 69B, 225 (1977).
[15] Aubert J.J. *et al* (EMC), *Nucl. Phys.* B248, 381 (1984).
[16] Osborne L.S. *et al*, *Phys. Rev. Lett.* 40, 1624 (1978).
[17] Arneodo *et al* (EMC), CERN-EP/86-42.

Figure Captions

Fig.1. Lowest order diagram for lepton-nucleon scattering.

Fig.2. $O(\alpha_s)$ QCD corrections to the QPM diagram.

Fig.3. Effect of the intrinsic k_T of the struck quark on the scattering process.

Fig.4. VDM diagram for $\mu N \rightarrow \mu N \rho^0$.

Fig.5. Distributions of a) polarisation parameter r and b) slope parameter b as a function of Q^2.

Fig.6. Distributions of $\sum$ as a function of x for μp and μd interactions.

Fig.7. Valence quark distribution determined from the structure functions and from the final state hadrons.

Fig.8. Fragmentation function for a leading π^+ as a function of z.

Fig.9. Distributions in x_F of ρ^0, K^{*0} and $\bar{K}^{*0}$.

Fig.10. Distributions in z for the vector mesons ρ, ω^0, ϕ and J/ψ. The elastic data is shown at $z = 1$.

Fig.11. Possible fragmentation mechanisms a) chain mechanism b) photon-gluon fusion.

Fig.12. Distributions in x_F of ρ^0, f and p.

Fig.13. Distribution in x_γ of observed photons in 200 GeV μp interactions.

Fig.14. Distributions of direct photons in a) x_γ and b) p_T^2. The curves are for the QED Compton process for different values of the quark masses.

Fig.15. $< p_T^2 >$ as a function of x_F. The Lund model curves with hard QCD, soft gluons and $< k_T^2 >= (0.44\ \mathrm{GeV})^2$ is called the standard curve. Variations from this are labelled.

Fig.16. Distributions of the transverse momenta balancing a trigger particle with $x_F > 0.5$ in a) and b) and $-0.5 < x_F < -0.2$ in c) and d). The curves in a) and c) are from the Lund model and in b) and d) from two variants of the independent jet model.

Fig.17. Distribution of $\sum (p_T^{in})^2$, the curves are for the Lund model.

Fig.18. Ratio of the distributions of $d\epsilon/d\lambda(W_2)/d\epsilon/d\lambda(W_1)$ for various intervals of W_2. For each W_2, $4 < W_1 < 8$ GeV. The curves are for the independent jet and the Lund models.

Fig.19. Maxima of $1/x$ distributions as a function of W^2 for identified $\pi^\pm$, $K^\pm$, K^0 and p.

Fig.20. Ratios of the z distributions of Cu/D_2 for different regions of ν.

Fig.21. Ratios of $< p_T^2 >$ for Cu and D_2, as a function of ν.

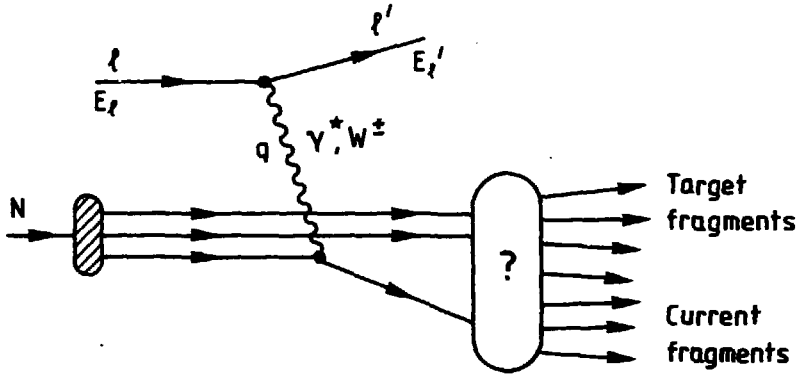

Fig. 1.

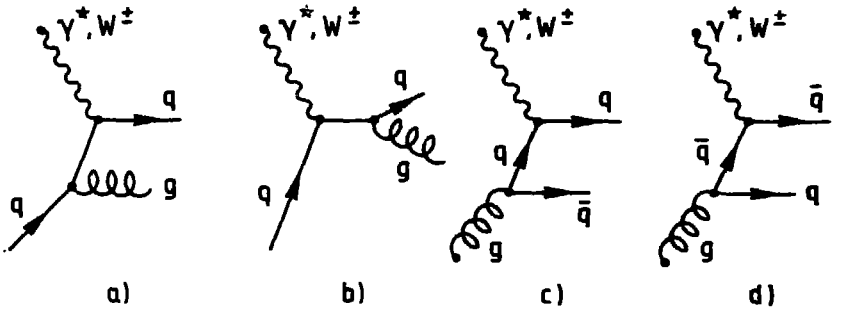

Fig. 2.

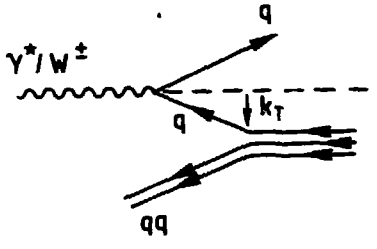

Fig. 3.

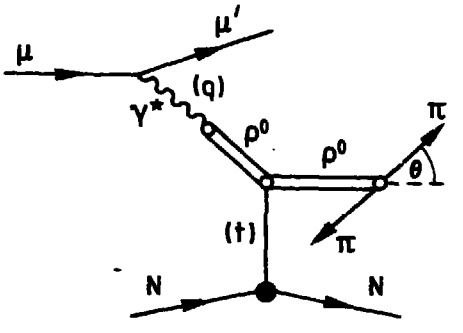

Fig. 4.

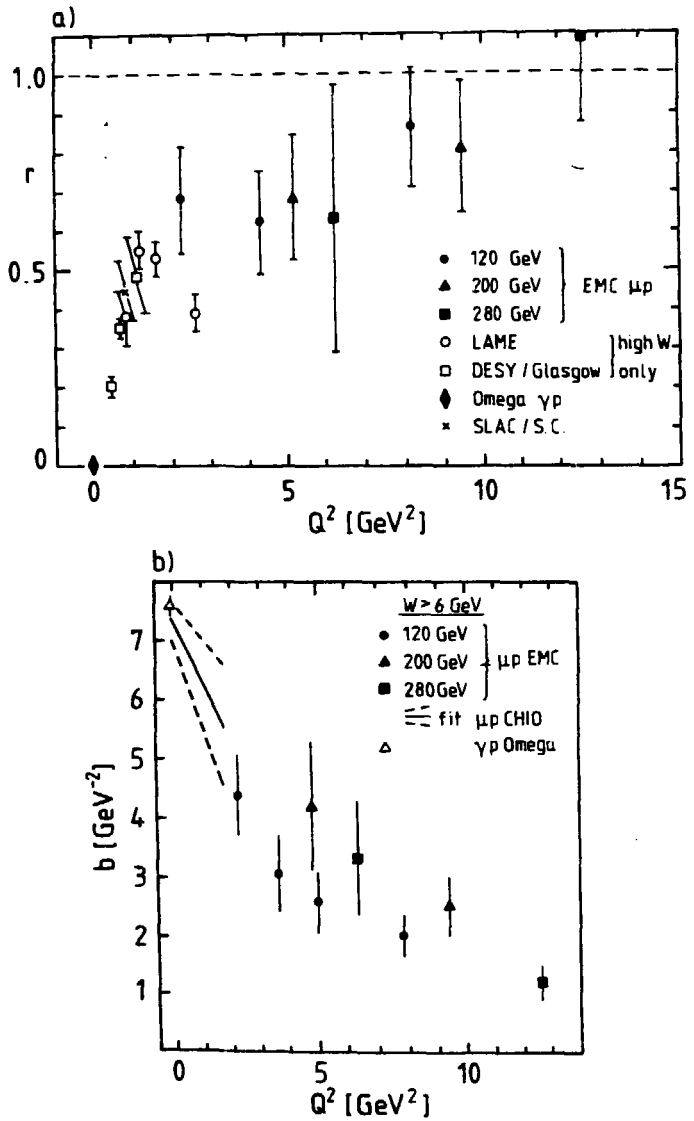
a)
1.0
R
0.5
0
0
5
10
15
Q² [GeV²]
120 GeV
200 GeV
280 GeV
EMC μp
LAME
DESY / Glasgow
high W only
Omega γp
SLAC / S.C.
b)
W > 6 GeV
120 GeV
200 GeV
280 GeV
μp EMC
fit μp CHIO
γp Omega
b [GeV⁻²]
7
6
5
4
3
2
1
0
5
10
Q² [GeV²]

Fig. 5.

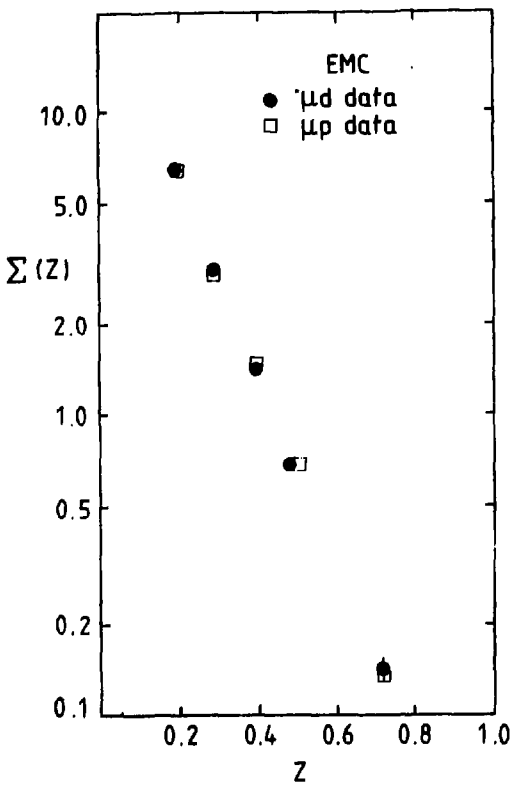
EMC
μd data
μp data
10.0
5.0
2.0
1.0
0.5
0.2
0.1
Σ(Z)
0.2
0.4
0.6
0.8
1.0
Z

Fig. 6.

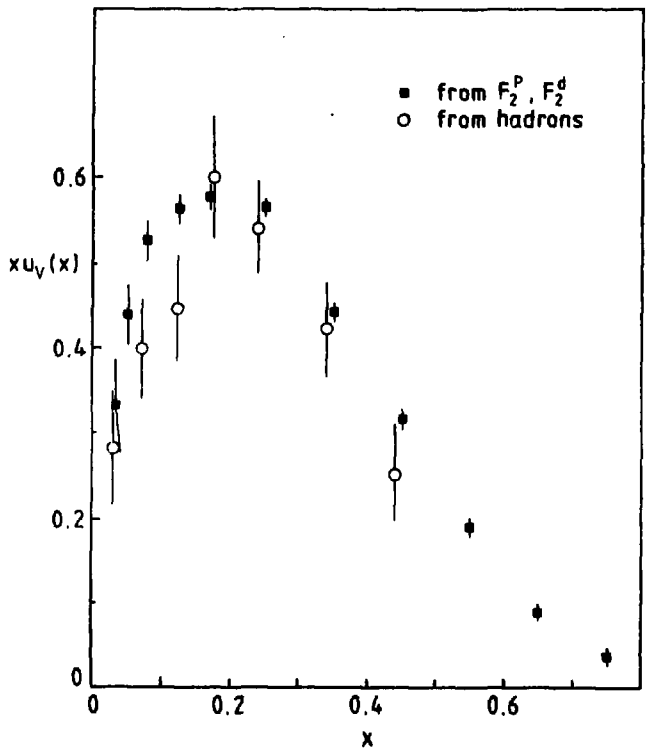
from F_2^p, F_2^d
from hadrons
0.6
0.4
0.2
0
$xu_v(x)$
0
0.2
0.4
0.6
x

Fig. 7.

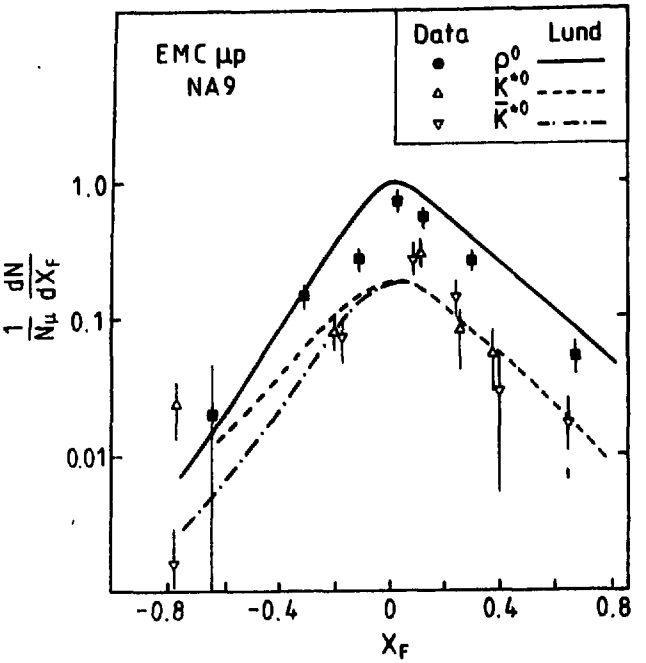
EMC μp
NA9
Data
Lund
ρ⁰
K*0
K̄*0
1.0
0.1
0.01
1/N_μ dN/dX_F
-0.8
-0.4
0
0.4
0.8
X_F

Fig. 9.

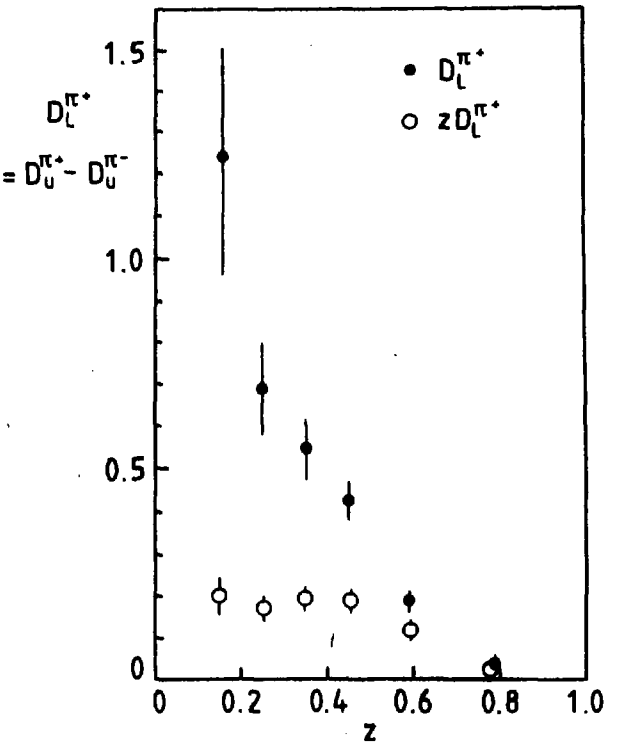
D_L^π+
= D_U^π+ - D_U^π-
D_L^π+
z D_L^π+
1.5
1.0
0.5
0
0
0.2
0.4
0.6
0.8
1.0
z

Fig. 8.

Fig. 10.

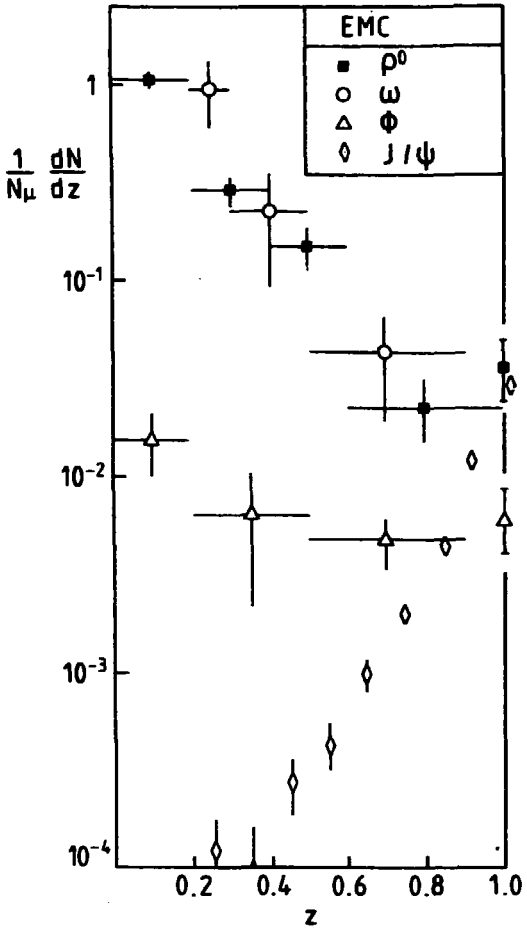
EMC
ρ⁰
ω
Φ
J/ψ
1
10⁻¹
10⁻²
10⁻³
10⁻⁴
1/Nμ dN/dz
0.2
0.4
0.6
0.8
1.0
z

Fig. 11.

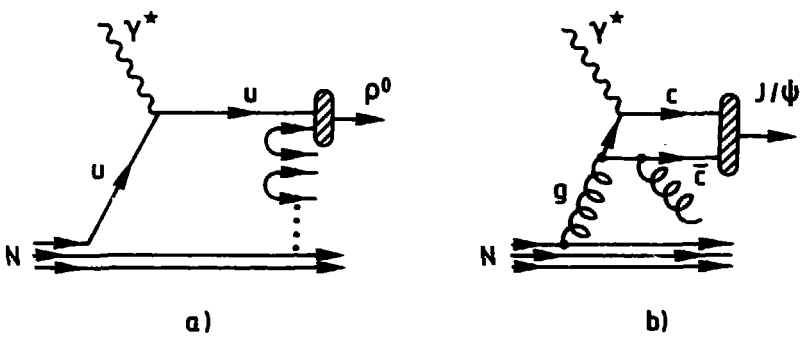
γ*
u
ρ⁰
u
N
a)
γ*
c
J/ψ
g
c̄
N
b)

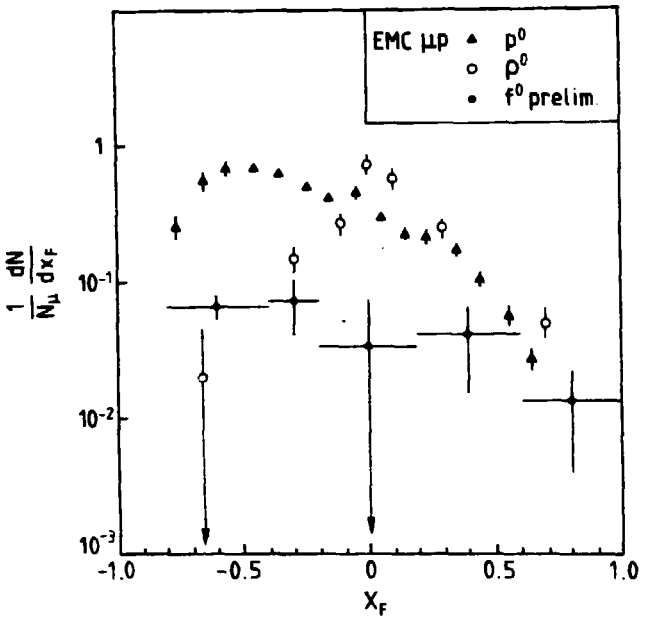
EMC μp
p⁰
ρ⁰
f⁰ prelim.
1
10⁻¹
10⁻²
10⁻³
-1.0
-0.5
0
0.5
1.0
X_F
1/N_μ dN/dx_F

Fig. 12.

Fig. 13.

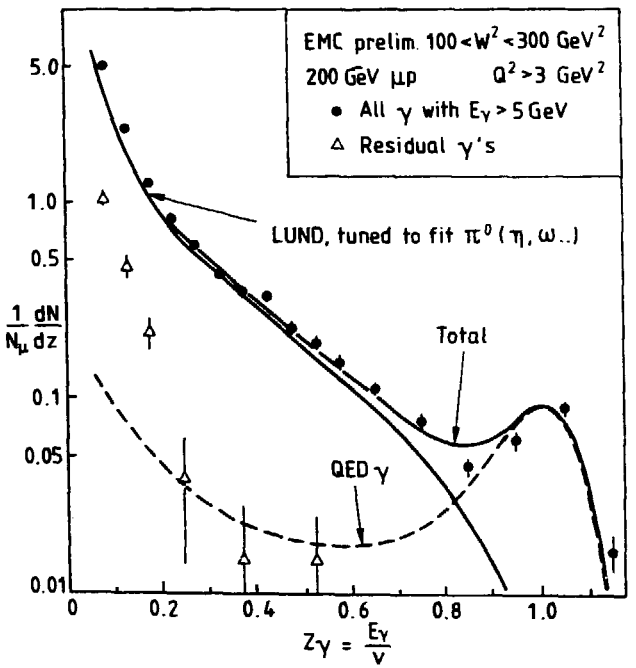
EMC prelim. 100<W²<300 GeV²
200 GeV μp
Q²>3 GeV²
All γ with E_γ > 5 GeV
Residual γ's
LUND, tuned to fit π⁰ (η, ω..)
Total
QED γ
5.0
1.0
0.5
0.1
0.05
0.01
0
0.2
0.4
0.6
0.8
1.0
1/N_μ dN/dz
Zγ = E_γ/ν

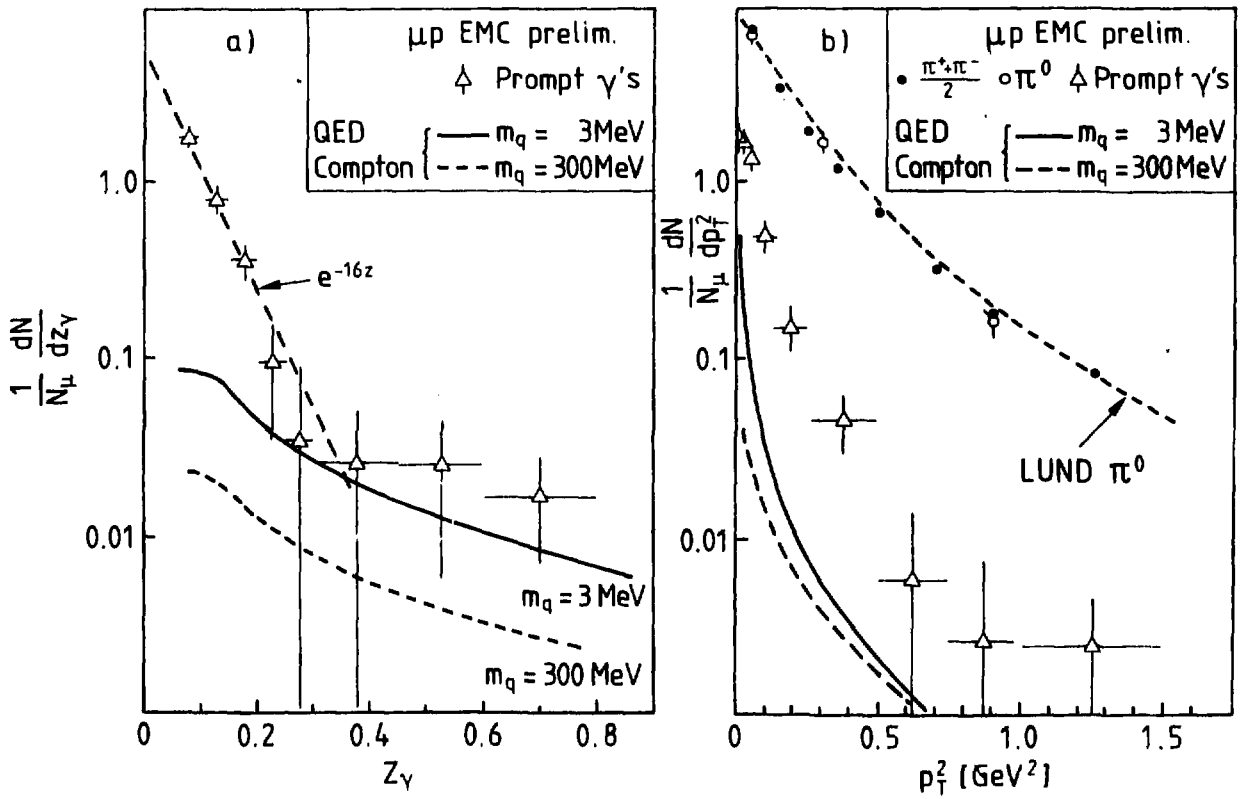
a)
μp EMC prelim.
Prompt γ's
QED Compton
m_q = 3MeV
m_q = 300MeV
e^{-16z}
m_q = 3 MeV
m_q = 300 MeV
$\frac{1}{N_\mu}\frac{dN}{dz_\gamma}$
z_γ
b)
μp EMC prelim.
$\frac{\pi^+\pi^-}{2}$ π^0 Prompt γ's
QED Compton
m_q = 3MeV
m_q = 300MeV
LUND π^0
$\frac{1}{N_\mu}\frac{dN}{dp_T^2}$
p_T^2 [GeV^2]

Fig. 14.

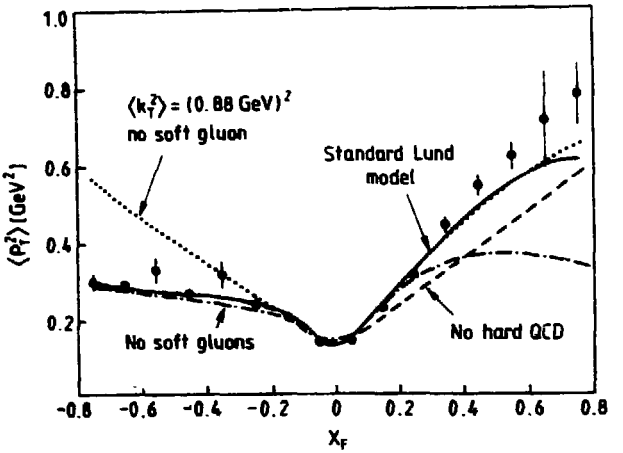
$\langle k_T^2 \rangle = (0.88\ \text{GeV})^2$
no soft gluon
Standard Lund model
No soft gluons
No hard QCD
$\langle P_T^2 \rangle\ (\text{GeV}^2)$
X_F

Fig. 15.

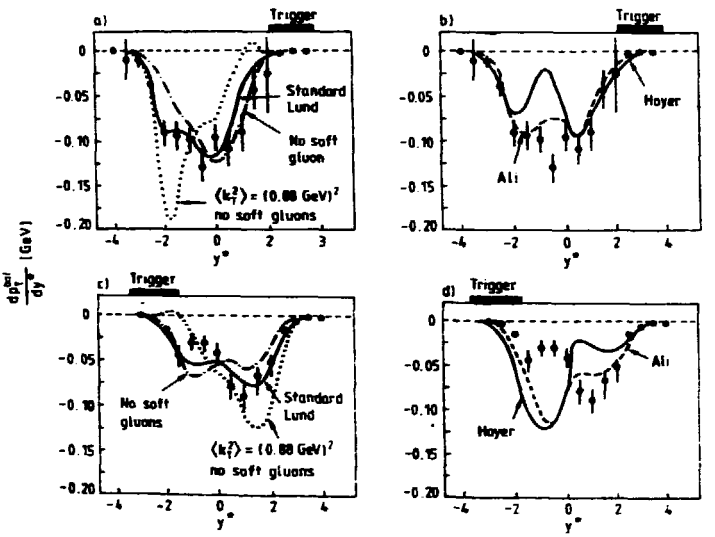
a)
Trigger
Standard Lund
No soft gluon
$\langle k_T^2 \rangle = (0.88\ \text{GeV})^2$
no soft gluons
b)
Hoyer
Ali
c)
No soft gluons
Standard Lund
$\langle k_T^2 \rangle = (0.88\ \text{GeV})^2$
no soft gluons
d)
Ali
Hoyer
$\frac{dp_T^{rel}}{dy^*}$ (GeV)
y^*

Fig. 16.

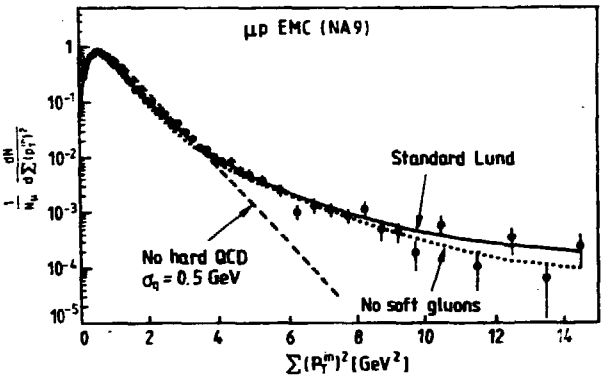
μp EMC (NA9)
Standard Lund
No hard QCD
σ_q = 0.5 GeV
No soft gluons
$\frac{1}{N_{ev}} \frac{dN}{d\sum(p_T^{in})^2}$
$\sum(P_T^{in})^2$ [GeV^2]

Fig. 17.

Fig. 18.

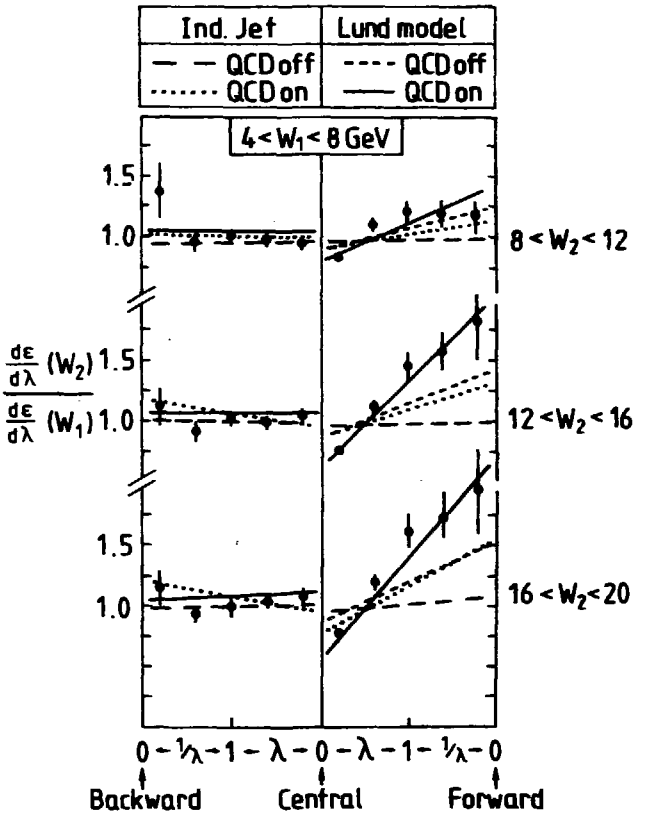
Ind. Jet
Lund model
QCD off
QCD on
QCD off
QCD on
4 < W1 < 8 GeV
8 < W2 < 12
12 < W2 < 16
16 < W2 < 20
$\frac{d\varepsilon}{d\lambda}(W_2) / \frac{d\varepsilon}{d\lambda}(W_1)$
0 - ½λ - 1 - λ - 0 - λ - 1 - ½λ - 0
Backward
Central
Forward

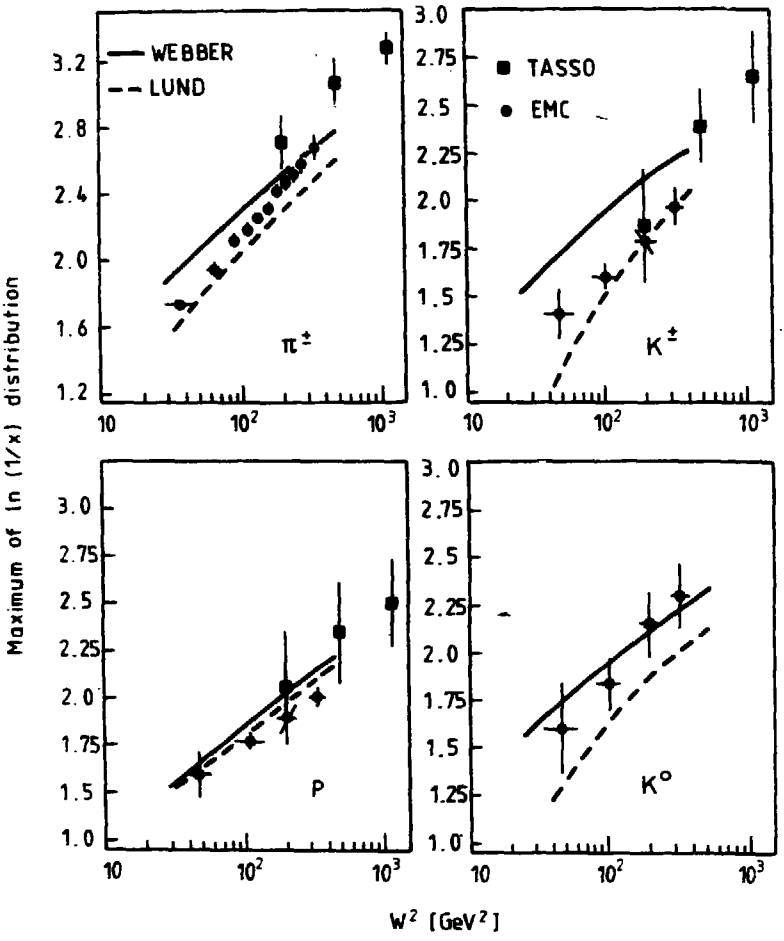
WEBBER
LUND
TASSO
EMC
π±
K±
P
K°
Maximum of ln (1/x) distribution
W² [GeV²]

Fig. 19.

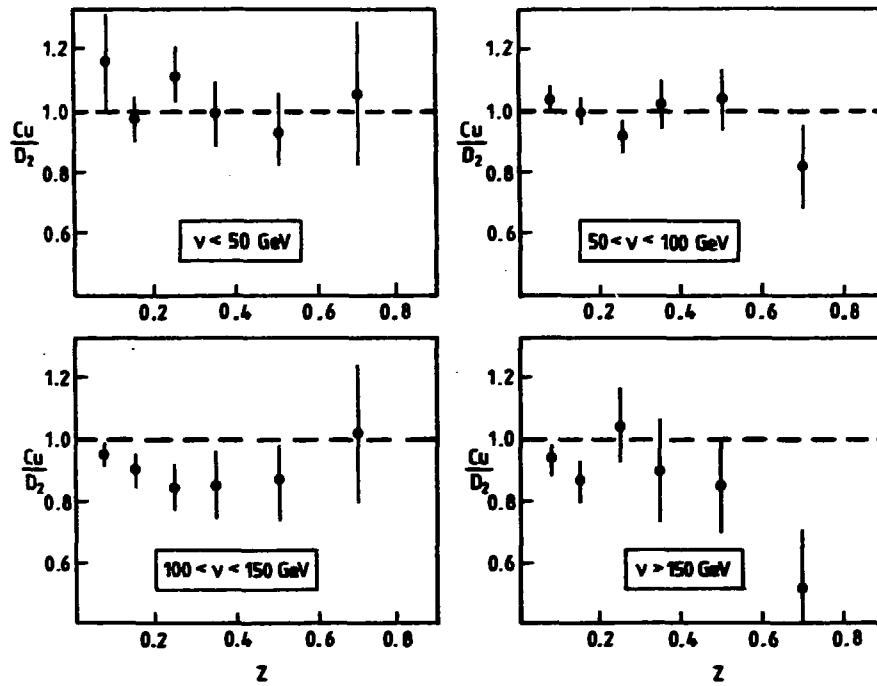
Cu/D2
1.2
1.0
0.8
0.6
ν < 50 GeV
50 < ν < 100 GeV
100 < ν < 150 GeV
ν > 150 GeV
0.2
0.4
0.6
0.8
z

Fig. 20.

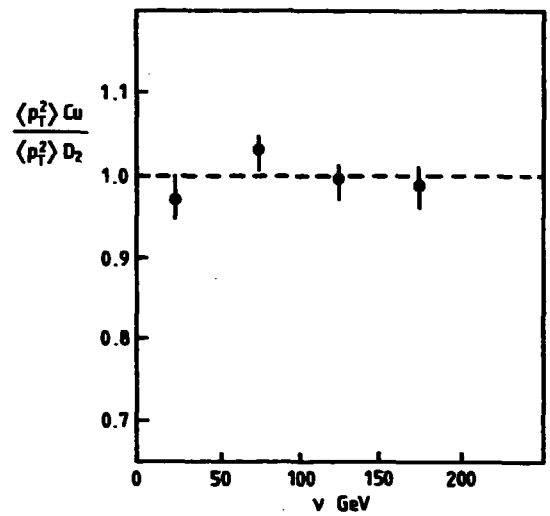
⟨p_T²⟩ Cu / ⟨p_T²⟩ D2
1.1
1.0
0.9
0.8
0.7
0
50
100
150
200
ν GeV

Fig. 21.

New Results from the UA5/2-Experiment[1]

Ch. Geich-Gimbel

Physikalisches Institut der Universität Bonn, F.R. Germany

This talk will cover recent results from the investigation of $p\bar{p}$-interactions at $\sqrt{s} = 200$ and 900 GeV with a streamer chamber detector (UA5/2-experiment) [1] at the CERN SPS Collider. I will present results on cross section measurements, diffraction dissociation, multiplicity distributions and forward-backward multiplicity correlations.

The data these preliminary results are based on were taken during a very successful run of the pulsed $p\bar{p}$-Collider at CERN in spring 1985. The UA5/2 detector [2] took 115,000 streamer chamber pictures and 500,000 electronic events (i.e. only containing information from the trigger hodoscopes and the hadron calorimeter), mainly at the flat bottom at 100 GeV beam energy and the four seconds flat top at 450 GeV of the cycle, see fig. 1. For part of the run, an additional photon converter plate was introduced between the beam pipe and the upper streamer chamber to increase the photon detection efficiency at large production angles.

The UA5/2-detector consists of two large streamer chambers ($6 \times 1.25 \times 0.5\,m^3$ visible volume), placed above and below the 2 mm thick beryllium beam pipe, see fig. 2. The azimuthal coverage of the chambers is 95% for a pseudorapidity[2] $|\eta| \leq 3$. At each end of the chamber there is a pair of trigger hodoscopes, designated A1 and A2, covering a pseudorapidity range of $2 < |\eta| < 5.6$. The large solid angle covered by these hodoscopes and their good time resolution made the trigger efficient for beam-beam interactions, suppressing a good part of the beam-gas background. At 90°, see fig. 2, a $4 \times 1 \times 1\,m^3$ sandwich calorimeter is located.

1. *Cross Section Measurements*

The count rate $\dot{N}_i(t)$ is related to the trigger cross section σ_i by the luminosity $L(t)$ as $\dot{N}_i(t) = \sigma_i \cdot L(t)$, thus requiring the knowledge of the luminosity to calculate the cross section from observed count rates. The absolute luminosity at the SPS Collider turns out to be hardly measurable to better than 10%.

In *pulsed* collider mode however, the fact that the same circulating bunches of protons (and antiprotons) are accelerated and slowed down between 100 and 450 GeV, allows

[1] Bonn-Brussels-Cambridge-CERN-Stockholm Collaboration

[2] $\eta = -\ln \tan \Theta/2$

for a measurement of the cross section *ratio* for $\sqrt{s}$ = 200 and 900 GeV:

$$R = \frac{\sigma_i^{900}}{\sigma_i^{200}} = \frac{\dot{N}_i^{900}}{\dot{N}_i^{200}} \cdot \frac{L^{200}}{L^{900}}, \tag{1}$$

where L^{200}/L^{900} only depends on machine parameters, and is essentially given by the ratio of the beam energies (nominally 2/9). Its precise, measured value [3] is $L^{200}/L^{900} = 0.224 \pm 1\%$, obtained by analyzing the radio frequency settings, the radial positions of the bunches in the machine and extracted beam measurements.

Two different triggers were used in parallel to record inelastic $p\bar{p}$-interactions in the UA5-detector: a 2-arm-trigger A1·A2 to select NSD (non-single diffractive) events, and an 1-arm-trigger A1 $\cdot\overline{A2}$ to select events of the reaction $\bar{p}p \to X + p$ ($\bar{p}$-diffractive)[1]. Fig. 3 schematically shows the trigger set-ups, and fig. 4 illustrates the distribution of the total cross section to the various triggers.

The relationship between $\sigma_{NSD}, \sigma_{SD}$ and the trigger cross sections σ_i reads

$$\begin{pmatrix} \sigma_1 \\ \sigma_2 \end{pmatrix} = \begin{pmatrix} \epsilon_{1,NSD} & \epsilon_{1,SD} \\ \epsilon_{2,NSD} & \epsilon_{2,SD} \end{pmatrix} \begin{pmatrix} \sigma_{NSD} \\ \sigma_{SD} \end{pmatrix}. \tag{2}$$

The fractions ϵ (trigger efficiencies) were obtained by the UA5 Cluster Monte Carlo [2]. Single diffractive events were generated with an s/M^2-dependence and a longitudinal phase space decay of the diffractive system of mass M, see also [4].

Solving eq. (2) for either $\sigma_{inel} = \sigma_{SD} + \sigma_{NSD}$, σ_{SD} or σ_{NSD} one obtains (at each $\sqrt{s}$) an equation of the form

$$\sigma = \kappa_1\sigma_1 + \kappa_2\sigma_2, \tag{3}$$

where the κ's are functions of the above efficiencies ϵ. The trigger cross sections σ_1 and σ_2 in eq. (3) finally follow from the counts N_i (in time t at a luminosity L), corrected for non beam-beam interactions as

$$\sigma_i = \frac{f_i N_i}{t\, L}. \tag{4}$$

The proportions of genuine events, f_i, were obtained by scanning and where neccessary measuring streamer chamber pictures from time intervals corresponding to the electronic triggers.

Combining eqs. (1), (3) and (4) one finally gets[2]

$$R = \frac{(2\kappa_1 f_1 N_1 + \kappa_2 f_2 N_2)^{900}}{(2\kappa_1 f_1 N_1 + \kappa_2 f_2 N_2)^{200}} \cdot \frac{L^{200}}{L^{900}} \cdot \frac{t^{200}}{t^{900}}. \tag{5}$$

[1] The corresponding $\overline{A1}$.A2 trigger was not used on account of more severe background conditions from the intense proton bunch.

[2] The factor 2 in eq. (5) arises from the use of only one of the possible 1-arm trigger combinations.

For the ratio R we have measured [5]

$$R_{inel}^{900/200} = 1.20 \pm .01 \pm .02,$$

the first error being statistical, the second systematic, reflecting the uncertainties in the trigger efficiencies and the luminosity ratio.

1.1. Absolute Cross Sections

To get absolute values of the cross sections we use the fit to $\sigma_{tot}(p\bar{p})$ by Amos et al., [6], which renders $\sigma_{tot}^{200} = 51.6 \pm 0.4$ mb, see fig. 5[1]. Additionally, from the UA4 measurement of σ_{el}/σ_{tot} at $\sqrt{s} = 546$ GeV [7] and ISR-measurements we interpolate $\sigma_{el}^{200}/\sigma_{tot}^{200} = 0.19 \pm .01$, compare fig. 6, and hence obtain $\sigma_{inel}^{200} = 41.8 \pm 0.6$ mb.

From this input, and the $R_{inel}^{900/200}$ value measured, it follows

$$\sigma_{inel}^{900} = 50.3 \pm 0.4 \pm 1.0\,\text{mb},$$

and, with $\sigma_{el}^{900}/\sigma_{tot}^{900} = 0.23 \pm .01$ (from extrapolation),

$$\sigma_{tot}^{900} = 65.3 \pm 0.7 \pm 1.0\,\text{mb}.$$

This agrees to a value of 65.8 mb, predicted by the dispersion relation fit [6] mentioned. As the ratio $\sigma_{el}/\sigma_{tot} \ll 1$, the additional error in the determination of σ_{tot} from σ_{inel} and σ_{el}/σ_{tot} is much smaller than the error in σ_{el}/σ_{tot}.

1.2. Diffraction Dissociation

Diffraction dissociation, i.e. the inelastic excitation of interacting particles with diffractive like signatures (sharp forward peak, no quantum number exchange) was predicted long ago [8]. Inelastic diffraction was viewed as a process which puts virtual hadronic states on the mass shell, the mass M of such states only being limited by a coherence condition, which in most analyses is taken as $M^2/s \leq 0.05$.

For the investigation of diffraction dissociation in the UA5 - experiment the measurements of σ_1 and σ_2 can be exploited to calculate σ_{SD} at each energy, as eq. (3) may also be expressed for σ_{SD}/σ_{NSD} in terms of σ_1/σ_2 and ϵ's, independent of the luminosity. The measurements give [9]

$$r = \sigma_{SD}^{200}/\sigma_{NSD}^{200} = 0.132 \pm .016 \pm .024$$
$$r = \sigma_{SD}^{900}/\sigma_{NSD}^{900} = 0.180 \pm .014 \pm .029,$$

[1] For the low energy data points see [10-14]

and with $\sigma_{SD} = \sigma_{inel} \cdot r/(r+1)$ and the values of the inelastic cross sections

$$\sigma_{SD} = (7.8 \pm 0.5 \pm 1.1) \text{ mb} \quad \text{at } \sqrt{s} = 900 \text{ GeV}$$
$$\sigma_{SD} = (4.8 \pm 0.5 \pm 0.8) \text{ mb} \quad \text{at } \sqrt{s} = 200 \text{ GeV}.$$

Table 1 summarizes the information on cross sections, also in comparison to ISR results [11-15].

Table 1	$p\bar{p}$ Cross Sections				
	ISR	SPS - Collider			
$\sqrt{s}$	53-63[a)]	200	540	900	GeV
σ_{tot}	~ 44	51.6 ± 0.4	61.9 ± 1.5	65.3 ± 2.2	mb
σ_{el}/σ_{tot}	~ 0.175	$0.19 \pm .01$[c)]	$0.215 \pm .005$	$0.23 \pm .01$[c)]	
σ_{el}	~ 7.7	~ 9.6	13.3 ± 0.6	~ 15	mb
σ_{inel}	~ 36	41.8 ± 0.6[c)]	48.6 ± 1.6[d)]	50.3 ± 1.4	mb
σ_{SD} [b)]	~ 7	4.8 ± 1.3	8.1 ± 0.8[e)]	7.8 ± 1.6	mb
σ_{NSD}	~ 29[f)]	~ 37	~ 41[f)]	~ 42.5	mb

a) All cross sections in this column averaged from different ISR-experiments [12].
b) For $M^2/s < 0.05$.
c) Input values from interpolation, see text.
d) Calculated from [7].
e) From [16].
f) By subtraction of σ_{SD} from σ_{inel}.

Figure 7 shows these results on diffraction dissociation together with a large number of measurements of the single-diffractive cross-section over a wide range of c.m. energies, where different experimental techniques were used to extract single-diffractive events. We have included measurements of the SD cross-section for different definitions of the M^2/s high mass limit and for various experimental methods of extracting the single-diffractive sample [17], resulting in partially inconsistent results at the same energies. For example, at ISR energies the measurements for $M^2/s \leq 0.06$ from one experiment give lower cross sections than for $M^2/s \leq 0.05$ from another experiment at about the same energy, indicating the difficulties of measurements of this cross-section. It appears that the single-diffractive cross-section increases only slightly with energy, in contrast with the tendency, suggested by the ISR data [15], that the the SD cross-section is a constant fraction of the total $p\bar{p}$ cross-section ($\sigma_{SD} = 0.17\ \sigma_{tot}$). This would yield a single-diffractive cross-section of about 11 mb at 900 GeV and 9 mb at 200 GeV, both of which are clearly ruled out by the Collider measurements.

All collider measurements, together with the values at highest ISR energies are in fact compatible with σ_{SD} being constant with a value between 5 and 8 mb.

In the analysis of diffraction dissociation at Collider energies also an attempt was made to estimate the contribution of double-diffractive processes. In analogy to the method described above, a third independent 'trigger' was used in order to enrich DD events in the 2-arm trigger sample. In practice, this 'trigger' consisted of an off-line cut, e.g. demanding no charged track within a certain central pseudorapidity region, for details see [9]. One ended up with

$$\sigma_{DD}^{900} = 4.0 \pm 2.5 \text{ mb}$$
$$\sigma_{DD}^{200} = 3.5 \pm 2.2 \text{ mb} .$$

One may compare these results with calculations assuming factorization of diffractive vertices. If factorization holds for the double-diffractive cross-section it may be written as [18]:

$$\sigma_{DD} = \frac{\sigma_{SD}^2}{4\sigma_{el}} \cdot \frac{b_{SD}^2}{b_{el}\, b_{DD}} \qquad (6)$$

with $b_{DD} = 2b_{SD} - b_{el}$, relating the slope parameters b of the exponential dependence of all three diffractive cross-sections on the 4-momentum transfer t ($d\sigma/dt = a \cdot e^{b \cdot t}$).

In the Collider energy range data for σ_{el}, b_{el} and b_{SD} are only available at $\sqrt{s} = 546$ GeV [7], so we compare our result with calculations based on 546 GeV measurements. Taking $\sigma_{el} = (13.6 \pm 0.6)$ mb, $b_{el} = 15$ GeV^{-2}, $b_{SD} = 8 \pm 1$ GeV^{-2} and $\sigma_{SD} = (7 \pm 1)$ mb the above formula yields a value for σ_{DD} between 2 and 4 mb in approximate agreement with our measurements.

The important question, whether the diffractively produced system of mass M tends to hadronize by an isotropic fireball-like decay, or rather according to p_T-limited phase space was investigated by means of the dispersion

$$\sigma_\eta^{obs} = \sqrt{\frac{1}{n_{obs}} \sum_{i=1}^{n_{obs}} (\eta_i - < \eta >_{obs})^2}$$

of the η-values of the observed particles around their mean per event. Whilst for the case of an isotropic decay the above quantity is expected to have a half width at half maximum of about 0.88 units in pseudorapidity, independent of the mass of the diffractively produced system, a multiperipheral decay implies a mass dependent HWHM of approximately $\ln(M/ < \mu >)$, where μ denotes the transverse mass of the final state particles. These different situations are illustrated in fig. 8.

Fig. 9 shows the observed pseudo- rapidity distribution of charged particles in 1-arm triggers at $\sqrt{s} = 900$ GeV in comparison with two different model predictions. A p_T-limited hadronization process in diffractive dissociation events is clearly favoured. In fact, only at collider energies the difference between the two possible hadronization schemes becomes large enough to be distinguished that way.

2. *Multiplicity Distributions*

Generally measurements of charged particle multiplicity distributions in hadronic interactions provide important constraints on models of multiparticle production, especially in lack of a *theory* of soft hadron production.

The mean charged multiplicity $< n_{ch} >$ from non-single diffractive reactions at various center-of-mass energies is shown in fig. 10. The new data points at $\sqrt{s} = 200$ and 900 GeV originate from the UA5/2 experiment [19]. The observed multiplicity has been corrected by standard techniques, see [2,20]. The lower energy data are from [21,22].

The energy dependence of the charged multiplicity is equally well described by

$$< n_{ch} > = A + B \ln s + C \ln^2 s \qquad (7)$$

$$< n_{ch} > = D + E\, s^F \qquad (8)$$

in the range $\sqrt{s} = 10$-900 GeV, as shown in fig. 10. The fit parameters are $A = 2.7 \pm 0.7$, $B = -0.03 \pm 0.21$ and $C = 0.167 \pm 0.016$ with $\chi^2/NDF = 17/9$, or $D = -7.0 \pm 1.3$, $E = 7.2 \pm 1.0$ and $F = 0.127 \pm 0.009$, respectively, with $\chi^2/NDF = 11/9$.

The result of the fit to the power law (8) definitively rules out an energy dependence of the mean charged multiplicity such strong as $s^{\frac{1}{4}}$, which had been favoured by statistical or hydrodynamical models [23], and still seemed possible at ISR energies [24] (already the first data from the Collider, namely $< n_{ch} >= 28.9 \pm 0.4$ at $\sqrt{s} = 546$ GeV [25,26] were in disagreement to the $s^{0.25}$ fit used in [24] at the ISR).

The quadratic ln s term (form (7)), which also gives a good fit to the data, gains plausibility by the observations made in inclusive pseudorapidity distributions (not shown here), where both the height (at $\eta = 0$) and the width of the inclusive pseudorapidity distributions were found to rise approximately with ln s.

2.1. *Inclusive Multiplicity Distributions*

In 1972 Koba, Nielsen and Olesen [27] predicted that the *normalized* charged particle multiplicity distribution for hadron-hadron interactions should become energy independent when $s \to \infty$, i.e.

$$< n_{ch} > \cdot P_n \to \Psi(z), \quad z = n_{ch} / < n_{ch} > \qquad (9)$$

with P_n being the probability for n charged particles to be produced and with the general definition of the normalized multiplicity distribution

$$\Psi(z,s) = < n_{ch} > \cdot P_n(s) \; . \qquad (10)$$

The KNO scaling law [27] had been derived from Feynman scaling [28]. Though Feynman scaling is known not to be valid, the KNO scaling apparently holds in an energy range of 11 to 63 GeV c.m. energy [24,29].

Clear evidence for the violation of KNO scaling at $\sqrt{s} = 546$ GeV was shown by the UA5 collaboration in 1983 [25,30], see fig. 11. The normalized multiplicity distribution $\Phi(z)$ for NSD events at $\sqrt{s}$= 546 GeV is much broader than that at ISR [21] or FNAL and Serpukhov [22] energies. This becomes manifest e.g. in the fraction of events with $z \geq 2$ increasing to 6% from about 2% at lower energies.

2.2. *Negative Binomial Distributions*

The UA5 collaboration has found [31,32] that charged particle multiplicity distributions for $p\bar{p}$ reactions at $\sqrt{s}$= 546 GeV and pp reactions between about 10 and 60 GeV c.m. energy may well be fitted by a *negative binomial distribution* (NegBin)

$$P(n;\bar{n},k) = \binom{n+k+1}{n} \left(\frac{\bar{n}/k}{1+\bar{n}/k}\right)^n \frac{1}{(1+\bar{n}/k)^k} . \qquad (11)$$

This NegBin distribution has two free parameters: $\bar{n}$, which denotes the mean charged multiplicity $< n_{ch} >$[1] and the (non neccessarily integer) parameter k, which affects the shape (width) of the distribution. The dispersion (second central moment) of a NegBin is given by

$$D^2 = \bar{n} + \bar{n}^2/k. \qquad (12)$$

The observed widening of the normalized multiplicity distribution with increasing energy is connected to a decrease of the parameter k with energy, as shown in fig. 12.

It may be recalled that k=1 in the NegBin leads to a geometrical (single-cell Bose-Einstein) distribution. For any integer value of k formula (11) leads to a generalized Bose-Einstein distribution, as used already in 1923 by Planck [33] to describe the number of identical photons coming from k independent phase space cells.

UA5 has found non-integer k values for the NegBin to fit multiplicity distributions best [32], with the binomial coefficient in eq. (11) written as

$$\binom{n+k+1}{n} = \frac{(n+k-1)\ldots(n+k-1-(n-1))}{n!} = \frac{k\,(k+1)\ldots(n+k-1)}{n!} . \qquad (13)$$

It had been remarked [34] that in the case of very high energy, such that the average multiplicity becomes large ($\bar{n} \gg k$) the NegBin can be expressed in terms of scaled quantities $z = n/\bar{n}$ and $\bar{n}P_n$ like

$$\Phi(z,k) = \bar{n}P_n = \frac{k^k}{\Gamma(k)} z^{k-1} e^{-kz} . \qquad (14)$$

[1] Henceforth we will not distinguish between $\bar{n}$ and $< n_{ch} >$

This asymptotic form (14) obviously requires constant k^{-1} for KNO scaling, such that the NegBin (11) is the correct form at current energies, to which a KNO-like scaling would appear as an asymptotic approximation [34].

At highest current accelerator energies ($\sqrt{s} = 900$ GeV) an asymptotic region has not been reached, as shown by the UA5/2 data [19], see fig. 12. The shape parameter k is still changing with energy. One obtains

$$k^{-1} = a + b \ln\sqrt{s} \tag{15}$$

with $a = -0.104 \pm 0.004$ and $b = 0.058 \pm 0.001$ (s in GeV^2).

Furthermore already in a previous publication of UA5 [32] it was concluded that the 'observed' KNO scaling in the c.m. energy range between 10 and 60 GeV was 'accidental', as in the C_q moments, e.g.

$$C_2 = 1 + (\frac{1}{\bar{n}} + \frac{1}{k}), \tag{16}$$

whose energy independence would be equivalent to KNO scaling, the term $(\frac{1}{\bar{n}} + \frac{1}{k})$ numerically dominates: The variation of $(\frac{1}{\bar{n}} + \frac{1}{k})$ with c.m. energy is shown in fig. 13, where the fortuitious approximate constancy of $\gamma_2 = C_2 - 1$ at the FNAL and ISR shows up.

There two new data points at $\sqrt{s} = 200$ and 900 GeV are added, which were obtained by fitting negative binomial distributions convoluted with the UA5 acceptance matrix to observed charged multiplicity distributions [19], see fig. 14.

Hence, the multiplicity distribution turns out to be governed by the negative binomial distribution (11), whose parameters $\bar{n}$ and k are *smoothly* varying with energy in a range of two decades (10-900 GeV) c.m. energy, confirming the result from the first collider runs at $\sqrt{s} = 546$ GeV on the violation of KNO scaling [30]. One might conclude, that up to now KNO scaling never was *valid* rather than calling the observations a *violation* of KNO scaling!

In conclusion, the negative binomial distribution, replacing KNO scaling, provides a new basis for predicting multiplicity distributions in hadronic interactions at higher energies.

2.2.1. *Physical Interpretation of the Negative Binomial Distribution*

Originally the NegBin was reached assuming stimulated emission of identical bosons by k identical phase space cells [33]. For a translation of this picture into high energy physics the condition of k being integer is quite unpleasant, as k has been found to be generally non-integer, varying smoothly with the energy available, and furthermore k is showing an energy dependence (eq. (15)) *opposite* to what seems natural from the above idea [19,32].

Before Collider data arrived, however, in the framework of stochastic cell models related interpretations of the NegBin and its shape parameter k have been advanced [35], which called for integer k and k to *increase* with energy.

Data from the Collider demonstrated the broadening of the multiplicity distribution with rising energy, independent of the framework of the NegBin, i.e. not involving any physical interpretation of the shape parameter k of the NegBin so far.

2.2.2. Superclusters

Recently a way was found to overcome the interpretational difficulties of the experimental result of k being non-integer and decreasing with energy, the idea of *superclusters* [36,37]: One assumes a fluctuating number c of independent (super-) clusters with a Poissonian distribution per event, branching into fluctuating numbers m_j (logarithmically distributed) of particles per cluster; such that

$$n = \sum_{j=1}^{c} m_j \quad \text{and} \quad \bar{n} = \bar{m} \cdot \bar{c} \,, \tag{17}$$

rendering the desired NegBin for n.

The average number of clusters $\bar{c}$ and the average cluster size $\bar{m}$ are related to the parameters $\bar{n}$ and k of the NegBin by [36]

$$\bar{m} = \bar{n}/\bar{c} \quad \text{and} \quad \bar{c} = k \ln(1 + \frac{\bar{n}}{k}) \,. \tag{18}$$

The average number $\bar{c}$ of superclusters and the mean cluster size $\bar{m}$ are shown in fig. 15, plotted versus the c.m. energy.

Surprisingly the average number of (super-) clusters seems to reach a constant value (about 8), at about the energy ($\sqrt{s} \simeq 60$ GeV), where the 'accidental' KNO scaling ceased to hold. The further increase of the total charged multiplicity then seems to be provided by an increase of the average cluster size, only. Why does the number of super-clusters saturate, and why does this saturation occur at the exquisite number of 8 primary clusters?

—

First referenced in 1713 [38] (based on gambling) negative binomials have been known and applied in biometrics since long. Two schemes have been developped in the application of NegBins in biometrics more recently:

The NegBin (11) has been derived in risk theory. An illustrative example is given in [39]: The frequency distribution of accidents occurring to women working on the manufacture of shells was found not to be described by a single Poisson distribution,

but rather by a superposition of individual Poisson distributions, with the condition of the mean values of the individual Poissons following a Gamma-type distribution. The working hypothesis supposes that the individuals investigated differ in their 'proneness' to the attribute under study, represented by different parameters of the individual Poisson distributions [40].

Mathematically such a mixture of Poisson distributions, with their mean values accordingly distributed (Gamma-distribution) is equivalent to a negative binomial distribution, cf. [39].

Elsewhere, in counting problems in biology (more precisely in bacteria and colony counts), it was found in 1948 [41], that if the colony counts c followed a Poisson distribution and the numbers m_j of bacteria per colony were logarithmically distributed the total bacteria counts were distributed according to a negative binomial.

A proof of this conjecture was first given by Quenouille in 1949 [42], relating the parameters $\bar{n}$ and k of the negative binomial (11) to the average number $\bar{c}$ (of colonies) and $\bar{m}$ (of bacteria) under the above suppositions in the same way as applied to particle multiplicities in high energy physics now [36,37], see eq. (18).

3. *Forward-Backward Multiplicity Correlations*

From the foregoing results on multiplicity distributions at the Collider, and the fact that the dispersion of the NegBin, see eq. (12), is larger than the dispersion of a pure Poisson distribution (for which $D_2 = < n >$) for any finite value of the parameter k, one may conclude onto the presence of *correlations* in the production of charged particles. Also, the investigation of correlations may provide a deeper understanding of the dynamics of multi-particle production.

Forward-backward multiplicity correlations appear as the easiest way to access correlations in the particle production. Defining n_B and n_F as the number of backward, resp. forward going particles, such that $n_S = n_B + n_F$, one has found experimentally

$$< n_B(n_F) >= a + b \cdot n_F \ . \tag{19}$$

where the slope parameter b is equivalent to the linear regression coefficient

$$b = \frac{cov(n_B, n_F)}{\sqrt{var(n_B)var(n_F)}} \ . \tag{20}$$

In order to decouple the two regions (forward and backward) from the (trivial) effect of resonances emitting their decay products into either region simultaneously, a central gap of $\delta\eta = 2$ was introduced. Fig. 16 shows for the 900 GeV data the average number of backward going charged particles $< n_B(n_F) >$ versus the number of forward going particles n_F. For the slope parameter b a value of 0.51 ± 0.03 [43] was obtained.

This result proves the existence of long-range correlations. Fig. 17 summarizes the results on the correlation parameter b at ISR [44] and Collider [43,45] energies. Still, the correlation parameter rises about linearly with the logarithm of the c.m. energy, reflecting quite strong correlations at Collider energies.

3.1. *Correlations and the Cluster Model*

Formally, for each n_S there exists a $f_s(n_F)$ distribution and its moments. It can be shown [45] that the following identity holds for the correlation parameter b:

$$b = \frac{\frac{1}{4}D_S^2 - < d_S^2(n_F) >}{\frac{1}{4}D_S^2 + < d_S^2(n_F) >} \quad . \tag{21}$$

For the physical interpretation of the correlations observed different assumptions may be distinguished. In the case of independent *single* particle production, i.e. having a binomial distribution with $p = 1/2$ for a particle to fall into either hemisphere, one obtains $d_S^2(n_F) = p(1-p)n_S = 1/4\, n_S$, and with the measured values of $< n_S >= 16.0 \pm 0.2$ and $D_S = 8.8 \pm 0.1$ (for a $\delta\eta = 2$ gap at 540 GeV [43], thus $b = 0.66$, in contradiction to a measured slope parameter of $b = 0.42 \pm 0.01$.

If instead inpendent production of *clusters* (groups of particles, possibly including resonances) is assumed, with a fixed cluster size k, one would get $d_S^2(n_F) = p(1-p)kn_S = 1/4\, kn_S$ (thus increasing b), or

$$k = 4\, d_S^2(n_F)/n_S \quad . \tag{22}$$

This picture is still unrealistic, as the cluster size may vary, at least due to various decay multiplicities of known resonances. Under the assumption of clusters of mixed size the cluster size k in eq. (22) turns into an effective cluster size k_{eff} [46]

$$k_{eff} = < k > + \mathrm{var}(k)/ < k > \quad , \tag{23}$$

which is a function of the first two moments of the (unknown) cluster decay multiplicity.

This quantity $4\, d_S^2(n_F)/n_S = k_{eff}$ is plotted in fig. 18 for different c.m. energies and different spans $\Delta\eta$ of the pseudorapidity intervals considered, in dependence of the overall charged multiplicity n_S in the intervals considered. It appears that, provided the multiplicity n_S is large enough as well as the interval $\Delta\eta$, the effective cluster size saturates at $k_{eff} \simeq 2.5$, also independent of the c.m. energy. As for smaller intervals and/or smaller multiplicities the relative probability for clusters to emit particles outside the control regions (leakage effects) is enhanced, naturally smaller values for k_{eff} emerge.

The curves in fig. 18 represent the results of Monte Carlo simulations, based on independent cluster emission (UA5 Cluster-Monte-Carlo [2]). There for the charged cluster decay multiplicity a truncated Poisson distribution was input, with $< k > \simeq 1.8$, resulting in $k_{eff} \simeq 2.6$.

This result ties in with the conclusions drawn from the analysis of two-particle pseudorapidity correlations [47] at $\sqrt{s} = 540$ GeV and also with earlier ISR results [48], where compatible values for k_{eff} were obtained.

4. *Search for Unusual Phenomena*

Cosmic ray physics have provided a variety of unexpected - from the viewpoint of extrapolating the behaviour of the hadronic interactions from ISR results known then - phenomena, as the so-called Centauros, Geminions and Chirons [49], at beam energies around 10^{14} eV. One major motivation to perform the UA5- and UA5/2-experiment [1,50] was to search for these suggested phenomena under 'laboratory conditions' in a similar energy range. Especially the Centauro hypothesis deserved attention. From the signature of events recorded in a two-storey emulsion chamber (Mt. Chacaltaya, Brazil-Japan Collaboration [51]) the presence of a sizeable fraction of photon-poor (compatible with no photons at all) and high multiplicity (possibly baryon-rich) events was inferred, with considerably bigger mean transverse momentum.

At $\sqrt{s} = 540$ GeV both the UA1 and the UA5-experiment [52,53] reached a negative result in the Centauro search. The cosmic ray data could however be interpreted to suggest a threshold for Centauro production just above that Collider energy [54]. This led to the proposal of raising the Collider energy to the equivalent of $E_0 = 430$ TeV, where the Centauro signature, if genuine, should occur at a frequency of 5-10% [1].

In our detecting system (fig. 2) such an event-type would materialise in events having relatively big signals in the calorimeter, preferentially in the deeper 'hadronic' layers of the calorimeter (caused by neutrons and anti-neutrons of high transverse momentum), and showing few or no photon shower initiated tracks in the streamer chamber, especially in the upper chamber, where the photon conversion probability is enhanced by a converter plate[1].

From a detailed analysis of the UA5 data at $\sqrt{s} = 900$ GeV [55] along these principles upper limits on the Centauro production were obtained, shown in fig. 19, being typically in the order of a few per thousand inelastic events.

In conclusion, no evidence for the existence of Centauro-like events has been found at the SPS Collider, suggesting either a threshold still higher, or alternatively that the Centauro phenomenon is an observational 'artefact', to which accelerator detectors might be less susceptible [55]. However, if the observed Centauro events were not

[1] Effective thickness of the converter plate, placed between the beam pipe and the upper streamer chamber, is 0.4 radiation lengths for tracks with $|\eta| \leq 3.6$.

caused by nucleon-nucleon collisions (but by some exotic object), laboratory experiments are not expected to see the phenomenon.

5. Summary

In this review of recent UA5 results from $p\bar{p}$-interactions at $\sqrt{s}$ = 200, 546 and 900 GeV, obtained at the CERN SPS Collider, the following points were discussed:

- From the measurement of the ratio of the inelastic cross sections at $\sqrt{s}$ = 200 and 900 GeV for the total $p\bar{p}$ cross section at 900 GeV a value of $65.3 \pm 0.7 \pm 1.0$ mb was determined.
- The investigation of single diffraction dissociation showed that at the Collider the single diffraction cross-section appears to be about 5 – 8 mb, being only weakly energy dependent.
- The hadronization of the diffractively excited system preferentially proceeds according to p_T -limited phase space, rather than by an isotropic fireball-like decay.
- Violations of the KNO scaling are well established. The multiplicity distributions can instead be parametrized by negative binomial distributions, whose parameters smoothly vary with the c.m. energy.
- Besides strong short range correlations in the particle production, which appear to be energy inpendent as far as ISR and Collider energies are concerned, the analysis of long range correlations revealed a linear increase of the correlation strength with the logarithm of the c.m. energy.
- The findings on correlations strongly favour the independent production of clusters (of mixed size) of particles, giving rise to multi-particle production. For the effective cluster size, which is defined by the first to moments of the cluster decay multiplicity, a value of about 2.5 charged particles is estimated.
- There is no evidence for Centauro events up to $\sqrt{s}$ = 900 GeV.

References

[1] UA5-Collaboration, CERN/SPSC/82-75, SPSC/P184, 15 October 1982.
[2] UA5-Collaboration, to be submitted to Physics Report.
[3] J.G. Rushbrooke, Invited Rapporteur's Talk at the Int. Europhysics Conf. on High Energy Physics, Bari, Italy, July 1985, CERN-EP/85-178.
[4] G. Chiefari, UA4-Collaboration, Int. Europhysics Conf. on High Energy Physics, Bari, Italy, July 1985.
[5] UA5-Collaboration, to appear in Zeitschrift für Physik C.
[6] N. Amos et al., Nucl. Phys. B262 (1985), 689.

[7] M. Bozzo et al., Phys. Lett. 147B (1984), 385 & 392.
[8] E.L. Feinberg and I. Pomeranchuk, Suppl. Nuovo Cimento 4 (1956), 652.
M.L. Good and W.D. Walker, Phys. Rev. 120 (1960), 1855.
[9] UA5-Collaboration, submitted to Zeitschrift für Physik
[10] CERN-HERA 79-03, Compilation of pp and $p\bar{p}$ Cross Sections.
[11] U. Amaldi and K.R.Schubert, Nucl. Phys. B166 (1980), 301.
[12] M. Ambrosio et al., Phys. Lett. 115B (1982), 495.
[13] N. Amos et al., Phys. Lett. 128B (1983), 343.
[14] N. Amos et al., Phys. Lett. 120B (1983), 460.
[15] J.C.M. Armitage et al., Nucl. Phys. B194 (1982), 365.
[16] G. Sciacca, UA4-Collaboration, XVI Symp. on Multiparticle Dynamics, Kiryat Anavim, Israel, June 1985.
[17] M.G. Albrow et al., Nucl. Phys. B108 (1976), 1.
J. Whitmore et al., Phys. Rep C10 (1974), 273.
J.W. Chapman et al., Phys. Rev. Lett. 32 (1974), 257.
S. Barish et al., Phys. Rev. D9 (1974), 2689.
H. Bialkowska et al., Nucl. Phys. B110 (1976), 300.
J. Schamberger et al., Phys. Rev. Lett. 34 (1975), 121.
J.C.M. Armitage et al., Nucl. Phys. B194 (1982), 365.
A. Breakstone et al., Phys. Rev. 30 (1984), 528.
[18] K. Gouilanos, Phys. Rep. 101 (1983), 169.
[19] G.J. Alner et al., UA5-Collab., Phys. Lett. 167B (1986),476.
[20] B. Åsman, UA5-Collab., Univ. of Stockholm Report USIP 85-17 (1985).
B. Åsman, UA5-Collab., Thesis, Stockholm University, Stockholm 1985.
[21] V.V. Ammosov et al., Phys. Lett. 42B (1972),519.
H.B. Białkowska et al, Nucl. Phys. B110 (1976),300.
W.M. Morse et al., Phys. Rev. D15 (1977),66.
S. Barish et al., Phys. Rev. D9 (1974),2689.
Firestone et al.,Phys. Rev. D10 (1974),2080.
C. Bromberg et al., Phys. Rev. Lett. 31 (1973),1563.
J. Whitmore, Phys. Rep. 10C (1974),273.
[22] A. Breakstone et al., Phys. Rev. D30 (1984),528.
[23] L.D. Landau, Izv. Akad. Nauk. SSSR, Ser. Fiz. 17 (1953),51; in Collected Papers, ed. by D. Ter Haar (Pergamon, Oxford, 1965), 569.
[24] W. Thomé et al., Nucl. Phys. B129 (1977),365.
[25] K. Alpgård et al., UA5-Collab., Phys. Lett. 121B (1983),209.
[26] K. Alpgård et al., UA5-Collab., Phys. Lett. 107B (1981),315.
[27] Z. Koba, H.B. Nielsen and P. Olesen, Nucl. Phys. B40 (1972),317.
[28] R.P. Feynman, Phys. Rev. Lett. 23 (1969),1415.
[29] P. Slattery, Phys. Rev. D7 (1973),2073.
[30] G.J. Alner et al., UA5-Collab., Phys. Lett. 138B (1984),304.
[31] G. Ekspong, 5th Topical Workshop on Proton-Antiproton Physics, Saint-Vincent, Italy, Feb. 25 - March 1, 1985.
[32] G.J. Alner et al., UA5-Collab, Phys. Lett. 160B (1985),199.
[33] M. Planck, Sitzungsber. Deutsch. Akad. Wiss. Berlin, 33 (1923),355.

[34] P. Carruthers and C.C. Shih, Phys. Lett. 127B (1983),242.

[35] W. Knox, Phys. Rev. D10 (1974),65.
A. Giovannini, Nuovo Cimento 15A (1973),543.
N. Suzuki, Prog. Theor. Phys. 51 (1974),1629.

[36] G. Ekspong, XVI. Symp. on Multiparticle Dynamics, Kiryat Anavim, Israel, June 9-14, 1985.

[37] A. Giovannini and L. Van Hove, CERN-TH.4230/85, July 1985.

[38] P.R. Montmort, Essay d'Analyse sur les Jeux de Hazard. Seconde Edition. Chez Jacque Quillau, Imprimeur-Juré-Libraire de l'Université, Paris, 1713.

[39] M. Kendall and A. Stuart, The Advanced Theory of Statistics, Charles Griffin & Company Ltd., London 1977.

[40] M. Greenwood and G.U. Yule, J.R.Statist.Soc. 83 (1920),255.

[41] P.C.T. Jones and J.E. Mollison, Journal of Microbiology 2 (1948),54.

[42] M.H. Quenouille, Biometrics 5 (1949),162.

[43] B. Holl, 21. Rencontre des Moriond, Les Arcs, France, March 1986.

[44] S. Uhlig et al., Nucl. Phys. B132 (1978), 15.

[45] K. Alpgård et al., UA5-Collab., Phys. Lett. 123B (1983), 361.

[46] G. Ekspong, Proc. of the 3rd Topical Workshop on Proton-Antiproton Collider Physics, CERN Yellow Report 83-04, 1983, p. 112.

[47] B. Eckart, XVIII. Rencontre de Moriond, La Plagne, March 19-25, 1983; ed. J. Tran Thanh Van, Editions Frontières, Gif-sur-Yvette, 1983; p.155.
K. Böckmann and B. Eckart, XV. Int. Symp. on Multiparticle Dynamics, Lund, Sweden, June 10-16, 1984; Bonn University, BONN-HE-84-22.

[48] S.R. Amendolia et al., Nuovo Cimento 31A (1976),17.
D. Drijard et al., NPB 155 (1979),269.
W. Bell et al., ZPC 22 (1984),109.

[49] S.G. Bayburina et al., Nucl. Phys. B191 (1981), 1.

[50] UA5-Collaboration, SPSC/P-92, 1978.

[51] C.M.G. Lattes, Y. Fujimoto and S. Hasegawa, Phys. Reports 65 (1980),151.

[52] G. Arnison et al., Phys. Lett. 122B (1983), 189.

[53] K. Alpgard et al., Phys. Lett. 115B (1982), 71.

[54] J.G. Rushbrooke, Proc. 21th Int. Conf. on High Energy Physics, Paris 1982, Journal de Physique, C3-177 (1982).

[55] UA5-Collaboration, to be submitted to Zeitschrift für Physik C.

Fig.1

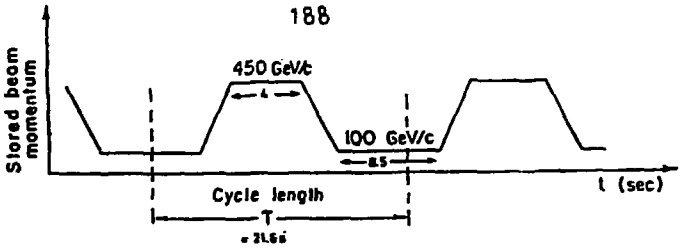

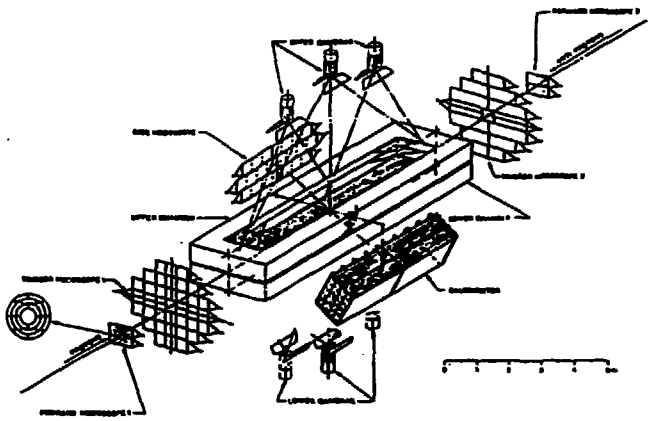

Fig.2

Fig. 3

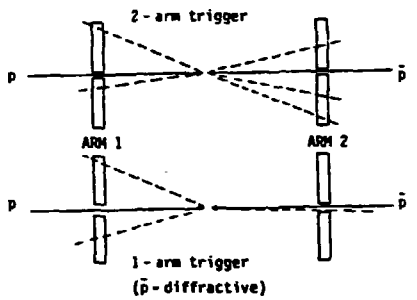

Fig.4

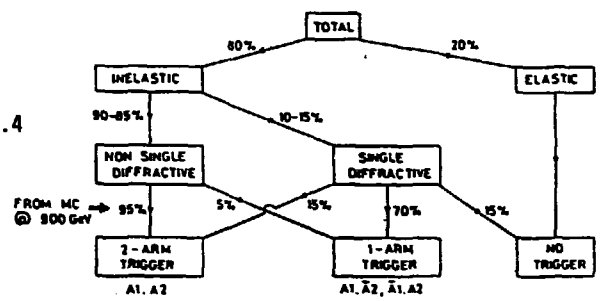

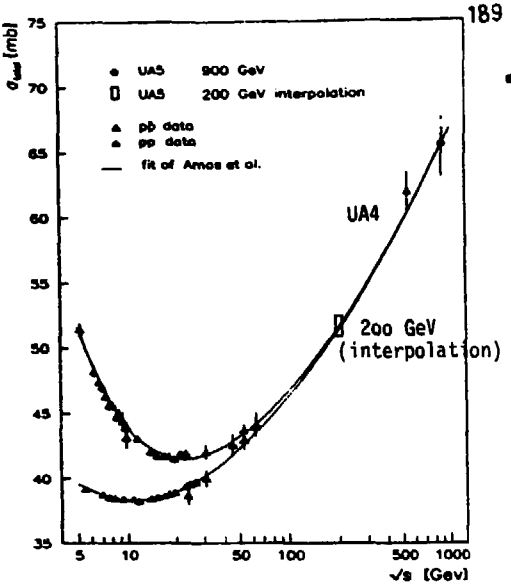

FIGURE 5

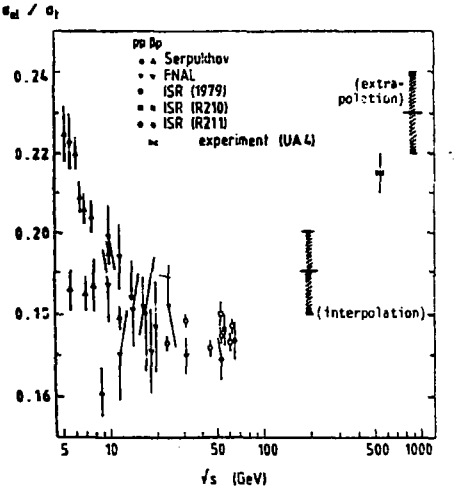

Fig. 6 The ratio of the elastic to the total cross section

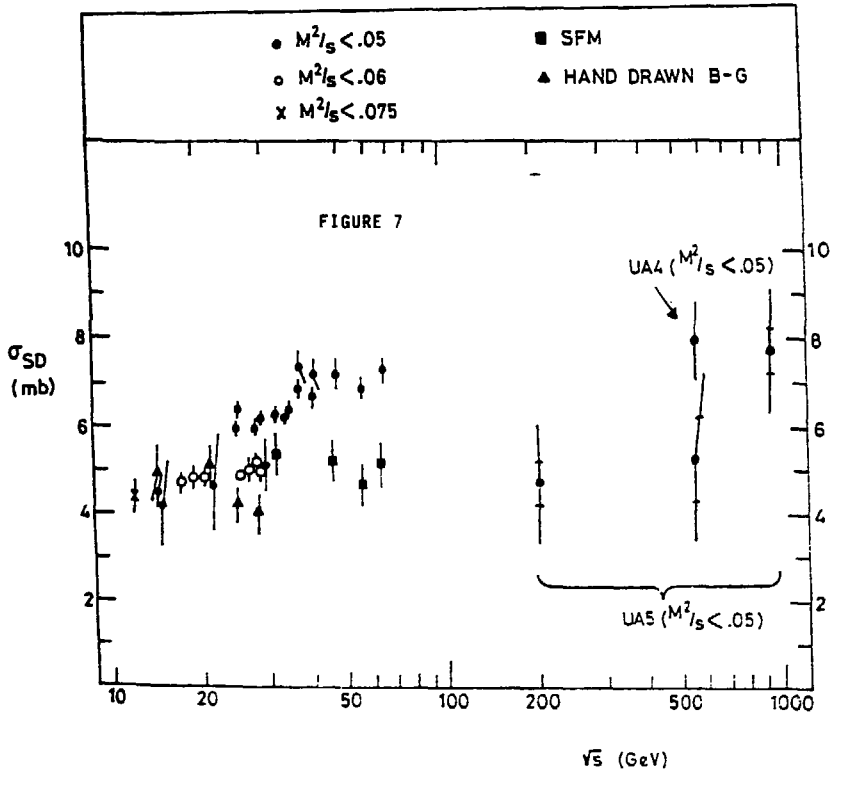

figure 8

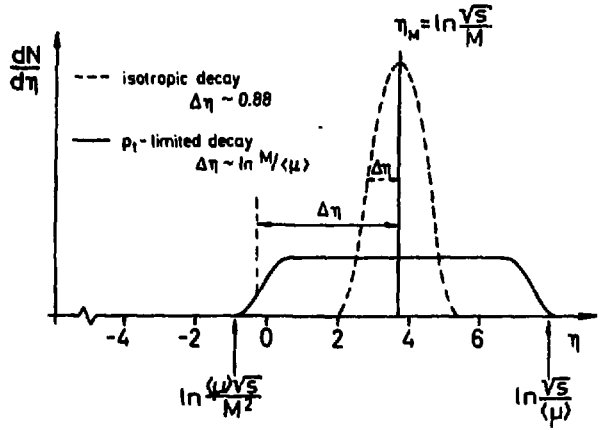

figure 9

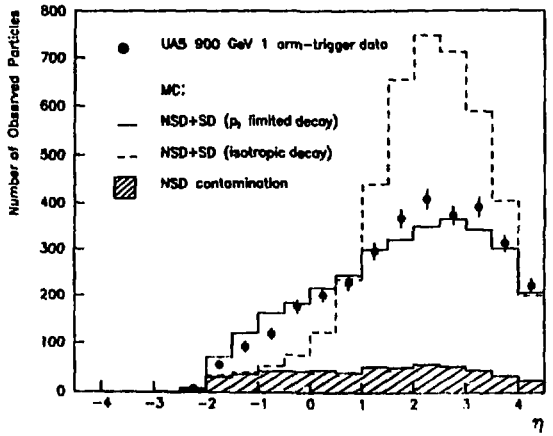

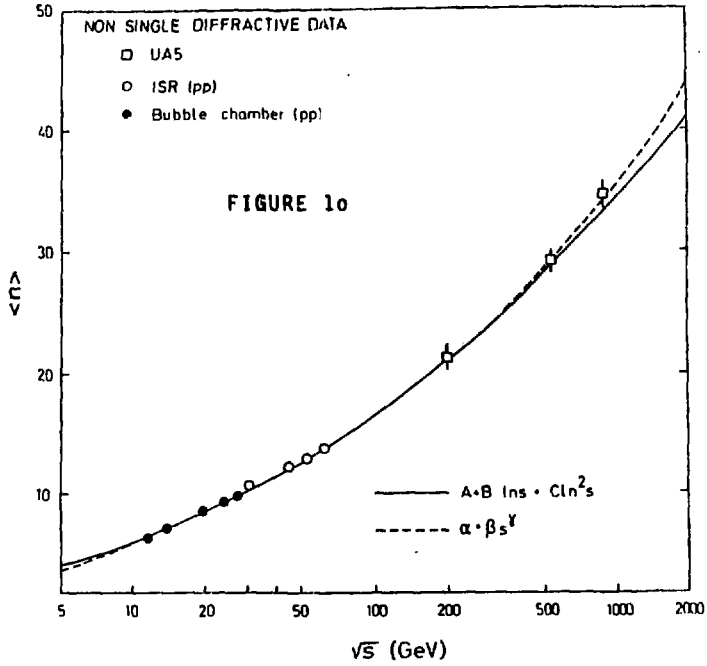

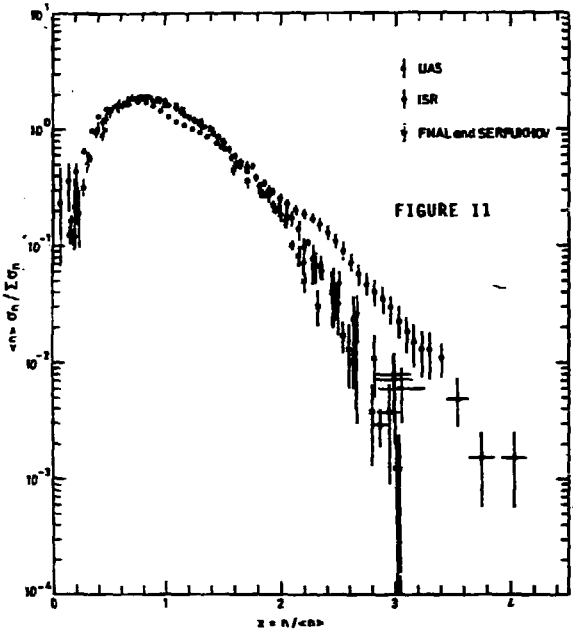
UA5
ISR
FNAL and SERPUKHOV
FIGURE 11

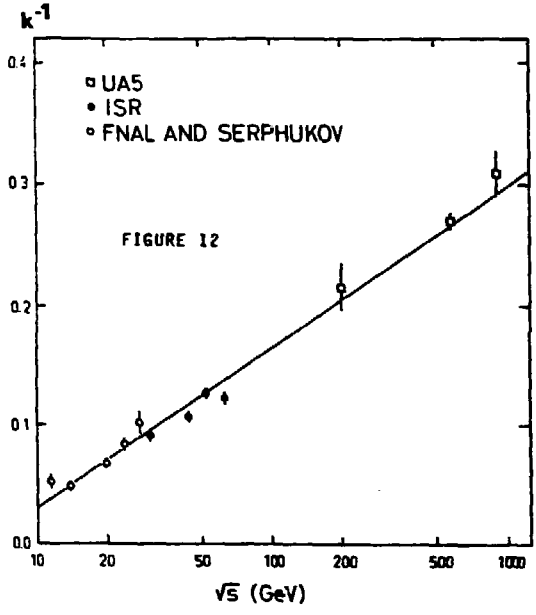
UA5
ISR
FNAL AND SERPHUKOV
FIGURE 12
√s (GeV)

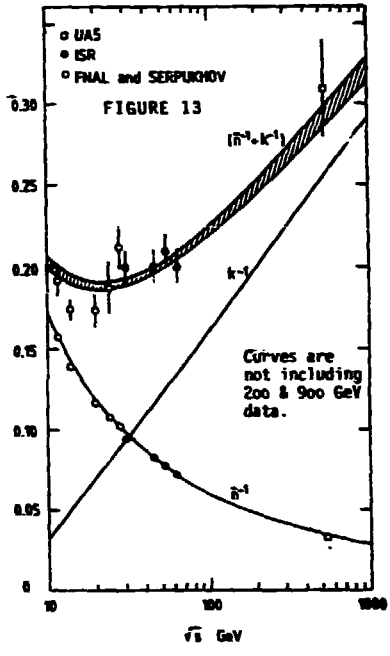
UA5
ISR
FNAL and SERPUKHOV
FIGURE 13
Curves are not including 200 & 900 GeV data.
√s GeV

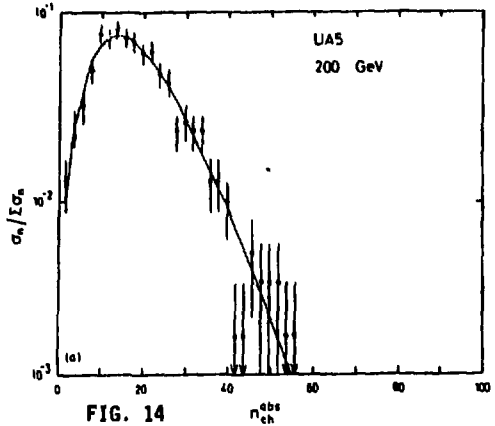
UA5
200 GeV
(a)

FIG. 14

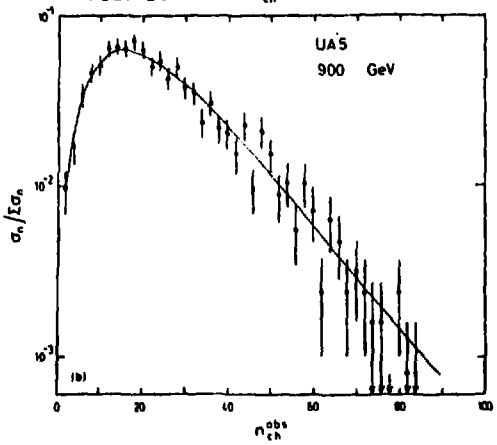
UA5
900 GeV
(b)

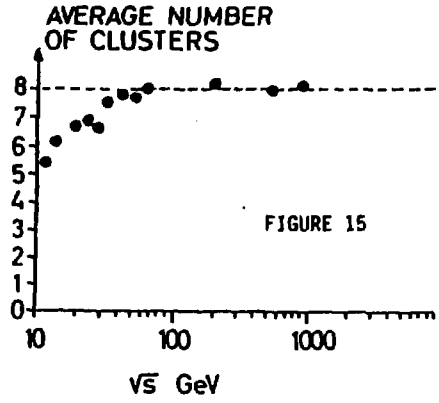
AVERAGE NUMBER
OF CLUSTERS
FIGURE 15
√s GeV

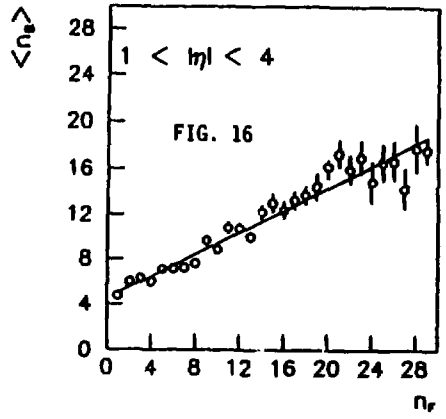
1 < |η| < 4
FIG. 16

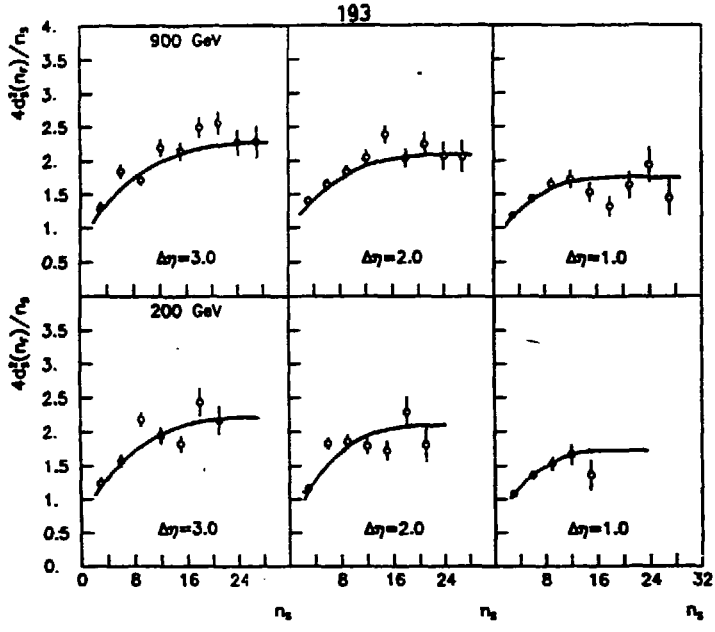

FIG. 18 The ratio $4d_S^2(n_F)/n_S$ as a function of the total multiplicity n_S for three different forward/backward intervals at 900 GeV and 200 GeV

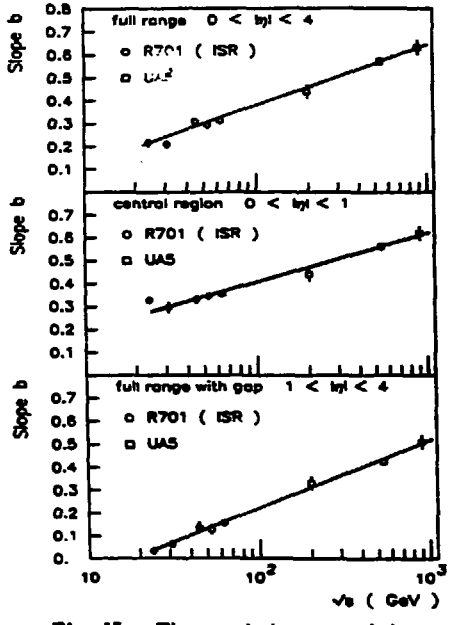

Fig. 17. The correlation strength b as function of the energy for three different η-intervals.

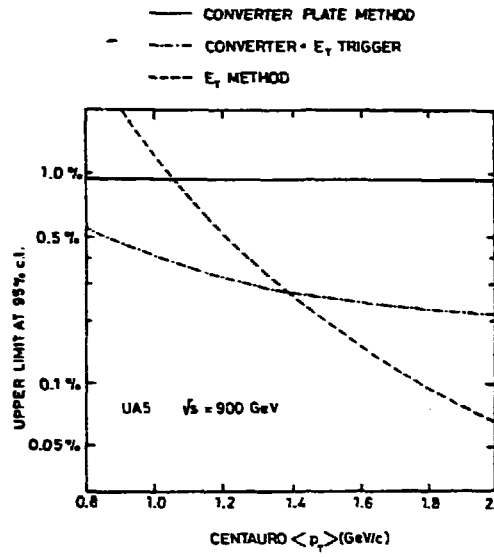

FIG. 19

CYGNUS X-3 AS EVIDENCE OF NEW PARTICLES, NEW INTERACTIONS OR EXPERIMENTAL ERRORS?

Maria Giler
Physics Institute, University of Łódź
Poland

The discovery of Cyg X-3 as a Galactic source of very high energy quanta /10^{15} - 10^{16} eV/ inducing in the Earth's atmosphere extensive air showers[1] has been causing a great interest among cosmic ray and also elementary particle physicists. The reason is that for the first time a confirmed cosmic source[2] of particles of such a great energy has been identified. Moreover, all the existing experimental data on Cyg X-3 are non compatible with any known particle traveling from that source to us, neither with their expected interactions extrapolated to high energies.

Cyg X-3 is a binary object on the edge of our Galaxy, lying some 10 kpc away from the Sun in the Galactic plane. It is a strong X-ray source displaying a periodical change of the intensity /the period being ~ 4.8 hours/ usually interpreted as a result of the orbital motion of the two components. It is observed in radio waves /where it exhibits strong outbursts with unexplained period of~367 days/ and in the infrared radiation where the 4.8 hr period is seen.

Measurements at higher energies are less consistent with each other. Some of the balloon and satellite missions detecting γ-rays at $10^8 \div 10^9$ eV do see Cyg X-3 [3], some of them don't [4]. It is plausible that at least some of these differencies might be attributed to the variability of the source over the time scale of years or even months.

Here we shall be concerned with the interpretation of the experimental results at the highest energies, corresponding to the energy of the primary quanta $E \geq 10^{12}$ eV. There are two sets of that data based on

1/ surface detectors registering
   a/ Cherenkov light produced by small /$E \geq 10^{12}$ eV/ electromagnetic cascades which themselves die out high in the atmosphere,
   b/ extensive air shower arrays /$E \geq 10^{15}$ eV for sea level/ and
2/ deep underground muon detectors with the typical muon energy of the order of several hundreds GeV.

The identification of Cyg X-3 was made by the observation of an enhancement of events coming from its direction and /or by a nonuniform distribution of the events in the phase plot for the 4.8 hr period/. Most experiments identity this source by the second method because, as it turns out, the excess events are concentrated in a rather narrow phase bin. However, in the first observation of Cyg X-3 by the extensive air shower array in Kiel both the enhancement of the shower counting rate and the nonuniform phase distribution was seen /fig 1

and 2a/. The angular resolution of the shower arrival direction was better than 1^{o}, due to a large number of scintillator detectors measuring the delays in detecting the shower front. An interesting thing is that Cyg X-3 was seen only in the shower sample with broader lateral distribution of particles /age parameter $s > 1.1$/ - as one would expect for showers iniciated by high energy /$E > 2 \times 10^{15}$ eV/ γ-rays. This is an imposing idea that the quanta producing showers in the atmosphere are γ-rays but it meets with a very serious difficulty. The γ-ray induced showers should produce much less /~ 10 times/ muons than the normal showers induced by strong interacting particles /protons, nuclei/ - whereas the muon content in the Cyg X-3 showers shows practically no indication of being smaller [5].

The Kiel observation was confirmed shortly later by the Haverah Park air shower array [1]. The phase analysis of the showers coming from Cyg X-3 direction shows an enhancement of events in the same bin /0.2 - 0.3/ as in the Kiel experiment although the time averaged flux is some 5 times lower /fig 4/. Further air shower and Cherenkov technique experiments displayed nonuniform phase distributions but the phase of the maximum was about 0.6 rather than 0.2. Fig 2 shows examples of the data obtained mainly in 1984 /appart from the last histogram produced from 1981/82 data/. A compilation of the phase analyses from many experiments in different energy ranges is presented in fig 3 where positions of the phases of highest peaks are marked. It can be seen that the phases are grouped around two values 0.25 and 0.6, the preferable phase for later measurements being rather 0.6. The statistical significance of the peaks exceeds 4 σ in many experiments. However, the primary γ-ray energy spectrum drawn in fig 4 shows a rather large scatter of the data, particularly for $E > 10^{14}$ eV. Some of the discrepancies may be attributed to the uncertainties in the primary energy determination /which are not shown on the graph/, some might be due to the variability of the source, some of course are caused by systematic errors. Nevertheless the overall shape of the observed integral spectrum can be roughly described by a power law $I(>E) \sim E^{-\delta}$ with $\gamma \simeq 1$. This is much flatter than the cosmic ray particle spectrum for which $\gamma = 1.7$ in that energy range. It also implies that the energy content in the γ-ray flux is the same in any constant logarithmic interval of energy. Thus the flux must steepen or cut off somewhere. Moreover if one wants to calculate the energy spectrum at the source the γ-ray interactions in the interstellar space must be taken into account. At 10^{15} eV the mean free path for pair production on the microwave background radiation reaches its minimum and is about equal to the distance to Cyg X-3. So the source spectrum may be even flatter. Fig 4 shows a hypothetical source spectrum with $\gamma = 0.7$ chosen so to fit the Kiel observations after absorption correction.

As it was already said γ-rays from Cyg X-3 should not produce many muons in the Earth atmosphere. So it was quite puzzling when within a short period of time two groups reported observations of high energy muon fluxes from Cyg X-3 direction [6]. These were proton decay experiments located deep underground which in addition are well suited for measurements of high energy muons produced by cosmic ray particles. However

other experiments have not confirmed these results[7]. Fig 5 shows phase distributions of muon events for the two positive results together with one of the negative ones, obtained with a large muon detector in Baxan /Caukasus/. The statistical significance of the latter is much better than the others, partly due to lower energies. What also is important is that the NUSEX data correspond to a rather large declination and right ascension interval /both 10^{o}/ around Cyg X-3 position chosen so to maximize the signal, although the angular uncertainty of muon arrival direction was about 1^{o}. Moreover the Soudan 1 data represent the events coming from the direction shifted by 2.7^{o} in declination from Cyg X-3 position. This was also chosen in such a way to maximize the signal in the phase plot, although it is less than the estimated pointing error.

If the observed muon enhancements were really due to some particles from Cyg X-3 then they are in conflict with the γ-ray hypothesis by several orders of magnitude. The muon flux from the Soudan experiment is $7.10^{-11}cm^{-2}s^{-1}$ for $E_{\mu} > 650$ GeV which is the same as the γ-ray flux of that energy /fig 4/. The NUSEX flux is not so drastically high but γ-rays of the intensity from fig 4 would also not produce it. However one should keep in mind that the source may be variable and divergent results of different groups might be at least partly due to it.

A very rough model for the high energy γ-ray production in Cyg X-3 is the following[8]. A compact object /probably a pulsar/ and a rather low mass normal star are orbiting around each other with the 4.8 hours period. This corresponds to the distance between them of the order of solar radius. X-rays are produced by the matter falling from the companion star into the deep gravitation potential well of the pulsar, heated to temperatures $10^{7} - 10^{8}$ K. The quickly rotating pulsar is probably the site of the acceleration of protons to the energies up to about 10^{17} eV. These protons produce γ's in the star's atmosphere /by $\pi^{o} \rightarrow 2\gamma$/, which shields the pulsar twice during one period. Phase zero corresponds to the minimum X-light so if it means that the pulsar is then behind the star we should expect the γ-ray pulses at phases somewhere in the regions 0.1 - 0.2 and 0.8 - 0.9. The observed situation is different /phases $\sim$ 0.25 and 0.6/. Particularily phase 0.6 corresponds to the situation when the pulsar is in front of the atmosphere.

A very interesting possibility to determine the pulsar's orbit arises by measurements of the derivative of the pulsars own period of rotation. The only observation of the pulsar's period was reported recently by Chadwick et al[9]. They observed the Cherenkov light flashes, corresponding to primary γ's of 1000 GeV, being periodical with 12.59 ms. So the pulsar may serve as a clock and due to the Doppler effect its own period should vary with the orbital phase. The data gives negative derivative at phase around 0.6 implying this being a rear part of the pulsar's orbit - in contrast with the simple model described above, but in agreement with the γ-ray peak for that phase. So the model of Cyg X-3 must be different and there are several attempts, assuming e.g. eccentricity of the orbit and or asymmetric gas distribution, trying to fit the data.

What in fact is most disturbing for elementary particle and cosmic ray physicists is the nature of the arriving quanta and their interaction in the atmosphere. The particle must obviously be neutral - otherwise it would be deflected by galactic magnetic fields from the straight line direction. We have already explained the problem with the photon hypothesis - there are to many muons /almost an order of magnitude/ in the extensive air showers. The photoproduction cross-section at $\sim 10^{15}$ eV would have to be comparable with the nuclear one which means an increase by two orders of magnitude in comparison with 10^{11} eV. The very large distance /$\geq$ 35 000 light years/ excludes neutron as a particle which would produce the muons. The neutron energy should be $\geq 10^{18}$ eV for its life time to be equal to the travel time but the primary energy of the showers is $\leq 2 \times 10^{16}$ eV. If neutrinos were the primary particles then their interaction cross-section in the atmosphere should be greater by about six orders of magnitude from what is expected from its linear rise with energy, implying $\sigma_\nu \sim E^2$. If neutrinos had normal cross-section and produced underground muons then the signal should not change with the zenith angle - contrary to the observations[6].

The duration of the signal Δt provides an interesting information about the particle mass - the relative time dispersion of particles with the energy greater than E is $\Delta t/t \simeq \frac{1}{2}(m/E)^2$, where t is the travel time. If $\Delta t < 0.5$ hour /$\Delta\psi = 0.1$/ then for $E \geq 10^{12}$ eV the particle mass must be less than about 100 MeV. Moreover if the observations of Cherenkov light pulsing with the 12.59 ms period are real then the upper limit for the mass is much smaller - $m \leq 0.1$ MeV. This puts severe limits to various exotic hypotheses concerning the nature of the particle. There has been suggested that the compact object might be a quark star rather than the neutron star and Cyg X-3 would emit bits of quark matter. They would produce showers with enough muons but their mass would be to large to give a short signal.

The assumptions that the primary particles are the supersymmetric ones /e.g. photinos/ meet with one common difficulty. They would imply a gigantic emissivity of the source. If we assume that the primaries are γ-rays the inferred emissivity is already extremely large - $L_\gamma / E_\gamma > 10^{15}$eV/ $\simeq 10^{37}$erg/s /if it is isotropic/. The emissivity in high energy parent protons /$E_p > 10^{16}$ eV/ would then amount to about 10^{39}erg/s if one allows for the inelasticity coefficient $K_{\pi^0} = 0.13$ and the fact that γ's are observed during 0.1 fraction of the period. This fraction may be even several times smaller increasing the total emissivity by the same factor. It is difficult to assume that protons of the energy 10^{16} eV produce supersymmetric particles instead of π^0's but the smaller is the fraction of these particles the larger would be the inferred total emissivity. $L \geq 10^{39}$erg/s is already almost two orders of magnitude greater than the energy input rate needed to fulfil the Galaxy with the cosmic ray intensity for $E > 10^{16}$ eV as observed at the Earth. It is only few times less than what is necessary for all the observed cosmic rays with $E > 10^8$ eV. If this large emissivity is transient that would relax the above discrepancy but we must then be quite lucky in observing an object like Cyg X-3 at all.

In concluding we would like to underline a rather low statistical significance of the two underground experiments claiming to observe high energy muons from Cyg X-3 direction. If these are statistical fluctuations or some detection biases then the photon hypothesis seems to be the best. However the large muon content in the showers still remains to be explained. Further measurements will hopefully clear out the whole phenomenon if only Cyg X-3 does not fade away.

The author wishes to thank prof.Jerzy Wdowczyk for many useful discussions.

REFERENCES

1 M.Samorski and W.Stamm, Astrophys.J.268,L17 /1983/.
J.Lloyd-Evans et al, Nature 305, 784 /1983/.

2 A shower excess from the direction of the Crab Nebula has been observed by Łódź group, but this awaits further confirmations. See T.Dzikowski et al, Proc.of the 18-th ICRC, Bangalore 2, 132 /1983/ and references therein.

3 R.C.Lamb et al, Astrophys.J. 212, L63 /1977/.
A.M.Galper et al,Proc.of the 15-th ICRC,Plovdiv, 1,131/1977/.
S.Danaher et al,Nature/Letters/ 289,568 /1981/.
R.C.Lamb et al, Nature 296,543 /1982/.
Ju.Neshpor et al, Ap.Space Sci.61, 349 /1979/.

4 R.S.White et al, Nature/Letters/ 284, 608 /1980/.
W.Hermsen et al, Proc.of the 19-th ICRC,La Jolla 1,95 /1985/.

5 M.Samorski and W.Stamm,Proc.of the 18-th ICRC,Bangalore 11, 244 /1983/.
However a Japan group observes an enhancement at phase 0.6 for muon-poor showers but with a rather low statistical significance /T.Kifune et al,Proc.of the 19-th ICRC,La Jolla 1, 67 /1985/ /.

6 M.L.Marshak et al, Phys.Rev.Lett.54, 2079 /1985/ .
G.Battistoni et al, Phys.Lett.155B, 465 /1985/.

7 Ju.Andreyev et al, results presented in the Soviet Cosmic Ray Conference, Tbilisi /1986/.
Ch.Berger et al, FREJUS collaboration, preprint /1986/.

8 W.T.Vestrand and D.Eichler, Astrophys.J. 261,251 /1982/.

9 P.M.Chadwick et al, Nature 318, 642 /1985/.

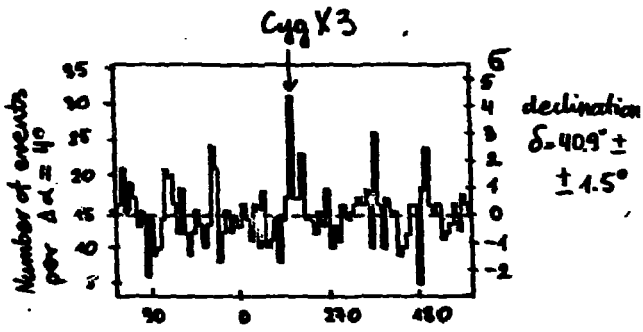

Fig.1. Number of air showers with size $N_e > 10^5$ particles, detected in Kiel.

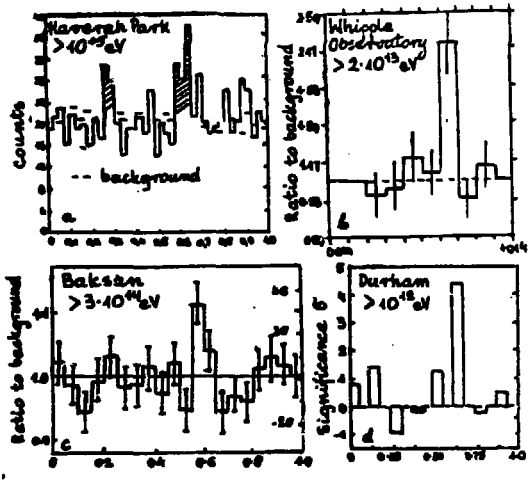

Fig.2. Phase plots from different experiments

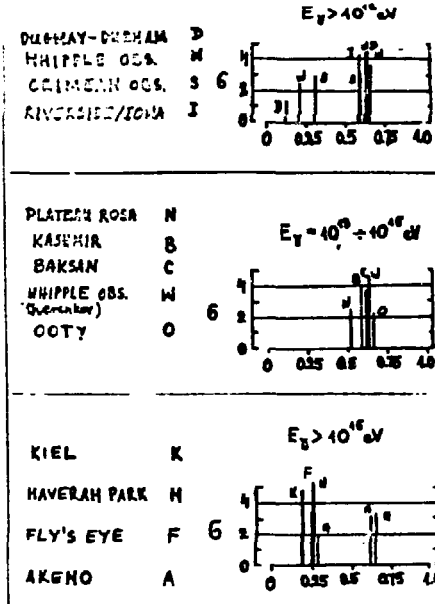

Fig.3. Phase positions of highest peaks and their statistical significance σ from different experiments.

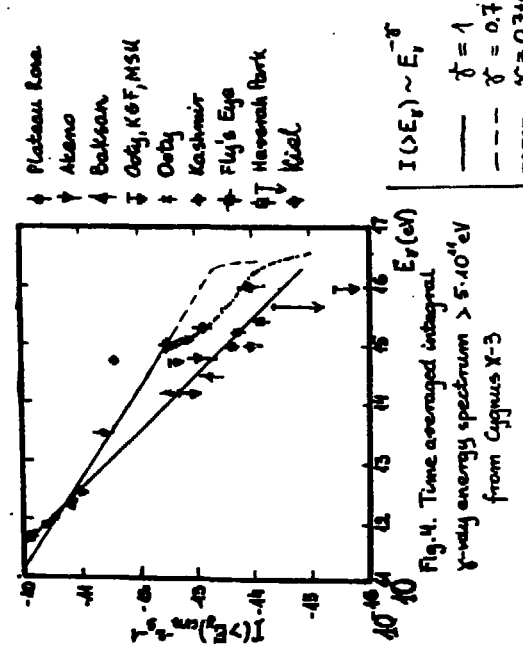

Fig.4. Time averaged integral γ-ray energy spectrum > 5·10^14 eV from Cygnus X-3

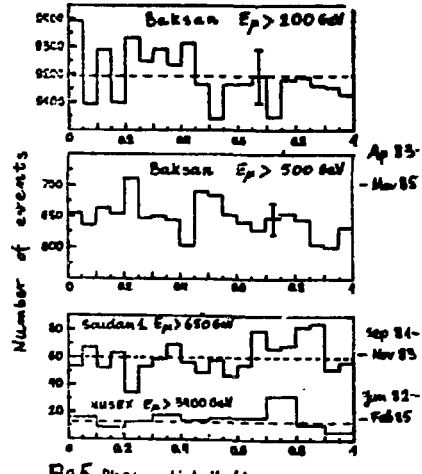

Fig.5. Phase distributions of underground muons from Cyg X3 direction

MEASUREMENT OF ELECTROWEAK EFFECTS IN e^+e^- ANNIHILATION

D. R. Saxon

Rutherford Appleton Laboratory, Chilton, Didcot, Oxon OX11 0QX, UK.

ABSTRACT

Electroweak interference effects in e^+e^- + leptons have been measured to an accuracy of about 5%. This allows for accurate comparison with theory, and the differences between theoretical schemes are discussed, together with the sensitivity of limits on deviations from theory to normalisation systematics. The weak coupling is seen in the hadronic total cross-section and the Z^0 propagator in leptonic forward-backward asymmetries. The weak isospins of heavy quarks have been measured.

1. INTRODUCTION

The first significant measurements of electroweak interference in $e^+e^- \to \mu^+\mu^-$ were made in 1982 [1-3]. Since then the field has evolved rapidly, with very high statistics (total 567 pb^{-1}) available at $s = 841$ GeV^2 from PEP, and 180 pb^{-1} of high energy data at PETRA, up to a maximum s of 2188 GeV^2 ($\sqrt{s} \leq 46.78$). Present running at PETRA is concentrating on a large improvement in the statistic at $\sqrt{s} \sim 35$ GeV, where there are some discrepancies from theory. The development of the study into its modern form can be seen in a number of reviews [4-7]. This report is written as an updating of a previous work by the same author [7].

The increase in experimental precision has been matched by sophistication in theoretical treatment. Full one-loop radiative corrections are needed to match the 5% accuracy of measurement of the interference ten, both pure QED $O(\alpha^3)$ and Z° self-energy, γ-Z° transitions, and double Z° and W^+W^- exchange. This introduces a dependence on the electroweak scheme, as we now discuss.

2. WEAK NEUTRAL CURRENT PARAMETERS

In the theory as developed by Glashow, Weinberg and Salam [8-10], the fermion vector and axial weak neutral couplings are related to the third components of the weak isospins of the fermions.

$$g_a^f = T_{3L}(f) - T_{3R}(f)$$

$$g_v^f = T_{3L}(f) + T_{3R}(f) - 2Q_f \sin^2\theta_w$$

The fermions are members of left-handed doublets and right-handed singlets, assuming the existence of a top quark. The couplings obtained are therefore:

Fermion	Q_f	g_a^f	g_v^f	$g_v^f(\sin^2\theta_w = 0.22)$
e,μ,τ	-1	$-\frac{1}{2}$	$-\frac{1}{2} + 2\sin^2\theta_w$	-0.06
u,c,t	$+\frac{2}{3}$	$+\frac{1}{2}$	$+\frac{1}{2} - \frac{4}{3}\sin^2\theta_w$	$+0.21$
d,s,b	$-\frac{1}{3}$	$-\frac{1}{2}$	$-\frac{1}{2} + \frac{2}{3}\sin^2\theta_w$	-0.35

The lowest order diagrams for $e^+e^- \to f\bar{f}$ are shown in Figure 1, with intermediate virtual γ and Z°.

For final states other than $e^+e^- \to e^+e^-$ we define the ratio of the total cross-section to the point-like pure QED cross-section for $e^+e^- \to \mu^+\mu^-$

$$R_{f\bar{f}} = \sum_c Q_f^2 - 2Q_f g_v^e g_v^f \mathrm{Re}\chi + (g_v^{e2} + g_a^{e2})(g_v^{f2} + g_a^{f2})|\chi|^2$$

The angular distribution is of the form

$$(1 + \tfrac{8}{3}A\cos\theta + \cos^2\theta)$$

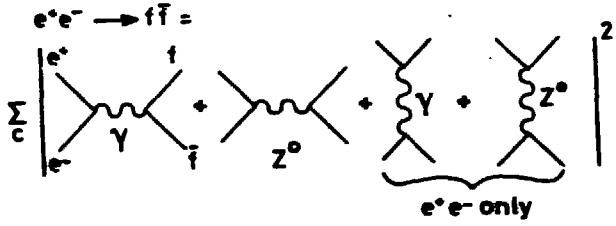

Figure 1 Lowest order Feynman graphs for $e^+e^- \to f\bar{f}$. The sum (for hadrons) runs over colours.

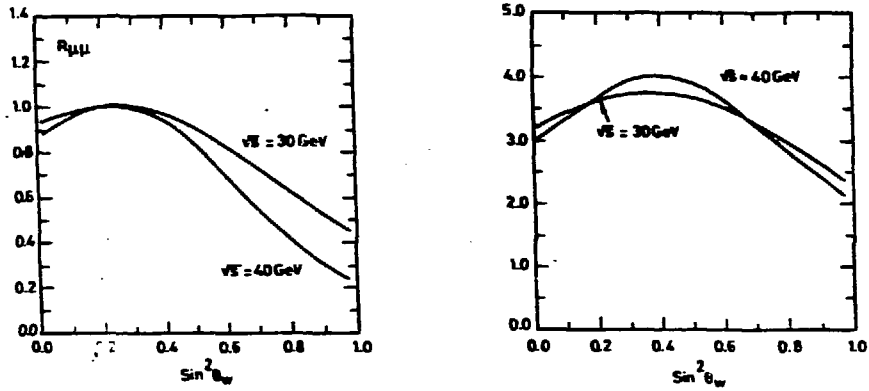

Figure 2 Lowest order cross-section, normalised to pointlike QED, plotted aginst $\sin^2\theta_W$. (a) $e^+e^- \to \mu^+\mu^-$. (b) e^+e^- → hadrons (5 flavours, ignoring QCD effects).

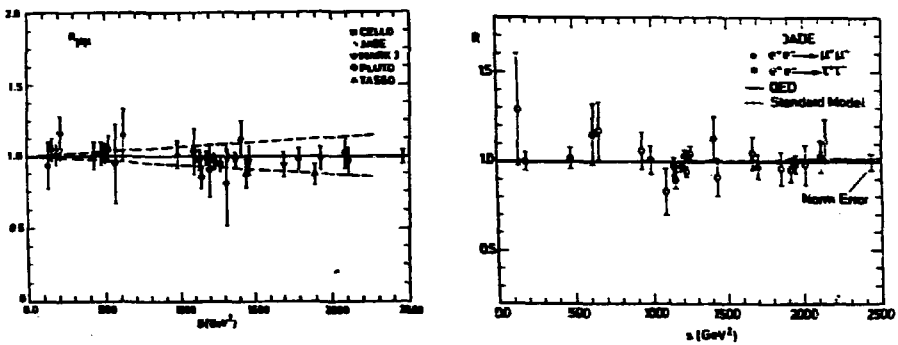

Figure 3 Measured cross-sections/QED predictions. (a) $\mu^+\mu^-$, many experiments. (b) $\mu^+\mu^-$ and $\tau^+\tau^-$, JADE.

where θ is the cm scattering angle between the initial state electron and the final state fermion. Thus we define the forward-backward asymmetry

$$A_{ff} = \frac{3}{2R_{ff}}\left[-Q_f g_a^e g_a^f \mathrm{Re}\chi + 2g_v^e g_a^e g_v^f g_a^f |\chi^2| \right]$$

The Z^0-propagator is contained in χ. This can be formulated in two ways. Conventionally one follows Weinberg and Salam [9,10,11]

$$\chi = \frac{\rho\, G_F}{2\sqrt{2}\pi\alpha} \cdot \frac{s\, m_Z^2}{s - m_Z^2 + i m_Z \Gamma}$$

In this case there are three free parameters (ρ, G_F, $\sin^2\theta_W$). The charged weak coupling, G_F, is obtained from μ-decay, and the Higgs mechanism is used to relate this to the weak neutral current, via the parameter ρ ($\rho = 1$ in the simplest case), and $m_Z = m_W/\rho\cos\theta_W$.

However, given that the Z^0 has now been discovered, it has been pointed out by Böhm [11] that it is perhaps more economical of theory to follow the original Glashow formalism and write

$$\chi = \frac{1}{4\sin^2\theta_W \cos^2\theta_W} \cdot \frac{s}{s - m_Z^2 + i m_Z \Gamma}$$

In this case there are two free parameters (m_Z and $\sin^2\theta_W$) [10,11]. Given the Z^0 mass, the Weinberg angle then measures the strength of the weak neutral coupling. There is no link to charged currents and hence neither ρ nor G_F occurs.

We shall analyse the data both ways below, and also compare the weak one-loop corrections in the two schemes.

Examining the formulae for R_{ff} and A_{ff} we notice some simplifications at PETRA/PEP energies. The terms in $|\chi|^2$ are negligible. Weak neutral current effects therefore enter only through their interference with the electromagnetic current. The cross-section is sensitive to the vector coupling $g_v^e g_v^f$, which is very small because $\sin^2\theta_W$ is close to $\frac{1}{4}$, and the asymmetry to the axial coupling $g_a^e g_a^f$. The signs of g_v and g_a are not measurable, nor is the relative sign, so that one is not sensitive to parity violation. We shall look at these topics in turn.

3. LEPTONIC CROSS-SECTION MEASUREMENTS AND THEIR INTERPRETATION

Figure 2(a) shows the dependence on $\sin^2\theta_W$ of the μ-pair cross-section at $\sqrt{s} = 30$ and 40 GeV. $R_{\mu\mu}$ depends on g_v^2. It is therefore very close to the QED value for $\sin^2\theta_W = 0.22$. The extraction of $\sin^2\theta_W$ from total cross-section is fraught with difficulty. If one measures $R_{\mu\mu}$ too high, a value of $\sin^2\theta_W = 0.25$ with a small "error" is found, apparently satisfactorily. If one measures $R_{\mu\mu}$ too low, two solutions are found for $\sin^2\theta_W$, both far from 0.25 and with large errors. This is in fact the major problem comparing to Glashow's theory (Section 7 below). Measurements of $R_{\mu\mu}$ and $R_{\tau\tau}$ are shown in Figure 3 [1-3, 12-16]. Because of the insensitivity to $\sin^2\theta_W$ one traditionally adopts another approach, to fix the electroweak terms at their standard value (or zero) and to look for deviations from QED in terms of cut-off parameters (or photon form-factors)

$$F_{\pm} = 1 \mp \frac{q^2}{q^2 - A_{\pm}^2}$$

No significant deviations from QED have been reported. 95% confidence level lower limits on $A_{\pm}$, based on data above 40 GeV are as follows. We also show a high-precision number based on 29 GeV (HRS).

Final State	Experiment	95% CL Limits (GeV)		Reference
		A_+	A_-	
e^+e^-	JADE	267	200	14
	MARK J	165	235	17
	HRS	154	220	29
$\mu^+\mu^-$	JADE	230	245	14
	MARK J	238	174	17
	HRS	172	172	29
$\tau^+\tau^-$	JADE	285	210	14
	MARK J	235	205	12
	HRS	92	246	18

(See Reference 19 for a summary of earlier work)

One must be cautious against taking such values too seriously, for three reasons:

a. The errors on A_+ and A_- are very asymmetric and embrace infinity. Making a substitution $K = 1/A_+^2$ $(K > 0)$ and $K = -1/A_-^2$ $(K < 0)$ one sees that Gaussian experimental errors on $R_{\mu\mu}$ lead to Gaussian errors on K. Since $K = 0$ is always within the experimental limits the errors on $A_{\pm}$ become singular [20].

b. The formalism is very specific about the form of any new theory. In particular a QED cut-off of 200 GeV is quite consistent with a Z^0 mass of 83 GeV.

c. The experimental error bars should be treated with care. Almost all the published results lie with 1σ of 1.0. This can, of course, be the result of proper caution by the experimenters, but it means that combining them to arrive at a cutoff parameter can be misleading in either sense.

QED cutoff parameters are a useful expression of ignorance but become out-dated when a deviation from QED is seen.

4. LEPTON-PAIR ASYMMETRIES. LEADING ORDER AND ONE-LOOP CORRECTIONS

The forward-backward asymmetry is given by

$$A(f\bar{f}) = -\frac{3g_a^e g_a^f}{2Q_f} \mathrm{Re}\chi + \ldots.$$

For $s \ll m_z^2$ this is always negative. At $\sqrt{s} = 35$, $m_z = 93$, $\sin^2\theta_w = 0.22$ the Glashow form gives

$A(\mu\mu, \tau\tau) = -.090$
$A(c\bar{c}) = -.135$
$A(b\bar{b}) = +.27$ which becomes $-.25$ after

corrections for finite mass (factor $2\beta/(3 - \beta^2) = 0.92$) and QCD corrections [21].

In comparing $\ell^+\ell^-$ final states data with theory one must always make radiative corrections. (This was already done in the cross-section data presented in Section 3 above.) Every theorist knows that it is impossible, in principle, to distinguish the $\ell^+\ell^-$ final state from $\ell^+\ell^-$ + soft or collinear photons. Every experimenter also knows this also for different reasons. What one does therefore is to make a cut at a position of one's choice, count those events within the cut and correct the theory accordingly. Figure 4(a) shows as an example the acollinearity angle distribution of the final state μ-pair, defined as shown, for events with $p_\mu > \frac{1}{2}$ E(beam), compared to QED predictions following Berends and Kleiss [22]. (Data from Mark-J [12].) A cut is made at $\xi < 20°$. Everything at $\xi < 20°$ is called $\mu^+\mu^-$ and everything at $\xi > 20°$ is called $\mu^+\mu^-X$. The correction, δ, is shown in Figure 4(b) for various values of the cut ξ, where

$$\frac{d\sigma}{d\Omega}(\alpha^3, \xi_{cut}) = \frac{d\sigma}{d\Omega}(\alpha^2)(1 + \delta)$$

The corrections alter both the normalisation and the asymmetry. Initial state bremsstrahlung, for example, lowers the effective cm energy and hence increases the cross-section. The asymmetry arises because of $O(\alpha^3)$ interference between the leading diagram ($O(\alpha^2)$), which leads to a final state ($\ell^+\ell^-$ + unresolved γs) with $C = -1$, and diagrams ($O(\alpha^4)$) with $C = +1$. (See Figure 4(c).) The pure QED asymmetry is positive (ie opposite in sign to the electroweak interference) and ~ 1%, depending on the cuts. In all the work presented here, QED corrections to $O(\alpha^3)$ are made to the data before they are presented. This is a reasonable procedure as the magnitude of corrections depends on the experimenters' cuts.

The calculation of the weak one-loop corrections was clarified by Böhm [11]. It includes corrections to the Z^0 propagator, γ - Z transitions, vertex corrections, and diagrams with two Z^0 exchanged or W^+ and W^- exchange. At $\sqrt{s} = 34.5$ the corrections have been calculated by Wetzel in the Weinberg-Salam scheme [23]. The Born term asymmetry is -9.23% and the one-loop corrections +0.60%, leading to a one-loop corrected asymmetry of -8.63%. Brown et al [24], Berends et al [25] and Böhm and Hollik [26] have made calculations on the Glashow scheme. They find a Born term asymmetry of -8.65%, one loop corrections of +0.05% and a one-loop corrected value of -8.60%.

In the early days, comparison was normally made to the data after $O(\alpha^3)$ QED correction to lowest order Weinberg-Salam. This is wrong, and misleading if one tries to reconcile resulting m_z values with collider measurements [27]. A consistent approach can be made if one uses either scheme at the one-loop corrected level (the difference is beyond experimental sensitivity) or, for the simple minded, the Glashow scheme in lowest order.

It has recently been advocated by Cashmore et al that one should make comparison of theory and data after making order α^3 corrections to Z^0 exchange diagrams within the Weinberg-Salam scheme [28]. Whilst this is clearly a self-consistent picture, it does not allow ready comparison with

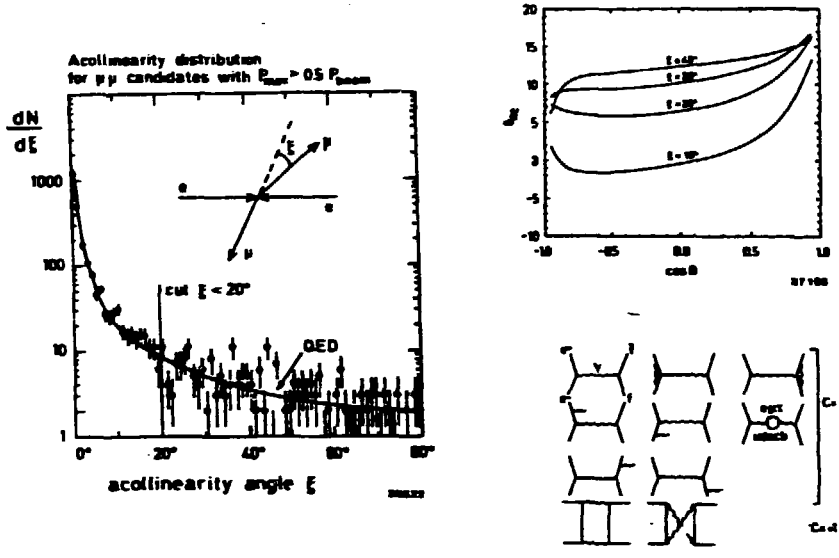

Figure 4 (a) Acollinearity distribution compared to QED predictions. Data from MARK J. (b) Radiative corrections as a function of cosθ for different acollinearity cuts. (c) Diagrams contributing to $O(\alpha^3)$ QED calculation.

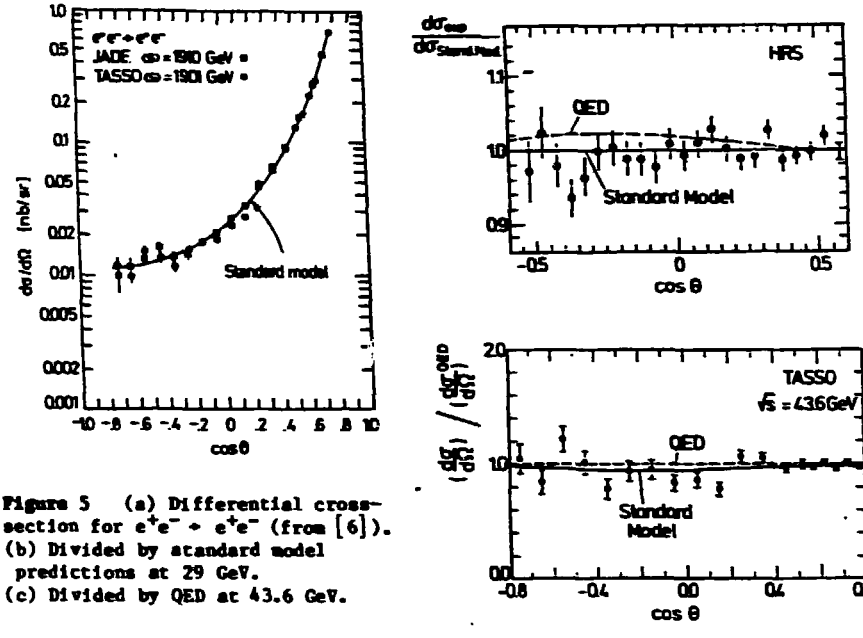

Figure 5 (a) Differential cross-section for $e^+e^- \to e^+e^-$ (from [6]).
(b) Divided by standard model predictions at 29 GeV.
(c) Divided by QED at 43.6 GeV.

the Glashow scheme and so we have retained the approach of the previous paragraph.

5. RESULTS ON LEPTONIC FINAL STATES

Figure 5 shows results on Bhabha scattering at high energies. The dominance of the forward peak due to one photon exchange is clearly seen. We also show the results divided by QED and standard model predictions. Because of the one-photon exchange term, the angular distribution is sensitive both to g_a^e and g_v^e. The highest statistics $\mu^+\mu^-$ and $\tau^+\tau^-$ results from MAC, shown in Figure 6, together with the highest energy JADE data. The $O(\alpha^3)$ corrected $\mu^+\mu^-$ and $\tau^+\tau^-$ asymmetries are as follows:

$\mu^+\mu^-$

Expt	$\sqrt{s}$(GeV)	N_{events}	$A_{\mu\mu}$ (%)	Theory (one loop)	Ref
MAC	29	16058	- 5.9 ± .7 ± .2	- 5.9	39
MARK 2	29	5312	- 7.1 ± 1.7	- 5.9	30
HRS	29	5057	- 4.9 ± 1.5 ± .5	- 5.9	29
Average	**29**		**- 5.9 ± 0.6**	**- 5.9**	
CELLO	34.2	387	- 6.4 ± 6.4	- 8.5	13
MARK J	34.6	3658	-11.7 ± 1.7 ± .5	- 8.8	12
JADE	34.4	3400	-11.1 ± 1.8 ± 1.0	- 8.7	1
PLUTO	34.7	1550	-13.2 ± 2.8 ± 1.0	- 8.9	16
TASSO	34.5	2673	- 9.8 ± 2.3 ± .5	- 8.7	3
Average	**34.5**		**-11.2 ± 1.1**	**- 8.7**	
CELLO	38.9	244	- 9.3 ± 7.3	-11.7	4
JADE	38.0	422	- 9.7 ± 5.2	-11.1	4
MARK J	39.1	684	-10.0 ± 4.1	-11.8	4
TASSO	38.3	173	+ 2.4 ± 8.6 ± .5	-11.2	31
Average	**38.6**		**- 8.5 ± 2.8**	**-11.4**	
CELLO	44.3	576	-18.8 ± 4.7	-16.2	4
JADE	43.7	1258	-19.1 ± 3.1	-15.6	4
MARK J	44.1	1316	-16.0 ± 3.0	-16.0	4
TASSO	43.6	614	-17.3 ± 4.4 ± .5	-15.4	31
Average	**43.9**		**-17.7 ± 1.8**	**-15.7**	

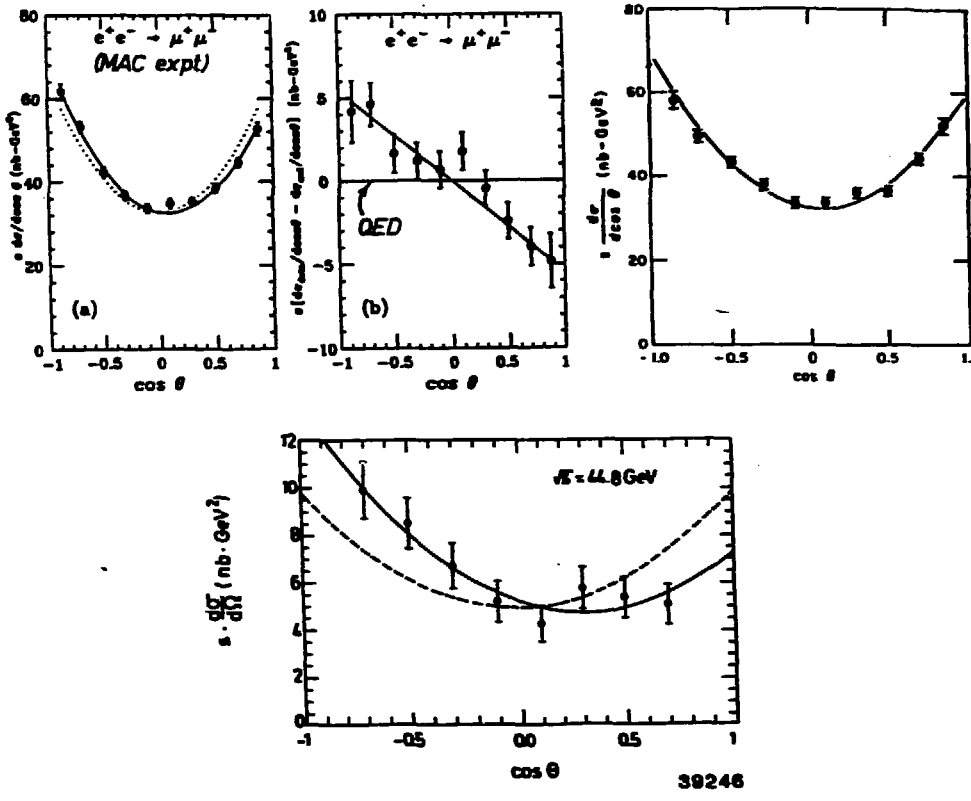

Figure 6 (a) Differential cross-section for $e^+e^- \to \mu^+\mu^-$. Solid line-fit: dotted line pure QED. (b) Same divided by QED prediction. (c) $e^+e^- \to \tau^+\tau^-$. All at 29 GeV. (d) $e^+e^- \to \mu^+\mu^-$ at 44.8 GeV (JADE). All data shown after $O(\alpha^3)$ corrections.

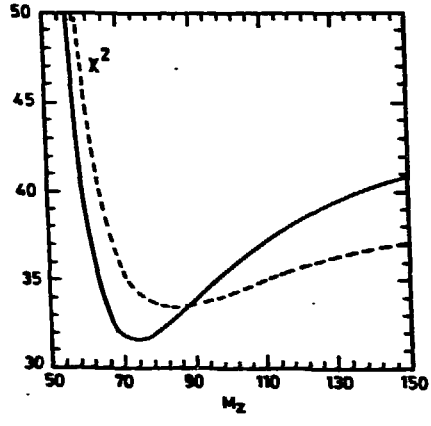

Figure 7 Determination of m_Z from electroweak asymmetry and cross-section. Solid line - one loop corrections. Dashed line - lowest order.

$\tau^+\tau^-$

Expt	$\sqrt{s}$(GeV)	N_{events}	$A_{\tau\tau}$ (%)	Theory (one loop)	Ref
MAC	29	1053	$-5.5 \pm 1.2 \pm .5$	-5.9	15
HRS	29	7372	$-4.4 \pm 1.4 \pm .5$	-5.9	18
MARK 2	29	3714	-4.2 ± 2.0	-5.9	30
Average	**29**		-4.9 ± 0.9	-5.9	
CELLO	34.2	434	-10.3 ± 5.2	-8.5	13
JADE	34.6	1998	$-6.0 \pm 2.5 \pm 1.0$	-8.8	32
MARK J	34.6	860	-7.8 ± 4.0	-8.8	12
TASSO	34.4	350	$-4.9 \pm 5.3 \pm 1.2$	-8.7	33
PLUTO	34.6	419	$-5.9 \pm 6.8 + 0 - 2.5$	-8.8	34
Average	**34.5**		-6.8 ± 1.8	-8.8	
JADE	38.0	336	$+7.5 \pm 6.3 \pm 1.0$	-11.1	4
CELLO	43.9	397	$-14.2 \pm 4.8 \pm 1.0$	-15.7	4,35
JADE	43.7	913	$-17.0 \pm 3.6 \pm 1.0$	-15.6	4,32
MARK J	43.9	222	$-12.8 \pm 7.0 \pm 1.5$	-15.5	12
Average	**43.8**		-15.5 ± 2.7	-15.6	

The results are shown graphically in Figure 8, compared to Weinberg-Salam predictions for $m_z = \infty$, and to Glashow predictions for $m_z = 93$ and $\sin^2\theta_w = 0.22$.

The 34.5 GeV $\mu^+\mu^-$ data lie 2.2 SD from theory, and this tends to pull up fitted values of ρ, or pull down fitted values of m_z, away from the expectation for $m_z = 93$ GeV, $\sin^2\theta_w = 0.22$.

6. MEASUREMENT OF WEINBERG-SALAM PARAMETERS

With ρ, G_F and m_z as parameters we find

$$A_{\mu\mu} = -\frac{3}{2} g_e^{\mu} g_a^{\mu} \frac{\rho G_F}{2\sqrt{2}\pi\alpha} \cdot s \cdot \frac{m_z^2}{m_z^2 - s} + \ldots.$$

We have combined the above $\mu^+\mu^-$ and $\tau^+\tau^-$ results and looked for finite m_z by deviations from a linear fit in the dependence of $A_{\mu\mu}$ on s. (See Figure 7.) Results are, from the one-loop corrected fit

$$m_z = 73^{+10}_{-6} \text{ GeV}$$

or

$$63 < m_z < 101 \text{ GeV} \quad (95\% \text{ CL}) \; [7]$$

in good agreement with $\bar{p}p$ collider results [27].

Using $m_z = 93 \pm 2$ GeV we can re-interpret the data as a measurement of ρ and obtain

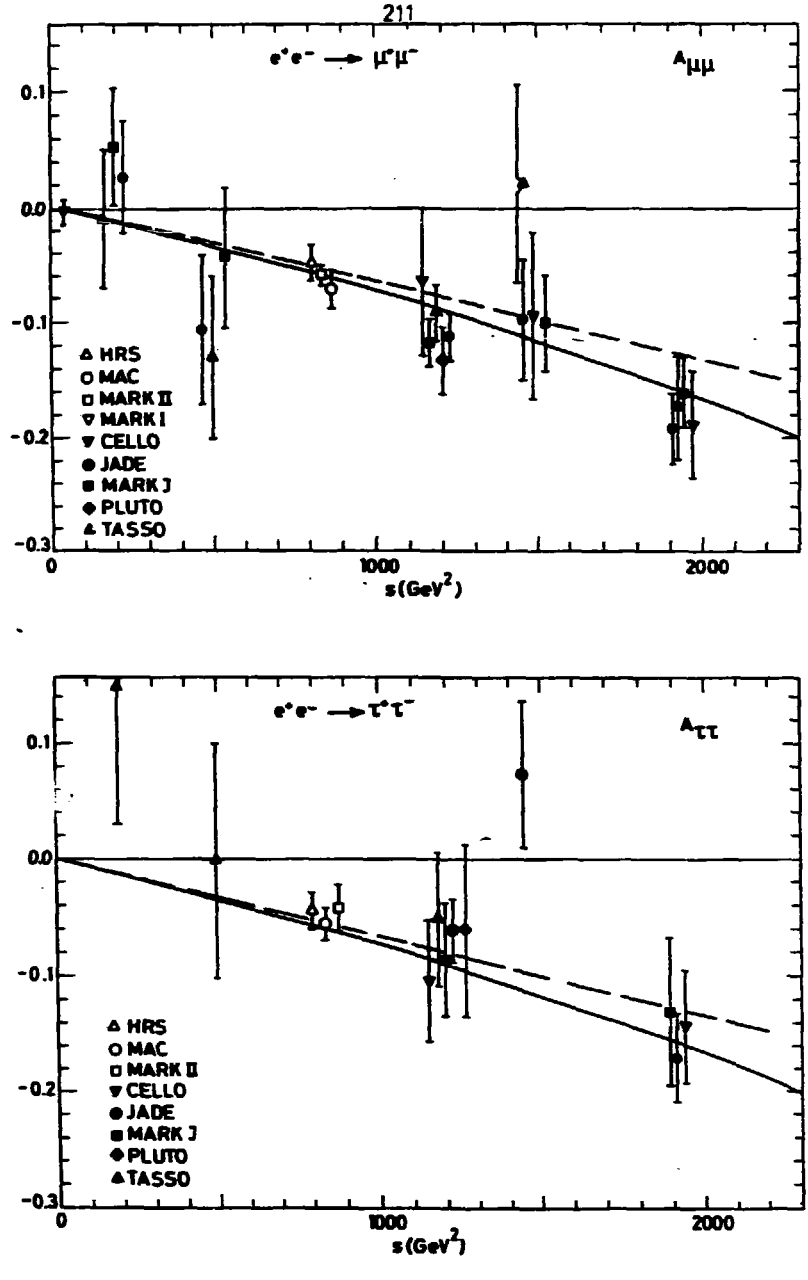

Figure 8 Measured asymmetries. Dashed line shows WS prediction for pointlike process ($m_z = \infty$). Solid line shows predictions for $m_z = 93$, $\sin^2\theta_w = 0.22$.

ρ	= $1.02 \pm .05$	$\mu\mu$, $\tau\tau$	1-loop
(ρ	= $1.11 \pm .07$	$\mu\mu$	1-loop
	$1.03 \pm .07$	$\mu\mu$	lowest order) [4]

or, setting $\rho = 1$ and assuming lepton universality, from e^+e^-; $\mu^+\mu^-$; $\tau^+\tau^-$

$$g_a^2 = 0.26 \pm 0.01$$

and

$$g_v^2 = 0.08^{+0.07}_{-0.04}$$

What is the significance of these results? We have seen in Section 3 that cross-section measurements in $e^+e^- \to \mu^+\mu^-$, $\tau^+\tau^-$ provide an unreliable measure of g_v^2. The interference with γ-exchange in $e^+e^- \to e^+e^-$ is much more sensitive, in the angular distribution, to g_v^2 than to g_a^2.

The measurements made from the asymmetry alone give low values of m_z, or high values of ρ from $\mu^+\mu^-$. These are just two ways of expressing the same experimental result. We should be cautious of over-interpreting the value of ρ obtained. As with a QED cut-off parameter, obtaining the expected value provides some reassurance, but a value of $\rho \neq 1$ arises in theory from a non-minimal Higgs structure. In such a model the radiative corrections would likely be different and so the precise value of ρ obtained after subtraction of assumed corrections would be incorrect.

7. MEASUREMENT OF GLASHOW PARAMETERS

With m_z, $\sin^2\theta_w$ as parameters we find

$$A_{\mu\mu} = -\frac{3}{8} \frac{g_a^e g_a^\mu}{\sin^2\theta_w \cos^2\theta_w} \cdot \frac{s}{m_z^2 - s}$$

The MARK J Collaboration were the first to analyse their data this way [11,12]. Figure 9(a) shows at $\sqrt{s} = 45$ the sensitivity to normalisation changes. An accurate measurement of $A_{\mu\mu}$ defines a locus in the ($\sin^2\theta_w$, m_z) plane and ± 2% variation in normalisation allows a considerable range along this locus. We have analysed data on $R_{\mu\mu}$, $R_{\tau\tau}$, $A_{\mu\mu}$ and $A_{\tau\tau}$ to obtain the allowed regions shown in Figure 9(b). Here we have allowed normalisations to move within the quoted systematic error, but adding a term to the χ^2 when this is done. Two solutions are clearly seen with g_v of opposite sign. However, if we impose a 2% normalisation change the other way the dashed contour is obtained, with only one solution.

Bearing in mind the problems of normalisation addressed in Section 3, we draw the conservative conclusion that the μ-pair and τ-pair final states do not allow an independent measure of m_z and $\sin^2\theta_w$ in the Glashow scheme. If we set $m_z = 93 \pm 2$, one obtains essentially from the strength of the asymmetry

$$\sin^2\theta_w = 0.19 \pm 0.016\ ^{+0.02}_{-0.01} \text{ from } \mu\mu$$

$$0.20\ ^{+\ 0.016}_{-\ 0.013}\ ^{+\ .02}_{-\ .01} \text{ from } \mu\mu, \tau\tau, ee$$

The analysis by Naroska that gives these results is illustrated in Figure 9(c) [4].

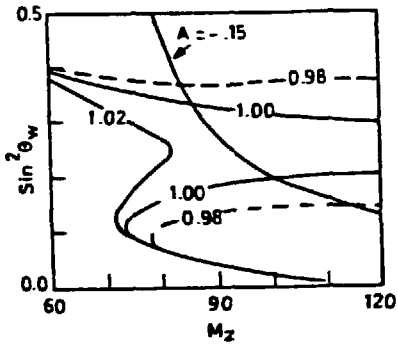

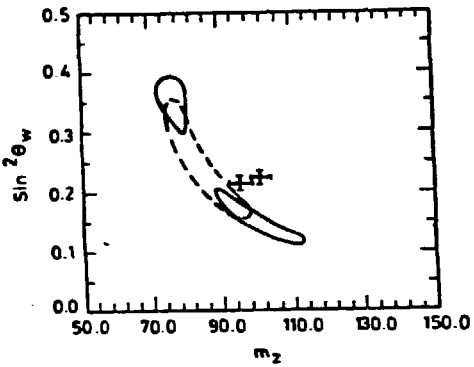

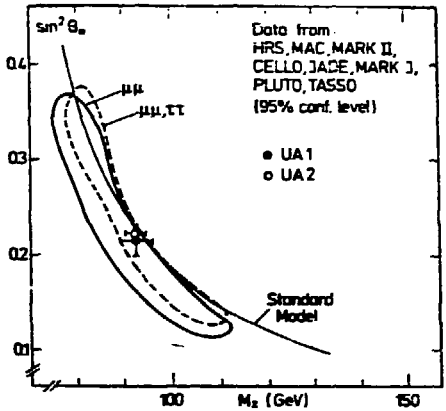

Figure 9 Determination of $\sin^2\theta_w$ and m_z from R,A. (a) Contours of constant $R_{\mu\mu}$ and locus $A_{\mu\mu} = -0.15$ at $\sqrt{s} = 45$ GeV. (b) 95% CL contours from $R_{\mu\mu}$, $A_{\mu\mu}$, $R_{\tau\tau}$, $A_{\tau\tau}$ data. Dashed contour shows result after imposing ZZ normalisation change. (c) 95% CL contour using all data, together with results from UA1, UA2 [4].

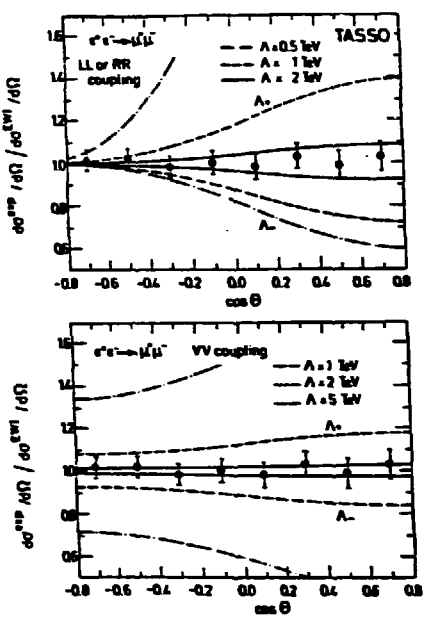

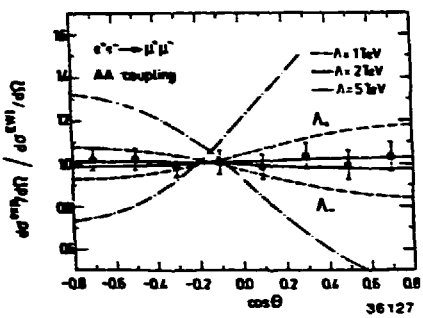

Figure 10 μ-pair differential cross-section divided by GWS prediction together with substructure effects.

8. SEARCH FOR PARITY VIOLATION

Parity violation is the best evidence for the presence of a weak-interaction. To establish parity violation one needs to measure a non-zero expectation value of a pseudoscalar. Lacking (to date) polarised beams, one looks at the final state lepton helicity. In the case of τ-leptons one can use the τ-decay as analyser. The τ helicity feeds into the laboratory momentum spectrum ($x = p/E_{beam}$) of the final state charged particle. The decays $\tau \to \pi\nu$, $\rho\nu$, $e\nu\nu$, $\mu\nu\nu$ have been used by the CELLO Collaboration [33] (see Figure 12).

The final-state τ helicity is given by

$$P(\theta) = \frac{-G_F s m_Z^2}{\sqrt{2}\pi\alpha(s-m_Z^2)} \left(g_v^e g_a^\tau + g_v^\tau g_a^e \frac{2\cos\theta}{1+\cos^2\theta}\right)$$

We expect $g_v = -0.06$ and hence a very small effect.

The statistical precision is as yet poor and the errors span the physical region. From the asymmetry of $P(\theta)$ they obtain $g_v^\tau = -0.1 \pm 1.4$ and from the average and asymmetry, assuming universality, $g_v g_a = 0.25 \pm 0.35$. (cf $g_v g_a = 0.07 \pm 0.09$ from μN DIS charge asymmetry [37].) We conclude that evidence for parity violation in $e^+e^- \to$ lepton pairs should await SLC operation with polarised beams.

9. LIMITS ON THE DEPARTURE FROM ELECTROWEAK THEORY

With modest ($\lesssim$ 2 SD) discrepancies, all the above results show experiments in agreement with electroweak theory. This limits the range of new phenomena that could contribute to $\ell^+\ell^-$ and $\ell^+\ell^-\gamma$ final states. We review these briefly.

Lepton substructure (preons) [38] can be searched for at energies below the preon threshold by looking for residual contact interactions. (Compare the study of weak interactions at low energies.) The effective Lagrangian is altered.

$$L_{eff} = L_{EWI} \pm \frac{g^2}{2\Lambda_\pm^2}\{\eta_{LL} j_L \cdot j_L + \eta_{RR} j_R \cdot j_R + \eta_{RL} j_R \cdot j_L\}$$

We set $g^2/4\pi = 1$ (by ansatz) and $\eta_{LL}, \eta_{RR}, \eta_{RL} = 0, \pm 1$ according to one's preferred model. Limits on $\Lambda_\pm$ of order 0.6 to 2 TeV in $e^+e^- \to e^+e^-$ have been presented by CELLO, HRS, JADE, MAC and TASSO. The reaction $e^+e^- \to \mu^+\mu^-$ is more sensitive (assuming e and μ to have common components). Results from TASSO are shown in Figure 11. One obtains 95% confidence level limits [3,14] as follows:

	TASSO		JADE	
	Λ_+	Λ_-	Λ_+	Λ_- (TeV)
LL,RR	2.1	2.6	4.4	2.1
VV	3.4	4.4	5.8	4.8
AA	3.1	3.4	7.5	2.8

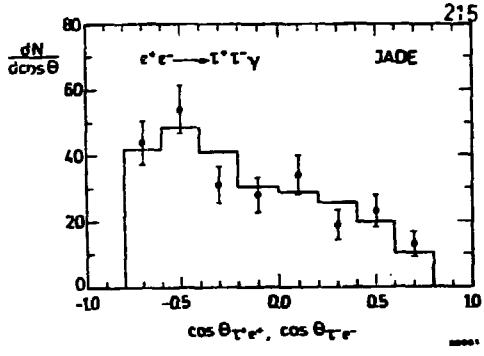

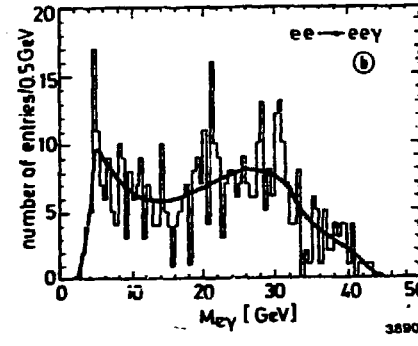

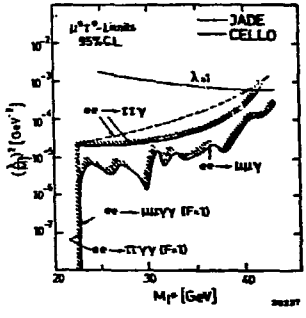

Figure 11 (a) Lepton angular distribution for the reaction $e^+e^- \to \tau^+\tau^-\gamma$. Points with bars-data, histogram-QED $O(\alpha^3)$ prediction. (b) $e\gamma$ mass spectrum compared to QED prediction for $e^+e^- \to e^+e^-\gamma$ (CELLO). (c) Limits to the coupling strength for μ^*, τ^* production.

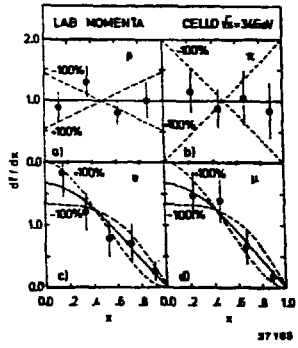

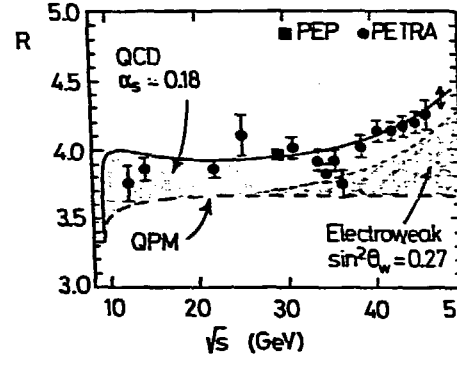

Figure 12 τ helicity analysis. Momentum spectra for various final state particles. Dashed lines show maximum possible effect.

Figure 13 Average values of R (e^+e^- → hadrons), showing the QPM prediction and the fitted contributions of QCD and electroweak effects.

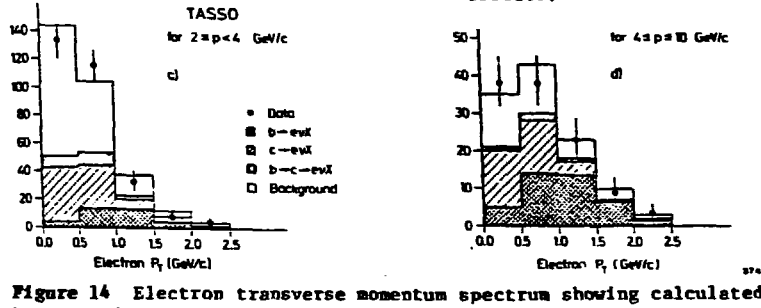

Figure 14 Electron transverse momentum spectrum showing calculated charm, beauty and background contributions.

The JADE results are the first to be published using data for $\sqrt{s} > 40$ GeV. As can be seen from the figure, the VV curve is equivalent fo a QED cutoff fit, and the remarks made in Section 3 apply again. The Λ limits are, of course, proportional to the input value of g.

Excited leptons can be searched for via the coupling $\ell^* \to \ell\gamma$, for which one sets a Lagrangian

$$L = \frac{\lambda e}{2M} \bar{\ell}^* \sigma_{\alpha\beta} \ell F^{\alpha\beta} + hc$$

(Beware of inconsistent conventions between and within experiments.)

There are three reactions of interest:

i. $e^+e^- \to \ell^*\ell^* \to \ell^+\ell^-\gamma\gamma$ (e^*,μ^* up to $\sqrt{s}/2$)

ii. $e^+e^- \to \ell^*\ell \to \ell^+\ell^-\gamma$ (e^*,μ^* up to $\sqrt{s}$)

iii. $e^+e^- \to \gamma\gamma$ (e,e^* exchange. $m(e^*) > \sqrt{s}$)

Excited electrons and muons are excluded totally for masses below 22 GeV. For masses up to 44 GeV e^* (and μ^*) are excluded for "reasonable" couplings λ [7,19,40,41].

New results have been presented this year on τ^* searches by CELLO and JADE [42,43]. In Figure 12(a) we show the forward-back asymmetry ($\cos\theta(\tau^+, e^+)$) for the reaction $e^+e^- \to \tau^+\tau^-\gamma$. This asymmetry arises from the interference of initial and final state bremsstrahlung. The angular distribution is compared to the predictions of a QED $O(\alpha^3)$ Monte Carlo. A new state would show up as an excess over this prediction at a fixed $m(\ell^\pm\gamma)$. The $e\gamma$ mass spectrum of CELLO is shown in Figure 12(b). The (absence of an) excess at a fixed $m(\ell^\pm\gamma)$ sets a limit on λ, and results on μ^* and τ^* are shown in Figure 12(c).

Supersymmetric leptons could contribute via reactions such as $e^+e^- \to \tilde{\mu}\tilde{\mu}$, each $\tilde{\mu}$ decaying via $\tilde{\mu} \to \mu\tilde{\gamma}$. The photinos might be unseen or decay $\tilde{\gamma} \to \gamma G$. The cross-section for scalar pair production is $R(\tilde{\mu}\tilde{\mu}) = \frac{1}{4}\beta^3$. The β^3 factor depresses the signal at high masses. The signatures are, for a low mass μ^*, an excess of $\mu^+\mu^-$ pairs, and for high mass μ^*, an excess of acoplanar $\mu^+\mu^-$ pairs.

The most sensitive limits on $\tilde{\mu}$ masses come from JADE and Mark J [44,45]. For $M_{\tilde{\gamma}} < 15$-16 GeV, at 95% $M_{\tilde{\mu}} > 20.9$ GeV. Similar limits exist from MAC, TASSO and CELLO [46-48]. For $M_{\tilde{\gamma}} < 13$ GeV, $M_{\tilde{\mu}} > 18$ GeV [45,48,49,50].

From the process $e^+e^- \to \tilde{e}\tilde{\gamma}e$, JADE and CELLO obtain $M_{\tilde{e}} > 25$ GeV for $M_{\tilde{\gamma}} = 0$, $M\tilde{e}_R = M\tilde{e}_L$ [51,52]. Similar limits are found by MAC and Mark 2 [53,54]. From $e^+e^- \to \tilde{e}^+\tilde{e}^-$ JADE and Mark J find [45,51], for $M_{\tilde{\gamma}} < 19$ GeV and $M\tilde{e}_R = M\tilde{e}_L$ that $M_{\tilde{e}} > 22$-23 GeV. However, the most sensitive limits on selectron production come from $e^+e^- \to \tilde{\gamma}\tilde{\gamma}\gamma$. These are strongly dependent on the assumed value of $M_{\tilde{\gamma}}$. For $M_{\tilde{\gamma}} = 0$ and $M\tilde{e}_R = M\tilde{e}_L$ the limits from MAC and CELLO are $M_{\tilde{e}} > 43.5$ and 37.7 GeV [49,55], and from ASP $M_{\tilde{e}} > 51$ GeV [56].

The conclusion is that over essentially all the available kinematic range, no significant deviations from electroweak theory are seen in leptonic final states.

10. HADRONIC TOTAL CROSS-SECTION

The total hadronic cross-section is sensitive to $\sum_{udscb} g_v^e g_v^q Q_q$. For $\sin^2\theta_w \sim 0.25$ therefore, no change is expected from pure QED ($g_v = 0$) for $s \ll m_z^2$, but the derivative with respect to $\sin^2\theta_w$ of R (hadronic) is non-zero, in contrast to the situation in $e^+e^- \to \mu^+\mu^-$ (see Figure 2). A measurement of R (hadronic) leads to two solutions for $\sin^2\theta_w$, one near 0.25 and one far away which is usually rejected. It may occur that the two solutions merge within errors. Since the $\sin^2\theta_w$ value comes from the energy dependence (or lack of it) of R the measurement is somewhat insensitive to energy-independent normalisation systematics. Results from individual experiments and from a combined analysis by Marshall are given below. This fit is shown in Figure 13. The fitted value of $\alpha_s = 0.188 \pm 0.056$.

Expt	$\sin^2\theta_w$	A_+	A_-(GeV)	Ref
JADE	0.23 + .03 − .04	> 277	> 266	7
MARK J	0.28 + .08 − .05	> 200	> 325	7,17
	($.18 < \sin^2\theta_w < 0.60$ at 2σ)			
TASSO	.30 + .23 − .07	> 288	> 372	3
Combined	.272 ± .035			6

11. QUARK FLAVOUR TAGGING

For a known quark flavour we expect an asymmetry

$$A_{q\bar{q}} = \frac{3}{2}\frac{g_e^e g_a^q}{Q_q} \cdot \frac{\rho G_F}{2\sqrt{2}\pi\alpha} \cdot s \cdot \frac{m_z^2}{m_z^2 - s}$$

At $\sqrt{s} = 35$ we expect $A = -0.090$ for $\mu\mu$, $\tau\tau$, $A = -0.135$ for $u\bar{u}$, $c\bar{c}$, and $A = 0.25$ for $d\bar{d}$, $s\bar{s}$, $b\bar{b}$, after QED corrections and mass corrections [21]. Thus the hadronic asymmetries are larger than the leptonic ones. The experimental problem is to identify the flavour and to distinguish q from $\bar{q}$. For u, d and s quark no reliable method has been found. For example, a primary K^+ meson is more likely to come from a u-quark jet than from an $\bar{s}$-quark jet [57]. For c- and b-quarks two methods had been used which take advantage of the fact that c- and b-mesons come from primary quarks and not from fragmentation. The methods are for charm, direct observation of D or D^* mesons, and for charm and beauty, observation of direct leptons. We discuss these in turn.

Charm asymmetries have been measured using D^* meson tag by HRS [58], JADE [59] and TASSO [60]. One takes advantage of a method first used by MARK 2 [61], that although the mass resolution on the D^0 meson or the D^* meson may be low, the mass difference $\Delta m = m(D^{*+}) - m(D^0)$ is only 145 MeV, so that the decay $D^{*+} \to D^0\pi^+$ has a very low Q-value. As a result the resolution on Δm is much better. All these experiments have used the decays $D^0 \to K^-\pi^+$, $K^-\pi^+\pi^+\pi^-$, $K^-\pi^+(\pi^0)$ unseen, and TASSO have used $K^-\pi^+\pi^0$ (seen) in addition. The charm signal is predominantly at $x > 0.4$, whereas the background is at lower x. Charm-tagging efficiencies are typically ~ ½%, and TASSO, for example, have a signal of 119 events including 26 background (see Figure 15(a)). The HRS D^* angular distribution is shown in Figure 15(b).

The HRS detector has sufficient resolution to observe $D^0 \to K^-\pi^+$ and $D^+ \to K^-\pi^+\pi^+$ directly with $\sigma = 13$ MeV for $x_D > 0.5$ (see Figure 15(c)).

Direct leptons have been used by several experiments as heavy-quark tags. The sources of e^- in hadronic events are as follows:

Lepton source	e^- asymmetry ($\sqrt{s} = 35$)
$b \to e^-$	- 0.25
$c \to e^+$	+ 0.14
$b \to c \to e^+$	+ 0.25
Misidentified hadron	0
γ conversion	0

The yields are low and the backgrounds to be distinguished high (one track in 700 is $b \to \mu$ direct), so that additional methods are needed to enhance the heavy-quark fraction. All the experiments look at the p_T of the lepton with respect to the jet axis, which peaks at 0.5 for muon candidates from u, d, s jets, 0.6 for c-jets and 1.3 for b-jets. MARK J use the event thrust as a heavy-quark selector [62]. TASSO have used a sphericity product. The event is cut into two halves, each half boosted by $\gamma = 1.6$ and its sphericity calculated. To suppress light-quark and gluon-bremsstrahlung events they demand that the product $S_1 \cdot S_2 > 0.1$ [63]. JADE define the jet transverse mass [64].

$$\langle M \rangle = \frac{2E_{beam}}{E_{vis}} \sum \left| p_T^{out} \right|$$

where the sum runs over charged and neutral tracks. They also use $p_T(\nu)$, the event missing momentum perpendicular to the jet axis.

TASSO study direct electrons and make a 4-dimensional fit in the variables (p, p_T, $\cos\theta$, $S_1 \cdot S_2$) to obtain A_c and A_b. For $1.0 < p_T < 2.5$ about 50% of the electron signal is from $b \to e\nu X$ (see Figure 14).

The TPC Collaboration [65] identify electrons by dE/dx and shower counters, so that the misidentified hadron contamination is much reduced. The main contamination is from γ conversions. In their c-enriched sample ($p > 1.5$, $p_T < 1.0$) they have 270 events, 57% charm and 24% background, and in the b-enriched sample ($p > 1.5$, $p_T > 1.0$) they have 80 events, 65% beauty and 11% background.

The most accurate results come from JADE inclusive muons [64]. At $\sqrt{s} = 34.6$ for $p_\mu > 1.8$ GeV/c they report on 1780 μ-candidates. They make a four dimensional maximum likelihood fit in the variables $\langle M \rangle$, $p_T(\mu)$, $p_T(\nu)$ and $\cos\theta$. The distribution in those variables and the reconstructed b-quark angular distribution are shown in Figure 19. They quote a b-quark asymmetry

$$A_b = -22.8 \pm 6.0 \pm 2.5\%$$

The main systematic errors are from uncertainties in fragmentation and the $b \to \mu X$ branching ratio, set to $(11.6 \pm 0.5)\%$.

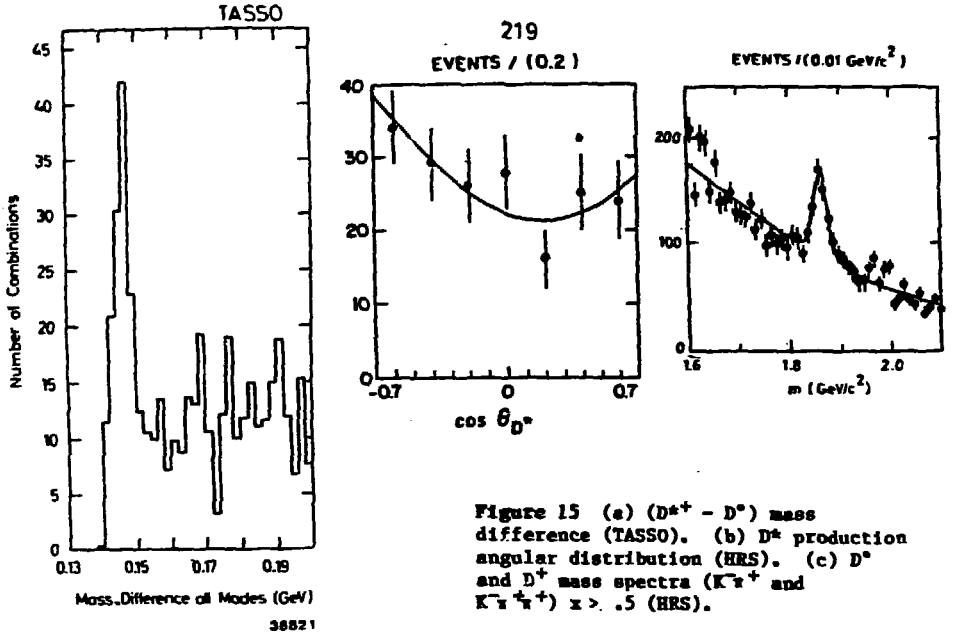

Figure 15 (a) ($D^{*+} - D^0$) mass difference (TASSO). (b) D^* production angular distribution (HRS). (c) D^0 and D^+ mass spectra ($K^-\pi^+$ and $K^-\pi^+\pi^+$) $x > .5$ (HRS).

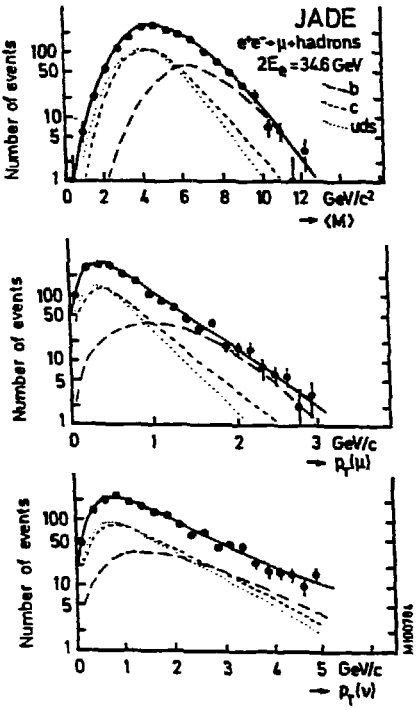

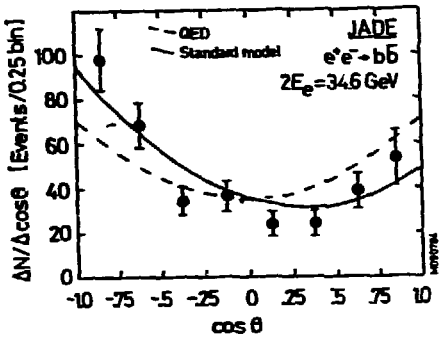

Figure 16 (a) Distributions in jet mass, $p_T(\mu)$ and missing p_T, together with the fitted distributions and the contributions to this of the various flavours.
(b) b-quark angular distribution resulting from a maximum likelihood fit in each cosθ bin.

12. QUARK WEAK ISOSPINS

The weak axial coupling, $g_a = T_{3L} - T_{3R}$. The results of the above measurements are summarised below.

Charm

Expt	$\sqrt{s}$	$A_{c\bar{c}}$	Expect	g_a^c	Method	Ref
MARK J	35.5	−16 ± 9%	−13.5	.59 ± .33	c → μ	62
JADE	34.4	−14 ± 9	−12.9	.54 ± .35	D*	59
PLUTO	34			.55 ± .51	c → μ	4
TASSO	34.4	−10 ± 9	−12.9	.39 ± .35	D*, c → e	63
TPC	29			.90 ± .46	c → e,μ	65
				.9 ± .9	D*	
HRS	29	−12 ± 8	− 8.8	.68 ± .91	D^0, D^+, D_s^+	58
MAC	29			.8 ± 1.8	c → μ	66

Combining these, $g_a^c = .56 \pm .17$, where we expect $\frac{1}{2}$.

Beauty

Expt	$\sqrt{s}$	$A_{b\bar{b}}$	Expect	g_a^b	Method	Ref
CELLO	34.0	−40 ± 17	−24.6	−.81 ± .69	b → μ, e	67
JADE	34.4	−22.8 ± 6.0 ± 2.5	−25.2	−.45 ± .12 ± .05	b → μ	64
MARK J	34.6	−21 ± 19	−25.5	−.41 ± .37	b → μ	62
PLUTO	34			−.65 ± .45	b → μ	4
TASSO	34.5	−30 ± 18	−25.4	−.59 ± .35	b → μ, e	63,68
TPC	29			−.69 ± .42	b → μ, e	65
MARK 2	29			$-.75 \,^{+.35}_{-.30}$	b → μ, e	69
MAC	29			−.3 ± .35	b → μ	66

Combining these, $g_a^b = -.49 \pm .10$, where we expect $\frac{1}{2}$.

Hence $T_{3L}(b) = -.49 \pm .10$ and the b-quark is definitely a member of a weak left-handed isodoublet. Many topless models were demolished previously by $b \to \ell^+\ell^- X$ limits (< .29% at 90% from CLEO [70], < .7% at 95% CL from JADE [71] and MARK J [72], where topless models require > 1.3% [73]. A possible escape devised by Tye and Peskin demanded a very short b lifetime [74]. Thus, independent of any direct observation of t-quarks, we conclude that weak interactions require a third generation of the same structure as the first two.

13. SUMMARY

In the leptonic sector the data are described well by GWS theory at the one-loop level. The μ-pair asymmetry is a little high at PETRA energies. Asymmetries have been measured up to 46 GeV. In the Weinberg-Salam scheme we need a finite $m_z = 73^{+10}_{-6}$ GeV, $63 < m_z < 101$ at 95% CL. ρ is consistent with 1 ($\rho = 1.02 \pm .05$). In the Glashow scheme, taking $m_z = 93 \pm 2$ GeV one obtains $\sin^2\theta_w = 0.20^{+.016}_{-.013}{}^{+.02}_{-.01}$. Combined fits to ee, μμ, ττ yield $g_v^2 = .08^{+.07}_{-.04}$ and $g_a^2 = .26 \pm .01$. One would like greater precision on

normalisation than is perhaps reasonable to expect. Parity violation effects are expected to be very small and a first search has been made. The success of electroweak theory in describing the data puts strong limits on lepton substructure, excited leptons and SUSY leptons.

In the hadronic sector the weak isospins of the c- and b-quarks have been measured and agree well with the standard model. Both quarks are members of weak isodoublets so that a t-quark is required.

REFERENCES

1. JADE Collaboration, W Bartel et al, Phys Lett 108B (1982) 140.
2. MARK-J Collaboration, B Adeva et al, Phys Rev Lett 48 (1982) 1701.
3. TASSO Collaboration, M Althoff et al, Phys Lett 110B (1982) 173; see also Z Phys C22 (1984) 13.
4. B Naroska, XXI ème Rencontre de Moriond (1986) DESY 86-051; see also Phys in Collision 5 (1985) p287 .
5. H-U Martyn, High Energy e^+e^- Interactions (AIP Conf Proc No 121, 1984) p215.
6. R Marshall, Trends in Physics 1984 (Proc 6th Gen Conf of EPS, Prague) p299, and Proc XVI Int Symp on Multiparticle Dynamics (Kiryat Anavim, 1985) (RAL 85-078).
7. D H Saxon, Phys in Collision 4 (1984) p295.
8. S L Glashow, Nucl Phys 22 (1961) 579; Rev Mod Phys 52 (1980) 539.
9. S Weinberg, Phys Rev Lett 19 (1967) 1264; Phys Rev D5 (1972) 1412; Rev Mod Phys 52 (1980) 515.
   A Salam in Elementary particle Theory, Ed N Svartholm, Stockholm, 1968, p361; Rev Mod Phys 52 (1980) 525.
   S L Glashow, J Iliopoulos, L Maiani, Phys Rev D2 (1970) 1285.
10. L M Sehgal, Aachen Report PITHA 84/03 (1984).
11. A Böhm, Proc XIX ème Rencontre de Moriond (1984) Vol 1, p191.
12. MARK-J Collaboration, B Adeva et al, Phys Reports 109 (1984) 131; Phys Rev Lett 55 (1985) 665; MIT Report LNS-153 (1986).
13. CELLO Collaboration, H-J Behrend et al, Z Phys C14 (1982) 283; Phys Lett 114B (1982) 282.
14. JADE Collaboration, W Bartel et al, Z Phys C30 (1986) 371.
15. MAC Collaboration, E Fernandez et al, Phys Rev Lett 50 (1983) 1238; 54 (1985) 1620.
16. PLUTO Collaboration, Ch Berger et al, Z Phys C21 (1983) 53; C27 (1985) 341.
17. MARK-J Collaboration, B Adeva et al, Phys Lett 152B (1985) 439.
18. K K Gan et al, Phys Lett 153B (1985) 116.
19. S L Wu, Phys Reports 107 (1984) 59.
20. D H Saxon, Hadronic Journal 6 (1983) 455.
21. J Jersak, E Laermann and P M Zerwas, Phys Lett 98B (1981) 363.
22. F A Berends and R Kleiss, Nucl Phys B177 (1981) 237.
23. W Wetzel, Nucl Phys B227 (1983) 1 and Heidelberg Preprint, May 1983.
24. R W Brown, R Decker and E A Paschos, Phys Rev Lett 52 (1984) 1192.
25. F A Berends, R Kleiss and S Jadach, Nucl Phys B202 (1983) 63.
26. M Böhm and W Hollik, Nucl Phys B204 (1982) 45; Phys Lett 139B (1984) 213.
27. UA1 Collaboration, G Arnison et al, Phys Lett 126B (1983), 398; 129B (1983) 273.
    UA2 Collaboration, P Bagnaia et al, Z Phys C24 (1984) 1.
28. R J Cashmore et al, Z Phys C30 (1986) 125.
29. D Bender et al, Phys Rev D30 (1984) 515; M Derrick et al, Phys Rev D31 (1985) 2352; M Derrick et al, Phys Lett 166B (1986) 463.

30. MARK 2 Collaboration, M E Levi et al, Phys Rev Lett 51 (1983) 1941.
31. TASSO Collaboration, Paper submitted to Berkeley Conference (1986).
32. JADE Collaboration, W Bartel et al, Phys Lett 161B (1985) 188.
33. TASSO Collaboration, M Althoff et al, Z Phys C26 (1985) 521.
34. PLUTO Collaboration, Ch Berger et al, Z Phys C28 (1985) 1.
35. CELLO Collaboration, Contributed Paper, Bari and Kyoto Conferences.
36. CELLO Collaboration, H-J Behrend et al, Phys Lett 127B (1983) 270.
37. A Argento et al, Phys Lett 120B (1983) 245.
38. E J Eichten, K D Lane and M E Peskin, Phys Rev Lett 50 (1983) 811.
39. W W Ash et al, Phys Rev Lett 55 (1985) 1871.
40. S Yamada, Proc Lepton Photon Symp (Cornell 1983) 525.
41. CELLO Collaboration, H-J Behrend et al, Phys Lett 103B (1981) 148; 123B (1983) 117.
JADE Collaboration, W Bartel et al, Z Phys C19 (1983) 197; C24 (1984) 273.
MAC Collaboration, W T Ford et al, Phys Rev Lett 51 (1983) 257.
MARK J Collaboration, B Adeva et al, Phys Rev Lett 48 (1982) 967.
PLUTO Collaboration, Ch Berger et al, Phys Lett 94B (1980) 87.
TASSO Collaboration, R Brandelik et al, Phys Lett 94B (1980) 259.
42. CELLO Collaboration, H-J Behrend et al, DESY 86-012 (1986).
43. JADE Collaboration, W Bartel et al, DESY 86-023 (1986).
44. JADE Collaboration, W Bartel et al, Phys Lett 152B (1985) 392.
45. MARK-J Collaboration, B Adeva et al, Phys Lett 152B (1985) 439.
46. E Fernandez et al, Phys Rev D28 (1983) 2721.
47. TASSO Collaboration, R Brandelik et al, Phys Lett 117B (1982) 365.
48. CELLO Collaboration, H-J Behrend et al, Phys Lett 114B (1982) 287.
49. R M Barnett, LBL-20492 (1986).
50. C Blocker et al, Phys Rev Lett 49 (1982) 517.
51. JADE Collaboration, W Bartel et al, Phys Lett 152B (1985) 385.
52. S Kowayima, Proc Lepton Photon Symp (Kyoto 1985, Ed M Konima, K Takaheshi) p612.
53. E Fernandez et al, Phys Rev Lett 52 (1984) 22.
54. L Gladney et al, Phys Rev Lett 51 (1983) 2253.
55. R Hollebeek SLAC-PUB-3846, E Fernandez et al, Phys Rev Lett 54 (1985) 118, CELLO Collaboration, H-J Behrend et al, DESY 86-050, LAL-86-11 (1986).
56. G Bartha et al, SLAC-PUB-3817, Phys Rev Lett to be published.
57. R J Cashmore, Phys in Collision 3 (1983) p167.
58. HRS Collaboration, M Derrick et al, Phys Rev Lett 53 (1984) 1971; Phys Lett 146B (1984) 261.
59. JADE Collaboration, W Bartel et al, Phys Lett 146B (1984) 121.
60. TASSO Collaboration, M Althoff et al, Phys Lett 126B (1983) 493; 138B (1984) 317.
61. S Nussinov, Phys Rev Lett 35 (1976) 1672; J M Yelton et al, Phys Rev Lett 49 (1982) 430; C Bebek et al, Phys Rev Lett 49 (1982) 610.
62. MARK-J Collaboration, B Adeva et al, Phys Rev Lett 51 (1983) 443.
63. TASSO Collaboration, M Althoff et al, Phys Lett 146B (1984) 443.
64. JADE Collaboration, W Bartel et al, Phys Lett 146B (1984) 437.
65. H Aihara et al, Phys REv D31 (1985) 2719; Z Phys C27 (1985) 39.
66. B Naroska, Proc 1983 Lepton-Photon Symposium, Cornell (1983) p96.
67. CELLO Collaboration, H-J Behrend et al, Z Phys C19 (1984) 291.
68. TASSO Collaboration, M Althoff et al, Z Phys C22 (1984) 219.
69. M E Nelson et al, Phys Rev Lett 50 (1983) 1542.
70. P Avery et al, Cornell Preprint CLNS 84/612 (1984).
71. JADE Collaboration, W Bartel et al, Phys Lett 132B (1983) 241.
72. MARK-J Collaboration, B Adeva et al, Phys Rev Lett 50 (1983) 799.
73. G L Kane and M E Peskin, Nucl Phys B195 (1982) 29.
74. S-H H Tye and M E Peskin, Cornell B Physics Workshop.
T A Ferguson, Phys in Collision 2 (1982) p387.

ANALYSIS OF e^+e^- ANNIHILATION IN TERMS OF THE WEBBER MODEL

Boaz Klima

DESY, Hamburg, FRG

ABSTRACT. e^+e^- annihilation data obtained at a c.m. energy of 34.6 GeV is compared with a modified version 2.2 of Webber Monte Carlo that has been developed. The model is found to reproduce well the gross features of the data, including the fraction of multijet events and the "string" effect in 3-jet events. The modified version's best parameters are : $\Lambda_{W_{ebber}} = 200^{+}_{-}90 MeV$ and $M_c = 4.2^{+}_{-}0.5 GeV$ where $\Lambda_{W_{ebber}}$ is the QCD scale in this model and M_c is the maximum cluster mass.

1. Introduction

The Webber model [1], the cluster model with interfering soft gluons, is one of the two successful fragmentation models, the other being the Lund model [2]. The Webber model does very well with very few parameters which is a particular success. It reproduces the "string" effect, the inclusive spectra and even a few higher order aspects which were studied so far. Its main failure up to now was that it could not give the correct fraction of 3-jet events. This in general has prevented a thorough overall comparison between model and data since no good fit to the data was obtained. The studies published so far concern the 3-jet analysis [3,4], but the model was used with the parameter set of the original version. These parameters did not reproduce the data satisfactorily. therefore one should first of all solve the 3-jet fraction problem, then find the model's best parameters and only then proceed with detailed comparisons.

A modified version 2.2 of the model has been developed which corrects this problem. This note describes briefly the features of the modified model in comparison with data from e^+e^- annihilations taken with the TASSO detector at PETRA.[1]

2. Modified Version 2.2 of Webber Model

In order to improve the model [1] two changes were made. The first one deals with the value of the boost. As it was explained in detail previously [1] the lack of manifest covariance means that it is incorrect to simulate multijet production by combining single cascades generated in different frames. This difficulty is avoided by requiring that all branching will take place in a single hemisphere, i.e. in e^+e^- annihilation the entire final state must be generated first of all as a "photon jet" and subsequently be transformed to its rest frame after computing the exact Q^2 of the virtual photon. The minimal boost, γ , required in order to have the initial quark - antiquark at 90 degrees is $\sqrt{2}$, but any larger value is also acceptable. Even though the calculations are performed in a non-infinite momentum frame it makes little effect both on most of the event distributions and on the fraction of multijet events. In the original version a value of 1.5 was chosen assuming that the physics results will not depend on this value. Unfortunately this is not the case and one better look for that value for which the Q^2 distribution is peaked exactly at E^2_{cm},the square of the c.m. energy. The value which gives that requirement was found to be $\gamma = 1.465$.

The second improvement deals with the energy distribution of the initial quark and antiquark. The energy of the quark in the boosted frame is

$$E_q = m_q + z(\gamma E_{cm} - 2m_q)$$

where m_q is the mass of the quark, E_{cm} is the c.m. energy, γ is the boost and z is a random number between 0 and 1. The energy of the antiquark in this frame is

$$E_{\bar{q}} = \gamma E_{cm} - E_q$$

In the original version it was assumed that the z distribution does not affect the physics results and a flat distribution was taken. However, since one deals with the virtual photon which is a vector rather than a scalar source one better uses the Altarelli - Parisi type distribution function $z^2+(1-z)^2$ instead of a flat one . Using the Altarelli - Parisi distribution function however results in harder gluons and consequently in a larger 3-jet rate.

3. Tuning of the Parameters

3.1 Assumptions

Using the modified version of Webber Monte Carlo described above there are few parameters which either should be tuned or should be chosen according to certain physics assumptions.

Assuming that the hadronizaion of the clusters is due to phase space and spin factors only, there are the following parameters : Λ_{Webber}, the QCD scale in this model, which is not identical to the commonly used $\Lambda_{\overline{MS}}$, M_c, the maximum cluster mass above which fission occurs, m_g, the gluon virtual mass cut-off and the quark masses, m_q's. These parameters have been explained in detail previously [1].

One has to remember that there are some constraints on these parameters which are built into the model which affect our choice. The constraints are : (1) $m_g \geq 2m_{u,d}$. (2) $m_{u,d} > 1.1\Lambda_{Webber}$. (3) $m_q > M_P$ where P is the lightest pseudoscalar which contains the quark q, e.g. $m_{u,d} > M_\pi$, $m_s > M_K$, $m_c > M_D$, $m_b > M_B$ etc.

Since the masses of the quarks were pushed up by the third constraint, at least for the heavy ones, the minimal values for the s, c and b quark mass were chosen.

A reasonable value for the light quark mass was taken and the virtual gluon mass which is the cut-off where the perturbative part is being stopped was chosen to have exactly twice the previously mentioned value, $m_g = 2m_{u,d}$. The value for the gluon virtual mass is the minimal available according to the first constraint. However the physics results turned out to be almost insensitive to reasonable changes in this value.

3.2 Event Selection

The experiment was performed with the TASSO detector at PETRA. The data used for this analysis were taken at c.m. energies in the range $32 < E_{cm} < 36GeV$. Details of the detector are described elsewhere [5]. Hadronic final states from e^+e^- annihilation were selected using the information on charged particle momenta measured in the central detector. The selection criteria for charged particles and for multihadron events were identical to those described previously [6]. A total of 21567 events were accepted. The experimental distributions were corrected for the effect of acceptance and for QED radiative effects [7].

3.3 Fit Procedure

Following the procedure of a previous analysis [8] the determination of the two remaining parameters, namely A_{Webber} and M_c, was done using a simultaneous fit to the following set of three distributions :$1/\sigma_{tot}d\sigma/dx_p$, $1/\sigma_{tot}d\sigma/dP_T^{in}$ and $1/\sigma_{tot}d\sigma/dP_T^{out}$ where x_p is the scaled momentum of the charged particles $x_p = 2|\vec{p}|/E_{cm}$ and P_T^{in}, P_T^{out} are the transverse momenta in and out of the event plane which is determined by diagonalizing the momentum tensor of second rank.

A lattice of 4x4 points in the A_{Webber} and M_c space was considered. For each lattice point about 3700 Monte Carlo events were generated and the distributions were calculated according to our definition (Sect. 3.1). The content of each bin of each distribution was parametrized by a 2nd order polynomial in A_{Webber} and M_c which gave a good description of the Monte Carlo data. The best values for A_{Webber} and M_c were obtained by a combined fit of these parametrizations to the corrected data using the computer code MINUIT [9].

3.4 The Best Parameters of the Model

Using the following values for the untuned parameters :

$$m_g = 2m_{u,d} = 0.70GeV$$
$$m_s = 0.50GeV$$
$$m_c = 1.87GeV$$
$$m_b = 5.30GeV$$

the modified Webber Monte Carlo best parameters are

$$A_{Webber} = 200^{+}\_90MeV$$
$$M_c = 4.2^{+}\_0.5GeV$$

The relatively big errors, especially in A_{Webber}, reflect two facts : (1) A_{Webber} always appears logarithmically in physics expressions so that they are not very sensitive to slight changes in this parameter. (2) The Monte Carlo distributions are not in a good agreement with the data. For very high momenta the model deviates from the data.

3.5 The Interpretation of A_{Webber} in the Webber model

It is very important to emphasize that A_{Webber} in this model is not the commonly used one, namely $A_{\overline{MS}}$.In order to compare our result with other experiments using different models one needs to know what is the connection between these two A's.

A recent theoretical publication [10] which might define and prove the connection between these parameters deals only with moments of multiplicity distributions so it cannot be applied to the present study. A more general theoretical proof is required in order to be able to interpret our result.

4. Comparison with the Data and with the Original Version

4.1 Results of Distributions

The χ^2/N_{DOF} of the fit, bearing in mind that it was done using the statistical errors only, is reasonably good. For the three different distributions χ^2/N_{DOF} values of 4.3 for x_p distribution, 4.5 for the P_T^{in} one, 3.2 for the P_T^{out} and 4.0 for all these three distributions were obtained. The quality of the fit is comparable to that of 2nd order Lund model [8].

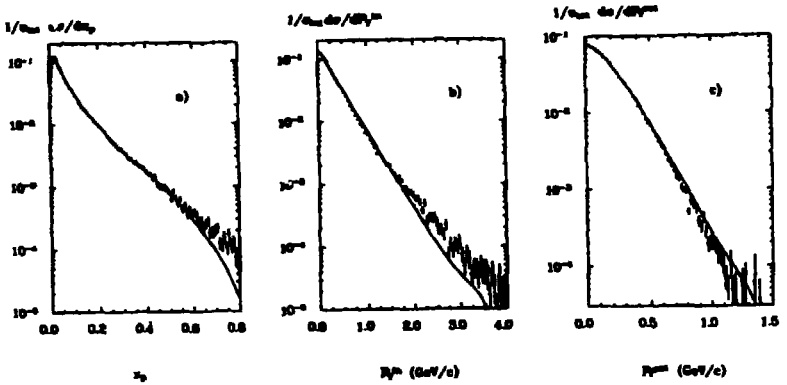

Figs. 1a-c: Webber model fit. The normalized distributions $1/\sigma_{tot} d\sigma/dY$, where Y is the quantity indicated on the horizontal scale, for the corrected data (+) and for the best fit predictions of Webber model (−). a) The scaled momentum distribution $x_p = 2p/E_{cm}$. b,c) The single particle inclusive P_T^{in} and P_T^{out} distributions.

In figures 1a-c one can see that up to certain values of P_T^{in} and P_T^{out} the fit results describe well the data. For relatively high values the fit is worse, even though one has to remember that the systematical errors which are much larger in this region were not included. Since these distributions were plotted using a logarithmic scale one should realize that the fit is good up to two orders of magnitude, i.e. the integrated deviation from the data is much less than one percent. In the x_p distribution it seems as if from a value of 0.5 on the model's curve deviates from the data points. This might reflect an intrinsic problem in the model [14]. Once again since one is dealing with a logarithmic plot it should be emphasized that the integrated deviation from the data in the x_p distribution is less than 0.1 percent.

4.2 The Fraction of Multijet Events

Since the fraction of multi (≥ 3) jet events was the main problem in the original version, the modified version's results are compared both with the original ones and with the data.

In table 1 the percentage of multi (≥ 3) jet events was summarized using two different methods. The first method, the angular cluster algorithm [11], was used in order to find the number of jets of charged particles while in the second one the generalized sphericity method[12] was used. In the first method any other cuts besides those which exist in that algorithm were not applied . The parameters $(\alpha, \beta, \epsilon_1, \epsilon_2)$ as defined previously [11] were chosen to be $(30°, 45°, 0.1, 0.11)$. In the second method exactly the same cuts as was done in the previous analysis [13] were applied.

The two methods might give a hint about possible systematic errors. Nevertheless, in both cases it is very clear that the modified version reproduces the data well.

4.3 The "String" effect in Webber model

Using the method of generalized sphericity [12] and applying exactly the same cuts as

	Method 1	Method 2
Data	$23.8^{+}_{-}0.6$	$11.1^{+}_{-}0.4$
Original Version	$18.9^{+}_{-}0.4$	$10.0^{+}_{-}0.3$
Modified Version	$22.9^{+}_{-}0.4$	$11.7^{+}_{-}0.3$

Table 1: Percentage of multi ($\geq$ 3) jet events in the Original and Modified versions of Webber Monte Carlo in comparison with the Data

was done previously [13] a multi ($\geq$ 3) jet event sample was obtained. This sample was studied with and without removing the 4 and 5 jet events. In table 2 the ratios of particle flow into the gap regions between jets for data and for the modified version 2.2 of Webber model were summarized.

	N(2)/N(3)		N(1)/N(3)	
	$\geq$ 3 jets	3 jets	$\geq$ 3 jets	3 jets
Data	$1.19^{+}_{-}0.03$	$1.26^{+}_{-}0.04$	$1.51^{+}_{-}0.04$	$1.64^{+}_{-}0.05$
Webber model	$1.16^{+}_{-}0.02$	$1.20^{+}_{-}0.02$	$1.46^{+}_{-}0.02$	$1.56^{+}_{-}0.03$

Table 2: The ratios of particle flow into the gap regions between jets for data and for the Webber modified version 2.2

In both cases, with and without removing the 4 and 5 jet events, it seems as if the "string" effect is reproduced in the Webber model even though its strength, the above mentioned ratios of particle flow into the gap regions between jets, might be a bit too small. Nevertheless our results are still compatible with previous studies [3,4] done using the original version's parameters.

Another investigation which was done using this sample concerned the momentum dependence of the density ratios. Figs. 2a and b show N(1)/N(3) and N(2)/N(3) in intervals

of $x_{in} = p_{in}/E_{beam}$ where p_{in} is the particle momentum projected into the event plane. We limit the analysis to $x_{in} < 0.1$ for reasons of statistics. In both ratios the Webber model reproduces the data reasonably well.

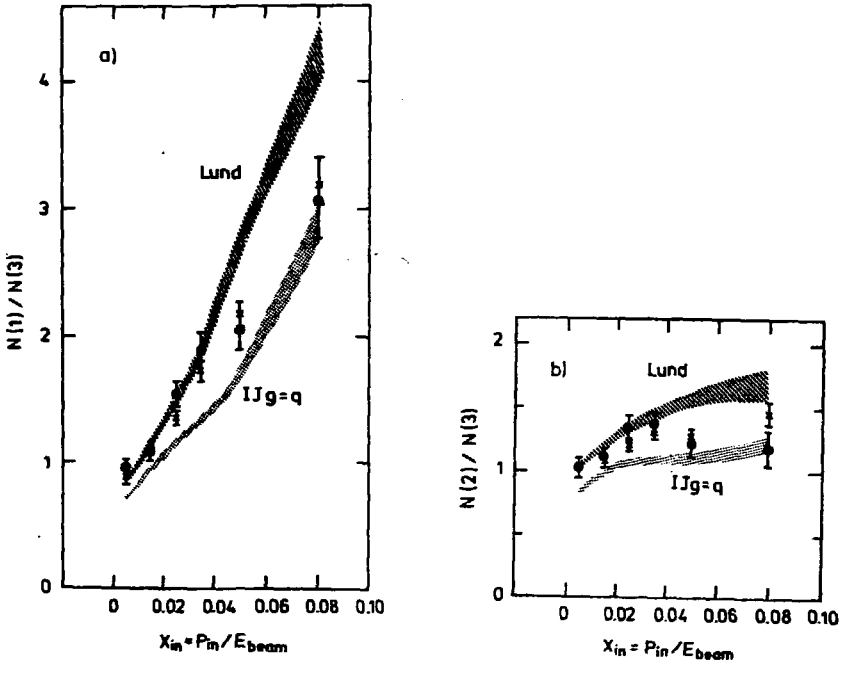

Figs. 2a,b: Ratios of particle densities in angular gaps between jet axes as a function of x_{in}. Superimposed on the data (⧳) are the Webber model (⧗) calculations. The Lund and Independent Jet models predictions are taken from reference (13).

5. Conclusions

A modified version 2.2 of Webber Monte Carlo which well reproduces the gross features of the data, including the fraction of multijet events and the "string" effect in 3-jet events, was developed. The two improvements included in this version gave a better description for the initial quark-antiquark energy distribution.

Using this model the best fit to e^+e^- data yields the values :

$$\Lambda_{Webber} = 200^{+}_{-}90 MeV$$

$$M_c = 4.2 \pm 0.5 GeV$$

The interpretation of Λ_{Webber} in this model or the connection between this parameter and the commonly used $\Lambda_{\overline{MS}}$ needs some more theoretical understanding.

Acknowledgement

I gratefully acknowledge the organisers for the lively and inspiring atmosphere during the conference. I am also indebted for disscussions with B. Webber.

REFERENCES

1. G. Marchesini and B. R. Webber, Nucl. Phys. **B238** (1984), p. 1;
   B. R. Webber, Nucl. Phys. **B238** (1984), p. 492.
2. D.H. Saxon, *Proceedings of the International Europhysics conference on High Energy Physics , Bari , Italy , 1985*, ed. L. Nitti and G. Preparata, p. 899;
   H. Yamamoto, *Proceedings of the 1985 International Symposium on Lepton and Photon at High Energies , Kyoto , Japan , 1985.*
3. JADE Collab. , W. Bartel et al., Phys. Lett. **101B** (1981), p. 129; Phys. Lett. **134B** (1984), p. 275; DESY preprint 85 - 036 (1985).
4. PEP-4 TPC Collab. , H. Aihara et al., Phys. Rev. Lett. **54** (1985), p. 270.
5. TASSO Collab. , R. Brandelik et al., Phys. Lett. **83B** (1979), p. 261; Z. Phys. C - Particles and Fields **4** (1980), p. 87.
6. TASSO Collab. , R. Brandelik et al., Phys. Lett. **113B** (1982), p. 499.
7. F. A. Berends and R. Kleiss, Phys. Nucl. Phys. **B177** (1981), p. 237; Phys. Nucl. Phys. **B178** (1981), p. 141.
8. TASSO Collab. , M. Althoff et al., Z. Phys. C - Particles and Fields **26** (1984), p. 157.
9. MINUIT CERN, Program Library.
10. E. D. Malaza, Cambridge preprint HEP85/9 (1985).
11. H. Daum, H. Meyer and J. Burger, Z. Phys. C - Particles and Fields **8** (1981), p. 167.
12. S. L. Wu and G. Zobernig, Z. Phys. C - Particles and Fields **2** (1979), p. 107.
13. TASSO Collab. , M. Althoff et al., Z. Phys. C - Particles and Fields **29** (1985), p. 29.
14. HRS Collab. , M. Derrick et al., ANL - HEP - PR - 85 - 77 (1985).

TRIPLE HADRONIC ENERGY CORRELATIONS IN HIGH ENERGY e^+e^- ANNIHILATION[x]

F.Csikor[1], G.Eszes[2], L.Garrido[3] and G.Pócsik[1]

1 Institute for Theoretical Physics, Eötvös University, Budapest, Hungary
2 Central Research Institute for Physics, Budapest, Hungary
3 Deutsches Elektronen - Synchrotron DESY, Hamburg, FRG

In the past few years hadronic energy correlations /EEC/ in high-energy e^+e^- annihilation [1] have been studied by many groups. While EEC could be calculated in perturbative QCD, it has been recognized soon that the fragmentation corrections to EEC are large at present energies. Since fragmentation corrections are expected to decrease as W^{-1} with increasing center of mass energy W /the perturbative part is proportional to $\ln W^{-1}$/, in order to be more sensitive to the QCD part, we recalculated EEC in the Z^0 resonance region [2] where a copious hadron production will appear. In $\gamma + Z^0$ exchange the normalized EEC is independent of initial state polarizations and weak interaction parameters [2].

Another possibility is to introduce such an energy weighted cross section whose fragmentation correction decreases faster than that of EEC. Such a quantity is the triple hadronic-energy correlation /TEC/ [3] for which the fragmentation correction is expected to decrease as W^{-2}, at least at asymptotic energies. TEC is defined as a threefold differential quantity

$$\sum_{\substack{\text{hadr.}\\ \text{events}}} \frac{\Delta E_1 \Delta E_2 \Delta E_3}{W^3 L T \Delta\Omega_1 \Delta\Omega_2 \Delta\Omega_3}$$

Presented by G.Pócsik

where in a hadronic event the ith hadronic calorimeter collects an energy ΔE_i in a solid angle $\Delta\Omega_i$ $(i=1,2,3)$ during a time T, L is the luminosity. TEC has many interesting properties. Here, we note only that normalizing TEC to the total hadronic cross section and integrating over at least one azimuthal angle, initial-state polarizations and 2^0 parameters are cancelled.

TEC has remarkable properties: 1. it is a symmetric way of treating three jets /in EEC only double correlations are measured/, 2. it does not require an event by event analysis /similar to EEC/, 3. in a large enough phase space it is completely independent of EEC and from all previously used methods in jet physics.

If we are interested in describing three-jet events, TEC must be defined in a plane [3] , this leads to the planar triple energy correlation /PTC/

$$PTC = \frac{1}{\Delta\chi_1 \Delta\chi_2 N} \sum_{A=1}^{N} \sum_{\substack{\text{planar} \\ \text{triplets}}} \frac{E_{Aa} E_{Ab} E_{Ac}}{W^3} ,$$

N is the number of hadronic events, in the event A E_{Aa}, E_{Ab}, E_{Ac} are the individual particle energies, and the momenta of particles a,b,c have relative angles χ_1 to $\chi_1+\Delta\chi_1$, χ_2 to $\chi_2+\Delta\chi_2$, χ_3 to $\chi_3+\Delta\chi_3$ with the planarity requirement $|2\pi-\chi_1-\chi_2-\chi_3| \leq 0.1$ rad. Each distinct triplet contributes only once, but a particle may contribute in several triplets. PTC is symmetric under the exchange $\chi_i \leftrightarrow \chi_j$. For PTC an $O(\alpha_s)$ QCD result is written down in [3] .

It is advantageous to sum up the various PTC values belonging to different χ_1, χ_2's, therefore, define [4]

$$I(\beta) = \int PTC \, d\chi_1 d\chi_2 \quad .$$
$$\chi_1 \leq \pi-\beta$$
$$\chi_2 \leq \pi-\beta$$
$$\chi_1+\chi_2 \geq \pi+\beta$$

β=0 cannot be taken for the presence of collinear singularities.

Recently, we have carried out a Monte Carlo simulation of $I(\beta)$ and shown that a statistically reasonable determination of $I(\beta)$ is feasible from the existing data and it provides an independent α_s determination [4]. 2-,3-,4-jet cross sections were computed in $O(\alpha_s^2)$ QCD using the Sterman-Weinberg ε,δ -prescription, as well as the scaled invariant mass squared cut, and Λ =100 MeV. Fragmentation corrections were computed in the Lund string model and in independent fragmentation models /IF/. We verified that for $\beta \geq 30^\circ$ $I(\beta)$ is infrared insensitive in both prescriptions for the pure QCD and also for the complete Monte Carlo in both models. Furthermore, for $\beta \geq 40^\circ$ the $q\bar{q}$ fragmentation gives a contribution of $\lesssim$ 8% for ε =0.1, W=44 GeV in both models. For measuring the fragmentation let us introduce the quantities

$$\Delta^{PTC}(W) = 1 - \frac{I(40^\circ)_{QCD+FR}}{I(40^\circ)_{QCD}},$$

$$\Delta^{Asym.}(W) = 1 - \frac{\int_{40^\circ}^{90^\circ} d\chi\, A(\chi)_{QCD+FR}}{\int_{40^\circ}^{90^\circ} d\chi\, A(\chi)_{QCD}},$$

where QCD+FR refers to the complete Monte Carlo and $A(\chi)$ is the normalized asymmetry of EEC. Table 1 shows the fragmentation corrections.

W/GeV/	Δ^{PTC}_{string}	Δ^{PTC}_{IF}	$\Delta^{Asym.}_{string}$	$\Delta^{Asym.}_{IF}$
34	0.40±0.05	0.23±0.05	0.44±0.07	0.31±0.06
44	0.30±0.015	0.16±0.03	0.32±0.08	0.18±0.08
90	0.22±0.07	0.08±0.04	0.22±0.10	0.08±0.05

Table 1

It follows that fragmentation corrections to the integrated PTC and $A(\lambda)$ are about the same, for IF they follow a W^{-1} type law, but for the string model they show a slower decrease up to 90 GeV.

Recently MARK J has carried out an α_s determination [5] based on the idea of PTC outlined above. From their data they found that for $\beta \geq 40^\circ$ $I(\beta)$ is infrared insensitive and two-jets contribute negligibly. Furthermore, Ali and Lund models give good descriptions of PTC data in the range 22-46 GeV. Table 2 shows their results for from PTC.

W/GeV/	α_s^{Ali}	α_s^{Lund}
22	0.071 ± 0.015	0.11 ± 0.018
35	0.112 ± 0.005	0.147 ± 0.005
41	0.097 ± 0.008	0.116 ± 0.010
44	0.105 ± 0.007	0.125 ± 0.007
46	0.130 ± 0.011	0.138 ± 0.007

Table 2

Errors are statistical ones in Table 2. There is a systematic error of 0.004 from data analysis and the same value from changing the planarity cut and β. The combined data on PTC and $A(\lambda)$ provide the fit [5]

$$\bar{\Lambda} = 105 \pm 25 \, {}^{+\,60}_{-\,40} \text{ MeV}$$

or

$$\alpha_s = \begin{cases} 0.124 \pm 0.004 \pm 0.012 & \text{at 35 GeV} \\ 0.12 \pm 0.007 \pm 0.01 & \text{at 44 GeV} . \end{cases}$$

This is to be compared to the results from EEC [6]:

$$\alpha_s = \begin{cases} 0.13 \pm 0.01 \pm 0.02 & \text{at 35 GeV} \\ 0.12 \pm 0.02 & \text{at 44 GeV} . \end{cases}$$

A virtue of [5] is that uncertainties were minimized in the α_s determination.

In summary, TEC offers a more detailed picture on jets, PTC probes 3-jet final states in a natural way, it is infrared insensitive. Fragmentation corrections to PTC are still large, the asymptotic W^{-2} law can be reached at best beyond the Z^0 region extending the validity of current models to about 90 GeV. PTC leads to an α_s determination independent of EEC. It would be worthwhile to reconsider the α_s determinations of various experimental groups in the light of PTC.

References

1. C.L.Basham, L.S.Brown, S.D.Ellis and S.T.Love: Phys.Rev.Lett. 41, 1585 /1978/; Phys.Rev. D17, 2298 /1978/; 19, 2018 /1979/; L.S.Brown and S.D.Ellis: ibid. 24, 2383 /1981/.
2. F.Csikor, G.Pócsik and A.Tóth: Phys.Rev.D28, 1206, /1983/; 28, 2877 /1983/.
3. F.Csikor, G.Pócsik and A.Tóth: Phys.Rev.D31, 1025 /1985/.
4. F.Csikor, G.Eszes, L.Garrido and G.Pócsik:ITP Budapest Report No. 432, 1985; Phys.Rev.D, 1986 in print.
5. M.Chen: Review talk, Proc.6. Rencontre de Moriond Conf., 1986; MIT TR148, 1986; L.Garrido: PhD Thesis, Barcelona, 1986.
6. B.Adeva et al.: Phys.Rev.Lett. 54, 1750 /1985/.

AN ANALYTIC RESULT ON BREMSSTRAHLUNG IN e^+e^- -ANNIHILATION

O.M. Fedorenko* and T. Riemann
Joint Institute for Nuclear Research, Dubna

We have determined the electromagnetic one-loop radiative corrections to the differential cross section $d\sigma/d\cos\theta$ (θ being the scattering angle) of the reactions

$$e^+e^- \to \mu^+\mu^-, \tag{1}$$

$$e^+e^- \to \mu^+\mu^-\gamma. \tag{2}$$

The Z -boson of the GWS-theory we took into account in Born approximation. The following diagrams are contributing:

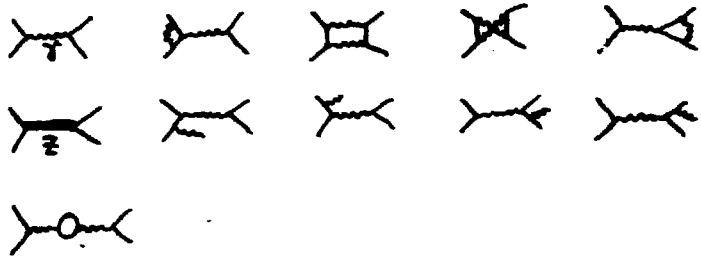

From the differential cross section, one usually derives

$$\sigma_{tot} = \int_{-1}^{+1} dc \, \frac{d\sigma}{dc}, \qquad c = \cos\Theta, \tag{3}$$

and the forward-backward (or charge) asymmetry,

$$A_{FB} = \frac{1}{\sigma_{tot}} \left[\int_0^1 dc \, \frac{d\sigma}{dc} - \int_{-1}^0 dc \, \frac{d\sigma}{dc} \right]. \tag{4}$$

* Dept. of Physics and Mathematics, State University of Petrozavodsk, USSR.

We obtain analytic expressions for the bremsstrahlung contribution after integration over the complete photon phase space. We rely on techniques developed in [1]. Our results are an upper limit on the radiative corrections in real experiments where due to cuts only part of the hard bremsstrahlung has to be included. In fact, one can use our result to simulate realistic experimental conditions if one subtracts with a Monte-Carlo program the observed photon events from the analytic cross section. In this way, one gets an alternative to the usual approach to realistic hard bremsstrahlung calculations [2]. In the ultra-relativistic approximation, the cross-section for (1,2) is:

$$\frac{d\sigma}{dc} = \frac{\pi\alpha^2}{2s}\Big\{Q^2\left[1+c^2+\frac{\alpha}{\pi}(F_e+QF_1+Q^2F_2)+\frac{\alpha}{\pi}F_{vp}\right] + 2\,\mathrm{Re}\,\chi\,|Q|\cdot\left[v_e v\,(1+c^2)+2a_e a\cdot c\right] + |\chi|^2\cdot\left[(v_e^2+a_e^2)\cdot(v^2+a^2)(1+c^2)+8v_e v a_e a\cdot c\right]\Big\} \tag{5}$$

Here, $s = 4E^2$, $a = 1$, $v = 1-4s_W^2\,|Q|$, $Q(\mu) = -1$, $s_W^2 = 1-M_W^2/M_Z^2$, $\chi = G_\mu\cdot M^2\cdot s/(8\cdot 8\pi\alpha\cdot(s-M^2))$, $M^2 = M_Z^2 - i\Gamma_Z M_Z$.

We got the following results:

$$F_{e,2} = f_{e,2}(c) + f_{e,2}(-c),$$
$$F_1 = f_1(c) - f_1(-c), \tag{6}$$

$$f_0 = \frac{1}{3}\left[\frac{19}{3}+4L_e-2L_\mu-2L_-+3c_-L_-\right] + c_-^2\left[\frac{19}{3}-\frac{4}{3}L_e+\pi^2+2(1-L_e)(L_++L_-)-L_-^2\right] + \frac{1}{c_-}\left[-\frac{11}{9}+\frac{5}{3}L_e+\frac{2}{3}L_\mu+\frac{2}{3}L_-+2L_+\right] + \frac{1}{c_-^2}\left[(L_e-2)L_++\frac{1}{2}L_+^2-\frac{5}{12}(c_-)\right], \tag{7}$$

$$f_1 = -\frac{3}{C_+^2} L_+ - \frac{3}{C_-} + 9L_+ + 12 C_-^2 L_i + C_- \left[6 + \frac{\pi^2}{3} + L_- + L_+ - 2 L_- L_+ \right], \tag{8}$$

$$f_2 = 1 - \frac{3}{2} C_+^2 \tag{9}$$

with the following abbreviations:

$$L_e = \ln \frac{s}{m_e^2}, \quad L_f = \ln \frac{s}{m_f^2},$$

$$C_+ = \cos^2 \frac{\vartheta}{2}, \quad C_- = \sin^2 \frac{\vartheta}{2},$$

$$L_+ = \ln \left(\cos^2 \frac{\vartheta}{2} \right), \quad L_- = \ln \left(\sin^2 \frac{\vartheta}{2} \right), \quad L_i = \ln \left(\tan^2 \frac{\vartheta}{2} \right),$$

$$I(x) = -\int_0^1 \frac{dt}{t} \ln (1 - xt).$$

$$G_{tot} = \frac{4}{3} \pi \frac{\alpha^2}{s} \left\{ Q^2 \left[1 + \frac{\alpha}{\pi} \left(F_e^{tot} + Q^2 F_2^{tot} \right) + \frac{3}{8} \frac{\alpha}{\pi} F_{vp} \right] + 2 \mathrm{Re} \chi |Q| v_e V + |\chi|^2 (v_e^2 + a_e^2)(V^2 + A^2) \right\}, \tag{10}$$

$$A_{FB} = \frac{A}{G_{tot}} \frac{3}{3} \pi \frac{\alpha^2}{s} \left[Q^2 \frac{\alpha}{\pi} F_A^{tot} + \frac{3}{2} \mathrm{Re} \chi |Q| a_e a + 3 |\chi|^2 v_e V a_e A \right], \tag{11}$$

$$F_{FB}^{tot} = \frac{3}{8} \int_{-1}^{+1} dx \, F_{FB}, \qquad F_A^{tot} = \frac{3}{8} \left[\int_0^1 dx \, F_A - \int_{-1}^0 dx \, F_A \right],$$

$$F_e^{tot} = \frac{2}{3} - \frac{\pi}{6} L_e + L_e L_f - L_f + \frac{\pi^2}{3}, \tag{12}$$

$$F_A^{tot} = \frac{3}{20} - \frac{15}{2} \ln 2 + \frac{3}{4} \ln^2 2 - \frac{\pi^2}{8} = -.457195, \tag{13}$$

$$F_2^{tot} = \frac{3}{4} \tag{14}$$

(14)

Wheareas one may find $F_{1,2}^{tot}$ in the literature[2], the f_i and F_1^{tot} have been derived here for the first time. Our formulae partly correct corresponding results published earlier[3].

We would like to thank D.Yu. Bardin for discussions and cooperation in the first stage of this work and the organizers of this Symposium at Kazimierz 1986 for the opportunity to present our results. An extended version will be submitted to Acta Physica Polonica.

REFERENCES

1. A.A. Akhundov, D.Yu. Bardin, O.M. Fedorenko, T. Riemann, Yad.Fiz. 42 (1985) 1204; Dubna-prepr. E2-84-787 (in English); and ref. cited therein.

2. F.A. Berends and R. Kleiss, Nucl.Phys. B177 (1981) 237; and refs. cited therein.

3. E.A. Kuraev, G.V. Meledin, Nucl.Phys. B122 (1977) 485.

A GLOBAL ANALYTIC MODEL OF THE PION ELECTROMAGNETIC STRUCTURE AND ITS UTILIZATION FOR OTHER PHYSICAL PROBLEMS

S.Dubnička and Ľ.Martinovič

Institute of Physics EPRC, Slovak Academy of Sciences
Bratislava, Czechoslovakia

It is well known that the pion-pion-virtual photon vertex in Feynman diagrams of different electromagnetic processes can not be considered as a point-like and the quark - gluon structure of the pion has to be taken into account. The latter is phenomenologically simulated in terms of a single structure function or form factor (ff) $F_\pi(t)$ where $t = -Q^2$ is the photon four-momentum transfer squared.

In this contribution we would like to present a global analytic model of $F_\pi(t)$ with an arbitrary number of radially excited rho-states and its application to other physical problems like a determination of $\rho'(1250)$ and $\rho''(1600)$ from data on $e^+e^- \to \pi^+\pi^-$, the prediction of the P-wave isovector $\pi\pi$ phase shift $\delta_1^1(t)$ and the inelasticity $\eta_1^1(t)$ in the whole experimentally measurable region and finally, the evaluation of the two-pion contribution to the muon anomalous magnetic moment.

I. A GLOBAL ANALYTIC PION ff MODEL

The idea was [1] to incorporate all well established properties of $F_\pi(t)$, respecting the analyticity as precisely as possible.

The analytic properties consist of the elastic branch point at $t = 4m_\pi^2$, the effective inelastic branch point*) at $t = t_{inel}$, the

*) Its position will be left as a free parameter in the fit of data and the data themselves will take as much inelasticity as they need.

pole $t_p = -15.36\ m_\pi^2$ and the zero $t_z = -8.96\ m_\pi^2$ on the second Riemann sheet by means of which the so-called left-hand cut is approximated [2,3] and the poles t_ρ, $t_{\rho'}$, $t_{\rho''}$, ... on the unphysical sheets, which correspond to the $\rho(770)$, $\rho'(1250)$, $\rho''(1600)$ ... resonances respectively.

The cut structure used generates the four-sheeted Riemann surface, on which our model of $F_\pi(t)$ is defined. By using the inverse Zhukovsky transformation

$$W(t) = i\,[(q_1+q)^{1/2} - (q_1-q)^{1/2}]/[(q_1+q)^{1/2} + (q_1-q)^{1/2}] \qquad (1)$$

with $i = (-1)^{1/2}$, $q_1 = 1/2(t_{inel} - 4)^{1/2}$, $q = 1/2(t-4)^{1/2}$, $m_\pi = 1$

we map all four sheets in t - variable onto the W - plane and all cuts disappear.

The variable $W(t)$ possess the assumed pion ff dominant cut structure in t - variable and the same holds for the expansion

$$F_\pi[W(t)] = \frac{(W^2-1)^m (W - W_z)\sum_{n=0}^{L} A_n W^n}{(W - W_p)\prod_{v=\rho,\rho',\rho''\ldots}(W - W_v)(W - W_v^*)} \qquad (2)$$

with arbitrary L and real coefficients A_n. The factor $(W^2-1)^m$ is present to ensure the asymptotic behaviour of the form $\sim t^{-m/2}$ with m being a positive integer.

In order to find explicit dependence of our model on the ratio $f_{v\pi\pi}/f_v$, which is the measure of a strength of residua at the corresponding poles, we employ the vector meson dominance (VMD) pole diagram contributions

$$F_\pi^{(VMD)}(t) = \sum_v \frac{m_v^2 (f_{v\pi\pi}/f_v)}{m_v^2 - t} = \sum_v F_\pi^{(v)}(t) \qquad (3)$$

transformed into the W - variable

$$F_{\pi}^{(v)}(t) = \frac{m_v^2 (f_{v\pi\pi}/f_v)\left[(1-W^2)(1-W_{vo}^2)\right]^2}{16 q_1^2 (1-W_{vo}^2 W^2)(W^2 - W_{vo}^2)} \qquad (4)$$

for $v = \rho, \rho', \rho'' \ldots$.

Here $W_{\rho o} = -W_{\rho o}^* = \lim_{\Gamma_\rho \to 0} W_\rho$, $W_{vo} = 1/W_{vo}^* = \lim_{\Gamma_v \to 0} W_v$ if $v \neq \rho$ since $\rho(770)$ is placed on the second sheet and $\rho'(1250)$, $\rho''(1600)$ ... are placed on the third sheet as we expect [1] $t_{inel} < m_{\rho'}^2, m_{\rho''}^2, \ldots$.

In expression (2), for every resonance only the complex conjugate pair of poles nearest to the physical region is considered. Therefore, we extract only the term with denominator of the form $(W - W_{vo})(W - W_{vo}^*)$ from (4) and demand its equality to the equivalent term from (2) in the limit $\Gamma_v \to 0$.

As a consequence we obtain the equations

$$\sum_{n=0}^{L} (C_{\rho o} W_{\rho o}^n - C_{\rho o}^* W_{\rho o}^{*n}) A_n = 2 r_{\rho o} \qquad (5)$$

$$\sum_{n=0}^{L} (C_{\rho' o} W_{\rho' o}^n + C_{\rho' o}^* W_{\rho' o}^{*n}) A_n = r_{\rho' o} + r_{\rho' o}^* \qquad (6)$$

$$\sum_{n=0}^{L} (C_{\rho'' o} W_{\rho'' o}^n + C_{\rho'' o}^* W_{\rho'' o}^{*n}) A_n = r_{\rho'' o} + r_{\rho'' o}^* \qquad (7)$$

.....

where

$$C_{\rho o} = \frac{(W_{\rho o}^2 - 1)^m (W_{\rho o} - W_z)}{(W_{\rho o} - W_p)(W_{\rho o} - W_{\rho o}^*)(W_{\rho o} - W_{\rho'})(W_{\rho o} - W_{\rho'}^*)(W_{\rho o} - W_{\rho''})(W_{\rho o} - W_{\rho''}^*) \ldots}$$

$$C_{\rho' o} = \frac{(W_{\rho' o}^2 - 1)^m (W_{\rho' o} - W_z)}{(W_{\rho' o} - W_p)(W_{\rho' o} - W_\rho)(W_{\rho' o} - W_\rho^*)(W_{\rho' o} - W_{\rho' o}^*)(W_{\rho' o} - W_{\rho''})(W_{\rho' o} - W_{\rho''}^*) \ldots}$$

$$C_{\rho'' o} = \frac{(W_{\rho'' o}^2 - 1)^m (W_{\rho'' o} - W_z)}{(W_{\rho'' o} - W_p)(W_{\rho'' o} - W_\rho)(W_{\rho'' o} - W_\rho^*)(W_{\rho'' o} - W_{\rho'})(W_{\rho'' o} - W_{\rho'}^*)(W_{\rho'' o} - W_{\rho'' o}^*) \ldots}$$

.....

and $r_{\rho o}, r_{\rho' o}, r_{\rho'' o}, \ldots$ are the residua of $F_{\pi}^{(v)}(t)$ at the poles

$W_{\rho o}$, $W_{\rho' o}$, $W_{\rho'' o}$, ... respectively.

Another two equations

$$A_o + R(v)\, A_1 = 0 \qquad (8)$$

with

$$R(v) = \left[(W_p^{-1} - W_z^{-1}) + \sum_{v=\rho,\rho',\rho'',\ldots} \frac{2\,\mathrm{Re}\, W_v}{|W_v|^2} \right]^{-1}$$

and

$$\sum_{n=o}^{L} A_n W_N^n = C_N(v) \qquad (9)$$

where

$$C_N(v) = \frac{(W_N - W_p) \prod_{v=\rho,\rho',\rho'',\ldots} (W_N - W_v)(W_N - W_v^*)}{(W_N^2 - 1)^m (W_N - W_z)}, \quad W_N = W(t)\big|_{t=0}$$

are obtained from the threshold behaviour requirements

$$\mathrm{Im}\, F_\pi(t)\big|_{q=0} = \frac{d}{dq}\, \mathrm{Im}\, F_\pi(t)\big|_{q=0} = \frac{d^2}{dq^2}\, \mathrm{Im}\, F_\pi(t)\big|_{q=0} = 0$$

and the normalization condition $F_\pi[W(0)] = 1$ respectively.

The summation parameter L takes the value K + 1, where K is the number of resonances under consideration.

The quark structure of hadrons leads to a general belief that with increased energy of e^+e^- always a new excitation of vector meson is produced. Then the number of resonances K taken in (2) depends on the range and preciseness of existing experimental data on $F_\pi(t)$ and is always chosen empirically according to an absolute minimum of χ^2 and the values of parameters of the model, which are controlled by other experiments, as they have a clear physical meaning.

The dependence of the coefficients A_n in (2) on the parameters m, t_{inel}, m_v, Γ_v, $f_{v\pi\pi}/f_v$ ($v = \rho$, ρ', ρ'', ...) with clear physical meaning is found by a solution of the linear algebraic equations (5),...(9).

Prior to the determination of $\varphi'(1250)$ and $\varphi''(1600)$ from $e^+e^- \to \pi^+\pi^-$ we present results on a compatibility check of space-like region pion ff data with time-like one.

II. A COMPATIBILITY CHECK OF SPACE-LIKE REGION PION ff DATA WITH TIME-LIKE ONE

The electroproduction of pions from nucleons $e^-N \to e^-\pi N$ is the only available source of the space-like region pion ff data at large momentum transfers [4] . However these are strongly model dependent [5] .

On the other hand the annihilation process $e^+e^- \to \pi^+\pi^-$ provides through the one photon exchange approximation very reliable time-like region data.

By using the analytic properties of $F_\pi(t)$, expressed through the following integral representation

$$F_\pi(Q^2) = \frac{1}{\pi}\int_{4}^{t_{\pi^*\omega}} \frac{\mathrm{Im}^E F_\pi(t)}{t+Q^2}\,dt + \frac{1}{\pi}\int_{t_{\pi^*\omega}}^{\infty} \frac{\mathrm{Im}^A F_\pi(t)}{t+Q^2}\,dt \qquad (10)$$

we have carried out a compatibility check of the space-like region electroproduction model dependent pion ff data [4] with time-like one.

The idea was to transfer the reliable experimental information on $e^+e^- \to \pi^+\pi^-$ by means of (10) into the space-like region and then to compare it (calculating the values of partial χ^2 's) with electroproduction data.

The data on $\mathrm{Im}^E F_\pi(t)$ in the first integral of (10) are obtained by equating the experimental cross section of $e^+e^- \to \pi^+\pi^-$ with theoretical one as follows

$$\sigma_{exp}(t) = \frac{\pi\alpha^2\beta^3}{3t}\left|F_\pi(t) + R\exp(i\phi)\,\frac{m_\omega^2}{m_\omega^2 - t - i\,m_\omega\Gamma_\omega}\right|^2 \qquad (11)$$

where

$$R = \frac{6}{\alpha\, m_\omega \beta^3}\left\{\Gamma(\omega \to e^+e^-)\cdot\Gamma(\omega \to \pi^+\pi^-)\right\}^{1/2}, \quad \beta = \left[1 - \frac{4m_\pi^2}{m_\omega^2}\right]^{1/2}$$

$\alpha = 1/137$ is the fine structure constant and $\phi = \text{arc tg}\,\dfrac{m_\rho\Gamma_\rho}{m_\rho^2 - m_\omega^2}$.

Now, if we take into account the identity between the pion ff phase and the P-wave isovector $\pi\pi$ phase shift $\delta_1^1(t)$ for $4 < t < t_{\pi^0\omega}$ (i.e. at the elastic region) the relation (11) gives the quadratic equation [3]

$$|F_\pi|^2 + |F_\pi|\frac{2R\,m_\omega^2}{(m_\omega^2 - t)^2 + m_\omega^2\Gamma_\omega^2}\left\{(m_\omega^2 - t)\cos(\phi - \delta_1^1(t)) - m_\omega\Gamma_\omega\sin(\phi - \delta_1^1(t))\right\} +$$
$$+\left\{\frac{R^2 m_\omega^4}{(m_\omega^2 - t)^2 + m_\omega^2\Gamma_\omega^2} - \left[\frac{3t}{\pi\alpha^2\beta^3}\,\sigma_{exp}(t)\right]^2\right\} = 0 \qquad (12)$$

the physical solution of which is

$$|F_\pi(t)| = -Z(t) + \left\{Z^2(t) + \left[\frac{3t}{\pi\alpha^2\beta^3}\,\sigma_{exp}(t)\right]^2 - \frac{R^2 m_\omega^4}{(m_\omega^2 - t)^2 + m_\omega^2\Gamma_\omega^2}\right\}^{1/2} \qquad (13)$$

where

$$Z(t) = \frac{R\,m_\omega^2}{(m_\omega^2 - t)^2 + m_\omega^2\Gamma_\omega^2}\left\{(m_\omega^2 - t)\cos(\phi - \delta_1^1(t)) - m_\omega\Gamma_\omega\sin(\phi - \delta_1^1(t))\right\}$$

Taking the experimentel information on $R, \phi, m_\omega, \Gamma_\omega, \delta_1^1(t)$ and $\sigma_{exp}(t)$ one can determine the data on $\mathrm{Im}^E F_\pi(t)$ for $4 < t < t_{\pi^0\omega}$ from (13) and $F_\pi(t) = |F_\pi(t)|\exp(i\,\delta_1^1(t))$ which through the first integral of (10) are giving more than 90% contribution to $F_\pi(Q^2)$ for $Q^2 = 0$.

For the $\mathrm{Im}^A F_\pi(t)$ in the second integral of (10) using the perturbative QCD result we have proved [1] that it has at least one

zero and is vanishing from negative values as $t \to +\infty$.
Therefore we have parametrized it as follows

$$\mathrm{Im}^{A} F_{\pi}(t) = a \frac{(t - t_0)}{(t - b)^{M}} \tag{14}$$

where the paremeters a, t_0, b and M are determined from the requirements

$$\mathrm{Im}^{E} F_{\pi}(t)\Big|_{t=t_{\pi\omega}} = a \frac{(t_{\pi\omega} - t_0)}{(t_{\pi\omega} - b)^{M}} \tag{15}$$

$$\frac{d}{dt} \mathrm{Im}^{E} F_{\pi}(t)\Big|_{t=t_{\pi\omega}} = \frac{d}{dt} a \frac{(t - t_0)}{(t - b)^{M}}\Big|_{t=t_{\pi\omega}} \tag{16}$$

$$\frac{d^2}{dt^2} \mathrm{Im}^{E} F_{\pi}(t)\Big|_{t=t_{\pi\omega}} = \frac{d^2}{dt^2} a \frac{(t - t_0)}{(t - b)^{M}}\Big|_{t=t_{\pi\omega}} \tag{17}$$

$$1 - \frac{1}{\pi}\underbrace{\int_{4}^{t_{\pi\omega}} \frac{\mathrm{Im}^{E} F_{\pi}(t)}{t} dt}_{0.93} = \frac{1}{\pi}\int_{t_{\pi\omega}}^{\infty} \frac{a(t - t_0)}{t(t - b)^{M}} dt \tag{18}$$

and the results are as follows

$$a = -.41557, \quad t_0 = 165.5762\ m_{\pi}^2, \quad b = 27.69067 \quad \text{and} \quad M = 1.31934 \tag{19}$$

There are 20 experimental points on $|F_{\pi}(t)|$ at different values of t in the space-like region [4] . Calculating the corresponding integrals with $\mathrm{Im}^{E} F_{\pi}(t)$ and $\mathrm{Im}^{A} F_{\pi}(t)$ of (10) at these values of t one gets the results presented in Table 1.

Comparing the corresponding partial χ^2 values we came to the conclusion that despite the ambiguities in extracting the pion ff data from the pion electroproduction cross section measurements of Bebek et al [4] the reported values are except for 4 points at $t = -1.19, -1.20, -2.01, -9.77$ consistent with reliable e^+e^- pion ff measurements.

III. DETERMINATION OF $\rho'(1250)$ AND $\rho''(1600)$ FROM DATA ON $e^+e^-\to\pi^+\pi^-$

In the first section of this talk we have costructed the pion ff model with an arbitrary number of radially excited rho-states which is suitable for a description of all existing pion ff data. As a result all parameters of the model are determined in this way.

All together 278 experimental points from $e^-N \to e^-\pi K$, $\pi^-e^- \to \pi^-e^-$ for $t<0$ and $\pi^-p \to e^+e^-n$, $e^+e^-\to\pi^+\pi^-$, $J/\psi\to\pi^+\pi^-$ for $t > 0$ were analysed including also the newest ORSAY [7] and NOVOSIBIRSK [8] data. The best description of the data was achieved by means of the pion ff model with three resonances ρ, ρ', ρ'' and the results are as follows (for data and our fit see fig.1)

$$\chi^2/ndf = 1.85, \quad m = 3, \text{ i.e. } F_\pi[W(t)] \underset{t\to\infty}{\sim} t^{-3/2}$$
$$t_{inel} = 1.46 \pm 0.01 \text{ GeV}^2$$

$$m_\rho = 760.1 \pm 1.9 \text{ MeV}, \quad \Gamma_\rho = 152.4 \pm 2.4 \text{ MeV}, \quad f_{\rho\pi\pi}/f_\rho = 1.24 \pm 0.01 \qquad (20)$$
$$m_{\rho'} = 1217.4 \pm 2.4 \text{ MeV}, \quad \Gamma_{\rho'} = 323.8 \pm 14.3 \text{ MeV}, \quad f_{\rho'\pi\pi}/f_{\rho'} = -.10 \pm 0.01$$
$$m_{\rho''} = 1531.6 \pm 54.5 \text{ MeV}, \quad \Gamma_{\rho''} = 454.0 \pm 64.8 \text{ MeV}, \quad f_{\rho''\pi\pi}/f_{\rho''} = -.07 \pm 0.03$$

Since the values of m_V, Γ_V can be determined reliably only in the case there are sufficiently precise experimental data around the points $t = m_V^2$ one can say that the parameters of $\rho'(1250)$ and $\rho''(1600)$ in (20) are determined from the data on $e^+e^-\to\pi^+\pi^-$. The errors in (20) correspond to the χ^2 change of 11.54 [9].

Here we would like to note that the values of $\rho'(1250)$ and $\rho''(1600)$ parameters published in [10] were obtained with a computer program faults and they have to be disregarded. On the other hand the errors of parameters in [11] correspond to the χ^2 change of 1.0 . So, only those errors of parameter values presented in (20) have to be considered as right one.

In order to carry out a further test of validity of our model

of the pion electromagnetic structure we use it for a prediction of the behaviour of the P-wave isovector $\pi\pi$ phase shift $\delta_1^1(t)$ and the inelasticity $\eta_1^1(t)$ at the experimentally measurable region.

IV. PREDICTION OF $\pi\pi$ PHASE SHIFT $\delta_1^1(t)$ AND INELASTICITY $\eta_1^1(t)$ FROM $e^+e^- \to \pi^+\pi^-$

The model of $F_\pi[W(t)]$ presented in section I. has one elastic and one effective inelastic cut. Only the inclusion of the latter into our model enables us to predict the phase and the inelasticity in agreement with existing experimental data.

The elastic unitarity condition, valid for $4 < t < t_{inel}$

$$\mathrm{Im}\, F_\pi(t) = F_\pi(t)\, A_1^{1*}(t) \tag{21}$$

can be used for the analytic continuation of the pion ff on the second Riemann sheet (generated by the elastic branch point) as follows

$$F_\pi^{II}(t) = \frac{F_\pi^{I}(t)}{1 + 2i\, A_1^1(t)} \tag{22}$$

or

$$A_1^1(t) = \frac{F_\pi^{I}(t) - F_\pi^{II}(t)}{2i\, F_\pi^{II}(t)} \tag{23}$$

The latter expression is valid in the whole complex t - plane. Further we restrict ourselves only to the physical region which is defined on the upper boundary of the cut in the t - plane.

The standard parametrization of the P-wave isovector $\pi\pi$ scattering amplitude at the physical region

$$A_1^1(t + i\varepsilon) = \frac{\eta_1^1(t + i\varepsilon)\, \exp(2i\delta_1^1(t + i\varepsilon)) - 1}{2i} \tag{24}$$

leads in (23) to

$$\eta_1^1(t + i\varepsilon)\exp(2i\,\delta_1^1(t + i\varepsilon)) = \frac{F_\pi^I(t + i\varepsilon)}{F_\pi^{II}(t + i\varepsilon)} \qquad (25)$$

from where it is straightforward to find [12]

$$\delta_1^1(t + i\varepsilon) = 1/2\ \mathrm{arc\ tg}\ \frac{\mathrm{Im}\left[F_\pi^I(t + i\varepsilon)/F_\pi^{II}(t + i\varepsilon)\right]}{\mathrm{Re}\left[F_\pi^I(t + i\varepsilon)/F_\pi^{II}(t + i\varepsilon)\right]} \qquad (26)$$

$$\eta_1^1(t + i\varepsilon) = \left|\frac{F_\pi^I(t + i\varepsilon)}{F_\pi^{II}(t + i\varepsilon)}\right| \qquad (27)$$

If we insert on the right-hand sides of (26) and (27) the explicit expression of our pion electromagnetic structure model with the values of the parameters (20) one gets the behaviour of $\delta_1^1(t)$ and $\eta_1^1(t)$ presented in fig.2a,b. The corresponding experimental data are reproduced quite well. This nontrivial result is beyond all expectations and it is rising a confidence to our model constructed in section I. The latter will be further used for the evaluation of the two-pion contribution to the anomalous magnetic moment of the muon.

V. TWO-PION CONTRIBUTION TO THE ANOMALOUS MAGNETIC MOMENT OF MUON

The anomalous magnetic moment $a_\mu = 1/2(g - 2)$ is one of the basic properties of the muon which is measurable with great precision and also calculable theoretically. So, it is a sensitive tool for testing the validity of our present theoretical ideas about the microworld. Its most accurate measurements are those obtained at the CERN muon storage ring [13]

$$a_{\mu^+}^{exp} = (116\ 591\ 000 \pm 1200)\times 10^{-11} \qquad (28a)$$

$$a_{\mu^-}^{exp} = (116\ 593\ 600 \pm 1200)\times 10^{-11} \qquad (28b)$$

or, if combining both

$$a_\mu^{exp} = (116\ 592\ 300 \pm 2500)\times 10^{-11} \qquad (29)$$

The largest uncertainties in the existing theoretical calculations come from the order $-\alpha^2$ hadronic contributions (see fig. 3a) to the anomalous magnetic moment of the muon, particularly the low-energy two-pion contribution (see fig. 3b).

Our global analytic model of the pion electromagnetic structure could contribute to diminishing of these uncertainties and this problem will be discussed in more detail elsewhere. Here we are interested only in the comparison oftwo-pion contribution with all other hadronic contributions given analytically [14] by

$$a_\mu(H) = \frac{1}{4\pi^3}\int_{4m_\pi^2}^{\infty} dt\ \sigma_H(t) \int_0^1 dx\ \frac{x^2(1-x)}{x^2 + (1-x)(t/m_\mu^2)} \qquad (30)$$

where $\sigma_H(t)$ is $\sigma_{tot}(e^+e^- \to \text{hadrons})$ measured in the form of

$$R = \frac{\sigma(e^+e^- \to \text{hadrons})}{\sigma(e^+e^- \to \mu^+\mu^-)}$$

The most recent evaluations of $a_\mu(H)$ are: using only experimental data on R [15]

$$a_\mu(H) = (7070 \pm 60 \pm 170)\times 10^{-11} \qquad (31)$$

or more refined procedure [16]

$$a_\mu(H) = (7100 \pm 105 \pm 49)\times 10^{-11} \qquad (32)$$

where the first error is statistical and the second is systematic.

By using our pion ff model (2) with the values of paremeters (20) and evaluating the contribution of the diagram (3b) one gets the following result

$$a_\mu(2\pi) = (6073 \pm 8)\times 10^{-11} \qquad (33)$$

Comparing (32) and (31) with our result (33) we come to the conclusion that two pion contribution to the anomalous magnetic moment of the muon is more than 85% of the total hadronic contribution represented by the diagram (3a).

REFERENCES:

[1] S.Dubnička and Ľ.Martinovič, Proc. of VII. Warsaw Symposium on Elementary Particle Physics in Kazimierz, Warszawa (1984) p.511 and Czech.J.Phys. B36 (1986)

[2] S.Dubnička and Ľ.Martinovič, Czech.J.Phys. B29 (1979) 1384

[3] S.Dubnička, V.A.Meshcheryakov and J.Milko, J.Phys. G7 (1981) 605

[4] C.J.Bebek et al, Phys.Rev. D17 (1978) 1693

[5] F.A.Berends, Daresbury study weekend series No.6,DNPL/R 30,(1973)

[6] S.Dubnička and M.Mojžiš, Proc. of VI Warsaw Symposium on Elementary Particle Physics in Kazimierz, Warszawa (1983)243

[7] D.Bisello et al, Preprint LAL/85 - 15, ORSAY (1985)

[8] L.M.Barkov et al, Nucl.Phys. B256 (1985) 365

[9] M.Roos, private communication

[10] S.Dubnička, Comm. of JINR, P2-85-869, Dubna (1985)

[11] S.Dubnička and Ľ.Martinovič, Proc.of XXI Rencontre de Moriond, Les Ares, March 16-22, 1986

[12] S.Dubnička and Ľ.Martinovič, Lett. Nuovo Cim. 44 (1985) 462

[13] J.Bailey et al, Phys.Lett. B68 (1977) 191

[14] M.Gourdin and E. de Rafael, Nucl.Phys. B10 (1969) 667

[15] T.Kinoshita, B.Nizić and Y.Okamoto, Phys.Rev. D31 (1985) 2108

[16] J.A.Casas, C.López and F.J.Yndurain, Phys.Rev. D32 (1985) 736

TABLE 1.

t (GeV^2)	$F_\pi^{exp.}$	$\Delta F_\pi^{exp.}$	$F_\pi^{predic.}$	$\chi^2_{partial}$
-9.77	0.0700	0.0190	0.0191	7.20
-6.30	0.0590	0.0300	0.0477	0.15
-3.99	0.0040	0.6780	0.0921	0.01
-3.33	0.0860	0.0330	0.1146	0.74
-3.30	0.1020	0.0230	0.1158	0.35
-2.01	0.1540	0.0140	0.1941	7.98
-1.99	0.1790	0.0210	0.1959	0.61
-1.94	0.1930	0.0250	0.2007	0.08
-1.71	0.2380	0.0200	0.2247	0.47
-1.31	0.2420	0.0150	0.2805	6.36
-1.22	0.2900	0.0300	0.2964	0.04
-1.20	0.2693	0.0082	0.3002	13.54
-1.19	0.2380	0.0170	0.3021	13.90
-1.18	0.2560	0.0260	0.3040	3.31
-1.07	0.3090	0.0190	0.3267	0.79
-0.79	0.3840	0.0140	0.4007	1.27
-0.62	0.4450	0.0160	0.4621	1.02
-0.40	0.5700	0.0160	0.5731	0.01
-0.29	0.6340	0.0290	0.6497	0.24
-0.18	0.8500	0.0440	0.7490	5.44

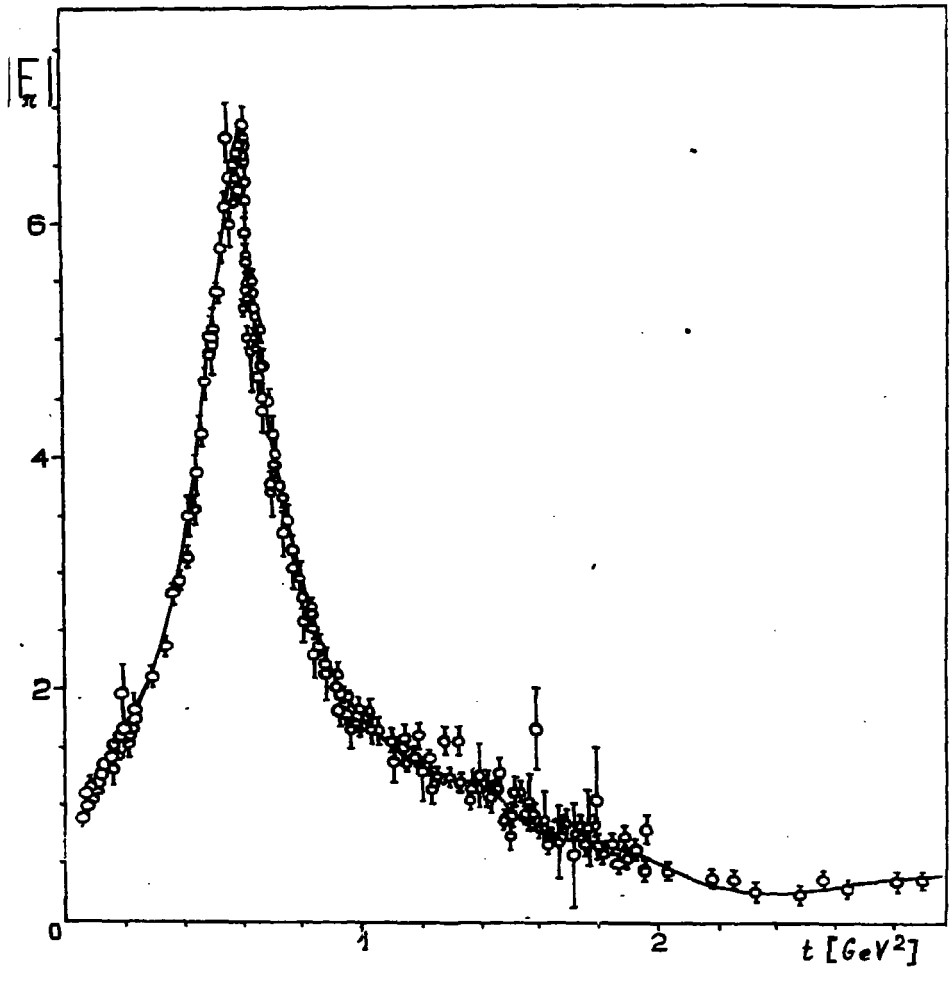

Fig. 1

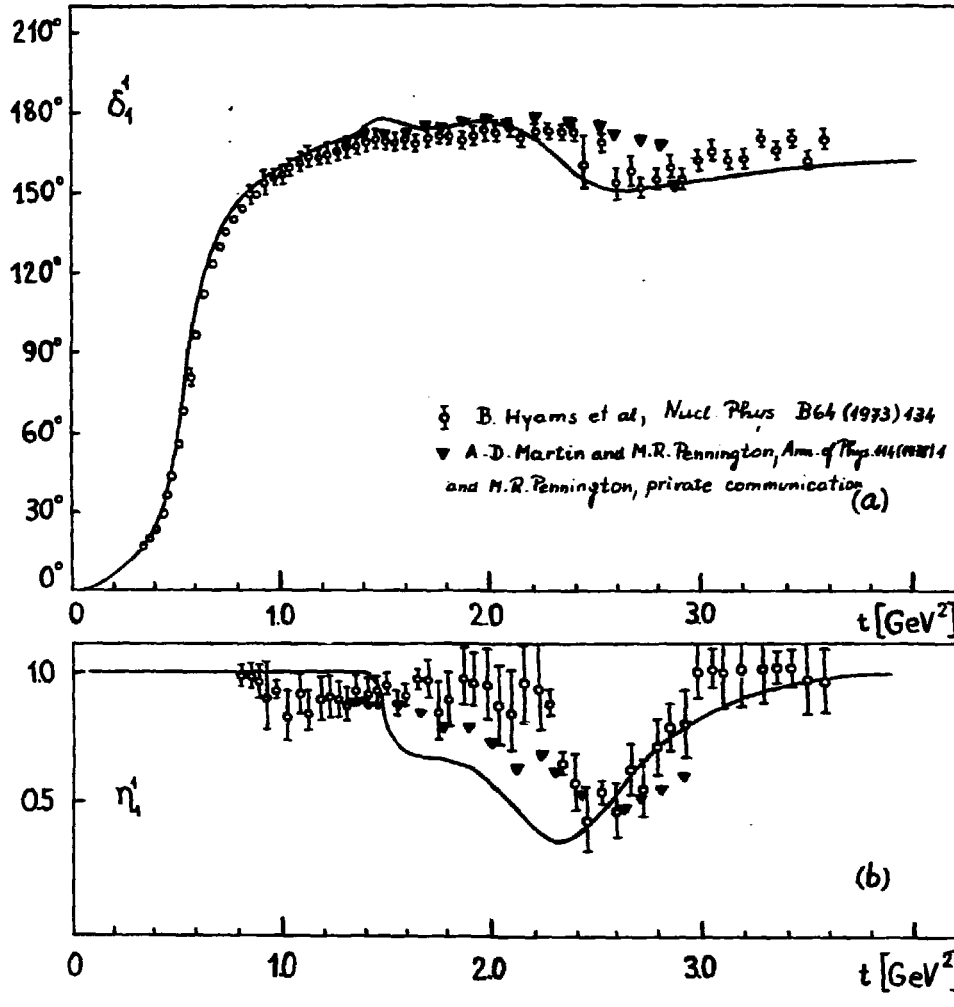
210°
180°
150°
120°
90°
60°
30°
0°
δ_1^1
B. Hyams et al, Nucl Phys B64 (1973) 134
A.D. Martin and M.R. Pennington, Ann. of Phys. 114 (1978) 1
and M.R. Pennington, private communication
(a)
0
1.0
2.0
3.0
t [GeV²]
1.0
0.5
η_1^1
(b)
0
1.0
2.0
3.0
t [GeV²]

Fig. 2

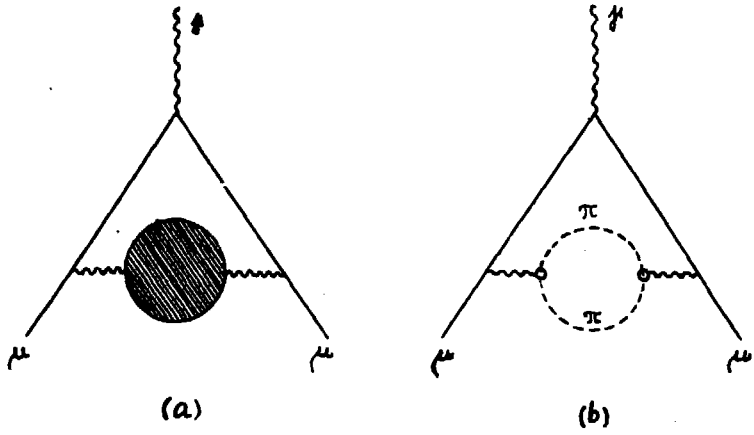

Fig. 3

THE NEUTRAL KAON MASS MEASUREMENT

L.M.Barkov, I.B.Vasserman, P.V.Vorob'ev, P.M.Ivanov, G.Ya.Kezerashvili, I.A.Koop, A.P.Lysenko, A.A.Mikhailichenko, V.S.Okhapkin, E.A.Perevedentsev, A.A.Polunin, S.I.Redin, N.M.Ryskulov, A.N.Skrinsky, V.P.Smakhtin, E.P.Solodov, B.I.Khazin, Yu.M.Shatunov, A.I.Shekhtman

Institute of Nuclear Physics, Siberian Branch, Academy of Sciences of the USSR

A b s t r a c t

The momenta and the emission angles of the pions in the reaction $e^+e^- \to K_L^0 K_S^0$, $K_S^0 \to \pi^+\pi^-$ have been measured with the help of the cryogenic magnetic detector at the VEPP-2M storage ring. The energy of the particles in the storage ring was determined by the resonance depolarization method. The preliminary value of the neutral kaon mass was found to be 497.644 ± 0.037 MeV by the analysis of 5197 events.

The experiment was carried out with the cryogenic magnetic detector [1] at the VEPP-2M electron-positron storage ring [2] . The cryogenic magnetic detector consisted of a superconducting solenoid and a cylindrical six gap optical spark chamber inside. The spark chamber had 26 cm diameter and 22 cm length. The spark chamber operated at 180°K and 2 atmosphere gas mixture pressure. The magnetic field was parallel to the beam axis. The amount of matter crossed by a charged particle inside the detector was about 0.014 radiation length. The Z-coordinate along the beam axis was measured by the spark displacement in the optical prismes.

Because of the magnetic field, the low temperature, and the increased pressure of the gas mixture in the spark chamber, the spatial resolution about 55 micrometers was achieved in the XY plane, which is perpendicular to the axis of the beams. The spatial resolution along the Z axis was 1.6 mm. The contribution of the pions multiple scattering into the momentum resolution was comparable with the contribution of the detector spatial resolution.

The neutral kaon mass measurement was performed in the reaction $e^+e^- \to K_L^0 K_S^0$, $K_S^0 \to \pi^+\pi^-$ at the total energy of the beams 2E =1018.64 ± 0.03 MeV on the left-hand slope of the φ-resonance curve. At this point the kinetic energy of the kaons is 11.7 MeV and both the kaon momentum and the minimum angle between decay pions which is about 150 degrees are sensitive to the relatively small variations of the neutral kaon mass.

The experiment was performed at two values of the magnetic field in the detector volume. The luminosity integrals $L = 28.3 nb^{-1}$ for the magnetic field H = 14.92 kGs and $L = 35.3\ nb^{-1}$ for H = 24.69 kGs were collected. The momentum resolution for kaons was equal to 8 MeV/c for H = 14.92 kGs and 5.6 MeV/c for H=24.69 kGs. The measurement accuracy of the angle between the decay pions was about 1.2 degree.

The optical features of the detector, the displacements of the sparks in the crossed magnetic and electric fields and the nonuniformity of the magnetic field were taken into account for the tracks reconstruction.

The trigger conditions allowed the detection of the two-particle events with the angular noncollinearity in the XY plane between 0° and 90°. The detection efficiency for the reaction $e^+e^- \to K_L^0 K_S^0 \to \pi^+\pi^-$ was about 20%. About 97000 events pictures were recorded in this experiment.

The primary selection of the useful events was connected with the fact that the sum of the pion momenta, (P1+P2), concentrated in the narrow interval near 416 MeV/c for this reaction.

Taking into account the radiation corrections and the momentum resolution of the detector the selection conditions 380 MeV/c $<$ $<(P1+P2)<$ 472 MeV/c for H = 14.92 kGs and 400 MeV/c $<(P1+P2)<$ $<$448 MeV/c for H = 24.69 kGs were used.

To reduce the contribution from the electroproduction reaction $e^+e^- \to e^+e^-e^+e^-$ the two-track events with the angular noncollinearity in the XY plane less than 10° were rejected. The events with three and less sparks on the track and with the spatial resolution three times more than average resolution were also rejected. Only kaon decays inside the vacuum tube of the accelerator were taken into account. Applying these conditions 5197 events were selected.

Using the resonance depolarization method [3,4] together with the feedback system [5] the average beam energy was keeping constant throughout the experiment within 15 keV for each beam. The absolute value of the magnetic field was determined by comparing the total energy of the pions measured in the detector and the known beam energy. Since the energy of the kaons after the

radiation corrections was known, one could obtain the neutral kaon mass from the kaon momentum distribution. The 0.1% uncertainty in the magnetic field contributed 23 keV into the mass determination error by this method. Note that the same uncertainty in the magnetic field caused a 320 keV change in the invariant mass of the pions if one did not take into account the known energy of the pions.

The kaon mass can be determined also by measuring the minimum angle between the decay pions.

For each value of the magnetic field the selected events were divided in two groups. One group contained events, in which the momenta of the pions differed more than 10%. It was used for neutral kaon mass measurement by the first method. It included 1781 events, collected with magnetic field H = 14.92 kGs, and 2448 events, collected with H = 24.69 kGs. From the kaon momentum distributions, shown in fig. 1,2, for these events, one can obtain the kaon mass. The 100 keV displacement in the kaon mass corresponds to 460 keV shift in the average kaon momentum. Applying the maximum-likelihood method over these events, the neutral kaon mass was found to be $M = 497.605 \pm 0.068$ MeV at H = 14.92 kGs and $M = 497.610 \pm 0.046$ MeV at H = 24.69 kGs. The errors here consist of the statistical errors and the errors which came from the optical distortions, the displacement of the sparks in the electric and magnetic fields, the imperfect calibration of the magnetic field in the detector, the uncertainty of the beam energy calibration and the momentum distribution generated by Monte-Carlo method.

The second group contained events, in which momenta of the pions differed less than 10%. This group included 406 events, collected with magnetic field H = 14.92 kGs, and 562 events, collected

with magnetic field H = 24.69 kGs. The angles between the decay pions in these events should concentrate in a narrow interval of 0.6 degree near the minimum angle, which was about 150 degrees. However, processes with emission of soft photons and the finite angular resolution of the detector broaden this distribution. From the angular distributions, shown in fig. 3,4, for these events one can obtain the kaon mass. The 100 keV displacement in the kaon mass corresponds to 0.12 degree shift of the distribution. Applying the maximum-likelihood method over these events the neutral kaon mass was found to be M = 497.754 ± 0.063 MeV at H = 14.92 kGs and M = 497.636 ± 0.056 MeV at H = 24.69 kGs. The errors here consist of the statistical errors and the errors which came from the optical distortions, the displacement of the sparks in the electric and magnetic fields, the uncertainty of the beam energy calibration and the uncertainty in the expected distribution in the angle between the pions which was generated by the Monte-Carlo method.

The correlations between errors in these four values were taken into account and the neutral kaon mass was found to be M = 497.644 ± 0.037 MeV.

This value is in agreement with the result, M = 497.742 ± 0.085 MeV obtained in our previous work [6], and with the average value M = 497.67 ± 0.13 MeV [7] based on the results of the other authors.

References

1. Barkov L.M. et al. Nucl. Instr. Meth., 1983, 204, 379.
2. Tumaikin G.M. Proceedings of the 10 International Conference on High Energy Particle Accelerators. Serpukhov, 1977, vol.1, p.443.
3. Bukin A.D. et al. Proceedings of the Fifth International Symposium on High Energy Physics and Elementary Particles. Warsaw, 1975, p.138.
4. Derbenev Ya.S. et al. Preprint INP 76-64, Novosibirsk, 1976.
5. Baklakov B.A. et al. Proceedings of the Seventh All Union Conference on Charged Particle Accelerators. Dubna, 1980, vol.1, p.338.
6. Barkov L.M. et al. Pis'ma Zh. Exp. Theor. Phys., 1985, 42, p.113. (JETP Lett. 42, 138 (1985)).
7. Reviews of Modern Physics, 1984, vol.56, No 2, part 2, s.105.

FIGURE CAPTIONS

Fig. 1. The kaon momentum distribution for the events from the first group. H = 14.92 kGs. Solid line - calculated with M = 497.605 MeV.

Fig. 2. The kaon momentum distribution for the events from the first group. H = 24.69 kGs. Solid line - calculated with M = 497.610 MeV.

Fig. 3. Two pion relative angle distribution of the events from the second group. H = 14.92 kGs. Solid line - calculated with M = 497.754 MeV.

Fig. 4. Two pion relative angle distribution of the events from the second group. H = 24.69 kGs. Solid line - calculated with M = 497.636 MeV.

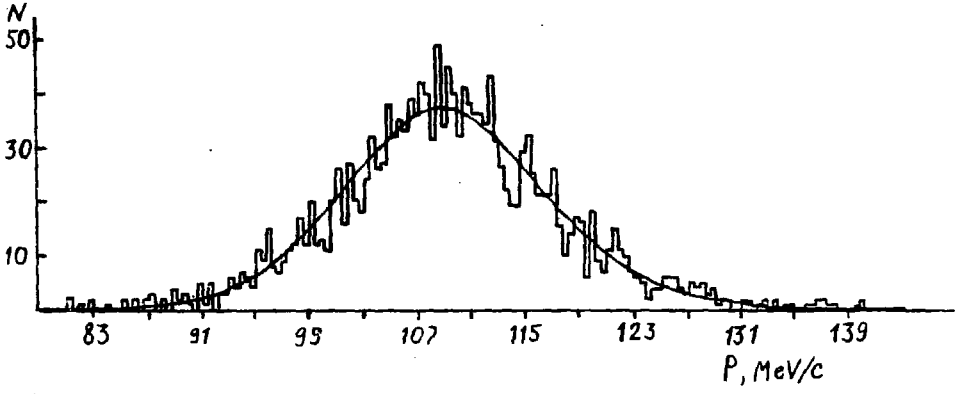
N
50
30
10
83
91
99
107
115
123
131
139
P, MeV/c

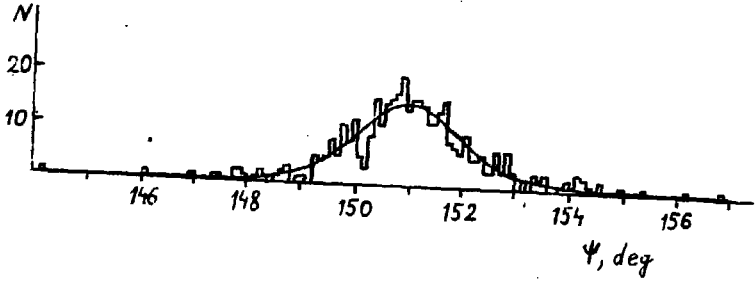
N
20
10
146
148
150
152
154
156
Ψ, deg

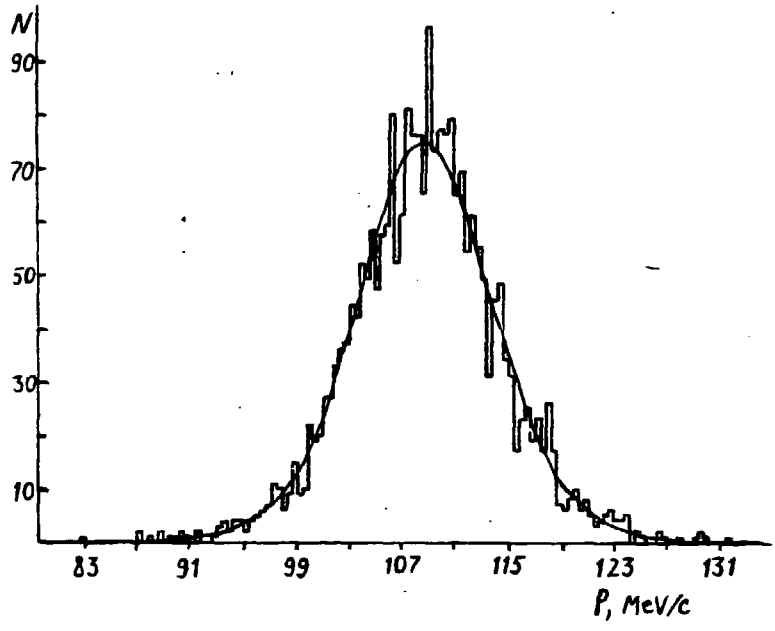
N
90
70
50
30
10
83
91
99
107
115
123
131
P, MeV/c

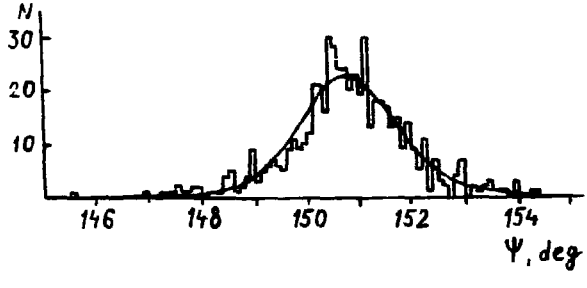
N
30
20
10
146
148
150
152
154
Ψ, deg

$\theta(1690)$ AS A GLUEBALL

Michał Majewski and Wacław Tybor

Institute of Physics, University of Łódź
Nowotki 149, 90-236 Łódź, Poland

1. The nonet of 2^{++} mesons: $A_2(1320)$, $K^{**}(1430)$, $f(1270)$, $f'(1525)$ is almost ideally mixed. The mixing angle is 28°, and deviations from ideal structures:

$$|f\rangle^{id} = |N\rangle \ , \quad |f'\rangle^{id} = |S\rangle \ ,$$

where

$$|N\rangle = \left|\frac{1}{\sqrt{2}}(u\bar{u} + d\bar{d})\right\rangle \ , \quad |S\rangle = |s\bar{s}\rangle \ , \qquad (1)$$

and ideal mass relations

$$m_f^{id} = m_{A_2} \ , \quad m_{f'}^{id} = 2\, m_{K^{**}} - m_{A_2} \qquad (2)$$

are small. These deviations were ignored for a long time, but in 1981 J. Rosner have made an attempt to treat them as a signal from an additional state, which could be a glueball [1]. The extra state is required mainly by the mass difference $m_{A_2} - m_f > 0$ and by the decay rate of $f \to \bar{\pi}\bar{\pi}$. However, it is probably not required by the present data, if only decay properties are considered [2] (but it is still allowed).

2. The meson θ ($J^{PC} = 2^{++}$) was discovered in 1982 by Cristal Ball Collaboration [3] in the gluon rich process

$$J/\psi \longrightarrow \gamma\theta \longrightarrow \gamma\eta\eta .$$

Its present values of mass and width are [4] :

$$m = (1710 \pm 5)\text{MeV}/c^2 , \qquad \Gamma = (153 \pm 10)\text{MeV}/c^2 .$$

It is regarded as a glueball candidate, but its decay pattern indicates that it can not be a pure glueball state. Its decay rates are:

$$\frac{\Gamma(\theta \to K\bar{K})}{\Gamma(\theta \to \pi\pi)} = \begin{cases} 3 : 6 & \text{(expected for pure glueball)} \\ 3 : 0{,}8 & \text{(observed).} \end{cases}$$

Therefore it is necessary to investigate the mixings in the 2^{++} multiplet for testing the glueball assignment of θ ; these mixings are more needed for θ than for the nonet.

3. The mixings of f, f', θ were investigated [5,6] with the assumption of their flavour independence. The appropriate mass operator has been taken in the form given by Fuchs [7] . Diagonalizing this operator Rosner and Tuan construct the mixing matrix V:

$$\begin{bmatrix} |f\rangle \\ |f'\rangle \\ |\theta\rangle \end{bmatrix} = V \begin{bmatrix} |N\rangle \\ |S\rangle \\ |G\rangle \end{bmatrix} \qquad (3)$$

where $|G\rangle$ is a glueball state, $|N\rangle$ and $|S\rangle$ are defined in (1).

The main feature of this matrix is that f is almost pure N state, but f' and θ are strongly mixed S and G states. For this matrix V:

a) The decay $f' \to \pi\pi$ is suppressed as a result of interference between states N and G, but not only as a result of OZI rule.

b) The decay $f' \to \gamma\gamma$ is almost totally suppressed in direct contradiction with data.

The failure of the flavour independent mixing is sometimes regarded as an argument against the gluonic nature of θ meson.

4. Rosner and Tuan construct also the phenomenological mixing matrix (desired one) describing all known experimental data on nonet and θ, but they do not justify it. It is completely different from the previous matrix.

We propose another mixing, which is based on exotic commutator method, and obtain the mixing matrix essentially identical with the phenomenological one. Hence there is no trouble with the decays of f' into $\pi\pi$ and $\gamma\gamma$.

5. Exotic Commutator Method rests on vanishing of the following commutators [8]:

$$\left[G_a,\left[m^2,G_b\right]\right] = 0 \tag{4a}$$

$$\left[G_a,\left[m^2,\left[m^2,G_b\right]\right]\right] = 0 \tag{4b}$$

$$\left[G_a,\left[m^2,\left[m^2,\left[m^2,G_b\right]\right]\right]\right] = 0 \tag{4c}$$

.....

.....

where m^2 is operator of the mass squared, $\{G_a\}$ are generators of flavour $U(3)$ group and (a,b) is the exotic combination of indices, i.e. such a combination for which the commutators (4) do not belong to an octet. These relations produce the mass formulae depending on mass squared.

We use below the particle symbols for its mass squared and the symbols of tensor mesons for any multiplet.

6. Let us consider a nonet. If $|f\rangle$ and $|f'\rangle$ are states of real particles then the isosinglet state from octet is expressible as

$$|f_8\rangle = \lambda_1 |f\rangle + \lambda_2 |f'\rangle$$

where the mixing parameters λ_i are real numbers and $\sum \lambda_i^2 = 1$.

If we impose the conditions (4a) and (4b) on the nonet states, then we obtain the Schwinger mass formula for nonet and calculate λ_1^2, λ_2^2, which are expressed by the masses of the particles from nonet.

If three constraints (4a),(4b) and (4c) are imposed, the ideal mixing is obtained:

$$f = A_2, \quad f' = 2K^{xx} - A_2, \quad \lambda_1^2 = \frac{1}{3}, \quad \lambda_2^2 = \frac{2}{3}.$$

Inclusion of the subsequent conditions from (4) does not disturb the ideality.

7. The ideality is broken if we include an extra state [9]. Then we have a decouplet and three isosinglets do mix. In this case

$$|f_8\rangle = \lambda_1 |f\rangle + \lambda_2 |f'\rangle + \lambda_3 |\theta\rangle . \qquad (5)$$

Restricting the decouplet states with the conditions (4a), (4b) and (4c) (the ideality conditions for a nonet) we obtain one mass formula and find λ^2's, which are expressed by the masses of all particles belonging to decouplet. The mass calculated from the formula, say θ, and λ^2's should be positive. We must require it additionaly, and this restricts the possible masses f and f'. One can deduce very simple necessary condition: if three states $|f\rangle, |f'\rangle, |\theta\rangle$ belong to a decouplet, then the masses of these states comply with the conditions:

$$f < A_2 < f' < 2K^{xx} - A_2 < \theta \qquad (6)$$

The necessary and sufficient conditions can be formulated as well.

These conditions are satisfied by multiplets 2^{++}, 0^{++}, 3^{--} and probably by 1^{++}, 1^{+-}, 4^{++}. The multiplets 0^{-+} and 1^{--} do not satisfy them and consequently can not be extended to decouplets. Obviously other mechanisms are responsible for their deviations from ideality.

8. The decouplet mixing matrix U defined as

$$\begin{bmatrix} |f\rangle \\ |f'\rangle \\ |\theta\rangle \end{bmatrix} = U \begin{bmatrix} |f_8\rangle \\ |f_0\rangle \\ |G\rangle \end{bmatrix} = V \begin{bmatrix} |N\rangle \\ |S\rangle \\ |G\rangle \end{bmatrix} ,$$

where $|f_0\rangle$ is $q\bar{q}$ singlet state (V is defined in (3)),

can be parametrized by three angles ϑ_1, ϑ_2, ϑ_3 :

$$U = \begin{bmatrix} c_1 \ (=\lambda_1) & -s_1c_2 & s_1s_2 \\ s_1c_3 \ (=\lambda_2) & c_1c_2c_3 - s_2s_3 & -c_1s_2c_3 - c_2s_3 \\ s_1s_3 \ (=\lambda_3) & c_1c_2s_3 + s_2c_3 & -c_1s_2s_3 + c_2c_3 \end{bmatrix}$$

where $c_j = \cos \vartheta_j$, $s_j = \sin \vartheta_j$ $(j=1,2,3)$. The elements of the first column are equal λ_1, λ_2, λ_3 respectively. Consequently, the angles ϑ_1, ϑ_3 can be expressed by the masses, but ϑ_2 remains free. It reflects the unknown mixing between two SU(3) singlets and can be determined only from decay rates.

9. The mixings occuring in the decouplet slightly change the masses of the two physical isosinglets attributed to the nonet. But the structures of these isosinglets can be drastically disturbed. It is possible to accomplish the displacement of the flavour from one particle to another, as is seen in the case of scalar mesons: we can easily get almost pure $s\bar{s}$ state for $S^X(970)$ meson [9] .

10. The mass formula for 2^{++} mesons is satisfied, if we accept the mass values presented in Table [10] . The PDG values are given for comparison [11] .

Table. The masses of 2^{++} mesons belonging to decouplet (in MeV/c^2)

	A_2	K^{XX}	f	f'	θ
Decouplet	1311	1432	1281	1522	1725
PDG	1318±5	1425±5	1274±5	1525±5	1690±30

The mixing matrix V is (in brackets the numbers from phenomenological mixing matrix [6]):

$$V = \begin{bmatrix} 0,9532 \ (0,95) & 0,0633 \ (0,07) & 0,2957 \ (0,3) \\ -0,0711 \ (-0,09) & 0,9973 \ (0,98) & 0,0157 \ (0,1) \\ -0,2940 \ (-0,3) & -0,0360 \ (-0,13) & 0,9551 \ (0,95) \end{bmatrix}$$

Obviously the decay $f' \to \pi\pi$ is suppressed by OZI rule.

We are dispenced from a duty to quote all decay rates calculable from this matrix since they are described by phenomenological matrix. As an example we cite the radiative width $f' \to \gamma\gamma$:

$$\frac{\Gamma(f' \to \gamma\gamma)}{\Gamma(A_2 \to \gamma\gamma)} = 0,124 \text{ x phase space correction.}$$

This is in agreement with the measured value of [12]

$$\Gamma(f' \to \gamma\gamma)\, B(f' \to K\bar{K}) = (0,11 \pm 0,06)\text{keV}/c^2 .$$

The decay rate $(\Theta \to K\bar{K}) : (\Theta \to \pi\pi) = 4$ is taken as an input.

We conclude, that according to available experimental data meson $\Theta(1690)$ can be understood as a particle containing about 90% of glueball state.

References

1. J.L.Rosner, Phys. Rev. D24 1347 (1981)
2. A.Bramon et al., Z. Phys. C28 573 (1985)
3. C.Edwards et al., Phys. Rev. Lett. 48 458 (1982)
4. K.Königsmann, DESY 86-009 (1986) preprint
5. H.Schnitzer, Nucl. Phys. B207 131 (1982)
6. J.L.Rosner, S.F.Tuan, Phys. Rev. D27 1544 (1983)
7. N.H.Fuchs, Phys. Rev. D14 1912 (1976)
8. M.Majewski, W.Tybor, Acta Phys. Pol. B15 267 (1984)
9. M.Majewski, W.Tybor, Acta Phys. Pol. B15 777 (1984)
10. M.Majewski, W.Tybor, Acta Phys. Pol. B17 333 (1986)
11. Particle Data Group, Rev. Mod. Phys 56 S1 (1984)
12. M.Althoff et al., Phys. Lett. 121B 216 (1983)

CHARGINO PRODUCTION AND DETECTION BY THEIR LEPTONIC DECAYS AT e^+e^- COLLIDERS

A. Leike, Sektion Physik, Karl-Marx-Universität, DDR

The chargino production at e^+e^- colliders with polarized and unpolarized electrons is considered for at least one sneutrino mass smaller than the chargino masses. The forward-backward asymmetries and the angular distributions are studied for charged leptons coming from the chargino decay. A left handed electron beam enhances the part of leptons detected in the backward region and vice versa.

Supersymmetric theories predict new particles with spins, differing from those of the known particles by half a unit. In detail they predict partners of the W bosons and the higgs, which are called wino and higgsino, respectively. These charged spin 1/2 particles may mix. Their mass eigenstates are called charginos.

The total cross section of chargino production (Fig.1a, Fig.1b) in e^+e^- collisions may exceed that of standard lepton production by a factor 10 /1/. So a rising cross section at c.m. energies $\sqrt{s} < 2m_W$ (m_W is the W-boson mass) may be a signal of chargino pair production.

As was shown in /1,2,3/, the polarization of the electrons may help in finding the origin of this increase.

We were interested in the leptons coming from the chargino decay. There are 3 leptonic and 5 hadronic decay diagrams of a chargino /4/. The branching ratio of the decays depends on the masses and mixings of SUSY particles. If at least one

sneutrino mass is smaller than the chargino masses, the leptonic two particle decay (Fig.2) is kinematically allowed and the leptonic branching ratio is almost 100%. In this case we have no background problems for c.m. energies $\sqrt{s} < 2m_W$. At c.m. energies $\sqrt{s} > m_W$ the W^+W^- pair production will give an important background, i.e. much charged leptons with missing energy.

Results

The forward-backward asymmetries of the charged leptons coming from the chargino decay (Fig.3) depend on the polarization of the electron beam and to a lower extend on the mixing model and the sparticle masses.

The angular distributions of leptons coming from chargino decay depend on the sparticle masses. Almost no dependence on the mixing model was seen for c.m. energies $\sqrt{s} \approx m_Z$.

A left handed electron beam enhances the excange (Fig.1b) of the sneutino and gives more leptons in the backward region (Fig.4).

The exchange is forbidden for a right handed electron beam. So less leptons from chargino decay will be detected in the backward region. A dependence of the angular distributions on the axial and vector couplings in the annihilation process (Fig.1a) may be seen only for detected leptons very closed to the beam.

Finally we may conclude that a polarized electron beam may help in detecting of new physics. Left handed electrons enhance the backward region of the detected leptons due to the exchange diagram (Fig.1b). The angular distributions of

the detected leptons show a strong dependence on the polarisation of the electron beam especially in regions closed to the beam ($|\cos\theta| > 0.8$).

References

/1/ P.Chiapetta et al. Nucl.Phys.B262, 495 (1985)

/2/ D.H.Schiller, D.Wänar, Si-84-18

/3/ H.Baer et al. in Physics at LEP, CERN 86-02 edited by J. Ellis and R.Peccei

/4/ A.Bartl, H.Fraas, W.Majerotto, UWThPh-1985-21

Figures

Fig.1a, Fig.1b: production diagrams of a chargino pair

Fig.2: The two particle decay diagram of the chargino

Fig.3: The forward-backward asymmetry for charged leptons coming from two particle wino decay, $m_{\tilde{W}} = 40$GeV, $m_{\tilde{\nu}} = 20$GeV
unpolarized electrons (dotted line)
right handed polarized electrons (dashed line)

Fig.4: The angular distributions for leptons coming from two particle wino decay, $m_{\tilde{W}} = 40$GeV, $m_{\tilde{\nu}} = 20$GeV for c.m. energies $\sqrt{s} = 82$GeV, $\sqrt{s} = 92$GeV and $\sqrt{s} = 102$GeV
left handed polarized electrons (dotted line)
right handed polarized electrons (dashed line)

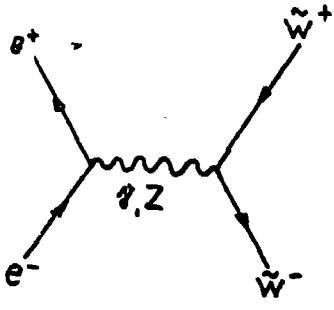

Fig. 1a

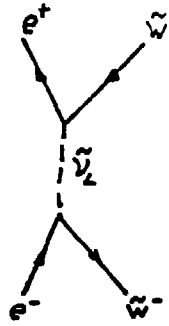

Fig. 1b

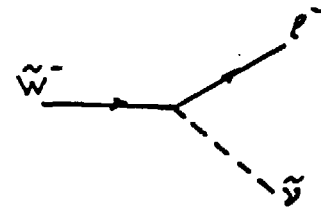

Fig. 2

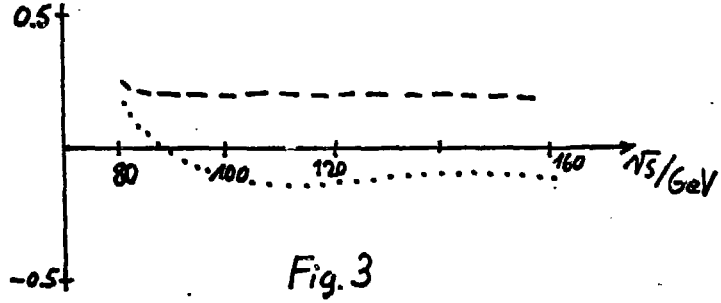

Fig. 3

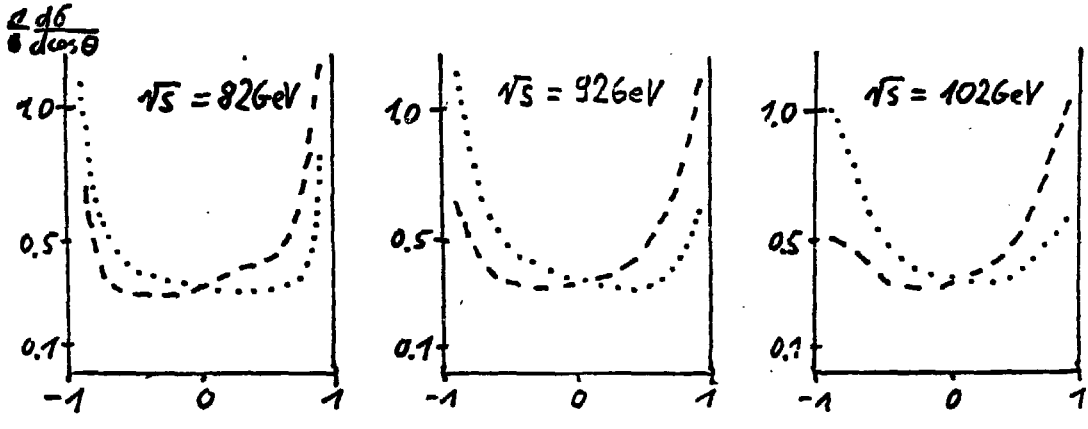

Fig. 4

THE STRONGLY COUPLED STANDARD MODEL*

R. L. Jaffe**

Center for Theoretical Physics
Laboratory for Nuclear Science
and Department of Physics
Massachusetts Institute of Technology
Cambridge, Massachusetts 02139 U.S.A.

Typeset in TEX by Roger L. Gilson

* This work is supported in part by funds provided by the U. S. Department of Energy (D.O.E.) under contract #DE-AC02-76ER03069.
** Supported in part by Boston University.

ABSTRACT

This is an abbreviated summary of work performed in collaboration with E. Farhi and M. Claudson.[1] We analyze an alternative formulation of the standard model in which the $SU(2)$ gauge interaction becomes confining at energies of order $G_F^{-1/2} \sim 300$ GeV. We show that, making reasonable dynamical assumptions, this model accounts for all electroweak phenomena up to and including the W and Z mass scale. At yet higher energies the model predicts a wealth of new phenomena.

I. INTRODUCTION

The standard electroweak theory has been completely successful in its description of physics up to 100 GeV. This success includes the predictions of the masses and couplings of the observed W and Z. The precision of the agreement between the low energy predictions of the theory and experiment indirectly tests the theory at even higher energy scales. Higher energy scales are also probed through radiative corrections and effects such as the $K_L K_S$ mass difference. To date, there is no convincing experimental data to evoke any doubt about the validity of the standard electroweak theory up to several hundred GeV.

In this paper, we explore the possibility that the success of the standard model may be shared by another theory. We will investigate the predictions of this specific theory and see how they differ from those of the standard model. Making certain reasonable dynamical assumptions, we find that the experimental predictions of this theory are also consistent with present data. However, deviations from the standard model predictions are expected and at energies well above the W mass a rich spectrum of new particles should emerge.

The theory we investigate here is the strong coupling or confining version of the standard model (SCSM).[1] This theory is based on the same lagrangian as the standard model with the parameters adjusted so that infrared growth of the gauge coupling is not cut off by symmetry breaking in the Higgs' sector. The $SU(2)_L$ gauge coupling becomes large at the weak interaction scale $\sim G_F^{-1/2} (= 293$ GeV) which is taken to be much larger than the mass parameter in the Higgs' sector. Physical particles which participate in the weak interactions, such as left-handed fermions and intermediate vector bosons, are composite particles bound by the strong $SU(2)_L$ force into $SU(2)_L$ singlets. The observed "weak interactions" are then residual interactions between these composites, analogous to the "strong interactions" between color singlets in QCD. It has already been demonstrated that this theory reproduces much of the experimental data of the weak interactions well below the W mass.[2] In this paper, we examine the dynamical assumptions required for the SCSM to produce the correct W and Z

phenomenology as well as all low energy results. We also describe some of the new physics above the W and Z mass which clearly distinguishes the SCSM from the standard model.

The SCSM is based on a renormalizable gauge field theory which cannot be analyzed perturbatively since it is strongly interacting at the energy scales of interest. Instead, we use methods of analysis familiar from hadronic physics such as symmetries, dispersion theory and effective lagrangians. Remarkably, these methods allow us to show that the long distance behavior of the theory corresponds to the observed weak interactions if we make three crucial assumptions about the dynamics of the strongly interacting theory. We must assume (i) chiral symmetry breaking is prevented by the presence of scalar fields, (ii) the effective fermion-anti-fermion-W coupling is small, and (iii) the W and Z are much lighter than the typical mass scale of the theory. We know of no compelling arguments against any of these assumptions, however, we are also unable to offer any firm justifications for them.

If the weak interactions are in fact described by this strongly interacting theory, then how has the standard model managed to masquerade as the truth for so long? Why does the impostor theory work so well? We will show, given our assumptions, that the low energy effective theory, consisting of operators of dimension four or lower which describes the interactions of the lightest bound states in the SCSM, is in fact the standard model in the unitary gauge. [Actually, certain "Higgs scalar" couplings may differ in the two theories and could, in principle, distinguish between them.] The standard model is then a very good approximation of the long distance behavior of the SCSM. The phenomenological successes of the standard model might in fact be successes of the SCSM. Ultimately, of course, the only reason to depose the standard model is if it fails to agree with experiment. Should this occur, then the SCSM may be the truth behind the charade of the standard model.

In the next section we summarize the SCSM and explain how it can account for the broad features of weak phenomenology. We describe its spectrum and its symmetries. We examine the light composite fermions and the composite bosons which arise in the model and find that under reasonable conditions they coincide with the observed quarks, leptons and weak bosons. We explore the implications for the model of the small observed value ($\bar{g} \simeq 0.66$) of the W-fermion antifermion coupling. We study electromagnetic effects in the SCSM and establish an equivalence between the SCSM at low energies and the standard model in unitary gauge.

Section III gives a brief summary of the SCSM interactions at energies up to of order m_W. For a more complete analysis, see Ref. [1]. We show that reasonable dynamical assumptions can render the SCSM indistinguishable from the standard model in all experiments to date. More accurate tests of certain standard model predictions (*e.g.*, $m_W^2 = \pi\alpha/\sqrt{2}G_F \sin^2\theta_W$) as well as searches for new phenomena at high energies can distinguish the SCSM from the perturbative version of the standard model.

In Section IV we examine the exotic particles expected at energies above m_W in the SCSM. We briefly discuss the phenomenology of excited quarks and leptons, excited weak bosons, dileptons, diquarks and leptoquarks. The lower limits on the masses of exotic particles in the SCSM which come from low energy tests of the standard model suggest that we shall have to wait for the next generation of accelerators to see these particles, if they do exist.

The possibility that neutral current phenomenology could be understood through a mixing between the photon and a neutral member of a global $SU(2)$ triplet, was first discussed by Bjorken[3] and Hung and Sakurai.[4] The fact that in strong coupling the standard model can have a low energy spectrum with quantum numbers that match those of the perturbative spectrum was shown by several groups.[5,6,7,8] That the SCSM could reproduce weak interaction phenomena in detail (at energies below the W mass) and might be an alternative to the standard theory was first demonstrated by Abbott and Farhi.[2] Many other composite models have been introduced.[9] As far as we are aware, the SCSM[1] is the only one among these without serious phenomenological flaws (*e.g.*, too many or too few unbroken chiral symmetries, trouble with anomalies, flavor changing neutral currents). Kögerler and Schildknecht[10] and Schrempp and Schrempp[11] have studied weak interactions in generic composite models aided by the assumption of "strong vector dominance".[12] Our work focuses on a single model, the SCSM, which is the only one we believe is viable and we show that it can account for *all* weak phenomena. Although we do not invoke vector dominance *per se*, the constraints on masses and couplings in the SCSM which enable it to reproduce experiment can be interpreted as limits on the corrections to strong vector dominance.

II. THE SCSM: SYMMETRIES, INTERACTIONS AND COMPOSITE PARTICLES

II.1 SYMMETRIES AND MASSLESS COMPOSITES

In this section, we review some of the basic features of the strongly coupled standard model. We begin with the standard electroweak lagrangian with the usual charge assignments. The gauge group is $SU(2)_L \times U(1)$ with N left-handed fermion doublets ψ_L^a ($a = 1,\ldots,N$). For now, we neglect QCD strong interactions so that the index a labels colors as well as flavors. Thus, $N = 4n_f$ for n_f families of quarks and leptons. Each doublet has $U(1)$ charge y_a with $y_a = 1/6$ for quarks and $y_a = -1/2$ for leptons. For each left-handed quark doublet, there are two right-handed $SU(2)_L$ singlets u_R and d_R with $U(1)$ charges 2/3 and -1/3, respectively. Also, for each lepton doublet, there is a right-handed $SU(2)_L$ singlet e_R with $U(1)$ charge -1. [Right handed neutrinos can be included; they have $y = 0$.] We collectively denote these right-handed singlets by ψ_R^b for $b = 1,\ldots,7n_f$ and their $U(1)$ charges by y_b. There is also one scalar field ϕ which is an $SU(2)_L$ doublet with $U(1)$ charge -1/2. The lagrangian is then

$$\begin{aligned}\mathcal{L} = {} & i\bar{\psi}_{La}\not{D}\psi_L^a + i\bar{\psi}_{Rb}\not{D}\psi_R^b + \frac{1}{2}\,tr\left[(D_\mu\Omega)^\dagger(D^\mu\Omega)\right] \\ & - \frac{1}{4}\mathcal{F}_{\mu\nu}\mathcal{F}^{\mu\nu} - \frac{1}{2}\,tr\,G^{\mu\nu}G_{\mu\nu} - \frac{\lambda}{2}\left[tr\,\Omega^\dagger\Omega - 2v^2\right]^2\end{aligned} \tag{2.1}$$

where the covariant derivatives are given by

$$\begin{aligned}D_\mu\Omega &= \partial_\mu\Omega - ig_2\omega_\mu\Omega + \frac{1}{2}ig_1\Omega\tau_3 a_\mu \\ D_\mu\psi_L^a &= \partial_\mu\psi_L^a - ig_2\omega_\mu\psi_L^a - ig_1 y_a a_\mu\psi_L^a \\ D_\mu\psi_R^b &= \partial_\mu\psi_R^b - ig_1 y_b a_\mu\psi_R^b\end{aligned} \tag{2.2}$$

with $\omega_\mu = \frac{1}{2}\omega_\mu^i \tau^i$ for $i = 1, 2, 3$. Also, we have written the scalar fields as a 2×2 matrix

$$\Omega = \begin{pmatrix} \phi_1 & -\phi_2^* \\ \phi_2 & \phi_1^* \end{pmatrix} \quad \Omega^\dagger \Omega = (\phi_1^* \phi_1 + \phi_2^* \phi_2) \begin{pmatrix} 1 & 0 \\ 0 & 1 \end{pmatrix} \ . \tag{2.3}$$

and

$$\begin{aligned} \mathcal{F}_{\mu\nu} &= \partial_\mu a_\nu - \partial_\nu a_\mu \\ G_{\mu\nu} &= \partial_\mu \omega_\nu - \partial_\nu \omega_\mu - i g_2 [\omega_\mu, \omega_\nu] \ . \end{aligned} \tag{2.4}$$

Later we will consider the effects of Yukawa couplings between the scalar field ϕ and the left- and right-handed fermions as well as QCD. However, it is first convenient to discuss the theory in the limit in which these effects are neglected.

There are two important dimensionful parameters which characterize this theory. The first, v^2, appears in the scalar field potential. Positive v^2 corresponds to ordinary spontaneous symmetry breaking, while, for v^2 negative, the gauge symmetries are unbroken and the scalar fields develop masses of order $\sqrt{-\lambda v^2}$. The other dimensionful parameter is Λ_2, the scale parameter of the $SU(2)_L$ gauge group. If v^2 is much less than Λ_2^2, the running coupling constant g_2 becomes large at energies of order Λ_2 just as the running coupling constant of QCD becomes large at $\Lambda_{\rm QCD}$. For $v^2 >> \Lambda_2^2$, the vacuum expectation value of the Higgs field cuts off the growth of the coupling and this coupling never gets much larger than $g_2(v)$. This is the case in the standard model where $g_2(v = 246 \text{ GeV}) \simeq 0.66$. When $g_2(v)$ is small, Λ_2 can be defined as the scale where the coupling would get large if v^2 where zero. We will characterize the theory as strongly coupled or confining for $\Lambda_2^2 >> v^2$ and we will use the language of spontaneous symmetry breaking for $v^2 >> \Lambda_2^2$.

There are two other couplings to consider. The first is the coefficient of the ϕ^4 term, λ, which we assume to be fixed and of order one or smaller. We will not attempt to study how the dynamics changes as λ is varied. The other coupling is g_1, which determines the strength of the ordinary electric charge in both the confining and the spontaneously broken modes. This coupling is always chosen to give the correct value of the fine structure constant. In all cases, g_1 is small.

For $g_1 = 0$, the lagrangian (2.1) possess the exact global symmetry group $SU(N) \times SU(2)_W$ where the $SU(N)$ is associated with the N fermions ψ_L^c. We are not concerned here with symmetries which act only on the right-handed fermions since these are neutral with respect to the $SU(2)_L$ force. The $SU(2)_W$ symmetry arises from the invariance of the lagrangian (2.1) under the transformation $\Omega \to \Omega h$ with $h \in SU(2)$. If $g_1 \neq 0$ or if color forces or the Yukawa couplings are included in the full theory, $SU(N) \times SU(2)_W$ is only an approximate symmetry. Because these symmetry breaking effects are small at the scale $G_F^{-1/2}$, we can sensibly discuss the exact symmetry limit.

We now consider the strong coupling version of the theory, that is $\Lambda_2^2 >> v^2$. The scale, Λ_2, characterizes the interactions of the SCSM and is of order $G_F^{-1/2} \simeq 300$ GeV. The spectrum of physical particles consists of $SU(2)_L$ gauge singlets, including fundamental particles which are neutral with respect to the $SU(2)_L$ force such as the right-handed fermions and the $U(1)$ gauge boson a_μ. In addition, we must consider bound state gauge singlets much like the mesons and baryons of QCD. We can classify the composite particles by writing down (low dimension) $SU(2)_L$-singlet composite

operators which create the states of interest from the vacuum. However, $SU(2)_L$ is strongly interacting so any attempt to attribute a *simple* particle content to a bound state should be done with caution. We can combine each fermion ψ_{La} with the scalar field ϕ in two different ways to make a gauge singlet fermion. With $\alpha, \beta = 1, 2$ being $SU(2)_L$ indices, we let

$$F_L^a = \begin{pmatrix} \phi^{*\alpha}\psi_{L\alpha}^a \\ \phi_\alpha \epsilon^{\alpha\beta}\psi_{L\beta}^a \end{pmatrix} = \Omega^\dagger \psi_L^a \quad , \qquad (2.5)$$

be an interpolating field which connects two spin 1/2 gauge singlet fermions for each ψ_L^a to the vacuum. F_L^a transforms as an $(N, 2)$ under the global group $SU(N) \times SU(2)_W$.

For the SCSM to be a viable model, these composite fermions must be massless in the exact symmetry limit. A necessary condition for the existence of massless composite fermions is that they satisfy 't Hooft's anomaly matching conditions. It is easy to see that the composite fermions F_L^a match the anomalies of the fundamental fermions ψ_L^a. The only diagram to consider is the $SU(N)^3$ triangle. The fermions ψ_L^a are doublets under the $SU(2)_L$ gauge group and transform as two N's of $SU(N)$, while the bound states F_L^a are doublets under the global $SU(2)_W$ and also transform as two N's. Thus, these bound states produce the same anomaly as the fundamental fermions and may, in fact, be massless composite fermions. However, it may be energetically favorable for condensates such as $\langle \psi_L^a \psi_L^b \rangle$ to form, in which case chiral symmetry is spontaneously broken. If so, all fermions would acquire mass and the anomalies would be saturated by Goldstone bosons. If $-v^2 >> \Lambda_2^2$, no $SU(2)_L$ gauge symmetry breaking is induced by the Higgs potential, and the scalar field ϕ has a mass of order $\sqrt{-v^2}$ which is much larger than the composite binding energy $\sim \Lambda_2$. In this case, we expect the bound states F_L^a to be massive because they contain a heavy constituent ϕ and chiral symmetry breaking occurs. [Another way to see this is to note that in the limit of very heavy scalar constituents the SCSM becomes a theory of N left-handed fermion doublets strongly interacting at the scale Λ_2. $N/2$ of the fermions may be replaced by their conjugate fields, which destroy right-handed anti-doublets. Since $SU(2)$ representations are real, these are equivalent to right-handed doublets. The resulting theory is $N/2$ flavor, two color QCD which certainly breaks its chiral symmetries.[13]] On the other hand, if $v^2 >> \Lambda_2^2$, the theory is in its familiar perturbative mode and the standard wisdom is that no spontaneous chiral symmetry breaking occurs. There must be a chiral symmetry breaking phase transition controlled by the parameter Λ_2^2/v^2. In the SCSM, we take $\Lambda_2^2 >> v^2$ and, in order to avoid spontaneous chiral symmetry breaking, we will also assume that, if v^2 is negative, its magnitude is not greater than of order Λ_2^2. Thus, our first assumption is that in the SCSM with a binding scale Λ_2 and scalar fields whose masses do not exceed Λ_2, chiral symmetry breaking does not occur and the fermions F_L^a are massless. There is no reason to expect any states other than the fermions F_L^a to be massless.

II.2 SCALAR-SCALAR BOUND STATES

The SCSM also contains gauge singlet bound states whose interpolating fields contain two fundamental scalars. These are interesting because their properties reproduce much of the phenomenology of the fundamental $W^\pm$ and Z of the standard model. The simplest interpolating field for such bound states is the $SU(2)_L$ invariant, spin-0

operator $H \equiv \phi_a^* \phi^a = 1/2\ tr\ [\Omega^\dagger \Omega]$. We identify the lowest mass state connected by this operator to the vacuum with the Higgs particle of the standard model. Its mass is determined by the mass of its constituents and the strong interaction dynamics and should be of order $G_F^{-1/2}$, although we have no way to compute its value reliably.

In the absence of fermion masses, this particle, like the usual Higgs particle, does not couple to fermion anti-fermion pairs. Dimension four operators of the form $H\bar{F}_L F_L$ vanish because of the left-handed nature of F_L. Couplings of the form $H\bar{F}_L \psi_R$ do not occur because the right handed fermions do not feel the $SU(2)_L$ force. The addition of a Yukawa coupling, $g_{ab}\bar{\psi}_L^a \Omega \psi_R^b$, to the underlying lagrangian (2.1) would induce $H\bar{F}_L\psi_R$ couplings in the effective theory and would generate masses for the lightest composite fermions with $m^{ab} \sim \Lambda_2 g^{ab}$. Therefore, $g^{ab} \sim m^{ab}/\Lambda_2$ are typically very small. In the standard model, the Higgs-Yukawa couplings are $\sim G_F^{1/2} m_f$ which are roughly as small. Thus, the observation of a scalar particle which couples to fermion anti-fermion pairs with an amplitude proportional to the fermion mass would not distinguish the SCSM from the usual form of the standard model.

Spin one bound states can be made using the interpolating fields $W_\mu^i = tr[\Omega^\dagger D_\mu \Omega \tau^i]$. These particles form a triplet under the global $SU(2)_W$ and are degenerate in the absence of electromagnetism. The two charged states are identified with the $W^\pm$, while the neutral component W^3 mixes with the photon and produces a state heavier than the $W^\pm$ which is identified as the Z. There is no analogous $SU(2)_W$ singlet operator so there is no reason to expect an $SU(2)_W$ singlet vector particle near in mass to the $\vec{W}$. The $SU(2)_W$ singlet operator $Tr[\Omega^\dagger D_\mu \Omega]$ is proportional to $\partial_\mu H$ which does not create a spin one particle from the vacuum.

In the absence of electromagnetism, we can write down an effective lagrangian consistent with the global symmetries which incorporates the self-interactions of the spin-one bound states and their interactions with the bound state fermions F_L^a. The most general $SU(2)_W$ invariant effective lagrangian including all terms of dimension 4 or less is

$$\begin{aligned}\mathcal{L}_{\rm eff}^0 = {} & i\bar{F}_{La}\not{D} F_L^a - \frac{1}{4}\vec{W}^{\mu\nu}\cdot\vec{W}_{\mu\nu} + \frac{1}{2}m_W^2 \vec{W}^\mu \cdot \vec{W}_\mu + \bar{g}\vec{W}^\mu \cdot \vec{j}_{L\mu} \\ & - \frac{1}{2}g_3 \vec{W}^{\mu\nu}\cdot(\vec{W}_\mu \times \vec{W}_\nu) + \frac{1}{4}g_4(\vec{W}^\mu \cdot \vec{W}_\mu)^2 + \frac{1}{4}g_4'(\vec{W}^\mu \cdot \vec{W}^\nu)(\vec{W}_\mu \cdot \vec{W}_\nu)\end{aligned} \tag{2.6}$$

where $\vec{W}_{\mu\nu} = \partial_\mu \vec{W}_\nu - \partial_\nu \vec{W}_\mu$ and $\vec{j}_L^\mu = \frac{1}{2}\bar{F}_L^a \vec{\tau} \gamma^\mu F_L^a$. Here, $\bar{g}$, g_3, g_4 and g_4' are dimensionless couplings which characterize the interaction between on-shell, physical composite particles much like the ρ-nucleon, ρ^3 and ρ^4 couplings. In the SCSM they are determined by the underlying gauge theory. However, their values are not equal to that of the gauge coupling and cannot be calculated in any known manner from the $SU(2)_L$ strong interaction dynamics.

The reason we include only operators of dimension four or lower is that higher dimension operators have coefficients which are proportional to the scale factor, Λ_2, to a negative power. As we will show, the model can account for W and Z phenomenology only if the scale Λ_2 is much larger than m_W, perhaps by a factor of five. In this case, higher dimension operators are suppressed at energies up to m_W. We do not include a four fermion operator at this stage because it has dimension six. However, a four

fermion operator will be induced through the exchange of W's. Its coefficient will be of order m_W^{-2} which is much larger, by assumption, than Λ_2^{-2}, so it is consistent to keep in the effective four fermion theory only operators induced by exchanges. [The fact that a compositeness scale much greater than m_W might be a desirable feature in composite models of the weak interactions has been suggested in other contexts.][14,15]

Of the many couplings in eq. (2.6) only $\bar{g}$ can so far be inferred from experiment. Notice that the exchange of W's between fermions via the lagrangian (2.6) leads to an effective four fermion theory at energies well below m_W of

$$\mathcal{L}_{\text{eff}} = i\bar{F}_L^a \not{\partial} F_L^a - \frac{\bar{g}^2}{2m_W^2} \vec{J}^{\mu}_L \cdot \vec{J}_{\mu L} \quad . \tag{2.7}$$

For this to match the usual four-fermion interaction we require

$$\frac{\bar{g}^2}{2m_W^2} = \frac{4G_F}{\sqrt{2}} \quad . \tag{2.8}$$

[We are neglecting electromagnetism, but our results are still strictly true for the charged current interactions.] We are assuming here that the dominant contribution to the effective four-fermion operator comes from W exchange. Clearly, there will be contributions from other states, *e.g.* excited W's. The reasonableness of this assumption will be examined later. Using measured values of the W mass (81 GeV) and G_F, eq. (2.8) implies that $\bar{g}$ takes the same value $\bar{g} \simeq 0.66$ as the gauge coupling of the standard model in the pertubative mode.

II.3 THE RISE AND FALL OF THE COUPLING

There is a remarkable similarity between the low energy spectrum of the SCSM and the usual spontaneously broken standard model. Assuming no chiral symmetry breaking in the SCSM, both theories have massless fermions transforming as an $(N, 2)$ under the unbroken global symmetry group $SU(N) \times SU(2)_W$. [In the standard model, the unbroken global $SU(2)_W$ is the diagonal sum of the $SU(2)$ discussed previously and global $SU(2)_L$ gauge transformations.] Both theories have a spin zero particle transforming as a $(1,1)$ and three spin one W's transforming as a $(1,3)$. This is an example of "complementarity"[5,6,7,8] which states that in a gauge theory with a Higgs field transforming in the fundamental representation, there is no phase transition between the confining and spontaneously broken regions of parameter space. This should not be taken to mean that all Green's functions are independent of the parameters. Rather, it says that the Green's functions change smoothly as underlying parameters are varied. In fact, complementarity cannot hold for all values of Λ_2^2/v^2 in this model since, as we have argued, when $-v^2$ is much greater than Λ_2^2 spontaneous breakdown of the $SU(N)$ chiral symmetry must occur.

Let us consider the interaction between the lightest spin one triplet of particles, W_μ^i, and the massless fermions F_L^a. The on-shell $WF_L\bar{F}_L$ coupling is given by eq. (2.6) regardless of the relative size of the parameters v^2 and Λ_2^2. The dimensionless coefficient $\bar{g}$ is a function of the ratio Λ_2^2/v^2. It is measured, for example, in the decay $W \to F_L\bar{F}_L$ or by independent measurements of G_F and m_W. To see how $\bar{g}(\Lambda_2^2/v^2)$

the anomaly-free condition is

$$D - D' - 10 = 0. \qquad (6)$$

Since we want to consider X^{α} as a component of a Majorana spinor, it follows that in our approach the relevant space-times are those for which the Majorana-Weyl [11] condition can be imposed, we see that $D'=2^{\frac{1}{2}(2mod8)}$ so D' = 2, 16 ... . However, only for two- and sixteen-component spinors we can have consistent supergravity theories in dimensions 2 and 10 and we see that D may be 12 or 26. This last dimension is of great interest since it corresponds to the heterotic strings construction [2], in which the number of bosonic and fermionic dimensions is respectively 26 and 16.

From what was said above it seems that the last, so-called doubly graded σ-model, has bright prospects. There are however many problems that must be solved including finding the correspondence with D=10, N=1 supergravity and/or Yang-Mills-supergravity system, anomaly-free and finiteness conditions. Work in this direction is in progress.

References

[1] for to-date collection of papers, see J.H. Schwarz ed., Superstrings; World Scientific (1985).

[2] D. Gross, J. Harvey, E. Martinec, R. Rohm, Nucl. Phys. B256 (1985) 253 and B267 (1986) 75.

[3] J.P. Candelas, G.T. Horowitz, A . Strominger, E. Witten, Nucl. Phys. B258 (1985) 46.

[4] L. Alvarez-Gaumé, D.Z. Friedman, S. Mukhi, Ann. Phys. 134 (1981) 85.

[5] E.S. Fradkin, A.A. Tseytlin, Nucl. Phys. B261 (1985) 1;
C.G. Callan, D. Friedau, E. J. Martinec, M.J. Perry, Nucl. Phys. B262 (1985) 593.

[6] J.W. van Holten, NIKHEF-H preprint 86-11, to be published in Nucl. Phys. B.

[7] J. Kowalski-Glikman, J.W. van Holten, NIKHEF-preprint 86-14.

[8] R. Arnowitt and P. Nath in Unification of the Fundamental Particle Interactions, Eds. S. Ferrara, J. Ellis and P. van Nieuwenhuizen, Plenum Press 1980 and references therein.

[9] B.E.W. Nilsson, Nucl. Phys. B188 (1981) 176.

[10] P. Bouwknecht, P. van Nieuwenhuizen, Leiden preprint, August 1985.

THEOREM PROVING WITH FIRST-ORDER PREDICATE LOGIC: II

B.Humpert*)

Institut de Physique Nucleaire
Universite de Lausanne
CH-1000 LAUSANNE, Switzerland

and

Artificial Intelligence Group
HASLER Research Laboratories
CH-3000 BERN 14, Switzerland

Abstract

We give an introduction into Theorem Proving by presenting in this second paper the basic resolution refinements: semantic resolution, linear resolution, and paramodulation. Semantic resolution introduces the predicate ordering and uses semantic criteria to split the set of input clauses into two groups; resolution is then blocked between the members of the same group. In linear resolution, one of the two parent clauses must be the preceding resolvent. If the second parent clause is an input/unit clause, the number of possible resolutions is further reduced. Combining the concepts of linearity and ordering, we arrive at ordered linear resolution. Due to its extended set of equality axioms, the equality predicate introduces an additional complexity into resolution which, to a large degree, is reduced by paramodulation. Paramodulation is compatible with several of the earlier mentioned resolution techniques. Since this tutorial is intended as a rapid introduction into the essential concepts of the resolution refinements, we skip all proofs but add illustrative examples.

*) also at CERN.

1. INTRODUCTION

The prospect of having a computer system that can draw logically correct conclusions is doubtless a reason for excitement. 'Theorem Proving' in the framework of first−order predicate logic [1] offers such a possibility with a range of applications going far beyond mathematics. Theorem Proving is in the title of this paper although perhaps 'Automated Reasoning' [2] would have been more appropriate.

This paper grew out of the interest to understand the notions and concepts which permitted the realization of 'Automated Reasoning Programs' or computer systems. It is the second part of a set of tutorial lectures and focuses on the refinements of Robinson's resolution principle. We sofar considered the resolution principle as an inference rule that can be used to generate new clauses from old ones. We also have seen that unlimited applications of the resolution may generate many irrelevant clauses besides of useful ones. Although the deletion strategy can be used to delete some of the irrelevant and redundant clauses after they are generated, time has already been wasted by generating them. Furthermore, if useless clauses are generated, many resources such as computer time and memory are required to determine whether they are indeed irrelevant and redundant. Therefore in order to have efficient theorem proving procedures, we must prevent large numbers of useless clauses from being generated. This leads us to the discussion of the refinements of resolution.

There are basically three different types of refinements: semantic resolution [3], linear resolution [4] and paramodulation [5]. Semantic resolution introduces the predicate ordering and uses semantic criteria to split the set of input clauses into two groups; resolution is then blocked between the members of the same group. In linear resolution, one of the two parent clauses must be the preceding resolvent. If the second parent clause is an input or unit clause, the number of possible resolutions is further reduced at the price that the completeness property in full generality is not valid any longer. Combining the concepts of linearity and ordering, we arrive at the ordered linear resolution. Due to its extended set of equality axioms, the equality predicate introduces an additional complexity into resolution which is reduced, to a large extent, by paramodulation. In addition, paramodulation has the advantage of being compatible with several of the earlier touched resolution refinements.

These notes are intended as a rapid introduction into the main resolution refinements and the needed terminology. We consequently leave aside all proofs and focus on the presentation of results and their practical use, refering for a deeper understanding of the subject to the specialized literature [2,6].

This paper is organized as follows: in section 2 we summarize some of the earlier insights from paper I concerning resolution, soundness and completeness. Section 3 focuses on the semantic resolution refinements such as: PI−Resolution [7], Hyper−Resolution [8], UR−Resolution [17], Set−of−Support Resolution [9], O−Resolution [10], OI−Resolution [11], Lock−Resolution [12]. The linear resolution refinements are discussed in section 4 where we consider in particular: Linear−Resolution [4], Input−Resolution [13], Unit−Resolution [13], and OL−Resolution [14]. Section 5 explains Paramodulation [5] and its combination with some of the earlier mentioned resolution refinements such as: Hyper−, Input−, Unit−, and Linear−Paramodulation [15]. In section 6 we give a few hints at the best applicability of the above resolution refinements, and section 7 is reserved for the conclusions.

2. RESOLUTION, SOUNDNESS, COMPLETENESS

This section summarizes the earlier insights from paper I concerning: −Resolution, Soundness and Completeness.

2.1 Resolution Principle [16]

The general inference technique to derive new clauses from known ones and their successive use to derive the empty clause □, is called the 'Resolution Principle' (denoted by ℜ). This principle makes use of 'Factorization' and 'Binary Resolution' on any (unsatisfiable) clause set without giving any preference to particular clauses or selecting a specific proof strategy. For completeness we repeate here the essential notions.

Factor:

If two (or more) literals with the same sign of a clause G have a most general unifier θ=MGU, then $G\theta$ is called a 'unit factor' of G:

Factor $\mathbf{F}$:

1) $G(..L_1..L_2..)$: same−sign L's
2) $\exists\, \theta = MGU(L_1,L_2)$:
3) $\mathbf{F}(G) = G\theta$: includes G

Binary Resolvent:
Let G and H be two clauses with no variables in common. Let L_1 and L_2 be two literals in G and H, respectively. If L_1 and $\sim L_2$ have a most general unifier θ=MGU, then the clause: $\mathbf{BR}(G,H) = \{G\theta - L_1\} \cup \{H\theta - L_2\}$ is called a 'binary resolvent'. The literals L_1 and L_2 are called 'literals resolved upon', and G,H are the 'parent clauses' of $\mathbf{BR}$:

Binary Resolvent $\mathbf{BR}$:

1) $G(..L_1..)$, $H(..L_2..)$: diff−sign L's
2) $\exists\, \theta = MGU(L_1,\sim L_2)$:
3) $\mathbf{BR}(G,H) = \{G\theta - L_1\theta\} \cup \{H\theta - L_2\theta\}$:

Resolvent:
A 'resolvent' of the (parent) clauses G and H is one of the following binary resolvents: (i) a $\mathbf{BR}$ of G and H, (ii) a $\mathbf{BR}$ of clause G and a factor of H, (iii) a $\mathbf{BR}$ of a factor of G and the clause H, (iv) a $\mathbf{BR}$ of a factor of G and a factor of H:

Resolvent $\mathbf{R}$: $\mathbf{R}(G,H) = \mathbf{BR}(\underbrace{\mathbf{F}(G),\mathbf{F}(H)}_{\text{Clause or Factor}})$

2.2 *Soundness*

The resulting process of deriving new clauses from old ones will eventually derive the empty clause, if and only if, the original clause set is unsatisfiable. The 'only if' part of this is the soundess theorem:

If a formula S, in conjunctive normal form, is satisfiable
and if C is derived from two clauses in S by $\mathbf{R}$−resolution,
then S∧C is satisfiable.

It thus states that we cannot produce an unsatisfiable conjunction of clauses, and in particular, one containing the empty clause, from a satisfiable one.

Soundness Theorem: If there exists an $\mathbf{R}$−refutation of a general clause set S, then S is unsatisfiable:
S unsatisfiable <= $S \vdash_{\mathbf{R}} \square$

Since the basic resolution step is common to all successive resolution refinements, the 'soundness property' is almost never endangered.

2.3 *Completeness*

That the inference of new clauses via $\mathbf{R}$ −resolution will always lead to the empty clause □, provided the original clause−set S is unsatisfiable, is guaranteed by '$\mathbf{R}$−completeness'.

Completeness Theorem: If a clause set S is unsatisfiable, then there is an $\mathbf{R}$ −deduction of the empty clause:
S unsatisfiable => $S \vdash_{\mathbf{R}} \square$

The completeness property is by no means a resolution-inherent property and it has to be ensured explicitly for each of the resolution refinements. Choosing a particular proof strategy by deleting specific types of clauses, or preventing sets of clauses from resolving amongst themselves, or other possible restrictions, can lead to the loss of refutation completeness, meaning that the empty clause might or might not be found. It therefore is necessary that the completeness property is explicitly ensured for each resolution refinement.

3. SEMANTIC RESOLUTIONS

In this section we present those resolution refinement which use semantic criteria to split the set of initial clauses into subsets. It is divided into several sub-sections each one considering a particular method.

3.1 Introduction

In order to illustrate the essentials of semantic resolution let us consider the following simple example. A set of clauses be given by

$$S = \{\ \underset{(1)}{\sim P \vee \sim Q \vee R}\ ,\ \underset{(2)}{P \vee Q}\ ,\ \underset{(3)}{Q \vee R}\ ,\ \underset{(4)}{\sim R}\ \}$$

To prove the unsatisfiability of the set S we will apply binary resolution by resolving first the original clauses against each other, and then the original clauses against the deduced resolvents. We thus arrive at the set of clauses

S =	(1) = ~P ∨ ~Q ∨ R	from S	} S
	(2) = P ∨ Q	from S	
	(3) = Q ∨ R	from S	
	(4) = ~R	from S	
$\overline{R}$=	(5) = ~Q ∨ R	from (1)+(2)	} S × S
	(6) = ~P ∨ R	from (1)+(3)	
	(7) = ~P ∨ ~Q	from (1)+(4)	
	(8) = P	from (2)+(4)	
	(9) = Q	from (3)+(4)	
	(10) = ~Q ∨ R	from (1)+(8)	} S × $\overline{R}$
	(11) = ~P ∨ R	from (1)+(9)	
	(12) = R	from (2)+(6)	
	(13) = ~Q	from (4)+(5)	
	(14) = ~P	from (4)+(6)	
	(15) = □	from (4)+(12)	

Among all these generated clauses, only (6) and (12) are actually used in the proof. All other clauses are irrelevant. Is it possible to have some mechanisms that can reduce the number of useless clauses being generated ? Indeed, there are such mechanisms and we shall now discuss them in detail.

Let us imagine that we can, in some way, divide the set of S clauses into two groups, S_1 and S_2. Let us further imagine that we do not allow clauses within the same group to be resolved with each other. This will obviously cut down the number of clauses being generated. Let us assume that in the above example the two clause sets are:

$$S_1 = \{\ \underset{(2)}{P \vee Q}\ ,\ \underset{(3)}{Q \vee R}\ \} \qquad S_2 = \{\ \underset{(1)}{\sim P \vee \sim Q \vee R}\ ,\ \underset{(4)}{\sim R}\ \}$$

Since clause (1) and clause (4) are both in S_2, (1) and (4) will not be resolved. Thus we have succeeded in blocking the resolution: (1)+(4). As we shall see, this blocking will not affect our ability to deduce the empty clause □.

The question is: how do we divide the clauses into two groups ? In semantic resolution, we use an interpretation to divide clauses. This is why this kind of resolution is called SEMANTIC RESOLUTION. Note that in the above example, the clauses (2) and (3) are falsified by the I−interpretation I = { ~P, ~Q , ~R }, while the clauses (1) and (4) are satisfied by I. Therefore, this interpretation can be used to divide S into S_1 and S_2, where S_2 contains the clauses falsified by I and S_2 contains those satisfied by I. The reader should remember that we are dealing with an unsatisfiable set of clauses. No interpretation can satisfy or falsify all clauses. Therefore, every interpretation divides S into two non−empty sets of clauses. We shall see in the following that any interpretation can be used.

Another means to block unnecessary resolutions is offered by the P−ordering of the predicate symbols. Suppose we order all predicate symbols appearing in the clauses of S by the relation

$$P > Q > R$$

and we consider the binary resolution of clauses (one from S_1 and one from S_2). We now require that the resolved literal L in the S_1−clause G shall be of higher or equal priority than (or contain) all predicate symbols in that clause

$$L_{\mathbb{R}} \geq \text{Predicates}(G)$$

In this way we have blocked the resolvants: (2)+(4) and (3)+(4) because R is not the largest literal in (2) and (3).

The foregoing ideas: the use of an I−interpretation to divide clauses into two groups and of a P−ordering of the predicate symbols to reduce the number of possible resolvents, are important concepts in semantic resolution which shall be further explained in the following.

3.2 *PI−Resolution*

This resolution allows the deduction of a resolvant with several (not only two) clauses being involved. This has the advantage of jumping over a whole set of binary resolution step. We first will introduce some new notions.

PI−Resolvent, PI−Clash:
Let I be an interpretation and P be an ordering of all predicate symbols. A finite set of clauses, composed of "Satellites" E_i which must be false in I and a "Nucleus" N ($\equiv R_1$):

$$[\underbrace{E_1, E_2, \ldots, E_q}_{\text{"Satellites" false in I}}, \underbrace{N}_{\text{"Nucleus" } (\equiv R_1)}]$$

is called a PI−Clash, if every satellite can be resolved with the preceding resolvent: $R_{i+1} = (E_i, R_i)$ whereby the literal resolved upon L in E_i must be of higher or equal priority than (or contain) all predicates in E_i, and furthermore if the last resolvent R_{q+1} ($\equiv$PI−Resolvent) is false in I:

1) Resolvents : $\exists R_{i+1} = \mathbb{R}(R_i, E_i)$ $(i = 1 \ldots q)$
2) $\mathbb{R}$−Literal : $L_{\mathbb{R}} \geq$ Predicates(E_i)
3) PI−Resolvent : R_{q+1} false in I

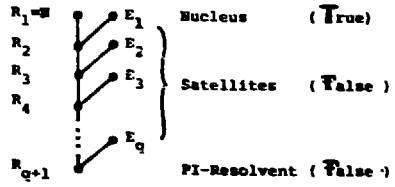

Note, the ordering the "Satellites" $\{ E_1, E_2, \ldots, E_q \}$ is immaterial; we always get the same PI−resolvents of this clash. An interesting thing about semantic resolution is that we can use any P−ordering and any I−interpretation.

Example 1:

. I-Interpretation = $[Q_a, \sim R_y, \sim S_c]$ = all T

. P-Ordering = $[Q > R > S]$

. Satellites : $E_1 \equiv \sim Q_x \vee \sim Q_a$ = F

$E_2 \equiv R_b \vee S_c$ = F

. Nucleus : $N \equiv Q_x \vee Q_a \vee \sim R_y \vee \sim R_b \vee S_c$ = T

. Resolvents : $R_1 \equiv N$

$R_2 \equiv R(E_1, R_1) = \sim R_y \vee \sim R_b \vee S_c$ } $\vdash_R$:largest in E_1

$R_3 \equiv R(E_2, R_2) = S_c$

. PI-Resolvent : S_c = F

PI−Deduction:
Suppose a clause set S is given. Let I be an interpretation, and let P be an ordering of all predicate symbols in the clauses of S. A deduction from S is called a PI−deduction if and only if each clause in the deduction is either a clause in S or a PI−resolvent:

PI−Deduction => S−Clauses, PI−Resolvents

Example 2 : $S \equiv \{1 \equiv Q \vee R, 2 \equiv Q \vee \sim R, 3 \equiv \sim Q \vee R, 4 \equiv \sim Q \vee \sim R\}$

I-Interpretation = $[Q, \sim R]$ => $S^+ = \{1 \equiv Q \vee R, 2 \equiv Q \vee \sim R, 4 \equiv \sim Q \vee \sim R\}$ = all T

P-Ordering = $[R > Q]$ $S^- = \{3 \equiv \sim Q \vee R\}$ } = all F

Clash-1 : $E_1 \equiv \sim Q \vee R$ $R_1 \equiv \sim Q \vee \sim R$

Clash-2 : $E_1 \equiv \sim Q$ $R_1 \equiv Q \vee R$

Clash-3 : $E_1 \equiv \sim Q$ $E_2 \equiv R$ $R_2 \equiv Q \vee \sim R$ $\square$

Completeness of PI−Resolution:
If P is an ordering of predicate symbols in a finite set S of clauses, and if I is an interpretation of S, then there is a PI−deduction of □ from S:

PI−Resolution => complete

PI−Resolution and Deletion−Strategy:
The PI−resolution can be used together with the Deletion−Strategy without loosing the completeness property:

PI−Resolution + Deletion−Strategy => complete

3.3 Pos./Neg. Hyperresolution

We now consider an inference rule which emphasizes the role of the positive/negative clauses. We first introduce some definitions.

Positive, Negative, Mixed Clauses:
A positive (negative) clause is composed of positive (negative) literals only. A mixed clause is composed of positive and negative literals.

Example 3 :

```
pos.clause = Q∨R∨S∨...    (pos.Ls only)
neg.clause = ~Q∨~R∨~S∨...  (neg.Ls only)
mxd.clause = ~Q∨R∨~S∨T∨...  (pos.+neg.Ls)
```

Positive Hyperresolution:
The inference rule 'positive hyperresolution' consideres simultaneously a set of clauses $\{E_1,E_2,...,E_Q\}$ ("Satellites") where each contains only positive literals, and a clause N ("Nucleus") that contains at least one negative literal. The resulting hyperresolvant $\mathcal{R}_{H+}$ is required to consist of positive literals only:

Pos. Hyperresolution $\mathcal{R}_{H+}$:

$$\{\underbrace{\text{Satellites}}_{\text{pos. Ls}} + \underbrace{\text{Nucleus}}_{1 \le \text{neg. Ls}}\} \Rightarrow \{\underbrace{\text{Hyperresolvent}}_{\text{pos. Ls only}}\}$$

Positive hyperresolution is a special case of PI−resolution in which the interpretation I consists of negative literals only: $I = [\sim L_1, \sim L_2, ...]$. The predicate ordering P is immaterial but it can further constraint the resolution possiblities.

Example 4 :

$$S = \{ Q_x \vee R_x, \sim Q_x \vee R_x, \sim R_a \vee \sim S_a, S_x \}$$

I-Interpretation = $[\sim Q_x, \sim R_x, \sim S_x]$ ⇒ $S^+ = \{\sim Q_x \vee R_x, \sim R_a \vee \sim S_a\}$

P-Ordering = $[S > Q > R]$ $S^- = \{ Q_a \vee R_x, S_x \}$

Clash-1 : $E_1 \equiv Q_a \vee R_x$ $R_1 \equiv \sim Q_x \vee R_x$

Clash-2 : $E_2 \equiv S_x$ $E_3 \equiv R_x \vee R_a$ $R_1 \equiv \sim R_a \vee \sim S_a$

$\square$

Negative Hyperresolution:
The inference rule 'negative hyperresolution' considers simultaneously a set of clauses $\{E_1,...,E_Q\}$ ("Satellites") where each contains only negative literals and a clause N ("Nucleus") that contains at least one positive literal. The resulting hyperresolvent $\mathcal{R}_{H-}$ is required to consist of negative literals only:

Negative Hyperresolution $\mathcal{R}_{H-}$:

$$\{\underbrace{\text{Satellites}}_{\text{neg. Ls}} + \underbrace{\text{Nucleus}}_{1 \le \text{pos. Ls}}\} \Rightarrow \{\underbrace{\text{Hyperresolvent}}_{\text{neg. Ls only}}\}$$

Negative Hyperresolution is a special case of PI−resolution in which the interpretation I consists of positive literals only: $I = [L_1, L_2, ...]$. The predicate ordering is immaterial, but it can further constraint the resolution possibilities.

Example 5 : $S \equiv \{ Q_a \vee R_x, \sim Q_x \vee R_x, \sim R_a \vee \sim S_a, S_x \}$

I-Interpretation = [Qx, Rx, Sx] $\Rightarrow$ $S^+ = \{ Q_a \vee R_x, \sim Q_x \vee R_x, S_x \}$ = all T
P-Ordering = [S > Q > R] $\Rightarrow$ $S^- = \{ \sim R_a \vee \sim S_a \}$ = all F

Clash-1 :
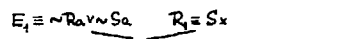

Clash-2 :
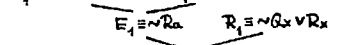

Clash-3 :
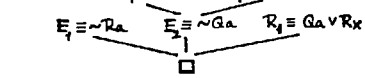

P-Ordering = [R > Q > S]

Clash-1 :
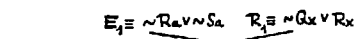

Clash-2 :
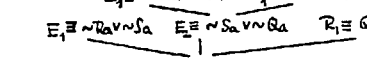

Clash-3 :
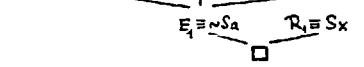

Completeness of Hyperresolution:
If P is an ordering of predicate symbols in a finite set S of clauses and if I is an interpretation of S, then there is a pos./neg. hyperresolution deduction of □ from S. If the ordering P is dropped the statement is still valid:

Pos./Neg. Hyperresolution => complete

Note, it is often the case that the axioms of a theorem are represented by some positive and mixed clauses, and the negation of the conclusion is represented by a negative clause ~C. In this case the positive hyperresolution roughly corresponds to "thinking forward", which means that the deduction starts with the axioms and derives a clause C which is contradictory to the negation of the conclusion ~C. The negative hyperresolution corresponds to "thinking backwards" which means that the deduction starts from the negation of the conclusion. Assuming that the conclusion is false, we derive a contradiction from this assumption in one of the other clauses.

3.4 UR – Resolution

Another special case of PI – Resolution is UR – resolution ("Unit Resulting"). The satellites are required to be Unit – clauses, the nucleus is constrained to have one more literal than the number of satellites and the result is required to be a unit clause. Thus UR – resolution requires that a set of unit clauses is used to yield a unit clause. Remember, a unit clause is a clause that contains exactly one literal, while a non – unit clause contains more than one literal. The inference rule 'UR – Resolution' ($\mathcal{R}_{UR}$) thus considers simultaneously a set of n unit clauses ("Satellites") and a non – unit clause ("Nucleus") with n + 1 literals. The resulting UR – resolvent is required to be a unit clause whereby the sign of the literals is immaterial. For UR – resolution to succeed, a simultaneous replacement of all variables in the set under consideration must exist that, when applied to each pair, makes the pair identical except for the sign:

UR – Resolution $\mathcal{R}_{UR}$:

$$\{ \underbrace{n \text{ Unit} - \text{Clauses}}_{1 \text{ Literal}} + \underbrace{1 \text{ Non} - \text{Unit} - \text{Clause}}_{n+1 \text{ Literals}} \} \Rightarrow \{ \underbrace{\text{Unit} - \text{Clause}}_{1 \text{ Literal}} \}$$

The UR−resolution removes the restriction that the derived clauses must have only positive literals (as is the case for pos. hyperresolution) but imposes the restriction that the derived clauses must be unit− clauses: { $E_1 \equiv P$, $E_2 \equiv \sim R$, $N \equiv \sim P \vee \sim Q \vee R$ } => $R_2 \equiv \sim Q$. UR−resolution would derive ~Q whereas pos. hyperresolution would be unable to derive anything. One thus might say that UR−resolution emphasizes unit−clauses in exactly the same way that hyperresolution emphasizes the positive clauses.

Example 6 :

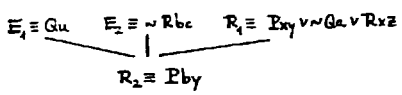

Completeness of UR − Resolution:
Given an unsatisfiable set S of n unit clauses and a non−unit clause with n + 1 literals, then there is a UR−resolution deduction of □ from S:

UR − Resolution => complete

Example 7 : see example 5.

3.5 Set−of−Support (SS) Resolution

The set−of−support strategy forbids an Automated Reasoning Program (ARP) from applying an inference rule unless at least one of the potential parents to which it is being applied has been deduced from some specified subset of the input clauses. A theorem, for instance, consists of a set of axioms $\{A_1, \ldots A_n\}$ and a conclusion C. To prove this theorem, we are essentially proving that: $A_1 \wedge A_2 \wedge \ldots A_n \wedge \sim C$ is unsatisfiable. Since the conjunction of the axioms: $A_1 \wedge A_2 \wedge \ldots \wedge A_n$ is usually satisfiable, it might be wise to avoid resolving clauses in $A_1 \wedge A_2 \wedge \ldots \wedge A_n$. This is what the set−of−support strategy tries to accomplish. Again we first give some definitions.

SS − Resolution:
A subset T of a set S of clauses is called a set−of−support of S if S−T is satisfiable. A set−of−support resolution ($\mathcal{R}_{SS}$) is a resolution of two clauses that are not both from (S − T):

SS − Resolution $\mathcal{R}_{SS}$:

$$\{(S) + \underbrace{(S-T)}_{\text{satisfiable}}\} \Rightarrow \{\text{SS}-\text{Resolvent}\}$$

The set T is chosen best to consist of the axiom expressing the negated conjecture (or query), or of the "special" axioms together with the negated conjecture.

SS − Deduction:
An SS − Deduction is a deduction in which every resolvent is a SS − resolvent:

SS − Deduction => S − Clauses, SS − Resolvent

Example 8 : $S = \{1 \equiv Pa, 2 \equiv \sim Dy \vee Lay, 3 \equiv \sim Px \vee \sim Qy \vee \sim Lxy, 4 \equiv Db, 5 \equiv Qb\}$

$T = \{4 \equiv Db, 5 \equiv Qb\}$, $S-T = \{1 \equiv Pa, 2 \equiv \sim Dy \vee Lay, 3 \equiv \sim Px \vee \sim Qy \vee \sim Lxy\}$

Deduction : $4+2=6$: Lab

$5+3=7$: $\sim Px \vee Lxb$

$6+7=8$: $\sim Pa$

$8+1=9$: $\square$

Completeness of the SS − Strategy:
If S is a finite, unsatisfiable set of clauses and T is a subset of S such that S − T is satisfiable, then there is an SS − deduction of □ from S with T as the set − of − support:

Set − of − Support Strategy => complete

SS − Strategy + other Refinements:
The SS − strategy is not compatible with most other resolution refinements. In particular, the combination of hyperresolution with the SS − strategy leads to the loss of resolution completeness:

SS − Strategy + most Refinements =/=> complete
SS − Strategy + Hyperresolution =/=> complete

3.6 *O − Resolution*

The ordering of predicate symbols may not be a sufficiently stringent condition to single out uniquely a literal. In a clause there may be more than one literal which is of higher or equal priority as the largest predicate symbol of the clause. Anyone of these can be a candidate to be resolved upon. We thus may be forced to generate from a clash more than one resolvent. In order to remedy this situation, we consider O(rdered) − Clauses and develop the O(rdered) − Resolution.

O − Clauses:
An O(rdered) − clause is a sequence of distinct literals. We introduce the ordering of literals in a clause by agreeing that a literal L_2 is greater than a literal L_1 in a clause if L_2 follows L_1 in the sequence specified by the clause. Thus, the last literal in an ordered clause will always be considered the largest literal in the clause:

$$\text{Clause} = [\, L_1 \vee \sim L_2 \vee \ldots \vee \sim L_n \,], \quad O-\text{Clause} = [\, \underbrace{L_1 < \sim L_2 < \ldots < \sim L_n}_{\text{ordering of literals}} \,]$$

Merging Left (ML):
In an O − clause, if there is more than one occurence of the same literal with identical arguments, we always keep only the leftmost one and delete the other identical literals:

$$O-\text{Clause} = [\, L_1 \vee L_2 \vee \ldots \vee \cancel{L_1} \vee \ldots]$$

Example 10 :

O-Clause : $Pa \vee Qx \vee Rz \vee \cancel{Pa} \overset{ML}{=} Pa \vee Qx \vee Rz$

$Qb \vee Ru \vee Pv \vee \cancel{Ru} \overset{ML}{=} Qb \vee Ru \vee Pv$

$Pv \vee Qu \vee \cancel{Rv} \vee \cancel{Qu} \overset{ML}{=} Pv \vee Qu$

O−Factor:
If two (or more) literals with the same sign of an O−clause G have a most general unifier Θ≡MGU, then the O−clause obtained from GΘ by deleting a literal that is identical to a smaller literal in the sequence is called an 'O−factor' of G:

O−Factor $\mathfrak{F}_O$:

1) $G[..L_i..L_j..]$	: same−sign Ls
2) $\exists\,\Theta \equiv MGU(L_i,L_j)$	:
3) $G\Theta$	: includes G
4) $\mathfrak{F}_O(G) = G[..L_i..\not{L_j}..]$	: merging left

Example 11 :

$G_i = Px \vee Qx \vee Pa \Rightarrow \mathfrak{F}_O(G_i) = G_1$ or $Pa \vee Qa$

$G_i = Pa \vee Px \vee Py \Rightarrow \mathfrak{F}_O(G_i) = G_i$ or $Pa \vee Px$ or $Pa \vee Py$ or Pa

$G_i = Px \vee Pfx \vee Qx \Rightarrow \mathfrak{F}_O(G_i) = G_1$ or $Pfy \vee Qfy$

O−Binary Resolvent:
Let G and H be two clauses with no variables in common. L_1 and L_2 be two literals in G and H, respectively. If L_1 and $\sim L_2$ have a most general unifier Θ≡MGU, then by concatenation: $\mathfrak{BR}_O(G,H) = [\,(G\Theta - L_1\Theta)\,,\,(H\Theta - L_2\Theta)\,]$, whereby the higher ones of possibly identical literals are dropped. $\mathfrak{BR}_O$ is called an 'O−Binary Resolvent' of G against H. Note that the ordering of the concatenated sequences is important: $\mathfrak{BR}_O(G,H) \neq \mathfrak{BR}_O(H,G)$.

O−Binary Resolvent $\mathfrak{BR}_O$:

1) $G(..L_1..)\,,\,H(..L_2..)$	: diff−sign Ls
2) $\exists\,\Theta \equiv MGU(L_1,\sim L_2)$	:
3) $[\,(G\Theta - L_1\Theta)\,,\,(H\Theta - L_2\Theta)\,]$	: concatenate
4) $\mathfrak{BR}_O = [..\not{L_a}..\not{\sim L_a}..]$	: merging left

Example 12 :

- $G \equiv Px \vee Qx \vee Rx$, $H \equiv \sim Pa \vee Qa$
  $L_1 \Rightarrow \theta = \{x/a\} \in L_2$
  $\mathfrak{BR}_0(G,H) = \{(G\theta - L_1\theta) \vee (H\theta - L_2\theta)\} = \{Qa \vee Ra \vee \not{Qa}\} \overset{ML}{=} \{Qa \vee Ra\}$
- $G \equiv Pa \vee Qx \vee Rx$, $H \equiv Py \vee \sim Qb \vee Sy$
  $L_1 \Rightarrow \theta = \{x/b\} \in L_2$
  $\mathfrak{BR}_0(G,H) = \{(G\theta - L_1\theta) \vee (H\theta - L_2\theta)\} = \{Pa \vee Rb \vee Py \vee Sy\}$
  $\mathfrak{F}_0(\mathfrak{BR}_0) \Rightarrow \theta = \{y/y\} \Rightarrow \quad = \{Pa \vee Rb \vee Sa\}$

O−Resolvent:
An 'O−Resolvent' of the clauses G and H is one of the following O−binary resolvents: (i) $\mathfrak{BR}_O$ of G against H, (ii) a $\mathfrak{BR}_O$ of the O−clause G against the O−factor of H, (iii) a $\mathfrak{BR}_O$ of the O−factor of G against the O−clause of H, (iv) a $\mathfrak{BR}_O$ of an O−factor of G against an O−factor of H:

O−Resolvent $\mathfrak{R}_O$: $\mathfrak{R}_O(G,H) = \mathfrak{BR}_O[\underbrace{\mathfrak{F}_O(G)}_{O-Clause\ or\ O-Factor}, \mathfrak{F}_O(H)]$

Example 13 :

$$G = P_x \vee Q_x \vee R_x \vee P_a \quad , \quad H = \neg P_a \vee Q_a$$

$$T_0'(G) = P_a \vee Q_a \vee R_a \quad , \quad H = \neg P_x \vee Q_a$$

$$\Leftarrow L_1 \Rightarrow \theta = \{x/a\} \Leftarrow L_2 \Rightarrow$$

$$R_0(G,H) = \{(Q_a \vee R_a) \vee (Q_a)\} \overset{ML}{=} \{\, Q_a \vee R_a \,\}$$

Completeness of O−Resolution:
If S is an unsatisfiable set of O−clauses and O−resolution is the inference rule to generate new clauses, the O−resolvents, then there is an O−deduction of □ from S.

O−Resolution => complete

3.7 OI−Resolution

We now consider semantic resolution for O−clauses. We still use the concepts of interpretation and clash. However we shall use the concept of ordered clauses rather than that of the ordering Γ of predicate symbols. We first give some definitions.

OI−Resolvent, OI−Clash:
Let I be an interpretation of a finite set of O−clauses in S. A finite sequence of O−clauses which is composed of the "Satellites" E_i, assumed to be false in I, and an "O−Nucleus" N ($=R_1$):

$$[\underbrace{E_1, E_2, E_3, \ldots, E_q}_{\text{"O−Satellites" false in I}}, \underbrace{N}_{\text{"O−Nucleus" } (=R_1)}]$$

is called an OI−Clash if:

1) Resolvents : $\exists\, R_{i+1} = \mathcal{R}_O(E_i, R_i) \quad (i = 1 \ldots q)$
2) $\mathcal{R}_0$−Literal : E_i(L = last literal), R_i(L = largest true in I)
3) OI−Resolvent : R_{q+1} false in I.

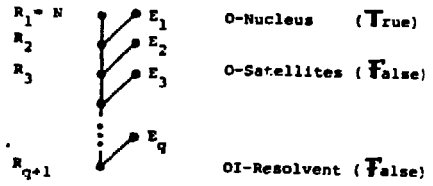

Note, the order of the O−Satellites is determined by the order of the literals in the O−Nucleus.

Example 14 :

- O-Clauses : $\{1 \equiv (P \vee Q),\ 2 \equiv (P \vee R),\ 3 \equiv (\sim R \vee \sim Q \vee P)\}$
- I-Interpret. : $[\sim P, \sim Q, \sim R] =$ all T_{rue}
- Satellites : $E_1 \equiv P \vee Q = F$
  $E_2 \equiv P \vee R = F$
- Nucleus : $N \equiv \sim R \vee \sim Q \vee P = T$
- Resolvents : $R_1 \equiv N$
- OI-Resolvent : $R_2 \equiv R(E_1, R_1) = P \vee \sim R$, $R_3 \equiv R(E_2, R_2) = P = F$ } L_R : last, last T

OI – Deduction:
Let I be an interpretation for a set of O – clauses. A deduction from S is called an OI – deduction if and only if each O – clause in the deduction is either an O – clause in S or an OI – resolvent

OI – Deduction => S – Clauses, OI – Resolvents

Example 15 :

$S = \{1 \equiv Q_a \vee R_x,\ 2 \equiv \sim Q_x \vee R_x,\ 3 \equiv \sim R_a \vee \sim S_a,\ 4 \equiv S_x\}$

$I \equiv \{\sim Q_x, \sim R_x, \sim S_x\} \Rightarrow S^+ \equiv \{\sim Q_x \vee R_x, \sim R_a \vee \sim S_a\}$

$S^- \equiv \{Q_a \vee R_x, S_x\}$

OI-Clash-1 : $E_1 \equiv S_x$ $E_2 \equiv Q_a \vee R_x$ $R_1 \equiv \sim R_a \vee \sim S_a$

OI-Clash-2 : $E_1 \equiv Q_a$ $R_1 \equiv \sim Q_x \vee R_x$

OI-Clash-3 : $E_1 \equiv S_x$ $E_2 \equiv R_a$ $R_1 \equiv \sim R_a \vee \sim S_a$ $\square$

Completeness of OI – Resolution:
OI – resolution is not complete: OI – Resolution $\not\Rightarrow$ complete

Example 16 : $S \equiv \{1 \equiv P \vee Q, 2 \equiv Q \vee R, 3 \equiv R \vee W, 4 \equiv \sim R \vee \sim P, 5 \equiv \sim W \vee \sim Q, 6 \equiv \sim Q \vee \sim R\}$

Unrestricted Resolution : $2+4=7$: $Q \vee \sim P$, $6+8=10$: $\sim R$
$7+1=8$: Q , $3+9=11$: R
$8+5=9$: $\sim W$, $11+10=12$: $\square$

OI-Resolution : $I \equiv [\sim P, \sim Q, \sim R, \sim W]$

$S_0^+ \equiv \{4 \equiv \sim R \vee \sim P, 5 \equiv \sim W \vee \sim Q, 6 \equiv \sim Q \vee \sim R\}$

$S_0^- \equiv \{1 \equiv P \vee Q, 2 \equiv Q \vee R, 3 \equiv R \vee W\}$

OI-Clash-1 : $E_1 \equiv P \vee Q$, $E_2 \equiv R \vee W$, $R_1 \equiv \sim W \vee \sim Q$
$R_2 = P \vee \sim W (= \overline{T})$, $R_3 = R \vee P (= \overline{F})$, $7 \equiv R \vee P$

OI-Clash-2 : $E_1 \equiv Q \vee R$, $E_2 \equiv P \vee Q$, $R_1 \equiv \sim Q \vee \sim R$
$R_2 = Q \vee \sim Q (= \overline{T})$, $R_3 = (P \vee Q)(= \overline{F})$, $8 \equiv P \vee Q$

OI-Clash-3 : $E_1 \equiv R \vee P$, $E_2 \equiv Q \vee R$, $R_1 \equiv \sim R \vee \sim P$
$R_2 = P \vee \sim R (= T)$, $R_3 = Q \vee R (= \overline{F})$, $9 \equiv Q \vee R$

No new clauses possible $\Rightarrow \square$ not possible.
$\Rightarrow$ OI-Resolution not complete !

3.8 *Lock – Resolution*

The idea of Lock – Resolution is similar to that of ordered clauses since indices are used to order the literals in the clauses of S. Each occurence of a literal in S is arbitrarily indexed by an integer and therefore different occurences of the same literal may be indexed differently. Resolution is then permitted only on literals of lowest index in each clause. If a literal in a resolvent has more than one possible index, the lowest index is assigned to this model. We introduce a few definitions.

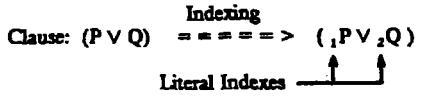

Merging Low (MLo):
In a clause, if there is more than one of the same literal with identical arguments, we always keep only the literal with the lowest index and delete the other identical literals. This operation is called 'merging low for identical literals'.

Example 17 :

$G = {}_1Q \vee {}_2P \vee {}_3Q \overset{MLo}{=} {}_1Q \vee {}_2P$

$G = {}_5Pa \vee {}_6Qy \vee {}_7Pa \overset{MLo}{=} {}_5Pa \vee {}_6Qy$

Lock Factor:
Let G be an indexed clause, meaning that each of its literals is given an integer index. If two (or more) literals with the same sign have a most general unifier $\Theta = MGU$, formation of $G\Theta$ and dropping any literal that is identical to a literal of lowest index ('merging low') is called a 'Lock Factor' of G:

Lock Factor $\mathbb{F}_L$:

1) $G(..L_\alpha..L_\beta..)$	: same – sign Ls
2) $\exists\,\Theta = MGU(L_\alpha, L_\beta)$	:
3) $G\Theta$	:
4) $\mathbb{F}_L(G) = G\Theta(..L_\alpha..\not{L_\beta}..)$	: merging low

Example 18 :

$G = {}_2Px \vee {}_3Qx \vee {}_4Pa \vee {}_6Qx \Rightarrow \mathbb{F}_L(G) = G$ or ${}_2Pa \vee {}_6Qa$

$G = {}_2Px \vee {}_3Qx \vee {}_4Pa \Rightarrow \mathbb{F}_L(G) = G$ or ${}_3Qx \vee {}_4Pa$

$G = {}_2Px \vee {}_3Qx \vee {}_5Pa \Rightarrow \mathbb{F}_L(G) = G$ or ${}_2Pa \vee {}_3Qa$

Binary Lock Resolvent:
Let G and H be two indexed (parent) clauses with no variables in common. Let L_1 and L_2 be two literals of "lowest" index in G and H, respectively. If L_1 and $\sim L_2$ have a most general unifier $\Theta = MGU$, then the clause: $\mathbb{BR}_L(G,H) = \{ (G\Theta - L_1\Theta) \cup (H\Theta - L_2\Theta) \}$ (+ merging low) is called a 'Binary Lock Resolvent' of G and H:

Binary Lock Resolvent $\mathbb{BR}_L$:

1) $G(..L_1..), H(..L_2..)$	: diff – sign Ls
2) $\exists\,\Theta = MGU(L_1, \sim L_2)$	:
3) $\{ (G\Theta - L_1\Theta) \cup (H\Theta - L_2\Theta) \}$	:
4) $\mathbb{BR}_L = [..L_\alpha..\not{L_\beta}..]$	: merging low

Example 19 :

$$G \equiv {}_1P_x \vee {}_2Q_x \vee {}_3R_x \;,\; H \equiv {}_4\sim P_a \vee {}_5Q_a \;,\; \{\theta = x/a\}$$

$$\mathbb{BR}_L(G,H) = \{\,(G\theta - L_1\theta) \vee (H\theta - L_2\theta)\,\}$$

$$= \{\,{}_2Q_a \vee {}_3R_a \vee {}_5Q_a\,\} \overset{ML\theta}{=} \{\,{}_2Q_a \vee {}_3R_a\,\}$$

Lock Resolvent:
A 'Lock Resolvent' of the indexed (parent) clauses G and H is one of the following binary lock resolvents: (i) a $\mathbb{BR}_L$ of the indexed clauses G and H, (ii) a $\mathbb{BR}_L$ of the indexed clause G and a Lock factor of H, (iii) a $\mathbb{BR}_L$ of a Lock factor of G and the indexed clause H, (iv) a $\mathbb{BR}_L$ of a Lock factor of G and a Lock factor of H:

$$\text{Lock Resolvent } \mathbb{R}_L : \mathbb{R}_L(G,H) = \mathbb{BR}_L(\underbrace{\mathbb{F}_L(G), \mathbb{F}_L(H)}_{\text{indexed clause or Lock factor}})$$

Example 20 :

$$S = \{\,1 \equiv {}_1P \vee {}_2Q,\; 2 \equiv {}_3P \vee {}_4\sim Q,\; 3 \equiv {}_5Q \vee {}_6\sim P,\; 4 \equiv {}_7\sim Q \vee {}_8\sim P\,\}$$

$3+4=5 : {}_6\sim P$, $2+6=7 : {}_4\sim Q$

$1+5=6 : {}_2Q$, $6+7=8 : \square$

Lock Deduction:
Let S be a set of indexed clauses. A deduction from S is called a 'Lock Deduction' if and only if every clause in the deduction is either a clause in S or a Lock resolvent:

Lock Deduction = > indexed S − clause, Lock Resolvents

Example 21 :

$$S = \{\,1 \equiv {}_1P[f_{3,1}] \vee {}_2P_{ya}\;,\; 2 \equiv {}_2P[y,f_{71}] \vee {}_6P_{ya}\;,\; 3 \equiv {}_3P[f_{3,1}] \vee {}_9\sim P_{xy}\;,$$

$$4 \equiv {}_4P[y,f_{71}] \vee {}_1\sim P_{xy}\;,\; 5 \equiv {}_7\sim P_{ya} \vee {}_{10}\sim P_{xy}\,\}$$

$1+5=6 : {}_5P_{aa} \vee {}_{10}\sim P[x,f_{71}]$, $8+2=9 : {}_6P_{aa}$

$3+5=7 : {}_8\sim P_{xa} \vee {}_{10}\sim P[y,f_{71}]$, $8+4=10 : {}_9\sim P_{xa}$

$6+7=8 : {}_{10}\sim P[x,f_{71}] \vee {}_{10}\sim P[y,f_{71}]$, $9+10=11 : \square$

Completeness of Lock Resolution:
Let S be a set of clauses with their literals indexed by integers. If S is unsatisfiable, then there is a Lock deduction of □ from S.

Lock Resolution = > complete

Lock Resolution and other Strategies:

Lock Resolution + Deletion Strategy	≠ >	complete
Lock Resolution + SS − Strategy	≠ >	complete
Lock Resolution + most other Strategies	≠ >	complete

Note, Lock − Resolution is a very efficient inference rule and refinement of the unrestricted resolution.

Example 22 :

$S = \{ 1 \equiv {}_1\sim E x_2 \forall x_3 S[x, f x] \;,\; 5 \equiv {}_5\sim S x_9 \vee_{10} P y$

$2 \equiv {}_4\sim E x_5 \forall x_6 C f x \;,\; 6 \equiv {}_{11}\sim P x \vee_{12} \sim V x$

$3 \equiv {}_7 P a \;,\; 7 \equiv {}_{13}\sim P x \vee_{14} \sim C x \;\}$

$4 \equiv {}_8 E a$

$4+4=8 : {}_2\forall a \vee_3 S[a, f a] \;,\; 10+8=12 : {}_3 S[a, f a]$

$2+4=9 : {}_5\forall a \vee_6 C f a \;,\; 10+9=13 : {}_6 C f a$

$3+6=10 : {}_{12}\sim V a \;,\; 12+5=14 : {}_{10} P f a$

$3+7=11 : {}_{14}\sim C a \;,\; 14+7=15 : {}_{14}\sim C f a$

$13+15=16 : \square$

4. LINEAR RESOLUTIONS

This is the summary name of a set of resolution procedures which all have in common that one of the two parent clauses in a resolution is the preceding resolvent.

4.1 Introduction

When applying an identity we often start with the left−hand side of the identity, apply an inference rule to it to obtain some other expression, then apply some inference rule again to the expression we have just obtained until the left−side expression is identical to the right−side expression of the identity. The idea of linear resolution is similar to a kind of chain reasoning. It starts with a clause, resolves it with another clause to obtain a resolvent, and resolves this result with some clause, until the empty clause □ is obtained. The special appeal of linear deduction is its simple structure allowing also for heuristic search methods.

4.2 Linear Resolution

We now consider the proper 'linear resolution'.

Linear Resolution:
Given a set S of clauses, a linear resolution $\mathbb{R}_L$ is an $\mathbb{R}$−resolution in which one of the two parent clauses is the preceding resolvent and the other parent clause is either from the set S of input clauses or it is an earlier resolvent

$$G_{i+1} = \mathbb{R}_L(G_i, B_i)$$

Center−Clause (preceding resolvent) — Side−Clause (from S or any earlier resolvent)

Example 23 : $S = \{ 1 \equiv P \vee Q \;,\; 2 \equiv \sim P \vee Q \;,\; 3 \equiv P \vee \sim Q \;,\; 4 \equiv \sim P \vee \sim Q \}$

$1+2=5 : Q$

$5+3=6 : P$

$6+4=7 : \sim Q$

$7+5=8 : \square$

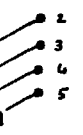

Linear Deduction:
Given a set S of clauses and a clause G_0 in S. A linear deduction of G_0 from S starts with the top-clause G_0 which is resolved with the clause B_0. The resulting resolvent G_1 (center-clause) is resolved against the side-clause B_1, and so on. All side-clauses are either from S or are earlier resolvents.

Example 24 :

$S = \{ 1 \equiv P[x, f_x, b], 2 \equiv \sim S_x \vee \sim S_y \vee \sim P[x, f_y, z] \vee S_z$
$3 \equiv S_a, 4 \equiv \sim S_b \}$
$4+2=5 : \sim S_x \vee \sim S_y \vee \sim P[x, f_y, b]$
$5+3=6 : \sim P[a, f_a, b]$
$6+1=7 : \square$

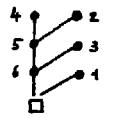

Completeness of Linear Resolution:
Given a finite set S of clauses, then there is a linear deduction of $\square$ from S.

Linear Deduction = = > complete

4.3 Input Resolution

When we consider a refinement of resolution, we would like it to be complete, that is, to guarantee that the empty clause can always be derived from the unsatisfiable set of clauses. However, efficiency is also important. Sometimes, we may like to trade completeness for efficiency. That is, there may be some refinements of resolution that are efficient, but incomplete. If a refinement of resolution is efficient and powerful enough to prove a large class of theorems, even though it is not complete, it may still be useful. Input resolution (and also unit resolution) is in this situation.

Input Resolution:
An input resolution is an $\mathcal{R}$-resolution in which one of the two parent clauses is an input clause (from the input set S).

$$G_{i+1} = \mathcal{R}_I(G_i, B_i)$$

Center-Clause (earlier resolvent) — Input-Clause (from S)

Example 25 :

$S = \{ 1 \equiv \sim P[x,y,u] \vee \sim P[y,z,v] \vee \sim P[x,v,w] \vee P[u,z,w]$
$2 \equiv P[g(x,y),x,u] \quad 3 \equiv P[x,h(x,y),y], 4 \equiv \sim P[h(x,y),g(x,y)] \}$

$4+2=5 : \sim P[y,z,v] \vee \sim P[g(y,t),v,w] \vee P[u,z,w]$
$5+2=6 : \sim P[v,z,v] \vee P[w,z,w]$
$6+2=7 : P[w, h(v,v), w]$
$7+4=8 : \square$

Input Deduction:
An input deduction is a deduction in which every resolution is an input resolution. Note, an input deduction is actually a linear deduction in which every side−clause is an input− clause, and hence it is a subcase of linear deduction.

Example 26 :

$S = \{ 1 \equiv P_x \vee Q_{yx} \vee \sim R_{xz}, 2 \equiv \sim P_x \vee Q_{xx}, 3 \equiv \sim Q_{ax}, 4 \equiv P_{xb} \}$

$1+4 = 5 : P_x \vee Q_{yx}$
$5+2 = 6 : Q_{xx} \vee Q_{yx}$
$6+3 = 7 : Q_{xx}$
$7+3 = 8 : \square$

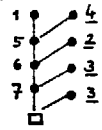

Completeness of Input Resolution:
The input resolution is not complete. However, given an unsatisfiable set S of Horn−Clauses (with at most one positive literal) there is a input deduction of □ from S (Input Refutation).

Input Resolution	(General)	=/=> complete
Input Resolution	(Horn−Clauses)	==> complete

4.4 Unit Resolution:

Unit resolution is essentially an extension of the one−literal rule by Davis−Putnam to the first−order predicate logic. This rule is especially important, for in order to deduce the empty clause, one must obtain successively shorter clauses, and unit resolution provides a means for progressing rapidly towards shorter clauses.

Unit Resolution:
A unit resolution is an $\mathcal{R}$−resolution in which a resolvent is obtained by restricting at least one parent clause to a unit clause or a unit factor of a clause:

$$R_i = \mathcal{R}_U(\underbrace{G, H}_{1 \leq \text{unit − clause/factor}})$$

None of the two parent clauses is required to be a preceding resolvent.

Unit Deduction:
A unit deduction is a deduction in which every resolution is a unit resolution.

Example 27 :

$S = \{ 1 \equiv P_x \vee Q_{yx} \vee \sim R_{xz}, 2 \equiv \sim P_x \vee Q_{xx}, 3 \equiv \sim Q_{ax}, 4 \equiv P_{xb} \}$

$1+4 = 5 : P_x \vee Q_{yx}$
$5+2 = 6 : \sim P_a$
$6+5 = 7 : Q_{ya}$
$7+3 = 8 : \square$

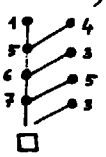

Completeness of Unit Resolution:
Unit resolution is not complete. However, given an unsatisfiable set S of Horn−Clauses (with at most one negative literal), there is a unit deduction of □ from S (Unit Refutation).

Unit Resolution	(General)	=/=> complete
Unit Resolution	(Horn−Clauses)	==> complete

Equivalence of Unit and Input Resolution:
There is a unit refutation from a set of S clauses if and only if there is an input refutation from S.

Input Refutation <= = > Unit Refutation

4.5 P1 – Resolution

For completeness we also mention here the P1 – resolution although it logically is close to the hyper-resolution.

P1 – Resolution :
A P1 – resolution is an $\mathbb{R}$ – resolution in which at least one of the twp parent clauses is a positive clause (which consists of positive literals only) :

$$G_i = \underbrace{\mathbb{R}(G,H)}_{1 \leq \text{pos. clause / factor}}$$

None of the parent clauses is required to be a preceding resolvent. Note that P1 – resolution is a special case of hyperresolution.

P1 – Deduction:
A P1 – deduction is a deduction in which every resolution is a P1 – resolution.

Completeness of P1 – Resolution:
The P1 – resolution is complete: P1 – resolution = = > complete

Example 28 : see example 27.

4.6 OL – Resolution

We can strengthen linear resolution by introducing two additional concepts into it: ordered clauses and information on the literals resolved upon. The concept of ordered clauses in linear resolution will not destroy its completeness. In resolution, when a resolvent is obtained, the literals resolved upon are deleted. Actually, the information provided by these literals is very useful since it can be used to improve further its efficiency without loosing the completeness property.

$\hat{O}$ – Clauses:
Let us consider the mechanism of recording information on the resolved literals. Suppose two O – clauses are resolved:

$$\begin{matrix} G = P \vee Q \\ H = \neg Q \vee R \end{matrix} \Rightarrow \mathbb{R}_O(G,H) = P \vee R \;\; = = > \;\; \mathbb{R}_O(G,H) = P \vee \boxed{Q} \vee R$$

from first clause

whereby Q and ~Q are the literals resolved upon. Since they are complementary to each other, we need only record one of them, namely Q in the first clause G (keep the order!). The ordered resolvent can be represented by $\mathbb{R}\,\hat{O}$ as indicated, whereby the framed literal is the literal resolved upon. That is, literals resolved upon are indicated by framed literals in an $\hat{O}$ – clause which we denote from now on by: $\hat{O}$ – clause. The framed literals are merely for recording those literals that have been resolved upon; they do not participate in resolution.

Example 29 :

$S = \{1 \equiv P \vee Q,\ 2 \equiv P \vee \sim Q,\ 3 \equiv \sim P \vee Q,\ 4 \equiv \sim P \vee \sim Q\}$

$4 + 2 = 5 : P \vee \boxed{Q} \Rightarrow P$

$5 + 3 = 6 : \boxed{P} \vee Q$

$6 + 4 = 7 : \boxed{P} \vee \boxed{Q} \vee \sim P$

$7 + 5 = 8 : \boxed{P} \vee \boxed{Q} \Rightarrow \square$

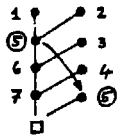

Deletion Convention: In the above scheme, if a framed literal is the last literal in an $\hat{O}$-clause, it shall be deleted.

$\hat{O}$-Clause = $L_1 \vee \boxed{L_2} \vee \sim L_3 \vee .. \vee \boxed{L_{10}} \vee L_{11} \vee .. \vee \boxed{L_{15}}$

literals resolved upon

last, delete if framed

Example 30 :

$G = R_x \vee Q_{xy} \vee \boxed{R_{zy}} \Rightarrow P_x \vee Q_{xy}$

Reducible $\hat{O}$-Clause:
An $\hat{O}$-clause G is called a 'reducible $\hat{O}$-clause' if and only if the last literal of G is unifiable with the negation of a framed literal of G.

Example 31 :

$G = \boxed{P_x} \vee Q_{xy} \vee \boxed{P_a} \vee \sim P_z \Rightarrow G = \boxed{P_x} \vee Q_{xy}$

reducible $\hat{O}$-clause — reduced $\hat{O}$-clause

Reduced $\hat{O}$-Clause:
Let G be a reducible $\hat{O}$-clause. Let the last literal L be unifiable with the negation of some framed literal using the most general unifier θ. The 'reduced $\hat{O}$-clause' is obtained from $G\theta$ by deleting $L\theta$ and every subsequent framed literal not followed by any unframed literal:

$G = ...\boxed{L}\vee...\vee\sim L \vee \boxed{M}...$

all framed literal

earlier framed literal

delete from here !

$\hat{O}$-Factor:
If two or more framed literals (with the same sign) of an $\hat{O}$-clause G have a most general unifier θ, the ordered clause obtained from $G\theta$ by merging left for identical (unframed) literals and by deleting every framed literal not followed by an unframed literal in the remaining clause, is called an '$\hat{O}$-Factor' of G:

$\hat{O}$-Factor $F_{\hat{O}}$:

1) $G[..L_i..L_j..]$: same sign
2) $\exists\, \theta = MGU(L_i, L_j)$:
3) $G\theta$:
4) $G[..L_i..L_j..]$: merging left
5) $F_{\hat{O}} = G[..\vee \boxed{L_m}]$: delete convention

Example 32 :

$$G = P_x \vee Q_{yz} \vee \boxed{\sim P_a} \vee Q_{bc} \quad , \quad \theta = \{x/y, z/z\}$$
$$G\theta = P_x \vee Q_{bc} \vee \boxed{\sim P_a} \vee Q_{bc} \Rightarrow F_\theta(G) = P_x \vee Q_{bc}$$

$\hat{O}$ – Binary Resolvent:
Let G and H be two $\hat{O}$ – clauses with no variables in common, and let L_1 and L_2 be two unframed literals in G and H, respectively. Let L_1 and L_2 have a most general unifier $\theta = MGU$, then by concatenation: $BR_{\hat{O}}(G,H) = [\, G\theta(\ldots \boxed{L_1\theta} \ldots), (H\theta - L_2\theta)\,]$ whereby 'merging left' for any identical unframed literals is applied and any framed literal, not followed by an unframed literal, is removed. $BR_{\hat{O}}$ is then called an '$\hat{O}$ – binary resolvent' of G against H. Note that the ordering of the concatenated sequences is important.

$\hat{O}$ – Binary Resolvent $BR_{\hat{O}}$:

1) $G(\ldots L_1 \ldots), H(\ldots L_2 \ldots)$	: diff – sign L's
2) $\exists\, \theta = MGU(L_1, \sim L_2)$	:
3) $G\theta(\ldots \boxed{L_1\theta} \ldots), (H\theta - L_2\theta)$	:
4) $[\ldots L_{i-1}, \ldots L_{i+1} \ldots]$	:
5) $BR_{\hat{O}} = [\ldots \vee \boxed{L_m}]$	: delete convention

Example 33 :

$$G \equiv P_x \vee Q_{yz} \vee R_b, \quad H \equiv R_b \vee W_z \vee \sim P_a \quad , \quad \theta = \{a/x\}$$
$$BR_{\hat{O}}(G,H) = [\boxed{P_a} \vee Q_{yz} \vee R_b \vee \boxed{W_z}\,]$$
$$= P_a \vee Q_{yz} \vee R_b$$

$\hat{O}$ – Resolvent:
An $\hat{O}$ – resolvent of the $\hat{O}$ – clauses G and H is one of the following $\hat{O}$ – binary resolvents: i) an $BR_{\hat{O}}$ of the $\hat{O}$ – clauses G against H, ii) an $BR_{\hat{O}}$ of the $\hat{O}$ – clause G against an $\hat{O}$ – factor of H. iii) an $BR_{\hat{O}}$ of an $\hat{O}$ – factor of G against the $\hat{O}$ – clause H, and iv) an $BR_{\hat{O}}$ of an $\hat{O}$ – factor of G against an $\hat{O}$ – factor of H.

$$\hat{O} \text{ – Resolvent } R_{\hat{O}} : R_{\hat{O}}(G,H) = BR_{\hat{O}}(F_{\hat{O}}(G), F_{\hat{O}}(H))$$
$$\hat{O} \text{ – Clause or } \hat{O} \text{ – Factor}$$

$\hat{O}L$ – Deduction:
Given a set S of O – clauses whereby G_0 shall be a particular element of S. An '$\hat{O}L$ – deduction' of (the $\hat{O}$ – clause) G_n from S is similar to a 'linear deduction': G_0 is the top – clause and there are center $\hat{O}$ – clauses G_i which are resolved against the side $\hat{O}$ – clauses B_i. The conditions are stated as follows:

1) Every B_i is either in S or it is an instance of an earlier $\hat{O}$ – resolvent $G_{j<i}$.
2) If the center $\hat{O}$ – clause G_i is reducible, then G_{i+1} is the reduced $\hat{O}$ – clause of G_i : $G_{i+1} = G_i(\text{reduced})$.
   If the center $\hat{O}$ – clause G_i is not reducible, then $R_{\hat{O}}(G_i, B_i)$ with B_i in S, whereby the literal L_R resolved upon (in G_i) is the last literal.
3) No tautology is admitted in the deduction.

$$G_{i+1} = \begin{cases} G_i(\text{reduced}) & : \text{if } G_i \text{ reducible (with } B_i = G_{j<i} \text{ – instance)} \\ R_{\hat{O}}(G_i, B_i) & : \text{if } G_i \text{ not reducible (with } B_i \text{ in S)} \end{cases}$$

center – clause, side – clause

Completeness of $\widehat{OL}$ – Resolution:
If G_o is a particular member of an unsatisfiable set S of O – clauses, and if $S - \{G_o\}$ is satisfiable, then there is an OL – deduction of □ from S with G_o at its top:

$$\widehat{OL} - \text{Resolution} + (S - \{G_o\}) \text{ satisfiable} \Longrightarrow \text{complete}$$

Example 34 : $S = \{1 \equiv Pvq, 2 \equiv \sim qv R, 3 \equiv Pv\sim R, 4 \equiv \sim qv\sim R, 5 \equiv \sim Pv\sim R\}$

$1+2 = 6$: $Pv\boxed{q}vR$
$6+4 = 7$: $Pv\boxed{q}v\boxed{R}v\sim q$
8 : $Pv\boxed{q}v\boxed{R} \Rightarrow P$
$8+3 = 9$: $\boxed{P}vR$
$9+5 = 10$: $\boxed{P}v\boxed{R}v\sim P$
11 : $\boxed{P}v\boxed{R} \Rightarrow \square$

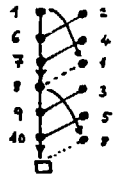

Example 35 : $S = \{1 \equiv \sim Rab, 2 \equiv \sim Pv\sim Myzuv\sim Pzuv\exists xy\forall x\exists z,$
$3 \equiv \sim Mxyzv\exists xz, 4 \equiv Ma\,fcfb, 5 \equiv Mxx\,fx, 6 \equiv Pa\}$

$1+2 = 6$: $\boxed{\sim Rab}v\sim Pav\sim Mybuv\sim Pauv\exists xy$
7 : $\boxed{\sim Rab}v\sim Pav\sim Mbbuv\sim Pau$
$7+3 = 8$: $\boxed{\sim Rab}v\sim Pav\sim Mbbuv\boxed{\sim Pau}v\sim Mayu$
$8+4 = 9$: $\boxed{\sim Rab}v\sim Pav\sim Mbbfb$
$9+5 = 10$: $\boxed{\sim Rab}v\sim Pa$
$10+6 = 11$: $\boxed{\sim Rab}v\boxed{\sim Pa} \Rightarrow \square$

5. PARAMODULATIONS

This is the summary name of a set of resolution techniques involving the equality – sign (predicate) such that its set of axioms can be left aside.

5.1 Introduction

We are in this section concerned with the equality relation. If only resolution is used there is no possibility to prove a theorem which involves the equality relation. There are additional axioms needed describing the properties of the equality relation. The extra axioms describe the reflexive, symmetric, transitive and substituitive properties of equality. Such an approach is however very clumsy. It not only requires more clauses for the generation of numerous useless resolvents. In order to curtail this problem and to disperse with the troublesome axioms of equality many remedies have been proposed among which 'Paramodulation' is simple and natural. We shall see that paramodulation can replace those axioms concerning the symmetric, transitive, and substituitive properties of equality. We shall also see that in conjunction with resolution, paramodulation can be used to prove theorems in a very natural and efficient way.

5.2 Equality Axioms

Let S be a set of clauses with function and predicate symbols. Then the set of 'equality axioms' for S consists of the following clauses:

1) EQ(x,x)
2) EQ(x,y) − > EQ(y,x)
3) EQ(x,y) ∧ EQ(y,z) − > EQ(x,z)
4) EQ(x_1,u_1) ∧ .. ∧ EQ(x_n,u_n) − > EQ(f(x_1,..,x_n) , f(u_1,..,u_n))
5) EQ(x_1,u_1) ∧ .. ∧ EQ(x_n,u_n) − > EQ(P(x_1,..,x_n) , P(u_1,..,u_n))

where the predicate EQ(x,y) stands for the equality−sign (x=y). Note that the axioms 4) and 5) apply for every n−place function symbol: f(x_1,..,x_n), and every m−place predicate symbol: P(x_1,..,x_m), occuring in S.

EQ−Interpretation:
An 'EQ−Interpretation' is an interpretation that satisfies all equality axioms.

EQ−(Un)Satisfiable:
Suppose we consider an interpretation that satisfies all equality axioms (EQ−interpretation). A set of clauses S is called 'EQ−satisfiable' if and only if all clauses in S are satisfiable in the EQ−interpretation. Otherwise, S is called 'EQ−unsatisfiable'.

EQ−Theorem:
Let S be a set of clauses and let K be the set of equality axioms for S. Then S is EQ−unsatisfiable if and only if (S ∪ K) is unsatisfiable.

S (EQ−unsatisf.) < = = = > S ∪ K (EQ−unsatisf.)

Equality Substitution Rule:
If a clause G[t,..] contains a term t and if there is a unit−clause EQ[t,s] (meaning: t=s) then infer a new clause by substituting s for one single occurence of t in G[t,..], giving G[s,..].

Example 36 : $G = P_a$, $H = EQ[a,b] \Rightarrow G' = P_b$

5.3 *Paramodulation*

The 'proper' paramodulation consists of binary paramodulation with a specific type of parent clauses (or their factors).

Binary Paramodulation:
Let two (parent) clauses be defined as

G ≡ L[t,..] ∨ A and H ≡ EQ[r,s] ∨ B

Unification

whereby no variables shall be in common. t,r,s are terms (constants, variables, functions), EQ[r,s] is the equality predicate and L[t,..] stands for any literal depending on the term t. A and B are arbitrary clauses. If t and r have a most general unifier θ ≡ MGU such that tθ and rθ become identical, the instantiated equality literal reads: EQ[rθ,sθ]. The 'Binary Paramodulant' then reads

$$\mathfrak{BR}_{para}(G,H) \equiv L\theta[s\theta,..] \cup A\theta \cup B\theta$$

where Lθ[sθ,..] denotes the result obtained by replacing one single occurence of tθ (≡rθ) in Lθ by sθ. The clause H is called the "from−clause" and the clause G is called the "into−clause". The literals L[t,..] and EQ[r,s] are called "literals paramodulated upon". Note, instead of unifying t with r we also could have unified t with s and applied the above procedure in an analogous way.

Example 37 :

- $G \equiv \underbrace{P_x}_{L[1]} \vee \underbrace{Q_b}_{A}$, $H \equiv EQ[a,b] \vee \underbrace{R_b}_{B}$

  $\Rightarrow \quad \mathbb{BR}_{para}(G,H) = P_b \vee Q_b \vee R_b$

- $G \equiv \underbrace{P[g(f_x)]}_{\text{Literal } L[1]} \vee G_x$, $H \equiv EQ[\underbrace{f(g_b)}_{\text{Term } t}, a] \vee R_{gc}$

  $t \equiv f_x, \; r \equiv f(g_b), \; s \equiv a \;\Rightarrow\; \theta = \{ {}^{g_b}/_{x} \}$

  $L\theta[t\theta] = P[g(f(g_b))] \Rightarrow L\theta[s\theta] = P[g_a]$

  $\Rightarrow \quad \mathbb{BR}_{para}(G,H) = P[g_a] \vee Q[g_b] \vee R[g_c]$

Paramodulation:
A Paramodulant of the two (parent) clause G and H is one of the following binary paramodulants: i, an $\mathbb{R}_{para}$ of the clause G and the clause H, ii) an $\mathbb{BR}_{para}$ of the clause G and a factor of H, iii) an $\mathbb{BR}_{para}$ of a factor G and the clause H, and iv) an $\mathbb{BR}_{para}$ of a factor of G and a factor of H.

Paramodulant $\mathbb{R}_{para}$: $\mathbb{BR}_{para}(\underbrace{\mathbb{F}(G), \mathbb{F}(H)}_{\text{Clause or Factor}})$

Completeness of Resolution + Paramodulation:
If S is an EQ – unsatisfiable set of clauses then there is a deduction of □ from S using resolution and paramodulation:

Resolution + Paramodulation = = > complete

5.4 *Demodulation*

The process called 'Demodulation' enables an ARP to simplify and canonicalize information. A demodulator is a positive unit – clause with an equality predicate that has been designated to rewrite expressions. A demodulator of the form

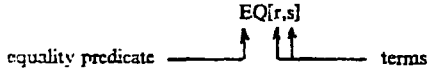

applies to a term t, if and only if t is an instance of either r or s. Suppose D[t] is a clause with its term t being an instance of say r, such that the demodulator: EQ[r,s] can be applied. Unifying r with t such that $r\theta = t$, we denote the instantiated modulator by: $EQ[r\theta, s\theta]$. Thus, the result of applying the demodulator EQ[r,s] to the clause D[t] changes it to the demodulator $D[s\theta]$. The procedure is graphically represented by

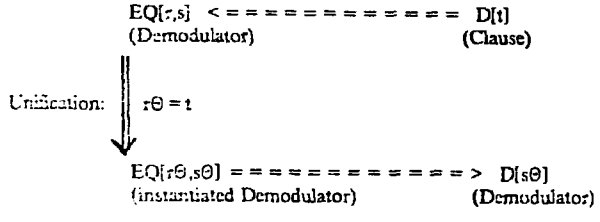

Sofar t was considered an instance of r with so called "left−to−right applications" of the demodulator. Instead we could have chosen that t is an instance of s leading in this case to a "right−to−left application" of the demodulator. Ordinarily, a term is treated to as many demodulators as possible. Only the final demodulator is retained.

Example 38 : $G \equiv Q[g(\underbrace{f(h_a)}_{t})]$, $H \equiv EQ[\underbrace{f_x}_{r}, \underbrace{x}_{s}]$ $\xrightarrow{\text{instance}}$ $G' \equiv Q[g(h_a)]$

Unification : $\theta = \{h_a/x\}$, $r\theta = f(h_a) = t$, $s\theta = h_a$

Back Demodulator:
When newly adjoined clauses are designated as demodulators and these are applied to already retained clauses, the process is termed: Back Demodulation.

Comments:
1) Employment of demodulation results in the loss of refutation completeness. Nevertheless, demodulation is heavily used for many problem domains by the ARP.
2) Unification in the framework of demodulation is constrained to making non−trivial variable replacements only in the analogue of the "from−clause" (demodulator) and not in the clause under consideration.
3) Demodulation requires that the EQ−literal resides in a (positive) unit−clause.
4) Demodulation discards the original clause into which the substitution takes place, while paramodulation retains the clauses before and after the substitution.

5.5 *Hyper−Paramodulation*

As in resolution, the purpose of refining paramodulation is to increase the efficiency; these refinements however are somewhat weaker than those of resolution. It now arises the question whether the paramodulation $\mathfrak{R}_{para}$ can be combined with some earlier discussed resolution schemes. There is no complete counterpart to PI−resolution and OL−resolution in paramodulation. The combination of paramodulation with hyperresolution, and of paramodulation with linear resolution, however, is possible. We therefore define first paramodulation $\mathfrak{R}_{para-X}$ under the constraints of the additional resolution X, and in a second step we investigate the possible consequences if both resolution schemes are applied. In this sub−section we analyze in particular the combination of paramodulation + hyperresolution: $\mathfrak{R}_{para-H} + \mathfrak{R}_{H}$.

Hyper Paramodulant:
Let P be an ordering of predicate symbols including those of the clauses: G ≡ L[t] ∨ A and H ≡ EQ[r,s] ∨ B. A paramodulant of these two clauses is called a 'Hyper Paramodulant' $\mathfrak{R}_{para-H}$ if and only if G and H are positive clauses and the literals paramodulated upon (L[t] and EQ[r,s]) are of higher or equal priority (or contain) the largest predicate symbols in G and H, respectively.

Hyper Paramodulant $\mathfrak{R}_{para-H}$:

1) P predicate ordering
2) G ≡ L[t] ∨ A, H ≡ EQ[r,s] ∨ B
3) G,H positive clauses
4) L[t] ≥ Predicates(G), EQ[r,s] ≥ Predicates(H)

Combination: Hyperresolution + Hyper Paramodulation
Let P be an ordering of the predicate symbols in a set S of clauses. A deduction that is obtained by using both: hyperresolution ($\mathfrak{R}_{H}$) and hyper paramodulation ($\mathfrak{R}_{para-H}$), is called a 'hyper deduction

by resolution and paramodulation', or short 'Hyper− Paramodulation': $\mathcal{R}_H + \mathcal{R}_{para-H}$. Every clause is either in S, or a hyper resolvent, or a hyper paramodulant:

Hyperresolution +	Hyper Paramodulation	= = >	
$\mathcal{R}_H$	$\mathcal{R}_{para-H}$		Clause in S Hyperresolvent Hyper Paramodulant

Completeness of Hyper − Paramodulation:
If P is an ordering of the predicate symbols in a finite EQ − unsatisfiable set S of clauses, then there is a Hyper− Paramodulation deduction of □ from the set: { S ∪ EQ(x,x) ∪ F }. F represents the set of functionally reflexive axioms for S.

Hyperresolution + Paramodulation = = > complete
(S' ≡ S ∪ EQ(x,x) ∪ F)

Note the above theorem says that for hyperresolution we need only consider clashes whose "satellites" are positive, and for paramodulation we need consider only positive clauses.

Corollary − Theorem:
If P is an ordering of the predicate symbols in a finite EQ − unsatisfiable set S of clauses such that the equality predicate EQ(..) is the smallest in P, and if F is the set of functionally reflexive axioms for S, then □ can be deduced from : { S ∪ EQ(x,x) ∪ F } by hyperresolution and paramodulation whereby: i) all resolvents are hyperresolvents, and ii) paramodulation is applied only from clauses consisting entirely of positive EQ − literals into positive clauses.

Example 39 : [Hyper − Paramodulation]

$S = \{ 1 \equiv \sim Q_a \vee \sim R_a \vee EQ[a,b],\ 2 \equiv Q_a \vee EQ[a,b],\ 3 \equiv R_a,\ 4 \equiv \sim EQ[f_a, f_b],\ 5 \equiv EQ[f_x, f_x] \}$

P - Ordering = [Q > R > EQ]

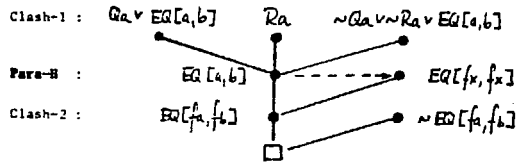

5.6 *Input − Paramodulation, Unit − Paramodulation*

The input and unit resolutions discussed earlier can be extended to include also paramodulation. In the following we go through the definitions and formulate the theorem.

Input Paramodulation:
A paramodulation in which one of the two parent clauses is an input clause is called an 'Input Paramodulation'

$$G_{i+1} = \mathcal{R}_{para-I}(R_i, B)$$

R_i: S − clause or Input Paramodulant; B: Input Clause (S − Clause)

Combination: Input Resolution + Input Paramodulation
A deduction that is obtained by employing both: input resolution ($\mathcal{R}_I$) and input paramodulation ($\mathcal{R}_{para-I}$), is called an 'input deduction by resolution and paramodulation', or short 'Input − Paramodulation' : $\mathcal{R}_I + \mathcal{R}_{para-I}$. Every clause is either in S, or is an input resolvent, or is an input paramodulant:

Input Resolution + Input Paramodulation = = >

$\mathcal{R}_I \qquad \mathcal{R}_{para-I}$

Clause in S
Input Resolvent
Input Paramodulant

Example 40 : $S = \{ 1 \equiv P[a,f_a] \vee Q_c, 2 \equiv EQ[a,b] \vee Q_c, 3 \equiv \sim P[a,f_b] \vee Q_a$
$4 \equiv EQ[a,c], 5 \equiv \sim Q_c \}$

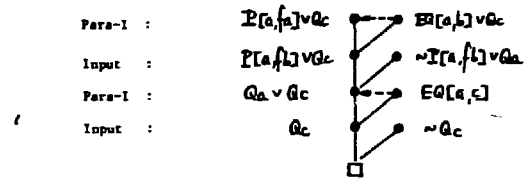

Theorem:
If G is a clause in an EQ−unsatisfiable set S' = { S ∪ EQ(x,x) ∪ F } of unit clauses, and if S'−{G} is EQ−satisfiable, then S' has an Input−Paramodulation ($= \mathcal{R}_I + \mathcal{R}_{para-I}$) :

S' = { S ∪ EQ(x,x) ∪ F } (EQ−unsatif.) = = > S' $\vdash_{\mathcal{R}_I + \mathcal{R}_{para-I}}$ □
S' − {G} (EQ−satisf.)

Unit Paramodulation:
A paramodulation in which a paramodulant is obtained by using at least one unit−clause or a unit−factor of a parent clause is called a 'Unit Paramodulant':

$G_{i+1} = \mathcal{R}_{para-U}(G_i, G_j)$

S−Clause or Unit Paramodulant — G_i ; G_j — Unit−Clause (S−clause or Unit Paramodulant)

Combination: Unit Resolution + Unit Paramodulation
A deduction that is obtained by using both: unit resolution ($\mathcal{R}_U$) and unit paramodulation ($\mathcal{R}_{para-U}$) is called a 'unit deduction by resolution and paramodulation', or short 'Unit−Paramodulation' : $\mathcal{R}_U + \mathcal{R}_{para-U}$. Every clause is either in S, or is a unit resolvent, or is a unit paramodulant:

Unit Resolution + Unit Paramodulation = = >

$\mathcal{R}_U \qquad \mathcal{R}_{para-U}$

Clause in S
Unit Resolvent
Unit Paramodulant

Example 41 : $S = \{ 1 \equiv EQ[a,b], 2 \equiv EQ[a,c], 3 \equiv EQ[x,x], 4 \equiv P_a \vee R_{ab}$
$5 \equiv \sim P_c \vee \sim EQ[a,b], 6 \equiv \sim R_{ab} \}$

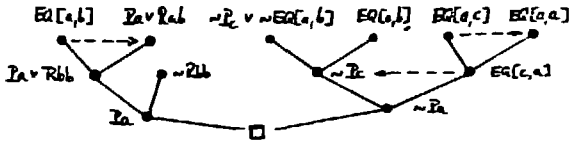

Theorem:
If a set of clauses has an input deduction by ($\mathcal{R}_I + \mathcal{R}_{para-I}$) of □, then { S ∪ F } has a deduction of □ by ($\mathcal{R}_U + \mathcal{R}_{para-U}$). F stands for the functionally reflexive axioms of S.

$$S \vdash_{R_I + R_{para-I}} \quad ==>> \quad (S \cup F) \vdash_{R_U + R_{para-U}} \square$$

There is not yet a proof of the inverse of the above theorem.

Example 42 : $S = \{ 1 \equiv \neg P_a,\ 2 \equiv P_d,\ 3 \equiv EQ[a, f_b],\ 4 \equiv EQ[b, c],$
$5 \equiv EQ[g_a, f_c],\ 6 \equiv EQ[g_a, d] \}$

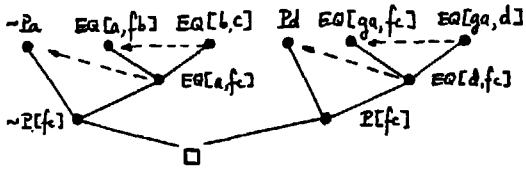

5.7 *Linear – Paramodulation*

As in the case of unit and input resolution there exists similarly an extension of linear resolution to include paramodulation. This is what we will consider in this section.

Combination: Linear Resolution + Paramodulation
Given a set of clauses with the selected member G_0 . A deduction that is obtained by using both, linear resolution (R_L) and paramodulation (R_{para}) is called a 'linear deduction by resolution and paramodulation' or short 'Linear – Paramodulation': $R_L + R_{para}$, from S of the clause G_n with:

$$G_{i+1} = R_L(G_i, B_i) + R_{para}(G_i, B_i)$$

Center – Clause (preceding linear resolvent or paramodulant) — Side – Clause (from S or any previous resolvent)

Every clause is either in S, or is a linear resolvent, or is a paramodulant:

Linear Resolution + Paramodulation	==>>	
		Clause in S
R_L		Linear Resolvent
	R_{para}	Paramodulant

Completeness of Linear – Paramodulation:
If G is a clause in an EQ – unsatisfiable set of clauses: $S' = (S \cup EQ(x,x) \cup F)$, and if $S' - \{G\}$ is EQ – satisfiable, then S' has a 'Linear – Paramodulation' ($= L + para$) of $\square$ with top – clause G:

$S' = (S \cup EQ(x,x) \cup F)$	(EQ – unsatisf.) ==>>	$S' \vdash_{R_L + R_{para}} \square$
$S' - \{G\}$	(EQ – satisf.)	

Example 43 : [Linear – Paramodulation]

$S = \{1 \equiv \sim Q_c \vee EQ[c,d], 2 \equiv \sim Q_c \vee \sim EQ[f_c, f_d]$

$3 \equiv Q_c \vee EQ[a,b], 4 \equiv Q_c \vee \sim EQ[f_a, f_b], 5 \equiv EQ[f_x, f_x]\}$

$1+2=6 : \sim Q_c \vee \sim EQ[f_d, f_d]$

$6+5=7 : \sim Q_c$

$7+3=8 : EQ[a,b]$

$8+4=9 : Q_c \vee \sim EQ[f_b, f_b]$

$9+5=10 : Q_c$

$10+7=11 : \square$

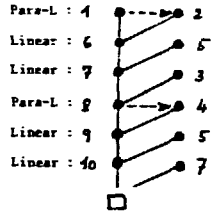

6. HELPFUL RULES

In the preceding section we have introduced several different resolution refinements giving any hints at their practical applicability and their use. In this section we aim to fill this gap by transmitting a few general rules which, although not universally applicable, can be quite helpful. We first introduce a few notions.

6.1 Strategies

Strategy is a means for guiding the refutation search process of an ARP. One distinguishes among others the ordering−, restricting−, pruning−, canonicalizing−,... strategies. Without a strategy a ARP would eventually, even for the most simple problem, generate too many conclusions to be effective. Two particular strategies have proven of quite some help:

Set−of−Support Strategy:
The set−of−support strategy prohibits the application of an inference rule to a set of clauses unless at least one of the two clauses has support. A clause 'has support' if it is an input clause and has been designated as having support, or if it is obtained by application of an inference rule to a set of clauses one of which has support. In other words, having support is inherited in the sense that in each step of the derivation of the clause, at least one of the clauses participating in the step has support. The recommended choices for the set−of−support are either the set of clauses that comprise the special hypothesis and also those that comprise the denial, or simply those that comprise the denial. Notice that either of these choices has the property that the complement of this set is expected to be a satisfiable clause set.

Unit Preference Strategy:
The 'unit preference strategy' is the strategy which causes an ARP to prefer for the application of an inference rule at set of clauses, one of which is a unit clause. Further, if a unit clause is found, the ARP employing this strategy seeks a clause with the fewest possible literals and containing a literal that unifies with the unit clause but is of opposite sign. If no such set exists, then the unit preference strategy causes an ARP to prefer a set in which one of the clauses has a number of literals as few as possible. The motivation for the unit preference strategy is the seeking of unit clauses, and especially of unit conflict.

Weighting:
One of the most powerful ordering strategies is that of weighting. With this strategy, priorities for variables, function symbols, and predicate symbols are assigned by the user. Thus the user informs the ARP about which concepts are thought to be keys to solving the problem at hand. These priorities or weights are relied upon to direct the ARP in its choice of the next clause on which to focus. The weighting strategy can be imposed regardless of the combination of inference rules being employed. Using weighting in this manner imposes an ordering strategy on the program's processing of clauses. In contrast, weighting also permits a threshold to be assigned that in turn causes the deletion of clauses whose weight exceeds that threshold. Used in this manner weighting imposes a restriction strategy. Whether used as an ordering strategy or as a restriction strategy, weighting can interfere with refutation completeness.

6.2 Guidelines

The application of the earlier discussed resolution refinements on many practical problems has lead to a set of guidelines for the representation problem in clausal−form, for the optimal choice of the inference rule and for the best strategy to choose. We summarize in the following the essential,but rarely available information:

Problem Representation:
1) Use unit clauses in preference to non−unit clauses.
2) Employ equality predicates.
3) Rely on shorter clauses in preference to longer.
4) Depend on implicit argument−typing in preference to literal−typing.
5) Include dependent information.

Inference Rules:
1) Use Paramodulation if equality units are present.
2) Use UR−resolution when unit−clauses are present or when unit−clauses are being sought.
3) Use Hyperresolution when positive clauses are being sought.
4) Avoid binary resolution.

Strategies:
1) Rely on the set−of−support strategy, with the choice for the set−of−support of the clauses that comprise the special hypothesis and the clauses that comprise the denial.
2) Weight functions and predicates to reflect your knowledge and intuition about how the problem being studied might be solved.
3) Include in the input demodulators that simplify and canonicalize.
4) Employ the unit preference strategy, if you need to employ binary resolution.

7. CONCLUSION

This paper is the second part of an introductory tutorial on "Theorem Proving/Automated Reasoning". It focuses on the basic resolution refinments which can be grouped into: semantic resolution, linear resolution, and paramodulation. Each of these techniques comprises a set of particular resolution refinements. Semantic resolution introduces the predicate ordering and uses semantic criteria to split the set of input clauses into two groups; resolution is then blocked between the members of the same group. In linear resolution, one of the two parent clauses must be the preceding resolvent. If the second parent clause is an input or unit clause, the number of possible resolutions is further reduced at the price that the completeness property in full generality is not valid any longer. Combining the concepts of linearity and ordering, we arrive at the ordered linear resolution. Due to its extended set of equality axioms, the equality predicate introduces an additional complexity into resolution which is reduced, to a large extent, by paramodulation. In addition, paramodulation has the advantage of being compatible with several of the earlier touched resolution refinements.

Having in mind the realization of a theorem proving/automated reasoning program and its practical applications, these notes are intended to give the reader a rapid introduction into the employed basic concepts, a kind of overview about the notions and theorems, without going into the technical details of the proofs.

Part I of this tutorial introduced the basic notions of propositional and predicate logic. The present part II concentrates on the resolution refinements, and part III will focus on the applications of theorem proving/automated reasoning in science, technology and every−day life.

ACKNOWLEDGEMENTS:
The author thanks Profs. C.Joseph and P.Minkowski for their kind interest and encouragements.
The author also thanks the CERN Theoretical Physics Division, where part of this work was done, for its kind hospitality.

REFERENCES

[1] B.Humpert
Theorem Proving with First – Order Predicate Logic: I.
Proc. of the 8th Warsaw Symposium on Elementary Particle Physics, 1985.

[2] L.Wos et al.
Automated Reasoning: Introduction and Applications,
Prentice Hall Inc., New Jersey, 1984.

[3] J.R.Slagle
Automatic Theorem Proving with renamable and semantic resolution.
Journal of the ACM 18 (1967) 630

[4] D.W.Loveland
A linear format for resolution.
Proc. IRIA Symp. Automatic Deduction, Versailles, France, 1968
Springer Verlag, New York (1970) p.163

[5] G.A.Robinson and L. Wos
Paramodulation and Theorem Proving in First – Order Theory with Equality: in "Machine Intelligence", Vol.4 (Eds. B.Meltzer and D.Michie), American Elsevier, New York (1969) p.135.

[6] C.L.Chang and R.C.T.Lee
Symbolic Logic and Mechanical Theorem Proving.
Academic Press, New York, 1973.

A.Bundy
The Computer Modelling of Mathematical Reasoning.
Academic Press, New York, 1983

D.W.Loveland
Automated Theorem Proving: A Logical Basis.
North Holland Publ. Co., Amsterdam, 1978.

J.A.Robinson
Logic: Form and Function
Edinburgh University Press, Edinburgh, 1979

Eds. J. Siekmann and G. Wrightson
Automation of Reasoning 1,2: Classical Papers on Computational Logic
Springer Verlag, new York, 1983.

[7] see first reference in ref.[6].

[8] J.A.Robinson
Automatic Deduction with Hyper – Resolution.
Intl. Journl. of Comp. Maths. 1 (1965) p.227

R.Overbeek
An Implementation of Hyper-Resolution.
Computers and Mathematics with Applications 1 (1975).

[9] L.Wos, D.Carson and G.Robinson
Efficiency and Completeness of the Set-of-Support Strategy in Theorem Proving.
Journal of the ACM 12 (1965) 536

[10] R.Reiter
Two Results on Ordering with Merging and Linear Format.
Journal of the ACM 18 (1971) 630

[11] J.R.Slagle and L.Norton
Experiments with an Automated Theorem Prover having Partial Ordering Rules.
Division of Computer Research and Technology, Natl. Inst. of Health, Bethesda, Maryland (1971).

[12] R.S.Boyer
Locking: A Restriction of Resolution.
Ph.D.Thesis, Univ. of Texas at Austin, Texas (1971)

[13] C.L.Chang
The Unit Proof and the Input Proof.
Journal of the ACM 17 (1970) p.698

L.Henschen and L.Wos
Unit Refutations and Horn Sets
Journal of the ACM 21 (1974) p.698

[14] R.Kowalski and D.Kuhner
Linear Resolution with Selection Function
Artificial Intelligence 2 (1971) p.227

D.Loveland
A Unifying View of Some Linear Herbrand Procedures.
Journal of the ACM 19 (1972) p.366

[15] L.Wos and G.Robinson
Paramodulation and Set-of-Support
Proc.Symp. Automatic Demonstration
Springer-Verlag, New York (1970) p.276

J.R.Slagle
Automatic Theorem Proving with Built-in Theories Including Equality.
in : Machine Intelligence, Vol.4 (Eds. B.Meltzer and D.Michie), American Elsevier, New York (1969) p.103

R.Kowalski
The Case for Using Equality Axioms in Automatic Demonstration.
Proc. Symp. Automatic Demonstration, Springer-Verlag, New York (1970) p.112.

L.Wos, G.Robinson, D.Carson and L.Shalla
The Concepts of Demodulation in Theorem Proving

Journal of the ACM 14 (1967) p.698

[16] J.A.Robinson
A Machine Oriented Logic Based on the Resolution Principle.
Journal of the ACM 12 (1965) p.23

[17] J.McCharen, R.Overbeek and L.Wos
Complexity and Related Enhancements for Automated Theorem-Proving Programs.
Computers and Mathematics with Applications 2 (1976) p.1

GLUONS AND QUARKS INSIDE HADRONS AND RISING HADRON CROSS SECTIONS

A.V.Kiselev*)

Institute for High Energy Physics, Serpukhov, USSR

Multiple production processes have always been regarded as a manifestation of a complex particle structure. These processes prove to be especially significant for strongly interacting particles (hadrons). Over the last few decades the concept of the hadron structure has evolved from the pion cloud of the nucleon to the quark-gluon structure of baryons and mesons.

As is now clear, the hadron structure is closely related to that of vacuum. Modern ideas of this problem are accumulated in the theory of two vacua, physical (hadronic) and perturbative (partonic). On small space-time scales, both vacuum and real hadrons are thought to be parton vacuum bubbles containing valence quarks. Inside the bubbles, partons are normal excitations. Various bag models that take into account this picture successfully describe static characteristics of hadrons.

As known the bulk of hadron interaction occurs at long distances (comparing with the scale of e^+e^--annihilation, for instance). Therefore, hadron periphery plays the major role in hadron-hadron collisions. In the picture above it is determined by the transition layer between two vacua. In the bag models there is no reliable quantum field description of the bag walls. It is not a surprise then that no noticeable advance has been

*) Report is based on the team-work with V.A.Petrov.

achieved in studying hadron interactions at high energies within the framework of bag models.

In our opinion, the "physical contents" of the transition layer should naturally be referred to the gluon field. Relative independence of gluon matter in forming the transition layer (wall) of the hadron is ensured by the gluon self-interaction.

At moderate energies, when hadrons have time to stick together, they interact via their internal constituents, valence quarks and hadron-hadron scattering processes are well described by additive quark model.

For high energies, the mechanisms associated with the interaction of gluon walls become dominant. The idea of gluon dominance in high-energy collisions goes back to refs.[1,2] in which it was endeavoured to estimate possible experimental manifestations of the gluon mechanism. As was pointed out in ref.[1], the presence of leading hadrons carrying about half the momenta of initial particles testifies to a relatively passive role of valence quarks. Additional arguments in favour of the gluon dominance model were given in ref.[3].

In ref.[1] the gluon interaction was allowed for "as a whole", by using distributions in the sum of momenta of all the gluons in the hadron. This approach obviously contradicts quantum field formalism. In this connection, the approach from ref.[2] is preferable since in it the interaction is mainly determined by the interaction of two gluons. As an argument favouring this mechanism it is pointed out that in the interaction of more than one gluon from each hadron, they will form (due to intense self-interaction) a virtual glueball. The interaction radius will be then greatly diminished. Another argument consists in the estimate of the relative density of gluons (in impact parameter) in colliding hadrons, which is of the order of 10-20%.

One should also mention ref.[4] in which the "bare" Pomeron is thought of as a simple exchange by a minimal number of gluons. This mechanism brings about a constant cross section.

Rising cross sections result from the gluon interaction mechanism[2,5,6]. It was first realized in ref.[5] where the model for the glueball resonance production in hadron collision was proposed.

In the following we shall proceed from the model which takes into account the main features of the above picture. For definiteness, it will be referred to as the "gluon dominance model" (GDM).

In the GDM the hadron multiple production amplitude is set by the graph in Fig. 1. After inelastic (in a general case) scattering of gluons from hadrons A and B, final hadronic states may be subdivided into three groups. There are fragments of hadron A, produced after the absorption of "return" gluon; "vacuum hadrons" as a result of the energy transfer from hadrons A and B to vacuum via active gluons; and fragments of hadron B.

The basic GDM ingradients are: $g_A(x,\vec{b})$ - the gluon distribution in the momentum fraction x and the impact parameter b in hadron A; and $t_{gg}(s,\vec{b})$ - the scattering amplitude for two gluons with the invariant mass s and the impact parameter b. Consider first the total cross section. For large invariant masses of final hadron groups, we replace in Fig. 1 summation over hadronic states by that over partonic (totally colorless) states. Note, that the parton-hadron duality hypothesis is extensively used in analysing hard processes, say e^+e^--annihilation into hadrons.

With the help of parton-hadron duality one can easily verify that in the GDM the unitarity condition is fulfilled. The total cross section for scattering of hadrons A and B is described in its main rising part by the following expression[2,6]

$$\sigma_{AB}^{tot}(s) = \int dx_1\, dx_2\, g_A(x_1) g_B(x_2)\, \hat{\sigma}_{gg}(s x_1 x_2) \qquad (1)$$

where

$$g_A(x) = \int d^2b\, g_A(x, \vec{b}),$$
$$\hat{\sigma}_{gg}(s) = Im\, \hat{\tau}_{gg}(s, 0), \qquad (2)$$
$$\hat{\tau}_{gg}(s, \vec{\Delta}) = \int d^2b\, \exp(i\vec{\Delta}\vec{b})\, \tau_{gg}(s, \vec{b})$$

In formula (1) there are restrictions on gluon momentum fractions showing the field of application of the parton description

$$m/\sqrt{s} \ll x_i \ll 1 \qquad (3)$$

m being a typical hadron mass.

In the composite quark model, the role of gluons reduces to formation of dressed quark-valons. One of the agruments favouring this model is approximate proportionality of cross sections to the numbers of valons in hadron collisions. In particular, hereout one obtains the known relation

$$\sigma_{\pi N}/\sigma_{NN} = 2/3 \qquad (4)$$

established in ref.[7].

What happens in our model? It has been estimated experimentally that in the proton (and in the pion, but not so difinitely) half the mcmentum is carried by gluons. We assume this to hold for all hadrons containing light quarks. Next, in different situations one can apply the constiturnt counting rules which for the gluon distribution read

$$x g_A(x)\Big|_{x\sim 1} = C_A (1-x)^{2n_A - 1} \qquad (5)$$

n_A being the number of valons in hadron A

It follows from above that

$$C_A = n_A \qquad (6)$$

This in its turn, leads to the following asymptotics for the total cross section

$$\sigma_{AB}^{tot}(s) \to n_A n_B\, \sigma_0(s) \qquad (7)$$

where

$$\sigma_0(s) = \int_{s_0}^{s} \frac{dM^2}{M^2} \hat{\sigma}_{gg}(M^2) \ln\frac{s}{M^2} \geq const \ln\frac{s}{s_0} \qquad (8)$$

is a universal function for all sorts of colliding hadrons.

Thus, the GDM mimicrizes the result of the additive quark model, but its nature here is quite different[8]. It should be underlined that in our model active gluons are collectivised and cannot be referred unambiguously to quark constituents. As for valence quarks, their interaction leads to a constant contribution to $\sigma_{AB}^{tot}(s)$ (which is also proportional to n_A, n_B).

Note that the rise of $\sigma_{AB}^{tot}(s)$ is associated with the singular behaviour of the gluon distribution, i.e. with the infinite number of gluons in the hadron. Demanding also that the Froissart bound on $\sigma_{AB}^{tot}(s)$ be fulfilled, one comes to strong limitations on the singular behaviour of function $g_A(x)$ at x=0. Up to the degrees of ln 1/x they are of the form

$$(\ln 1/x)^{-1} \leq x g_A(x) \leq (\ln 1/x)^{1/2} \qquad (9)$$

Remember that these conclusions hold for any behaviour of the gluon-gluon scattering amplitude.

Now we turn to choosing a particular form for g_A and $\hat{\tau}_{gg}$ We assume that the gluon-gluon scattering amplitude is described by the pole Regge theory with asymptotics

$$\hat{\tau}_{gg}(s,\vec{b}) = i\,\frac{1+e^{-i\pi\alpha(t)}}{2}\,\beta^2(t)\left(\frac{s}{s_0}\right)^{\alpha(t)}, \quad t \equiv -\vec{\Delta}^2 \qquad (10)$$

The basic assumption is that the Regge trajectory $\alpha(t)$ is a glueball linear trajectory:

$$\alpha(t) = 1 + \alpha_p'(0)t \qquad (11)$$

Then for small -t, the gluon-gluon amplitude is specified by expression

$$\hat{\tau}_{gg}(s,\vec{b}) = i\hat{\sigma}_0 s \exp\left(t\alpha_p'(0)\ln s/s_0\right) \qquad (12)$$

where we denote $\hat{\sigma}_0 = \beta^2(0)/s_0$.

Based upon the straight-line glueball vacuum trajectory, we predict the existence of condensate of 0^{++} "glueballs" with the "mass" $-1/\alpha_p'$*). As shown in ref./9/, instability of the perturbative vacuum can actually lead to the creation of condensate of gluon bound states with vacuum quantum numbers filling in the hadron vacuum.

The Pomeron pole in the gluon amplitude causes a double logarithm rise of the total cross section:

$$\sigma_{AB}^{tot}(s) = 1/2\, n_A n_B \hat{\sigma}_0 \ln^2 s/s_0 \qquad (13)$$

Using formulae (1), (12), find the average momentum fractions for interacting gluons, $\langle x_i \rangle = 2/\ln s$. In other words with the energy of colliding hadrons growing still softer gluons participate in the interaction.

The choice of the gluon spatial distribution in hadrons $g_A(x,\vec{b})$ should agree with the physical picture in which the softest gluons are located in periphery. Under the chosen Regge behaviour of the gluon-gluon amplitude, the size of the gluon cloud is strictly fixed by the condition $\sigma_{AB}^{el} < \sigma_{AB}^{tot}$. We require further that the gluon distribution function, integrated over the impact parameter, $g_A(x)$, should be the same as the one measured in deep inelastic scattering and charm photoproduction. Our grounds are the results from refs./10/ where it was shown that the inclusive hadron-hadron and deep inelastic lepton-hadron processes can be described by universal structure functions.

---

*) In fact glueball trajectory being linear at high angular momenta may exhibit a highly nonlinear behaviour in "quantum region". So, our estimate of the tachyon mass may change drastically.

Finally we choose the soft gluon distribution to be

$$x g_A(x,\vec{b}) = \frac{n_A(1-x)^{2n_A-1}}{\pi R_A^2 \ln^2 x} \exp\left(-b^2/R_A^2 \ln^2 x\right) \qquad (14)$$

In elastic hadron scattering each gluon in Fig. 1, after being elastically scattered on the gluon from another hadron coverts the excited parton configuration into the initial hadron.

Present now the results of calculations. The slope of the elastic differential cross section $B_{AB}(s,t)$ depends on the variable t. When t=0, it has the following asymptotics

$$B_{AB}(s,0) = \frac{d}{dt}\left(\ln \frac{d\sigma_{AB}^{el}}{dt}\right)\Big|_{t=0} = \frac{1}{12}\left(R_A^2 + R_B^2\right) \ln^2 \frac{s}{s_0} \qquad (15)$$

With -t rising, the behaviour of the differential cross section becomes Regge-like:

$$\frac{d\sigma_{AB}^{el}}{dt}\Big|_{-tR_{AB}^2 \ln^2 s/s_0 \gg 1} = \frac{(n_A n_B \hat{\sigma}_0)^2}{(R_A R_B t)^2} \exp\left(2t\alpha_P'(0) \ln s/s_0\right) \qquad (16)$$

The slope parameter in this region is determined by the slope of the leading glueball trajectory $\alpha_P'(0)$

$$B_{AB}(s,t)\Big|_{-tR_{AB}^2 \ln^2 s/s_0 \gg 1} = 2\alpha_P'(0) \ln s/s_0$$

Finally at high s the total elastic cross section is proportional to

$$\sigma_{AB}^{el}(s) = \frac{1}{4\pi} \frac{(n_A n_B \hat{\sigma}_0)^2}{R_{AB}^2} \ln^2 \frac{s}{s_0} \qquad (17)$$

where

$$R_{AB}^{-2} = \int du_1 du_2\, \theta(1-u_1-u_2)\, dv_1 dv_2\, \theta(1-v_1-v_2) \cdot \left[R_A^2(u_1^2+v_1^2) + R_B^2(u_2^2+v_2^2)\right]^{-1} \qquad (18)$$

In particular, $R_{AA}^2 = 1.85\, R_A^2$.

In the single diffraction without a quantum number exchange $AB \to AX$, hadron A is a kind of a probe for the gluon distribution in hadron B similarly as the lepton serves as that for the quark distribution in deep inelastic lepton-nucleon processes.

The GDM allows one to calculate the single diffraction differential cross section in the kinematic region

$$s \gg M^2 \gg -t \tag{19}$$

with M^2 being an invariant mass of final hadron states. The high M^2 allows to apply again parton-hadron duality and express the cross section through the quantities g_A and $\hat{\tau}_{gg}$. Here is the result of the calculations:

$$\left.\frac{d\sigma^{SD}_{AB\to AX}}{dt\,dM^2}\right|_{-tR_A^2\ln^2 s/s_0 \gg 1} = \frac{1}{16}\frac{(n_A\hat{\sigma}_0)^2 n_B}{M^2 R_A^2 |t|}\exp\left(2t\alpha_p'(0)\ln\frac{s|t|}{s_0 M^2}\right) \tag{20}$$

The contribution coming from the large M^2 region to the asymptotics of the single diffraction total cross section, is given by the formula

$$\sigma^{SD}_{AB\to AX} = \frac{1}{16}(n_A\hat{\sigma}_0)^2 n_B \frac{1}{R_A^2}\ln\frac{s}{s_0}\ln\ln\frac{s}{s_0} \tag{21}$$

To study the resonance region in the diffraction process ($M^2 \sim m^2$), one has to introduce some additional quantities which would describe overlapping of gluon clouds of hadron B and associated hadron resonances.

Similarly, the differential cross section of double diffraction without a quantum number exchange $AB \to X_1X_2$ in the kinematic region

$$s \gg M_1^2, M_2^2 \gg -t \tag{22}$$

looks like

$$\frac{d\sigma^{DD}_{AB\to X_1X_2}}{dt\,dM_1^2\,dM_2^2} = \frac{1}{16\pi}\frac{n_A n_B \hat{\sigma}_0^2}{M_1^2 M_2^2}\exp\left(2t\alpha_p'(0)\ln\frac{st^2}{s_0 M_1^2 M_2^2}\right) \tag{23}$$

Accordingly, the total cross section of double diffraction (except the contribution from resonance production of the hadron groups X_1 and X_2) behaves as follows:

$$\sigma^{DD}_{AB\to X_1X_2} = \frac{1}{32\pi}\, n_A n_B \hat{\sigma}_0^2 \frac{1}{\alpha_P'(0)} \ln\frac{s}{s_0} \ln\ln\frac{s}{s_0} \qquad (24)$$

Note that its scale is dictated by the glueball trajectory slope.

In some respects the consequences of the GDM coincide with those of other approaches. For instance, for the single difiraction the M^{-2} law for large M^2 can be also obtained in the three-reggeon mechanism[11]. Our model shares also with the three-reggeon mechanism such a result as factorization. Indeed, from (15), (20), (21) we conclude that for high enough -t, namely, in the range $-t R_{AB}^2 \ln^2 s/s_0 \gg 1$ the following equality is satisfied:

$$\frac{d\sigma^{el}_{AB}}{dt}\,\frac{d\sigma^{DD}_{AB\to X_1X_2}}{dt\,dM_1^2 dM_2^2} = \frac{d\sigma^{SD}_{AB\to AX_1}}{dt\,dM_1^2}\,\frac{d\sigma^{SD}_{AB\to X_2B}}{dt\,dM_2^2} \qquad (25)$$

As for the total, elastic, single and double diffraction cross sections they are determined in the GDM by the behaviour of corresponding differential cross sections at parametrically small momentum transfers ($-t R_{AB}^2 \ln^2 s/s_0 \lesssim 1$) and are not connected via an analogous relation.

REFERENCES

1. S.Pokorski, L. Van Hove.Acta Phys. Pol., B5 (1974) 229; L.Van Hove, S.Pokorski. Nucl. Phys., B86 (1975) 243.
2. G.L.Kane. York-Peng Yao. Nucl. Phys., B137 (1978) 313.
3. Carruthers P. Preprint LA-UR-84-1084.
4. F.E.Low. Phys. Rev., D12 (1975) 163.
5. S.S.Gershtein, A.A.Logunov. Yad. Fiz., 39 (1984) 1514.
6. V.A.Petrov. Preprint IHEP 85-48, Serpukhov, 1985.
7. E.M.Levin, L.L.Frankfurt. Pis'ma ZhETF 31 (1965), 105.
8. G.Sh.Dzhaparidze, A.V.Kiselev, V.A.Petrov. Preprint IHEP 85-50, Serpukhov, 1985.
9. C.E.Carlson, T.H.Hansson, C.Peterson. Phys. Rev., D26 (1982) 2069.
10. A.A.Logunov, M.A.Mestvirishvili, V.A.Petrov. Preprint IHEP 74-66, Serpukhov, 1974; Particles and Nuclei 14 (1983) 493.
11. A.B.Kaidalov. Phys. Rep., 50 (1979) 157.

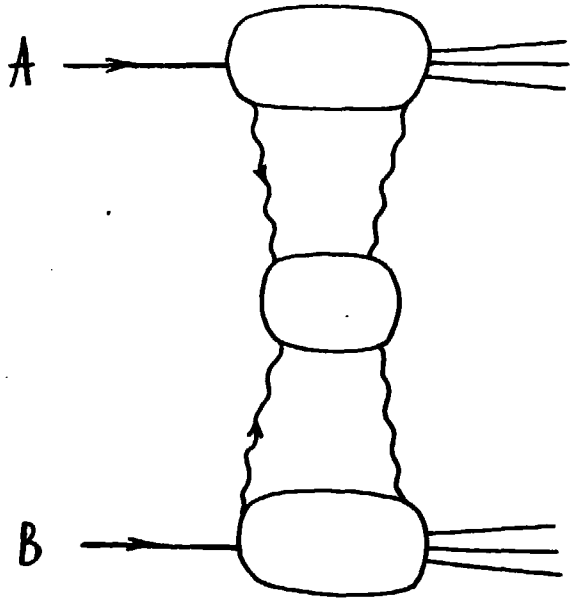

Fig. 1

RECENT RESULTS FROM NEUTRINO SCATTERING EXPERIMENTS

C. GUYOT
CEN, Saclay, France

Abstract :

The recent results from neutrino experiments at high energies are reviewed. Emphasis is given on their impact on the knowledge of the structure of the weak neutral current and the nucleon structure.

Outline :

1ère PART : STRUCTURE OF THE WEAK CURRENT. PURELY LEPTONIC INTERACTIONS

1.1 Neutrino scattering and the structure of the weak current

1.1.1 - *Basic formalism for the weak interactions of neutrinos with matter [1]* :

The lagrangian for neutrino interactions with ordinary matter at "low" energies ($Q^2 \ll M_z^2$) can be written as follow :

$$L = L_{CC}^{\nu N} + L_{NC}^{\nu N} + L^{\nu e}$$

where we have separated the charged current (CC) and neutral current (NC) interactions with nucleons. If one assumes a current-current form with only Vector and Axial terms, no flavor changing neutral current, the lagrangien for the interactions of a left-handed neutrino with a fermion f can be written :

$$L_{NC}^{\nu f} = \frac{G_F}{\sqrt{2}} \bar{\nu} \gamma^\mu (1+\gamma_5) \nu \; \bar{f} \gamma_\mu \left(g_V^f + g_A^f \gamma_5 \right) f \; , \quad f = e, q_i$$

where we have introduced the phenomenological chiral couplings $g_{V,A}^f$.

The weak hadronic current will be described in the framework of the Quark Parton Model :

$$L_{NC}^{\nu N} = - \frac{G_F}{\sqrt{2}} \bar{\nu} \gamma_\mu (1+\gamma_5) \nu \; J_\mu^N$$

with $J_\mu^N = \sum_{q_i} \bar{q}_i \gamma_\mu \left(g_V^{q_i} + g_A^{q_i} \gamma_5 \right) q_i$, the q_i being the quark flavours.

Also used are the chiral couplings $C_L = \frac{g_V + g_A}{2}$, $C_R = \frac{g_V - g_A}{2}$. In the SU(2)xU(1) model, the chiral couplings are related to the weak isospin and the electric charge of the fermion :

$$g_V = \rho \left(T_3 - Q \sin^2\theta_W \right) \; , \; g_A = - \rho \; T_3$$

with $\rho = \frac{M_W^2}{M_Z^2 \cos^2\theta_W} = 1$ in the standard model.

1.1.2 *Structure of the weak charged current*

For the CC interactions, we will assume a pure V-A structure (no right-handed currents) : $g_V = g_A = +1$ or $C_L = 1$, $C_R = 0$. This is supported by data on μ decay [2] and by neutrino scattering data [3].

If one assumes an admixture of right-handed current in the transition $u \leftrightarrow d$ given by $\rho = |C_R/C_L|$, then it is easy to demonstrate that :

$$|\rho^2| < \frac{d^2\sigma^{\bar{\nu}}/dxdy - (1-y)^2\ d^2\sigma^{\nu}/dxdy}{d^2\sigma^{\nu}/dxdy - (1-y)^2\ d^2\sigma^{\bar{\nu}}/dxdy}$$

which gives experimentally : $|\rho| < 0.009$ (90 % CL).

These limits can be interpreted in the framework of the left right symetric model $SU(2)_R \times SU(2)_L \times U(1)$ with 2 bosons W_L, W_R which mix with an angle ζ into 2 mass eigenstates W_1 and W_2.

$$\text{Then,}\quad C_L = \frac{\cos^2\zeta}{M_1^2} + \frac{\sin^2\zeta}{M_2^2},\ C_R = \sin\zeta\cos\zeta\left(\frac{1}{M_2^2} - \frac{1}{M_1^2}\right)$$

W_1 is the recently discovered W boson. The limits in the plane ζ, $\alpha = M^2(W_1)/M^2(W_2)$ are given in Fig.1.

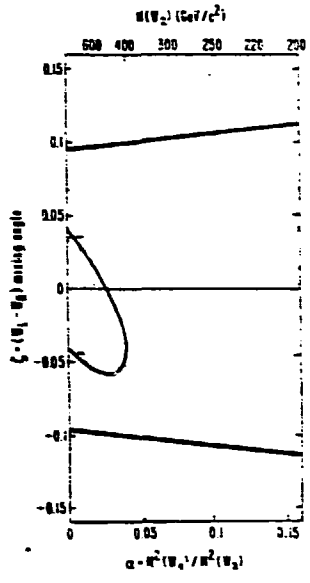

Fig. 1 : Experimental 90 % CL limits on ζ and $\alpha = M_1^2/M_2^2$. The allowed region contains $\zeta = \alpha = 0$. The limits from the neutrino scattering experiment (═══) apply for all ν_R mass, whereas the limits from the μ decay (——) apply for some assumption about the nature and the mass of the ν_R (e.g. $m_{\nu_R} = 0$).

1.2 Purely leptonic interactions :

Neglecting terms of the order m_e/E_ν, the cross sections for ν_e scattering are expressed in terms of the vector and axial couplings as follow :

$$\sigma(\nu_\mu e \to \nu_\mu e) = K\left[\left(g_V^e + g_A^e\right)^2 + (1-y)^2\left(g_V^e - g_A^e\right)^2\right]$$

$$\sigma(\bar{\nu}_\mu e \to \bar{\nu}_\mu e) = K\left[\left(g_V^e - g_A^e\right)^2 + (1-y)^2\left(g_V^e + g_A^e\right)^2\right]$$

$$\sigma(\nu_e e \to \nu_e e) = K\left[\left(g_V^e - g_A^e + 2\right)^2 + (1-y)^2\left(g_V^e + g_A^e\right)^2\right]$$

$$\sigma(\bar{\nu}_e e \to \bar{\nu}_e e) = K\left[\left(g_V^e - g_A^e\right)^2 + (1-y)^2\left(g_V^e + g_A^e + 2\right)^2\right]$$

with $K = \frac{G_F^2 M_e}{2\pi} E_\nu$, $y = E_e/E_\nu$.

Using only $\overset{(-)}{\nu}_\mu e$ interactions does not allow the separation of g_V^e and g_A^e, and the knowledge of their sign. Further information comes from $\overset{(-)}{\nu}_e e$ cross section due to the interference between the CC and NC diagrams.

1.2.1 - *Muon neutrino scattering* :

Two experiments gather most of the world statistics on $\bar{\nu}_\mu e$ interactions. Their results are presented in the following table 1 :

EXP.	number of events ν	number of events $\bar{\nu}$	$\sigma_{\nu_\mu e}/E_\nu$ x 10^{-42} cm^2/GeV	$\sigma_{\bar{\nu}_\mu e}/E_\nu$ x 10^{-42} cm^2/GeV	$R=\frac{\sigma_\nu}{\sigma_{\bar{\nu}}}$	$\sin^2\theta_W$
CHARM [4]	107 ± 17	147 ± 23	1.90 ± 0.90	1.5 ± 0.5	$+ 0.80$ $1.27 - 0.32$	0.215 ± 0.034
BNL E734 [5]	59 ± 9	59 ± 10	1.60 ± 0.39	1.16 ± 0.25	$+ 0.44$ $1.38 - 0.38$	0.209 ± 0.032

R and $\sin^2\theta_w$ are related : $R = 3\,\dfrac{1-4\sin^2\theta_w + \frac{16}{3}\sin^4\theta_w}{1-4\sin^2\theta_w + 16\sin^4\theta_w}$.

Combining the 2 results leads to : $\sin^2\theta_w = 0.212 \pm 0.023$. This result will be significantly improved ($\pm$ 0.005) by the next CHARM II experiment which expects to gather $\sim$ 2000 events by the end of 1988.

1.2.2 - *Electron neutrino-electron scattering :*

Experiment E225 at LAMPF [6] is continuously taking data. Neutrinos are produced in the following cascade :

$$p\ (780\ \text{MeV}) + Cu \rightarrow \ldots\ldots + \pi^0 \rightarrow \mu^+ \nu_\mu \rightarrow e^+ \bar{\nu}_\mu \nu_e\ , \qquad \langle E_{\nu_e} \rangle \sim 20\ \text{MeV}.$$

The $\overset{(-)}{\nu}_\mu$ contributions are subtracted using CHARM and E734 cross sections. The present statistics is 99 $\pm$ 25 events after $\overset{(-)}{\nu}_\mu$ background subtraction (7 $\nu_\mu e$, 14 $\bar{\nu}_\mu e$). One expects 94 $\pm$ 13 events if there is a destructive interference between NC and CC diagrams (as in the standard model), 187 $\pm$ 27 for no interference and 292 $\pm$ 39 for a constructive interference.

The measured cross section is :

$$\sigma(\nu_e e) = 9.8 \pm 2.7_{stat.} \pm 1.6_{syst.}\ \ E_e/\text{GeV} \times 10^{-42}\ \text{cm}^2$$

which gives in the standard model : $\sin^2\theta_w = 0.23\ ^{+\,0.06}_{-\,0.05}{}_{stat}\ ^{+\,0.05}_{-\,0.06}{}_{syst}$

There may be a great future for this kind of experiment. Projects exists at LAMPF which aim at a large statistics (λ 10 000 evts) and a precise measurement of $\sin^2\theta_w$ ($\pm$ 0.0025) [7].

1.2.3 - *The chiral couplings for charged leptons :*

Using only the data from $\nu_\mu e$ scattering gives the following ambiguous results :

$$|g^e_{V,A}| = 0.08 \pm 0.05, \quad |g^e_{A,V}| = 0.496 \pm 0.04$$

Further information is necessary in addition to $\nu_e e$ data. Forward-backward asymetry of muons pairs produced in $e^+e^- \rightarrow \mu^+\mu^-$ provides essentially a measurement of $g^e_A\, g^\mu_A$. Universality ($g^e = g^\mu$) will be assumed. These results gathered in fig. 2 define only one solution :

$$g^e_V = -0.08 \pm 0.05, \quad g^e_A = -0.496 \pm 0.040$$

n agreement with the standard model prediction :

$$g^e_V = -\frac{1}{2} + 2\sin^2\theta_w, \quad g^e_A = -\frac{1}{2}.$$

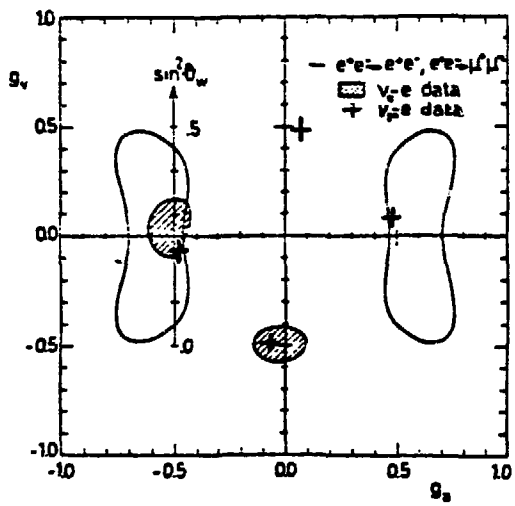

Fig. 2 : Allowed region in the plane g^e_V, g^e_A from data on $\bar{\nu}_\mu e$, $\nu_e e$ and $e^+e^- \rightarrow \mu^+\mu^-$.

2ème PART : NEUTRINO INDUCED DEEP INELASTIC SCATTERING AND THE STRUCTURE OF THE NUCLEON

2.1 Total cross-sections

A proper measurement of the total cross section of neutrinos on nucleon involves a good (but difficult) calibration of the neutrino flux. It is essential for the extraction of the structure functions. Up to now no experiment has ever reported a departure from the linearity with the total energy of the neutrino and the antineutrino cross sections. The history of the most accurate measurements of σ_t on isoscalar targets is given in fig. 3.

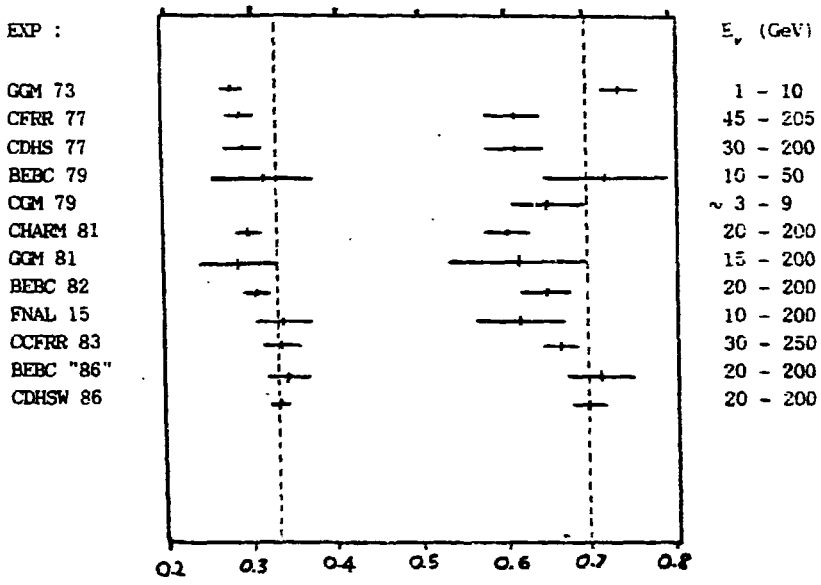

Fig. 3 : Summary of available accurate measurements of $\sigma_t^{\nu(-)}/E$ on the nucleon. This slope is assumed to be constant over the quoted energy range.

The present most accurate measurements are given in table 2.

Table 2

EXP	σ^{ν}/E . 10^{38} cm^2 GeV^{-1}	$\sigma^{\bar{\nu}}/E$
CDHS 77 [8]	0.62 ± 0.04	0.30 ± 0.02
CHARM 81 [9]	0.604 ± 0.032	0.301 ± 0.018
CCFRR 83 [10]	0.669 ± 0.024	0.340 ± 0.020
BEBC revised [11]	0.723 ± 0.040	0.351 ± 0.022
CDHSW 86 [12]	0.686 ± 0.020	0.339 ± 0.010
BEBC νp [11]	0.474 ± 0.028	0.500 ± 0.032
CDHS νp [14]	0.44 ± 0.02	0.44 ± 0.03

From the new results of the CDHSW group, the energy dependence of the cross sections has been derived by 2 independent methods : first by separating the contributions of the neutrinos from K or π decays in 3 different NBB exposures (Fig. 4a), and secondly by the determination of the neutrino energy from its radial position in the high statistics 160 GeV NBB (Fig. 4b). Again no departure from the linearity with E_ν can be seen.

As a conclusion, there is now a better agreement between CERN and FNAL experiments at a value $\frac{\sigma}{E} \simeq 0.70\ 10^{-38}$ cm^2 GeV^{-1}. As a consequence previous CERN structure functions have to be rescaled upward by $\sim$ 12 %.

2.2 Structure function measurements

2.2.1 - *The differential cross sections*

Assuming a current-current form for the interactions and zero lepton masses, the differential cross sections can be written :

$$\frac{d^2\sigma^{(-)}_{\nu}}{dxdy} = \frac{G_F^2\, ME_\nu}{\pi}\left[xy^2\, F_1(x,Q^2) + \left(1 - y - \frac{xyM_N}{2E}\right) F_2(x,Q^2) \pm y\left(1-\frac{y}{2}\right) xF_3(x,Q^2)\right]$$

where x, y are the standard scaling variables :

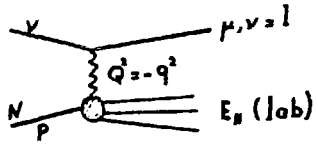

$$y = \frac{E_H - M_H}{E_\nu}, \quad x = \frac{Q^2}{2M_H \nu}, \quad \nu = \frac{p \cdot q}{M_H} = E_\nu - E_l$$

The $F_i = F_i^{\nu,nc,cc}$ are the structure functions which are "a priori" different for ν and $\bar{\nu}$ interactions, and for CC and NC. The F_i's are related to cross-sections of left (+), right (-) and longitudinally (L) polarized W (or Z) bosons :

$$2x F_1 = \frac{2 M_N K}{\pi} \cdot \frac{1}{2} (\sigma_+ + \sigma_-)$$

$$F_2 = \frac{2 M_N K}{\pi} \cdot \frac{1}{1+Q^2/\nu^2} \left\{ \frac{1}{2} (\sigma_+ + \sigma_-) + \sigma_L \right\}$$

$$xF_3 = \frac{2 M_N K}{\pi} \cdot \frac{1}{\sqrt{1+Q^2/\nu^2}} \cdot \frac{1}{2} (\sigma_+ - \sigma_-)$$

where $K = \frac{W^2 - M^2}{2M_N}$ is a somewhat arbitrary flux factor.

This introduces the longitudinal structure function :

$$F_L = \left(1 + \frac{Q^2}{\nu^2}\right) F_2 - 2x F_1 .$$

In the quark parton model (with $m_q = p_T = 0$) :

$$\sigma_L = 0 \rightarrow F_L = 0$$

$$\sigma_+ \propto C_L^{q\,2}\, q(x) + C_R^{q\,2}\, \bar{q}(x)$$

$$\sigma_- \propto C_R^{q\,2}\, \bar{q}(x) + C_L^{q\,2}\, \bar{q}(x)$$

In the leading order of QCD (and to a very good precision, in the next to leading order), F_L and $\overset{(-)}{q}(x)$ can be replaced by the QCD prediction $F_L^{QCD}(x,Q^2)$ and $\overset{(-)}{q}(x, Q^2)$ with a Q^2 variation given by the Altarelli-Parisi equations [15].

For the CC interactions on an isoscalar target with no KM mixing, $s = \bar{s}$, $c = \bar{c}$, $q = x(u+d+s+c)$, one gets :

$$2xF_1^{\nu}(x,Q^2) = 2xF_1^{\bar{\nu}}(x,Q^2) = q + \bar{q}$$

$$xF_3^{\nu}(x,Q^2) = q - \bar{q} + 2x(s-c)$$

$$xF_3^{\bar{\nu}}(x,Q^2) = q - \bar{q} - 2x(s-c)$$

But, one may also include the Kobayashi-Maskawa mixing and the threshold for d or s $\longrightarrow$ c production e.g. by using a slow rescaling model [16] :

Then

$$F_2^{\nu N} = x\,(c_c^2 + \frac{\xi}{x} S_c^2)\,(u+d) + 2x\,(S_c^2 + \frac{\xi}{x} C_c^2)\,s + x(\bar{u} + \bar{d}) + 2\,\bar{c} \neq F_2^{\bar{\nu}N},$$

with $\xi = x\left(1 + \frac{m_c^2}{Q^2}\right)$, $C_c = \cos\theta_c$, $S_c = \sin\theta_c$, $\qquad \xi q = \xi q(\xi, Q^2)\,\theta(1-\xi)$

In addition F_L develops a non zero value in addition to the QCD contribution. As a consequence, there are ambiguities in the definition of the measured structure functions. In principle, they are corrected for :

- The non isoscalarity of the heavy target $\left(\frac{d_v}{u_v} \simeq 0.5\,(1-x)\right)$.
- The strange sea term (s-c) in $2xF_1$ and F_2 (See 2.2.2).
- The radiative corrections.

They are sometimes corrected for the charm threshold effect (slow rescaling), the propagator term, the target mass effect, the Fermi motion, etc...

The present most accurate measurements are described with their assumptions in the following table. Emphasis will be given to the new CDHSW results presented for the first time. Only preliminary results were reported at Bari 1985 [17].

Table 3

Assumptions	CCFRR [18]	CHARM [19]	CDHS 79 [20]	CDHSW new [21]
σ_i/E	0.67	0.60	0.62	0.70
s-c	$\bar{s} = \frac{\bar{u}}{2} = \frac{\bar{d}}{2}$	$\bar{u} = \bar{d} = \bar{s}$	$\bar{s} = \frac{\bar{u}}{2} = \frac{\bar{d}}{2}$	$\bar{s} = \frac{\bar{u}}{2} = \frac{\bar{d}}{2}$ *
C threshold	$m_c = 1.5$	No	No	No
$R = \frac{F_L}{2x F_1}$	R_{QCD}	R = 0	R = 0.1	R_{QCD}
Fermi motion	No	Yes	No	No
Rad. Cor.	<	De Rujula et al. [13]	>	Bardin et al. [35]
# evts ν	150 K	50 K	90 K	650 K
$\bar{\nu}$	23 K	110 K	25 ± 175 K	550 K
Beam	NBB	WBB	NBB ($\nu+\bar{\nu}$) WBB ($\bar{\nu}$)	WBB
Target	Fe	$CaCO_3$	Fe	Fe

* *The strange sea correction takes into account its suppression by the charm threshold.*

2.2.2 - *Extraction of the structure functions*

Ignoring the already discussed corrections, the differential cross sections can be simply written as :

$$\overset{(-)}{\sigma}^{\nu} = \frac{1}{G^2 \frac{ME}{\pi}} \frac{d^2 \overset{(-)}{\sigma}^{\nu}}{dx\, dy} =$$

$$\underbrace{2xF_1}_{q+\bar{q}} \left[\frac{1 + (1-y)^2}{2}\right] + F_L(1-y) + \left[\frac{1 - (1-y)^2}{2}\right] x(s-c) \overset{(-)}{+} \left[\frac{1 - (1-y)^2}{2}\right] \underbrace{xF_3}_{q-\bar{q}}$$

Starting from these expressions, the usual procedure goes as follow :

i) *Determination of the longitudinal structure function* F_L *and the sea :*

F_L can be extracted from the y dependence of the following combination :

$$\frac{\sigma^{\nu} + \bar{\sigma}^{\nu} - \left[1 - (1-y)^2\right] x(s-c)}{1 + (1-y)^2} = 2xF_1 + \frac{(1-y)}{1 + (1-y)^2} F_L$$

Another combination, used by the CDHS collaboration, is :

$$\frac{\bar{\sigma}^{\nu} - (1-y)^2 \sigma^{\nu} + 2x(s-c)\left[(1-y)^2 - (1-y)^4\right]}{1 - (1-y)^4} = \bar{q}^{\nu} + \frac{(1-y) - (1-y)^2}{1 - (1-y)^4} F_L$$

with $\bar{q}^{\nu} = \bar{u} + \bar{d} + 2\bar{s}$.

Taking only the domain y>0.5 minimizes the effect of the s-c correction and the $\bar{\sigma}^{\nu}/\sigma^{\nu}$ normalisation.

The CDHS collaboration has presented at the Bari Conference [17] a new determination of F_L (fig. 5). Fig. 6 shows the measurements of $R = \frac{F_L}{2xF_1}$ from the CHARM and CDHSW groups. A good agreement with the QCD prediction is found although the sensitivity to the value of Λ is very weak.

At the same time, the sea $\bar{q}$ can be extracted from the above equation. Thus, the values of $\bar{q}$ are strongly correlated to F_L and show big errors. A standard procedure consists in using an analytic form of F_L compatible with the previous measurement (e.g. F_L^{QCD}). Final results on F_L and $\bar{q}$ will be presented at the Berkeley Conference [21].

For what follows, a QCD like parametrisation is used for $R = \frac{F_L}{2x\,F_1}$.

ii) *Determination of F_2 :*

F_2 is derived from the following combination :

$$F_2 = \frac{\sigma^{\nu} + \sigma^{\bar{\nu}} - 2x(s-c)\,[1 - (1-y))^2]}{1 + (1-y)^2 - y^2\,\frac{R}{1+R}}$$

A similar formula for $2xF_1$ would involve a correction term for F_L of the form $(1-y)R$ in average larger than $\frac{y^2 R}{1+R}$. This shows that F_2 is in general "better" measured than $2xF_1$, being more free from assumptions on R, especially if one considers only low y data.

The new measurement of F_2 from CDHSW is shown on Fig. 7. A comparison with the previous measurement of the same group using the assumptions and the corrections with the old analysis is shown on Fig. 8. A difference of the order 10 % remains at low x. The agreement with CCFRR (Fig. 9) is now acceptable given the statistical errors.

A significant test of the quark model (or of the consistency of the data) is provided by the comparison with the measurement of $F_2^{\nu N}$. Neglecting the charm threshold and the charm sea, these functions are related according to :

$$\frac{18}{5}\,F_2^{\bar{\nu}N} = F_2^{\nu N}\,\left(1 - \frac{3}{5}\,\underbrace{\frac{s+\bar{s}}{q+\bar{q}}}_{0.05}\right) \quad \text{in average}$$

Figure 10 and figure 11 show comparisons between the right hand side from CDHSW and the left side of the above equation from the EMC [22] and BCDMS [23] collaborations. Rather than pointing to physics problems, the disagreements seem to indicate some experimental inconsistencies especially between the two muon measurements.

iii) The determination of $xF_3 = \frac{1}{2}(xF_3^{\nu} + xF_3^{\bar{\nu}})$

This measurement does not need any assumptions on R and s-c :

$$xF_3 = \frac{\sigma^{\nu} - \sigma^{\bar{\nu}}}{1 - (1-y)^2}$$

Figures 12, 13, 14 show the new measurements of the CDHSW group with the comparisons with the old CDHS and CCFRR data. The improvement in statistics is significant although the data are concentrated at lower Q^2 values where the standard perturbative QCD predictions may be invalided.

2.2.3 - *QCD fits to the structure functions*

They are all based on the Altarelli-Parisi equations. In the early eighties, the study of scaling violations appeared to be very promising to test QCD. The interest has been decreasing due to the appearance of several difficulties :

i) The higher twist effects ($1/Q^2$ terms) may be present at low Q^2 where scaling violations are maximum.

ii) Nuclear effects (EMC effect) are still an open problem although some data seem to indicate no Q^2 dependence.

iii) The data suffer from statistical and systematics limitations for xF_3 which has the only well understood QCD behaviour. Uncertainties from R, s-c, $G(x,Q^2)$ (gluons), may have a non negligible impact on F_2.

iv) Finally, several programs exist on the market which integrate the Altarelli-Parisi equations and fit the expected Q^2 evolution to the observed data. There are still inconsistencies in the results of different programs. But these technical problems should be overcome soon.

The results of QCD fits to available data, which do not involve assumptions on the glue (Non Singlet fits), are summarized in the following table. Results are given in term of the value of Λ (lowest order or next to leading order fit).

Table 4

EXP	target	type of fit	Q^2 range (GeV^2)	Λ_{LO}	$\Lambda_{\overline{MS}}$ (MeV)
CDHS 83	Fe	xF_3	$W^2 > 11$		$200 \,^{+\,300}_{-\,100}$
		F_2 (x>0.35)	$Q^2 > 2$	275 ± 80	300 ± 150
		xF_3	$W^2 > 10$	$88 \,^{+\,163}_{-\,60}$	$155 \,^{+\,250}_{-\,150}$
CCFRR	Fe	F_2	$Q^2 > 5$	360 ± 100	340 ± 110
CHARM	$CaCO_3$	xF_3	$Q^2 > 3$	187 ± 150	310 ± 160
WA25	D_2	xF_3	$Q^2 > 1$	250 ± 90	
(BEBC)		$F_2^n - F_2^p$		$170 \,^{+\,180}_{-\,140}$	
EMC	Fe	F_2, x>0.25	$Q^2 > 5$	$125 \,^{+\,120}_{-\,80}$	$170 \,^{+\,170}_{-\,110}$
BCDMS (Preliminary)	C	F_2, x>0.25	$Q^2 > 25$		$220 \pm 20 \,^{+\,80}_{-\,60}$ stat syst

Preliminary results on a second order QCD fit to the new CDHSW data have been reported (fig. 15) [21]. An agreement with QCD can be found only if one restricts the data to the high Q^2, high W^2 domain e.g. $Q^2 > 20$, $W^2 > 11$. Still the value of Λ seems to depend upon the W and Q^2 cuts. A preliminary range of [50 - 300] MeV for $\Lambda_{\overline{MS}}$ is given. The departure from the QCD behaviour at low x and low Q^2 may point to interesting physics outputs, given the fact that systematic errors seem too small to bring the data points back to the theoretical curve.

The extraction of the gluon distribution suffers from the strong correlation with σ_t and α_s. Better data are needed at high Q^2. But it should be noticed that such a determination which uses the QCD evolution makes sense only if the QCD fits agree with the data over the whole range in x, including the low x region where the glue is concentrated.

2.2.4 - *Conclusions on the structure function measurements*

There is now a better agreement between the experiments mainly due to the new values of the total cross sections. Comparison have to be made with the same assumptions to be relevant. The situation with QCD fit is still confused. The new CDHS data are promising if the systematics can be properly understood and may lead to interesting physics outputs (may be not QCD).

2.2.5 - *x-distributions from NC interactions*

The previous formalism for CC interactions can be reproduced for NC interactions up to the different chiral couplings which introduces small changes in the structure functions :

$$\frac{d\sigma^{\bar{\nu}}}{dx} = \frac{G^2\, ME_\nu}{2\pi} F_\pm(x)$$

in the scaling approximation with

$$F_\pm(x) = \frac{4}{3} F_2^{NC}(x) \pm \frac{2}{3} xF_3^{NC}(x)$$

$$F_2^{NC} = \underbrace{(C_L^{u\,2} + C_L^{d\,2} + C_R^{d\,2} + C_R^{d\,2})}_{\sim 0.33\ (\sin^2\theta=0.23)} (q+\bar{q})$$

$$- \underbrace{(C_L^{u\,2} - C_L^{d\,2} + C_R^{u\,2} - C_R^{d\,2})}_{\sim 0.44} 2x(s-c)$$

$$xF_3^{NC} = \underbrace{(C_L^{u\,2} + C_L^{d\,2} - C_R^{u\,2} - C_R^{d\,2})}_{\sim 0.27} (q-\bar{q})$$

Thus, x distributions for CC and NC are similar. They have been measured in experiments which use fine grain calorimeters allowing the measurement of the shower direction. Results have been reported by the CHARM [24] and the FMM [25] collaborations (fig. 16) which show a good agreement with the expected distributions.

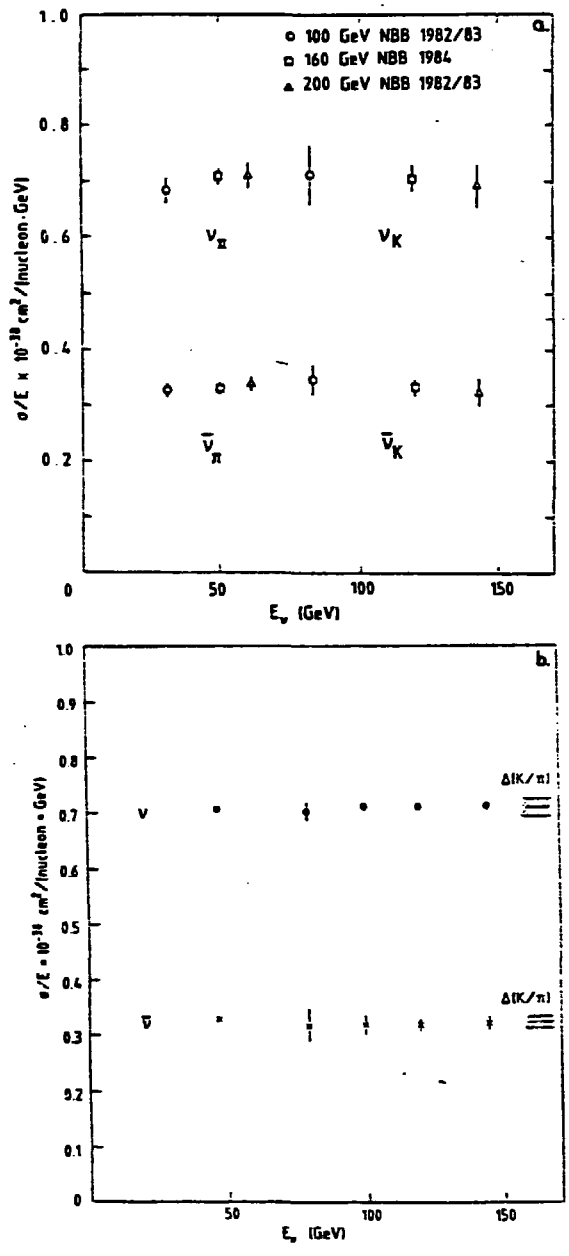

Fig. 4 : Energy dependence of the slope σ_t/E as measured by the CDHSW collaboration from 2 different methods (Fig. a and b. See text).

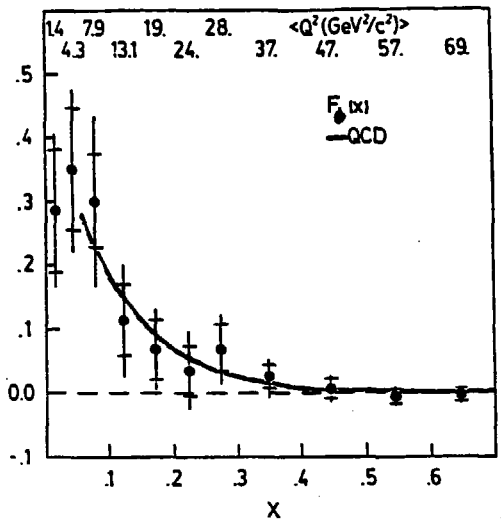

Fig. 5 : The longitudinal structure function F_L measured by CDHSW [17]. Each point is an average over a different Q^2 range.

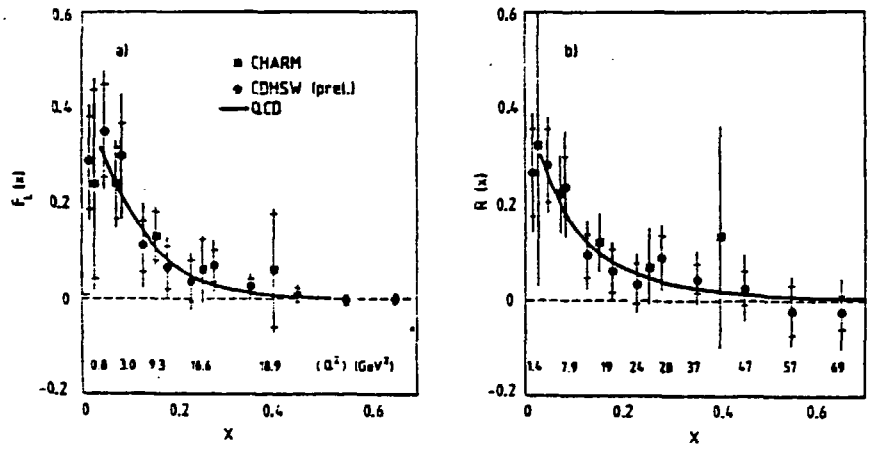

Fig. 6 : Comparison of the measured ratio $R = F_L/2x F_1$ from the CDHSW [17] and CHARM [19] groups. Also shown is the QCD prediction for $\Lambda \sim 250$ MeV.

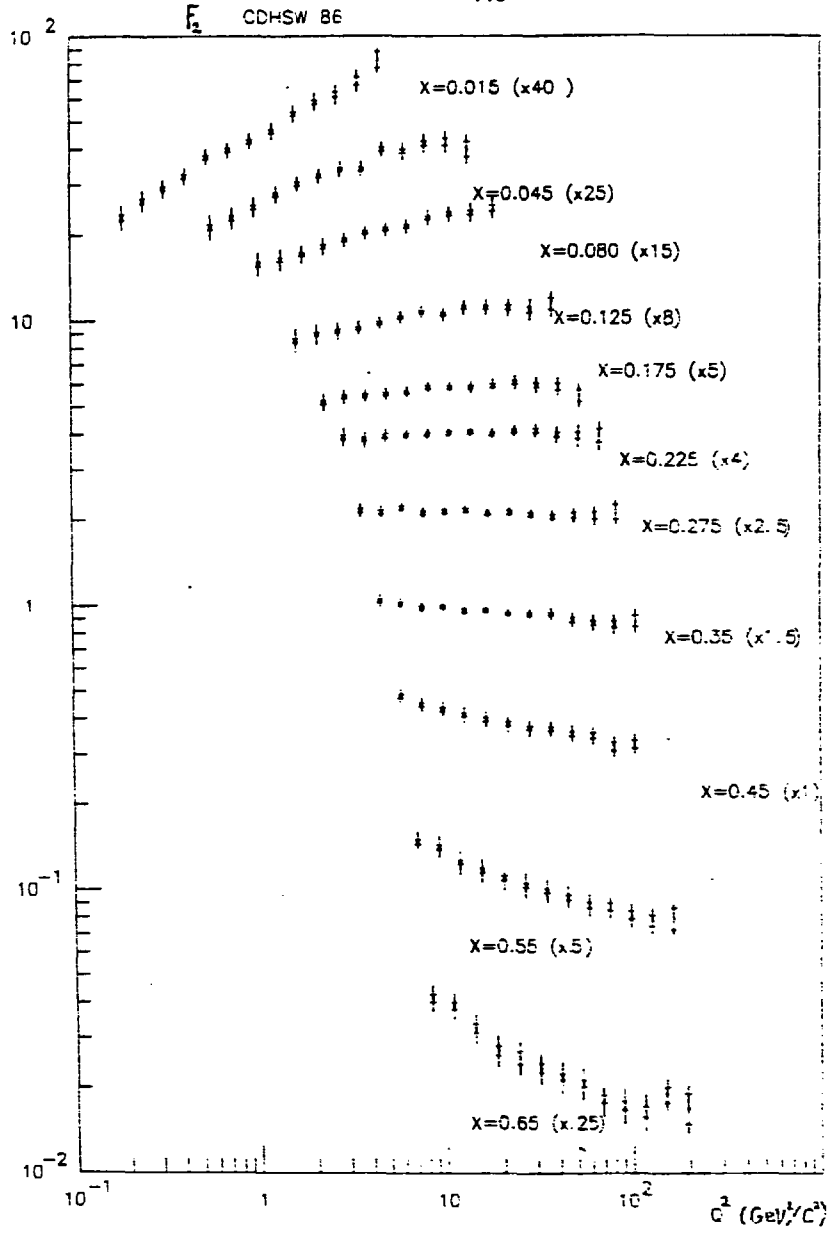

Fig. 7 : The structure function F_2 measured by the CDHSW collaboration. The points are not corrected for the charm threshold effect which may introduce of shift of a few percent at small Q^2. The systematic errors are given for each point and added quadratically to the statistical errors.

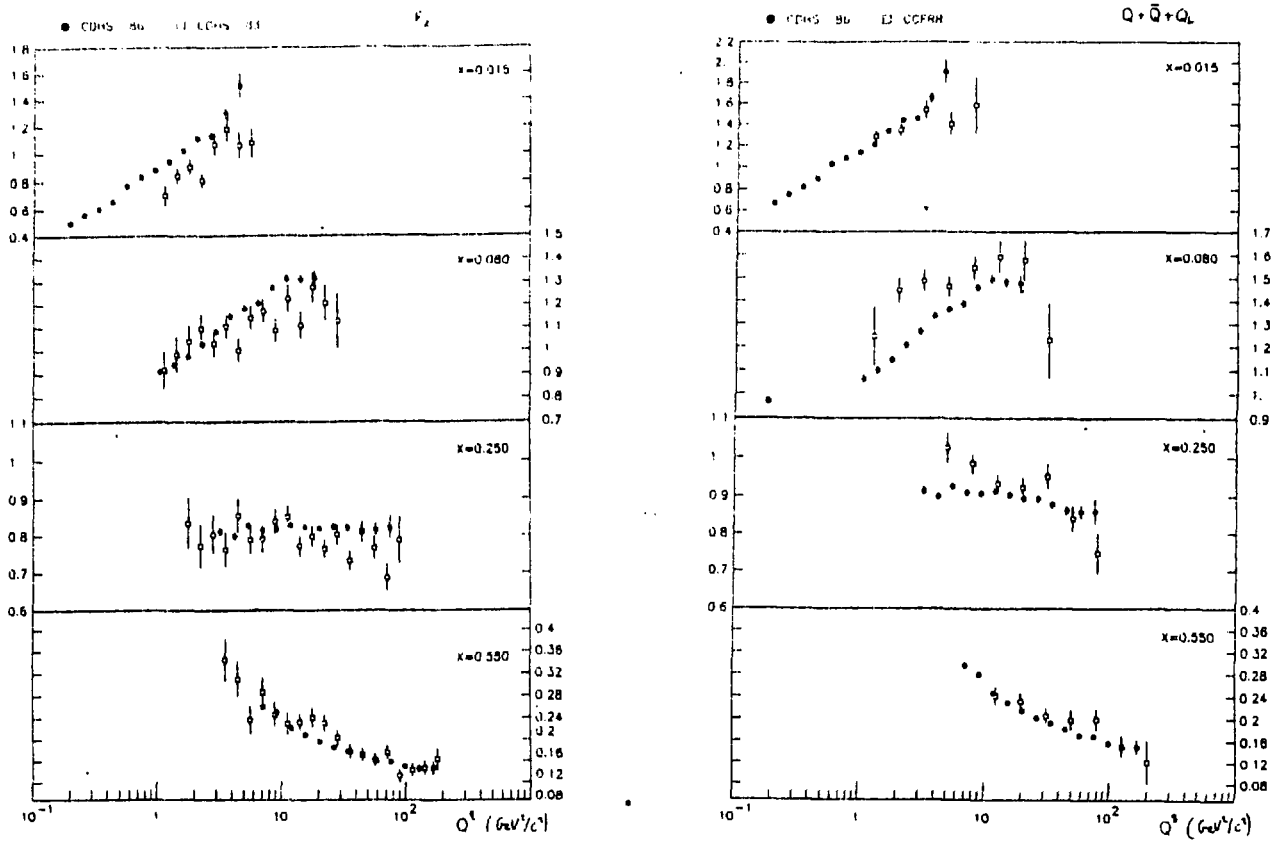

Fig. 8 : Comparison of the new and the old measurements of F_2 by the CDHSW group. The assumptions for the calculation are those of the old measurement.

Fig. 9 : Comparison of the new measurement of F_2 by CDHSW and the published F_2 of CCFRR. The physical assumptions are identical.

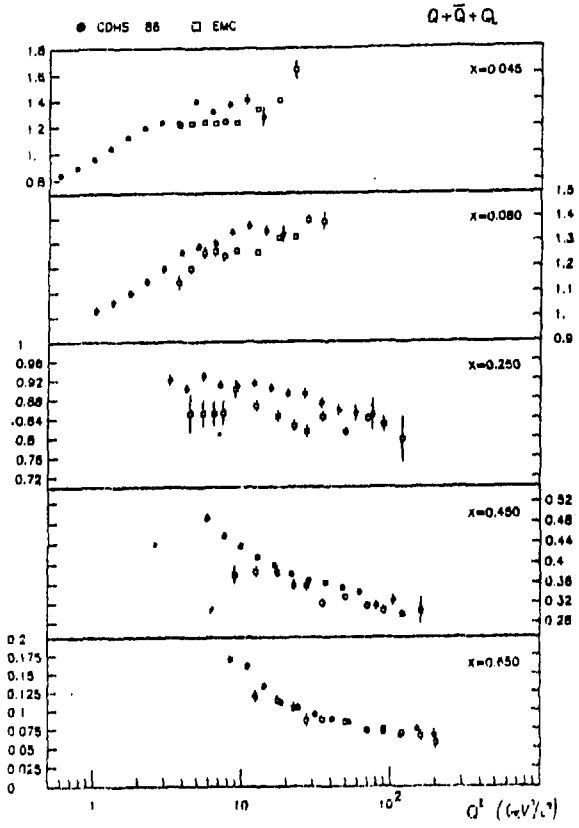

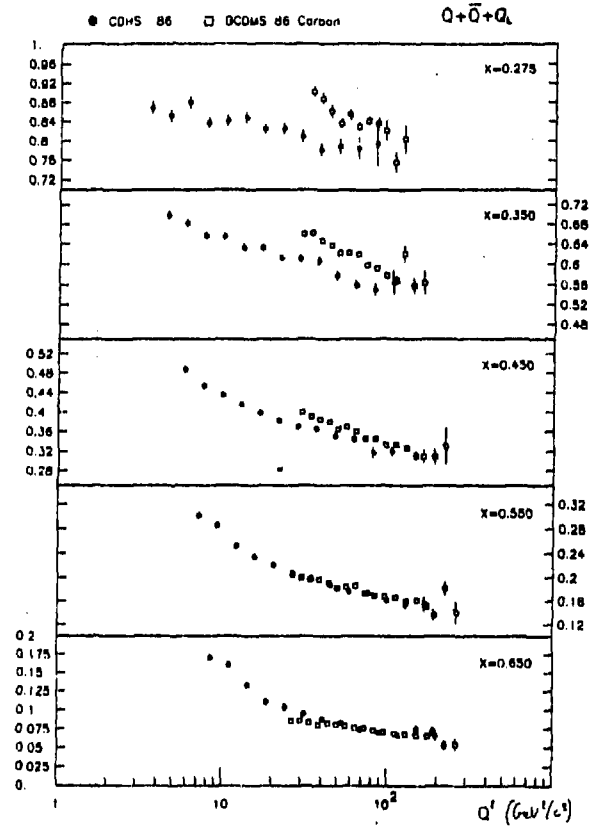

Fig. 10 : Comparison of the measured points for $\frac{18}{5} F_2^{\mu N}$ from the EMC group and the measurement of $F_2^{\nu N}\left(1 - \frac{3}{5} \cdot \frac{s+\dot{s}}{q+\dot{q}}\right)$ from CDHSW.

Fig. 11 : The same comparison with $F_2^{\mu N}$ from the BCDMS collaboration [21].

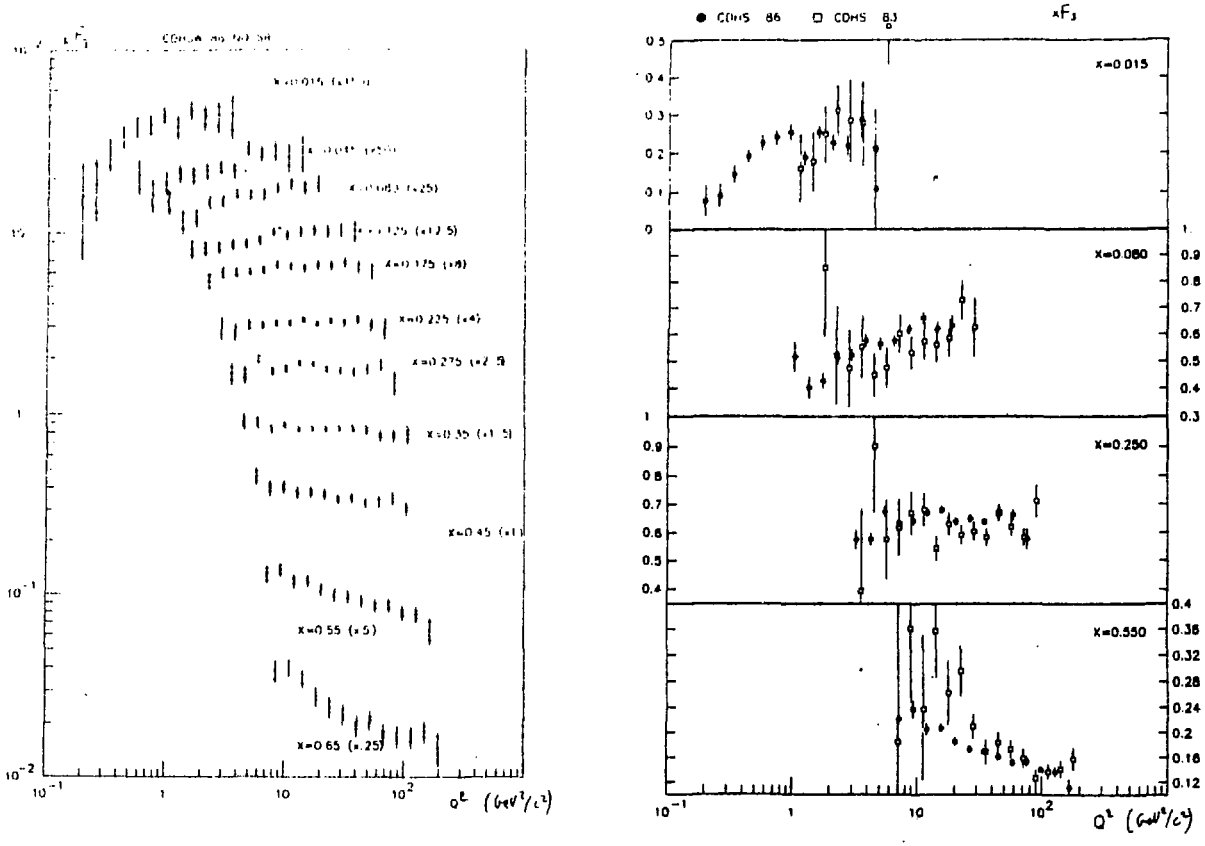

Fig. 12 : The new measurement of $xF_3 = \frac{1}{2}(xF_3^{\nu} + xF_3^{\bar{\nu}})$ by the CDHSW group.

Fig. 13 : Comparison of the new and the old measurement of xf_3 (assumptions of the old measurement).

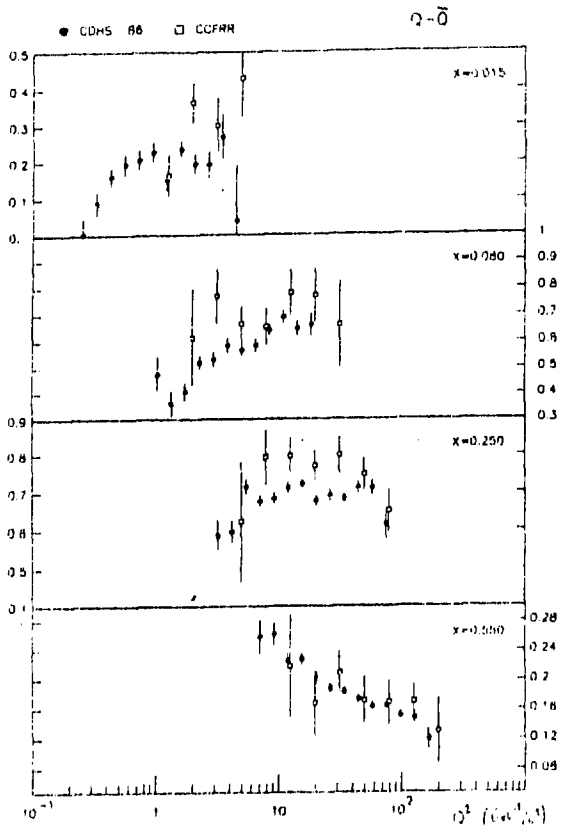

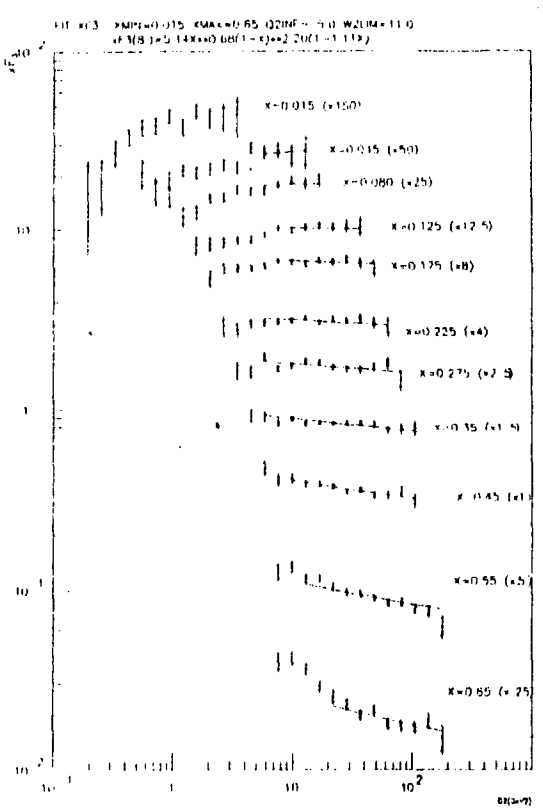

Fig. 14 : Comparison of xf_3 from CDHSW and CCFRR.

Fig. 15 : Result of a second order QCD fit to the new xF_3 data of CDHSW. The kinematical domain is restricted to $Q^2 > 5$ GeV^2 and $W^2 > 11$ GeV^2.

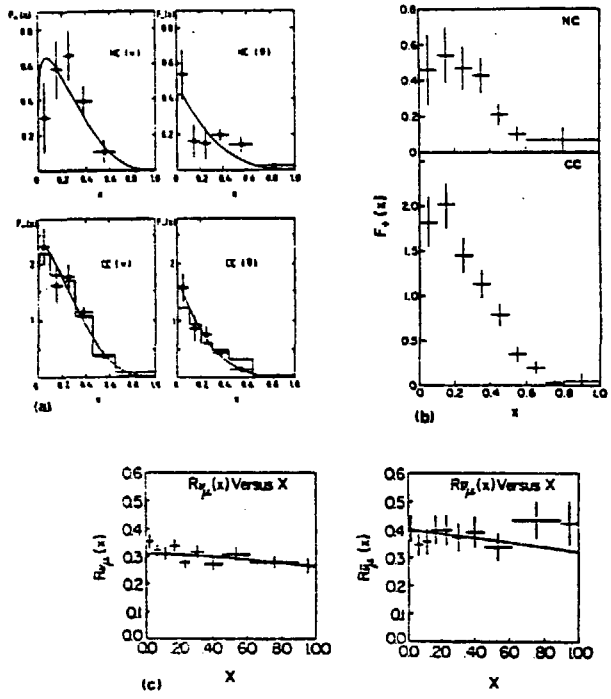

Fig. 15 . The x-distributions for neutral current interactions. CHARM has measured the functions $F_{\pm}(x)$ (a and b) and FMM has measured the ratios R_{ν} (x)(c).

3rd PART : NEUTRAL CURRENT RESULTS FROM EXPERIMENTS ON SEMI-LEPTONIC NEUTRINO SCATTERING

3.1 The measurement of $R^{\nu} = NC/CC$ and the determination of $\sin^2\theta_w$.

Experimentally, the measurement of R^{ν} is the determination of the ratio of the number of events without any muon in the final state (neutral current events) to the number of events with a muon (charged current events). A cut on the hadron energy, E_{hc}, is necessary to ensure a full detection efficiency. Additionnal corrections are needed to correct for background events such as ν_e events (see [26] for more details).

Theoretically, this ratio is related to the chiral couplings, and so to $\sin^2\theta_w$, in the following formula :

$$R^{\nu} = \frac{\int_{E_{hc}}^{\infty} dE_\nu \, \phi(E_\nu) \int_{E_{hc}/E_\nu}^{1} dy \int_0^1 dx \, \frac{d\sigma^{nc}}{dxdy} (C_L^q, C_R^q)}{\int_{E_{hc}}^{\infty} dE_\nu \, \phi(E_\nu) \int_{E_{hc}/E_\nu}^{1} dy \int_0^1 dx \, \frac{d\sigma^{cc}}{dxdy}}$$

where $\phi(E_\nu)$ is the neutrino flux function of the energy.

The differential cross-sections of neutrinos on the target nucleus may calculated in the framework of the quark parton model if the experiments is in the deep-inelastic regime. In addition, radiative corrections have to be taken into account.

The motivation for high precision measurements of $\sin^2\theta_w$ are the possible test of the presence of radiative corrections from a comparison of the measured value of $\sin^2\theta_w$ in different processes and the check of GUTs predictions.

Several difficulties arise which lead to a theoretical error in the extraction of $\sin^2\theta_w$:

i) The knowledge of the quark distributions :
It is actually good enough for isoscalar targets. Small non isoscalarity (Fe Target) can be corrected for by using the measured ratio $\frac{U_v}{D_v}$ of the valence u and d quarks in the proton. Fortunately x distributions are similar for NC and CC.

ii) The existence of the Kobayashi-Maskawa mixing and the threshold for charm production (for CC only).
This is the largest uncertainty. The correction rests on the use of the slow rescaling model [16] involving the charm quark mass m_c. Which value of m_c to be used is still an open problem : constant m_c, QCD "running mass" (with Q^2 or W^2)... There are some constraints from data on $\mu^+ \mu^-$ production in neutrino interactions and on D decay which indicates $m_c \simeq 1.5 \pm 0.3$ leading to an uncertainty $\Delta \sin^2\theta_w = 0.004$.

iii) The possible breaking of the QCD Quark Parton Model due to higher twist terms [27]. It has been shown [28] that these effects may be small if one could use an isoscalar target containing only u and d quarks. Then the weak isospin symetry is identical to the strong isospin symetry and the following relation can be deduced :

$$\frac{d\sigma^{NC,\ \nu}}{dxdy} = \rho^2 \left((\frac{1}{2} - \sin^2\theta_w + \frac{5}{9}\sin^4\theta_w) \frac{d^2\sigma^{CC\ \nu}}{dxdy} + \frac{5}{9}\sin^4\theta_w \frac{d^2\sigma^{CC\ \bar{\nu}}}{dxdy} \right)$$

up to small twist 4 terms ($\Delta \sin^2\theta \lesssim 0.002$).
But corrections to this formula in order to apply to the "real" world are calculated in the QPM leaving the main uncertainty from the charm threshold unchanged.
Another possibility would involve the use of the Paschos-Wolfenstein relation :

$$R^- = \frac{\sigma^{\nu}_{NC} - \sigma^{\bar{\nu}}_{NC}}{\sigma^{\nu}_{CC} - \sigma^{\bar{\nu}}_{CC}} = (\frac{1}{2} - \sin^2\theta_w)\ \rho^2$$

Then, due to the cancellation of the sea contribution, the uncertainty from the charm threshold effect is roughly divided by 2. But this would require a very high statistics in $\bar{\nu}$ and asks for a relative normalisation $\sigma_{\bar{\nu}}/\sigma_{\nu}$ not achievable at present.

3.2 The results for isoscalar targets

The most accurate measurements are given on table 5. The new CDHSW result is now final. Values of $\sin^2\theta_W$ are expressed in the Sirlin scheme [35].

Table 5

EXP	E_{cut} (GeV)	R_ν	$R_{\bar\nu}$	ϵ_c (GeV)	$\sin^2\theta_W$ (ρ=1)
CDHS II [29]	10	0.301 ± 0.005 ± 0.005	0.363 ± 0.015	~ 1.1	0.226 ± 0.012
CHARM I [30]	2	0.320 ± 0.010	0.377 ± 0.020	1.5	0.220 ± 0.014
FMM [31]	10	0.307 ± 0.011	0.384 ± 0.023	1.5	0.246 ± 0.018
CCFRR [32]	*			1.5	0.242 ± 0.011 ± 0.005
CDHS III [33]	10	0.3072 ± 0.0025 ± 0.0020	0.381 ± 0.015 ± 0.003	1.5	0.225 ± 0.005
CHARM II [34]	4	0.3098 ± 0.0025 ± 0.0018		1.5	0.236 ± 0.005

* *This result uses Paschos-Wolfensteins ratios $R^\pm$ with a radius dependent y cut to reduce the background of short CCs. The systematic error includes the theoretical error.*

The present experimental situation including measurements from other processes is summarized on Fig. 17. Given the statistical errors and the theoretical errors, there is an acceptable agreement.

Several remarks have to be done :

i) The value of $\sin^2\theta_W$ of a given process may depend upon the renormalisation scheme. Two sets of radiative corrections have been used : one is expressed in the $\overline{MS}$ scheme [36] where $\sin^2\theta_W$ is a running parameter $\sin^2\theta_W(Q^2)$ expressed at $Q^2 = M_W^2$, the second is calculated in the on-shell renormalisation scheme of Sirlin [35] where $\sin^2\theta_W$ is defined by $\rho \cos^2\theta_W = \frac{M_W^2}{M_Z^2}$, M_W and M_Z beeing the physical (measured masses of the heavy

bosons. The corrections to the measured values of $\sin^2\theta_w$ are the following for a standard high energy neutrino experiment ($E_{\nu cut}$ = 10 GeV)

$$\Delta \sin^2\theta_w^{MS} \simeq - 0.013$$

$$\Delta \sin^2\theta_w^{Sirlin} \simeq - 0.011.$$

At present, uncertainties in the available programs are og the order of magnitude of the difference between the two schemes. This technical difference is likely to be understood in a near future.

ii) A theoretical error ~ 0.005 is common to all neutrino experiments. As it comes from the unknown value of m_c, CDHS choosed to give its result including explicitely the m_c dependence :

$$\sin^2\theta_w = 0.225 + 0.013 \cdot (m_c - 1.5)$$

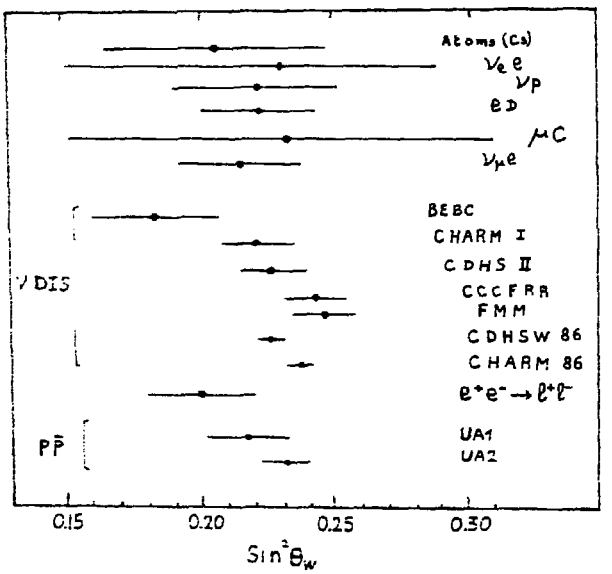

Fig. 17 : The measured values of $\sin^2\theta_w$ from different processes involving different Q^2 ranges. The results are given independentely for the high energy neutrino experiments.

3.3 Experiments on neutron and proton targets.

From experiments on isoscalar targets, one can derived only the sum of the chiral couplings $g^2_{L(R)} = C^{u\,2}_{L(R)} + C^{d\,2}_{L(R)}$. In order to extract separately $C^u_{L(R)}$ and $C^d_{L(R)}$, experiments on proton or (and) neutron target are necessary. In bubble chamber data, it is possible to identify the nature of the target nucleon on an event by event basis. Results have been reported on the measurement of the ratios $R^{p}_{(\bar{\nu})}$, $R^{n/p}_{\nu} = \frac{\sigma^{\nu n}_{NC}}{\sigma^{\nu p}_{NC}}$, $r_{(\bar{\nu})} = \frac{\sigma^{\nu p}_{NC} - \sigma^{\nu n}_{NC}}{\sigma^{\nu p}_{CC} - \sigma^{\nu n}_{CC}}$. The latter ratio minimizes the systematic errors which originate mainly from the rescattering probability. The most interesting results are given in table 6 :

Table 6

EXPERIMENT		RESULTS	
BEBC (TST)	[37]	$R^p_\nu = 0.455 \pm 0.038$	$R^p_{\bar{\nu}} = 0.320 \pm 0.038$
BBCLMO	[38]	$R^p_\nu = 0.384 \pm 0.028$	$R^p_{\bar{\nu}} = 0.338 \pm 0.021$
FNAL 15'	[39]	$R^{n/p}_\nu = 1.08 \pm 0.09$	
	[40]	$R^{n/p}_\nu = 1.01 \pm 0.14$	
BEBC Deut.	[41]	$r_\nu = 0.06 \pm 0.06$	$r_{\bar{\nu}} = 0.02 \pm 0.09$

3.4 Comparison with the standard model predictions : evidence for radiative corrections

3.4.1 *Determination of the quark chiral couplings*

What follows is based on a combination of the most accurate results on neutral currents from neutrino experiments using isoscalar targets or proton or neutron targets. Dependence of the measured quantities upon the electroweak parameters and a fit to the experimental results have been worked out by G.L. Fogli [42]. These results are preliminary and do not use the most up to data experimental results. It uses the value of R^{ν} from CHARM presented at Bari's conference ($R^{\nu} = 0.215 \pm 0.010$) which has been revised since to the value given in table 5. Still, this analysis gives an estimate of what can be achieved if one accepts to combine independently nearly all the available experimental results. A criterium for such a combination to make sense could be that the statistical errors are dominant which is no longer true for the recent measurements of R^{ν}.

The measured quantities (R^{ν}, $R^{\bar{\nu}}$, $R^{\nu/\bar{\nu}}$, $r^{\bar{\nu}}$) are parametrized in terms of the chiral couplings :

$$\text{e.g.} \quad R^{\nu} = a_1 g_L^2 + a_2 g_R^2 + a_3 \delta_L^2 + a_4 \delta_R^2$$

$$\text{with} \quad g^2_{L,R} = C^{u\,2}_{L,R} + C^{d\,2}_{L,R}$$

$$\delta^2_{L,R} = C^{u\,2}_{L,R} - C^{d\,2}_{L,R}$$

The a_i's are coefficients which depend on the experimental conditions (beam spectrum, cuts), the quark distributions (QCD, QPM), the K.M. mixing matrix elements, the charm threshold parameter m_c and the radiative corrections (m_t = 36 GeV) if required. The uncertainties on the a_i's reflect the theoretical misunderstanding of the semi-leptonic neutrino scattering.

The result of a 4 parameters fit to $g^2_{L,R}$, $\delta^2_{L,R}$ is given in figure 18 restricted to the planes (g_L^2, g_R^2) and (δ_R^2, δ_L^2). A comparison of the 1σ domains with the lines of fixed ρ and $\sin^2\theta_W$ giving the constraints of the SU(2) x U(1) model shows that the data are consistent with this model, whether or not the radiative corrections are included.

3.4.2 *Evidence about radiative corrections ? Comparison with UA's results*

A test of the radiative corrections may be provided by a comparison of the electroweak parameters determined by two different processes. In the following comparison, we use the data from the neutrino DIS experiments given in table 5 and the masses of the heavy intermediate bosons measured by the UA experiments as given in table 7.

Table 7

EXP	M_W (GeV)	M_Z (GeV)
UA1 [43]	83.5 ± 1.1 (± 2.7)	93.0 ± 1.4 (± 3.0)
UA2 [44]	81.2 ± 1.1 (± 1.3)	92.5 ± 1.3 (± 1.5)
UA2 (Prelim.) [45]	80.3 ± 0.8 (± 1.3)	91.5 ± 0.9 (± 1.5)

The second error stands for a calibration uncertainty common to M_Z and M_W.

In the Sirlin scheme, one has the following relation [46] :

$$\frac{M_W^2}{M_Z^2} = \rho\ (1 - \sin^2\theta_W)$$

$$M_W^2 = \frac{A^2}{\sin^2\theta_W} \quad \text{with} \quad A^2 = \frac{37.281^2}{1 - \Delta r}$$

$$\Delta r\ (m_{Higgs} = m_Z,\ m_t = 3\ 6\ \text{GeV}) = 0.0696$$

$$\sin^2\theta_W = \sin^2\theta_W^{EXP}\ (1 - \epsilon_s)$$

$$\rho = \rho^{EXP}\ (1 + \epsilon_\rho)$$

$\sin^2\theta_W^{EXP}$ and ρ^{EXP} are the values derived experimentally in the neutrino experiment ignoring the radiative corrections $\epsilon_s \sim 5$ % and $\epsilon_\rho \lesssim 1$ %.

Assuming $\rho = 1$, the average value of $\sin^2\theta_w$ from table 5 is $\sin^2\theta_w = 0.232 \pm 0.003$ (EXP) $\pm$ 0.005 (THEO) . The comparison with the values derived from M_w and M_z is shown on Fig. 19. While the agreement is very good when both radiative corrections are included, ignoring them leads to a $\sim 2\,\sigma$ discrepancy. From this comparison a value of Δr can be derived :

$$\Delta r = 0.077 \pm 0.030\ (\bar{p}p) \pm 0.030\ (\nu N)$$

The contribution from νN includes the present theoretical error. Given the variation of Δr with m_t [46], one can set a limit on m_t within the standard model :

$$m_t < 200\ \text{GeV} \quad (90\ \%\ \text{CL})$$

A value of the parameter ρ can be determined from R^ν and $R^{\bar{\nu}}$ only. Using the CDHS data only (table 5), one gets :

$$\rho = 0.991 \pm 0.020$$

$$\sin^2\theta_w = 0.216 \pm 0.021$$

In his fit to nearly all the available neutrino data, G.L. Fogli gets [42] :

$$\sin^2\theta_w = 0.224 \pm 0.010\ (\text{EXP}) \pm 0.007\ (\text{THEO})$$

$$\rho = 1.004 \pm 0.008\ (\text{EXP}) \pm 0.007\ (\text{THEO})$$

A more reliable method to get ρ is the comparison of R^ν with the measured M_w and M_z through the relations :

$$M_w^2 = \frac{38.65^2}{\sin^2\theta_w}$$

$$\sin^2\theta_w = 1 - \frac{M_w^2}{\rho\, M_z^2}$$

$$R^\nu = \rho^2 \left[\frac{1}{2} - \sin^2\theta_w + \frac{5}{9}\sin^4\theta_w\ (1 + r)\right]$$

A 2 parameters fit to M_W, M_Z and R^ν from CDHSW and CHARM gives :

$$\rho = 0.997 \pm 0.011$$

$$\sin^2\theta_W = 0.229 \pm 0.007$$

This set of results gives the best presently available determination of the electroweak parameters.

3.5 Conclusions

The high statistics neutrino data presented this year represent presumably a sort of final word on the study of NC coupling using the Deep inelastic neutrino scattering. A good agreement with GA results needs the radiative corrections to be taken into account. Is it a reliable test of the electroweak theory ? Actually, $\sim$ 70 % of the effect on the DIS corrections is due to "trivial" electromagnetic effect at the vertex of the CC interaction. In addition, the value of Δr comes mostly from the renormalisation of α through pure photonic effects (at least for small m_t). It is certainly too early to claim that we have seen the presence of the one loop weak corrections.

Another test of the radiative corrections may be available when CHARM II results on $\bar{\nu}_\mu e, \nu_\mu e$ are available ($\Delta\sin^2\theta \simeq 0.005$ almost free of radiative corrections). This will be the next important round for neutrino experiments.

I am grateful to my colleagues of the Saclay group of the CDHSW collaboration for their help in preparing this review, in particular Frédéric Perrier, Bertrand Vallage and Patrice Perez.

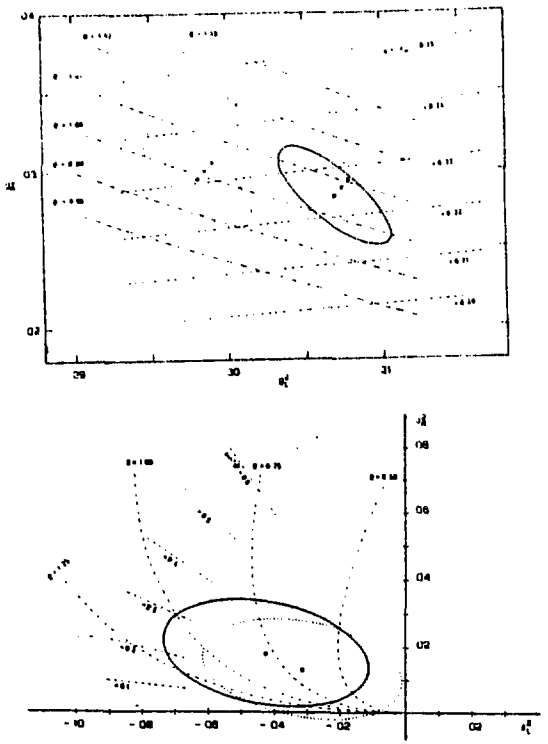

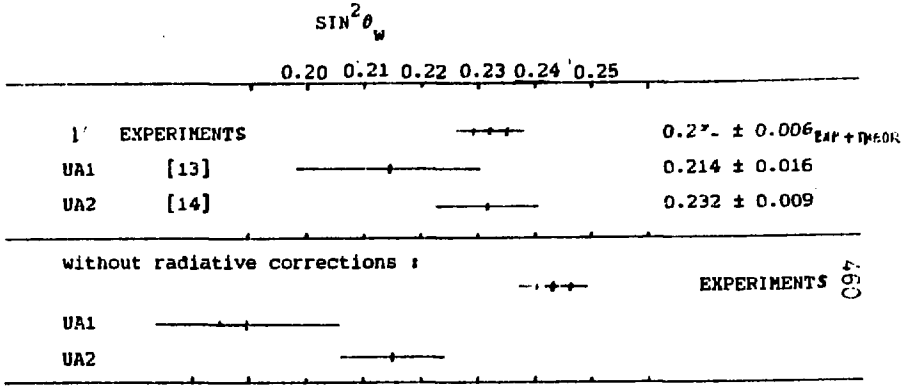

Fig. 18 : The 1σ allowed regions for the chiral couplings (g_L^2, g_R^2) and (δ_L^2, δ_R^2) from the general fit to neutrino data by G.L. Fogli [42].

Fig. 19 : Comparison of the values of $\sin^2\theta_W$ derived from the measured masses of the W and Z bosons and from the measured ratios R^{ν}. The stantard model (ρ = 1) is assumed.

REFERENCES

[1] For a review : P.Q. Hung, J.J. Sakurai, Ann. Rev. Nucl. Part. Sci., 31 (1981) 375.

[2] J. Carr et al., Phys. Rev. Lett. 51 (1983) 627.
M. Strovink, proceeding of the 11th neutrino conference, Dortmundt (1984)
H. Burkard et al., submitted to Phys. Lett.

[3] H. Abramowicz et al., Z. Phys. C12 (1982) 225.

[4] F. Bergsma et al., Phys. Lett. 147B (1984) 481.

[5] L.A. Ahrens et al., Phys. Rev. Lett. 54 (1985) 18.

[6] H.H. Chen, talk at the 12th neutrino conference, Sendai (1986).

[7] e.g. D. Hywel White, talk given at the LAMPF User's Meeting, November 2, 1985. Proposal for a large cherenkov detector (Los Alamos 1986).

[8] J.G.H. de Groot et al., Z. Phys. C1 (1979) 143.

[9] M. Janker et al., Phys. Lett. 99B (1981) 265 and Phys. Lett. 100B (1981) 520(E).

[10] R. Blair et al., Phys. Rev. Lett. 51 (1983) 343.

[11] M. Aderholz et al., CERN/EP 86-31 to be published in Phys. Lett. B.

[12] A. Blondel et al., to be published in Z. Phys. C.

[13] De Rujula et al., Nucl. Phys. B154 (1979) 394.

[14] H. Abramowicz et al., Z. Phys. C25 (1984) 29.

[15] For a review : G. Altarelli, Phys. Rep. 81 (1982) 1.

[16] R.M. Barnett, Phys. Rev. D14 (1976) 70.
H. Georgi and H.D. Politzer, Phys. Rev. D14 (1976) 1829.

[17] P.Buchholtz, Proceedings of the Europhysics conference on H.E.P. Bari (1985).

[19] F. Bergsma et al., Phys. Lett. 123B (1983) 269.

[20] H. Abramowicz et al., Z. Phys. C17 (1983) 283.

[21] See also, P. Perez, talk at Neutrino 86 conference, Sendai (1986).

[22] J.J. Aubert et al., Phys. Lett. 150B (1981) 322.

[23] M. Virchaux, talk at the XXth Moriond meeting, Les Arcs (1986).

[24] M. Jonker et al., Phys. Lett. 128B (1983) 117.

[25] D. Bogert et al., Phys. Rev. Lett. 55 (1985) 574.

[26] R. Geiges, talk at this conference.
A. Blondel et al., to be published in Z. Phys. C .

[27] J.L. Miramontes et al., CERN-TH 4184/85.

[28] C.H. Llewellyn Smith, Nucl. Phys. B228 (1983) 205.

[29] H. Abramowicz et al., Z. Phys. C24 (1985) 51.

[30] M. Jonker et al., Phys. Lett. 99B (1981) 265.

[31] D. Bogert et al., Phys. Rev. Lett. 55 (1985) 1969.

[32] P.G. Reutens et al., Phys. Lett. 152B (1985) 404.

[33] H. Abramowicz et al., to be published in Phys. Rev. Lett. See also [26] [26].

[34] J. Panman, talk at the XXI^{e} rencontre de Moriond (1986).

[35] A. Sirlin, Phys. Rev.D22 (1980) 971.
A. Sirlin and W.J. Marciano, Nucl. Phys. B189 (1981) 442.
Yu. Bardin et al., Nucl. Phys. B197 (1982).

[36] J.F. Wheater and C.H. Llewellyn Smith, Nucl. Phys. B208 (1982) 27 and Nucl. Phys. B226 (1983) 547.

[37] N. Armenise et al., Phys. Lett. 122B (1983) 448.
Moreels et al., Phys. Lett. 138B (1984) 230.

[38] M.M. Mobaygen, talk at the XXI^{e} Rencontre de Moriond (Les Arcs 1986).

[39] J. Marriner et al., Phys. Rev. D27 (1983) 2569.

[40] T. Kafka et al., Phys. Rev. Lett. 48 (1982) 910.

[41] D. Allasia et al., Phys. Lett. 133B (1983) 129.

[42] G. L. Fogli, talk given at the 1986 Lake Louise Winter Institute and talk at the XXI° Rencontre de Moriond (Les Arcs 1986).
G.L. Fogli, Nucl. Phys. B260 (1985) 593.

[43] G. Arnison et al., Phys. Lett. 166B (1986) 484.

[44] J.A. Appel et al., CERN-EP/85-166 (1985).

[45] B. De Lotto, talk at the XXI° Rencontre de Moriond (Les Arcs 1986).
G. Parrour talk at this conference.

[46] W.J. Marciano and A. Sirlin, Phys. Rev. D29 (1984) 945.

ROLE OF SINGLE PARTICLE NUCLEAR POTENTIAL IN THE EMC EFFECT

Jacek Rozynek

Institute for Nuclear Studies, Warsaw, Poland

The simple single particle model of the nucleus is proposed to explain the EMC effect. The good agreement with data is obtained. The essential features of the change of the nucleon structure function in nuclear medium are explained by kinematical effect only.

1. *Single Particle Energies in Nuclear Medium*

It is known[1] that the mean free path of the nucleon in a nucleus is large in comparison to nucleon sizes. Therefore the nucleon can be treated as a quasifree object, which moves in the average potential coming from the interactions with all others nucleons. For the two body nucleon-nucleon interaction $V_{N,M}$ we can write the following relation for the single nucleon energy e_N and the single nucleon potential U_N in the nuclear medium:

$$e_N = (M^2+P_N^2)^{1/2} + U_N \,, \tag{1}$$

where $U_N = \sum_{M=1}^{A} V_{N,M}$, P_N is the three-momentum of Nth nucleon. A is the mass number and M nucleon mass.

From the definition of the average binding energy per nucleon ϵ_N we have the following relation:

$$E/A = M+\epsilon_N = \frac{1}{A}\sum_{N=1}^{A}\left[(M^2+P_N^2)+\frac{1}{2}U_N\right] = (M^2+\langle P_N^2\rangle)^{1/2} + \frac{1}{2}\langle U_N\rangle \tag{3}$$

where E is the nucleus energy and $\langle p_N^2 \rangle$ and $\langle U_N \rangle$ are the average values of the nucleon square momentum and the single particle potential in the nucleus.

Now we want to determine the value of $\langle U_N \rangle$. First we have to calculate $\langle p_N^2 \rangle$. In the Fermi-gas model the average nucleon square momentum $\langle p_N^2 \rangle \approx 0.6 p_F^2$ and Fermi momentum $p_F = \hbar(1.5\pi^2\rho)^{1/3}$, is the function of a density ρ.

The nuclear density $\rho(r)$ is almost constant for $0<r<R_A-d/2$ ($R=1.11A^{1/3}$) and equal $\rho(0) \approx .17$ fm^{-3}. The surface width is also almost constant for nuclei and equals $d \approx 2.4$ fm. The density decreases at the distance d from $\rho(R_A-d/2) \approx 0.9\rho(0)$ to $\rho(R_A+d/2) \approx 0.1\rho(0)$. These numbers allow us to estimate the average nuclear density ρ_A which varies from $\rho_{A\approx 12} \approx 0.4\rho(0)$ for light nuclei to $\rho_{A>200} \approx 0.7\rho(0)$ for heavy nuclei. Now using Fermi-gas model relation we calculate $\langle p_N^2 \rangle$, then using (1)-(2) we calculate $\langle U_N \rangle$ and the average single particle energy $\langle e_N \rangle$.

For light ($A \approx 12$) nuclei we obtain: (4)

$$\langle p_N^2 \rangle / 2M \approx 12 \text{ MeV}, \qquad \langle U_N \rangle \approx 2(12\text{MeV}+\epsilon) \approx 40 \text{ MeV}, \qquad \langle e_N \rangle - M \approx 28 \text{ MeV}$$

In the limit $A>200$ we have: (5)

$$\langle p_N^2 \rangle / 2M \approx 18 \text{ MeV}, \qquad \langle U_N \rangle \approx 2(18\text{MeV}+\epsilon) \approx 51 \text{ MeV}, \qquad \langle e_N \rangle - M \approx 33 \text{ MeV}$$

In our calculation we will use single particle energy e_N as the zero component p_0 of the four vector p_N. In our LAB frame (nucleus at rest) the average value of p_0 will be $\langle e_N \rangle$.

2. Deeply Inelastic Electron-Nucleus Scattering

The differental cross section for deeply inelastic electron nucleus scattering is given by[2]:

$$\frac{1}{A}\frac{d^2\sigma^A}{dE'd\Omega'} = \frac{4\alpha^2E'^2}{AQ^4}\left[2W_1^B(Q^2, P_N1)\sin^2(\theta/2) + W_2^B(Q^2, P_N1)\cos^2(\theta/2)\right]. \quad (6)$$

In our model the electron-nucleus cross section is a sum of single nucleon cross sections. If we use the Fermi distribution for nucleons we obtain:

$$\frac{1}{A}\sum_{N=1}^{A}\frac{d^2\sigma^N}{dE'd\Omega'} = \frac{3}{4\pi P_F^3}\int \frac{ME'}{16\pi^2(P_N1)}\,|M|^2\,d\cos\vartheta\,d^3p\,, \quad (7)$$

where $|M|^2 = (e/q)^4\,L^{\mu\nu}W_{\mu\nu}$, $\quad L^{\mu\nu}W_{\mu\nu} = 2W_1Q^2 + V_2\left[\ldots(P_N1)(P_N1')\ldots Q^2\ldots\right]$

and $P_N = (P_O, \mathbf{P}_N)$.

Now we want to calculate all scalar products which appear in (6)-(7) in LAB frame. They are .av means average value over nucleon orientation:

$(P_N1)_{av} = P_OE$, $\quad (P_N1')_{av} = P_OE'$, $\quad P_N^2 = (M+U_N)^2$,

$x' = Q^2/2P_N(q) = Q^2/[P_O\nu - |\mathbf{p}|\cos\vartheta\sqrt{\nu^2+Q^2}] = Q^2/\nu(P_O - |\mathbf{p}|\cos\vartheta - \ldots)$

$x' = Q^2/2\nu(P_O - |\mathbf{p}|\cos\vartheta) = x(P_O - |\mathbf{p}|\cos\vartheta)$ with $x = Q^2/2M\nu$.

We can obtain from (6)-(8) the following relation between this structure function W_2^B of bound nucleon and V_2:

$$W_2^B[x', (P_Nq)] = (3/4\pi p_F^3)\int (P_O/M)\,V_2(Q^2, P_Nq)M^2\,d^3p\,. \quad (9)$$

Calculating $V_2(Q^2, P_Nq)M^2$ in the parton model[3] we obtain:

$$V_2(Q^2, P_Nq)M^2 = (M\nu/P_Nq)W_2(x') = (M/P_O)W_2(x'). \quad (10)$$

W_2 is the structure function for free nucleon. The factor ... from integration of the delta function in the definition of W_2.

Finally we obtain from (9) for $F_2^B(x') = \nu W_2^B(x')$ the following expression:

$$F_2^B(x) = (3/4\pi p_F^3)\int F_2(Mx/(p_0 - |p|\cos\varphi)\,d^3p\,, \qquad (11)$$

where x is the Bjorken variable for free nucleon and F_2 its structure function.

The factor (p_0/M) in (9) is cancelled and the influence of the nuclear medium is included only in the change of Bjorken variable x' as we see from (8) (the variable x', as x, from its definition varies from 0 to 1). This conclusion does not depend on our particular Fermi-model distribution of the nucleons in the nucleus.

3. *Results and conclusions.*

In the table we present the results for the ratio $R(x)=F_2^B(x)/F_2(x)$ for two limits of nuclear mass number A (A≈12 and A>200).

Table. The ratio R(x) for A≈12 and A>200.

x	.05	0.1	0.2	0.3	0.4	0.5	0.6	0.7	0.8	0.9
A≈12	1.01	1.00	.99	.97	.94	.92	.89	.88	.96	1.69
A>200	1.01	1.00	.98	.96	.93	.90	.88	.88	1.03	2.14

They were obtained from (11) for $p_0=(M^2+p^2)^{1/2}+\langle U_N\rangle$. The values of $\langle U_N\rangle$ were taken from (4)-(5). For $F_2(x)$ we choose after[4] $F_2(x)=x^{1/2}(1-x)^3$. Neglecting the small binding effects for deuteron, and also negligible contribution to the cross section from structure function W_1^B, we can compare our results for R(x) with the SLAC experiments[5]. The general agreement with the data supports our model. The fast increase of the R(x) for x>0.7 is much stronger for large A and it exhibits the essential feature of single particle mechanism. The asymptotic value of R(x) for x=0 is $R(x=0)=(M/p_0)^{1/2}=(M/\langle e_N\rangle)^{1/2}$. But for small values of x

for x=0 is $R(x=0)=(M/p_0)^{1/4}=(M/\langle e_N\rangle)^{1/4}$. But for small values of x ($x\approx 0(1/2R_A M)$ one can expect strong overlapping between quarks from different nucleons and the single nucleon mechanism can be invalid in this region[6].

The idea of single particle mechanism in deep inelastic electron scattering was formulated in[7]. The Fermi-smearing[8] expresions for R(x) are very similar to ours but witout single nucleon potential U_N. The inclusion of U_N is essential to obtain the minimum of R(x) for x=0.7 and $R(x)>0$ for $x<0.15$. In the paper[9] we can find the calculation of R(x) which use also the single nucleon mechanism. They calculate R(x) from the expression similar to (11) with more sophisticated distribution of the nucleons in a nucleus. But they do not show the cancellations of (M/p_0) factors which appear when we derive the structure function F_2 from the cross section.

Acknowledgments

The author thanks Dr. M. Staszel for many useful discusions.

References

1. A. Bohr, B. R. Mottelson, Nuclear Structure, Benjamin, Massachusets, vol 1 (1969).
2. Ch. Quigg, Gauge Theories of the Strong, Weak and Electromagnetic Interaction , Benjamin, Massachusets, (1983).
3. J. D. Bjorken, E. A. Paschos, Phys. Rev. 85 1975 (1969).
4. The European Muon Collaboration, J.J. Aubert et al., Phys. Lett. 105B, 315 (1981).
5. R. G. Arnold et al., Phys. Rev. Lett., 52, 727 (1984).
6. M. Staszel, J. Rozynek and G. Wilk, Phys. Rev. D 29, 2638 (1984).
7. G. B. West, Ann. Phys. (N.Y.)74, 646(1972). W. B. Atwood and G.B. West, Phys. Rev. D 7, 773 (1973).
8. A. Bodek, J.L. Richtie, Phys. Rev. D 23, 1070 (1981).
9. B.L. Birbrair et al., Phys. Lett., 166B, 119 (1986).

ASYMPTOTIC PROPERTIES OF HIGH ENERGY HADRON INTERACTIONS

J.Wdowczyk and A.W.Wolfendale

Institute of Nuclear Studies
90-950 Łódź, Poland

Department of Physics, University
of Durham, Durham DH1 3LE, UK

ABSTRACT

Using both accelerator and cosmic ray data it is shown that Feynman's scaling is strongly violated also in the fragmentation region at least up to 10^6 GeV.

1. INTRODUCTION

In analysis of cosmic ray propagation in the atmosphere the knowledge of the properties of high energy interactions at various energies is critical. Those properties are usually taken by extrapolation of accelerator experimental data using certain phenomenological formulae. In early cosmic ray works the so called CKP formula given by Cocconi Koester Perkins /1961/ was used. Later in many works the scaling formula suggested by Feynman /1969/ has been applied. That formula due to its simplicity is still used in spite of the fact that it has never been really confirmed by experimental observations. First of all, shortly after the formula was suggested, it has been pointed out by us that it leads to an extensive air shower development picture completely different from observations /Wdowczyk and Wolfendale,1972/.

Accelerator observations, as soon as the energy range available became wide enough, also showed that there exist significant deviations from that formula particularly in the so called central region where accurate data were available. It has been pointed by the present authors that the degree of scaling violation may be the same in the whole secondary energy range /Wdowczyk and Wolfendale,1979/. The formula suggested in that paper and generalised in our later paper /Wdowczyk and Wolfendale,1984/ has the following form

$$\frac{1}{\sigma_t}\frac{d\sigma}{dp_t\,dp_l} = \frac{K(s,s_0)}{E}\left(\frac{s}{s_0}\right)^{\alpha} f\left[x\left(\frac{s}{s_0}\right)^{\alpha}, p_t\right] \qquad /1/$$

where α gives the degree of scaling violation. That formula leads to Feynman's scaling if $\alpha = 0$. The best fit to the accelerator data gives now the value of $\alpha = 0.18$. That value is in very good accordance with results earlier deduced from cosmic ray observations which were summarised by Wdowczyk /1980/ as giving the value $\alpha = 0.20 \pm 0.05$.

2. UA5 DATA AND THE SCALING

The most recent measurements of the paeudorapidity distributions by UA5 group are given in figure 1. The distribution are plotted in coordinates $\eta^* = \eta - y$. If Feynman's scaling was valid the experimental points for all distributions should be identical. There is seen clear deviation from scaling. In addition to the well known deviations in the central region it should be noted that in the region of highest available energies of secondaries there is no sign of saturation, the curves show a clear tendency for crossing over. That gives strong indication of the scaling violation in the fragmentation region. More definite conclusions about scaling violation at the region of high energy secondary particles /fragmentation region/ are limited by the restrictions on available measurements at very small angles. The regions accesible for measurements as a function of x and p variables are given in figure 2.

The same UA5 data are used in figure 3 for verification of the above given formula describing scaling violation. The axes are choosen in such way that if the formula is valid the cross-sections should be independent of the primary energy. It is seen that the points really follow one line in spite of the fact that $\sqrt{s}$ varies from 53 to 900 GeV. It is important to point out that a single value of $\alpha = 0.18$ was taken in deriving that figure.

In figure 3 were omitted points for the cms rapidity below unity. The justification comes from the fact that in the figure there should be used the distribution in function of the rapidity. The most significant differences between distributions in rapidity and pseudorapidity occurs for small values of those variables.

Figure 3 shows that formula 1, very well describes the changes of the invariant cross-section in the region accessable for accelerators. The question which remains open

is the behaviour of the invariant cross-section at high x and low p_t. That region can be accessed only on the basis of cosmic ray data.

3. CONSEQUENCIES OF SCALING IN THE FRAGMENTATION REGION

The picture we would like to investigate here is the following. It is assumed that high energy interaction is characterised by the existence of a leading particle which conserves its identity /baryon number/. The energy taken by the secondary particle E = KEo so the energy taken by the leading particle is E = /1-K/Eo. The basic and fundamental question for cosmic ray research is how the energy is shared among the secondaries. In general there are two possibilities either the fraction of energy taken by every particle is decreasing when energy and consequently the multiplicity of the secondaries is increasing or there exist some particles which always take a constant fraction of the primary particle energy. The second case is normally called preservation of scaling in the fragmentation region.

If scaling was preserved in the fragmentation region at the accelerator energies that would require an increase of the total inelasticity coefficient. That follows from the fact that the fraction of primary energy seen in the central region increases with that energy. If at the same time we assume scaling in the fragmentation region we suppose that the fraction of energy in that region remains constant. Those two facts lead to the statement that total energy of the secondaries increases faster then primary energy.

Estimation made by us earlier /Wdowczyk and Wolfendale,1986/ lead to an increase of the inelasticity coefficient according to the following formula

$$K = 0.44 + 0.0326 \ln(s/1000\,\mathrm{GeV})$$

That behaviour, although unlikely, can not be ruled by accelerator data. It can be however verified on the basis of cosmic ray data. We intend to verify that formula on the basis of the cosmic ray hadron and γ-ray propagation in the atmosphere. It has been demonstrated that the rate of γ-ray families observed in emulsion experiments can be made to agree with expectations only in the case that primary cosmic rays are predominantly heavy nuclei. On the basis of

calculations of Wrotniak et al /1985/ we have found that, for the normal mass composition with the assumption of scaling in the fragmentation region, the expected intensity of -ray families with $\Sigma E > 100$ TeV is 8.5×10^{-8} m^{-2}s^{-1}sr^{-1}

The observed intensities for the same observation level vary from 1.1×10^{-8} /Mt Fuji recalculated to Pamir level/ to 2.5×10^{-8} /Japan USRR experiment at Pamir/. To make the expectations agree with observations it is necessary either to change the model of high energy interaction or to reduce drastically the proton content in the primary cosmic ray flux at energies around 10^{15} eV.

In the so called constant mass composition the proton flux amounts to about 35% of the total flux of the primary particles. To obtain the above quoted observed flux we would have to reduce the proton content to the level of 5-9%.

4. COSMIC RAY HADRONS IN THE ATMOSPHERE

Above we have discussed two consequencies of the scaling in the fragmentation region. It is important to note that both are leading to a reduction of the expected hadron flux in the atmosphere. The hadron flux is dominated by the leading particles. If the inelasticity coefficient increases the energy of the leading particle decreases so their flux become lower. The increase of the heavy particle content in the primary flux lead to a reduction of the flux of nucleons. This is due to a steep spectrum of cosmic rays. If we replace protons by nuclei with mass A we reduce the flux of nucleons by a factor $A^{(\gamma-1)}$ where γ is the integral spectral index of the primary spectrum approximately equal to 1.6. The reduction in nucleon intensity also gives a reduction of hadron flux in the atmosphere.

Detailed calculations lead to a result which is shown in figure 4. In that figure the flux of hadrons at Tien-Shan level is compared with the expected flux calculated under the assumption of the validity of scaling in the fragmentation region. It is seen that the joint effect of the two above stated phenomena is so drastic that it become clearly impossible to made the predictions and observations agree.

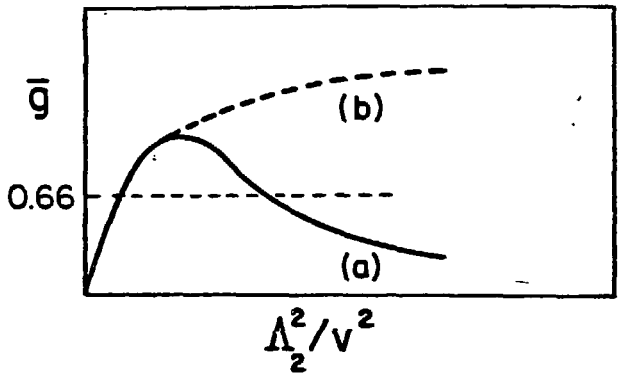

Fig. 1: Possible behavior of the effective $W F_L \bar{F}_L$ coupling as a function of Λ_2^2/v^2. (a) admits a SCSM which can agree with experiment; (b) does not.

must behave for the SCSM to make sense experimentally, we restrict our attention to $\Lambda_2^2/v^2 \geq 0$. When this ratio is small, the theory is analyzed perturbatively and $\bar{g}$ is just the gauge coupling g_2 evaluated at v, $g_2(v)$, which goes to zero as Λ_2 approaches zero. For small Λ_2^2/v^2, $\bar{g}$ rises monotonically from zero at least as long as the perturbative analysis is valid, that is, for $\bar{g} = g_2(v) \lesssim 1$.

We believe that the SCSM may describe weak interaction data. For this to be true, $\bar{g}$ must take the value of 0.66 at some large value of Λ_2^2/v^2. This can happen only if $\bar{g}$ falls back to the value 0.66 after its monotonic rise in the perturbative region. Furthermore, the value of Λ_2^2/v^2 at which $\bar{g}$ falls back through 0.66 must be within the domain in which chiral symmetry remains unbroken. This behavior is sketched in curve (a) of Fig. 1. It seems clear that $\bar{g}$ should approach a non-zero asymptotic value, since for Λ_2^2/v^2 large enough, v becomes irrelevant and there is no reason for the effective coupling between the bound states in a strongly interacting theory to vanish.

This picture of $\bar{g}$ helps us to understand how the perturbative standard model may have mistakenly been taken to describe the weak interactions: if the weak interactions are actually described by SCSM, then $\bar{g}$ must equal 0.66 for two values of Λ_2^2/v^2. It will require more experimental data, involving quantities other than $\bar{g}$, to determine which value of Λ_2^2/v^2 best describes all weak interaction phenomena.

The behavior of $\bar{g}$ which we have described is required for the SCSM to be the correct theory of the weak interactions. However, $\bar{g}(\Lambda_2^2/v^2)$ is a dynamically determined quantity whose behavior may be quite different from what we require. For example, $\bar{g}$ may continue to rise monotonically and approach a large asymptotic value as in curve (b). In this case, the only solution to $\bar{g}(\Lambda_2^2/v^2) = 0.66$ is the usual weak coupling solution and the SCSM cannot reproduce experimental weak interaction data. In fact, the value 0.66 for the effective interaction between strongly interacting bound states may be unnaturally small. In comparison, the corresponding ρ-nucleon coupling is roughly 5. However, it is difficult to make direct comparisons between the SCSM and a

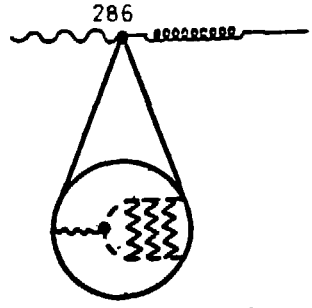

Fig. 2: Photon mixing with a composite W^3, bound by $SU(2)_L$ gauge boson exchange.

vector theory such as QCD, since the gauge groups, the constituents and the patterns of chiral symmetry breaking are all different. Because we are unable to calculate $\bar{g}(\Lambda_2^2/v^2)$ from the underlying gauge theory, we must impose the dynamical assumption that there is a large value of Λ_2^2/v^2 for which $\bar{g} = 0.66$.

II.4 ELECTROMAGNETISM AND THE EMERGENCE OF A YANG-MILLS STRUCTURE IN THE SCSM

In the SCSM, there is no spontaneous symmetry breaking and the $U(1)$ gauge boson, a_μ, remains massless. The $U(1)$ coupling, g_1, is the QED coupling e and the $U(1)$ charges of states are their electric charges. The scalar field ϕ has charge $-1/2$ and the left-handed doublet ψ_L^a has charge y_a. The two right-handed fermions associated with ψ_L^a have charges $y_a + 1/2$ and $y_a - 1/2$ which are 2/3 and -1/3 for quarks and 0 and -1 for leptons. The upper component of the bound state F_L^a is made of ϕ^* and ψ_L^a so it has charge $y_a + 1/2$ while the lower component is made of ϕ and ψ_L^a so its charge is $y_a - 1/2$. These match the charges of the corresponding right-handed states and electromagnetism is vectorial as it must be. The Higgs particle, H, is made of ϕ^* and ϕ so it is electrically neutral. The three W's are bound states of ϕ^* with ϕ^*, ϕ^* with ϕ, and ϕ with ϕ which carry charges of $+1$, 0 and -1, respectively.

The inclusion of electromagnetism allows the W^3 to mix with the photon and the resulting mass eigenstate, the Z, is heavier than the $W^\pm$. This mixing occurs because the W^3 is made of charged constituents and is illustrated in Fig. 2. To study the effect of this mixing let us add electromagnetism to the effective lagrangian eq. (2.6). Because the quarks, leptons, and W are composite, their couplings to the photon need not be minimal, but they must be $U(1)$ gauge invariant. Non-minimal couplings include anomalous magnetic moments, quadrupole moments for the W and electromagnetic form factors for quarks and leptons. Couplings involving operators of dimension five and higher are suppressed by powers of q/Λ_2 at low energies. Their effect on weak phenomenology at energies up to and including m_W is explored in Section III. Here we study the effects of including all electromagnetic couplings of dimension four or less. In addition to the electromagnetic interactions obtained by gauging the $U(1)$ in the usual (minimal) way, two other couplings can occur, $-\frac{k}{2}\mathcal{F}_{\mu\nu}W^3_{\mu\nu}$, which mixes the photon with the W^3; and $ie\lambda W_\mu^+ W_\nu^- \mathcal{F}_{\mu\nu}$ which generates an anomalous magnetic moment for

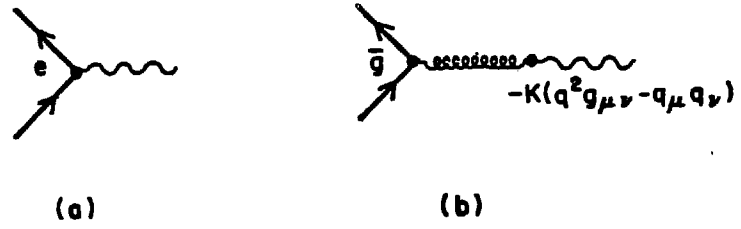

Fig. 3: Direct (a) and W^3-dominated (b) couplings of the photon to the massless composite fermion.

the $W^\pm$. The complete effective lagrangian (including right-handed fermions) through dimension four is

$$\begin{aligned}\mathcal{L}_{\rm eff} &= \mathcal{L}^0_{\rm eff} + i\bar{\psi}_{Rb}\,\partial\!\!\!/\,\psi^b_R - \frac{1}{4}\mathcal{F}^{\mu\nu}\mathcal{F}_{\mu\nu} + ea^\mu j^{em}_\mu - iea^\mu(W^{+\nu}W^-_{\mu\nu} - W^{-\nu}W^+_{\mu\nu}) \\ &\quad - e^2(a^\mu a_\mu W^{+\nu}W^-_\nu - a^\mu a^\nu W^+_\mu W^-_\nu) + eg_3(a^\mu W^-_\mu W^{+\nu}W^3_\nu \\ &\quad + a^\mu W^+_\mu W^{-\nu}W^3_\nu - 2a^\mu W^3_\mu W^{+\nu}W^-_\nu) - \frac{k}{2}\mathcal{F}^{\mu\nu}W^3_{\mu\nu} - ie\lambda\mathcal{F}^{\mu\nu}W^+_\mu W^{-\nu}\end{aligned} \tag{2.9}$$

where j^{em}_μ is the fermion electromagnetic current.

The presence of W^3-photon mixing gives rise to form factors for all electromagnetic vertices involving composite particles, even at tree level. For every direct photon-composite particle coupling there is an analogous graph with the same tensor structure in which the photon goes first into a W^3 and the W^3 then couples to the composite particles by an $SU(2)_L$ "strong interaction" (see Fig. 3). If the composite dynamics is based on an asymptotically free gauge theory, as it in the SCSM, then the electromagnetic form factors of composite particles should vanish at asymptotically large momentum transfer. Suppose, for the sake of argument, that the form factors generated at the tree level from eq. (2.9), satisfied this constraint; that is, they vanish as $q^2 \to \infty$ (q^2 being the virtual photon mass). As we will show, this requires certain relations among the parameters in $\mathcal{L}_{\rm eff}$, namely

$$\begin{aligned} k &= e/g \\ \lambda &= 1 \\ g_3 &= g \\ g_4 &= -g'_4 = g^2 \end{aligned} \tag{2.10}$$

The W^3-photon mixing term also makes the quadratic part of the lagrangian non-diagonal. To diagonalize it we make the transformation

$$\begin{aligned} Z_\mu &= \sqrt{1-k^2}\,W^3_\mu \\ A_\mu &= a_\mu + kW^3_\mu \end{aligned} \tag{2.11}$$

Rewritten in terms of A and Z, $\mathcal{L}_{\rm eff}$ is quite complicated. If, however, the relations given in eq. (2.10) hold, then a remarkable simplification occurs: the result is exactly the standard model lagrangian (in unitary gauge and not yet including the H particle or fermion masses) with $\sin\theta$ replaced by $k = e/\bar{g}$!

Let us recapitulate. The SCSM has an effective long distance lagrangian, involving composite W's, massless fermions and the photon, which can be rewritten in the form of eq. (2.9). The parameters of the effective theory are e, $\bar{g}$, g_3, g_4, g_4', k, λ and m_W. If we can justify saturating the electromagnetic form factors of the charged composite states with the contributions generated at tree level from eq. (2.9) then the relations of eq. (2.10) must hold and this theory shares all of the phenomenological successes of the standard model including the W and Z masses. In Section III we will study the use of eq. (2.9) as an effective theory through the energy region of roughly 100 GeV. In doing so, we will explain the relations of eq. (2.10).

In the SCSM the physical photon is an admixture of the gauge boson a_μ appearing in the original lagrangian and the bound state W^3. The photon already contains an admixture of the ρ^0, ω and all other spin one bound states with which it can mix, so including the bound state W^3 is perfectly natural. What is perhaps troubling is the amount of mixing. The parameter k has the value .46 which implies a rather large mixing. The corresponding $\rho - \gamma$ parameter is $\approx .05$. However, again, the ρ and the bound state Z are very different beasts. Also, if $k = e/\bar{g}$, the smallness of $\bar{g}$ previously discussed and the largeness of k are really the same issue and not two separate concerns.

III. THE SCSM: DYNAMICS AT $Q^2 \lesssim$ (100 GeV)^2

III.1 THE SCSM AND VECTOR MESON DOMINANCE

The ordinary nucleon is a bound state in a confining gauge theory with $\Lambda_{\rm QCD} \sim$ 200 MeV and therefore has form factors characterized by this mass scale. At very high momentum transfer one probes the constituent quarks and gluons interacting within the nucleon, so one can use QCD to study the asymptotic behavior of the form factors. At lower energies the form factors reflect the interactions of the nucleon with other bound states in the spectrum. This connection can be made precise by means of dispersion relations based on analyticity and unitarity. The low q^2 behavior of, for example, the proton's electromagnetic form factor has been successfully related to the strong interaction coupling of the proton with the ρ, ω and ϕ.

All composite particles in the SCSM should have non-trivial form factors characterized by a scale $\Lambda_2 \sim G_F^{-1/2}$. As an example, consider the electromagnetic form factor of F_L^a and begin by considering the contributions from the minimal sector described by the effective lagrangian (2.9). To lowest order in e and k there are two contributions shown in Fig. 3. The first is the direct photon coupling and the second arises because the photon is mixed with the W^3 which interacts with the fermion. Thus, to this order,

$$e\langle F_L^a, \bar{F}_L^a | J_{em}^\mu | 0\rangle = e\bar{U}_L\gamma^\mu Q^a V_L - k\bar{g}\frac{q^2}{q^2 - m_W^2}\bar{U}_L\gamma^\mu\frac{\tau_3}{2}V_L \qquad (3.1)$$

Using $Q^a = y^a + \tau_3/2$ we can decompose the current into $SU(2)_W$ singlet and vector pieces

$$e\langle F_L^a, \bar{F}_L^a | J_{em}^\mu | 0\rangle = e\bar{U}_L\gamma^\mu y^a V_L + e\left(1 - \frac{k\bar{g}}{e}\,\frac{q^2}{q^2 - m_W^2}\right)\bar{U}_L\gamma^\mu\frac{\tau_3}{2}V_L \qquad (3.2)$$

The $SU(2)_W$ vector form factor is then

$$F_V(q^2) = \left(1 - \frac{k\bar{g}}{e}\,\frac{q^2}{q^2 - m_W^2}\right) \qquad (3.3)$$

which has the required value of unity at $q^2 = 0$.

Since the light left-handed fermions are $SU(2)_L$ composites and $SU(2)_L$ is asymptotically free, the electromagnetic form factors of F_L^a must vanish as $|q^2| \to \infty$. If there were no other bound states coupled to the $SU(2)_W$ vector channel, then the two graphs of Fig. 3 would have to satisfy this constraint by themselves. This implies $k = e/\bar{g}$, which is one of the relationships we need to match the phenomenology of the minimal sector of the SCSM with that of the standard model (see Section II.4). The other three relationships of eq. (2.10) are obtained by applying the same reasoning to the charge and magnetic moment form factors and two photon (seagull) couplings of the $W^\pm$.

The relationship $k = e/\bar{g}$ has counterparts in ordinary hadronic physics.[11] The isovector part of the nucleon electromagnetic form factor has a direct contribution from the photon as well as a piece where the photon mixes with the ρ which then interacts with the nucleon. The assumption of "vector meson dominance" is that these two contributions are sufficient to saturate a form factor which vanishes as $q^2 \to \infty$, yielding the relationship $k_{\rho\gamma} = e/g_{\rho N\bar{N}}$. Remarkably, this works at the 10% level as does the isoscalar VMD relationship $k_{\omega\gamma} = e/g_{\omega N\bar{N}}$. Similarly, VMD works quite well for pion form factors where it implies $g_{\rho\pi\pi} = g_{\rho N\bar{N}}$, much like our relation $g_3 = \bar{g}$. The successes of VMD in hadronic physics embolden us in our application of these ideas to the SCSM.

We have shown that the effective theory describing the interactions of light fermions, the $W^\pm$, Z and photon in the SCSM, ignoring the exotic sector, is precisely the standard model lagrangian in the unitary gauge. We do not expect relations like $k = e/\bar{g}$ to be exact in the SCSM. Intermediate states involving exotic particles not present in the standard model also contribute to $F_V(q^2)$ and alter the relation between k and $e/\bar{g}$. Potentially, there are many sources of corrections: anomalous thresholds, polynomials and exotic coupling among familiar particles, to name a few. In fact, all significant deviations between the low energy SCSM and the standard model can be expressed in terms of the masses and couplings of the exotic particles in the SCSM. To ensure that the deviations are small we must assume that the particles in the exotic sector are heavy and/or weakly coupled. We will demonstrate this and show how to parameterize these deviations in the next subsection.

The equivalence of these two theories applies to radiative corrections as well. We can separate all radiative corrections into minimal and exotic parts. The former may be relatively large ($O(\alpha)$, $O(\bar{g}^2/4\pi)$, large logarithms) but are identical to radiative

corrections expected in the standard model. The latter are novel but small because they are corrections to exotic processes already required to be small in order to reproduce weak interaction phenomenology at tree level. We conclude that radiative corrections do not place new restrictions on the SCSM beyond those already required at tree level.

III.2 DISPERSION THEORY ANALYSIS OF THE SCSM

To study the modifications of weak phenomena which come from new physics in the SCSM, we use dispersion relations to separate the contributions to processes into parts coming from the minimal sector and from the exotic sector. We do not analyze all vertices since it would be rather tedious, but instead confine ourselves, for the purposes of illustration, to the photon vacuum polarization.[1] We use dispersion theory rather than effective lagrangians because we are interested in momenta as large as the compositeness scale of the confining $SU(2)_L$ *i.e.*, $|q^2| \sim m_W^2$. Also, by using dispersion relations we can entirely avoid ambiguous notions like the off-shell couplings of composite particles.

We are interested in the contributions to the photon propagator coming from the strong interactions of the SCSM. We are not interested in purely electromagnetic corrections so we work to lowest order in e. The photon propagator can be written as

$$D_{\mu\nu}(q^2) = \left(-g_{\mu\nu} + q_\mu q_\nu/q^2\right) \frac{1}{q^2\left(1 - e^2\tilde{\Pi}(q^2)\right)} \tag{3.4}$$

where

$$\Pi_{\mu\nu} = \left(-g_{\mu\nu}q^2 + q_\mu q_\nu\right)\Pi(q^2) \tag{3.5}$$

and the vacuum polarization

$$\Pi_{\mu\nu}(q) = i\int d^4x\, e^{iq\cdot x}\langle 0|T\left(J_\mu^{em}(x)J_\nu^{em}(0)\right)|0\rangle \tag{3.6}$$

has the electromagnetic current, J_μ^{em} evaluated to zeroth order in e. $\tilde{\Pi}$ has been subtracted to guarantee that the pole at $q^2 = 0$ has unit residue,

$$\tilde{\Pi}(q^2) = \Pi(q^2) - \Pi(0) \quad . \tag{3.7}$$

$\tilde{\Pi}(q^2)$ is an analytic function of q^2 with cuts beginning at $q^2 = 4m_a^2$, the threshold for creating each fermion-anti-fermion pair. The large q^2 ($q >> m_W^2$) behavior of $\tilde{\Pi}(q^2)$ is calculable because $SU(2)_L$ is an asymptotically free gauge theory: $\tilde{\Pi}(q^2)$ grows like $ln\ q^2$ for large q^2 and no polynomial in q^2 is allowed. Using standard techniques of dispersion theory, $\tilde{\Pi}(q^2)$ can be written as:

$$\tilde{\Pi}(q^2) = q^2\int_0^\infty \frac{d\sigma^2}{\sigma^2}\,\frac{\lambda(\sigma^2)}{\sigma^2 - q^2} \tag{3.8}$$

with $\lambda(\sigma^2)$ real,

$$\lambda(\sigma^2) = \frac{1}{\pi}\,Im\,\tilde{\Pi}(q^2) \tag{3.9}$$

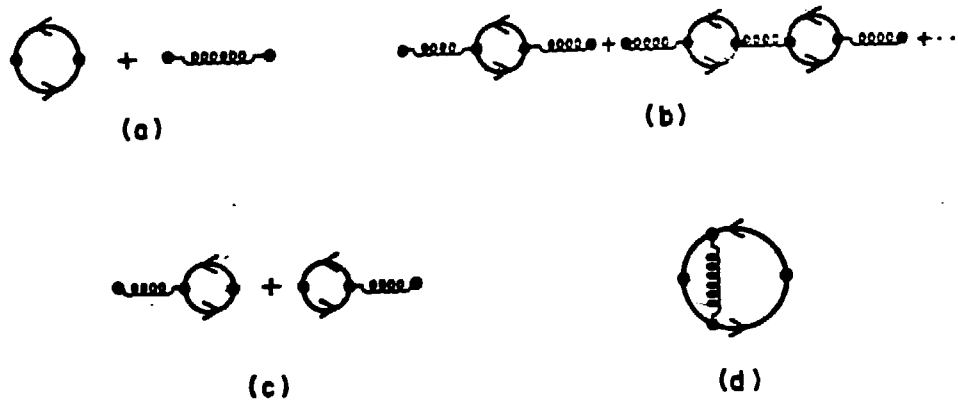

Fig. 4: Minimal sector contributions to $\mathrm{Im}\,\tilde{\Pi}(\sigma^2)$ in the SCSM.

and determined entirely by physical on-shell intermediate states which can be created from the vacuum by J_μ^{em}:

$$Im\ \Pi_{\mu\nu} \propto \sum_n \delta^4(q - p_n)\langle 0|J_\mu^{em}|n\rangle\langle n|J_\nu^{em}|0\rangle \tag{3.10}$$

In the minimal sector of the SCSM, to zeroth order in $\bar{g}$, the only states which couple to the photon are W_μ^3, the neutral member of the $SU(2)_L$ triplet, and the $F\bar{F}$ continuum. For non-vanishing $\bar{g}$ the W^3 also appears as a pole in the $F_L\bar{F}_L$ continuum, so we must take care to avoid double counting when calculating $\lambda(\sigma^2)$. The bookkeeping is simplified because $\bar{g}$ is small ($\bar{g} \approx 0.66$), making it possible to order contributions to $\lambda(\sigma^2)$ in powers of $\bar{g}^2/4\pi$. To zeroth order in $\bar{g}$, the only contributions to $\lambda(\sigma^2)$ come from the (zero width) W^3 pole and the $F\bar{F}$ cut (with no form factor at the $\gamma F\bar{F}$ vertex):

$$\lambda(\sigma^2) = \frac{k^2}{e^2} m_W^2 \delta(\sigma^2 - m_W^2) + \sum_a \frac{Q_a^2}{12\pi}\theta(\sigma^2 - 4m_a^2)\left(1 - \frac{4m_a^2}{\sigma^2}\right)^{1/2}\left(1 + \frac{2m_a^2}{\sigma^2}\right) \tag{3.11}$$

Here k is the on-shell $W^3 - \gamma$ coupling. These two contributions are shown in Fig. 4a. The first term will result in a pole in the photon propagator at a mass somewhat greater than m_W. We identify this state with the physical Z. Higher order contributions in $\bar{g}$ shift the Z mass and give it a finite width (Fig. 4b), generate off diagonal couplings (Fig. 4c) and contribute to the F_L electromagnetic form factor (Fig. 4d). All of the contributions to $\lambda(\sigma^2)$ shown in Fig. 4 are also found in the standard model, so they do not represent novel features of the SCSM. All except the direct $W^3 - \gamma$ mixing are classified as radiative corrections in the standard model. So up to radiative corrections which are the same as in the standard model, the minimal sector contribution to $\lambda(\sigma^2)$ is just the first term in (3.11).

$$\lambda^{\rm min}(\sigma^2) = \frac{k^2}{e^2} m_W^2 \delta(\sigma^2 - m_W^2) + \text{radiative corrections} \tag{3.12}$$

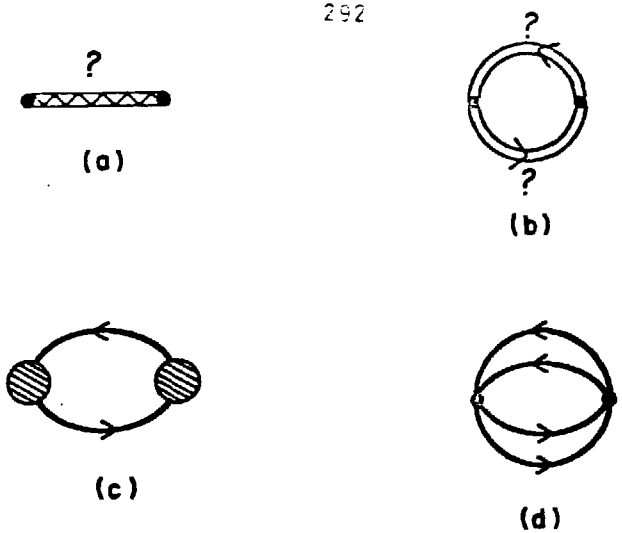

Fig. 5: Exotic contributions to $\mathrm{Im}\,\tilde{\Pi}(\sigma^2)$ in the SCSM: (a) excited vectors: (b) excited fermion anti-fermion pairs, etc.; (c) exotic contributions to light fermion form factors: (d) direct couplings to four or more light fermions.

Truly novel contributions to $\lambda(\sigma^2)$ do come from the exotic sector of the SCSM and are shown in Fig. 5. These include a) heavy particles which can mix with the photon *e.g.*, excited W's or $SU(2)_W$ singlet vectors: b) heavy particles which couple in pairs to the photon, *e.g.*, excited quarks and leptons, dileptons, diquarks or leptoquarks: c) exotic sector contributions to the light composite fermion electromagnetic form factor: and d) exotic direct couplings between the photon and four (or more) ordinary light composite fermions. The enhancements in the fermion form factor (c) all come from exotic resonances in the $F_L\bar{F}_L$ channel so a) b) and c) all arise from exotic particles in the SCSM. This leaves only d) as an exotic contribution not directly associated with novel states in the SCSM. We will now show that d) is small so that to a good approximation any structure in $\lambda(\sigma^2)$ not coming from the minimal sector can be attributed to new particles in the SCSM.

The lowest dimension gauge invariant operator which couples the photon to two left-handed fermion anti-fermion pairs may be written as

$$\mathcal{L}_{\gamma F\bar{F}F\bar{F}} = \frac{e\tilde{g}}{m_W^4} \mathcal{F}^{\mu\nu} \sum_{ab} \bar{F}_{La}\gamma_\mu Q^c F_L^a \bar{F}_{Lb}\gamma_\nu F_L^b \tag{3.13}$$

This interaction may be thought of as arising from preon line diagrams like those of Fig. 6. At low energy its contribution to $\lambda(\sigma^2)$ is suppressed by σ^8/m_W^8 relative to the contributions we keep. For $\sigma^2 \sim m_W^2$, the suppression is not operative and we estimate

$$\lambda_{\gamma F\bar{F}F\bar{F}}(\sim m_W^2) \sim 12\tilde{g}^2\Phi_4 \sum_a Q_a^2 \tag{3.14}$$

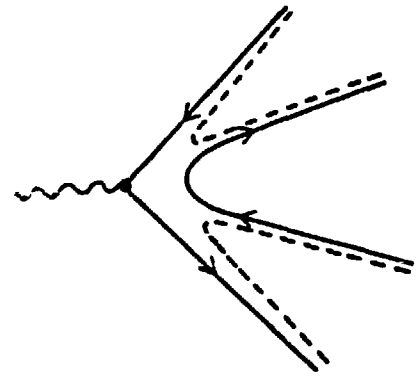

Fig. 6: Preon line diagram for a direct $\gamma \to F_L\bar{F}_L F_L\bar{F}_L$ coupling.

where the factor of 12 comes from the sum on b and Φ_4 is four body (massless) phase space.

$$\Phi_N = \frac{2\pi}{(16\pi^2)^{N-1}} \frac{1}{(N-1)!(N-2)!} \tag{3.15}$$

For $N = 4$, $\Phi_4 \approx 10^{-7}$ so $\lambda_{\gamma F\bar{F}F\bar{F}}(\sim m_W^2) \approx 10^{-5}\tilde{g}^2$. This is to be compared, for example, with the $F\bar{F}$ cut given by (3.11). For these two to be comparable $\tilde{g}$ must be around 150 which seems unreasonably large and even then this new contribution is only as large as a small radiative correction. The same argument does not forbid many body decays of heavy mesons in QCD. There are two differences: first, the masses of heavy mesons ($M > 1$ GeV) are much greater than the confinement scale, $\Lambda_{QCD} \sim 300$ MeV; and second, the decays can proceed through nearly on-shell two body intermediate states. No such quasi-two body channels exist below $2m_W$ in the SCSM so we conclude that many ($n \geq 4$) light fermion intermediate states have a negligible effect on the photon propagator.[16]

We are left then with poles and cuts, Figs. 5a and b, associated with heavy particles as the only possible significant contributions to the photon polarization which are not already present in the standard model. We can then write

$$\lambda(\sigma^2) = \frac{k^2}{e^2} m_W^2 \delta(\sigma^2 - m_W^2) + \theta(\sigma^2 - \sigma_0^2)\tilde{\lambda}(\sigma^2) \\ + \text{radiative corrections.} \tag{3.16}$$

where σ_0 is the mass of the lightest exotic threshold in the photon channel. Substituting into (3.8) and ignoring radiative corrections, gives

$$e^2\tilde{\Pi}(q^2) = \frac{k^2 q^2}{q^2 - m_W^2} + e^2 q^2 \int_{\sigma_0^2}^{\infty} \frac{d\sigma^2}{\sigma^2} \frac{\tilde{\lambda}(\sigma^2)}{q^2 - \sigma^2} \tag{3.17}$$

For the moment, we set $\tilde{\lambda} = 0$ and look at the photon propagator:

$$\left[q^2\left(1 - e^2\tilde{\Pi}(q^2)\right)\right]^{-1} = \frac{1}{q^2} + \frac{(k^2/(1-k^2))}{q^2 - m_W^2/(1-k^2)} \tag{3.18}$$

Recall that in first approximation, k is equal to the phenomenological parameter, $\sin\theta$, measured in weak interaction experiments. The new pole is at $m_W/\cos\theta$ and has residue $\tan^2\theta$. These correspond to the familiar values of m_Z and the coefficient of the $\left(J_\mu^{em}\right)^2$ term arising in the standard model from Z exchange. $\tilde{\lambda} \neq 0$ alters these results. If we assume

$$\epsilon \equiv e^2 m_W^2 \int_{\sigma_0}^{\infty} \frac{d\sigma^2}{\sigma^4}\tilde{\lambda}(\sigma^2) << 1 \tag{3.19}$$

then the photon propagator, to order ϵ, can be written as two poles and a constant

$$\left[q^2\left(1 - e^2\tilde{\Pi}(q^2)\right)\right]^{-1} = \frac{1}{q^2} + \frac{r}{q^2 - m_Z^2} + A + O(\epsilon^2) \tag{3.20}$$

with

$$r = \frac{k^2}{1-k^2} + O(\epsilon)$$
$$m_Z = m_W/\sqrt{1-k^2} + O(\epsilon)$$
$$A = O(\epsilon)$$

We see that the exotic sector leads to differences between the phenomenology of the SCSM and that of the standard model. To be useful in practice, it is necessary to extend this analysis to fermion form factors, the W-boson anomalous magnetic moment and to fermion four point functions. That analysis can be found in Ref. [1]. Here, we will now turn to the new physics of the exotic sector.

IV. PHENOMENOLOGY OF EXOTIC STATES AND EXPERIMENTAL CONSTRAINTS

There are $SU(2)_L$ single bound states expected in the SCSM which have no counterparts in the usual standard model. The presence of these particles makes the phenomenology of the SCSM richer than that of the standard model. These particles may be produced at accelerators in the near future so it is important to characterize their properties. In this section we present a brief phenomenological description of the lowest excitations expected in the SCSM. In Section III we showed how the exotic sector leads to differences between the low energy phenomenology of the SCSM and that of the usual weak interaction theory. These differences can be turned into lower bounds on the masses and upper bounds on the couplings of certain exotic states. We point this out where applicable. More detailed studies can be found in the work of

	State	Spin	$SU(N) \times SU(2)_{\text{global}}$
Excited Fermions	$F^{*a}_{L,R}$	$\frac{1}{2}$	$(N,2)$
	$F^{*a\mu}_{L,R}$	$\frac{3}{2}$	$(N,2)$
Excited Bosons	$W^{*\mu}, Z^{*\mu}$	1	$(1,3)$
	H^*	0	$(1,1)$
Two Fermion Bound States	S^{ab}	0	$\left(\frac{1}{2}N(N-1),1\right)$
	$V_{\mu a}{}^b$	1	$\left(N^2-1,1\right),(1,1)$
	$K^{ab}_{\mu\nu}$	1	$\left(\frac{1}{2}N(N+1,1\right)$

TABLE I: Exotic Resonances in the SCSM.

Wudka,[17] and Korpa and Ryzak,[18] and Kaidalov and Nogteva.[19] The states we shall be considering are listed, together with their quantum numbers, in Table I.

V.1 EXCITED FERMIONS

The left-handed quarks and leptons of the SCSM can be regarded as bound states of a strongly interacting fermion doublet with a strongly interacting scalar doublet. [This is only an approximate description since they also contain $SU(2)_L$ bosons and pairs.] These states have both radial and orbital excitations which mix to form massive fermions with masses of order $G_F^{-1/2}$. For example, the left-handed interpolating field $F^a_L = \Omega^\dagger \psi^a_L$ introduced in Section II connects not only the light composite fermion states to the vacuum, but also radial (spin 1/2) excitations which also transform as $(1/2,0)$ and $(N,2)$ under the Lorentz and global symmetry groups. Right-handed spin 1/2 operators such as $F^a_R = \Omega^\dagger \not{D} D^2 \psi^a_L$ also exist and are associated with orbital excitations transforming as $(0,1/2)$ and $(N,2)$. [Simpler operators like $\Omega^\dagger \not{D} \psi^c_L$ vanish by the equations of motion.] The unbroken chiral symmetry group $SU(N) \times SU(2)_W$ does not prevent these states from mixing, so Dirac mass terms of the form $\bar{F}_{Ra} F^a_L$ will appear in an effective theory describing these particles. [Mass terms of the form $\bar{F}^a_L F^b_L$ are forbidden by the unbroken global symmetry.] Because of the t' Hooft consistency conditions, one and only one $(N,2)$ of left-handed fermions will not mix with right-handed states and will remain in the spectrum as a light composite fermion.

The spectrum also contains spin 3/2 excited quarks and leptons. These fermions can be associated with the interpolating fields

$$\begin{aligned} F^a_{L\mu} &= \Omega^\dagger P_{\mu\nu}(D^\nu \psi^a_L) \\ F^a_{R\mu} &= \Omega^\dagger \not{D} P_{\mu\nu}(D^\nu \psi^a_L) \end{aligned} \tag{4.1}$$

which transform as $(1,1/2)$ and $(1/2,1)$ under the Lorentz group and as $(N,2)$ under the global group. Here $P_{\mu\nu} = g_{\mu\nu} - \frac{1}{4}\gamma_\mu\gamma_\nu$ is the projection operator which eliminates the $(0,1/2)$ component of $D^\nu\psi^a_L$. These states also have masses of order $G_F^{-1/2}$. Excited quarks and leptons of higher spin also exist but will not be discussed in the following.

In the absence of the perturbative $SU(3)\times U(1)$ gauge forces and the fundamental Yukawa couplings, the excited states of each spin would form degenerate $(N,2)$'s under the global symmetry group. This degeneracy is primarily removed by $SU(3)$ color forces which provide splittings of order $\alpha_S G_F^{-1/2}$ between excited quarks and leptons (7a). In addition, graphs such as Fig. 7b lead to flavor splittings between the excited fermions of order $m^2 G_F^{1/2}$ where m denotes a typical quark or lepton mass. Note that graphs which provide the light fermion masses also mix the excited spin-1/2 fermions with the fundamental right-handed fermions (Fig. 8c). This leads to small violations of unitarity in the Kobayashi-Maskawa matrix for the light composite fermions with the mixing angles between light and heavy (excited) fermions being of order $mG_F^{1/2}$.

Excited fermions have not been seen in any accelerator experiment to date. The most direct mass limit, arising from failure to produce these particles in e^+e^- collisions, sets a lower bound of 20 GeV on the masses of any charged excited fermions. If the excited fermion is less massive than the Z, it should be seen in decays such as $Z \to Q^*q$ or $Z \to E^*e$. The latter decay mode has been looked for by UA1. Under reasonable assumptions, a mass limit of 80 GeV can be obtained from present data.[20] It is perhaps possible to place a mass limit on excited quarks using existing $p\bar{p}$ collision data, although the limit is less reliable because of the complications of fragmentation functions, jet signatures, etc.

An excited fermion F^{*a} will contribute to the anomalous magnetic moment of the associated light fermion F^a. Because of the chiral nature of the underlying theory, these contributions are of order m^2/m_*^2 where m and m_* are the F^a and F^{*a} masses. The present limit on exotic contributions to $(g-2)/2$ for the muon is $\simeq 10^{-8}$ implying as an order of magnitude $m_* \gtrsim 1$ TeV. In attempting an actual calculation, one must assume a form for the coupling between F^a and F^{*a} and in general cut off loop integrals at m_* or perhaps $G_F^{-1/2}$. The loop integral introduces a factor of $(16\pi^2)^{-1}$ and if the coupling is unity, the bound is lowered to $m_* \gtrsim 80$ GeV. [Remember the expected weak contribution to $g-2$ has yet to be observed.] Detailed calculations bear this point out.[21] Planned improvements in the measurement of $(g-2)_\mu$ could give significant limits on excited fermion masses and couplings.[22] A similar discussion of the effect on $g-2$ can be given for each of the excitations we discuss below.

IV.2 EXCITED BOSONS

In the SCSM the $W^\pm$, Z and H are bound states, and in contrast to the usual weak interaction theory, we expect excitations of these particles with masses of order $G_F^{-1/2}$. The first orbital excitations of the H are the $W^\pm, Z$. The first radial excitation, H^*, has spin zero and is a singlet under the global group $SU(N)\times SU(2)_W$. The H^* couples to light fermions, much like the H, with coupling proportional to the fermion masses. Finding it would be roughly as difficult as finding the H. The H^* has decay

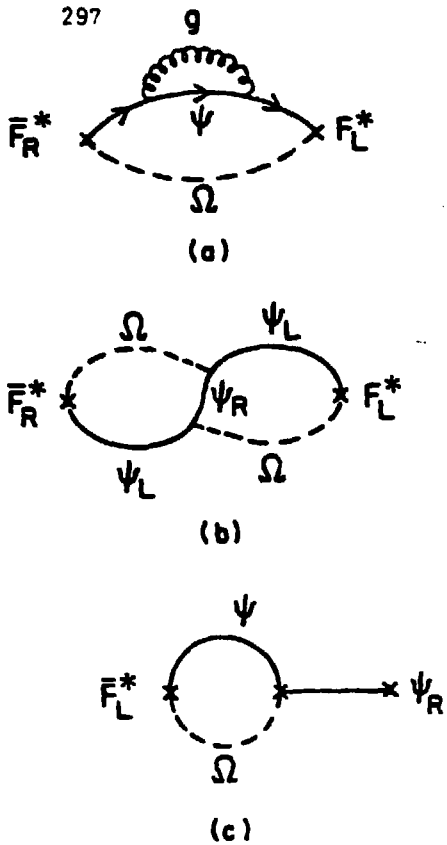

Fig. 7: Mass splittings of heavy fermions generated by (a) QCD gluons; (b) Yukawa couplings; and (c) mixing of excited fermions with light right handed fermions via Yukawa couplings.

channels not open to the H such as $H^* \to \gamma H$ or $H^* \to ZH$ if it is heavy enough. The exchange of the H^* will not lead to any significant modification of low q^2 physics.

The $W^\pm$ and Z have spin one radial excitations $W^{\pm *}$ and Z^* which are a triplet under $SU(2)_W$. As before, mixing with the photon makes the Z^* heavier than $W^{\pm *}$. These particles have couplings to light fermions which are very similar in structure to the couplings of the $W^\pm$ and Z. Of course, the size of the couplings are *a priori* unknown but typically excitations couple more weakly and already $\bar{g} = 0.66$ so perhaps these couplings are small. These excitations should be sought in the same channels which produce the $W^\pm$ and Z. These states also have novel decay modes such as $Z^* \to ZH$ or $W^{+*} \to W^+\gamma$. The UA1 collaboration reports[23] a lower limit of 210 GeV on the mass of the W^* assuming its coupling to fermions is equal to $\bar{g} = 0.66$.

		$\psi_L^a\ \psi_L^b$				$\psi_{La}^\dagger\ \psi_L^b$			
		Q	Color	B	L	Q	Color	B	L
$a=\ell$	$b=\ell$	-1	$\underline{1}$	0	2	0	$\underline{1}$	0	0
$a=\ell$	$b=q$	$-1/3$	$\underline{3}$	1/3	1	2/3	$\underline{3}$	1/3	-1
$a=q$	$b=q$	1/3	$\underline{6}+\underline{\bar{3}}$	2/3	0	0	$\underline{1}+\underline{8}$	0	0

TABLE II: Quantum numbers of two fermion bound states. ℓ, q indicate if ψ_L^a and ψ_L^b carry lepton or baryon number. Q = electric charge. B = baryon number. and L = lepton number.

The exchange of $W^{\pm *}$ and Z^* will lead to modifications of the four fermion interaction of light fermions. Most. but not all. of these modifications can be absorbed into redefinitions of the parameters G_F and $\sin^2\theta_W$. For example. the relation (2.8) will be modified to read

$$\frac{\bar{g}^2}{m_W^2}+\frac{\bar{g}^{*2}}{m_{W^*}^2}=\frac{8G_F}{\sqrt{2}}\ . \tag{4.2}$$

The bounds on m_{W^*} depend on $\bar{g}^*$.[18,24] If $\bar{g}^*$ is very small we get no significant bound on m_{W^*}. If $\bar{g}^*=\bar{g}$ a detailed fit including all the modifications of the low energy neutral current interactions coming from the exchange of the Z^* yields a bound $m_{W^*}>170$ GeV at the 68% confidence level.[18] If the analysis is extended to include the exchange of particles with other quantum numbers. the bounds only weaken.

There should also be orbital excitations of the W and Z with spin 2. In fact. if QCD is any guide. these would be more strongly coupled to the light fermions than are the radial excitations. However. their couplings to fermions vanish at low energies. so there are no significant bounds on their masses or couplings.

IV.3 TWO FERMION BOUND STATES

The SCSM has bound states which cannot be viewed as excitations of familiar particles. These are $SU(2)_L$ singlets of the form $\psi_L^a\,\psi_L^b$ and $\psi_{La}^\dagger\,\psi_L^b$ where ψ_L^a is the fundamental strongly interacting fermion. Again we expect masses of order $G_F^{-1/2}$. The simplest interpolating fields have no derivatives. The fermion number two states. $\psi_L^a\,\psi_L^b$. transform as (0,0) or (1,0) under the Lorentz group while the fermion number zero. $\psi_{La}^\dagger\,\psi_L^b$. transforms as a vector. (1/2, 1/2). We call these particles S^{ab}, $K_{[\mu\nu]}^{ab}$ and $V_\mu{}^b{}_a$ as in Ref. [18]. S is anti-symmetric in a and b while K is symmetric.

These particles have rather unusual quantum numbers as can be seen in Table II. They can be categorized as di-leptons. di-quarks and lepto-quarks. They decay into ordinary quarks and leptons via processes that always conserve the usual quantum numbers of charge. color. baryon number and lepton number. For example. the charge 2/3 lepto-quark with lepton number -1 might decay into $u\bar{\nu}$ or de^+.

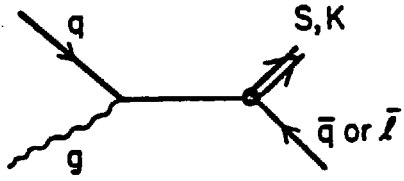

Fig. 8: Leptoquark production via quark-gluon fusion.

The most obvious place to look for leptoquarks is at HERA where, if they are light enough, they could be produced in the S-channel. Heavy leptoquarks might still produce measurable deviations from QCD predictions in ep scattering.[19] Leptoquarks could be produced in $p\bar{p}$ collisions in association with a single light fermion via gluon quark fusion as shown in Fig. 9. The fermion number zero states may appear as S-channel resonances in e^+e^- or $\bar{p}p$ collisions. Clearly the phenomenology of these states is very rich and be much further work is needed.

One linear combination of the N^2 vector states $V_\mu{}^b{}_a$ mixes with the photon. This $SU(2)_W$ singlet state makes an important contribution to the singlet sum rule of eq. (3.26). The exchange of V's leads to modifications of the four-fermion weak interactions. Assuming that the V's are the only novel contribution, Korpa and Ryzak[18] obtained the constraint $m_V/g_V \gtrsim 550$ GeV where g_V is the V-fermion–anti-fermion coupling, normalized like $\bar{g}$. If the V which mixes with the photon saturates the sum rule they obtain the additional constraint $g_V \gtrsim 0.45$ which implies $m_V \gtrsim 250$. Again including other resonance structure loosens the bounds.

The exchange of S particles also leads to a modification of the four-fermion effective theory, whereas K, due to its tensor properties, makes no contribution at $q^2 = 0$. Data from neutrino nucleon scattering[18] give $m_S/g_S \gtrsim 275$ GeV. We see that if either of the couplings g_S or g_V were as large as 2, the exotic excitations in the SCSM would be required to much more massive than the low lying $W^\pm$ and Z.

V. CONCLUSIONS

We have shown that the standard electroweak lagrangian, with its parameters reset so that it is strongly coupled and confining at weak interaction mass scales, may be able to account for all observed weak phenomena with the same level of success as the usual perturbative version of the theory. We say "may be able to" because our demonstration relies on unproven assumptions about the strong interaction dynamics. The assumptions are not unreasonable; whether they are correct is, at present, undecidable. If they are correct and the SCSM can account for weak interactions phenomena, we still have not shown on theoretical grounds that the SCSM is *preferable* to the perturbative theory. Since the SCSM is based on the same renormalizable lagrangian as the usual model with precisely the same field content, it offers no more, or less, insight into the origin of that lagrangian or into questions such as the origin of fermion masses and family replication. The SCSM is not consistent with the perturbative picture of

coupling constant unification required by grand unified theories. Observation of proton decay could be an argument against the SCSM.

Nonetheless, the ability of the SCSM to reproduce weak interaction phenomenology is remarkable. If the standard model should disagree with future experiments or if new particles such as a heavy W are found in the few hundred GeV range, the SCSM should be looked at as a possible explanation. The resonance structure found in the SCSM is rather rich and may serve as a more general guide to the implications of compositeness.

For the SCSM to work, the masses of the excitations must be in the few hundred GeV range. However, the $W^{\pm}$ and Z have masses below 100 GeV. In this case, the scale, Λ_2, of the SCSM is high, say around 500 GeV, and all bound states other than the massless chiral fermions would be expected to occur at this scale. The puzzle is then to explain why the $W^{\pm}$ and Z are so much lighter than the rest of the spectrum. They would have to be as light relative to the other states as the pions are to the other QCD excitations. In the case of pions and QCD, this is not a mystery since there exists a limit in which the pions are massless.

The SCSM requires a rather large value of the photon W^3 mixing parameter k. This parameter could be determined by lattice calculations. The W^3 is a bound state of two scalars interacting via an $SU(2)$ gauge force and scalar self interactions. A measurement of $\langle 0|J_\mu^{em}|W^3\rangle$ as a function of Λ_2, the scalar field mass and the scalar self coupling would show if k could be as large as is required for the SCSM to work. A lattice calculation could also determine the masses of the excited $W^{\pm}$ and Z as well as the Higgs mass. The inclusion of fermions in the lattice calculation would shed light on questions of chiral symmetry breaking and the value of $\bar{g}$.

REFERENCES

1. A complete exposition may be found in M. Claudson, E. Farhi, and R. L. Jaffe, MIT preprint-CTP-1331, to be published in *Physical Review D*.
2. L. F. Abbott and E. Farhi, *Phys. Lett.* **101B**, 69 (1981); *Nucl. Phys.* **B189**, 547 (1981).
3. J. D. Bjorken, *Phys. Rev.* **D19**, 335 (1979).
4. P. Q. Hung and J. J. Sakurai, *Nucl. Phys.* **B143**, 81 (1978).
5. T. Banks and E. Rabinovici, *Nucl. Phys.* **B160**, 349 (1979).
6. F. Fradkin and S. Shenker, *Phys. Rev.* **D19**, 3682 (1979).
7. G. t' Hooft, in *Recent Developments in Field Theory*, G. t' Hooft, *et al.* (Plenum Press, New York, 1980).
8. S. Dimopoulos, S. Raby and L. Susskind, *Nucl. Phys.* **B173**, 208 (1980).
9. M. Peskin, "Proceedings of the 1981 International Symposium on Lepton and Photon Interactions", (Bonn) W. Pfeil, ed., p. 880.
10. R. Kögerler and D. Schildknecht, CERN preprint TH.3241-CERN (1982).
11. B. Schrempp and F. Schrempp, DESY preprint, DESY 84/055, May 1984.
12. J. J. Sakurai, *Currents and Mesons*, (University of Chicago Press, Chicago, 1969).
13. We thank H. Georgi for this argument.
14. H. Fritzsch and G. Mandelbaum, *Phys. Lett.* **109B**, 224 (1982).
15. P. Chen and J. J. Sakurai, *Phys. Lett.* **110B**, 481 (1982).
16. The same effect was noted many years ago in $\pi \to \bar{\ell}\ell\bar{\ell}\ell$ decays by L. B. Okun', B. M. Pontecorvo and C. Rubbia, *Yad. Fiz.* **4**, 1202 (1966) [*Sov. J. Nucl. Phys.* **4**, 864 (1967)]; *Rev. Roum. Phys.* **11**, 819 (1966).
17. J. Wudka, MIT-preprint, MIT-CTP-1288, to appear in *Phys. Lett. B*.
18. C. Korpa and Z. Ryzak, MIT preprint, MIT-CPT-1313, December 1985.
19. Kaidalov and Nogteva, *Yad. Fiz.* **42**, 233 (1985).
20. K. Enqvist and J. Maalampi, *Phys. Lett.* **135B**, 329 (1984).
21. C. Korpa and J. Wudka, MIT preprint in preparation.
22. V. H. Hughes, *et al.*, AGS proposal 821, and private communication.
23. UA1 Collaboration, CERN preprint CERN-EP/85-185 (1985).
24. S. A. Devyanin and R. L. Jaffe, MIT preprint, MIT-CTP-1296, to appear in *Phys. Rev. D*.

STANDARD AND NON-STANDARD HIGGS BOSONS ~~IN~~ IN ELECTROWEAK RADIATIVE CORRECTIONS

by

Wolfgang Hollik*)

II. Institut für Theoretische Physik der Universität Hamburg

Hamburg, FRG

Abstract:

The influence of the standard Higgs and of the additional charged and neutral Higgs bosons in a 2-doublet model with enhanced Yukawa couplings on the 1-loop radiative corrections to leptonic processes is discussed. The magnitude of the Higgs effects is compared with the theoretical uncertainty and the accuracy of present experiments and of precision measurements at LEP and SLC.

1. Introduction

In spite of the great success of the electroweak standard model the hunt for the Higgs as the signal for spontaneous symmetry breaking is still a challenge to future collider experiments. In an electroweak gauge theory gauge bosons and fermions get their masses via the Higgs mechanism; as a consequence the particle spectrum is enlarged by at least one scalar boson.

The standard model has the minimal number of Higgs fields in SU(2) x U(1): a single scalar doublet with one physical neutral boson. This minimal version predicts the ratio

$$\rho = \frac{M_W^2}{M_Z^2 \cos^2\theta_W} = 1.$$

The converse, however, is not true: $\rho = 1$ remains valid for any number of Higgs doublets automatically.

The investigation of models with more than one Higgs doublet [1] was motivated by the discussion of CP violation [2], the Peccei-Quinn solution of the strong CP problem [3], SUSY extensions of the standard model [4] which need at least two scalar doublets, and finally the richer phenomenological implications and their experimental signatures at future colliders.

Whereas the direct production of Higgs bosons in the near future is limited to relatively light bosons ($\lesssim 50$ GeV), indirect effects may manifest in the radiative corrections to the standard fermionic processes: μ-decay, ν-scattering, and e^+e^- annihilation. In this talk we put together the Higgs effects in the standard model 1-loop corrections and discuss in a similar way the minimal extension which has two scalar doublets within SU(2) x U(1).

In order to avoid additional hadronic uncertainties we restrict the discussion to purely leptonic processes.

2. The minimal model

The scalar doublet

$$\Phi = \begin{pmatrix} \phi^+ \\ \frac{v + H_0 + i\chi}{\sqrt{2}} \end{pmatrix}$$

contains the physical Higgs field Ho (mass M_{Ho}) and the vacuum expectation value $v \neq 0$. v determines the $W^\pm$, Z masses

$$M_W = \frac{1}{2} g_2 v , \qquad M_Z = \frac{1}{2}\sqrt{g_1^2 + g_2^2}\, v$$

as well as the masses of the charged fermions:

$$m_f = g_f v \qquad (g_f: \text{Yukawa coupling})$$

Since for the known fermions $m_f \ll M_W$, the Yukawa coupling

$$g_f = \frac{1}{2} g_2 \frac{m_f}{M_W} \qquad (2.1)$$

is a very small quantity. This restriction is typical for the minimal model and is lowered in more-doublet models.

Virtual Higgs contributions in 1-loop diagrams appear in the W and Z self energy, e. g.

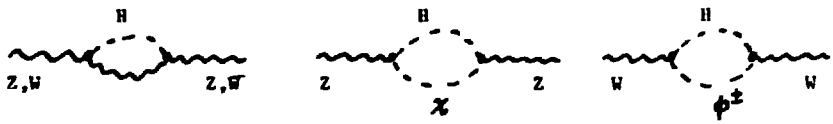

in the fermionic vertices, typically:

and in box diagrams, e. g.

Due to the small Yukawa couplings (2.1) vertex and box diagrams for fermions involving virtual Higgs lines are suppressed at least by a factor $(m_f/M_W)^2$ and can therefore be neglected unless very heavy fermions are involved. Consequently, in the minimal model a virtual Higgs contributes only via the W, Z propagators to the 1-loop corrections for fermionic processes.

Loop calculations require the choice of a renormalization scheme. We perform our discussion in the on-shell scheme with the particle masses M_W, M_Z, M_{Ho}, m_f and the electromagnetic fine structure constant α in the Thomson limit as renormalized parameters. The corresponding renormalization conditions are the on-shell subtractions of the self energies for the physical fields and the definition of α in the Thomson limit. For details see ref. [6].

Since field renormalization is performed, all the self energies and vertex corrections are finite after renormalization.

The mixing angle as an auxiliary quantity is defined in terms of the gauge boson masses:

$$\sin^2\theta_W = 1 - M_W^2 / M_Z^2 \qquad (2.2)$$

3. The 2-doublet model

The minimal extension of the standard model is the SU(2) x U(1) model with two scalar doublets

$$\Phi_1 = \begin{pmatrix} \phi_1^+ \\ \dfrac{v_1 + \eta_1 + i\chi_1}{\sqrt{2}} \end{pmatrix}, \qquad \Phi_2 = \begin{pmatrix} \phi_2^+ \\ \dfrac{v_2 + \eta_2 + i\chi_2}{\sqrt{2}} \end{pmatrix} .$$

3 of their eight degrees of freedom form the longitudinal polarization states of W^+, W^-, Z and 5 remain as physical particles. These split up into a pair of charged Higgs bosons $\phi^\pm$, 2 neutral scalars H_0, H_1, and a neutral pseudoscalar H_2. They are the mass eigenstates of the Higgs potential, which is chosen to be CP-symmetric [1]

$$V(\Phi_1, \Phi_2) = -\mu_1^2 |\Phi_1|^2 - \mu_2^2 |\Phi_2|^2 + \lambda_1 |\Phi_1|^4 + \lambda_2 |\Phi_2|^4$$
$$+ \lambda_3 |\Phi_1|^2 |\Phi_2|^2 + \lambda_4 (\Phi_1^+ \Phi_2)(\Phi_2^+ \Phi_1)$$
$$+ \frac{\lambda_5}{2}\left[(\Phi_1^+ \Phi_2)^2 + (\Phi_2^+ \Phi_1)^2\right] \qquad (3.1)$$

The vacuum expectation values v_1, v_2 determine the gauge boson masses:

$$M_W = \frac{1}{2} g_2 \sqrt{v_1^2 + v_2^2}\,, \qquad M_Z = M_W / \cos\theta_W\,. \quad ^{1)} \qquad (3.2)$$

If one assumes that only Φ_2 has Yukawa couplings to fermions (restricting our selves to leptons), the fermion masses arise as

$$m_f = g_f v_2 \qquad (3.3)$$

which implies for the Yukawa couplings:

$$g_f = \frac{1}{2} g_2 \frac{m_f}{M_W} \frac{\sqrt{v_1^2 + v_2^2}}{v_2}\,. \qquad (3.4)$$

In the limit of very different vacuum expectation values $v_1 \gg v_2$ (according to the different mass scales of gauge bosons and fermions) the Yukawa couplings (3.4) become essentially larger than in the minimal modal (2.), enhanced by the factor

$$\beta = \frac{\sqrt{v_1^2 + v_2^2}}{v_2} \simeq \frac{v_1}{v_2}\,. \qquad (3.5)$$

Besides the masses β is a further input parameter of the model. In addition, the scalars H_0, H_1 can mix by a further mixing angle ζ, which

---

1) Note that $\cos\theta_W = M_W/M_Z$ is also valid in more-doublet models

in the case $v_1 \gg v_2$ is of the order

$$\tan \zeta = v_1 / v_2$$

if the quartic couplings in (3.1) are all of the same order of magnitude.

In such a 2-Higgs model with enhanced Yukawa couplings the physical structure becomes very transparent:
One of the neutral scalars, Ho, behaves like the standard Higgs in the minimal model; in addition, there is a pair of a neutral scalar and pseudoscalar H_1, H_2, and a pair of charged Higgs bosons $\phi^{\pm}$, each of which has enhanced couplings to fermions. H_1 and H_2 can be lighter than the standard Higgs, whereas the mass of the charged Higgs is restricted from e^+e^- experiments [7] to $M_\phi \gtrsim 18$ GeV. Limits on v_1/v_2 from leptonic reactions are not very severe: g - 2 for the muon restricts $v_2/v_1 > 0.015$ [8] for a non-degenerate H_1, H_2 pair (H_1 = 6 GeV); a degenerate H_1, H_2 pair gives essentially weaker bounds [8]. More stringent limits can be deduced from heavy quark systems [9] but this depends on additional assumptions about the Higgs-quark sector.

The strategy of calculating radiative corrections to processes where at least one fermion pair is light (e^+e^-, νe) is as follows:

a) Calculate the additional contributions of H_1, H_2, $\phi^{\pm}$ to the boson self - and mixing energies, boson - fermion vertices, and fermion self energies.

b) Perform the on-shell renormalization as in 2., but now extended by the on-shell conditions for the additional physical Higgs fields. The renormalized input parameters are then α, M_W, M_Z, M_{Ho}, M_1, M_2, M_ϕ; Ho can be identified with the standard Higgs (M_1, M_2, M_ϕ denote the masses of H_1, H_2, $\phi^{\pm}$).

For the details see ref. [10] .

4. Radiative Corrections

4.1 The M_Z - M_W and M_Z - $\sin^2\theta_W$ interdependence

Application of the radiative corrections to the μ lifetime and identification with the Fermi model result lead to the formula

$$M_Z^2 = \frac{\pi\alpha}{\sqrt{2}\,G_F}\cdot\frac{1}{\sin^2\theta_W\cos^2\theta_W(1-\Delta\tilde{r})} \qquad (4.1)$$

with $$\Delta\tilde{r} = \Delta r(\alpha, \sin^2\theta_W, M_Z, M_{H_0}) + \Delta r_1 \,. \qquad (4.2)$$

Δr is the standard model correction [11]

$$\Delta r = \frac{\Sigma_W(0)}{M_W^2} + \frac{\alpha}{4\pi\sin^2\theta_W}\left[6 + \frac{7-4\sin^2\theta_W}{2\sin^2\theta_W}\log(\cos^2\theta_W)\right] \qquad (4.3)$$

with the renormalized W self energy $\Sigma_W(k^2)$, which contains the dependence on the Higgs mass M_{H_0}.

The extension to the 2-doublet case adds the additional term Δr_1, essentially given by

$$\Delta r_1 \approx \frac{\Delta\Sigma_W(0)}{M_W^2} \equiv \Delta r_1(\alpha, \sin^2\theta_W, M_Z; M_{A_1}, M_{H_2}, M_\phi) \qquad (4.4)$$

with the contributions of the extra bosons to the (renormalized) W self energy, $\Delta\Sigma_W(k^2)$.

Eq. (4.1) allows to derive a $\sin^2\theta_W$ value if M_Z is given; together with $M_W = M_Z\cos\theta_W$ this yields also the M_Z - M_W interdependence. These relations depend on the Higgs mass(es).

First we figure out the dependence on M_{H_0} in the minimal model (see also ref's [12 - 14]): Fixing $M_Z = 93.2$ GeV and varying M_{H_0} the following changes in $\sin^2\theta_W$ resp. M_W appear:

M_{Ho}	$\Delta \sin^2\theta_W$	ΔM_W
10 - 500 GeV	0.0035	-19 MeV
10 - 1000 GeV	0.0048	-25 MeV

The present experimental uncertainty of $\sin^2\theta_W$ is $\Delta\sin^2\theta_W \gtrsim \pm 0.005$, and that of M_W: $\Delta M_W = \pm 1.7$ GeV [15]. These do not allow to look where the Ho is settled between the conservative limits 10 GeV and 1 TeV.

The situation becomes somewhat better if (with LEP II) the ratio $\sin^2\theta_W = 1-M_W^2/M_Z^2$ can be measured with the precision ± 0.0015. The inherent hadronic uncertainty in the relation (4.1) from the light quarks leads to a theoretical uncertainty of $\Delta \sin^2\theta_W = 0.0002$ if the update analysis of Jegerlehner [14] is used. A further uncertainty of similar magnitude is due to the renormalization scheme dependence [16].

In the 2-doublet model, the effects of the extra Higgs bosons are listed in table 1. Significant deviations from the standard result are obtained if either $\phi^\pm$ or H_1, H_2 are heavy, and exceed the variation with Ho discussed above. All the other cases lead only to small modifications (see also ref. [17]). The value for M_W in case of $M_\phi \simeq 5\, M_Z$ is about the $1-\sigma$ limit of the measured M_W [15].

M_1	M_2	M_ϕ	$\sin^2\theta_W$	M_W (GeV)
M_Z	M_Z	M_Z	0.2208	82.27
10	10	M_Z	0.2194	82.35
0.1	0.1	M_Z	0.2194	82.35
M_Z	M_Z	$5\,M_Z$	0.1995	83.39
10	10	$5\,M_Z$	0.1916	83.80
1	1	$5\,M_Z$	0.1915	83.80
0.1	0.1	$5\,M_Z$	0.1915	83.80
$5\,M_Z$	$5\,M_Z$	M_Z	0.2005	83.33
$5\,M_Z$	M_Z	M_Z	0.2212	82.25
$5\,M_Z$	M_Z	$5\,M_Z$	0.2207	82.28
Standard			0.2208	82.27

Table 1.
$\sin^2\theta_W$ and M_W for $M_Z = 93.2$ GeV. (pure numbers mean masses in GeV)

4.2 Neutrino electron scattering

A sensitive quantity to measure $\sin^2\theta_W$ in a leptonic ν scattering process is the ratio

$$R = \frac{\sigma(\nu_\mu e)}{\sigma(\bar{\nu}_\mu e)} \quad , \tag{4.5}$$

in lowest order given by

$$R^0 = \frac{1+\xi+\xi^2}{1-\xi+\xi^2}, \qquad \xi = 1 - 4\sin^2\theta_W . \tag{4.6}$$

In 1-loop order this becomes

$$R^0 \longrightarrow R(\sin^2\theta_W, \alpha, M_Z, M_{H_0}\ [M_{A_1}, M_{A_2}, M_\phi]) . \tag{4.7}$$

R is therefore dependent on the Higgs mass(es).

First we compare the variation of $\sin^2\theta_W$ with M_{H_0} for a given $R^{exp} = 1.26$ [18] in the minimal model with the other sources of uncertainties in (4.7):

$M_{H_0} = 10 - 1000$ GeV	0.0024
$m_t = 30 - 60$ GeV	0.0008
$\Delta M_Z = \pm 5$ GeV	±0.0003
hadronic uncertainty	±0.0003
exp. uncertainty (expected)	±0.005

Although the Higgs gives the theoretically largest effect, it is completely within the experimental noise even for the highest expected precision in the CHARM experiment.

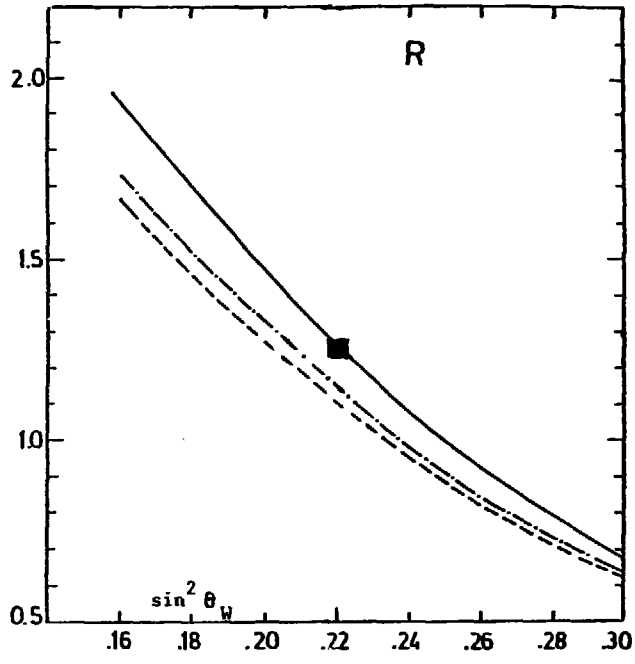

Fig. 1. R from eq. (4.7) in lowest order (——) and for different extra Higgs masses with radiative corrections.

——·——· $M_1 = M_2 = M_Z$, $M_\phi = 5\, M_Z$

— — — — $M_1 = M_2 = 10$ GeV, $M_\phi = 5\, M_Z$ $M_Z = 93.2$ GeV.

In the 2-doublet model, the effects of the extra Higgs bosons are depicted in Fig. 1 for the case of large mass splitting between ϕ^+ and H_1, H_2 (other situations give only small deviations from the standard model). The shaded areas indicate the expected accuracy of a measured R (CHARM experiment) and of $\sin^2\theta_W = 1-M_W^2/M_Z^2$ (from LEP) if the present mean values would persist. One can see that forthcoming experiments will become decisive.

4.3 $e^+e^- \longrightarrow l^+l^-$ ($l = \mu, \tau$)

With a longitudinal e-beam polarization P_L the differential cross section has the form

$$\frac{d\sigma}{d\Omega} \quad \frac{\alpha^2}{4s} \left\{ \sigma_U(\theta) + P_L \, \sigma_L(\theta) \right\}, \quad \theta = \sphericalangle(e^-, \mu^-) \; . \tag{4.8}$$

The observables of interest are:

(i) the integrated cross section:

$$\sigma = \int \frac{d\sigma}{d\Omega} \, d\Omega \tag{4.9}$$

(ii) the forward - backward asymmetry A_{FB}:

$$A_{FB} = \frac{1}{\sigma} \left\{ \int_{\cos\theta > 0} d\sigma \; - \int_{\cos\theta < 0} d\sigma \right\} \tag{4.10}$$

(iii) the polarization asymmetry A_L:

$$A_L = \frac{\sigma(P_L) - \sigma(-P_L)}{\sigma(P_L) + \sigma(-P_L)} \cdot \frac{1}{P_L} \tag{4.11}$$

The electromagnetic and weak corrections in the minimal model have already been discussed in ref's [11, 12, 19 - 25]. In our context here we only concentrate on the Higgs dependence via the weak corrections.

a) Standard model:

Weak corrections (and therefore Higgs effects) at PETRA energies are completely negligible for σ; in A_{FB} the M_{Ho} dependence is also too small to be of practical interest ($\Delta A_{FB} \approx -0.001$ for M_{Ho} from 10 GeV to 1 TeV).

A quantity of particular interest is the on-resonance polarization asymmetry A_L (for $s = M_Z^2$):

Calculating in 1-loop order

$$A_L = A_L^{\circ}(\sin^2\theta_W, M_Z) + \delta A_L(\sin^2\theta_W, M_Z, M_{H_o}) \quad (4.12)$$

and substituting $\sin^2\theta_W$ (α, G_F, M_Z, M_{Ho}) from (4.1) shows the sensitivity of A_L to the Higgs mass for a given M_Z (here: M_Z = 93.2 GeV)

M_H = 10 - 500 GeV: $\Delta A_L = -0.015$
M_H = 10 - 1000 GeV: $\Delta A_L = -0.018$

Comparing this result with the expected experimental accuracy of $(\Delta A_L)_{exp} = \pm 0.005$ at the SLC one gets a chance to decide at least whether the Higgs is very light or very heavy.

For the unpolarized on-resonance A_{FB} the change ΔA_{FB} with M_{Ho} is about 1/3 of the values for ΔA_L given above.

b) 2-doublet model:

The forward - backward asymmetry for PETRA energy is displayed in Fig. 2 for the case of a heavy ϕ^+ (heavy H_1, H_2 similar).

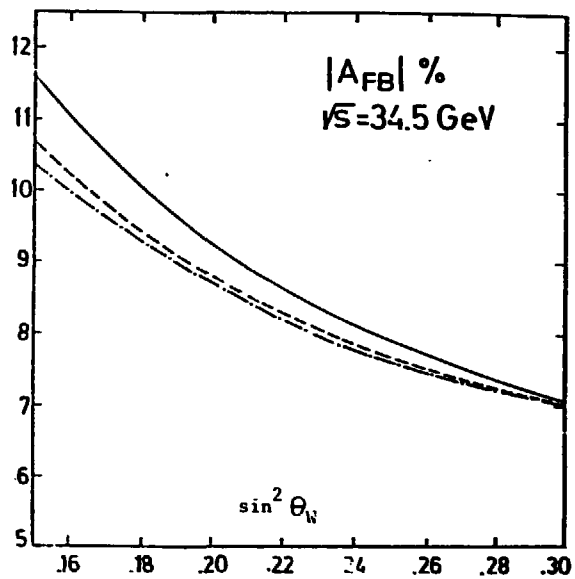

Fig. 2.

A_{FB} as function of $\sin\theta_W$.

– – – $M_1=M_2=M_Z$, $M_\phi=5M_Z$

—·— $M_1=M_2=10$GeV, $M_\phi=5M_Z$

——— lowest order

M_Z = 93.2 GeV.

As in the case of R in 4.2 the extraction of $\sin^2\theta_W$ from a measured A_{FB}^{exp} would yield smaller values than in the minimal model. This is largely independent of the enhancement factor β and does not lead to a difference between μ and τ final states.

If, however, $\sin^2\theta_W$ is eliminated by (4.1) in favor of α, G_F together with the scalar masses the predicted value for A_{FB} deviates only by +0.003 (for the lower curve in Fig. 2) from the standard model and is below the experimental sensitivity. The reason is that the W self energy in (4.1) and the Z self energy in $e^+e^- \longrightarrow l^+l^-$ largely cancel each other also in their scalar components.

As a last example we consider A_L at $s = M_Z^2$. We show the $\sin^2\theta_W$ dependence of $A_L = A_L^0(\sin^2\theta_W, M_Z) + \delta A_L(\sin^2\theta_W, M_Z, M_{H_0}, M_1, M_2, M_\phi)$ in Fig. 3 for various masses of the extra Higgs bosons. The sensitive dependence on the mass splittings between charged and neutral bosons is obvious.

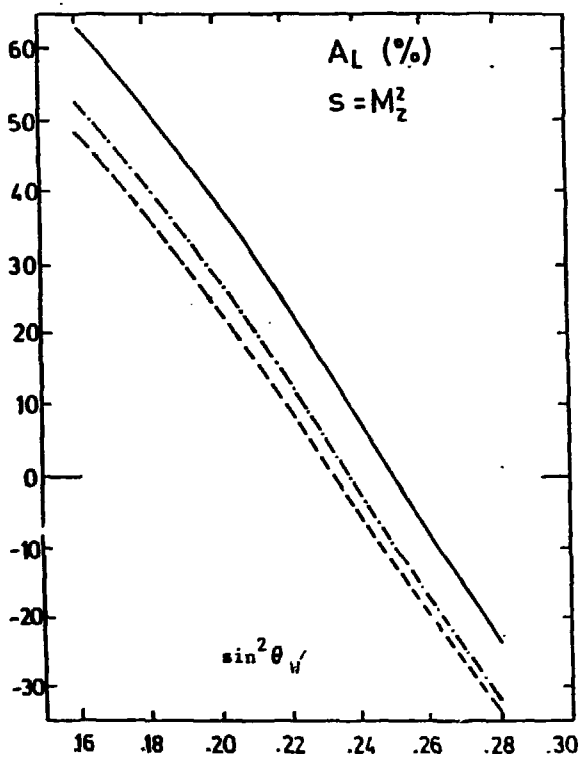

Fig. 3.

On-resonance polarization asymmetry A_L, dependence on $\sin\theta_W$.

——— lowest order

—·—·— $M_1 = M_2 = M_Z$, $M = 5\,M_Z$

– – – – $M_1 = M_2 = 10$ GeV, $M = 5\,M_Z$.

$M_Z = 93.2$ GeV.

Eliminating $\sin^2\theta_W$ by (4.1) in each of the models leads to differences in A_L which are measurable at the SLC; e. g. A_L is by 0.07 larger than the standard A_L if $M_\phi = 5\ M_Z$, $M_1 = M_2 = 10$ GeV. Again the situation is practically the same for μ and τ pair production, largely independent of v_1/v_2. Precision measurements of A_L could therefore tightly restrict the possible mass range in 2-doublet models.

In contrast to the asymmetries, the integrated cross section shows a dependence on v_1/v_2 (and on the masses of H_1, H_2, but it is insensitive to a heavy ϕ^+): At PETRA/PEP energies there is a difference between $\sigma(e^+e^- \to \mu^+\mu^-)$ and $\sigma(e^+e^- \to \tau^+\tau^-)$ by a few percent, mainly due the γ-vertex correction:

From the experimental error [26] on $\sigma(e^+e^- \to \tau^+\tau^-)/\sigma_0$, $\sigma_0 = 4\pi\alpha^2/3s$, of ~5 % one can derive the limits

$$v_1/v_2 \leq 200 \quad \text{for } M_1 = M_2 = 10 \text{ GeV}$$
$$v_1/v_2 \lesssim 140 \quad \text{for } M_1 = M_2 = 5 \text{ GeV}$$

This is a tighter restriction than from $(g-2)_\mu$ in the degenerate H_1, H_2 case.

5. Conclusions:

The effects of the standard Higgs in 1-loop corrections to fermionic processes are rather small ("screening" [5]). They are too small to be observable in present experiments. In precision experiments at LEP/SLC the Higgs effects will match the experimental accuracy.

In the 2-doublet model measurable effects appear if either the charged Higgs mass or the extra neutral boson masses are heavy. Effects of a light neutral scalar/pseudoscalar could be observed in terms of differences between $(e^+e^- \longrightarrow \mu^+\mu^-)$ and $(e^+e^- \longrightarrow \tau^+\tau^-)$.
The experimental uncertainty in the τ cross section can be used to put limits on v_1/v_2 and the neutral masses.

Acknowledgement:

I want to thank Z. Ajduk and all the organizers for the pleasant stay during the Symposium.

References:

1 For a review see: R. A. Flores, M. Sher, Ann. Phys. (N.Y.) 148 (1983) 95

2 A. J. Buras, Proceedings of the EPS meeting, Bari 1985, MPI-PAE/PTh 64/85 and references therein

3 R. D. Peccei, H. R. Quinn, Phys. Rev. Lett. 38 (1977) 1440; Phys. Rev. D 16 (1977) 1791

4 H. E. Haber, G. L. Kane, Phys. Rep. 117 (1985) 75

5 M. Veltman, Acta Phys. Pol. B8 (1977) 475

6 M. Böhm, W. Hollik, H. Spiesberger, DESY 84-027 (to appear in Fortschr. Phys.)

7 S. Komamiya, Int. Symp. on Lepton and Photon Interactions, Kyoto 1985

8 H. E. Haber, G. L. Kane, T. Sterling, Nucl. Phys. B 161 (1979) 493

9 G. G. Athanasiu, P. J. Franzini, P. J. Gilman SLAC/PUB 3648 (1985)

10 W. Hollik, DESY 86-047 (to appear in Z. Phys. C)

11 M. Böhm, W. Hollik, H. Spiesberger, Z. Phys. C27 (1985) 523

12 B. W. Lynn, R. G. Stuart, Nucl. Phys. B 253 (1985) 216

13 A. A. Akhundov, D. Yu. Bardin, T. Riemann, Phys. Lett. 166B (1986) 111

14 F. Jegerlehner, Bielefeld Preprint BI - TP 1985/28

15 E. Radermacher, Progress in Particle and Nuclear Physics 14 (1985) 231;
J. M. Gaillard, CERN - EP/86-07

16 F. Jegerlehner, Bielefeld Preprint BI - TP 1986/8;
W. Hollik, H.-J. Timme, DESY 85-099

17 S. Bertolini, New York University Preprint, NYU/TR 10/85

18 J. Panman, CERN - EP/85-35

19 M. Greco, G. Pancheri, Y. Srivastava, Nucl. Phys. B171 (1982) 118; E: B197 (1982) 543

20 F. A. Berends, R. Kleiss, S. Jadach, Nucl. Phys. B202 (1982) 63

21 M. Böhm, W. Hollik, Nucl. Phys. B204 (1982) 45;
Z.Phys. C23 (1984) 31

22 W. Wetzel, Nucl. Phys. B227 (1983) 1

23 M. Böhm, W. Hollik, Phys. Lett. 139B (1984) 213

24 R. W. Brown, R. Decker, E. A. Paschos, Phys. Rev. Lett. 52 (1984) 1192

25 W. Hollik, Phys. Lett. 152B (1985) 121

26 E. Fernandez et al, Phys. Rev. Lett. 54 (1985) 1620;
M. E. Levi et al, Phys. Rev. lett. 51 (1983) 1941

Monte Carlo Study of the standard SU(2) Higgs model on the Lattice

W. Langguth*
Institut für theoretische Kernphysik
Universität Karlsruhe
Postfach 6980
D7500 Karlsruhe
FRG

Abstract

The status of the standard SU(2) Higgs model on the lattice is summarized, and a report on recent Monte Carlo calculations at strong ($\beta = 2.3$) and weak ($\beta = 8$) gauge coupling for various values of the scalar selfcoupling λ is given. New results for the masses at $\beta = 8$ show a weak λ dependence for $\infty \geq \lambda \geq 1$ and lead to an upper bound of the Higgs/W-boson mass ratio of 7.5 ± 0.8.

* partially supported by Deutsche Forschungsgemeinschaft.

1. Introduction

Higgs models are of interest in various areas of physics, such as in cosmology, superconductivity and in elementary particle physics as part of the $SU(2) \otimes U(1)$ electroweak theory of Glashow, Salam and Weinberg. This interest is founded in the Higgs mechanism which allows to give the gauge bosons a mass without destroying gauge invariance and renormalizability of the theory. However, this mechanism is understood only perturbatively. For the potential $V(\phi)$ of the Higgs field ϕ,

$$V(\phi) = \mu^2\phi^2 + \lambda_c\phi^4 \equiv \lambda_c(\phi^2 - v^2)^2 - \frac{\mu^4}{4\lambda_c}$$

in the Higgs phase ($v^2 = \frac{-\mu^2}{2\lambda_c} \geq 0$) the well known tree-level results for the masses of the gauge invariantly coupled vector boson and of the scalar Higgs boson are $M_W = gv$ and $M_H = \sqrt{2}\mu$, respectively (g = gauge coupling); outside the Higgs phase ($v^2 = 0$), the vector boson stays massless and the mass of the Higgs boson is μ. During the last years this model has been studied intensively within the lattice formulation of gauge theories by means of numerical and analytical methods [1]. The tree-level picture has been found to be somewhat too naive since nonperturbative contributions change it not only quantitatively but also qualitatively. Rather than in two phases the model exists only in one phase with the Higgs and the confinement phase as its two extremes. Nonperturbative effects also lead to only a weak dependence of physical quantities like the Higgs/W-boson mass ratio from the bare self-coupling, λ, which is a fact of some phenomenological importance.
In the following, after introducing the lattice model and its global properties, I shall report on Monte Carlo calculations of masses and couplings in the strong and in the weak (physical) coupling regime.

2. Definition and properties of the model

2.1 Definition of the model

The euclidean action in the continuum is given by

$$S_c = \int d^4x \Big\{ \quad \frac{1}{2}TrF_{\mu\nu}(x)F_{\mu\nu}(x) + (D_\mu\phi(x))^\dagger(D_\mu\phi(x)) + \lambda_c(\phi^\dagger(x)\phi(x) - v^2)^2 \quad \Big\} \qquad (1)$$

where $F_{\mu\nu}(x)$ denotes the field strength of the $SU(2)$ gauge fields, $D_\mu = \partial_\mu + igA^a_\mu\tau^a/2$ the covariant derivative and ϕ a scalar Higgs doublet.
Its transcription to the lattice reads

$$S = \beta\sum_p\Big\{1 - \frac{1}{2}U(p)\Big\} + \sum_x\Big\{ \quad \lambda(\phi^\dagger_x\phi_x - 1)^2 + \phi^\dagger_x\phi_x - 2\kappa\sum_{\mu>0}\phi^\dagger_{x+\mu}U(x,\mu)\phi_x \quad \Big\} \qquad (2)$$

Here we have introduced a four-dimensional hypercubic lattice of lattice spacing a. $\sum_x$ denotes the sum over all lattice sites x, $\sum_\mu$ the sum over all positve directions $\mu = 1,..,4$, $\sum_p$ the sum over all positively oriented plaquettes. The gauge fields are defined on links $l = (x,\mu)$ and denoted by $U(x,\mu) \in SU(2)$. $U(p)$ is the oriented product of link variables $U(l)$ around the elementary plaquette p. The Higgs fields ϕ_x may be written in the form

$\phi_x = \rho_x \alpha_x, \rho_x > 0, \alpha_x \in SU(2)$. In this case the action becomes

$$S = \beta \sum_p \left\{ 1 - \frac{1}{2} U(p) \right\} + \sum_x \left\{ \lambda(\rho_x^2 - 1)^2 - 3 \log \rho_x + \rho_x^2 - \kappa \sum_{\mu > 0} \rho_{x+\mu} \rho_x Tr(\alpha_{x+\mu}^{\dagger} U(x, \mu) \alpha_x) \right\} \tag{3}$$

where we have changed the integration measure $d^4\phi_x d^3U(x,\mu)$ to $d\rho_x d^3\alpha_x d^3U(x,\mu)$, where d^3g denotes the Haar-measure in $SU(2)$.
The lattice action depends on three parameters : the gauge coupling $\beta = 4/g^2$, the bare ϕ-selfcoupling λ, and the hopping parameter κ, which are related to the continuum parameters by

$$\lambda_c = \frac{\lambda}{\kappa^2} \qquad \text{and} \qquad (a\mu)^2 = \frac{(1 - 2\lambda - 8\kappa)}{\kappa}. \tag{4}$$

The lattice formulation eqns(2,3) of the standard Higgsmodel allows the nonperturbative calculation of physical quantities like masses and couplings by analytical and numerical methods. For the existence and properties of its continuum limit, the phase structure which we shall describe next is of great importance.

2.2 The phase structure

The phase structure is displayed in fig.1. The critical surface $\kappa_{crit}(\beta, \lambda)$ separates the Higgs-phase ($\kappa > \kappa_c$) from the confinement phase ($\kappa < \kappa_c$) in the three dimensional parameter space spanned by β, λ and κ. This separation, however, is not complete since both phases are continuously connected at small β and large λ and thus are only two different pictures of one single phase. Since the continuum limit can only be performed at second order phase transition points, or lines, most of the early numerical work was devoted to the determination of location and the order of the critical surface [2]. But still it is known for only a few points and very special limits. For small λ and small β it is of first order and weakens for increasing β and/or λ. At $\beta = \infty$ the model becomes the linear σ-model which has a second order transition line $\kappa_\infty(\lambda)$. For some finite values of $\beta = 2.3$ and $\lambda = 1.0, \infty$, high statistic measurements have shown the transition to be of first order [3]. So far there exists no evidence for a tricritical line for finite λ and β, like the one indicated in fig.1. Recent analytical [4] and Monte Carlo [5] renormalization group calculations have shown that at the Gaussian fixed point ($\beta = \infty, \lambda = 0$) the continuum limit of the model is a free field theory of massive gauge bosons and a massive scalar field.
The present situation concerning the continuum limit may be summarized by the following three possibilities:

i) There exists a tricritical line for finite λ and β; then a nontrivial continuum limit (c.l.) is likely to exist.
ii) There exists no tricritical line but a non-Gaussian fixed point at large λ and $\beta = \infty$; then a nontrivial c.l. may exist.
iii) There exists no nontrivial c.l.. In this case an effective theory with an arbitrary high cut-off can be defined.

In any of these cases the lattice regularization serves as a tool for nonperturbative calculation of all physical quantities. In the following I shall turn my attention to the calculation of masses and couplings in the strong and weak coupling regime [6,7].

3.Monte Carlo results at $\beta = 2.3$

We have calculated masses and couplings of the vector and scalar boson on a 12^4 and 8^4 lattice with periodic boundary conditions for $\lambda = 0.5, 1.0$ and also for $\lambda = 0.1$ for various values of κ in the vicinity of the phase transition. We used the unitary gauge and full $SU(2)$ gauge group variables. The updating was done with the Metropolis algorithm with 6 links per variable at an acception rate of 1/3 per hit. The error estimation was done by 2^k - binning (k=1,2,3,..).

3.1 Masses

The masses were determined from the exponential decay of the two-point correlation functions, which on a periodic L^4 lattice behaves for large separations like

$$< h_0 h_d > \quad \xrightarrow{d \to \infty} \quad 2A_0 \cosh\left(am_h\,(d - L/2)\right)$$

with various operators $h_x^{(j)}, j = 1,2,3$ and $w_x^{(k)}, k = 1,2$ carrying the quantum numbers of the Higgs-boson and W-boson channel respectively. The masses can be estimated from

$$am_h(d) = \frac{1}{d_{max} - d} \log\left\{ \frac{C_d}{C_{d_{max}}} + \sqrt{\left(\frac{C_d}{C_{d_{max}}}\right)^2 - 1} \right\} \qquad (0 \le d \le d_{max}) \qquad (5)$$

where $C_d =< h_0 h_d >$ and $d_{max} \le L/2$. The results for the dimensionless masses am are shown in fig.2 as a function of the link expectation value $L =< 1/2TrV(x,\mu) >, V(x,\mu) = \alpha^{\dagger}_{x+\mu} U(x,\mu) \alpha_x$, for fixed λ and β. We observe the following important features:

i) $m_w < m_h$ within the Higgsphase, well above the phase transition, and $m_w > m_h$ at and below the phase transition
ii) the phase transition is driven by the Higgs boson (e.g. at $\beta = 2.3, \lambda = 1.0, \kappa = 0.3041$ on the 12^4 lattice: $am_h = .16(1), am_w = .53(4)$).
iii) outside the Higgsphase the W-mass does not, vanish in contrast to the starting point of the perturbative approach.
iv) both masses are at $\beta = 2.3$ for all measured values of κ *independent* of λ for all $\lambda \ge 0.1$ within the statistical errors. This again is a nonperturbative result which differs from the tree level expectations and which might be of some phenomenological consequences for the Higgs/W-boson mass ratio of the continuum or effective theory.

3.2 Couplings

We determined the zero-momentum n-Higgs and Higgs-WW couplings in the two points A: $(\lambda = 1.0, \kappa = 0.307)$ and B: $(\lambda = 0.1, \kappa = 0.196)$. The n-Higgs couplings have large errors due to cancellations and also show a strong dependence on the interpolating fields $h^{(j)}$. The HWW coupling has smaller errors, a negligible dependence on the choice of the fields $h^{(j)}$, but some dependence on the fields $w^{(k)}$.

$$\text{A:} \quad a^{-2}\Delta_{hww}^{k=1} = 1.66 \pm 0.28, \quad a^{-2}\Delta_{hww}^{k=2} = 2.56 \pm 0.24$$
$$\text{B:} \quad a^{-2}\Delta_{hww}^{k=1} = 1.60 \pm 0.21, \quad a^{-2}\Delta_{hww}^{k=2} = 3.34 \pm 0.27$$

Within the errors no strong λ-dependence can be observed.

4.Monte Carlo results at weak, physical gauge coupling

4.1 The choice of the bare parameters

The physical $SU(2)$ gauge coupling, defined by the strength α_w of the Yukawa potential at distance $1/M_W$ in the region $\beta = 2-3$ is too strong ($\alpha_w \approx 0.2$) compared to the physical situation ($\alpha_w \approx 0.04$) we are interested in. Adjusting the parameters β, λ and κ to the physical situation we have to fulfill the constraints $0.1 \leq am \leq 1.0$ for both, am_h and am_w. (The lower bound results from our finite lattice $L = 12$, $2/L \approx 0.1$, the upper bound keeps the correlation length larger than one lattice spacing.) These constraints make it impossible to reach $\alpha_w = 0.04$ at $\beta = 2.3$ since though with increasing κ, α_W decreases, am_w and am_h increase beyond 1.0 (λ seems to be irrelevant for $\lambda \geq O(1)$). Therefore β has to be increased. As a first good guess we took $\beta = 4/g^2 = 8$ which gives in first order $\alpha_w \doteq g^2/4\pi = 0.04$, and tuned κ to adjust the masses in the allowed range. On a 10^4 lattice we find for $\kappa = 0.28-0.30$ a mass ratio of $R_{hw} = m_h/m_w \approx 6$. For our high statistics measurements we selected two points on a 10^4 and a 12^4 lattice:

$$\text{C:}\quad \beta = 8, \lambda = 1.0, \kappa = 0.30 \quad \text{on } 10^4, \quad (5 \cdot 10^4 \text{ sweeps})$$

$$\text{D:}\quad \beta = 8, \lambda = 1.0, \kappa = 0.28 \quad \text{on } 12^4, \quad (2 \cdot 10^5 \text{ sweeps})$$

For the gauge coupling as a function of the distance R we obtained using a lattice Yukawa potential,

$$\text{C}: \quad \alpha_{SU(2)}(\text{R} = 2,3) = 0.0478(5), 0.051(4)$$

$$\text{D}: \quad \alpha_{SU(2)}(\text{R} = 2,3,4) = 0.0476(2), 0.0496(12), 0.051(7)$$

4.2 Masses and zero momentum couplings

The masses and couplings were determined as before. An example for the good quality of the fit of the W-mass in point D is shown in fig.3. All fits for zero momentum are strongly dominated by a single low mass state and are independent from the interpolating field $w^{(k)}$. From the lowest non-zero momentum correlations we obtain almost the same masses as from the zero momentum states which shows that Lorentz-invariance is restored at $\beta = 8$ at least for these type of operators. In detail we find

$$\text{C:}\quad am_{--} = 0.24(2), \qquad \text{D}: \quad am_w = 0.19(1).$$

Due to the presence of $2W$ contributions the determination of the Higgs mass is much more complicated. The result of a four parameter fit can be summarized in that there is a strongly coupled high mass state $am_h \approx 1.2-1.3$ and a weakly coupled (1%)low mass state $am_{2w} \approx 2am_w$ consistent with a $2W$ state. If we let vary the mass m_f of the lower state only below $2m_w$, we may summarize the results of the fit by

$$\text{C:}\quad am_h = 1.39(12), \qquad \text{D}: \quad am_h = 1.22(8).$$

This yields a mass ratio of $m_H/m_W = 6.4 \pm 0.8$ which is by a factor three smaller than the tree level ratio. As expected the couplings become smaller at larger β. The n-Higgs couplings in point C disappear completely in the noise. In point D some of them are measureable due to the better statistics, but still the errors are still quite large. For the HWW coupling we obtain for the different $w^{(k)}, k = 1,2$

$$\text{C:}\quad a^{-2}\Lambda_{hww}^{k=1} = 1.56 \pm 0.42, \quad a^{-2}\Lambda_{hww}^{k=2} = 2.29 \pm 0.41$$
$$\text{D:}\quad a^{-2}\Lambda_{hww}^{k=1} = 0.79 \pm 0.32, \quad a^{-2}\Lambda_{hww}^{k=2} = 1.54 \pm 0.35$$

A comparison between the lattice and tree level results for the dimensionless quantity $l_{hww} = m_h m_w \Lambda_{hww}$,

$$l_{hww} = 0.27(10), \qquad \text{(lattice)},$$
$$l_{hww} = 0.8 = g_{ren}, \qquad \text{(tree)},$$

shows again the large nonperturbative effects. For a Higgs boson mass of 500GeV this would reduce the partial HWW width, assuming pole dominance of the zero momentum HWW amplitude by one order of magnitude. Of course, one has to keep in mind that, besides the statistical errors, these numbers may have systematic errors, too, due to e.g. finite lattice size effects.

In order to test the λ dependence of the physical quantities, we measured masses and couplings in three additional points for $\lambda = 0.1$ and ∞ [7]:

$$\text{E:}\quad \beta = 8, \lambda = 0.1, \kappa = 0.177 \quad \text{on } 12^4, \quad (10^5 \text{ sweeps})$$
$$\text{F:}\quad \beta = 8, \lambda = 0.1, \kappa = 0.182 \quad \text{on } 12^4, \quad (10^5 \text{ sweeps})$$
$$\text{G:}\quad \beta = 8, \lambda = \infty, \kappa = 0.37 \quad \text{on } 12^4, \quad (10^5 \text{ sweeps})$$

The link expectation values in points D, E, G and, respectively, C, F are nearly equal. Our results for the masses show an extremely weak dependence on λ for $\lambda \geq 1$, but there is a significant deviation in am_h for $\lambda = 0.1$:

$$\text{E}: \quad am_w = 0.208(10), \qquad \text{F}: \quad am_w = 0.246(11), \qquad \text{G}: \quad am_w = 0.198(12)$$
$$\text{E}: \quad am_h = 0.96(5), \qquad \text{F}: \quad am_w = 1.17(6), \qquad \text{G}: \quad am_w = 1.49(6).$$

This yields the rather low Higgs/W-boson mass ratios

$$\text{E}: \quad R_{HW} = 4.6(5), \qquad \text{D}: \quad R_{HW} = 6.4(8), \qquad \text{G}: \quad R_{HW} = 7.5(8).$$

Since the λ-dependence is monotonous, the value of R_{HW} at $\lambda = \infty$ (point G) can be considered as an upper limit, in the sense of Dashen and Neuberger [8], for the Higgs-W mass ratio.

5.Conclusions

Let me conclude by summarizing some of the important points of the MC calculation:

i) The approximate λ independence of the W-boson and Higgs boson mass has been verified for strong gauge coupling at $\beta = 2.3$ within small statistical errors. At weak, physical gauge couplings ($\beta = 8$) new results have shown the λ dependence to be only weak and we obtain a rather low upper bound on the Higgs/W-mass ratio of $R_{HW} \leq 7.5(8)$.

ii) The measurement of the zero-momentum n-Higgs and HWW coupling is numerically difficult. At $\beta = 2.3$ only for the HWW coupling results with acceptable errors could be obtained. The dependence on λ again is weak for λ between 0.1 and 1.0.

Further high statistics MC calculations are required to improve on the determination of the zero-momentum couplings and to extend the existing measurements down to perturbative λ values. Also more analytic work is necessary for a better understanding of the model in the physical weak coupling range. For phenomenologically realistic calculations, the fermions still have to be included.

Acknowledgements

I would to thank the organizers, especially Dr. Z. Ajduk for their kind and warm hospitality.Financial support of the Deutsche Forschungsgemeinschaft is gratefully acknowledged.

6.References

[1] For a recent review see J.Jersák, *Lattice Higgs models*, talk given at the Wuppertal Workshop on Lattice Gauge Theory, November 1985, Aachen Preprint PITHA 85/25 (1985).

[2] see ref.[1], references therein, and J.Jersák, C. B. Lang, T. Neuhaus, G. Vones, *Properties of the phase transition of the lattice SU(2) Higgs model*, Aachen preprint PITHA 85/05 (1985).

[3] W. Langguth, I. Montvay, Phys. Lett. **165B** (1985) 135.

[4] A. and P. Hasenfratz, *The continuum limit of an SU(2) gauge theory with a scalar doublet*, Florida State University preprint FSU-SCRI-86-30, (1986).

[5] D. J. Callaway, R. Petronzio, *Can elementary scalar particles exist?*, CERN-TH 4270/85 preprint (1985); *Can elementary scalar particles exist? II. Scalar electrodynamics*, CERN-TH 4369/86 preprint (1986).

[6] W. Langguth, I. Montvay, P. Weisz, Nucl. Phys.**B277** (1986) 11, for earlier work see also I. Montvay, Nucl. Phys **B269** (1986) 170; DESY preprint 85-005 (1985).

[7] W. Langguth, I. Montvay, work in progress.

[8] R. Dashen, H. Neuberger, Phys. Rev. Lett. **50** (1983) 1897

Figure captions

Fig.1 The phase structure of the SU(2) Higgs model. Possible positions of critical areas are shaded.

Fig.2a The mass in lattice units of the W-boson channel as a function of the link expectation value $L = \frac{1}{2} < TrV(x,\mu) >$.

Fig.2b Same as Fig.2a for the Higgs boson channel.

Fig.3 The correlation $C_w^{(2)}$ in the W-channel at $\lambda = 1, beta = 8, \kappa = 0.28$ compared to a single cosh fit for distances $3 \leq d \leq 6$.

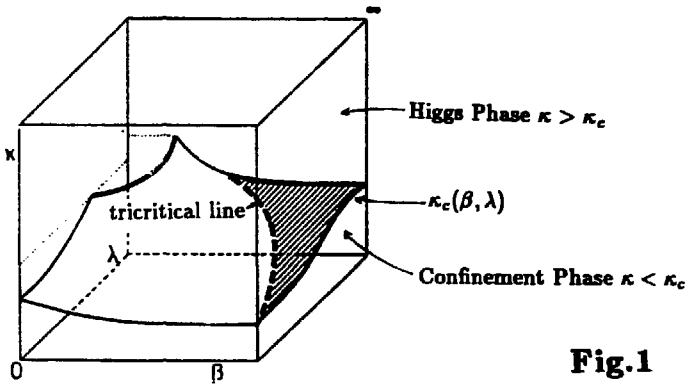
Higgs Phase $\kappa > \kappa_c$
$\kappa_c(\beta, \lambda)$
tricritical line
λ
Confinement Phase $\kappa < \kappa_c$
κ
0
β

Fig.1

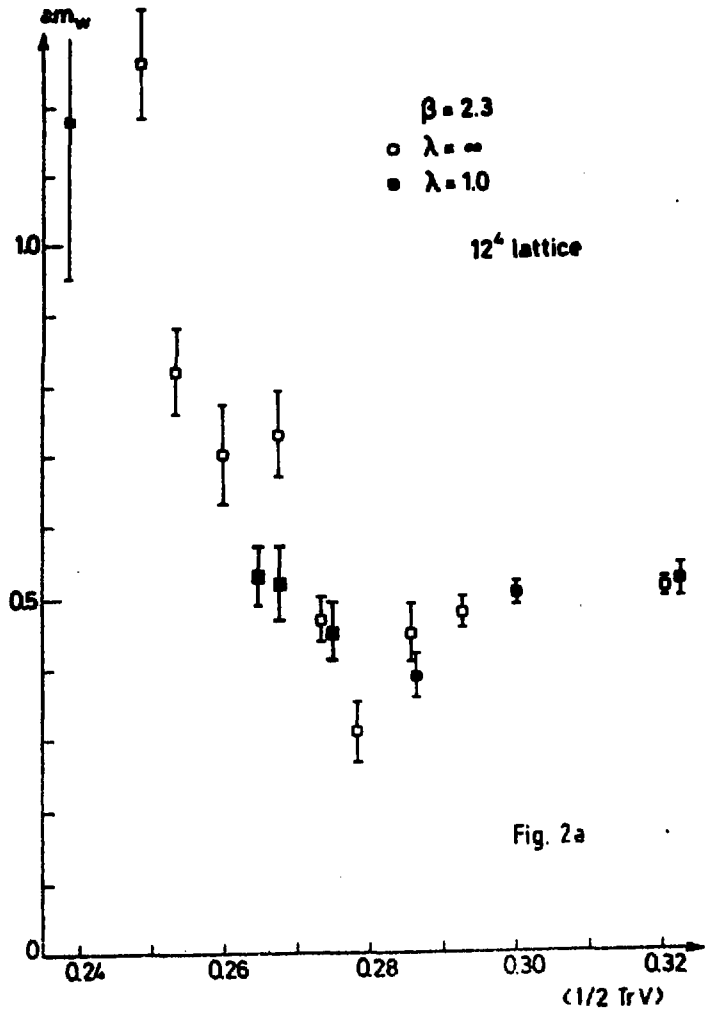
am_W
β = 2.3
λ = ∞
λ = 1.0
12^4 lattice
1.0
0.5
0
0.24
0.26
0.28
0.30
0.32
⟨1/2 Tr V⟩

Fig. 2a

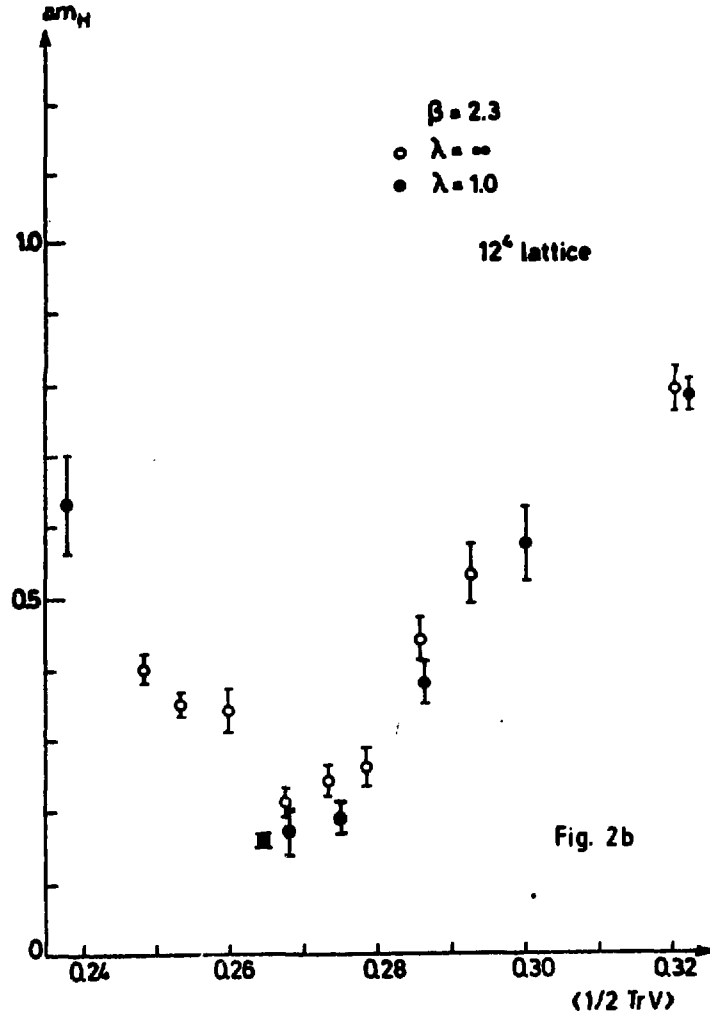
am_H
β = 2.3
λ = ∞
λ = 1.0
12^4 lattice
1.0
0.5
0
0.24
0.26
0.28
0.30
0.32
⟨1/2 Tr V⟩

Fig. 2b

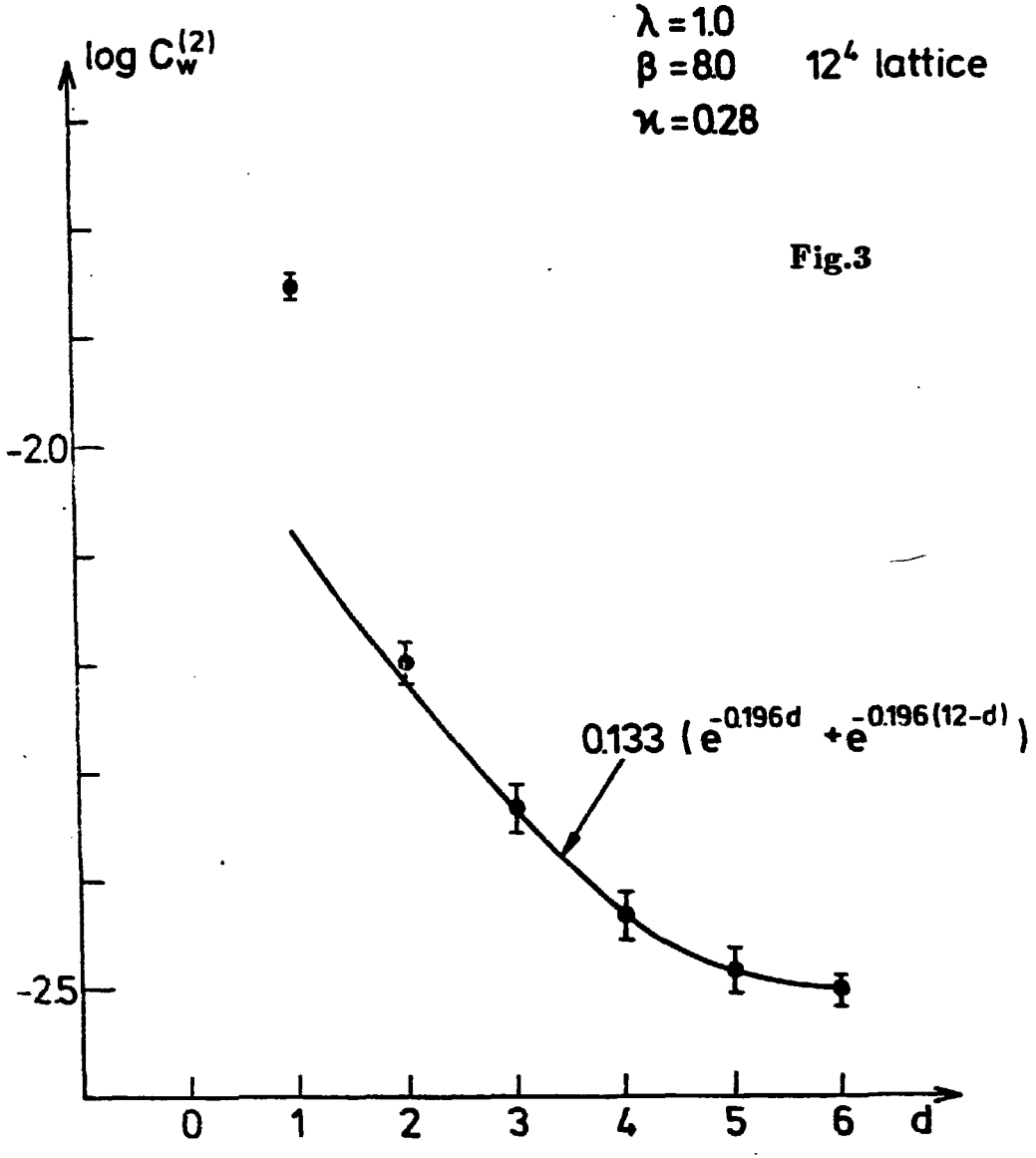
λ = 1.0
β = 8.0
κ = 0.28
12⁴ lattice
log C_w^(2)
-2.0
-2.5
0.133 (e^-0.196d + e^-0.196(12-d))
0
1
2
3
4
5
6
d

Fig.3

ON THE POSSIBLE ASTROPHYSICAL EVIDENCE FOR A RADIATIVELY DECAYING NEUTRINO

J. Maalampi
Research Institute for Theoretical Physics
University of Helsinki, Helsinki, Finland

K. Mursula
NORDITA, Copenhagen, Denmark

M. Roos
Department of High Energy Physics
University of Helsinki, Helsinki, Finland

ABSTRACT

We consider the possibility that the step-like structure observed in the cosmic background radiation at $\lambda = 1667 \pm 10$ Å would indicate radiative decays of massive cosmic neutrinos. In the standard electroweak theory the corresponding radiative lifetime is several orders of magnitude longer than observed, due to the purely left-handed structure of the charged weak currents. We point out that in models which include also right-handed currents, the lifetime can naturally be short enough to account for the astrophysical observations.

The cosmic ultraviolet background radiation may contain information on the decay of a big bang relic massive neutrino[1-4]. For a neutrino ν_2 with mass m_2 in the eV region, the radiative decay into a lighter neutrino ν_1

$$\nu_2 \to \nu_1 + \gamma , \tag{1}$$

would manifest itself as a monochromatic line at E_0 in the far UV spectrum. Decays during the distant past would redshift this line, producing a step-like increase at $E \lesssim E_0$.

A first hint of such a step reported[5] an increase in the intensity of the diffuse high-latitude spectrum from 260 ± 40 (in photons/s·cm^2·sr·Å units) in the range 1300 - 1525 Å, to ∿ 600 in the range 1680 - 1800 Å. However, since different detectors were used in the two wavelength bands, systematic errors could have caused the step.

Subsequently, rocket observations[6] with three UV broad band photometers covering the bandpasses 1450 - 1780 Å (peak sensitivity at 1590 Å), 1610 - 1950 Å (peak 1720 Å), and 1700 - 2420 Å (peak 2125 Å) indicated extragalactic diffuse radiation intensities of 550 ± 150, 900 ± 150, and $\lesssim$ 1300, respectively.

Recently, a compilation[7] of exposures at high galactic latitudes with the International Ultraviolet Explorer claims a step-like signal of 5σ significance at $\lambda_0 \approx (1667 \pm 10)$ Å in the otherwise flat continuum. This corresponds to a photon energy $E_0 \approx 7.4$ eV or, due to the relation $m_1^2 \approx m_2\,(m_2 - 2E_0)$, a neutrino mass of $m_2 \approx 14.9$ eV, assuming $m_1 \approx 0$ eV. Note that photons of this energy propagate freely through the intergalactic medium as well as through the interstellar medium and are consistent with the existence of neutral hydrogen clouds in galactic haloes[8].

The intensity change ΔI_0 at the step is[7] 454 ± 274, or within errors the same as in the previous observations[5,6]. One then deduces the lifetime of a hypothetical ν_2 from[1,2]

$$\tau_{obs} = \frac{c\,n(\nu_2)}{4\pi\,\Delta I_0\,H_0\,\lambda_0} , \tag{2}$$

where $n(\nu_2)$ is the number density of ν_2's in the Universe today. Assuming $n(\nu_2) \approx 100$ cm^{-3} for the decaying neutrinos, one finds

$$2\cdot10^{15}\ \text{yr} \lesssim \tau \lesssim 16\cdot10^{15}\ \text{yr}. \tag{3}$$

Note that this result does not contradict the lower bound, $\tau \geq 3\cdot10^{15}$ yr, derived[2,3] from other astrophysical data. It is remarkable that the upper limit is several orders of magnitude smaller than the lifetime one would expect within the standard $SU(2)_L \times U(1)_Y$ theory of electroweak interactions.

The effective matrix element for the decay (1) compatible with gauge invariance is of the general form[10]

$$\mathcal{M} = \varepsilon^{\mu} q^{\nu} \bar{\nu}_1(p_1)\sigma_{\mu\nu}(a + b\gamma_5)\nu_2(p_2), \tag{4}$$

where ε^{μ} and $q^{\nu} = (p_2 - p_1)^{\nu}$ are the polarization vector and the momentum of the photon, respectively. From (4) one derives

$$\frac{1}{\tau} = \Gamma(\nu_2 \to \nu_1\gamma) = \frac{1}{8\pi}\left(\frac{m_2^2 - m_1^2}{m_2}\right)^3 (|a|^2 + |b|^2) = E_0^3 (|a|^2 + |b|^2)/\pi \tag{5}$$

The decay (1) in the standard model proceeds (in the unitary gauge) through the two one-loop diagrams shown in Fig. 1.

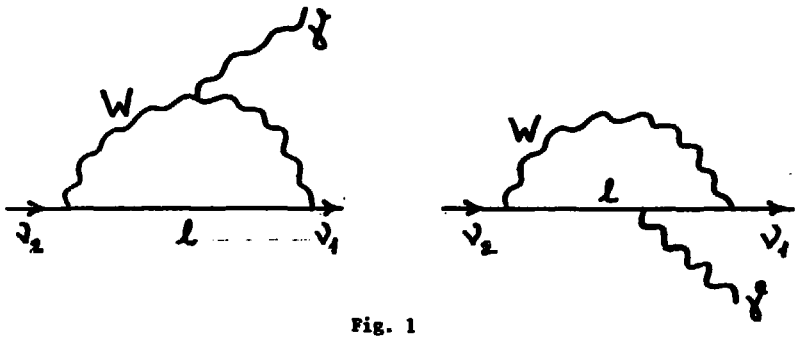

Fig. 1

A full standard model calculation[9] with $m_2 = 15$ eV and $m_1 = 0$ gives

$$\tau^{-1}_{\text{Stand.}} = \Gamma(\nu_2 \to \nu_1\gamma) = \frac{K\alpha G_F^2}{128\pi^4} m_2^5 \left|\sum_{\ell} U_{1\ell} U_{2\ell} F(r_\ell)\right|^2 \simeq K(3\cdot 10^{23}\,\text{yr})^{-1} \left|\sum_{\ell} U_{1\ell} U_{2\ell} F(r_\ell)\right|^2 \tag{6}$$

where $K = 1$ (or 2) for Dirac (or Majorana) neutrinos, U is the leptonic mixing matrix and $F(r_\ell) = O(1)$ is a smooth function of $r_\ell = m_\ell/M_W$. With three light charged leptons ($r_\ell \ll 1$), the leading term in the sum is cancelled due to the unitarity of U, and the rate is thus additionally suppressed by the factor r_ℓ^2. Nevertheless, even if this GIM cancellation were avoided by adding new heavy generations[9] or by making the unitarity sum incomplete (e.g. with an extra singlet ν), the natural lower bound is $\tau \geq 10^{23}$ yr for a 15 eV neutrino in the $SU(2)_L \otimes U(1)_Y$ gauge theory.

The essential feature of Eq. (6) is that the scale is (apart from G_F) set solely by the mass of the neutrino as a consequence of the pure left-handed structure of $W^{\pm}$-lepton interactions in the standard model. Indeed, if the two $W\ell\nu_i$ vertices in the decay amplitude (see Fig. 1) are both of the same chirality, only the momentum part of the internal charged lepton propagator $(\not{p}_\ell - m_\ell)^{-1}$ contributes to the matrix element. All terms of the gauge invariant form (4) are then proportional to the neutrino mass, thus $\Gamma \sim m_2^5$. However, if the $W\ell\nu$

vertex would contain a right-handed piece, also the mass part of the lepton propagator would contribute to the amplitude.

In the first model based on the $SU(2)_L \times SU(2)_R \times U(1)$ gauge group, a RH neutrino $\nu_R(1,2,-1)$ can decay radiatively to an LH neutrino $\nu_L(2,1.-1)$, provided the vector bosons $W_R^{\pm}$ and $W_L^{\pm}$ mix (see Fig. 2). The lighter of the

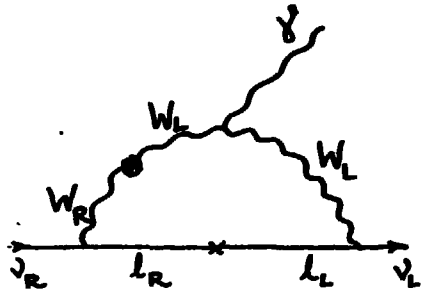

Fig. 2

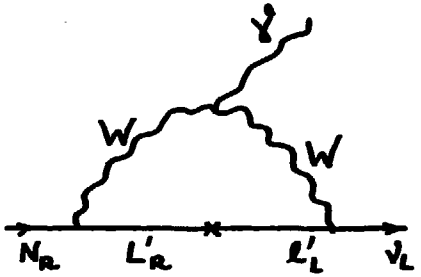

Fig. 3

two vector boson mass eigenstates, $W_1 \equiv \cos\zeta W_L + \sin\zeta W_R$, couples to leptons according to

$$\mathcal{L} = -W_1^{\mu} \frac{g}{\sqrt{2}} (\cos\zeta\, \bar{\nu}_L \gamma \ell_L + \sin\zeta\, \bar{\nu}_R \gamma_{\mu} \ell_R) + \text{h.c.}, \tag{7}$$

where ζ is the bosonic mixing angle. We neglect here the possible intergenerational mixing and the mixing between ν_L and ν_R, which are inessential to our argument. The contribution of the diagrams mediated by the heavier vector boson W_2 can be neglected since $M_{W_2} \geq 20\, M_{W_1} = 1.6$ TeV from the $K_L - K_S$ mass difference and other low-energy constraints[14]. The decay width for $\nu_R \to \nu_L \gamma$ (or $\nu_L \to \nu_R \gamma$) is given by

$$\tau_{LR}^{-1} = \Gamma(\nu_R \to \nu_L \gamma) \simeq (4 \cdot 10^{13}\,\text{yr})^{-1} \left(\frac{E_0}{7.4\ \text{eV}}\right)^3 \left(\frac{m_\ell}{\text{MeV}}\right)^2 \sin^2 2\zeta \tag{8}$$

independently of the neutrino masses for fixed E_0.

The lifetime one deduces from astrophysics depends on the present cosmological density $n(\nu_R)$ of the ν_R. This may be smaller than the density of the standard LH neutrinos, $n(\nu_L) \simeq 100\ \text{cm}^{-3}$, since the more weakly interacting RH neutrinos decouple from the thermal equilibrium earlier[15]. If they decoupled after the muons were annihilated they would today be as abundant as the ν_L. This corresponds to the situation when $M_{Z_R} \lesssim 3$ TeV. In this case we obtain, by comparing Eqs. (3) and (8), the condition

$$0.05 \leq \frac{m_\ell}{\text{MeV}} \sin 2\zeta \leq 0.14\,. \tag{9}$$

If ν_R belongs to the electron family, Eq. (9) requires $\zeta \gtrsim 0.05$. This possibility is clearly excluded since the experimental upper bound from the $K_L - K_S$ mass difference is $\zeta_{exp} \lesssim 0.004$[14]. On the other hand, the ν_R could still be a member of the μ or τ families: then Eq. (9) predicts $\zeta = (2\text{-}7)\cdot 10^{-4}$ or $\zeta = (1\text{-}4)\cdot 10^{-5}$, respectively.

If the ν_R density $n(\nu_R)$ is less than the standard neutrino density $n(\nu_L)$, the value of τ_{obs} in Eq. (3) is reduced by a factor $n(\nu_R)/n(\nu_L)$ and correspondingly larger values of the angle ζ are required.

In the mirror model[12] the situation is favourable in two respects. Firstly, the cosmological density of mirror neutrinos N_R is never suppressed since their neutral current interactions have the same strength as those of the standard LH neutrinos. Secondly, charged mirror leptons, L, must be heavy, $20 \lesssim m_L \lesssim 250$ GeV, and therefore the radiative width increases. The relevant part of the weak Lagrangian is given by[16]

$$\mathcal{L} = -W^\mu \frac{g}{\sqrt{2}} (-\sin\theta_\ell \bar{\nu}_L \gamma^\mu L_L + \cos\theta_\ell \bar{N}_R \gamma^\mu L_R) + \text{h.c.}, \qquad (10)$$

where θ_ℓ is the ℓL mixing angle parametrizing the mixing between the weak eigenstates of the charged lepton ℓ and its mirror partner L. One typical diagram contributing to the decay $N_R \to \nu_L \gamma$ is shown in Fig. 3. The width is, independently of the neutrino masses for fixed E_0, given by

$$\tau^{-1}_{Mirror} = \Gamma(N_R \to \nu_L \gamma) = K(2\cdot 10^5 \text{ yr})^{-1} \left(\frac{E_0}{7.4 \text{ eV}}\right) \left(\frac{m_L}{20 \text{ GeV}}\right) \sin^2 2\theta_\ell . \qquad (11)$$

Comparing this to τ_{obs} of Eq. (3), we find for $20 \leq m_L \leq 250$ GeV

$$2\cdot 10^{-7} \lesssim \theta_\ell \lesssim 1\cdot 10^{-5} \qquad (12)$$

which is far below the present experimental upper limit[16], $\theta_\ell \lesssim 0.1$. Let us note that values of the mixing angle in this range are suggested by some specific mirror models[17].

We conclude that the standard electroweak model cannot account for the short radiative lifetime, $\tau_{obs} \lesssim 10^{16}$ yr, of a massive neutrino, as suggested by astrophysical observations[5-7]. This is due to the purely LH structure of the weak interactions which makes the radiative width $\Gamma_{rad}(\nu_2 \to \nu_1 \gamma)$ proportional to $E_0^3 m_2^2$, where $E_0 = 7.4$ eV is the observed photon energy and m_2 is the mass of ν_2. Accordingly, in the standard model the radiative lifetime for neutrinos in the allowed range ($m_i \lesssim 50$ eV) is always larger than 10^{22} yr.

In non-standard electroweak models which encompass also RH currents, Γ_{rad} is proportional to $E_0^3 m_\ell^2$, where ℓ is a charged lepton. Consequently, the lifetime is shortened by the enormous factor $(m_\ell/m_2)^2$ compared to the standard model.

This enables RH models to explain the astrophysical observation[18]. The predictions for the model parameters are given in Eqs. (9) and (12), respectively. The implied small mixing angles would make it very hard to see the effects of RH interactions of known particles in laboratory experiments. However, N_R would contribute to the total width of Z^0 by an equal amount as the standard neutrino.

We note that ν_R or N_R will together with ν_{eL}, $\nu_{\mu L}$ and $\nu_{\tau L}$ saturate the famous cosmological bound of at most 4 light neutrinos, derived from the present helium abundance in the Universe. If this limit is taken seriously, the RH or mirror neutrinos of the other families should be much heavier or much more unstable than the one discussed here.

Although the astrophysical information used is controversial[5], or scanty[6], or preliminary[7], there is hope for very precise data in the near future, when the Berkeley Extreme Ultraviolet/Far Ultraviolet Shuttle telescope will be launched on the Space Shuttle[19].

It is a pleasure to acknowledge the useful and stimulating discussion we have had (K.M. and M.R.) with D. Fargion, Rome, and (M.R.) with S. Bowyer and C. Martin, Berkeley. J.M. has been supported by Bundesministerium für Forschung und Technologie, Bonn, F.R. Germany.

REFERENCES

1. R. Cowsik, Phys. Rev. Lett. 39, 784 (1977);
D. Dicus, E. Kolb and V. Teplitz, Astrophys. J. 221, 327 (1978);
A. de Rujula and S. Glashow, Phys. Rev. Lett. 45, 942 (1980).
2. F.W. Stecker, Phys. Rev. Lett. 45, 1460 (1980);
F.W. Stecker, and R.W. Brown, Astrophys. J. 257, 1 (1982).
3. R. Kimble, S. Bowyer and P. Jacobsen, Phys. Rev. Lett. 46, 80 (1981).
4. D. Fargion and M. Roos, Phys. Lett. 147B, 34 (1984).
5. M. Maucherat-Joubert, P. Cruvellier and J.M. Deharveng, Astron. Astrophys. 70, 467 (1978); R.C. Anderson et al., Astrophys. J. 234, 415 (1979).
6. P. Jakobsen et al., Astron. Astrophys. 139, 481 (1984).
7. G. Auriemma et al., INFN-Rome preprint 447 (1985, unpublished).
8. A. Melott and D. Sciama, Phys. Rev. Lett. 46, 1369 (1981);
Y. Rephaeli and A. Szalay, Phys. Lett. 106B, 73 (1981).
9. P.B. Pal and L. Wolfenstein, Phys. Rev. D25, 766 (1982), and references quoted therein.
10. W. Marciano and A. Sanda, Phys. Lett. 67B, 303 (1977);
S. Petcov, Sov. Nucl. Phys. 25, 340 (1977); E 25, 698 (1977).
11. J.C. Pati and A. Salam, Phys. Rev. D10, 275 (1974);
R.N. Mohapatra and J.C. Pati, Phys. Rev. D11, 566 (1975); ibid. 2558;
G. Senjanovic and R.N. Mohapatra, Phys. Rev. D12, 1502 (1975).
12. See e.g., J.C. Pati and A. Salam, Phys. Lett. 58B, 333 (1975);
J. Maalampi and K. Enqvist, Phys. Lett. 97B, 217 (1980);
F. Wilczek and A. Zee, Phys. Rev. D25, 553 (1982).
13. K. Enqvist, K. Mursula and M. Roos, Nucl. Phys. B226, 121 (1983).
14. See e.g., L. Wolfenstein, Phys. Rev. D29, 2130 (1984).
15. G. Steigman, K.A. Olive and D.N. Schramm, Phys. Rev. Lett. 43, 239 (1979).
16. J. Maalampi, K. Mursula and M. Roos, Nucl. Phys. B207, 333 (1982).
17. K. Enqvist and J. Maalampi, Z. Phys. C21, 345 (1984).
18. See also J. Maalampi, K. Mursula and M. Roos, Phys. Rev. Lett. 56 (1986).
19. S. Bowyer, private communications.

SEARCH FOR THE 2 γ - DECAY OF AXION-LIKE PARTICLES AT THE S I N - BEAM DUMP

Aachen - Berlin - SIN - Collaboration

(presented by Chr. Spiering , IHEP Berlin/Zeuthen, GDR)

ABSTRACT

A search was made for pairs of almost collinear photons, as expected from the decay of axion-like particles emitted from the SIN 585 MeV proton beam-dump. No 2 γ - decay signal was found in excess of the background. Limits on production and decay of axion-like particles are derived.

1. INTRODUCTION

Attempts to avoid strong CP-violation in QCD led to the postulate of a new, global U(1)-symmetry for the total (QCD+electroweak) Lagrangian. This symmetry would rotate away strong CP-violation /1/. As has been recognized by Weinberg /2/ and Wilczek /3/, the spontaneous breaking of the new symmetry would lead to a pseudoscalar particle with low mass and semi-weak coupling to quarks and leptons, the axion a^0. For the standard (PQWW) axion, the scale of symmetry breaking is fixed to $F_a \approx 250$ GeV. The only free parameter of the model, X, is the ratio of the vacuum expectation values of the two Higgs doublets within the model. Mass, lifetime, production- and interaction cross sections of the axion are computed from X.
Axions could be produced:
(i) in competition with π^0 and η in proton beam dumps,
(ii) in competition with photons in nuclear deexitation processes,
(iii) in K^+, ψ, Υ decays ($K^+ \rightarrow \pi^+ a^0$; $\psi, \Upsilon \rightarrow \gamma a^0$)
(iv) in electron beam dumps.
The existence of standard axions was excluded by (ii) and (iii) /4/. However, one may construct non-standard axion schemes /5/. Furthermore, light pseudoscalars appear in some SUSY-formalisms /6/. Therefore, the search for axion-like particles is still alive.

In 1978, the Aachen group searched for axions produced in the beam-dump of the 585 MeV proton cyclotron of the Swiss Institute of Nuclear Research (SIN), and set a limit on the decay $a^0 \rightarrow e^+ e^-$ /7/. With a modified set-up, however,

indications for radiative axion decays were found, i.e., an excess of photons pointing back to the beam-dump compared to the estimated accelerator and cosmic ray background/6/. Interpreted in terms of axion production and decay, the effect corresponded to

$$X = 0.4\ ,\ m_a = 220\ \text{keV}\ ,\ \tau_a = 15\ \text{msec (solution I)};$$
$$X = 3.5\ ,\ m_a = 285\ \text{keV}\ ,\ \tau_a = 3.8\ \text{msec (solution II)}.$$

This result was not beyond doubt. Objections were raised about the statistical significance /9/. There were also systematical uncertainties. In addition, the experiment strongly disagreed with upper limits from ψ - and Υ -decays. It was the purpose of the present experiment to check the effect observed in the first experiment with improved methods and, if confirmed, to measure it with better accuracy.

2. SET-UP AND DATA TAKING

Fig. 1 shows the set-up. The idea was, to detect both photons from the $a^0 \to \gamma\gamma$ decay in two identical modules, each consisting of a ten-gap optical spark chamber and scintillation counters. The a^0 was supposed to decay in a 2m region between the 8m shielding and counter A. This decay region could be blocked by a moveable Fe/Pb wall. For $m_a \approx 250$ keV, the angle of the decay photons with respect to the primary direction is about 2 mrad, i.e., the two photons would be nearly collinear. Photons were converted with $\approx 50\%$ probability in Pb-foils mounted in front of the spark chambers. The connection line of the conversion points and the beam-dump direction form an angle α , which should be small ($\alpha^2 < 10\ \text{deg}^2$) for axion decays.
Scintillation walls B and C measured energies and time of passing particles. Energy information was used to reject background (e.g. from bremsstrahlung photons). Photon energies and the 2γ-opening angle allow a raw determination of the mass of the parent particle.
In order to reduce the background trigger rate and possible artefacts due to cosmic ray and accelerator background, active and passive shielding was added compared to the 1976 experiment (veto counters D, E (top) and F (side), passive shielding as shown in Fig.1 by the cross-hatched areas). In addition, the timing of the experiment was sharpened.
The trigger consisted of

(i) veto signals from counters A,D,E,F,
(ii) a coincidence $B_i C_k$ with the C-signal delayed by (3.5 -15) nsec in respect to the B signal (7 nsec correspond to a relativistic particle flying from B to C),
(iii) a fast look-up table decision, selecting hit patterns $B_i, B_k, \ldots, C_l, C_m, \ldots$, which correspond to particles moving under an angle $\alpha \lesssim 20$ deg with respect to the beam-dump direction,
(iv) an additional coincidence of any of the elements of

the thin counter B' with the B_1C_1 coincidence.
With this conditions, the cosmic induced triggers were supressed to a level of 25 per hour.
Data were taken under four different running conditions:

Decay region open:
(Fe/Pb wall at the beginning of the decay region)
beam on - 810 hours , 386 Coul. ("signal run")
beam off - 663 hours ("background run")
Decay region blocked:
(Fe/Pb wall at the end of the decay region)
beam on - 261 hours , 146 Coul. ("background run")
beam off - 315 hours ("background run")

3. ANALYSIS

First, the films were scanned for $a^0 \to \gamma\gamma$ candidates. A candidate was defined to be an event with a "V" in at least one chamber (i.e. a pair of tracks with common origin in the Pb foil), at least one track in the other chamber and (to avoid confusion) not more than 5 tracks per chamber. Accepting only "2V" patterns would have been to restrictive, since one particle of the e^+e^- - pair often gets lost in the Pb foil.
The rate of selected events were:

Decay region open:	
beam on	20+-2 per 100 h
beam off	25+-2 "
Decay region blocked:	
beam on	23+-5 per 100 h
beam off	24+-3 "

So, the total rate of selected events does not exhibit any signal effect.
The selected events were measured with an accuracy of 0.6 mm (in space). Due to multiple scattering in the Pb foil, vertices of conversion pairs were reconstructed with a lower accuracy: ≈ 0.7 cm. This, plus other statistical and systematical errors led to an average error of the angle α, $\Delta\alpha \approx 0.9$ deg.

4. RESULTS

Fig.2 shows the angle distributions for the four different running conditions and for $\alpha^2 < 100$ deg^2. Hatched parts result from applying the following additional cuts:
(i) TOF(B to C) less than 10.2 nsec. This cut accepts 99% of particles travelling with the speed of light.
(ii) Average direction of all tracks in a chamber not pointing down by more than 10° with respect to the horizontal. This cut accepts almost all decaying particles emerging from the beam-dump.

From the hatched histograms, the following conclusions can be drawn: During 810 hours of running with beam on and decay region open, only one single $\pi^0 \to \gamma\gamma$ candidate was registered in the effect bin $\alpha^2 < 10\ deg^2$. The runs with beam off (663 hours) yield an expected background in the same bin of 3.2+-0.26 events. These numbers yield a 90% upper confidence limit for an effect of $N = 2.6$ events.

Fig. 3 compares expected rates and measured upper limits from our experiment ("SIN II") and from the CHARM beam dump experiment /10/. Differences between the two curves are due to different assumptions about the contribution of η-mesons to the expected axion flux. The level of the SIN I experiment and a limit obtained recently at SLAC/11/ are also indicated. Our limit is close to that derived by CHARM and excludes the standard axion, except for the range $0.7 < X < 2.1$.
Without referring to a specific theoretical model, limits for production and decay of axion-like particles can be given in the F_x-m_x plane, F_x being the scale of symmetry breaking. Fig.4 shows the 90% confidence limits as a function of F_x and m_x.

REFERENCES

1) R.Peccei, H.Quinn, Phys.Rev.Lett.38, 1440(1977)
2) S.Weinberg, Phys.Rev.Lett.40, 223(1978)
3) F.Wilczek, Phys.Rev.Lett.40, 279(1978)
4) See e.g. the reviews
   A.Zehnder, SIN preprint 84-08
   J.Bluemlein, Proceedings of the Georgenthal-Symposium, Georgenthal, GDR, 1984
5) See the rewiev of J.Bluemlein and references therein
6) P.Fayet, Nucl.Phys.B187(1981)184; B.R.Kim, Phys.Lett.117B (1982)329
7) H.Faissner et al., Phys.Lett.96B, 201(1980)
8) H.Faissner et al., Phys.Lett.103B, 234(1981)
9) N.Fetscher, Journ. of Phys.G8, L147, (1982)
10) F.Bergsma et al., Phys.Lett.157B, 458(1985)
11) J.D.Bjorken, FERMILAB-84/33-T(1984)

FIGURE CAPTIONS

Fig.1 Experimental set-up
Fig.2 Angular distributions of 2γ-events (hatched parts: see text)
Fig.3 Limits on properties of the standard axion
Fig.4 Model independent limits on mass and symmetry breaking scale of axion-like particles

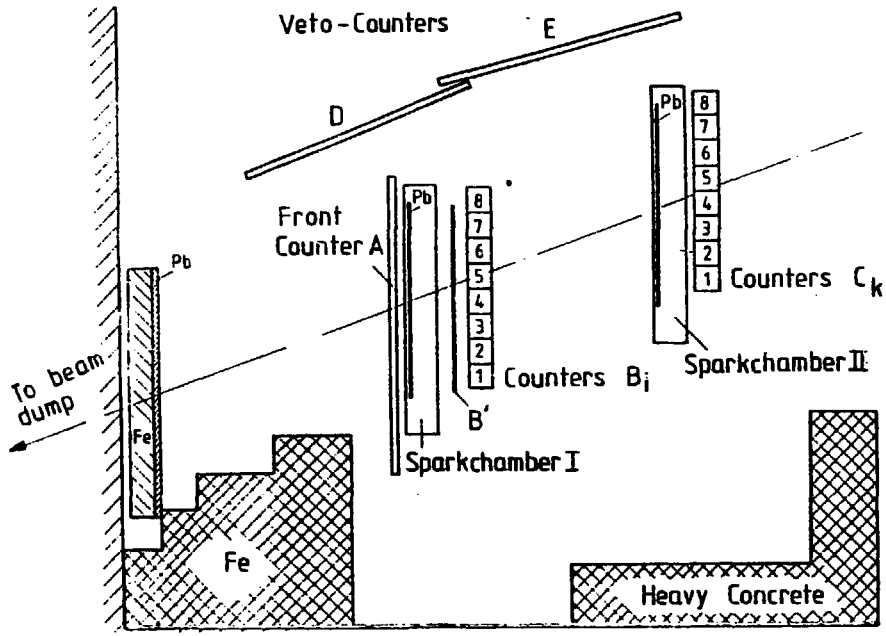
Veto-Counters
E
D
Pb
8
7
6
5
4
3
2
1
Front
Counter A
Counters C_k
Sparkchamber II
Counters B_i
B'
Sparkchamber I
To beam
dump
Fe
Heavy Concrete

Fig . 1

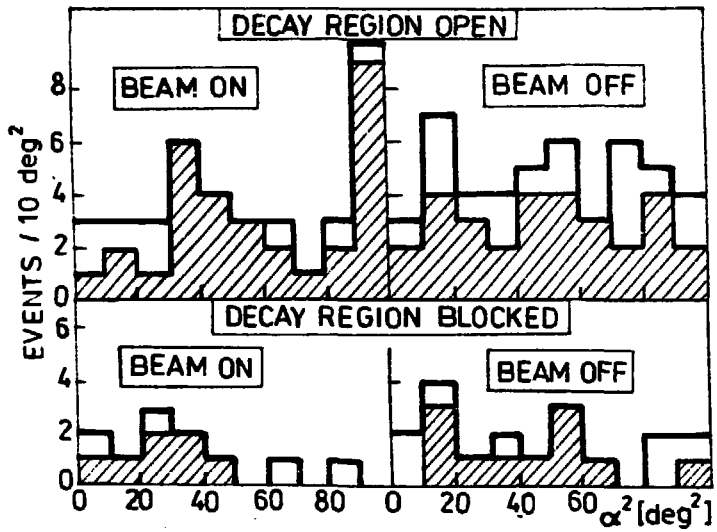
DECAY REGION OPEN
BEAM ON
BEAM OFF
DECAY REGION BLOCKED
BEAM ON
BEAM OFF
EVENTS / 10 deg²
0
2
4
6
8
0
20
40
60
80
α^2 [deg²]

Fig.2

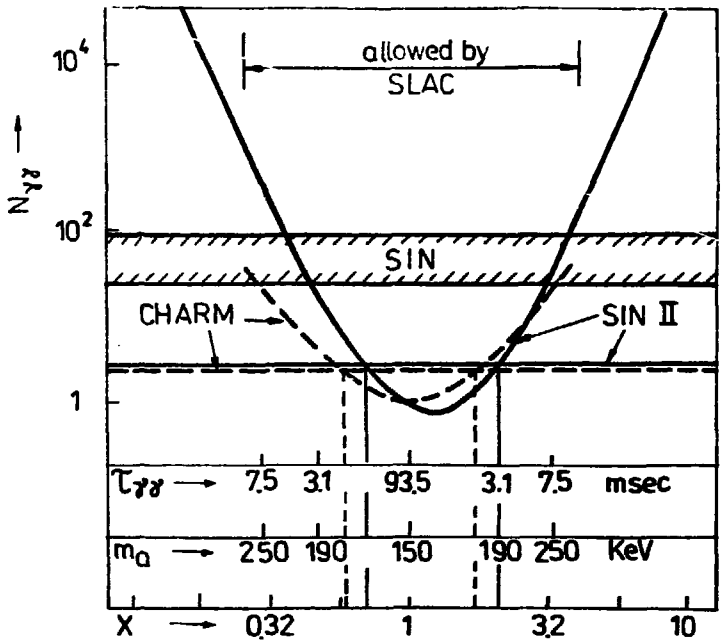
allowed by
SLAC
SIN
CHARM
SIN II
$N_{\gamma\gamma}$
10^4
10^2
1
$\tau_{\gamma\gamma}$ → 7.5 3.1 93.5 3.1 7.5 msec
m_a → 250 190 150 190 250 KeV
X → 0.32 1 3.2 10

Fig.3

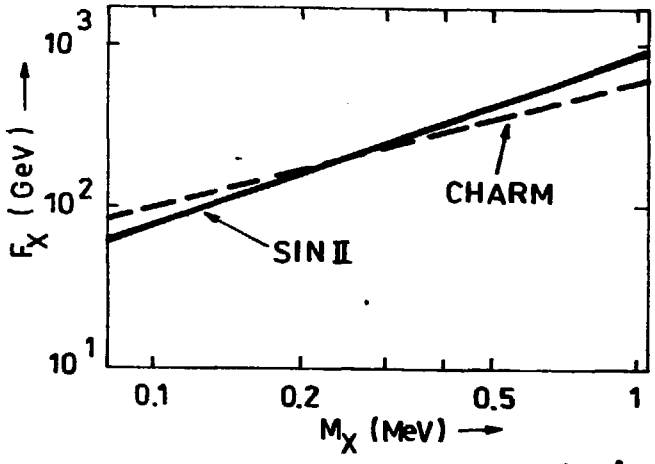
10^3
10^2
10^1
F_X (GeV) →
CHARM
SIN II
0.1
0.2
0.5
1
M_X (MeV) →

Fig.4

LIGHT COMPOSITE FERMIONS

H. Høgaasen
Physics.Dept, University of Oslo,
Norway

Abstract

We show how a model with bagged superfields, through the breaking of a G@G global symmetry group, give rise to quasi - Goldstone multiplets transforming under the adjoint representation of G. The confining boundary condition breaks supersymmetry such that the pseudo-Goldstone fermions are light, the bosons heavy.

It is not completely straightforward to describe quarks and leptons as composite particles.

If we form the product of mass m and extension R of bound states that we are used to, we find a product mR which is bigger than one. For humans it is $\sim 10^{44}$, for atoms $\sim 10^{6}$, for nuclei $\sim 10^{2}$ and for nucleons $mR \sim 5$. (For pions which is exceptional mR is slightly smaller than one). These results are natural consequences of Heisenbergs uncertainty relation

$$\Delta x \cdot \Delta p \geq \frac{h}{2} \qquad 1)$$

Even a massless particle wil have an energy $E=p$ which is of order of R^{-1} if it is confined to a region of extension R.

One of the most beautiful results in physics is the fantastic agreement between the observed magnetic moment of the electron and its calculated value from QED. The assumption of a point electron give the correct results with 11 digits. If the electron has an extension R then $R \leq 5 * 10^{-17}$cm.

The energy due to confinement of a preon inside such a distance is something as 200 GeV and not $0.5.10^{-3}$ GeV which is the energy of an electron at rest. If the electron with $mR \leq 10^{-5}$ or the neutrino, where probably $mR \leq 10^{-10}$ are composite systems, they are definitely of a kind that is different from ordinary bound states. Among the hadrons only the pion could serve as a model. The small mass of the pion is most easily explained by looking at it as a quasi Goldstone particle generated by a spontanous breaking of global SU(2) x SU(2) chiral symmetry. Naive $q\bar{q}$ models for the pion often has trouble to get the pion light enough, the Goldstone picture represents it as a collective exitation with an indefinite number of $q\bar{q}$ pairs.

In a supersymmetric extension of the Nambu-Goldstone mechanism the Goldstone bosons will also have assosiated fermionic partners[1-3]. This is the most elegant way I know of to obtain very light or even massless composite fermions.

It is also quite compatible with the ideas of superstrings being the ultimate degrees of freedom at distances comparable to or even smaller than the Planck length. On distance scales some

order of magnitudes greater, an exellent description of nature should be obtained by a supersymmetric theory with pointlike particles.
What is not so pleasant however is that the nice supersymmetry that was introduced to get fermions as light as bosons, has to be broken at the spatial extensions or the energy ranges that are probed by experiments to day, if we want to make a model of reality. And it has to be broken such that the bosons become much heavier than the fermions.
I shall describe just this last kind of symmetry breaking in a model very similar to the MIT bag modal. The bagged particles[4] will be called urons and will be represented by superfields confined to a small sphere of radius R where R is extremely small. Uron bags have an energy $\sim R^{-1}$ and have themselves nothing to do with quarks and leptons. The minimum number of constituents in a uron bag is two, we can imagine some kind of urcolour to be the dynamical mechanism that leads to the confinement.
It is assumed that the confinement give rise to a spesific boundary condition for the confined fields:
The energy of the bagged urons of spin 1/2 will be determined by the Bogoliubov-MIT boundary condition

$$-i\gamma \cdot \hat{r}\, \phi = \phi \qquad \text{at} \quad r = R \qquad 2)$$

We make a supersymmetry transformation of this to find the boundary condition for scalar urons:

$$m_{ur}\, \phi = \frac{d\phi}{dr} \quad \text{at} \quad r = R \qquad 3)$$

m_{ur} is the uron mass.
As we want to have Direc particles we need a minimum of two chiral superfields: ϕ_L and ϕ_R.
Here

$$\phi_L = (L, \lambda, F_L) \text{ and } \phi_R^+ = (R, \rho, F_R)$$

Each of these chiral superfields also carry an index, characte-

rizing the transformation property under a global flavour symmetry group G of the uron Lagrangian inside the bag. To each generator t_a of this group there corresponds supercurrents

$$V_a = \varphi_L^+ t_a \varphi_L - \varphi_R^+ t_a \varphi_R \qquad 4)$$

and

$$A_a = \varphi_L^+ t_a \varphi_L + \varphi_R^+ t_a \varphi_R \qquad 5)$$

These supercurrents, transforming under the adjoint representation of the group G (=E_8?) fullfil conservation equations (inside the bag)

$$\begin{aligned} D^2 V_a &= D^2 V_a = 0 \\ D^2 A_a &= 8 m_{ur} \varphi_L^+ t_a \varphi_L \\ D^2 A_a &= 8 m_{ur} \varphi_R^+ t_a \varphi_R \end{aligned} \qquad 6)$$

By expanding the chiral superfields in number and θ components one find that V_a and A_a contain the ordinary vector and axial currents as well as currents with spinorial nature.

For vanishing uron masses the currents A_a are strictly conserved inside the bag, but they have (as in the MIT bag where quarks are confined) a delta function source term on the surfece. This is because the boundary condition breaks chiral symmetry.

In the MIT bag one uses PCAC and ensures the continuity of the isovector axial currents by introducing an external Goldstone pion field coupled to the bag surface[5]. By a supersymmetric extension of PCAC - SUSY PCAC, we ensure the continuity of the axial supercurrents A_a and their divergences[6] through the uron bag surface by introducing chiral superfields on the outside of the bag.

If urons are massless so are the Goldstone fermions and bosons associated with the long distance properties of the axial currents. If we give the urons a mass m_{ur} we get relations between m_{ur} and the masses of the psendo Goldstone fermions (μ_f) and bosons (μ).

As the boundary conditions break supersymmetry μ_f and μ are different[4]:

$$m_{ur} = \frac{1}{2}\hat{\mu}_f \qquad 7)$$

$$m_{ur} = \frac{\mu}{2}\frac{\mu R(1+\mu R)}{2+2\mu R+\mu^2 R^2} \qquad 8)$$

For a very small radius R of the uron bag ($\mu R \ll 1$) one has

$$\mu = \sqrt{\frac{4m_{ur}}{R}}\,, \quad \tilde{\mu}_f = \frac{R}{2}\mu^2 \qquad 9)$$

The psendo Goldstone fermions are therefore much lighter than the bosons: this was the desired result. We note from eq 8) that if $R \to \infty$ then $\mu \to \mu_f$ and it can be shown that supersymmetry is recovered. The supercurrent that is obtained from the uron Lagrangian by the use of Nöthers theorem, due to the invariance under the supersymmetry generator is

$$s^m = s^m_L + s^m_R$$

with
$$s^m_L = \sqrt{2}\,[\sigma^n\bar{\sigma}^m \lambda\, \partial_n\bar{L} + i\,\sigma^m\bar{\lambda}\,\bar{F}_L] \qquad 10)$$

$$s^m_R = \sqrt{2}\,[\sigma^n\bar{\sigma}^m \rho\, \partial_n\bar{R} + i\,\sigma^m\bar{\rho}\,F_R] \qquad 11)$$

Explicit calculations give

$$\partial_j \tilde{s}^j = \sqrt{2}\,[\frac{1}{2}\frac{\partial}{\partial r}\,\delta(r_B - r=) + (m + \frac{1}{2}/\,\delta(r_B - r)]\,(\bar{\lambda}L + \bar{\rho}R).$$

And one may easily show that the flux of the susy current is bounded:

$$\int d^3r\, \partial_j\, \tilde{s}^j \leq \frac{C}{r_B} \qquad 12$$

As seen from eq.9 it is not possible to make a fermion massless without getting its SUSY boson partner massless. If one wants to build a realistic theory for quarks and leptons from this model then neutrinos necessarily have a mass. Another general property regardless of the group G is that quarks and leptons must transform under the adjoint representation of this internal flavour symmetry group of the urons.

The energy of uron bags and the energy scale Λ relevant for the confinement of urons is proportional to R^{-1}. Therefore it is only at extremely high energy that the fundamental dynamical variables which are the uron fields will come into play.
To day their only manifestation would be through the effective interaction of the pseudo Goldstone fermions arising from the simultanous breaking of supersymmetry and chiral symmetry.

Acknowledgements
It is always a pleasure to come to Warsaw and Kazimierz and I thank my Polish friends for their kind invitation to this most useful and enjoyful conference.

REFERENCES

1) W. Buchmüller, S.T. Love, R.D. Peccei and T. Yanagida, Phys.Lett. 115B (1982) 77.
W. Buchmüller, R.D. Peccei and T. Yanagida, Phys.Lett. 124B (1983) 67; Nucl.Phys. B227 (1983) 503.

2) W.A. Bardeen and V. Visnjic, Nucl.Phys. B194 (1982) 422;
W.A. Bardeen, T.R. Taylor and C.K. Zachos, Nucl.Phys. B231 (1984) 235.

3) W. Buchmüller CERN-TH 4189/85, Lectures at the XXIV International Universitätswochen für Kernphysik Schladming and W. Buchmüller in "Phenomenology of Gauge Theories" ed J. Tran Than Van, Editions Frontierès Paris 1984 are good comprehensive reviews with many relevant references.

4) G. Girardi et al. Phys.Lett. 164B (1985) 80.

5) G.E. Brown and M. Rho, Phys.Lett. 82B (1979) 177.
R.L. Jaffe, Ettore Majorana School vol. 17, ed. A. Zichichi, Plenum Press 1982.

6) H. Høgaasen, Inst.Phys.Report Series 82-27 University of Oslo; Physica Scripta 29 (1984) 193.

FERMION MASSES FROM SUPERSTRINGS

K. Tanaka

Department of Physics

The Ohio State University

Columbus, Ohio 43210, U.S.A.

Abstract

It is assumed that the E_8 gauge group of the $E_8 \times E_8'$ heterotic superstring can be broken into SO(10) x SU(4). The mass relations among fermions $m_u/m_d = m_c/m_s = m_t/m_b$ and $m_{\nu e}/m_e = m_{\nu\mu}/m_\mu = m_{\nu\tau}/m_\tau$ are discussed.

I. Introduction

Superstring theory offers an exciting possibility of unifying all the known particle interactions.[1-3] It is interesting to examine the experimental consequences of the heterotic string,[2] in particular, the fermion mass relations.

The most promising theory is the $E_8 \times E_8$ heterotic string theory in ten dimensions. The dynamics of compactification from ten to four dimensions is not known. The popular vacuum configuration is $M^4 \times K$, where M^4 is the four-dimensional Minkowski space-time and K is the compact six-dimensional, Ricci-flat Kahler manifold, with SU(3) holonomy, the Calabi-Yau manifold. Models build on Calabi-Yau manifolds give an $E_6 \times E_8$ internal symmetry group when the spin connection of K is embedded in E_8. This leads to a four-dimensional theory with N=1 supersymmetry.

A great deal is not known about Calabi-Yau manifolds if the ground state of the string theory is represented by such a manifold. Consequences of phenomenology is expected to determine the required manifold. There is some recent development that casts some questions on the approach based on Calabi-Yau manifold to which we shall comment on later. But first let us briefly continue on with the present popular scenario.

The topological properties of K have important implications for the four-dimensional low-energy theory that results from the superstring theory. One considers the compactification on $K = K_0/H$ if K_0 is simply connected and admits a discrete group of transformations H. This choice reduces the number of generations by a factor of the

order of H and allows symmetry breaking by Wilson loops called flux breaking mechanism[4]

$$U_g = Pexp\ [i\int A_m dx^m]$$

because there may be on K non-trivial E_6 gauge field configurations that have $F_{\mu\nu} = 0$. The integration is over non-contractible loops in K. Since the group H is finite, it follows that $U_g^n = 1$ for some integer n. These matrices act similarly to vacuum values of the Higgs fields and break E_6.

The matter fields of the zero modes transform as 27 or $\overline{27}$ of E_6. The 27 of E_6 contains unobserved particles that if not extremely heavy can mediate proton decay. Also it does not seem possible to give small masses to neutrinos.[5] Various authors checked whether it is possible to avoid both these problems in various pattern of superstring compactification.[6]

The two dimensional supersymmetric σ-models are relevant to the compactification (from ten-dimensions) of the superstring theories. If compactification takes place on a manifold $M^4 \times K$ the dynamics is described by a σ-model and one must require that the generalized β-function of the σ-model vanish. But at the four-loop level a non-zero contribution to the β-function is found on a Ricci-flat Kähler manifold[7]. This suggests that Calabi-Yau manifold can be considered as a start of a perturbative determination of acceptable manifolds[8] or one can consider alternative manifolds[9].

If K allows stable and holomorphic SU(4) or SU(5), the possible breaking $E_8 \to SO(10) \times SU(4)$ or $SU(5) \times SU(5)$ was suggested by Witten[8] rather than the much examined

$E_8 \to E_6 \times SU(3)$. Further reduction of the gauge group may be assumed by flux breaking via Wilson loops. This means for the former case that the gauge field must belong to the subgroup SU(4) of E_8 that commutes with SO(10). Various authors[10] enumerated the possible scenarios with SU(5) and SO(10) groups that inhibit proton decay and allow light weak Higgs doublets. It is not obvious that the manifolds that are considered are Calabi-Yau manifolds. The subgroup of SO(10) generated by the U_g is called $\bar{G}$.

II. Fermion Masses

Let us start with the Yukawa interaction in ten-dimensions[12,13] which is invariant under $E_8 \times E_8'$

$$L_Y^{(10)} = -g f_{ABC} \bar{\psi}^A \Gamma^M A_M^B \psi^C \quad , \tag{1}$$

where the fermions and gauge fields transform as (496,1) of $E_8 \times E_8'$. Here after we suppress E_8', expand the fields in ten-dimensional space in harmonics on K, keep only the zero modes on K, and take the reduced gauge group to be SO(10). The decomposition of the 248 representation of E_8 into $SO(10) \times SU(4)$ is[14]

$$248 \to (16,4) + (\overline{16},\bar{4}) + (45,1) + (10,6) + (1,15)$$

For fermions

$$\psi^A(x,y) \to \psi_i^a(x)\eta_i^\alpha(y) + \bar{\psi}_i^{\dot{a}}(x)\bar{\eta}_i^{\dot{\alpha}}(y) + \tag{2}$$

$$248 \quad \to \quad (16,4) \quad + \quad (\overline{16},\bar{4}) \quad +$$

For Bosons

$$A_M^B(x,y) \to \chi_i^b(x) A_{mi}^{\beta}(y) + \ldots . \qquad (3)$$

$$248 \to (10,6) + \ldots .$$

where x,y are the coordinates of M^4 and K manifolds, respectively.

The four-dimensional Lagrangian $L_Y^{(4)}$ is obtained by substituting (2) and (3) in (1) and integrating out the y coordinates

$$L_Y^{(4)} = d_{abc} f_{ijk} \psi_i^{aT} C \psi_k^c \chi_j^b + \text{h.c.} \quad , \qquad (4)$$

where C is the charge conjugation matrix in M^4, and f_{ijk} is the effective Yukawa coupling given by an integral over zero mode wave functions, and d_{abc} is the symmetric coupling. The quarks and leptons in the 16 representation acquire a mass due to the coupling 16 x 16 x 10 when χ_j^b acquires a VEV.

The mass matrices of charges $\frac{2}{3}$, $-\frac{1}{3}$ quarks and charged leptons and neutrinos are given by[15]

$$\begin{aligned} M_u^o &= f\langle 10\rangle_u \quad , \\ M_d^o &= f\langle 10\rangle_d \quad , \\ M_\nu^o &= f\langle 10\rangle_u \quad , \\ M_l^o &= f\langle 10\rangle_d \quad , \end{aligned} \qquad (5)$$

where $\langle 10\rangle_u = \langle 10(5)\rangle$, $\langle 10\rangle_d = \langle 10(\bar{5})\rangle$

with the transformation property under the subgroup SU(5) is indicated. In the n generation model, f is a n x n matrix whose elements are the Yukawa coupling f_{ijk} in (4). We have not constructed a Calabi-Yau manifold so the number of generations is treated as a parameter.

After SO(10) is broken by the flux breaking mechani .m the new states of charge $\frac{2}{3}$ quarks in the 16 representation will become a linear combination of the original states, etc. The corresponding mass matrices M_u in the broken SO(10) may be written in terms of M_u^o with the aid of (5)

$$
\begin{aligned}
M_u &= U_R^u M_u^o U_L^{u\,-1} = U_R^u f U_L^{u\,-1} \langle 10\rangle_u = f_u \langle 10\rangle_u \\
M_d &= U_R^d M_d^o U_L^{d\,-1} = U_R^d f U_L^{d\,-1} \langle 10\rangle_d = f_d \langle 10\rangle_d \\
M_\nu &= U_R^\nu M_\nu^o U_L^{\nu\,-1} = U_R^\nu f U_L^{\nu\,-1} \langle 10\rangle_u = f_\nu \langle 10\rangle_u \\
M_\ell &= U_R^\ell M_\ell^o U_L^{\ell\,-1} = U_R^\ell f U_L^{\ell\,-1} \langle 10\rangle_d = f_e \langle 10\rangle_d
\end{aligned}
\tag{6}
$$

If the flux breaking mechanism preserves the $SU(2)_L$ symmetry of the charged $\frac{2}{3}$ and $-\frac{1}{3}$ quarks so that[15]

$$
U_L^u = U_L^d \quad , \quad M_u^\dagger M_u \propto M_d^\dagger M_d \tag{7}
$$

Equation (7) leads to[15,16]

$$
m_u/m_d = m_c/m_s = m_t/m_b = \cdots . \tag{8}
$$

Similarly for charged and neutral Dirac leptons

$$U_L^{\nu} = U_L^{\ell} \quad M_{\nu}^{\dagger} M_{\nu} \propto M_{\ell}^{\dagger} M_{\ell} \tag{9}$$

which leads to[17]

$$m_{\nu e}/m_e = m_{\nu\mu}/m_{\mu} = m_{\nu\tau}/m_{\tau} \tag{10}$$

If we take $m_c = 1.35\text{GeV}$, $m_s = 0.175\text{GeV}$, $m_d = 8.9\text{MeV}$, $m_b = 5.3\text{GeV}$, we obtain $m_t = 41$ GeV and $m_u = 68$ MeV. The relation (10) has been found to be consistent with phenomenology on the basis of Stech and Fritzsch hypothesis in the leptonic sector[18]

$$m_{\nu e}/m_e = 33\text{eV}/0.51\ \text{MeV} = 6.47 \times 10^{-5}$$

$$m_{\nu\mu}/m_{\mu} = 6.8\ \text{KeV}/105.6\ \text{MeV} = 6.44 \times 10^{-5}$$

$$m_{\nu\tau}/m_{\tau} = 120\ \text{KeV}/1784\ \text{MeV} = 6.72 \times 10^{-5}$$

The explicit flux breaking of SO(10) that maintains the relations (8) is being worked out with T. Kitazoe. One alternative way is to break SO(10) via $G = Z_5$ in which case the unbroken group after flux breaking is $SU(2)_L \times SU(2)_R \times SU(3) \times U(1)$.[10] The possible light fields are

$$n16 + \delta\,(16 + \overline{16}) + c\ 10.$$

The VEVs $\langle s \rangle$ and $\langle \bar{s} \rangle$ which are $SU(2)_L$ singlets of $(16 + \overline{16})$ break $SU(2)_R$ at the intermediate mass scale M_I. The $SU(2)_L$ doublets H and $\bar{H}$ of $(16 + \overline{16})$ break $SU(2)_L \times U(1)$ to $U_{em}(1)$. Assume $\delta = 1$, i.e. only one pair of H, $\bar{H}$ exists so as to prevent flavor changing neutral

currents. In this scheme, the diagram Fig. 1 gives the

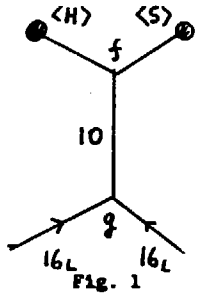

Fig. 1

mass matrix M_u and a similar diagram with the appropriate changes yields the mass matrix M_d:

$$M_u = \frac{f\langle H\rangle\langle s\rangle}{M_{10}}\, g$$

$$M_d = \frac{f'\langle \bar{H}\rangle\langle \bar{s}\rangle}{M_{10}}\, g'$$

Here f, f', g, g' are effective couplings originating from the higher order diagrams. The couplings f and f' have magnitude of M_I, g and g' are matrices in the generation space. Since g and g' are almost diagonal with respect to the 2,3 generation space, we can obtain with the aid of the assumption $\langle s\rangle = \langle \bar{s}\rangle$,

$$m_c/m_s = m_t/m_b \ .$$

This relation at the intermediate scale will receive a small modification due to the renormalization equation below this scale.

The author thanks T. Kitazoe and U. Sarkar for discussions, and Z. Ajduk and S. Pokorski for their hospitality at the Warsaw Symposium. This work was supported in part by the U.S. Department of Energy under Contract Number EY-76-C-02-1415 00.

References

1. M.B. Green and J.H. Schwarz, Phys. Lett, 151 B, 21(1985).
2. D.J. Gross, J.A. Harvey, E. Martinec, and R. Rohm, Phys. Rev. Lett. 54, 502(1985) and Nucl. Phys. B 256, 253(1985).
3. P. Candelas, G.T. Horowitz, A. Strominger and E. Witten, Nucl. Phys. B 258, 46(1985).
4. E. Witten, Nucl. Phys. B 258, 75(1985); Y. Hosotani, Phys. Lett. 126 B, 309(1983).
5. J.L. Rosner, Comments Nucl. Part. Phys. 15, 195(1986); For a possible solution see, for example, S. Nandi and U. Sarkar, Phys. Rev. Lett. 56, 564(1986; R.N. Mohapatra, Phys. Rev. Lett. 56, 561(1986).
6. M. Dine, V. Kaplunovsky, M. Mangano, C. Nappi, and N. Seiberg, Nucl. Phys. B 259, 549(1985); J.D. Breit, B.A. Ovrut, and G. Segre, Phys. Lett. 158B, 33(1985).
7. M.T. Grisaru, A.E.M. Van de Ven, and D. Zanon, Brandeis Univ. preprint.
8. E. Witten, Nucl. Phys. B 268, 79(1986).
9. K. Pilch and A.N. Schellekens, Nucl. Phys. B 259, 637(1985).
10. B.R. Greene, K.H. Kirklin and P.J. Miron, Univ. of Oxford preprint.

11. R. Holman and D.B. Reiss, Fermilab preprint; D. Bailin, A. Love and S. Thomas, University of Sussex and University of London preprint.

12. G.F. Chapline and N.S. Manton, Phys. Lett. 120 B, 105(1983).

13. A. Strominger and E. Witten, Comm. Math. Phys. 101, 341(1985).

14. R. Slansky, Phys. Rep. 79, 1(1981).

15. H. Sato, Hyogo Univ. of Education preprint.

16. D. Chang, R.N. Mohapatra, P.B. Pal and J.C. Pati, Phys. Rev. Lett. 55, 2756(1985).

17. M. Fukugita and T. Yanagida, Phys. Lett. 157B, 403(1985).

18. T.G. Rizzo and J.L. Hewett, Phys. Rev. D34, 298(1986).

DOWN QUARK MIXING IN SUPERSTRING MODELS

K. Enqvist, J. Maalampi and M. Roos

Research Institute for Theoretical Physics and
Department of High Energy Physics
University of Helsinki, Helsinki, Finland

ABSTRACT

Compactified superstring models contain exotic SU(2)-singlet "down" quarks (h_d, h_s, h_b) which are the supersymmetric partners of the color triplet Higgs bosons, and which may survive down to low energies. We study a simple scheme in which the h_b and b quarks mix, giving rise to the observed slight deviations from unitarity of the 3-family Kobayashi-Maskawa matrix V. This scheme has various consequences for the the lifetimes and decay modes of mesons containing b,t and h_b quarks. In particular we find that $m_{h_b} > 15$ GeV, $|V_{cs}| < 0.90$ and $|V_{tb}| < 0.11$.

A plausible low-energy spectrum of the E_8 superstring models[1-4] contains, in addition to the particles of the susy standard model, the following extra fields for each generation: N(1,1,0); ν^c(1,1,0); h(3,1,-1/3) and h^c(3,1,1/3), where the SU(3) x SU(2) x $U(1)_Y$ quantum numbers are displayed in the brackets. This is the situation[5] especially in the so called no-scale models[6] which may be [7] the effective d = 4 supergravity theory of the superstring. The singlet N has been shown[6] to play an important role in the dynamical breaking of the low-energy gauge group. The h-fields are the supersymmetric partners of the traditional Higgs triplets. As they carry the charge and color quantum numbers of the ordinary down quarks, they can mix with these. This mixing will have an important phenomenological consequence: the standard three -generation Kobayashi-Maskawa matrix[8] will no longer appear unitary.

Experimentally, the KM matrix V does in fact deviate to some extent from unitarity. The $|V_{ud}|$ element has recently been re-evaluated by Marciano and Sirlin [9] who considered the leading log radiative correction to β-decay via the renormalization group and structure dependent O(α) effects in a form factor analysis. The result is somewhat smaller than before (see below).

The most precise evaluation[10] of the $|V_{us}|$ element is dominated by K^+_{e3} and K^0_{e3} decays, for which the symmetry breaking in $f_+(0)$ can be estimated. Including also hyperon decays, one can only account for symmetry breaking by leaving several parameters free. The combined result is smaller than what hyperon data alone suggest. With the upper limit[11] for $|V_{ub}|$ we thus know

$$|V_{ud}| = 0.9729 \pm 0.0012 \quad ,$$

$$|V_{us}| = 0.221 \pm 0.002 \quad ,$$

$$|V_{ub}| < 0.0067 \quad (90\%\ \text{C.L.}). \tag{1}$$

The missing piece required by unitarity is then $|V_{u,\text{missing}}| > 0.045$ (90% C.L.). This has led to a flurry of speculations on the existence of a fourth family of quarks[12].

In this paper we shall study the alternative that the apparent deviations from unitarity in the KM matrix are due to the mixing of the SU(2) singlet h quarks with the ordinary down quarks. Some aspects of this mixing have also been discussed in refs.13-15.

The Yukawa couplings in the model are limited by E_6 invariance and renormalizability (possible non-renormalizable terms are not important for the present considerations). The superpotential contains mass terms for both down quarks d and singlet quarks h

$$f_0 = g_d\, d^c d\bar{H} + k\, hh^c N \quad , \tag{2}$$

where $\bar{H}$ is the standard Higgs doublet and we have suppressed the generation indices. Other terms relevant for dh-mixing are

$$f_1 = \lambda_1\, h^c LQ + \lambda_2\, he^c u^c + \lambda_3\, hd^c \nu^c \quad ,$$

$$f_2 = \lambda_4\, hQQ + \lambda_5\, h^c u^c d^c, \tag{3}$$

where L is a lepton SU(2) doublet and Q a quark doublet. As has been discussed in ref.5, the terms in Eqs.(3) do not violate baryon number separately, but only in combination. The Yukawa couplings in Eqs.(3) can indeed be absent in the low-energy theory of the superstring because of the topology of the internal manifold, although no proof of this exists.

If the right-handed sneutrino gets a vev, d and h will mix, and one has the following general form for the mass terms:

$$L_m = m_h^{ij}\, \bar{h}_L^i\, h_R^j + m_d^{ij}\, \bar{d}_L^i\, d_R^j + \mu_h^{ij}\, \bar{h}_L^i\, d_R^j + \text{h.c.} \tag{4}$$

where i and j are generation indices. Note that only the right-handed d mixes with the h.

In the general case the mass matrix for the Q = - 1/3 quarks is thus a 6x6 non-symmetric matrix which has the pattern

$$M = \begin{pmatrix} m_d^{ij} & \mu^{ij} \\ 0 & m_h^{ij} \end{pmatrix} \quad , \tag{5}$$

where the basis is (d,s,b,h_d,h_s,h_b). This can be diagonalized by a bi-unitary

transformation $D_R M D^{\dagger}_L = M$, where D_R and D_L are unitary and M is a diagonal mass matrix. Denoting $\tilde{U}_{L,R}$ the unitary matrices that diagonalize the 3x3 mass matrix of the $Q = 2/3$ quark sector, the charged current interactions depend on the following KM matrix

$$V = U_L D^{\dagger}_L, \quad \text{with} \quad U_L = \begin{pmatrix} \tilde{U}_L & 0 \\ 0 & 0 \end{pmatrix} \tag{6}$$

where the blocks are 3x3 matrices.

Hence the KM matrix is effectively a 3x6 matrix in the case of three mixing flavors. However, for the clarity of the argument we shall in the following consider the simplest possible case, when the mixing involves just one h quark, h_b. It is reasonable to assume that h_b couples considerably only with the b quark, since the much lower masses of the d and s quarks indicate that their mixing angles would be much smaller than those of the b quark*). Of course, all the qualitative effects of the mixing of importance to phenomenology will appear in this simplified mixing scheme.

Starting from a general 4x4 mass matrix M in the down quark system (h_b is numbered 4) we first apply a bi-unitary transformation which carries the 3x3 submatrix associated with the d,s and b quarks to a diagonal form. The matrices D_L and D_R generating this transformation are unitary block diagonal 4x4 matrices with zeros in the fourth column and row, and $(D_{L,R})_{44} = 1$. The assumption that only the b quark has considerable mixing with h_b leads at this stage to a mass matrix of the form

$$M' = D_R M D^{\dagger}_L = \begin{pmatrix} m_d & 0 & 0 & 0 \\ 0 & m_s & 0 & 0 \\ 0 & 0 & m & \mu \\ 0 & 0 & 0 & M \end{pmatrix} \tag{7}$$

in the basis (d,s,b,h_b). Let us assume for the time being that M' is a real matrix. It can then be diagonalized by a bi-orthogonal transformation generated by

$$\tilde{D}^{\dagger}_L = \left(\begin{array}{c|cc} 1 & 0 & \\ \hline 0 & c_\alpha & s_\alpha \\ & -s_\alpha & c_\alpha \end{array}\right), \qquad \tilde{D}_R = \left(\begin{array}{c|cc} 1 & 0 & \\ \hline 0 & c_\alpha & s_\alpha \\ & -s_\alpha & c_\alpha \end{array}\right). \tag{8}$$

---

*) The case of h_d-d mixing has been considered in ref.13. The mixing angle is obviously then very small, and some of the phenomenological consequences are quite different from our case. For instance, the mass limit m(h) > 30 GeV, derived[13] from data on $p\bar{p} \to e^- + 2$ (or more) jets does not apply to our case, where the presence of heavier quarks makes the isolated electron considerably softer.

Thus the angles α,β and the masses m_b, m_{h_b} get determined:

$$s_\alpha = \left[\tfrac{1}{2}\left(1 + \frac{R}{\sqrt{R^2+4}}\right)\right]^{\frac{1}{2}}, \qquad s_\beta = \left[\tfrac{1}{2}\left(1 + \frac{S}{\sqrt{S^2+4}}\right)\right]^{\frac{1}{2}},$$

$$\left.\begin{matrix} m_{h_b} \\ m_b \end{matrix}\right\} = \left[\tfrac{1}{2} T \left(1 \pm \sqrt{1-(2Mm/T)^2}\right)\right]^{\frac{1}{2}}, \tag{9}$$

where

$$R = (M^2 + \mu^2 - m^2)/ m\mu, \qquad S = (M^2 - \mu^2 - m^2)/ M\mu, \qquad T = M^2 + \mu^2 + m^2 . \tag{10}$$

The W couplings to quarks are covered by the generalized KM matrix $U_L D_L^\dagger \tilde{D}_L^\dagger$ where $U_L D_L^\dagger$ is a matrix with zeros in the fourth column and row, of the form (in the KM parametrization)

(11)

$$V = \begin{pmatrix} c_1 & s_1c_2 & s_1s_2c_\alpha & -s_1s_2s_\alpha \\ -s_1c_2 & c_1c_2s_3-s_2c_3e^{i\delta} & (c_1c_2s_3+s_2c_3e^{i\delta})c_\alpha & -(c_1c_2s_3+s_2c_3e^{i\delta})s_\alpha \\ -s_1s_2 & c_1s_2c_3+c_2s_3e^{i\delta} & (c_1s_2s_3-c_2c_3e^{i\delta})c_\alpha & -(c_1s_2s_3-c_2c_3e^{i\delta})s_\alpha \\ 0 & 0 & 0 & 0 \end{pmatrix}$$

The zeros in the fourth row indicate that the h_b -quark is a singlet under SU(2) and that it therefore does not couple to the up-quarks. The standard couplings among the conventional quarks are recovered when $\alpha \to 0$.

From the unitarity of $\tilde{U}_L$ and $D_L\tilde{D}_L$ it follows that the non-vanishing rows of V are orthogonal and normalized to unity,

$$\sum_{k=1}^{4} V_{ik} V_{jk}^* = \delta_{ij} \qquad i,j = 1,2,3 \tag{12}$$

as can be checked from Eq.(17). The same is not true for the column vectors, as it should be if V were unitary. Note that one cannot obtain the matrix (11) from 4x4 generalizations of the unitary KM-matrix by just deleting one row.

From the experimental values in Eq.(1) it follows that the mixing between b and h_b must be close to maximal:

$$\left|\frac{V_{ub}}{V_{uh}}\right| = \left|\frac{s_1s_2c_\alpha}{s_1s_2s_\alpha}\right| = |\cot\alpha| \lesssim 0.11 \quad (90\%\ \text{C.L.}) . \tag{13}$$

According to the heavy quark search in e^+e^- collisions at PETRA [16] the mass of the h_b quark should obey

$$m_{h_b} > 21\ \text{GeV} . \tag{14}$$

The signal for the h_b production would be extra muons from primary ($h \to$) and secondary ($h \to q \to \mu$) decays and, of course, a step of 1/3 in the R ratio. It is interesting to note that the MARK-J collaboration has recently reported[17] such extra muons at the topmost PETRA energy $\sqrt{s} = 46.7$ GeV, although this discovery has not been confirmed by the other detectors. The characteristics of the observed muons show[18] that the events are due to a pair production of $Q = -1/3$ quarks rather than of $Q = 2/3$ quarks or heavy leptons. Let us also mention that $h\bar{h}$ production in $p\bar{p}$ collisions should lead to final states with a single isolated lepton as already noted in ref.13.

It is easy to convince oneself that the experimental constraints (13) and (14) do not force us to any extreme corner in the (m,μ,M) parameter space . The $h_b b$-mixing considered here may thus appear naturally. For example, taking $m = \mu$ we have $R = (M/m)^2$ and from Eq.(9) then follows that

$$R = \tan\alpha - \cot\alpha \quad , \quad \frac{m_{h_b}}{m_b} = \tfrac{1}{2}\left(\sqrt{R} + \frac{2}{\sqrt{R}} + \sqrt{R + \frac{2}{R}}\right) . \qquad (15)$$

Eqs.(3) and (15) then lead to a lower limit for the h_b-quark mass

$$m_{h_b} \geq 3.0\, m_b \simeq 15 \text{ GeV}. \qquad (16)$$

Of course, more precise measurements of the KM matrix elements would allow one to put more severe limits on m_{h_b}. It is interesting that such a limit could compete with the limit that can obtained in e^+e^- collisions.

The presence of a fourth quark mixing with the first three down quarks of course explains why the B lifetime is so long: its predominant coupling is to an inert or kinematically disallowed channel. We note, however, that the ratio $\Gamma(b \to u l\nu)/\Gamma(b \to c l\nu)$ is not changed due to bh_b-mixing so that the determination of the B lifetime from experiment[11] need not be reconsidered. The main decay mode of the h_b quark would be to the top channel, if not kinematically prohibited, but also decays to the u and c channels would be substantial. The lifetime of the appropriate "honium" or "open h" meson states, H, would be shortened by the factor $\sim \cot^2\alpha\,(m_B/m_H)^3 \leq 10^2 (m_B/m_H)^3$ relative to that of B. Thus h_b-mesons would be a copious source of b-quarks.

The structure of the V matrix (11) permits us to make some predictions for the physics of c and t quarks. The c quark matrix elements have the experimental values[11] $|V_{cd}| = 0.24 \pm 0.03$, $|V_{cs}| = 0.85 \pm 0.15$, $|V_{cb}| = 0.042 \pm 0.005$. From the V matrix we have

$$|V_{ch}| = |V_{cb}| \tan\alpha > 0.37 \ (90\%\ \text{C.L.}) \quad . \qquad (17)$$

Using the condition

$$|V_{cd}|^2 + |V_{cs}|^2 + |V_{cb}|^2 + |V_{ch}|^2 = 1 \qquad (18)$$

and the experimental values for all the elements except the poorly determined $|V_{cs}|$, we can predict

$$|V_{cs}| < 0.90 \quad (90\% \text{ C.L.}) \quad . \tag{19}$$

For the t quark elements we obtain the predictions

$$|V_{tb}| / |V_{th}| = \cot \alpha < 0.11 \ (90\% \text{ C.L.}) \quad . \tag{20}$$

Neglecting the (presumably) small values of $|V_{td}|$ and $|V_{ts}|$, we can use the condition $|V_{tb}|^2 + |V_{th}|^2 < 1$ to predict

$$|V_{tb}| < \cos \alpha < 0.11 \qquad (90\% \text{ C.L.}) \tag{21}$$

Thus the t → b decay channel is disfavored in contrast to the 3-family standard model where $|V_{tb}| \approx 0.99$. Depending on which of the quarks t or h_b is heavier, this has dramatic effects on open t or h_b decay modes.

In conclusion, we have considered the mixing of the conventional Q = -1/3 quarks with the SU(2) singlet quarks h which may exist in the effective low energy theory of the superstring models. The mass of these new quarks may be relatively low and their mixing, especially with the b quark, can be large. Roughly, provided that the Nhh^c and $\nu^c d^c h^c$ coupling strengths are about equal, the limit from the KM mixing matrix would entail only that $\langle \nu^c \rangle \leq \langle N \rangle$. Such a large vev for ν^c would push the masses of the extra Z's to higher scales; for instance, in an SU(3)xSU(2)xU(1)² no-scale model[6] $m^2_{Z'} \alpha \langle \nu^c \rangle^2 + \langle N \rangle^2$. However, it should be remembered that a large vev for ν^c may not be a feasible outcome of a detailed dynamical calculation. As the b quark is in the standard model, in agreement with experiment. If the h_b mass exceeds the t quark mass, also the T lifetime is predicted to be much longer than in the standard 3-family model. For the c and t quarks the model predicts

$$|V_{cs}| < 0.90 \quad \text{and} \quad |V_{tb}| < 0.11 \qquad (90\% \text{ C.L.}) \quad ,$$

whereas the standard 3-family model prediction is $|V_{tb}| \approx 0.99$. If the h_b is heavier than the t quark, the decay t → h_b is kinematically forbidden and the dominant decay t → b is slow due to the smallness of $|V_{tb}|$. Then all searches for the t quark have been based on erroneous Monte Carlo calculations. If the h_b quark is lighter than the t quark, the decay chain t → h_b → b proceeds almost as if no h_b existed, and present Monte Carlo calculations are correct.

References

1) M.B. Green, Surv.High Energy Phys. 3 (1983) 127;J.H. Schwarz, Phys.Rep. 89 (1982) 323.

2) P. Candelas, G.T. Horowitz, A. Strominger and E. Witten,Nucl.Phys. B258 (1985) 46.

3) A. Strominger and E. Witten, Comm.Math.Phys. 101 (1985) 341.

4) E. Witten, Nucl.Phys. B258 (1985) 75.

5) E. Cohen, J. Ellis, K. Enqvist and D.V. Nanopoulos, Phys. Lett. 161B (1985) 85; 165B (1985) 76; J. Ellis, K. Enqvist, D.V. Nanopoulos and F. Zwirner, CERN preprint TH 4329 (1985); J. Ellis, K. Enqvist, D.V. Nanopoulos and F. Zwirner, CERN preprint TH 4350 (1985).

6) J. Ellis, A.B. Lahanas, D.V. Nanopoulos and K. Tamvakis, Phys.Lett. 134B (1984) 429; J. Ellis, C. Kounnas and D.V. Nanopoulos, Nucl.Phys B2 41 (1984) 406.

7) E. Witten, Phys.Lett. 155B (1985) 151.

8) M. Kobayashi and K. Maskawa, Progr.Theor.Phys. 49 (1973) 652.

9) W.J. Marciano and A. Sirlin, Phys.Rev.Letters 56 (1986) 22.

10) H. Leutwyler and M. Roos, Z.Phys.C 25 (1984) 91.

11) G. Barbiellini and C. Santoni, CERN-EP/85-117 (1985), and Riv.Nuovo Cimento (to appear).

12) S.K. Bose and A. Paschos, Nucl.Phys. B169 (1980) 384; A. Davidson, K.C. Wali, and P. Mannheim, Phys.Rev.Letters 45 (1980) 1135; H. Sugawara, Phys.Rev. D30 (1984) 2396; J. Bagger and S. Dimopoulos, Nucl.Phys. B244 (1984) 247; J. Bagger et al. SLAC-PUB-3441 (1984) and SLAC-PUB-3586 (1985); V. Barger et al., Phys.Rev. D30 (1984) 947 I. Bigi, Z.Phys. C27 (1985) 303; M. Gronau and J. Schechter, SLAC-PUB-3451; S. Pakvasa, KEK-TH 110 (1985); Xiao-Gang He and S. Pakvasa, Univ. of Hawaii preprint UH-SII-572-85 (1985); F.J. Botella and Ling-Lie Chau, BNL 37415 (1986); Ling-Lie Chau, BNL 37541-R (1986).

13) V. Barger, N. Deshpande, R.J.N. Phillips and K. Whisnant, Phys.Rev. D33 (1986) 1912.

14) F. Cornet, E.W.N. Glover, K. Hagiwara, A.D. Martin and D. Zeppenfeld, DESY 86-017 (1986).

15) R.W. Robinett, Phys.Rev. D33 (1986) 1908; B.A.Campbell, J. Ellis, K. Enqvist, M.K. Gaillard and D.V. Nanopoulos, CERN preprint in preparation.

16) M. Althoff et al. Phys.Letters 138B (1984) 441.

17) B. Adeva et al., MIT technical report 146 (1986).

The One-Loop Open Bosonic String Amplitude with External Vector Particles *

P. Jetzer
Département de Physique Théorique
Université de Genève
1211 Genève 4, Switzerland

Abstract

The one-loop amplitude of the open bosonic string with M external vector particles is calculated in the operator formalism.

In the zero-slope limit the model reduces to scalar electrodynamics, provided the ground-state mass and the dimensionless coupling constant, g, are kept fixed.

* Partially supported by the Swiss National Science Foundation.

1. Introduction

We discuss in this talk the one-loop amplitude of the open bosonic string containing external vector particles [1], which has not been performed so far [2,3]. This is mainly because of the tediousness of the calculations. The structure of the vertex operator, which is linear in the polarisation vector but not in the oscillators, does not allow a factorization of the trace over the oscillators as for the amplitudes containing external tachyonic states. However, if it is represented as an exponential of the external polarisation vector the factorization of the trace is recovered. The calculation then follows that of the tachyonic amplitudes with a simple shift of the external momenta. The terms linear in each of the polarization vectors are picked up at the end [4]. In a similar manner we can also calculate the one-loop amplitudes of the nonplanar orientable and nonorientable diagrams. As for the tachyonic amplitude we find that in leading order the integrand defining the amplitude diverges like q^{-3} (for $q \to 0$), and that the nonplanar orientable amplitude has "bound-state" poles for $S/4 = -2,0,2,\ldots$ [3].

We further investigate the zero-slope limit of the one-loop amplitude. This limit was first analysed by Scherk [5], who showed that the conventional model with external tachyonic states reduces to the ϕ^3 Lagrangian in the limit where the ground-state mass of the tachyon and $g/\sqrt{\alpha'}$ are kept fixed (g is a dimensionless coupling constant). Here we find that the one-loop amplitude of the open bosonic string containing external vector particles reduces in the zero-slope limit to the corresponding one-loop amplitudes of scalar electrodynamics, provided the ground-state mass and the dimensionless coupling constant g are kept fixed.

2. M-particle one-loop amplitude

As mentioned in the introduction, we write the vertex for the emission or absorption of a massless vector particle having momentum k and polarisation η (both transverse) in the following way [4]

$$V(\eta,k)=\frac{g}{\sqrt{2\alpha'}}\eta^i\frac{\partial}{\partial\xi^i}:e^{ik^iX^i(\sigma=0,\tau)+\xi^iP^i(\tau)\sqrt{2\alpha'}}:\Big|_{\xi^i=0} \tag{1}$$

where

$$X^i(\sigma=0,\tau)=x^i+p^i\tau+i\sqrt{2\alpha'}\left[\sum_{n=1}^{\infty}\left(\frac{a_n^i}{\sqrt{n}}e^{-in\tau}-\frac{a_n^{+i}}{\sqrt{n}}e^{in\tau}\right)\right]$$

$$P^i(\tau)=\frac{\partial}{\partial\tau}X^i(\sigma=0,\tau) \tag{2}$$

(g is a dimensionless coupling constant) which yields

$$V(\eta,k)=\frac{g}{\sqrt{2\alpha'}}\eta^i\frac{\partial}{\partial\xi^i}\left[e^{\sum_{n=1}^{\infty}(\xi_n^i+k^i\sqrt{2\alpha'})\frac{a_n^{+i}}{\sqrt{n}}e^{in\tau}}e^{ik^i(x^i+p^i\tau 2\alpha')}\times\right.$$
$$\left.\times e^{\xi^ip^i\sqrt{2\alpha'}}e^{\sum_{n=1}^{\infty}(\xi_n^i-k^i\sqrt{2\alpha'})\frac{a_n^i}{\sqrt{n}}e^{-in\tau}}\right]\Big|_{\xi^i=0}, \tag{3}$$

where normal ordering was used. The main advantage of this representation is that the expression inside the bracket resembles formally the tachyonic vertex

$$V(k)=\lambda e^{\sum_{n=1}^{\infty}\sqrt{2\alpha'}k^i\frac{a_n^{+i}}{\sqrt{n}}e^{in\tau}}e^{ik^i(x^i+p^i\tau 2\alpha')}e^{-\sum_{n=1}^{\infty}\sqrt{2\alpha'}k^i\frac{a_n^i}{\sqrt{n}}e^{-in\tau}}. \tag{4}$$

We note that the coefficients multiplying the oscillator (a_n, a_n^+) in Eqs (3) and (4) are related by $k\to\pm k+\frac{\xi n}{\sqrt{2\alpha'}\tau}$. With this observation we can simply use the expression for the trace over the oscillators in the tachyonic case [3] with the above replacement. The derivatives with respect to ξ will be taken at the end of the calculation.

To calculate the one-loop M-particle planar amplitude we use :

$$A_p(1,..,M) = \int d^{26}p \; Tr\left[\Delta V(\eta_1,k_1)\Delta \dots \Delta V(\eta_M,k_M)\right] \tag{5}$$

(Δ is the propagator and we set $\tau = 0$ in the vertex operator (3) according to the "cancelled propagator argument" [3]). With the insertion of the vertex operator Eq. (3), the trace part of the amplitude can be easily evaluated since it factorizes into an infinite product of traces over the single oscillators just as in the tachyonic case. After some standard manipulations [3], we obtain for the amplitude

$$A_p(1,..,M) = (\alpha' g)^M \int d^{26}p \int dx_1 .. dx_M \, \omega^{-2} f(\omega)^{-24} \prod_{j=1}^{M} k_j^{\alpha' P_j^2} A \cdot$$

$$\cdot \prod_{i=1}^{M}\left(\frac{1}{\sqrt{2\alpha'}}\eta_i \frac{\partial}{\partial \xi_i}\right)\left[\prod_{j=1}^{M} e^{-\frac{1}{2}k_j\xi_j\sqrt{2\alpha'} + \xi_j P_j \sqrt{2\alpha'}} \cdot B \cdot D\right]\Bigg|_{\xi_i=0} \tag{6}$$

where

$$P_j = (p - k_1 - k_2 - \dots - k_{j-1})$$

$$f(\omega) = \prod_{n=1}^{\infty}(1-\omega^n)$$

$$A = \prod_{i<j} e^{-2\alpha' k_i k_j \cdot A_{ij}}$$

$$B = \prod_{i<j} e^{\sqrt{2\alpha'}(\xi_j k_i - \xi_i k_j) B_{ij}}$$

$$D = \prod_{i<j} e^{\xi_i \xi_j \cdot D_{ij}} \prod_{i=1}^{M} e^{\xi_i^2 \sum_{n=1}^{\infty} \frac{n\omega^n}{1-\omega^n}}$$

$$A_{ij} = \sum_{n=1}^{\infty} \frac{1}{n}\left(c_{ji}^n + c_{ij}^n \omega^n\right)\frac{1}{1-\omega^n} \tag{7}$$

$$B_{ij} = \sum_{n=1}^{\infty}\left(c_{ji}^n - c_{ij}^n \omega^n\right)\frac{1}{1-\omega^n}$$

$$D_{ij} = \sum_{n=1}^{\infty} n \left(c_{ji}^{n} + c_{ij}^{n} \omega^{n} \right) \frac{1}{1-\omega^{n}}$$

$$C_{ij} = \frac{\rho_i}{\rho_j} \;, \quad \rho_i = x_1 x_2 \cdots x_i \;, \quad \omega = x_M \;. \qquad \text{(7 cont.)}$$

Here we used momentum conservation ($\sum_{j=1}^{M} k_j = 0$) and the mass-shell condition, $k_j^2 = 0$. Our notations follow those of Schwarz [2].

We perform the momentum integration and putting everything together we obtain for (6)

$$A_p(1,..,M) = (\alpha' g)^{M} \int_0^1 \prod_{i=1}^{M} dx_i \left(\frac{-\pi}{\alpha' \ln \omega} \right)^{13} \omega^{-2} f(\omega)^{-24} \times$$

$$\times \prod_{i<j} e^{-2\alpha' k_i \cdot k_j \left[\ln \omega (1-v_i)(1-v_j) + A_{ij} \right]} C_{ji}^{-\alpha' k_i \cdot k_j} \times$$

$$\times \prod_{\ell=1}^{M} \frac{1}{\sqrt{2\alpha'}} \eta_\ell \frac{\partial}{\partial \xi_\ell} \left[\prod_{i<j} e^{\sqrt{2\alpha'} \xi_i \cdot k_i (B_{ij} - v_i)} e^{\sqrt{2\alpha'} \xi_j \cdot k_j (-B_{ij} + (1-v_j))} \times \right. \qquad (8)$$

$$\left. \times e^{\xi_i \cdot \xi_j \left(D_{ij} - \frac{1}{\ln \omega} \right)} \right] \Big|_{\xi_\ell = 0} \;,$$

where we introduced $v_i \equiv \frac{\ln \rho_i}{\ln \omega}$.

In (8) we dropped all the factors in the exponent involving contractions $\xi_i k_i$ since they vanish after differentiation due to the transversality condition, $\eta_i k_i = 0$. We also neglected quadratic terms ξ_i^2 in the exponent, as they do not contribute to the amplitude. Multiple use of the Leibniz rule and the observation, that the term proportional to $\xi_i \xi_j$ in the exponent has to be differentiated an even number of times in order to get a nonvanishing contribution, show that we obtain at the end a sum of kinematical terms of the form

$$(\eta_{i_1} k_{j_1})(\eta_{i_2} k_{j_2}) \cdots (\eta_{i_L} k_{j_L})(\eta_{r_1} \eta_{s_1}) \cdots (\eta_{r_k} \eta_{s_k}) \;, \qquad (9)$$

where all the η_i appear exactly once; $i_\ell \neq j_\ell$, $r_i < S_i$ and $M = L + 2k$. Each such term is multiplied by a product of factors coming from the exponentials.

Introducing $q = \exp(2\pi^2/\ell n\omega)$ and using the properties of the Jacobi theta-functions [8] we obtain for the amplitude (6) (with $\sum_{i<j} k_i k_j = 0$),

$$A_p(1,..,M) = \frac{(\alpha' q)^M}{\pi} \int_0^1 dq \int_0^1 \prod_{i=1}^{M-1} \vartheta(\nu_{i+1} - \nu_i)\, d\nu_i \, f(q^2)^{-24} \frac{1}{q^2} \left(\frac{-2\pi^2}{\ell n q}\right)^M \times$$

$$\times \prod_{i<j} \left\{ \sin \pi(\nu_j - \nu_i) \prod_{n=1}^{\infty} (1 - 2q^{2n} \cos 2\pi(\nu_j - \nu_i) + q^{4n}) \times \right. \tag{10}$$

$$\left. \times \exp\left[\left(\frac{2\pi^2}{\ell n q}\right)(\nu_i + \nu_j - \tfrac{1}{2}(\nu_i^2 + \nu_j^2)) \right] \right\}^{2\alpha' k_i k_j} \cdot \prod_{i<j} F(B_{ij}, D_{ij}) \,,$$

where F is the sum of terms (9) resulting from the differentiations. Each such term is multiplied essentially by a product of B_{ij}, D_{ij}.

The expression for B_{ij} and D_{ij} in terms of the ν, q variables are [7]

$$B_{ij} = -\frac{1}{2} + (\nu_j - \nu_i) - \frac{\ell n q}{2\pi} \left[\cot \pi(\nu_j - \nu_i) + 4 \sum_{n=1}^{\infty} \frac{q^{2n}}{1 - q^{2n}} \sin(2\pi n(\nu_j - \nu_i)) \right]$$

$$D_{ij} = \frac{\ell n q}{2\pi^2} - \left(\frac{\ell n q}{2\pi}\right)^2 \left[\frac{-\pi^2}{\sin^2 \pi(\nu_j - \nu_i)} + 4\pi \sum_{n=1}^{\infty} \frac{q^{2n}}{1 - q^{2n}} \cos(2\pi n(\nu_j - \nu_i))\, 2\pi n \right] \tag{11}$$

We see that the general kinematical term (9) is multiplied by a function containing terms proportional to $(\ell nq)^M$, $(\ell nq)^{M-1}, \ldots, 1$. The term $(\ell nq)^M$ cancels the $(1/\ell nq)^M$ appearing in (10) so that the leading divergence in the integrand of (10) is of the type q^{-3} (for $q \to 0$) as in the corresponding tachyonic amplitude.

In a similar way, we can also study the nonplanar one-loop amplitudes. The integrand of the nonplanar orientable amplitude has poles, when the limit $q \to 0$ is performed, which can be interpreted as closed string bound states as in the

tachyonic case [3].

3. Zero-slope limit of the loop amplitudes

In this section we discuss the zero-slope limit of the one-loop amplitudes with external vector particles.

For clarity, we present here in some detail the calculations for the amplitude with two external states. This can be easily generalized to amplitudes with any number of external vector particles.

The compactified [2] (from 26 to 4 dimensions) planar one-loop amplitude is obtained from Eq. (6) :

$$A_p(1,2) = g_{26}^2 \frac{1}{R^{22}} \int d^4p \; \alpha' \int_0^1 dx_1 \, x_1^{\alpha'(p^2+m^2)-1} \; \alpha' \int_0^1 dx_2 \, x_2^{\alpha'((p-k_1)^2+m^2)-1} \cdot$$

$$\cdot \; \theta_3^{22}\left(0 \middle| \frac{\alpha^2 \ln\omega}{i\pi}\right) f(\omega)^{-24} \prod_{n=1}^{\infty} \left[(1-\omega^{n-1}c_{21})\left(1-\frac{\omega^n}{c_{21}}\right)\right]^{2\alpha' k_1 k_2} \cdot \tag{12}$$

$$\cdot \left[\frac{1}{2\alpha'} \eta_1 \eta_2 \sum_{n=1}^{\infty} (c_{21}^n + \omega^n c_{12}^n) \frac{n}{1-\omega^n} \; + \right.$$

$$\left. + \left(-\eta_1 k_2 \sum_{n=1}^{\infty} \frac{(c_{12}^n \omega^n - c_{21}^n)}{(1-\omega^n)} + \eta_1 p\right)\left(\eta_2 k_1 \sum_{n=1}^{\infty} \frac{(c_{21}^n - \omega^n c_{12}^n)}{(1-\omega^n)} + \eta_2 (p-k_1)\right)\right]$$

with $\omega = x_1 x_2$, $C_{21} = x_2$, $\omega C_{12} = x_1$, $a^2 = \alpha'/R^2$ and R is the radius of compactification. The dimensionless coupling constant in 4-dimensions is defined as [2] : $g^2 = g_{26}^2/R^{22}$. The only contributions to $A_p(1,2)$ in the zero-slope limit come from the corners of the integration region in the x_1 , x_2 plane. The corner x_1 , $x_2 \to 1$ (or $\omega \to 1$) can be neglected since the amplitude is divergent when $\omega \to 1$. Here one should consider the renormalized quantity, which turns out to be proportional to α' and thus vanished when $\alpha' \to 0$ [5]. For the corner x_1 , $x_2 \to 0$ we get :

$$G = g^2 \int d^4p \, \frac{(\eta_1 p)(\eta_2 (p-k_1))}{(p^2+m^2)((p-k_1)^2+m^2)} \tag{13}$$

which corresponds in scalar electrodynamics to the amplitude of the following Feynman graph :  .

From both corners $x_1 \to 1$, $x_2 \to 0$ and $x_1 \to 0$, $x_2 \to 1$ we obtain the same result, which is :

$$J = \frac{-\eta_1\eta_2}{4} g^2 \int d^4p \, \frac{1}{(p^2+m^2)} + \frac{\eta_1\eta_2}{4\mu^2} g^2 \int d^4p \tag{14}$$

where the first term corresponds to the amplitude of the Feynman diagram :

 .

The second term in Eq. (14) results from the infrared divergence; in order to avoid it we had to give a small mass μ^2 to the "photon".

This additional term can be interpreted as being originated from a mass counterterm of order g^2 in scalar electrodynamics with mass $\delta m^2 = \frac{1}{2\mu^2}\int d^4p$. We note also that this problem does not arise, when one considers amplitudes with more than two external legs.

Similar to the analysis of the planar amplitude, we can study the nonplanar orientable and nonorientable one-loop amplitudes.

In conclusion we find that, taking into account all the one-loop amplitudes of the string model, the relative weights of the Feynman diagrams we obtain are the correct ones for scalar electrodynamics.

Note that one has also to sum over all the cyclically inequivalent permutations of the external legs. This is important because for the amplitudes with more than two external vector particles one finds terms, which do not correspond to ordinary Feynman graphs in scalar electrodynamics, and once the sum over all permutations is performed they cancel.

Acknowledgements

It is a great pleasure to thank the organizers of the Symposium, in particular Professor S. Pokorski and Dr. Z. Ajduk for the enjoyable meeting.

I would like to thank J. Lacki for the collaboration on this subject.

References

[1] P. Jetzer and J. Lacki, University of Geneva preprint UGVA-DPT 508 (1986).

[2] For reviews see e.g. J.H. Schwarz, Phys. Rep. 89 (1982) 223 and references therein.

[3] D. Gross, A. Neveu, J. Scherk and J. Schwarz, Phys. Rev. D2 (1970) 697, see also J. Schwarz, Phys. Rep. 89 (1982) 223.

[4] H. Kawai, D.C. Lewellen and S. Tye, Nucl. Phys. B269 (1986) 1.

[5] J. Scherk, Nucl. Phys. B31 (1971) 222; N. Nakanishi, Progr. Theor. Phys. 48 (1972) 355.

[6] A. Neveu and J. Scherk, Nucl. Phys. B36 (1972) 155; Nucl. Phys. B81 (1974) 118.

[7] P. Frampton, P. Moxhay and Y.J. Ng, Phys. Rev. Lett. 55 (1985) 2107; University of North Carolina preprint IFP-256-UNC and IFP-269-UNC (1986).

[8] A. Erdély et al., Higher Transcendental Functions, McGraw-Hill (1953).

DOUBLY GRADED σ-MODEL AND THE SUPERSTRINGS

J. Kowalski-Glikman*

National Institute for Nuclear Physics and High Energy Physics, Amsterdam, The Netherlands

---

* On leave of absence from the Institute of Theoretical Physics, University of Warsaw, Warsaw, Poland.

Two-dimensional σ-models have recently become important in the context of string theory as they provide a description of strings moving on some curved background space-time. From the other point of view (which I will follow) one can also consider the σ-model as a generalization of string theory.

The two-dimensional σ-model as well as a string theory can be considered as a theory of mappings from the/a two-dimensional manifold into some higher (usually 26- or 10-) dimensional one. The underlying geometric picture is rather simple (see fig. 1).

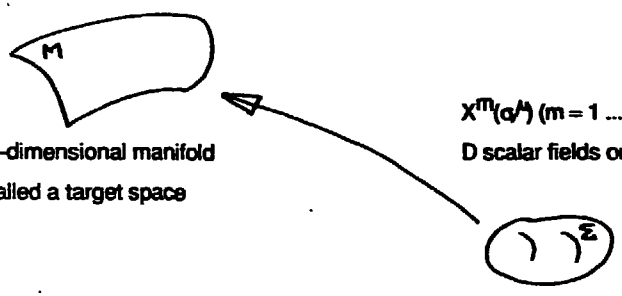

D-dimensional manifold called a target space

$X^m(\sigma^\mu)$ $(m = 1 \ldots D)$
D scalar fields on S providing coordinates on M

2-dimensional manifold called a world-sheet with co-ordinates σ^μ (may be compact)

We can define a string model as a one governed by the lagrangian [1]

$$L_I = \sqrt{\gamma^{(2)}}\, \gamma^{(2)\mu\nu}\, \partial_\mu X^m\, \partial_\nu X^n\, \eta_{mn}, \qquad (1)$$

where $\gamma^{(2)\mu\nu}$ is a metric of the world sheet and η_{mn} a flat metric of the target space. This model possesses a two-dimensional reparametrization and even conformal invariance. From the first sight it may look somehow trivial (as a free scalar fields theory), however since $\gamma^{(2)}$ is considered as an independent field its field equations provide constraints (energy-momentum tensor $T_{\mu\nu}$ of X^m's is zero) which make a theory highly non-linear.

Observe that since $T_{\mu\nu}=0$ its trace also vanishes which is equivalent to the above mentionec conformal symmetry of the theory. This symmetry however becomes anomalous on the quantum level unless D=26.

Therefore the theory can be consistently quantized only if the dimension of the target manifold is exactly 26. The dimension for which conformal anomaly is absent is usually called a critical dimension.

A usual way of generalizing of some physical theory is to enlarge its symmetry. The theory described by (1) has symmetries: a conformal symmetry on the world sheet and a local Lorentz one on the target space.

The obvious way of extending the world sheet symmetry is to have it supersymmetrized, i.e. to introduce a two-dimensional superconformal supersymmetry.

It can be done easily by extending the variable of (1) into corresponding supermultiplets:

$$\gamma^{(2)\mu\nu} \rightarrow (\gamma^{2\mu\nu}, \psi_\mu{}^{(2)}),$$

plus the field which gauges a superconformal symmetry which, however, decouples from the lagrangian;

$$X^m \rightarrow (X^m, \lambda^m, F^m) \qquad (2)$$

where $\psi_\mu{}^{(2)}$ is a two-dimensional gravitino, λ^m a Majorana spinor and F^m an auxiliary field. It turns out that a superconformal invariance of the resulting theory is again an anomalous one unless D=10. The theory governed by supersymmetrization of (1)

$$L_{II} = L_I + \text{"SUSY"}$$

is called superstrings[1] or heterotic strings[2] depending on some additional assumption we make. These theories are expected to be finite and since their low-energy limit seems to be a D=10 N=1 supergravity coupled to Yang-Mills fields (which is anomaly-free for Yang-Mills group $E_8 \times E_8$ or (SO(32)) we can consider them as (an) ultimate unification theories. Also a dimensional reduction down to 4 dimensions is expected to be consistent with phenomenology[3].

Even if one could consider the theories described above as quite satisfactory we can go further in generalizations of L_I. It can be done by extending a global Lorentz invariance in the target space into a local one i.e. by replacing a flat target manifold by a curved one with metric tensor $g_{mn}(x)$ point-dependent. Then the lagrangian L_{II} (2) changes into

$$L_{III} = \gamma^{(2)\mu\nu} \sqrt{\gamma}\, \partial_\mu X^m \partial_\nu X^n g_{mn}(x) + \text{"SUSY"}. \qquad (3)$$

Lagrangian (3) is invariant under the general coordinates transformation

$$\begin{aligned} & X^m \to X^m + \xi^m(x), \\ & g_{mn} \to \xi^{@}\partial_p g_{mn} + g_{mp}\, \partial_n \xi^p + g_{pn}\, \partial_m \xi^p \end{aligned} \qquad (4)$$

and the theory described by (3) is called a two-dimensional supersymmetric σ-model. If we quantize it by using the background field method[4], the effective lagrangian is an Einstein one plus terms proportional to the higher powers of Riemann tensor.

We can further modify a lagrangian (3) introducing two new fields that together with g_{mn} are contained in the bosonic spectrum of ten-dimensional supergravity namely the two-index antisymmetric tensor field A_{mn} and the scalar Φ. The resulting lagrangian reads

$$\begin{aligned} L_{IV} = \sqrt{\gamma}\, \gamma^{\mu\nu} \partial_\mu X^m \partial_\nu X^n g_{mn} + \varepsilon^{\mu\nu} \partial_\mu X^m \partial_\nu X^n A_{mn} + \\ + \Phi R^2 \sqrt{\gamma} + \text{"SUSY"}. \end{aligned} \qquad (5)$$

where $R^{(2)}$ is a curvature scalar of the world sheet. It turns out [5] that the effective quantum fields equation resulting from (5) are those of the bosonic part of D=10, N=1 supergravity with the additional terms non-linear in Riemann tensor and a field strength H_{mnp} of A_{mn}. Observe that if we do not introduce the additional scalar field [6] the term $\Phi R^{(2)}\sqrt{\gamma}$ breaks a superconformal invariance down to super-Poincaré symmetry. The former can be, however, re-established on the quantum level.

The reason of constructing σ-models described above was to have a direct correspondence between the resulting effective theory on the target space and the ten-dimensional supergravity.

Since the ten-dimensional supergravity contains also a fermionic part we should make a one additional generalization replacing the fields X^m by $X^M = (X^m, X^\alpha)$ [7] (X^α - anti-commuting), which means that we assume a target space to be a super-manifold, and change g_{mn} and A_{mn} by corresponding superfields. It follows that we can drop the last term in (5) since there is enough room for the field Φ in the superfields below and thus we have a final lagrangian [7]

$$L = G_{MN}\,\partial_\mu X^M \partial_\nu X^N \gamma^{mn}\sqrt{\gamma} + A_{MN}\,\partial_\mu X^M \partial_\nu X^N \varepsilon^{mn} + \text{"SUSY"}. \qquad (6)$$

The effective theory coming from (6) is not in direct correspondence with ten-dimensiona supergravity. The reason is that if we assume two-dimensional SUSY which is crucial from the point of view of superstrings, the supergeometry of the target space must be Riemannian (without torsion). Thus the effective model corresponds more to the Arnowitt-Nath approach to superspace [8] rather than to the direct Wess-Zumino one [9].

The first problem one should solve in our model is to find what is a critical dimension. To do so let us assume that the super target space is flat, i.e. $G_{MN} = (\eta_{mn}, C_{\alpha\beta})$ where $C_{\alpha\beta}$ is a charge-con- jugation matrix. Then using the Fujikawa method [10] we find that the contribution from D commuting fields X^m, D' anticommuting fields X^α and the ghosts to the factor that multiplies anomaly are respectively $^3/_4\,D$, $-\,^3/_4\,D'$, $-\,^{15}/_2$. It follows from the fact that anticommuting variables give the same results as commuting ones except for sign-flip. Thus

5. CONCLUSION

The result clearly shows that cosmic ray data contradict the assumption of the validity of scaling in the fragmentation region. The scaling is violated in such a way that the spectrum of the secondary particles becomes softer. This effect goes in the same direction as that following from the above given formula. The increase of the invariant cross-section in the central region is followed by a decrease of it in the fragmentation region. Somewhere in between there must be a cross over point. The accelerator observations practically do not pass that point and that fact sometimes leads to the statement about the existence of scaling in the fragmentation region simply because the invariant cross-sections for different energies appear to come together. In actual fact a closer look in the data shows that on the contrary they indicate a tendency to cross over since the slopes are different. The existence of the cross over point is strongly required by the cosmic ray data.

6. REFERENCES

Amenomori M et al. 1985, Proc. 19-th Int. Cosmic Ray Conf., La Jolla 6, 208 /and 348/. /The Mt. Fuji experiment./

Cocconi G, Koester L G, Perkins D H, 1961, Lawrence Radiation Laboratory High Energy Phys. Study Seminary, 28, part 2, UCID - 1444, 1.

Feynman R P, 1969, Phys. Rev. Lett. 23, 1415.

Machavariani S K, Nikolski S I and Chubenko A P, 1985, Proc. 19-th Int. Cosmic Ray Conf., La Jolla 6, 96. /The Tien Shan experiment./

Wdowczyk J, 1980, Proc. of Int. Seminar on Cosmic Ray Cascades, Sofia, 185.

Wdowczyk J and Wolfendale A W, 1972, Nature 236, 29.

Wdowczyk J and Wolfendale A W, 1979, Nuovo Cimento A 54, 433.

Wdowczyk J and Wolfendale A W, 1984, J. Phys. G: Nucl. Phys. 10, 257.

Wdowczyk J and Wolfendale A W, 1986, J. Phys. G: Nucl. Phys. - in press.

Wrotniak J A, Gaisser T K and Stanev T, 1985, Proc. 19-th Int. Cosmic Ray Conf., La Jolla 6, 328.

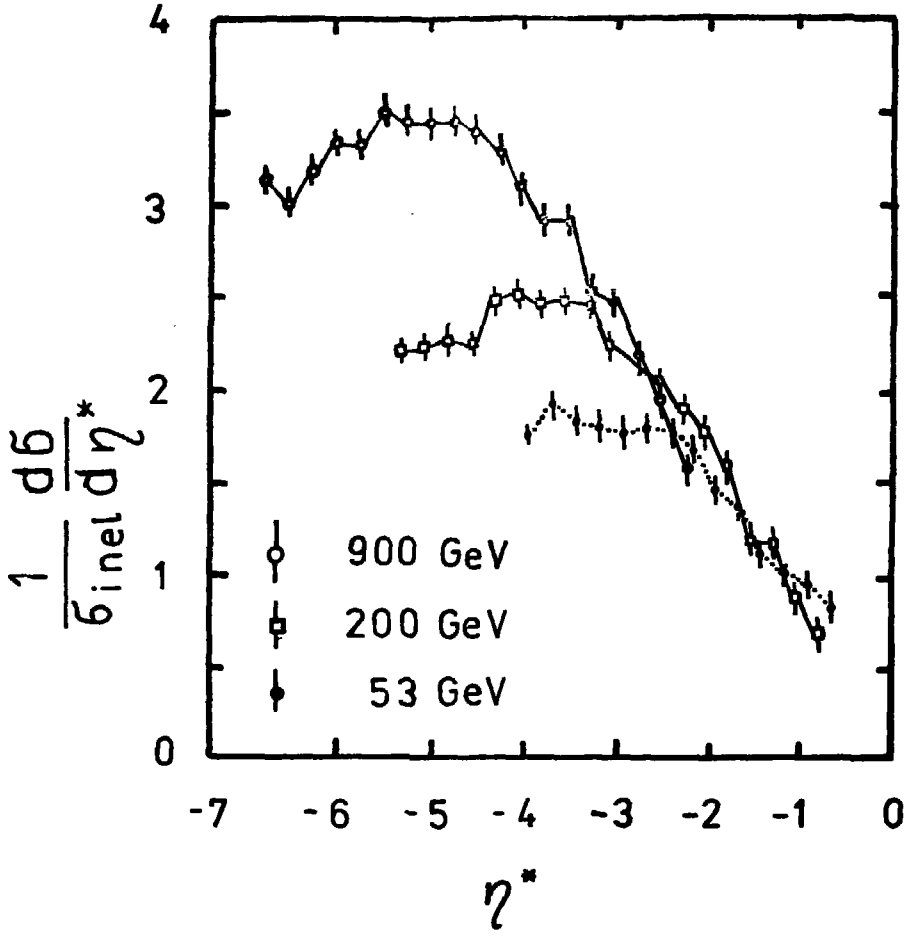

Fig 1. pseudorapidity density plotted against $\eta^* = \eta - y$ as a test of the scaling.

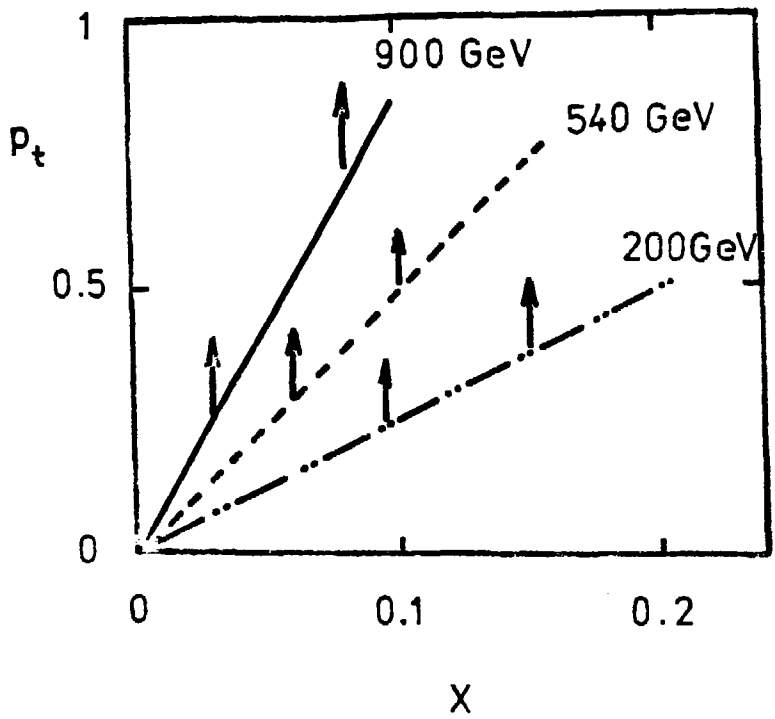

Fig. 2. Amplitude parameter p_t versus x for $\sqrt{s}$ = 900, 540 and 200 GeV. The solid lines are the parameterizations used in the UA2 experiment.

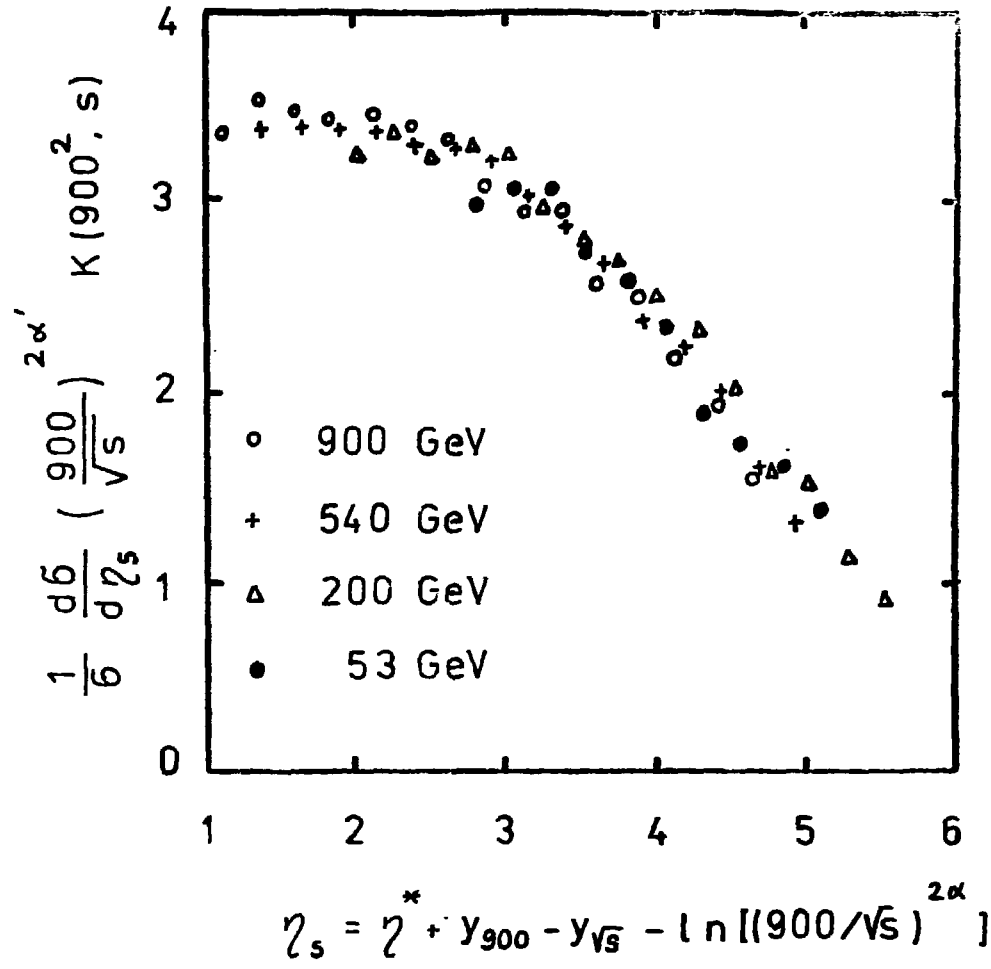

Fig. 3. Values of $\frac{1}{\sigma}\frac{d\sigma}{d\eta_s}\left(\frac{900}{\sqrt{s}}\right)^{2\alpha'} K(900^2, s)$ where $\alpha' = .1$ and $K/\pi = .5$, .74, .605, .55 respectively for $s = 53$, 200, 540 and 900 GeV, plotted against $\eta_s = \eta^* + y_{900} - y_{\sqrt{s}} - \ln[(900/\sqrt{s})^{2\alpha}]$ where $\alpha = 0.206$. The last value follows from $\alpha' = .1$ if the allowance for increasing $\langle p_t \rangle$ is made. Here it is assumed that $\langle p_t \rangle = .388(s/900)^{.224}$.

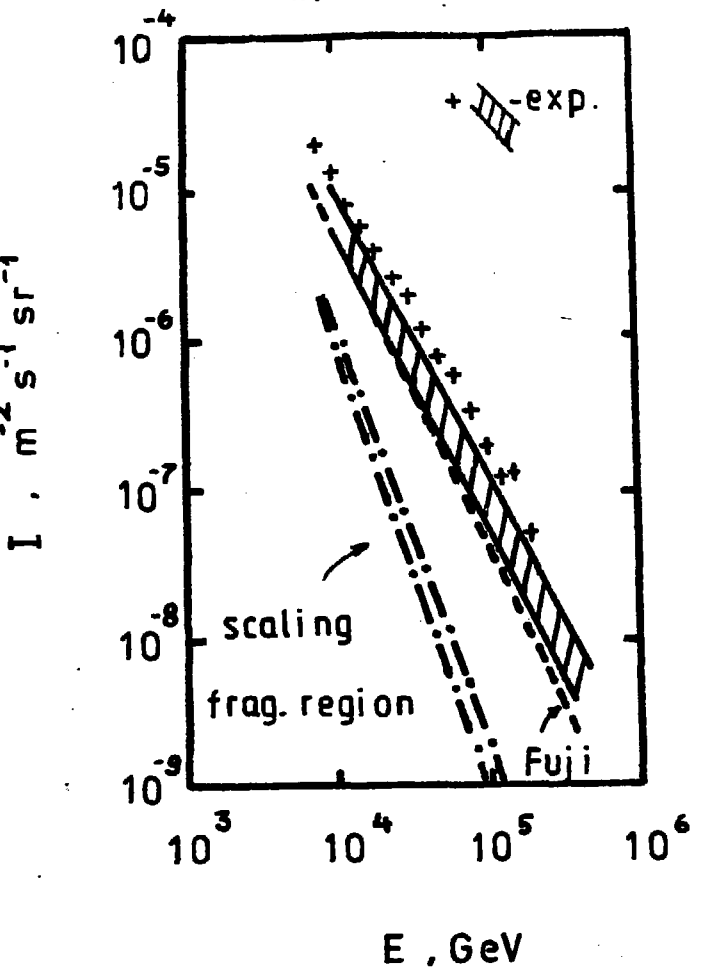

Fig 4. Hadron spectra relaxed to the depth of Mt. Fuji experiment /650 g cm^{-2}/. Experimental data of Machavariani et al /1985/ marked by points and those of Arenomori et al. /1985/ /dashed area/ are compared with the predictions based on the assumption of scaling validity in the fragmentation region. The two lower lines give the limits of the predictions. The effect of Mt. Fuji primary mass composition alone is also marked.

COSMIC MUONS AND NEUTRINOS.

NEUTRINOS FROM CYGNUS X-3

J.Kempa

University of Łódz, Department of Physics
90-236 Łodz, ul Nowotki 149-153 , Poland

J.Wdowczyk

Institute of Nuclear Studies,
90-950 Łodz, ul Uniwersytecka 5, Box 447,
Poland

ABSTRACT

Expected flux of high energy neutrinos from Cygnus X-3 is calculated on the basis of the model developed for the ultra high energy γ - ray emission.The expected fluxes are on the limit of the detectability by the existing underground devices and would be easily detectable by the future large detectors. The phase profiles of the expected neutrino fluxes are shown. The differences are pointed out between the ratios of the electron[1] to muon neutrino fluxes in the case of the atmospheric neutrinos and those originated in Cygnus X-3.

---

[1] In that paper under the term electron neutrino ν_e we understand together $\nu_e + \overline{\nu}_e$. Similarly for muon neutrino.

INTRODUCTION

The discovery of the ultra high energy γ - ray from Cygnus X-3 / Samorski and Stamm 1983 / and the latter indications at some underground proton decay detectors / Battistoni et al 1985 / of the existence of some sort of signal associated with Cyg X-3 phase caused very great excitement about that source. In particular a number of theoretical papers about the source itself and about the carrier particles have been published.

At the present moment only the photon hypothesis has some degree of understanding of the possible scenario. That hypothesis however is also facing several difficulties and is in clear contradiction with the underground observations. The last fact may not be so serious a drawback as the fact that the underground observations are still not well founded statistically. It should be remembered that this effect is not confirmed by other experiments for instance Baxan array / Chudakov 1986 / .

The scenario which seems to be the best is that based on the picture of the binary system with a compact object as one of the companions and relatively massive star as the other / Vestrand and Eichler 1982 /. The cosmic rays accelerated somehow by the compact object afterwards interact with the massive companion and produce secondaries which partly turn into ultra high energy γ - rays. In those interactions are also produced different particles. In appears that anong those an important role can be played by neutrinos firstly becouse in principle they can be detected at the Earth and secondly since there exists the possibility that they can play an important role in the stabilisation of the star as whole / Stecker et al 1985 /.

The possible flux of neutrinos has been calculated by Gaisser and Stanev 1985 using some sort of semi - scaling model. In the present work we describe results of calculations based on a model which better describes both accelerator and cosmic ray data.

ASSUMPTIONS ABOUT CYGNUS X-3 SOURCE

It has been assumed that the parameters characterising Cyg X-3 were as follows:

$$R = 2\ R_{\odot} = 1.4\ 10^{9}\ m \quad : \quad r = 1.2\ R = 1.7\ 10^{9}\ m$$

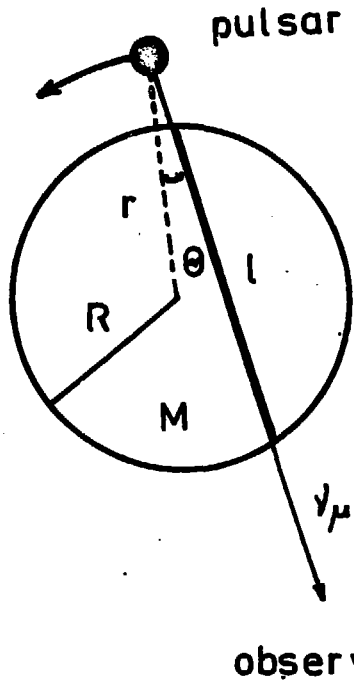

Fig.1 The schematic view of the Cygnus X-3 binary system. The symbol used in the paper are indicated.

$$M = 2\ M_\odot = 4\ 10^9\ kg \quad : \quad -57^\circ \lesssim \theta \lesssim 57^\circ$$

The distance Cygnus - Earth ~ 10 kpc.

The density of matter in the companion as a function of distance is taken as

$$\varrho = \varrho_0 \exp\left(-12\ x / R\right) \quad : \quad \varrho_0 = 38\ g/cm^3$$

In the center of the star there is a region with density of order of ϱ_0.

In the present calculations from the two discussed spectra the power law one has been chosen; the other being the monoenergetic one proposed by Hillas 1984.

It was aasumed that the total energy output of the cosmic source is $2\ 10^{40}$ erg/s for the energy above 10^8 eV. The actual shape of the energy spectrum is

$$j(E)\ dE = A \cdot E^{-2}\ dE\ ,$$

where A is obtained from the expression

$$\int_{.1}^{10^9} E \cdot j(E)\, dE = 1.25\ 10^{43}\ \text{GeV/s} .$$

The distribution of the matter as function of the angle between the direction of the beam and the straight line connecting the center of stars is shown in figure 2. It ranges from 0 to $1.9\ 10^{12}$ g/cm^2 .

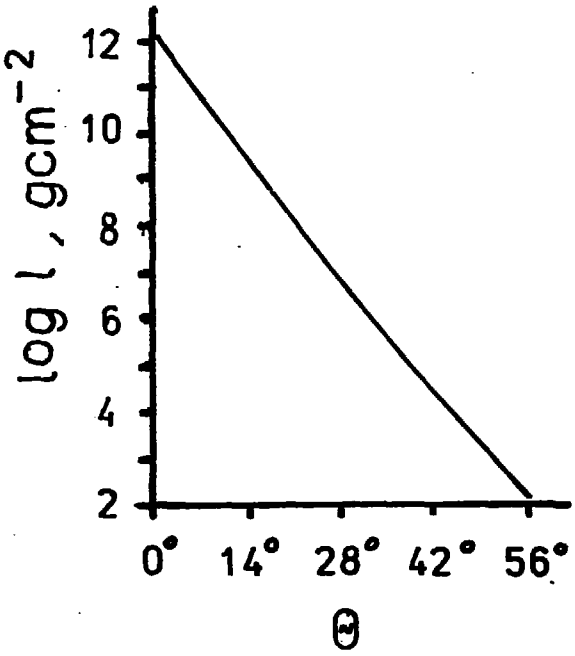

Fig.2 Column density of the matter in the star along the direction towards the Earth as the function of the angle Θ .

THE MODEL OF HIGH ENERGY INTERACTION

The model applied in the calculations is based on the scaling violation picture suggested by Wdowczyk and Wolfendale /1984/ . The parametrization of the formula is taken from the accelerator data up to $\sqrt{s}$ = 900 GeV / $4.5\ 10^{14}$ eV in lab system /.

That model has been verified in cosmic ray investigations . In particular the verification has been done in our work / Kempa and Wdowczyk 1985 / in respect to cosmic ray muons in the atmosphere . In

observations.

The flux of the horizontal atmospheric neutrinos

$$j_{\nu_\mu} \sim 10^{-7}\ cm^{-2}\ s^{-1}\ ,$$ / Chudakov 1986 /

is in good agreement with the calculations.

It can be concluded that the discussed model gives a description of the experimental data on cosmic ray muons and neutrinos produced in the atmosphere .

THE RESULTS

As it was stated earlier the object of the present calculations is to obtain the expected flux of the neutrinos from Cyg X-3 . The calculations were performed assuming that the companion is a source of cosmic rays with a flat spectrum / $j(E)\,dE \sim E^{-2}$ / extending up to at least 10^{18} eV. The transport equations of the cosmic rays in the matter of massive companion have been solved by the same method as that used in the calculation of the atmospheric muons and neutrinos / details can been found in Kempa and Wdowczyk 1985 /. All the decay

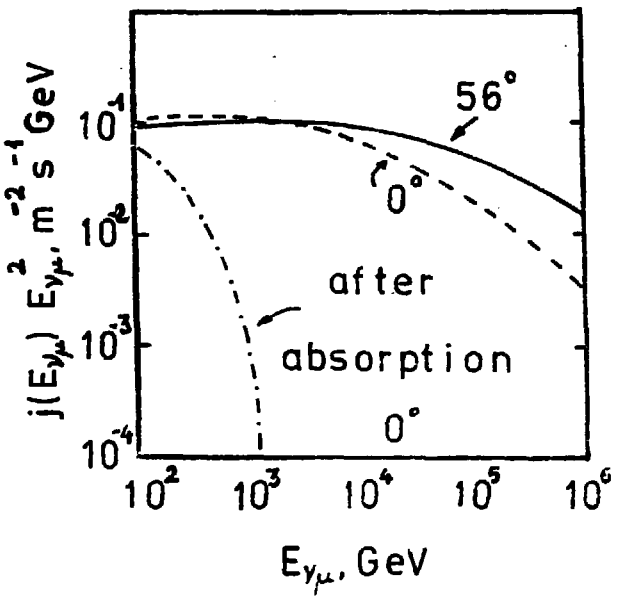

Fig.4 The neutrino production spectra at Cyg X-3 , for $\Theta = 0°$ and $56°$. The spectrum modified by the absorption in the star is also marked .

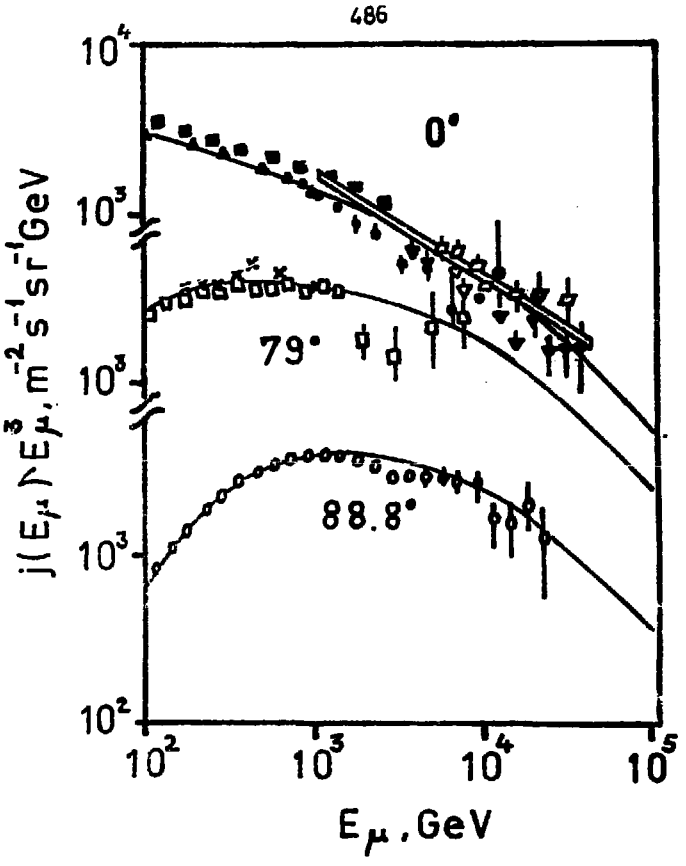

Fig.3 Atmospheric muon energy spectra for various zenith angles. Figure is taken after Kempa and Wdowczyk 1985. The experimental data are taken from following works:

at $\theta = 0^\circ$ Thompson et al /1977/,Allkofer et al /1971/,Khalchukov et al /1985/,Khrenov /1977/,Ivanenko et al / 1985 / , Krishnaswamy et al /1983/;

at $\theta = 79^\circ$ Jokish et al /1979/, Allkofer et al /1981/;

at $\theta = 88.8^\circ$ Matsuno et al /1984/ .

figure 3 taken from that work the results of calculations are compared with the data from various experiments. The agreement with the predictions is really very good. It should be of course remembered that the agreement is also dependent on assumptions concerning primary mass composition. However the mass composition taken is based on EAS data / Gawin et al 1984 / and is in good agreement with JACEE

processes which can be sources of neutrinos / $\pi^{\pm}, K^{\pm}, K^{o}$ / and have probability of occurence higher then 10^{-2} were taken into account .

The cascades originated in the external part of the star are absorbed not far from the surface with exception of the neutrinos which penetrate deep into but eventually are also absorbed / the exceptions here are only the most outer parts of the star where the thickness of the matter traversed is relatively small see figure 2 / .

The effect of the neutrino absorption in the companion star is shown in figure 4. For the neutrinos crossing the central part of the star, the star is practically opaque for all neutrinos with energies above 10^3 GeV . The absorption has been calculated assuming that the cross section for the neutrino interaction is increasing with energy according to the formula / Gaisser and Stanev 1985 /:

$$\sigma_y^{tot} = \frac{0.7\ 10^{-38}\ E}{1 + E\left(\frac{M_W^2}{2 m_p} \ln (E/50)\right)} .$$

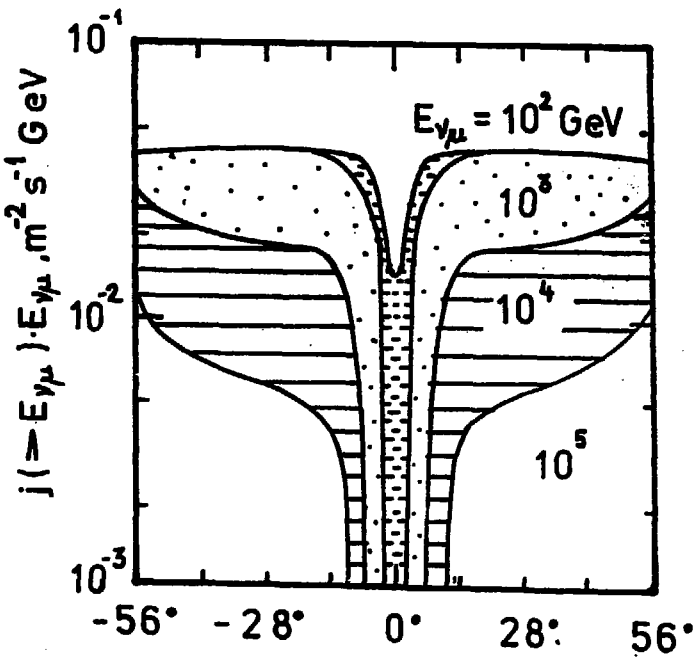

Fig.5 The neutrino curves as a function of the angle Θ and neutrino threshold energy .

A similar formula is used to described the total cross - section of the antineutrino interactions. Those assumptions are indentical with those taken by Gaisser and Stanev .

The analysis has been done also for the hypothetical linear increase with energy of neutrino cross - section / σ_ν / E = const. / .

The obtained results are basically the same. The difference concerns only the spatial distribution of the deposition in the star .

In figure 5 there is shown the dependence of the muon neutrino fluxes as the function of the pulsar position on the orbit .The latter is described by the angle between the earth direction and the line joining the centers of the stars. It is seen that for relatively low energy thresholds Cyg X-3 is emitting neutrinos semi-uniformly for about 40% of its orbital period. For the higher energy thresholds the neutrinos are emitted more in the form of two spikes gradually becoming narrower when energy increases .

The obtained estimation of the flux $\sim 8\ 10^{-8}\ cm^{-2}\ s^{-1}$ gives some hope for the possibility of the detection by the large underground detectors / Baxan , IMB / .

THE RATIO OF ELECTRON / ν_e / TO MUON / ν_μ / NEUTRINO FLUXES

The large size detectors allow one to observe neutrinos interacting inside of them / or very close to their surface /. That in turn gives a possibility of detection and identification of the two types of neutrinos / ν_e and ν_μ /.

The ratio of $N\nu_e$ / $N\nu_\mu$ appears to be an interesting parameter as it allows for differentiation of the atmospheric neutrinos from those coming from Cyg X-3. For the atmospheric neutrinos that ratio in the case $E \gtrsim 1000$ GeV, is clearly below 0.1 . Our calculations here are in good agreement with calculations of other authors / Osborne 1966;Mitsui and Minorikawa 1985;Volkova 1983/ for different models. So that conclusion appears to be model independent. In figure 6 we show the dependence of the ratio $R = N\nu_e / N\nu_\mu$ on neutrino energy both for atmospheric neutrinos and for Cyg X-3 neutrinos.It is seen that for Cyg X-3 that ratio is at least 5 times higher then in the case of the atmospheric neutrinos .

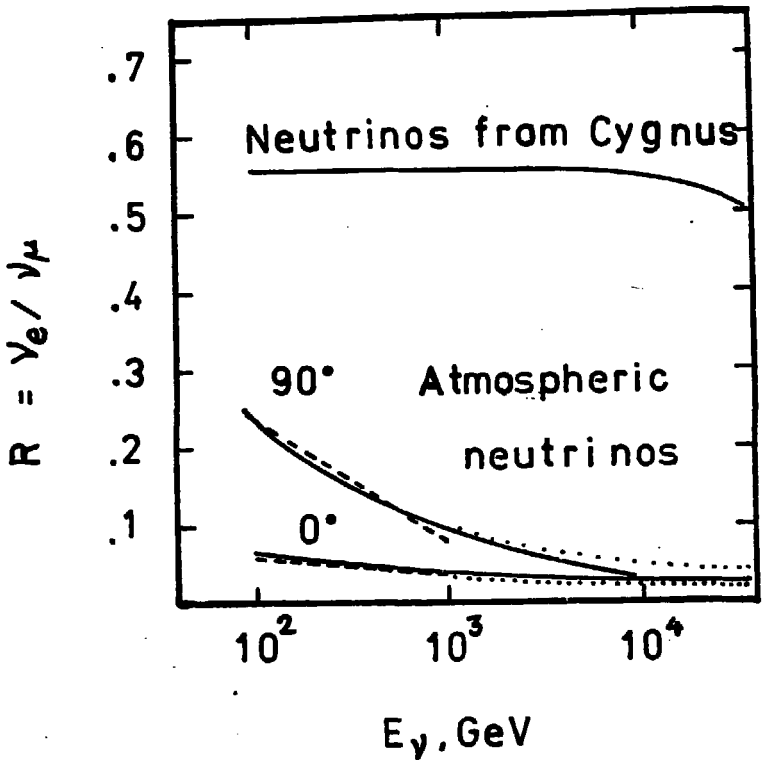

Fig.6 The ratio of the number of electrons neutrino to muon neutrinos as the function of neutrino energies / ------ Osborne 1966 ····· Mitsui and Minorikawa 1985, ———— Volkova 1983 /

CONCLUSIONS

The flux of neutrinos averaged over the orbital period of the Cyg X-3 of order of 10^{-7} cm^{-2} s^{-1} for 100 GeV threshold is on the limit of detectibility for the existing underground detectors. The flux would be detectable for larger detectors planned in future .

The detection of the neutrino flux from Cyg X-3 and its phase dependence could provide important information about model of the γ - ray and neutrino emission .

It is worthwile to notice that the results presented here are valid also in the case when the cosmic ray emissivity of Cyg X-3 is much lower and the high observed γ - ray intensity is due to strong beaming of the emission towards earth .

An additional possibility of verification of theoretical models and identification of neutrinos from point sources is the measurement of the ratio of the electron to muon neutrino.

In the considered scenario for Cyg X-3 and any other scenarios where the high energy photons originate as the result of π^0 decay the ratio $R = N_{\nu_e} / N_{\nu_\mu}$ must be a few times higher then that expected for atmospheric neutrinos .

ACKNOWLEDGEMENTS

The autors are indebted to Professor A.W.Wolfendale for discussions and comments and to Professor A.E.Chudakov for information about the Baxan experiment .

REFERENCES

Allkofer O C et al 1971 Proc.12th ICRC,Hobart,7,1314
---------- 1981 Proc.17th ICRC,Paris,10,321
Battistoni G et al 1985 Phys.Lett.,155B,465
Chudakov A E 1986 in press
Gaisser T K and Stanev T 1985 Preprint BA - 85 - 12
Gawin J et al 1984 Acta Universitatis Lodzienais,7,59
Hillas A M 1984 Lett. to Nature,312,50
Ivanenko I P et al 1985 Proc.19th ICRC, La Jolla,8,210
Jokish H et al 1979 Phys.Rev.D,19,1368
Kempa J and Wdowczyk J 1985 Proc.VIII Warsaw Symposium on Elementary Particles Physics,603
Khalchukov F F et al 1985 Proc.19th ICRC,La Jolla,8,12
Khrenov B A 1977 Proc.15th ICRC,Plovdiv,10,252
Krishnaswamy M R et al 1983 Proc.18th ICRC,Bangalore,11,450
Matsuno S et al 1984 Phys.Rev.D,29,1
Mitsui K and Minorikawa Y 1985 Proc.19th ICRC,La Jolla,8,144
Osborne J L 1966 Ph.D.Thesis,University of Durham
Samorski M and Stamm W 1983 Astrophys.J.Lett.,268,17
Stecker F W et al 1985 Lett. to Nature,316,418
Thompson G et al 1977 Proc.15th ICRC,Plovdiv,8,21
Vestrand W T and Eichler D 1982 Astrophys.J.,261,251

Volkova L V 1983 Proc.18th ICRC,Bangalore,7,22
Wdowczyk J and Wolfendale A W 1984 J.Phys.G:Nucl.Phys.,10,257

FERMION MASSES AND MIXING ANGLES FROM RADIATIVE CORRECTIONS IN SUPERSYMMETRIC STANDARD MODEL*

P. Krawczyk and A. Turski
Institute of Theoretical Physics
Warsaw University
Hoża 69, 00-681 Warsaw, Poland

Abstract

We show that in the framework of the supersymmetric standard model, masses of light quarks and leptons together with mixing angles can be generated by radiative corrections . The ratio of the electron mass to the up/down masses as well as the hierarchy of mixing angles are obtained in a natural way.

* Supported in part by Polish Ministry of Science, High Education and Technology, Problem CPBP01.03.

Introduction

The well known arguments suggest that the supersymmetric extension of the standard model may be a reasonable low energy theory (see Ref. [1] and references therein). In a widely accepted class of such models supersymmetry (SUSY) is explicitly broken by the additional soft terms in the Lagrangian. One can regard these terms as emerging from a theory with local supersymmetry at very high energies [2] but it is not necessary and we allow for the most general soft SUSY breaking.

All possible soft SUSY breaking terms have been classified [3]. They belong to one of the following classes:

$m_\lambda \overline{(\lambda^a)^c}\,\lambda^a$ - Majorana mass term for gauginos

$m^2_{ij}\,(\tilde{s}^{ia}_L)^*\,\tilde{s}^{ja}_L$ - mass term for left sfermions

$m'^2_{ij}\,(\tilde{s}^{i}_R)^*\,\tilde{s}^{j}_R$ - mass term for right sfermions

$h^k_{ij}\,H^a_k\,(\tilde{s}^{i}_R)^*\,\tilde{s}^{ja}_L + \text{h.c.}$ - coupling of left and right sfermions to Higgs bosons (generates mixing matrices for left and right sfermions).

The above terms allow practically arbitrary mass matrices for the up- and down-type squarks and sleptons. The only limitations come from experiment which suggests that sfermions of a given charge are almost degenerate in mass (differences do not exceed few GeV whereas masses must be larger than 20 GeV) [1,4].

Models with softly broken SUSY differ in a certain important aspect both from models with exact supersymmetry and those without supersymmetry. In the limit of exact SUSY all the masses are not renormalized, i.e. radiative corrections are zero [5]. On the other hand, when SUSY is absent, radiative corrections to masses are divergent and must be absorbed by renormalization procedure*. In the intermediate case considered by us, corrections are neither zero nor divergent. Rather they are finite and calculable. This suggest that some elements of the

---

* This is a general statement. Additional symmetries (e.g. chiral symmetry) can protect some masses from getting divergent contributions (see e.g. [6]).

tree level fermion mass matrix can be significantly modified by radiative corrections. We discuss this problem in the one-loop approximation.

Quark masses

Let us assume for simplicity that we have only one quark q and two squarks $\tilde{q}_1$ and $\tilde{q}_2$ with masses m_q, m_1 and m_2, respectively ($m_q \ll m_1, m_2$). In general, the physical states $\tilde{q}_1$ and $\tilde{q}_2$ are different from the interaction states $\tilde{q}_L$ and $\tilde{q}_R$ which are associated with two possible chiralities of the quark. The two sets of fields are related by an orthogonal matrix:

$$\begin{bmatrix} \tilde{q}_1 \\ \tilde{q}_2 \end{bmatrix} = \begin{bmatrix} \cos\theta_{LR} & \sin\theta_{LR} \\ -\sin\theta_{LR} & \cos\theta_{LR} \end{bmatrix} \begin{bmatrix} \tilde{q}_L \\ \tilde{q}_R \end{bmatrix} . \qquad (1)$$

The leading correction to the quark mass comes from the SUSY QCD and is given by the limit $p^2 = m_q$ of diagrams depicted in Figs. 1 and 2. Due to supersymmetry, divergent contributions from these two diagrams cancel each other. The crosses denote the places where the helicity flip must occur. In the diagram of Fig. 1 the helicity flip is related to the mass of the quark, so this diagram is proportional to $g_S^2 m_q/16\pi^2$ (where g_S is called the strong coupling constant renormalized at the gluino mass scale) and can be neglected in comparison with the tree-level mass m_q. In the diagram of Fig. 2 the helicity flip must occur on the gluino line. Also, the mixing between $\tilde{q}_L$ and $\tilde{q}_R$ states is required. The mixing is effective only when physical squarks differ in mass. Therefore, the finite contribution to the quark mass from the second diagram is proportional to the mass difference between squarks and to the gluino mass, but not to the quark mass itself. Observe that the $\tilde{q}_L$ - $\tilde{q}_R$ mixing violates the generalized chiral symmetry (for which chiral rotations of quarks are associated with identical transformations of $\tilde{q}_L$ and $\tilde{q}_R$ states). Thus, it is possible to generate non-zero one-loop contribution to the quark mass even if it vanishes at the tree level.

In the limit $\Delta m = m_1 - m_2 \ll \bar{m} = (m_1+m_2)/2$ the contribution to the quark mass from the diagram in Fig. 2 has the form:

$$\delta m_q = \frac{4}{3}\,\frac{1}{16\pi^2}\,g_s^2\,\sin(2\theta_{LR})\,\Delta m\,f\left(\frac{\bar{m}^2}{m_{\tilde{g}}^2}\right) \quad , \tag{2}$$

where the dimensionless function

$$f(x) = 2\sqrt{x}\,\frac{x-1-\ln x}{(1-x)^2}$$

has been plotted in Fig. 3. To estimate the value of δm_q we put

$$f\left(\frac{\bar{m}^2}{m_{\tilde{g}}^2}\right) \approx 1 \ , \quad \frac{g_s^2}{4\pi} \approx 0.1 \ , \quad \sin(2\theta_{LR}) = \frac{1}{\sqrt{2}} \tag{3}$$

and obtain

$$\delta m_q \approx 7.5\ \text{MeV} \cdot \left(\frac{\Delta m}{1\text{GeV}}\right) \quad .$$

This value is close to the current masses of the *up* and *down* quarks. Thus, it is possible that the masses of quarks from the first family come entirely from radiative corrections.

Lepton masses

Since leptons do not interact strongly the whole one-loop radiative corrections to their masses must be of electroweak origin. Therefore, we may expect them to be naturally one order of magnitude smaller than those for quarks. Similarly to the quark case, lepton mass corrections are dominated by diagrams analogous to that of Fig. 2 with quarks (squarks) replaced by leptons (sleptons) and the gluino replaced by one of the charginos or neutralinos. In the minimal supersymmetric extension of the standard model there are two physical charginos and four neutralinos which are the mixtures of the following interaction states: gauginos $\tilde{b}^0$ (bino), $\tilde{w}^0$, $\tilde{w}^\pm$ (winos) and higgsinos $\tilde{h}^0$, $\tilde{h}^0$, $\tilde{h}^\pm$ [1]. Of course, the contributions to lepton masses depend on these mixings. To estimate the leading corrections, let us notice that higgsinos interact very weakly whereas winos do not interact with right-handed leptons. Thus, the dominating contribution is given by the diagram with the bino. Let us assume for simplicity that the bino is the physical particle with the mass $m_{\tilde{b}}$. Then, we get

$$\delta m_l = \frac{1}{2}\,\frac{1}{16\pi^2}\,g'^2\,\sin(2\theta_{LR})\,\Delta m\,f\left(\frac{\bar{m}^2}{m_{\tilde{b}}^2}\right) \quad , \tag{4}$$

where g' is called the coupling constant of the U(1) gauge group.

Under the assumptions analogous to Eqs. (3):

$$f\left(\frac{\bar{m}^2}{m_{\tilde{g}}^2}\right) = 1 \quad , \quad \sin(2\theta_{LR}) = \frac{1}{\sqrt{2}} \quad ,$$

together with

$$\frac{g'^2}{4\pi} = \frac{\alpha}{\cos^2\theta_W} \approx \frac{4}{3}\,\frac{1}{137} \quad ,$$

Eq. (4) takes the form

$$\delta m_j \approx 0.27\ \text{MeV} \cdot \left(\frac{\Delta m}{1\text{GeV}}\right) \quad .$$

Once again, we have been able to produce a number close to the physical mass of the first family fermion (in this case - the electron). Therefore, it is natural to assume that the masses of first family fermions are of the radiative origin. This way, we get the proper mass hierarchy. The experimental values of the masses can be easily obtained by appropriate adjustment of the sfermion parameters.

Mixing angles

So far, we have been neglecting the existence of various families of fermions and the mixings between them. Now, we are going to relax this limitation. To simplify our discussion, let us assume the existence of only two generations. The more general case can be worked-out in a similar way

We assume that the tree-level quark mass matrices are diagonal but there is non-zero mixing between squarks of various families. Together with our earlier discussion, this means that the tree-level quark mass term has the form

$$(\bar{u}\ \ \bar{c}) \begin{bmatrix} 0 & 0 \\ 0 & m_c \end{bmatrix} \begin{bmatrix} u \\ c \end{bmatrix} + (\bar{d}\ \ \bar{s}) \begin{bmatrix} 0 & 0 \\ 0 & m_s \end{bmatrix} \begin{bmatrix} d \\ s \end{bmatrix} \qquad (5)$$

whereas the physical squarks are expressed in terms of right and left fields by the formulae (replacing Eq. (1))

$$\begin{bmatrix} \tilde{u}_1 \\ \tilde{u}_2 \\ \tilde{u}_3 \\ \tilde{u}_4 \end{bmatrix} = \begin{bmatrix} & U_{ij} & \end{bmatrix} \begin{bmatrix} \tilde{u}_L \\ \tilde{u}_R \\ \tilde{c}_L \\ \tilde{c}_R \end{bmatrix} , \quad \begin{bmatrix} \tilde{d}_1 \\ \tilde{d}_2 \\ \tilde{d}_3 \\ \tilde{d}_4 \end{bmatrix} = \begin{bmatrix} & D_{ij} & \end{bmatrix} \begin{bmatrix} \tilde{d}_L \\ \tilde{d}_R \\ \tilde{s}_L \\ \tilde{s}_R \end{bmatrix} .$$

In general, mixing matrices (U_{ij}) and (D_{ij}) are arbitrary. However, in the supergravity models they are determined by the tree-level quark mass matrix [2]. In particular, the diagonal quark mass matrix (c.f. Eq. (5)) would imply the lack of family mixing (both in the quark and squark sectors) up to all orders of perturbative expansion. Thus, it is essential for our approach to consider a model in which squark mixing is independent of the mass term for quarks.

Up to terms of order $O(g_s^2)$ there are two types of diagrams generating non-zero quark mixing. Diagrams of the first type (shown in Fig. (4)) contribute directly to the quark mass matrix. They are of the same order of magnitude as the diagram depicted in Fig. (2) (discussed previously), i.e. $g_s^2 \Delta m/16\pi^2$. The other type of corrections to the quark mass matrix is generated by the different renormalization of the left- and right-handed wave functions (c.f. Fig. (5)). These corrections are suppressed in comparison with those of Fig. (4) by the factor $m_q/m_{\tilde{g}}$ [*]. Within the approximation employed by us, they can be safely neglected. The resulting quark mass term at the one-loop level has the following structure:

$$[\bar{u} \quad \bar{c}] \begin{bmatrix} O(g_s^2 \Delta m/16\pi^2) & O(g_s^2 \Delta m/16\pi^2) \\ O(g_s^2 \Delta m/16\pi^2) & O(m_c) \end{bmatrix} \begin{bmatrix} u \\ c \end{bmatrix} \tag{6}$$

$$+ \quad [\bar{d} \quad \bar{s}] \begin{bmatrix} O(g_s^2 \Delta m/16\pi^2) & O(g_s^2 \Delta m/16\pi^2) \\ O(g_s^2 \Delta m/16\pi^2) & O(m_s) \end{bmatrix} \begin{bmatrix} d \\ s \end{bmatrix} .$$

---

[*] Diagram in Fig. (5) can be also drawn as a direct mass correction. One should add a cross denoting helicity flip on one of the external lines. In this case the proportionality to the quark mass is obvious.

Diagonalizing mass matrices of Eq. (6), we can find the quark mixing angle θ_C. It is of the order $O(g_S^2/16\pi^2\ \Delta m/m_S)$. Since the masses of the *up* and *down* quarks are generated radiatively we get

$$\theta_C = O(g_S^2/16\pi^2\ \Delta m/m_S) = O(m_d/m_S) = O(1/20) \quad . \tag{7}$$

The last number should be compared with the experimental value of the Cabibbo angle, $\sin\theta_C \approx 0.22$. The agreement isn't striking but we should remember that Eq. (7) gives only an order of magnitude estimate. It is unnatural to expect that Δm_{ij} for each pair of squarks is exactly the same. With different Δm's the factor of 4 can be easily generated leading to a good agreement with the experimental value [*].

Eq. (7) is only slightly modified if more families are taken into account. In this case the mixing of the n-th quark with lighter quarks is of the order

$$O(g_S^2/16\pi^2\ \Delta m/m_{q_n}) = O(m_d/m_{q_n})$$

Thus, mixing angles of heavier quarks are naturally smaller then those of lighter ones. This way we reproduce the observed pattern of the mixing matrix.

References

[1] H. E. Haber and G. L. Kane, Phys. Rep. 117 (1985) 75.

[2] J. Ellis, Lectures presented at the Advanced Study Institute on Quarks, Leptons and Beyond (1983);
J. Ellis, Talk presented at the 4th Workshop on Grand Unification, Brown University, Providence (1984).

[3] L. Girardello and M. T. Grisaru, Nucl. Phys. B194 (1982) 65.

[4] A. Campbell, Phys. Rev. D28 (1983) 209.

[5] J. Wess and B. Zumino, Phys. Lett. 49B (1974) 52;
J. Iliopoulos and B. Zumino, Nucl. Phys. B76 (1974) 310;
S. Ferrara, J. Iliopoulos and B. Zumino, Nucl. Phys. B77 (1974).

[6] M. Olechowski, *these proceedings*.

[7] S. Pakvasa and H. Suguwara, Phys. Lett. 73B (1978) 61.

[*] Relations of the type of Eq. (7) have been also discussed in the framework of models with discrete flavour symmetries, see e. g. Ref. [7].

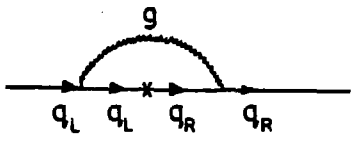

Fig. 1

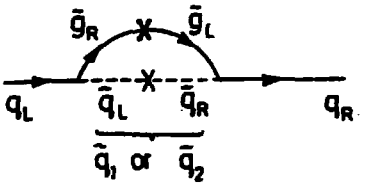

Fig. 2

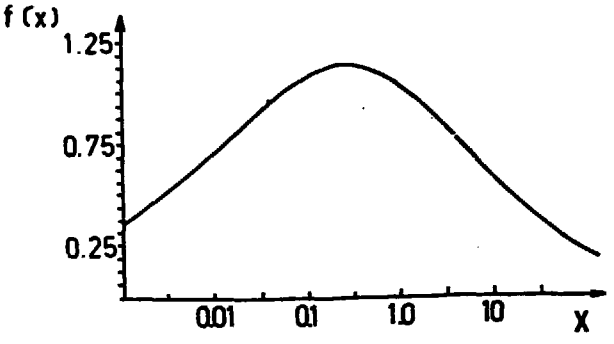

Fig. 3

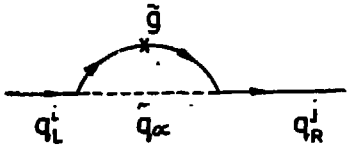

Fig. 4

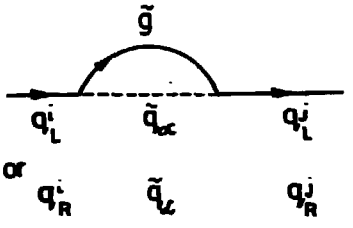

Fig. 5

Lifetimes of Heavy Mesons and the Kobayashi-Maskawa Matrix

Bernd Löhr
DESY, Hamburg, FRG

I. The Kobayashi-Maskawa Matrix ; Part 1

Throughout this talk the expression "heavy meson" is used for mesons containing at least one charm or bottom quark or the respective antiquark. In general quarks are not stable. They decay by their couplings to the weak charged current. The mass eigenstates of the quarks are however different from the weak eigenstates to which the charged current couples. The relation between these two sets of eigenstates is given by the Kobayashi-Maskawa matrix.

$$\begin{pmatrix} u \\ d' \end{pmatrix}_L, \begin{pmatrix} c \\ s' \end{pmatrix}_L, \begin{pmatrix} t \\ b' \end{pmatrix}_L \Longleftrightarrow \begin{pmatrix} u \\ d \end{pmatrix}_L, \begin{pmatrix} c \\ s \end{pmatrix}_L, \begin{pmatrix} t \\ b \end{pmatrix}_L$$

weak eigenstates mass eigenstates

By convention the mass mixing in the left handed weak isodoublets is chosen to occur only between the charge -1/3 members of the isodoublets.

$$\begin{pmatrix} d' \\ s' \\ b' \end{pmatrix} = \begin{pmatrix} V_{ud} & V_{us} & V_{ub} \\ V_{cd} & V_{cs} & V_{cb} \\ V_{td} & V_{ts} & V_{tb} \end{pmatrix} \begin{pmatrix} d \\ s \\ b \end{pmatrix}$$

For the presently known three generations of quarks the matrix V is a unitary 3 × 3 matrix with four real parameters. M. Kobayashi and K. Maskawa parametrized this matrix [1] in terms of three real angles and one complex phase.

$$V = \begin{pmatrix} c_1 & -s_1c_3 & -s_1s_3 \\ s_1c_2 & c_1c_2c_3 - s_2s_3e^{i\delta} & c_1c_2s_3 + s_2c_3e^{i\delta} \\ s_1s_2 & c_1s_2c_3 + c_2s_3e^{i\delta} & c_1s_2s_3 - c_2c_3e^{i\delta} \end{pmatrix}$$

$$s_i = sin\theta_i,\ c_i = cos\theta_i;\quad i = 1,\ldots,3$$

The parameters of this mixing matrix can be determined by analyzing processes which involve

weak charged current interactions. From the experimental point of view there are two kinds of such processes.

- The "weak production" processes, like e.g. deep inelastic lepton nucleon scattering, shown in fig. 1a. The measured quantity is the cross section.
- Decays of quarks, as shown in fig. 1b. In this case the experimentally determined quantity is the lifetime.

In both cases a straightforward extraction of the K.-M. matrix elements is not possible because free quarks don't exist. In deep inelastic scattering experiments the target is always a nucleon and one has to know the structure functions of the bound quarks. The decays of quarks cannot be observed directly. Only the lifetimes of visible hadrons can be measured and it is a priori not clear how to relate them to hypothetical quark lifetimes.

For the determination of the matrix element V_{ud} mainly data on nuclear β decays and a comparison to the μ-decay have been used [2]. In the μ-decay the virtual W-boson couples to (μ, ν_μ) with full strength, as shown in fig. 2a. In a nuclear β-decay the W couples to the u quark proportional to V_{ud}, as indicated in fig. 2b. The result of a recent analysis [3] is

$$|V_{ud}| = 0.9729 \pm 0.0012$$

The determination of V_{us} involves processes with strange quarks. An analysis [4] of K_{l3} and hyperon decays leads to

$$|V_{us}| = 0.221 \pm 0.002$$

Under the assumption that only three generations of quarks exist one can determine $|V_{ub}|$ from unitarity, once $|V_{ud}|$ and $|V_{us}|$ are known.

$$|V_{ud}|^2 + |V_{us}|^2 + |V_{ub}|^2 = 1 \quad \Rightarrow \quad |V_{ub}|^2 = 0.005 \pm 0.003$$

The disadvantage of this procedure is that the large relative error, which makes the result compatible with zero, is mainly given by theoretical uncertainties in extracting $|V_{ud}|$ and $|V_{us}|$ from the data. Thus an improvement can only be achieved by the determination of $|V_{ub}|$ from the lifetimes of bottom hadrons.

For the determination of K.-M. matrix elements involving charm quarks one can use lifetime measurements of charm and bottom hadrons and charm production in deep inelastic scattering processes. In the rest of this talk I will report on lifetime measurements and concentrate mainly on results from e^+e^- storage ring experiments.

II. Lifetime Measurements of Charm Mesons at PEP and PETRA

The typical lifetime τ of charm mesons is of the order of $10^{-13}s$ to $10^{-12}s$. In the laboratory the mean decay length l of a hadron is $l = \gamma\beta c\tau$, with $\gamma = p/E$ and $\gamma = 1/\sqrt{1-\beta^2}$. At the center of mass energies of the PEP and PETRA storage rings one finds for the produced charm mesons a value for $\gamma\beta$ of 2 to 5. This leads to decay lengths of approximately $0.1mm$ to

1.0mm. High precision drift chambers offer a spatial resolution which is adequate to measure the tracks of the decay products and reconstruct the decay vertex for such decay lengths.

In the following I will describe the experimental methods applied to measure the lifetimes of various charm mesons in e^+e^- storage ring experiments and present results.

Measurement of the D^o-Lifetime

For the identification of D^o mesons in e^+e^- annihilation events one takes advantage of the charged D^* decay into D^o mesons [5].

$$D^{*+} \rightarrow D^o\pi^+; \quad BR = (49 \pm 8)\%$$

The D^o mesons subsequently decay mainly into the following final states

$$\begin{aligned} D^o \rightarrow \; & K^-\pi^+ && ; \; BR = (5.4 \pm 0.4)\% \\ & K^-\pi^+\pi^o && ; \; BR = (17.3 \pm 1.7)\% \\ & K^-\pi^+\pi^-\pi^+ && ; \; BR = (10.9 \pm 1.0)\% \end{aligned}$$

The mass difference $\Delta m = m_{D^{*+}} - m_{D^o}$ is hardly above the charged pion mass. This results in a very small Q-value for the D^* decay. The distribution of calculated mass differences between reconstructed D^* and D^o candidates exhibits a narrow peak for real D^*, D^o combinations. This can be seen in fig. 3, where TASSO data on the decay $D^o \rightarrow K^-\pi^+$ are shown. The small Q-value for the D^* decay not only facilitates the identification of D^o mesons but also helps in the reconstruction of the D^o decay vertex. It allows only a very small transverse momentum for the transition pion which therefore passes through the D^o decay vertex within the measuring accuracy. The situation is visualized in fig. 4. The transition pion can thus be used as an additional track in the fit for the decay vertex and for the determination of the D^o decay length.

Most of the present detectors at e^+e^- storage rings measure much more accurately the coordinates of a reconstructed vertex in a plane perpendicular to the e^+e^- beams (x-y plane) than in a plane containing the beam axis. The primarily measured quantity is the x-y projection l_{xy} of the decay length l. The direction of the D^o momentum can be determined sufficiently well to calculate the three dimensional decay length according to

$$l = \frac{l_{xy}}{sin\theta_D} \quad \text{with } \theta_D = \text{ polar angle of the } D^o \text{ direction}$$

Technically the determination of the decay length for an individual decay proceeds as follows. First the decay vertex is reconstructed and fitted in the x-y plane using the identified decay products and including the transition pion. Propagation of the measuring errors for the tracks results in an error matrix for the decay vertex position in the transverse plane. Second the origin of the D^o meson in this plane has to be determined. This is the decay vertex of the charged D^* meson which for all practical purposes coincides with the event vertex because the D^* lifetime is very short. The event vertex could in principle be determined from all tracks not coming from decays of long lived particles, e.g. K^o,Λ. However, given the measuring accuracy of present detectors, it is preferable to use a nominal event vertex determined by averaging over many events. The beam profiles in the x-y plane determine

then a probability distribution for individual event vertices around the nominal interaction point. This can be well described by a two dimensional Gaussian distribution with variances σ_x, σ_y which are calculable from the storage ring parameters. Typical values are $\sigma_x \approx 500\mu$ and $\sigma_y \approx 10\mu$. In this way one determines origin and decay point of the D^o, both with uncertainties described by error ellipses. The geometrical situation is shown in fig. 5. The most probable two dimensional decay length comes out to be

$$l_{xy} = \frac{x_v\sigma_{yy}t_x + y_v\sigma_{xx}t_y - \sigma_{xy}(x_v t_y + y_v t_x)}{t_x^2\sigma_{yy} - 2\sigma_{xy}t_x t_y + t_{xx}^2\sigma_{xx}}$$

with :

x_v, y_v : coordinates of decay vertex
t_x, t_y : direction cosines of the D^o momentum
σ_{ij} : quadratic sum of the error ellipses of decay vertex and event vertex

The individual decay time τ of the D^o is then

$$\tau = \frac{l_{xy}}{sin\theta_D} \cdot \frac{1}{\gamma\beta c}\ ; \quad \text{with } \beta = \frac{p_{D^o}}{E_{D^o}}$$

Fig. 6 shows a distribution of individual D^o decay times measured by the MarkII experiment [6]. The shape of this distribution is a result of a convolution of several contributions.

- The "prompt" D^o decays: These are the genuine D^o decays . They give rise to an exponential decay time distribution, folded however with a Gaussian distribution due to measurement errors.
- Background under the D^o signal: This amounts to approximately 10% to 30% depending on the decay mode. Its contribution to the decay time distribution is a Gaussian.
- D^* mesons coming from B meson decays: Approximately 5% of the identified D^o mesons originate from B meson decays via the chain $B \rightarrow D^* \rightarrow D^o$. Their contribution to the decay time distribution is a convolution of two exponentials and a Gaussian.
- Background containing tracks from B meson decays: The contribution of this background gives a non zero average decay time. Its shape is derived from a Monte Carlo simulation.

The lifetime τ_D of the D^o meson is determined from the measured decay time distribution by a maximum likelihood fit taking into account all the above listed contributions. Fig. 7 shows the collection of measured D^o lifetimes as they were presented at the 1985 International Symposium on Lepton and Photon Interactions in Kyoto [7]. Included are also measurements from fixed target experiments. The only new result from an e^+e^- experiment since the Kyoto conference comes from the TASSO collaboration [8]. Their updated value is $\tau_{D^o} = (4.3^{+2.6}_{-1.4} \pm 0.8) \cdot 10^{-13}s$.

Measurement of the $D^{\pm}$ Lifetime

For the charged D lifetime there exists up to now only one measurement from e^+e^- storage ring experiments. This is the MarkII result [9]. It was derived using the decay sequence

$$D^{*+} \rightarrow D^+\pi^0 \; ; \; D^+ \rightarrow K^-\pi^+\pi^+.$$

The difficulty with this final state is the detection of the low momentum neutral transition pion which is necessary to make use of the mass difference distribution for the identification of the $D^{\pm}$. All other results for the charged D lifetime come from fixed target experiments. Fig. 8 shows a compilation of $D^{\pm}$ lifetimes as presented at the Kyoto conference [7].

Measurement of the $F^{\pm}$ Lifetime

The production of the charmed strange meson $F^{\pm}$ in e^+e^- interactions has been reported by several experiments [10]. The only published $F^{\pm}$ lifetime measurement from storage ring experiments comes from the HRS collaboration [11]. The F mesons were identified by the decay

$$F^{\pm} \rightarrow \phi\pi^{\pm} \; ; \; \phi \rightarrow K^+K^-.$$

In total 17 F-decay vertices have been reconstructed. The result is

$$\tau_{F^{\pm}} = (3.5^{+2.4}_{-1.8} \pm 0.9) \cdot 10^{-13}s.$$

Fig. 9 shows this result together with two other values from fixed target experiments.

III. Lifetime Measurements of Bottom Hadrons at PEP and PETRA

At e^+e^- storage rings individual B mesons have been identified up to now only by experiments at CESR at Cornell and DORIS at DESY [12]. These storage rings operate at center of mass energies near the $b\bar{b}$ production threshold. The boost parameter γ for B mesons is very small and the decay lengths in the laboratory system are too short to be resolved by the used experimental techniques. At the PEP and PETRA storage rings no experiment succeeded so far in reconstructing individual B hadrons. For the measurement of B hadron lifetimes methods other than in the case of charm mesons have to be applied. Most methods to determine the bottom lifetime start with a procedure to select a data sample with enriched B hadron content. One way to achieve that is to exploit the momentum spectrum of leptons from semileptonic B hadron decays. Because of the high B hadron mass their transverse momenta w.r.t. the jet axis, which is approximately the B hadron flight direction, are large. Fig. 10 shows a Monte Carlo simulation result for lepton p_t spectra from decays of charm and bottom mesons. By selecting events containing identified leptons with $p_t \geq 1.0 GeV/c$ one

arrives at a data sample which is enriched with B hadrons. Other procedures for enrichment use the event topology of $b\bar{b}$ events which is determined by the large mass of B hadrons. As an example I will describe here the "boosted sphericity product" method used by TASSO [13]. Hadronic events from e^+e^- annihilations are devided into two jets. Each jet is then boosted approximately to its rest frame. A value of $\beta \approx 0.7$ has been found appropriate by Monte Carlo simulations for this transformation. For the particles of each jet the sphericity is calculated in the boosted frame. Jets containing bottom hadrons will have a large sphericity. By requiring that the product of boosted sphericities of an event is bigger than 0.1 one arrives at a data sample which contains approximately 32% $b\bar{b}$ events. 35% $c\bar{c}$ events and 33% u,d,s events. In addition one can prepare with the same method a B hadron depleted data sample by demanding the sphericity product to be less than 0.1. This is of advantage for comparison and studies of sytematic errors.

Once the enriched data sample has been prepared the most common way to determine the bottom lifetime is the impact parameter method. The impact parameter is the distance of closest approach of a track to the event vertex. Tracks originating from decays of long lived particles have large impact parameters. High transverse momentum tracks coming from the decay of heavy particles enhance the effect as shown in fig. 11a. Tracks from decays of long lived particles in general intersect the sphericity axis in that hemisphere which contains the jet the particle belongs to. For such tracks the impact parameters are positive. Because of measuring errors the intersection can be in the opposite hemisphere in which case the impact parameters are given a negative sign. The procedure is explained in fig. 11b.

Experiments which use the semileptonic decays of bottom hadrons to enrich the data sample generally analyze the impact parameter distribution of the lepton tracks. Fig. 12 shows such distributions from several experiments. The mean values of these distributions are positive and indicate contributions from long lived, heavy particles. In fig. 13 an impact parameter distribution is presented which was obtained by TASSO using the sphericity product method for enrichment and plotting the impact parameters of all tracks in an event. For comparison the same distribution is shown also for a bottom depleted data set. A clear difference can be seen.

A measurement for the bottom lifetime is obtained by comparing the mean value of the impact parameter distribution to Monte Carlo simulations with different bottom lifetimes as input parameters. Such a comparison is shown in fig. 14. Results for bottom lifetime measurements are collected in fig.15 which was presented at the Kyoto conference [7]. A weighted average of all results gives

$$\tau_b = (1.26 \pm 0.16) \cdot 10^{-12} s.$$

One remark is appropriate concerning this result. The experiments use different bottom enrichment procedures. This can result in different mixtures of various bottom hadron species in each data sample. If the different bottom hadrons have different lifetimes then the experiments do not measure all the same quantity. Fig. 14 shows that within the present experimental errors all results are still consistent with a unique bottom lifetime.

In addition to the impact parameter method several experiments tried alternative procedures to determine the bottom lifetime. Although individual bottom mesons cannot be identified yet at PEP and PETRA one can try to find candidates for decay vertices of long lived particles by combining a certain number of tracks. Tbe so derived unspecific decay

length distribution is still sensitive to the contribution of bottom hadron decays. By a comparison with a Monte Carlo simulation the bottom lifetime can be extracted. This has first been demonstrated by the Mark II experiment [14]. They used their data sample enriched with bottom hadrons by selecting high p_t lepton events. In each jet secondary decay vertices were searched for by combining at least three tracks with momenta $p \geq 600 MeV/c$. The obtained decay length distribution is shown in fig. 16. The Mark II result for the bottom lifetime from this method is

$$\tau_b = (1.25^{+0.26}_{-0.19} \pm 0.23) \cdot 10^{-12} s$$

This value is in good agreement with the world average.

The TASSO experiment used the same method of vertex candidate reconstruction but with an unbiased data sample, not enriched with bottom hadrons [15]. This avoids the systematic uncertainties in modelling the enrichment procedure in the Monte Carlo simulation. They took all combinations of three tracks not having the same charge. If several vertex candidates in one jet were found the one with the lowest χ^2 was chosen. From the obtained decay length distribution, which is shown in fig. 17 , they obtained the preliminary result

$$\tau_b = (1.29^{+0.37+0.26}_{-0.25-0.24}) \cdot 10^{-12} s.$$

The TASSO experiment applied still another method. It exploits the fact that if one bottom hadron is present in a jet the other jet must contain also one. This is because at PEP and PETRA energies bottom hadrons are the primary hadrons in the fragmentation chain. A simplistic picture of a typical e^+e^- annihilation event containing bottom mesons is shown in fig. 18. The B and $\overline{B}$ mesons, together with some other tracks, emerge from the event vertex. After some time each bottom meson decays into a charm meson and other particles at a secondary decay vertex. The charm mesons in turn decay to complete the observable final state. The sphericity axis of the event is a good approximation for the flight directions of the bottom mesons which are almost back to back. The intersections of tracks from the two jets with the sphericity axis cluster therefore at separate positions for events with bottom hadrons. The situation is illustrated in fig. 19. The average cluster positions r_1 and r_2 along the jet axis define a distance $\rho = r_1 - r_2$, which is called the dipole length of the event. Cluster positions can be positive or negative depending on which side of the event vertex they are located along the jet axis. In detail the determination of the dipole length procedes in several steps. First one determines the sphericity axis in the ususal way. Then tracks are given weights

$$g_i = \frac{sin^2 \alpha_i}{\sigma_i^2},$$

where α_i is their angle with the sphericity axis and σ_i is the error of the track fit. With these weighted tracks the sphericity axis is redetermined such that

$$\sum_{i=1}^{N} \frac{(r_i - \langle r \rangle)^2}{\sigma_i^2}$$

becomes a minimum. N is the number of tracks in the event. In a second step new cluster positions and the dipole length are recalculated using different weigths for the tracks

$$\tilde{g}_i = g_i \cdot g_i$$

where y_i is the rapidity of a track. This emphasizes tracks from bottom hadron decays because of the hard bottom fragmentation function. The resulting dipole length distribution is shown in fig. 20a. A comparison of the average dipole length with results of Monte Carlo simulations using different bottom lifetimes as input is displayed in fig. 20b. It yields a preliminary value [15] of

$$\tau_b = (1.62^{+0.32}_{-0.29} \pm 0.25) \cdot 10^{-12} s \ .$$

well in agreement with the other values quoted by the TASSO experiment.

IV. The Kobayashi-Maskawa Matrix ; Part 2

In the previous chapter it was explained how lifetimes of charm and bottom hadrons were measured in e^+e^- experiments. In this chapter we will discuss how the Kobayashi-Maskawa matrix elements can be extracted from the experimental results.

The simplest picture for the decay of a heavy meson is the spectator model. The meson is a bound state of, let's say, a heavy quark and a ligth antiquark. It is assumed that irrespective of the strong binding forces the heavy quark decays independently into a lighter quark and a virtual W boson and the light spectator antiquark does not influence this process. The lighter quark and the antiquark fragment into final state hadrons. The virtual W boson decays into a pair of leptons or quarks, the latter fragmenting into hadrons as an independent system. This is illustrated by the diagram in fig. 21. The spectator model predicts that the lifetimes of all hadrons containing the same species of heavy quarks should be equal. In the case of charm, where the lifetimes of individual types of particles have been measured, one finds however that the lifetimes of the D^o and the $D^\pm$ differ by roughly a factor of two. This means that processes other than those described by the spectator diagrams must contribute significantly.

Fig. 22 shows a collection of diagrams which in addition to the spectator diagrams can contribute to the D^o and $D^\pm$ decays. The exchange diagram exists only for the D^o decay and the annihilation diagram only for the $D^\pm$ decay. It is at present not clear to what extent these processes are responsible for the different lifetimes. The color mixing diagram exists for both decays. In the case of the $D^\pm$ mesons the final state quark configuration is the same as for the spectator process. The two processes therefore interfere. A quantitative analysis shows that this interference is destructive. This increases the $D^\pm$ lifetime w.r.t. the D^o. We see that one can at least qualitatively understand the difference in lifetimes of the charged and neutral D mesons.

The non spectator diagrams discussed above do not contribute to the semileptonic decays of D^+ and D^o mesons. Then at least the semileptonic decay rates should be equal. For the semileptonic decay branching ratios one finds:

$$\frac{BR(D^+ \to e^+\nu X)}{BR(D^o \to e^+\nu X)} = 2.3^{+0.5}_{-0.4} \pm 0.1$$

With the ratio of measured lifetimes

$$\frac{\tau_{D^+}}{\tau_{D^o}} = 2.07 \pm 0.23$$

one gets

$$\Gamma(D^- \to e^- \nu X) = (1.14 \pm 0.20) \cdot 10^{-10} MeV$$

$$\Gamma(D^0 \to e^+ \nu X) = (1.24 \pm 0.18) \cdot 10^{-10} MeV$$

Within the quoted errors these partial decay widths are indeed equal. This suggests that the respective K.-M. matrix elements can be obtained from the semileptonic decays of D mesons. The spectator model predicts:

$$\Gamma(D \to e\nu X) = \Gamma(\mu \to e\bar{\nu}\nu) \left(\frac{m_c}{m_\mu}\right)^5 [f_{ps}|V_{cs}|^2 + |V_{cd}|^2] \cdot f_{QCD}$$

with

$$f_{ps} = 0.5 \pm 0.1 \quad ; \quad \text{phase space factor}$$

$$f_{QCD} = 0.85 \pm 0.05 \; ; \quad \text{QCD correction factor}$$

Since there is only one measured value, the partial decay width, but two quantities, $|V_{cd}|$ and $|V_{cs}|$, to be determined, one needs extra information. The ratio $|V_{cd}|/|V_{cs}|$ can be obtained from an analysis of the momentum spectrum of leptons from charm decays (see fig. 10). Accounting for all uncertainties in the analysis, and using also data on charm production in neutrino nucleon scattering [16] one arrives at [17]

$$0.219 \leq |V_{cd}| \leq 0.225$$

$$0.973 \leq |V_{cs}| \leq 0.975$$

In the case of the bottom quark matrix elements one proceeds very similar. Here we do not have the problems of different bottom hadron lifetimes. The spectator model prediction, with all the numbers inserted already, is:

$$|V_{cb}|^2 = \frac{(2.78 \pm 0.16) \cdot 10^{-15}}{1 + R_B} \cdot \tau_b$$

$$|V_{ub}|^2 = \frac{R_B(1.23 \pm 0.09) \cdot 10^{-15}}{1 + R_B} \cdot \tau_b$$

where τ_b is measured in seconds and

$$R_B = \frac{\Gamma(B \to e\nu u)}{\Gamma(B \to e\nu c)}$$

The ration R_B can again be extracted from the lepton momentum spectrum of semileptonic bottom decays. Up to now only upper limits have been derived experimentally. Taking the limit $R_B \leq 0.08$, which was reported at the Kyoto conference [7] one finds, accounting for all uncertainties

$$|V_{ub}| \leq 0.008$$

$$0.037 \leq |V_{cb}| \leq 0.053$$

Using unitarity and the assumption that there are only three generations of quarks, one can now calculate the whole Kobayashi-Maskawa matrix. The present state of our knowledge on the matrix elements is summarized in [17].

After the determination of the K.-M. matrix elements for charm and bottom quarks one can make the following remarks:

1. The fact that the bottom quark lives much longer than the charm quark, inspite of its much bigger mass, is related to $|V_{cb}|$ being very small and $|V_{ub}| \ll |V_{cs}|$

2. We recognize that

$$\frac{|V_{ub}|}{|V_{cb}|} \ll \frac{|V_{cd}|}{|V_{cs}|} .$$

This means that the mixing is smaller in the higher generation.

Concluding this talk one can state that our knowledge of the Kobayashi-Maskawa matrix has very much improved with the results from lifetime mesurements of heavy quarks.

References

[1] M.Kobayashi, T.Maskawa, Prog.Theor.Phys. 49,652(1973)

[2] M.Roos, Nucl.Phys. B77,420(1974);
K.Kleinknecht, Proc. of the XVII Int.Conf. on High Energy Physics , p. III-23, London 1974, ed. J.R.Smith;
M.Nagels et al., Nucl.Phys. B109,1(1976)

[3] W.J.Marciano, A.Sirlin, Phys.Rev.Lett. 56,22(1986)

[4] H.Leutwyler, M.Roos, Z.Phys. C25,91(1984)

[5] S.Nussinov, Phys.Rev.Lett. 35,1674(1975);
G.J.Feldman et al., Phys.Rev.Lett. 38,1313(1977)

[6] J.M.Yelton et al., Phys.Rev.Lett. 52,2019(1984);
L.D.Gladney, SLAC-Report 279, March 1985

[7] E.H.Thorndike, 1985 Symposium on Lepton and Photon Interactions, Kyoto,Japan

[8] TASSO collaboration, DESY-Report 86-027

[9] L.D.Gladney, SLAC-Report 279, March 1985

[10] A.Chen et al., Phys.Rev.Lett. 51,634(1983);
M.Althoff et al., Phys.Lett. 136B,130(1984);
H.Albrecht et al., Phys.Lett. 153B,343(1985);
M.Derrick et al., Phys.Rev.Lett. 54,2568(1985)

[11] C.Jung et al., ANL-HEP-PR-86-01

[12] S.Behrends et al., Phys.Rev.Lett. 50,881(1983);
R.Giles et al., Phys.Rev. D30,2279(1984);
A.Chen et al., Phys.Rev. D31,2386(1985);
D.B.MacFarlane, H.Schröder, XXIst Rencontre de Moriond, ed. J.Tran Thanh Van, Les Arcs, France, and DESY-Report 86-067

[13] M.Althoff et al., Phys.Lett. 149B,524(1984)

[14] L.Golding, Ph.D. Thesis, LBL 1985;
W.T.Ford, Univ. Colorado Preprint COLO-HEP-87, and Proceedings of the Aspen Winter Physics Conference, 1985

[15] A.Caldwell, XXIst Rencontre de Moriond, Perspectives in Electroweak Interactions and Unified Theories, ed. J.Tran Thanh Van, Les Arcs, France, March 1986

[16] H.Abramowicz et al., Z.Phys. C15,19(1982)

[17] Review of Particle Properties, Phys.Lett. 107B.1(1986)

Figure Captions

Figure 1 a.) Diagram for the "weak production process" in deep inelastic lepton nucleon scattering.
b.) Diagram for the decay of heavy quarks.

Figure 2 a.) W-boson coupling in μ-decay.
b.) W-boson coupling in nuclear β-decay.

Figure 3 Mass difference plot for reconstructed D^*, D^o combinations.

Figure 4 Geometry of the $D^* \rightarrow D^o\pi^+$ and subsequent $D^o \rightarrow K^-\pi^+$ decays.

Figure 5 Schematic picture of the reconstruction of the most probable decay length.

Figure 6 D^o decay time distribution measured by MarkII.

Figure 7 Compilation of measured D^o lifetimes.

Figure 8 Compilation of measured D^+ lifetimes.

Figure 9 Compilation of measured $F^{\pm}$lifetimes.

Figure 10 Monte Carlo simulation of lepton p_t spectra from charm and bottom decays.

Figure 11 a.) Schematic drawing of bottom decays leading to tracks with large impact parameters.
b.) Definition of the sign of an impact parameter.

Figure 12 Impact parameter distribution for identified leptons.

Figure 13 Distribution of impact parameters from all tracks in an event as measured by TASSO using a data sample which is enriched by the sphericity product method. For comparison also the result from a depleted sample is shown.

Figure 14 Determination of the bottom lifetime by comparing the measured average impact parameter with Monte Carlo simulations by TASSO.

Figure 15 Compilation of measured bottom lifetimes.

Figure 16 Decay length distribution obtained by MarkII for secondary vertex candidates; enrichment of bottom content by high p_t leptons.

Figure 17 Decay length distribution obtained by TASSO for secondary vertex candidates; no enrichment procedure.

Figure 18 Simplistic picture of an e^+e^- annihilation event containing bottom mesons.

Figure 19 Definition of a dipole length of an e^+e^- annihilation event.

Figure 20 a.) Dipole length distribution measured by TASSO.
b.) Determination of the bottom lifetime from the measured average dipole length by comparison with Monte Carlo simulations.

Figure 21 Spectator model diagram for the decay of heavy mesons.

Figure 22 Non spectator diagrams contributing to the $D^{\pm}$ and D^o decays.

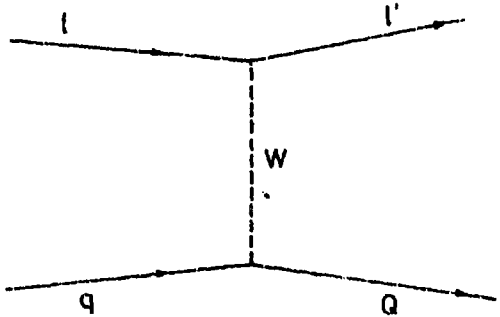

Fig. 1a) Diagram for "weak production"

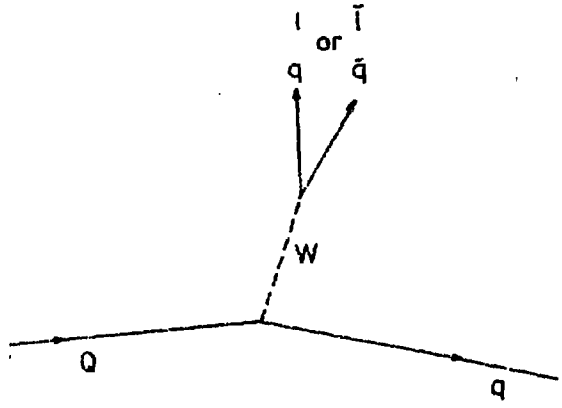

Fig. 1b) Diagram for the decay of heavy quarks

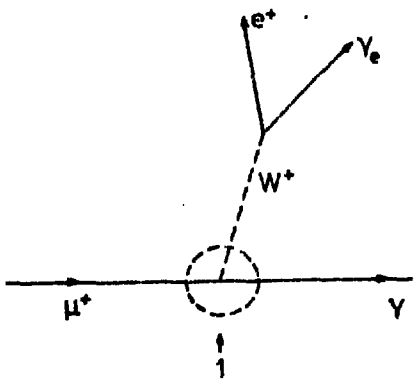

Fig. 2a) W - boson coupling in μ - decay

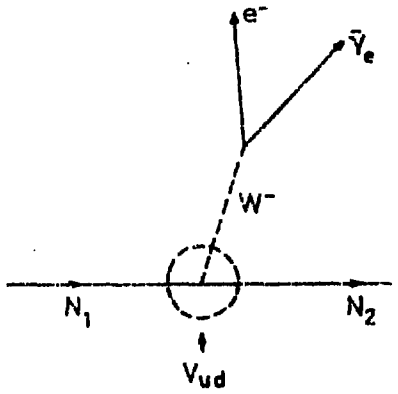

Fig. 2b) W - boson coupling in nuclear β - decay

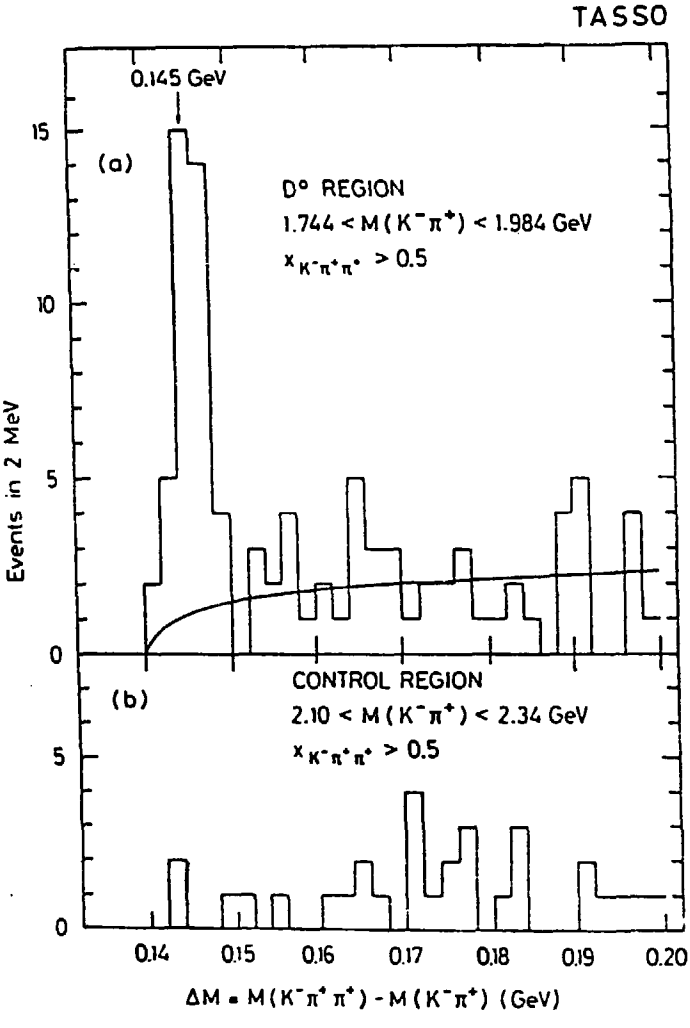

Fig. 3 Mass difference plot

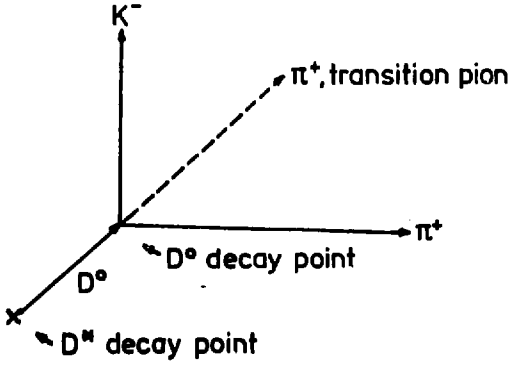

Fig. 4 Geometry of the decay
$D^* \to D^0\pi^+$, $D^0 \to K^-\pi^+$

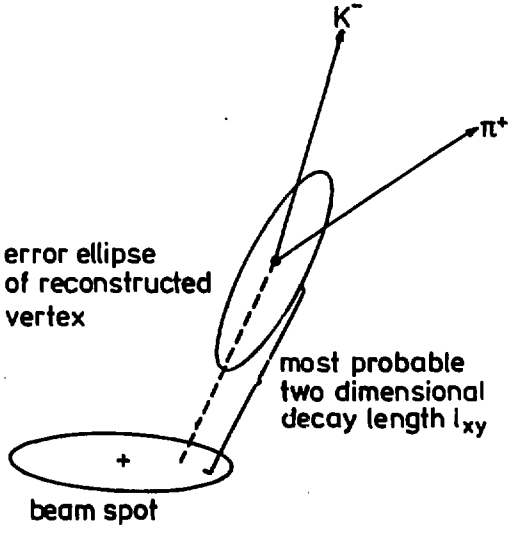

Fig. 5 Reconstruction of the
decay length

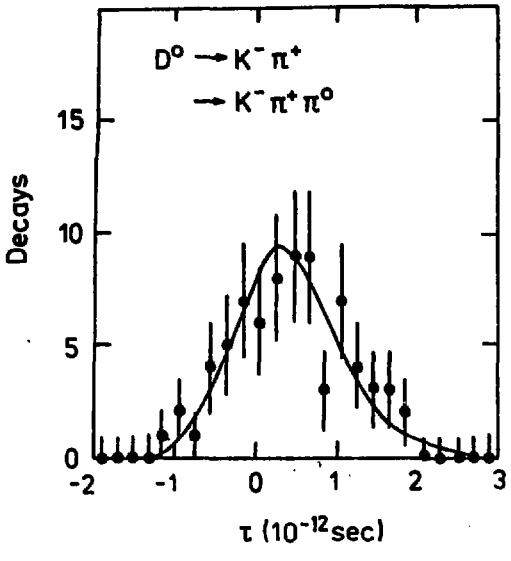

Fig. 6 D° decay time distribution from MARK II

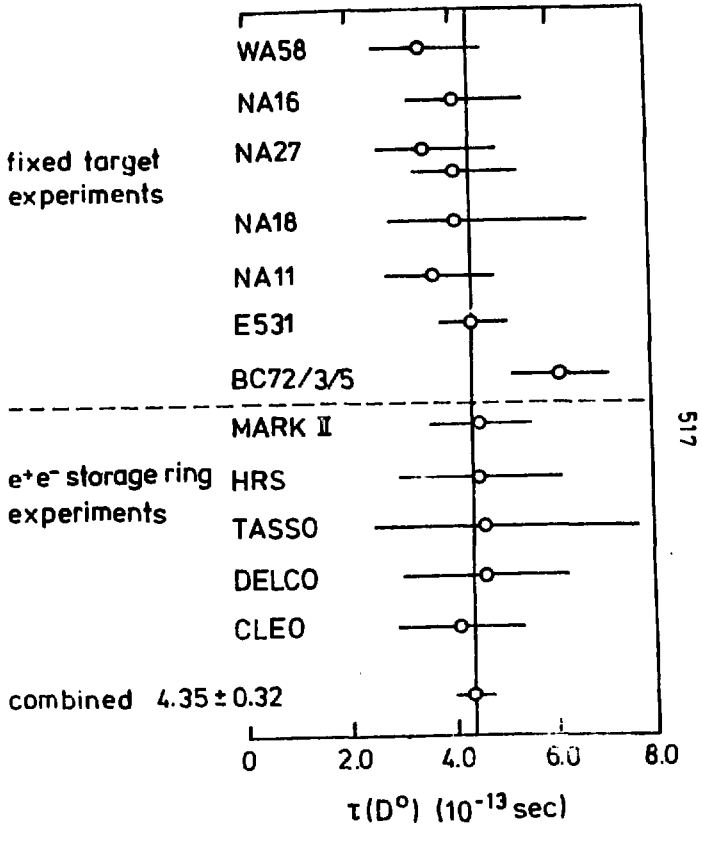

Fig.7 D° Lifetimes

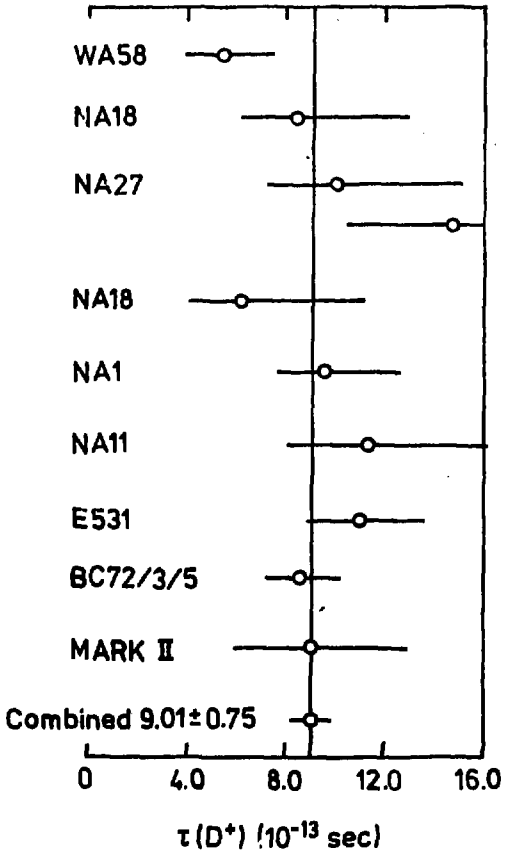

Fig. 8 $D^{\pm}$ Lifetimes

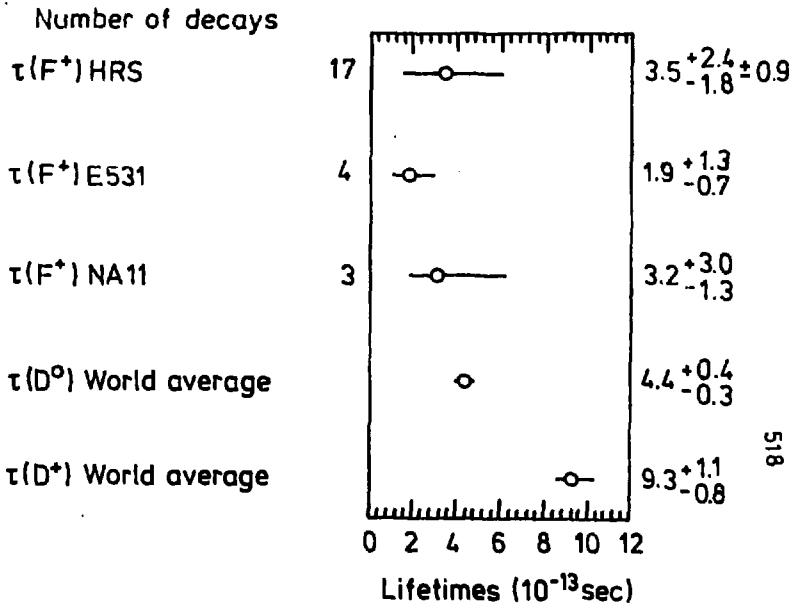

Fig. 9 $F^{\pm}$ Lifetimes

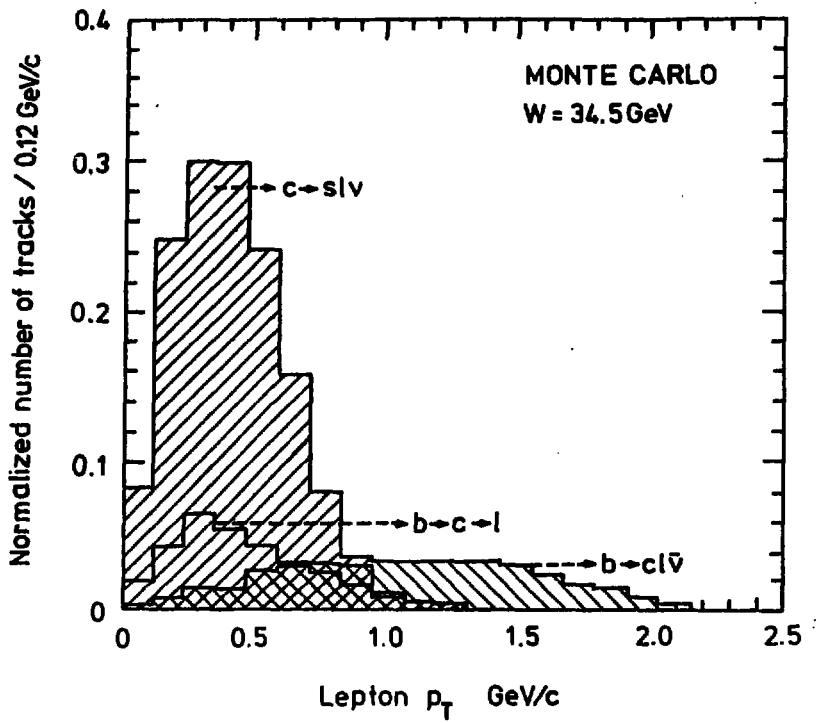

Fig. 10 Lepton p_T spectra from Monte Carlo simulation

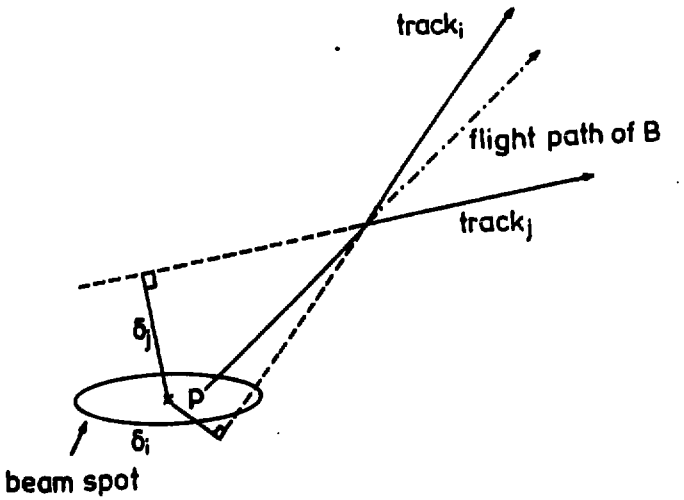

Fig. 11a) Geometry of bottom decays

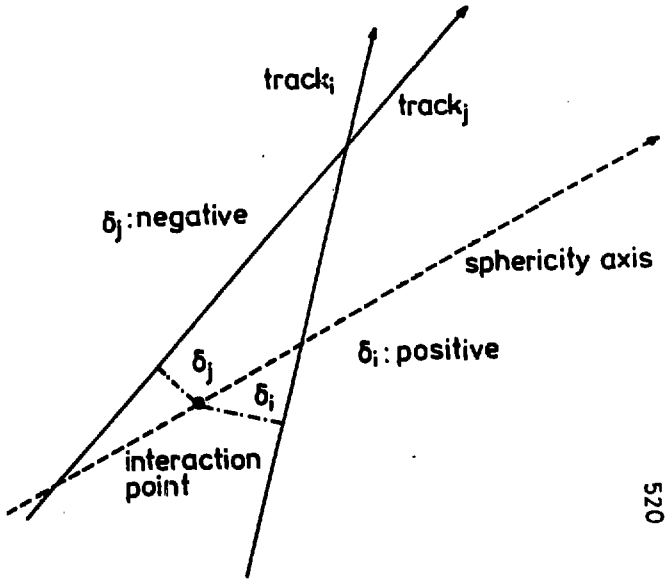

Fig. 11b) Definition of the sign of an impact parameter

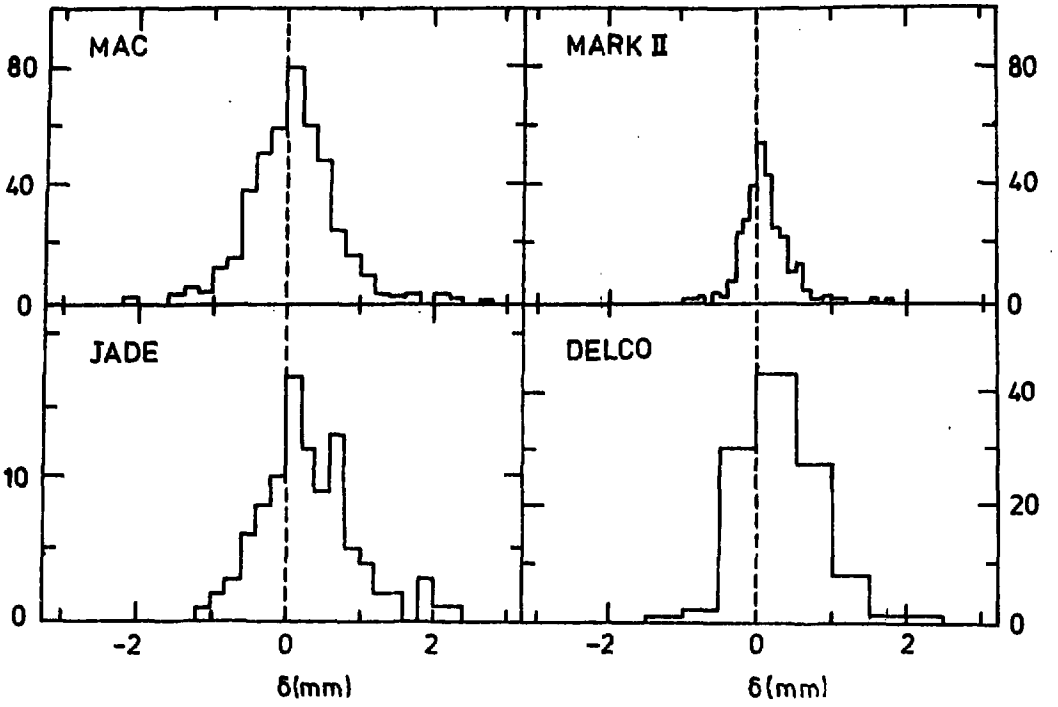

Fig. 12 Impact parameter distributions for high p_T leptons

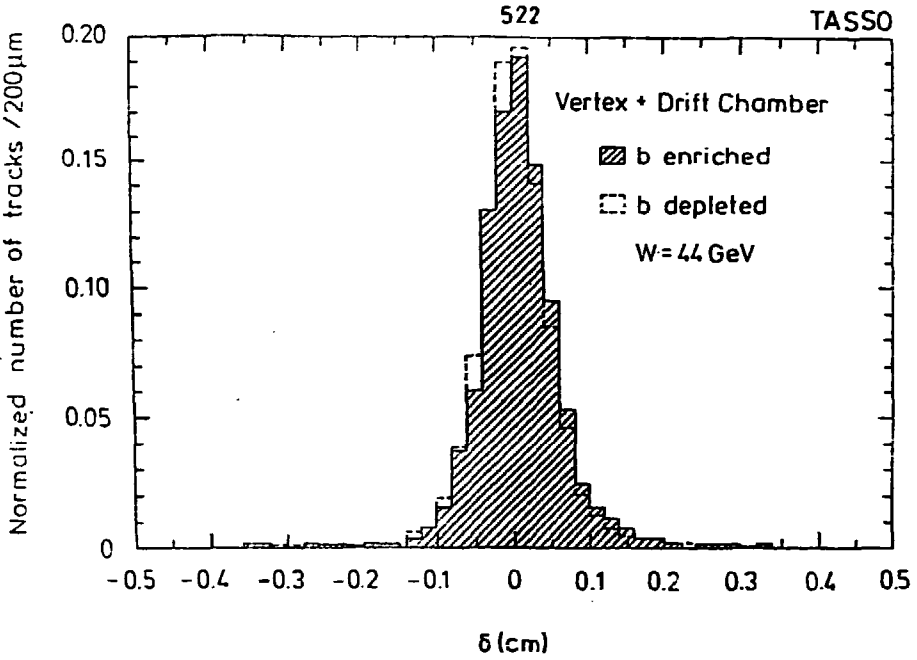

Fig. 13 Impact parameter distributions from TASSO

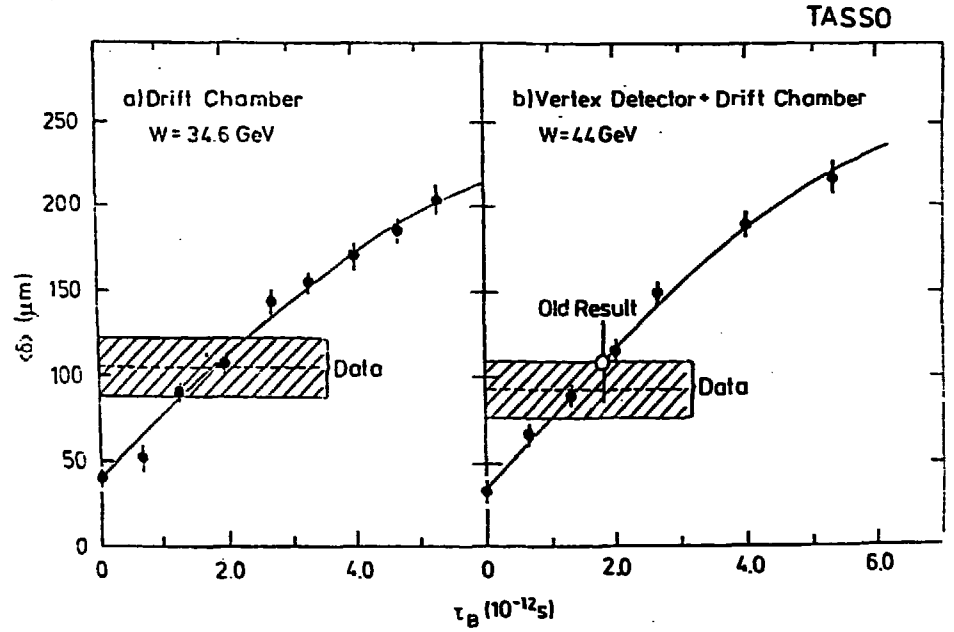

Fig. 14 Comparision of mean impact parameters with Monte Carlo simulations

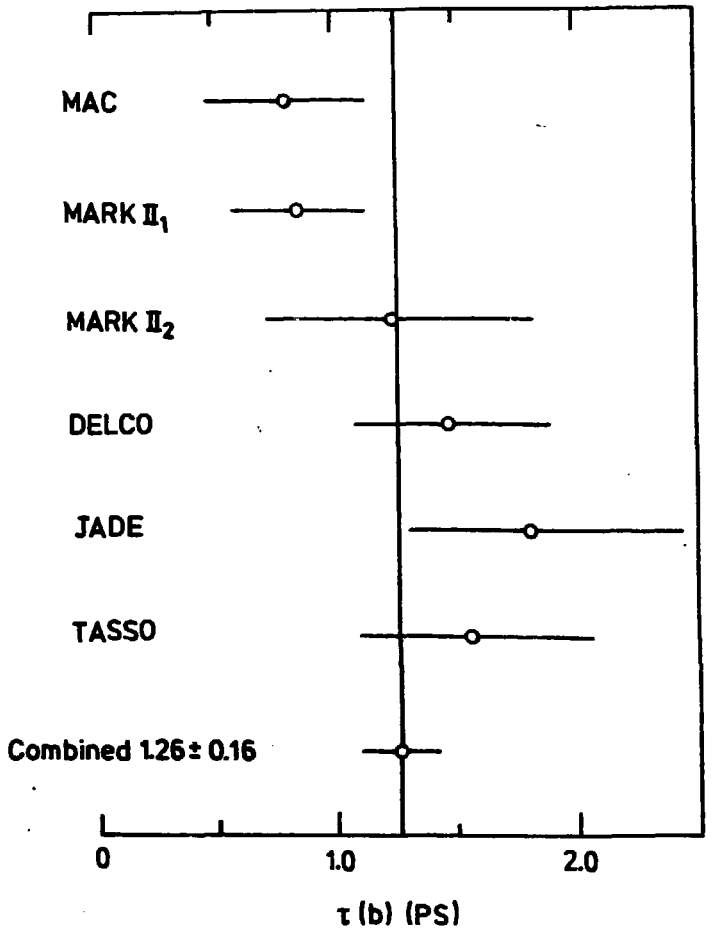

Fig. 15 Bottom hadron lifetimes

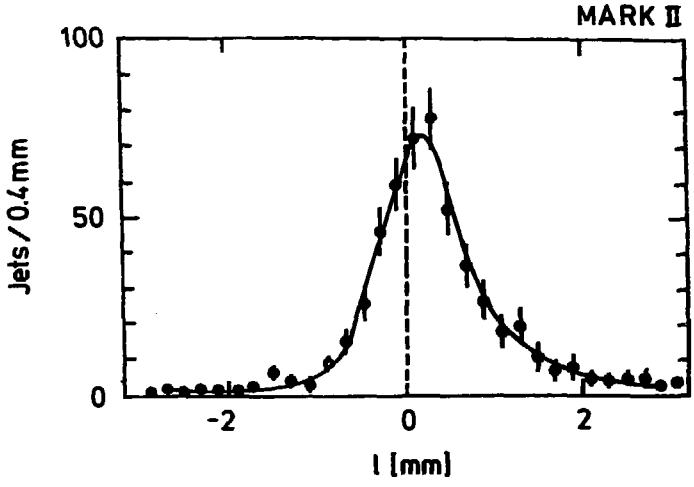

Fig. 16 Decay length distribution from MARK II

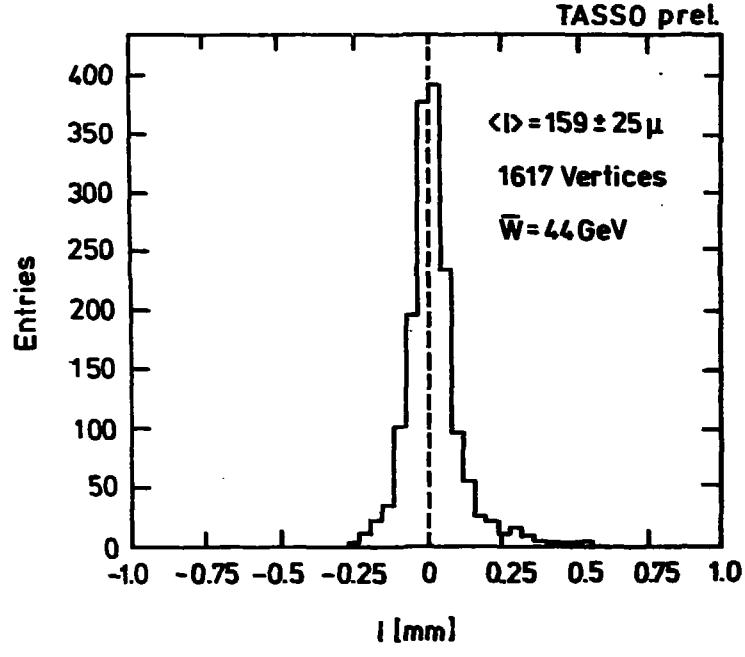

Fig. 17 Decay length distribution from TASSO

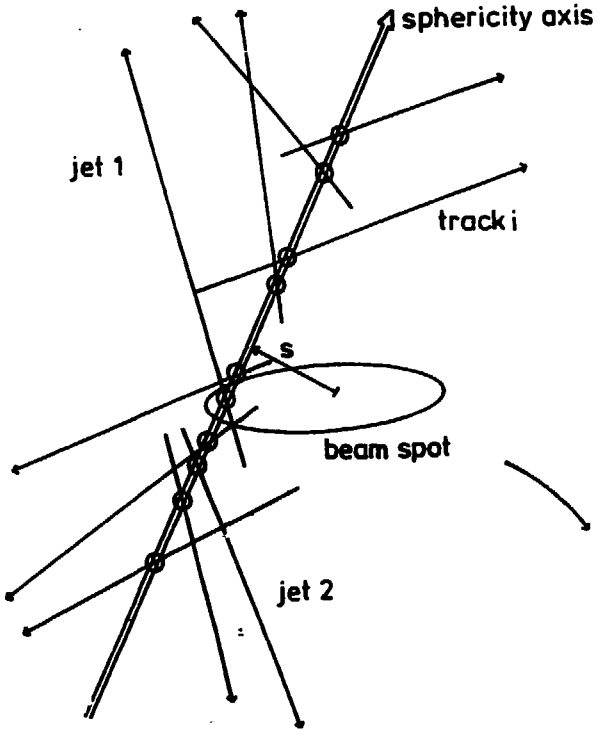

Fig.18 e^+e^- event containing bottom hadrons

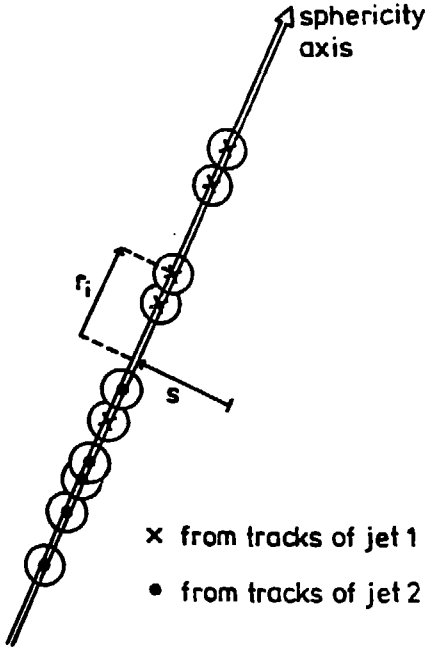

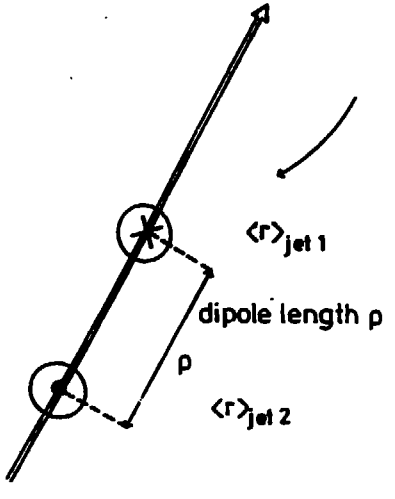

Fig.19 Definition of a dipole length

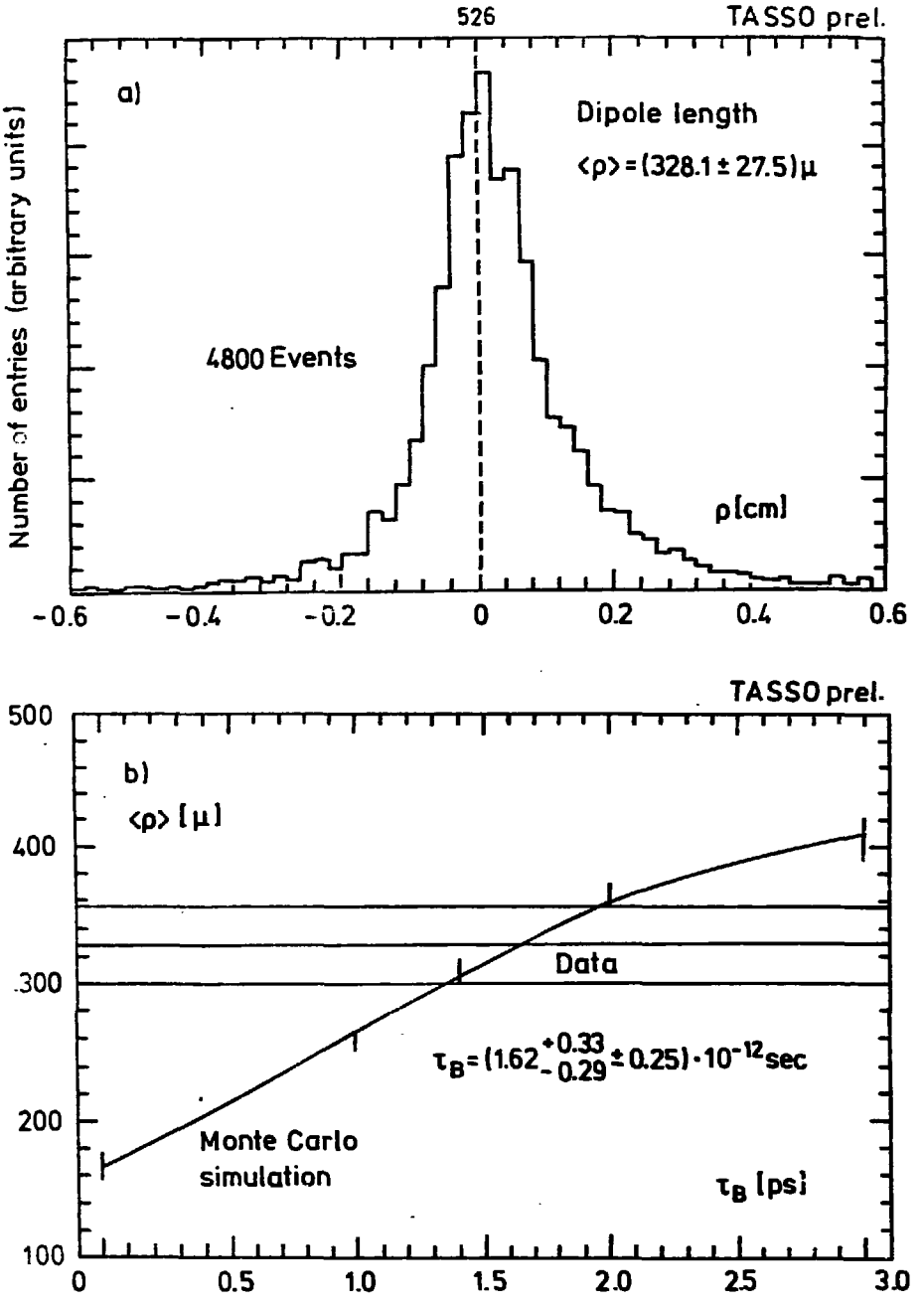

Fig. 20 Dipole length distribution and comparison with Monte Carlo simulations

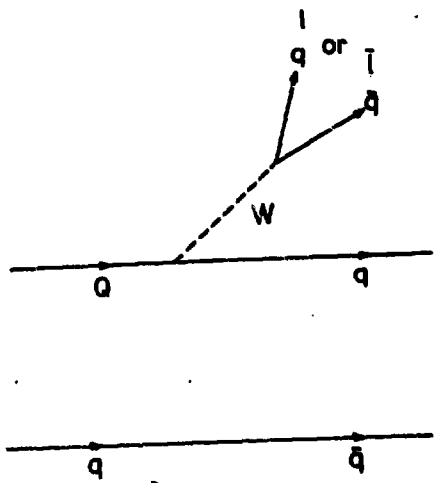

Fig. 21 Spectator diagram for the decay of heavy mesons

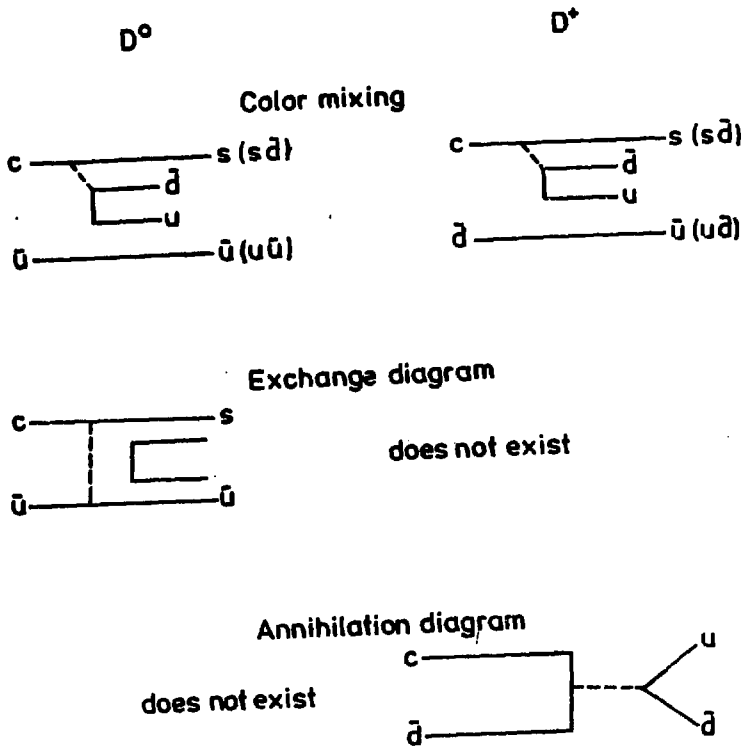

Fig. 22 Non spectator contributions to D meson decays

INFRARED FIXED POINT STRUCTURE OF THE FERMION MASSES IN THE STANDARD MODEL: THE TWO-LOOP ANALYSIS

P. Krawczyk and M. Olechowski,

Institute of Theoretical Physics, Warsaw University,

Hoża 69, 00-681 Warsaw

POLAND

(presented by P. Krawczyk)

A B S T R A C T

In the standard model, the renormalization group equation for the Yukawa couplings has the infrared fixed point which determines the upper bound for the masses of fermions present in the theory. We review this effect within the two loop approximation and report the 10% increase of the bound compared to the one loop results. We also notice and investigate the strong dependence of the bound on the precise value of the Weinberg angle.

In this talk we present a brief and preliminary survey of our original paper [1] to which an interested reader should refer for more detailed discussion.

None of various intriguing features of the fermion mass spectrum has been fully understood or explained. Thus, it seems extremely interesting that some of them may result from the infrared fixed point structure of the renormalization group equations within the standard model. This possibility has been pointed out by Pendleton and Ross [2] who noticed that in gauge theories, the evolution of the Yukawa couplings is determined by the competition between diagrams with gauge boson and scalar loops. This competition leads to the occurrence of the infrared fixed point in the evolution equations. If the fixed point were reached, it would determine the Yukawa couplings and (after spontaneous symmetry breaking) also the fermion masses.

This line of reasoning has been followed by several authors [2-7]. Up to now, the most extensive analysis has been performed by Bagger et al. [5]. They noticed that since the gauge group is spontaneously broken at the energy scale of order of the weak boson mass M_W, the evolution equations as given by the unbroken group become invalid and thus, the mathematical fixed point is never reached. In some cases, the evolution of the Yukawa couplings may last long enough to pull them close to the fixed point (so called "physical

fixed point"), in some others the initial values of the couplings may be left unchanged. After the detailed numerical "experiments" the authors of Ref. [5] have showed that under the assumption of the validity of perturbative unification, one can get the upper limit on masses of fermions present in the theory:

$$\Sigma\, m_Q^2 \lesssim (355\ \mathrm{GeV})^2 \qquad (1)$$

for quarks and

$$\Sigma\, m_L^2 \lesssim (330\ \mathrm{GeV})^2 \qquad (2)$$

for leptons. Similarly, if the theory contained N_H+3 families, the masses of the lightest new particles would satisfy the inequalities

$$m_Q \lesssim 250/\sqrt{N_H}\ \mathrm{GeV} \qquad (3.a)$$

$$m_L \lesssim 235/\sqrt{N_H}\ \mathrm{GeV} \qquad (3.b)$$

We have refined the analysis of Ref. [5] using the two-loop renormalization group equations [8]. Although we confirm the general features of the results of Bagger et al., we find that some of their conclusions are somewhat premature and must be corrected.

The inclusion of the two-loop radiative corrections leads in general to 5-10% relaxation of the bounds (1-3). We illustrate this fact in Fig. 1 which shows the quantity

$$T_Q = \Sigma\, Y_q^2$$

(Y_q is the Yukawa coupling of a quark q; we assume the lack of mixing) taken at the weak scale as a function of its initial value $T_Q(M_X)$. The two-loop curves has been obtained by the numerical integration of the evolution equation as given in Ref. [8].

There is also another effect which acts in the same direction as the inclusion of the two-loop corrections: the bounds show strong dependence on the value of the Weinberg angle. The main cause for this dependence is the relation between the unification mass scale M_X and the Weinberg angle: smaller Θ_W requires larger M_X and thus longer evolution time [9]

$$t_W = -1/(4\pi)^2 \log(M_W/M_X).$$

Of course, this effect is present already at the one-loop level but it has been overlooked in Ref. [5] (t_W has been fixed with the value $t_W = 0.2$).

With the present data (see for instance [10])

$$\sin^2\Theta_W(M_W) = 0.215 \pm 0.015 \qquad (4)$$

and the weakest limit on fermion masses is obtained for $\sin^2\Theta_W = 0.20$. Since the relations (1-3) have been calculated

for $\sin^2\theta_W \geq 0.215$, one has to correct them by another 10%. This can be easily seen in Fig. 2 in which we have plotted the bound on the quantity $T_Q(M_W)$ as a function of $\sin^2\theta_W(M_W)$ for the case of 4, 7 and 8 families (the curve for eight generations do not cover the full range of $\sin^2\theta_W$; it could not be continued for $\sin^2\theta_W < 0.215$ since it would violate the assumption of perturbative unification).

Inspecting Fig. 2, we can find the corrected bounds on the quark masses in the standard model ($m_q = Y_q$ 175 GeV). The relation (1) has to be replaced by

$$\Sigma\, m_q^2 \leq (400\ \text{GeV})^2 \tag{5}$$

whereas instead of Eq. (3.a) we get

$$m_q \leq 285/\sqrt{N_H}\ \text{GeV} \tag{6}$$

If however the Weinberg angle were found close to its present upper limit, the bounds would be much tighter. For instance, for the lightest new quark

$$m_q \leq 215/\sqrt{N_H}\ . \tag{7}$$

Similar considerations would give as the corrected limits for lepton masses. Since they are of rather little practical importance we do not list them here.

REFERENCES

1. P. Krawczyk and M. Olechowski, Warsaw University preprint, in preparation.

2. B. Pendleton and G. Ross, Phys. Lett. 98B (1981) 291.

3. C.T. Hill, Phys. Rev. D24 (1981) 691.

4. E. Paschos, Z. Phys. C26 (1984) 235.

5. J. Bagger, S. Dimopoulos and E. Masso, Nucl. Phys. B253 (1985) 397.

6. J. Bagger, S. Dimopoulos and E. Masso, Phys. Rev. Lett. 55 (1985) 920.

7. J. Bagger, S. Dimopoulos and E. Masso, Phys. Lett. 156B (1985) 357;
P.-Y. Xue, SLAC-PUB-3877 (January 1986), submitted to Phys. Lett. B;
C.T. Hill, C.N. Leung and S. Rao, Nucl. Phys. B262 (1985) 517;
C.N. Leung, talk presented at the DPF Meeting, University of Oregon, Eugene, OR, August 12 - 15, 1985.

8. M.E. Machacek and M.T. Vaughn, Nucl. Phys. B222 (1983) 83, B236 (1984) 221, B249 (1985) 70.

9. C.H. Llewellyn Smith, G.G. Ross and J.F. Wheater, Nucl Phys. B177 (1981) 263.

10. W.J. Marciano and A. Sirlin, Phys. Rev. D22 (1980) 2695;
A. Sirlin and W.J. Marciano, Nucl. Phys. B189 (1981) 442;
J.F. Wheater and C.H. Llewellyn Smith, Nucl. Phys. B208 (1982) 27.

FIGURE CAPTIONS

Fig. 1 The quantity $T_Q(M_W)$ versus $T_Q(M_\chi)$ for 4 and 8 families within the two-loop (solid lines) and one-loop (dashed lines) approximation. The Weinberg angle has been defined at the weak mass scale.

Fig. 2 The upper bound on the quantity $T_Q(M_W)$ as a function of $\sin^2\theta_W(M_W)$ for 4, 7 and 8 families. Solid lines denotes the two-loop results and dashed lines denotes the one-loop results.

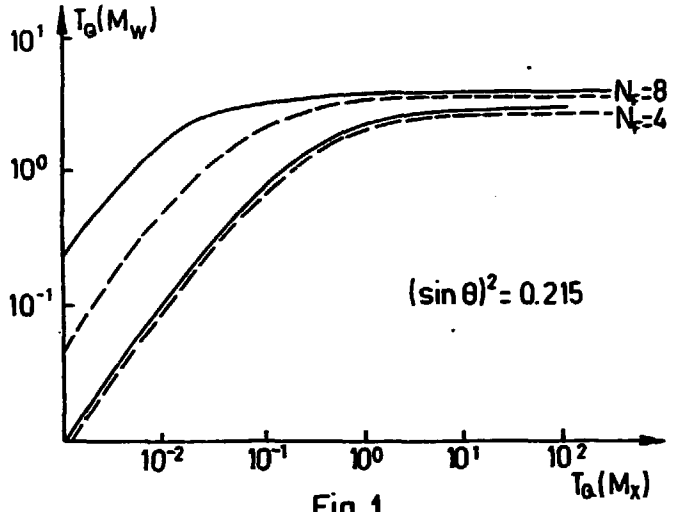
$T_Q(M_W)$
10^1
10^0
10^{-1}
$N_f=8$
$N_f=4$
$(\sin\theta)^2 = 0.215$
10^{-2}
10^{-1}
10^0
10^1
10^2
$T_Q(M_X)$

Fig. 1

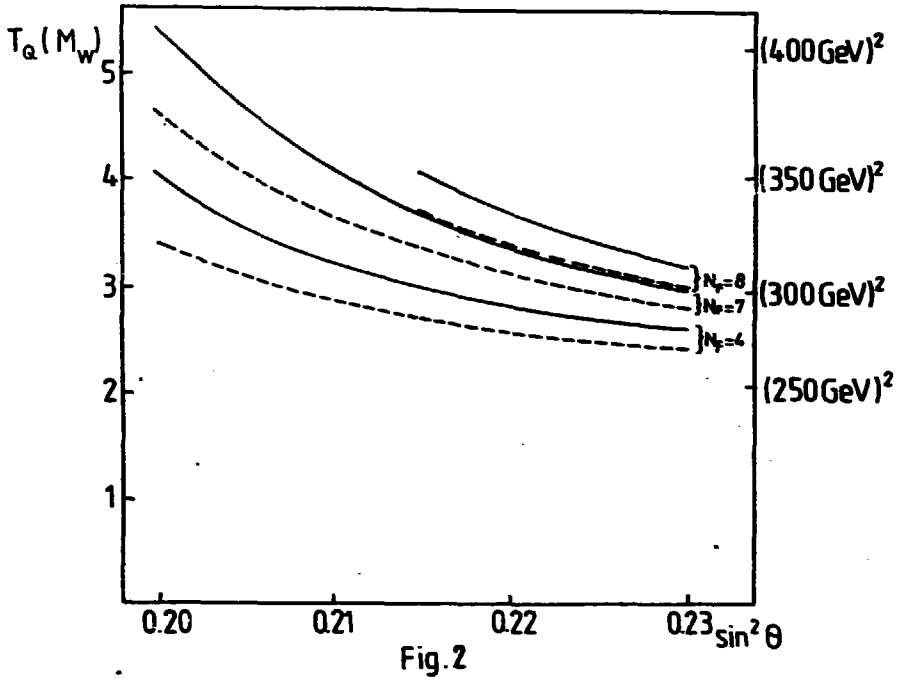
$T_Q(M_W)$
5
4
3
2
1
$(400\,GeV)^2$
$(350\,GeV)^2$
$(300\,GeV)^2$
$(250\,GeV)^2$
$N_f=8$
$N_f=7$
$N_f=4$
0.20
0.21
0.22
0.23
$\sin^2\theta$

Fig. 2

NEW BOUNDARY CONDITION IN THE BAG MODEL[#1)#2)]

Paweł Górnicki[#3)], Andrzej Szymacha[#4)]

The aim of this paper is to investigate a modification of the MIT Bag Model [1,2], namely, a possible change of the linear boundary condition:

$$-in_\mu \gamma^\mu \psi = \psi \qquad (1)$$

We propose its generalization:

$$-in_\mu \gamma^\mu \psi = \frac{1+\xi\gamma^0}{\sqrt{(1-\xi^2)}} \psi \qquad (2)$$

where $\xi \in]-1,1[$ is a parameter we are going to determine. For the purpose of the quark confinement any value of $\xi \in]-1,1[$ is acceptable.

The boundary condition (2) has an interesting physical interpretation.

Let ψ be a Dirac field inside a fixed finite square well formed by a mixture of the scalar and vector ('electric') potentials[#5)] with the ratio (vector potential)/(scalar potential) equal to ξ. The equation of motion for the quark field ψ has the form :

$$i\gamma^\mu \partial_\mu \psi - \gamma^0 \xi S\psi - S\psi = 0 \qquad (3)$$

where

$$S = \begin{cases} 0 & \text{inside the well} \\ S_0 > 0 & \text{outside the well .} \end{cases}$$

If $|\xi|<1$ and the well is not too shallow

#1) Work supported in part by the Research Program 01.03.

#2) Abbreviated from P. Górnicki, A. Szymacha, Phys. Lett. B (1986)

#3) Institute for Theoretical Physics, Polish Academy of Sciences, Lotników 32/46, PL-02-668 Warsaw, Poland

#4) Institute for Theoretical Physics, Warsaw University, Hoża 69, PL-00-681 Warsaw, Poland

#5) The mixed scalar-vector potential was considered by many authors in a somewhat different context [3,4,5].

there exists the bound state for the Dirac particle in this well. Note that the Klein paradox is avoided here as for the discussed range of ξ the scalar potential is dominating. Thus, the barrier may be arbitrary high and one can take $S_0 \to \infty$. In this limit solutions (continuous) of the eq. (3) corresponding to the bound states are the same as solutions of the free Dirac equation inside the cavity with the boundary condition (2) at its surface. The derivation of the modified boundary condition is analogous to that of the original MIT one, where only the scalar potential was considered - see [1]

One could be worried by the fact that the boundary condition (2) is not Lorentz covariant (for $\xi \neq 0$). However, there is nothing wrong in it. The condition (2) is applied in the fixed cavity approximation where the frame of reference is already chosen by the cavity itself. Then the proper treatment of the CM motion allows us to relate quantities obtained in this approximation to the relativistically covariant quantities describing the physical hadron.

The more serious problem is that the condition (2) seems to break the charge conjugation symmetry. It would be the case if the bag potential is produced by the vacuum itself. However, the bag describes the effective field acting on quarks inside a given hadron. If properly applied the C operator will act not only on the quark field but also on the effective confining field itself (this results in the change of ξ to $-\xi$)[#6]. In this situation the charge conjugation symmetry of the model will not be broken.

We come to the conclusion that the bag model with the modified boundary condition does not contradict any general theoretical principle. There is no good reason to put $\xi = 0$ (a priori) as this was done in the MIT model.

Unfortunately, we are not able to predict the ξ value directly from QCD. Instead, we shall try to determine it by fitting the model to the experimental data.

We propose to see what value of ξ fits the static properties of nucleon - ie. two magnetic moments (μ_p, μ_n), two mean charge radii (r_p, r_n), the axial formfactor (g_A) and the Roper resonance mass (m_{Roper}).

For simplicity we put quark masses equal to zero. Calculations of all the nucleon properties are rather straightforward and analogous to the $\xi=0$ case, so we will not discuss them here in detail.

[#6] Compare [6] .

In order to take care of the CM motion the point of view presented in [7,8] is adopted. We assume that the bag state describes the physical nucleon confined in an fictious, suitably chosen potential well. For the simplicity the potential is taken in the form of an infinite square well of the radius R_{well}.

The pionic cloud effects were treated within the framework given in [9,10]. The pionic cloud correction was applied additively which means that no mass and pion coupling constant renormalization was performed and the boundary condition was not changed due to the interactions with pions. Those effects are relatively small for the bag radii considered. Besides in our philosophy the bag pressure describes all the forces acting on quarks, also those resulting from the interactions with pions. Values of the parameters necessary to perform the pionic cloud calculations ie. the Δ and π masses and coupling constant f_π were taken from the experiment.

The constant B is determined by the proton mass which fixes the scale, hence, the ξ is the only free parameter of our model. The Table 1 shows all six quantities in question as the functions of ξ. In addition, the quantity $\sqrt{(\langle r_p^2\rangle + \langle r_n^2\rangle)}$ is shown as it is not influenced by the pionic corrections and thus independent of that part of the model. We observe that for ξ=-0.20 all six quantities come particularly close to their experimental values.

Authors would like to thank dr. J. Bartelski and dr. S. Tatur for many very interesting discussions.

References

[1] A. Chodos et al.: Phys. Rev. D9 (1974) 3471 .
[2] A. Chodos et al.: Phys. Rev. D10 (1974) 2599 .
[3] G. B. Smith, L. J. Tassie: Ann. Phys. 65 (1971) 352 .
[4] P. L. Ferreira, N. Zagury: Lett. Nuovo Cimento 20 (1977) 511; P. L. Ferreira et al. Nuovo Cimento 55A (1980) 215.
[5] N. Barik, M. Das: Phys. Lett. 120B (1983) 403; Phys. Rev. D28 (1983) 2823 .
[6] M. Villani: Phys. Rev. D30 (1984) 206;
[7] A. Szymacha: Phys. Lett. 146B (1984) 350 .
[8] A. Szymacha, S. Tatur: Phys. Lett. 146B (1984) 353 .
[9] C. E. DeTar: Phys. Rev. D24 (1981) 762 .
[10] S. Theberge et al.: Can. J. Phys. 60 (1982) 59 . Phys. Rev. D31 (1985) 645 .

Table 1. Parameters and results of the model as functions of ξ .

	units.									
ξ		-.30	-.25	-.20	-.15	-.10	-.05	.00	.05	.10	experimental
Parameters:											
x_0		1.72	1.78	1.83	1.89	1.94	1.99	2.04	2.09	2.13	
R_{bag}	$[m_p^{-1}]$	5.52	5.77	6.00	6.23	6.46	6.67	6.88	7.09	7.29	
R_{well}	$[m_p^{-1}]$	3.73	3.86	3.98	4.10	4.21	4.32	4.42	4.52	4.62	
Results:											
$\sqrt{\langle r_p^2 \rangle}$	$[m_p^{-1}]$	3.95	4.05	4.15	4.25	4.34	4.45	4.54	4.64	4.74	(3.99)
$\sqrt{-\langle r_n^2 \rangle}$	$[m_p^{-1}]$	2.00	1.92	1.85	1.77	1.71	1.65	1.59	1.54	1.49	(1.62)
$\sqrt{\langle r_p^2 \rangle + \langle r_n^2 \rangle}$	$[m_p^{-1}]$	3.40	3.56	3.71	3.86	4.00	4.13	4.26	4.38	4.50	(3.64)
μ_p	$[e/(2m_p)]$	2.65	2.73	2.82	2.91	2.99	3.08	3.16	3.25	3.32	(2.79)
μ_n	$[e/(2m_p)]$	-1.81	-1.85	-1.90	-1.95	-2.00	-2.05	-2.10	-2.15	-2.19	(-1.91)
g_A		1.32	1.29	1.26	1.23	1.21	1.18	1.15	1.13	1.10	(1.25)
m_{Roper}	$[m_p]$	1.67	1.63	1.60	1.57	1.55	1.52	1.50	1.48	1.47	(1.49 - 1.58)

STATUS REPORT ON CP VIOLATION IN NEUTRAL K SYSTEM

B. TURLAY

Département de Physique des Particules Elémentaires
C.E.N. Saclay
France

"At present our experimental understanding of CP violation can be summarized by the statement of a single number. If we state that the mass matrix which couples K and $\bar{K}$ has an imaginary off-diagonal term given by

$$\mathrm{Im}\, M_{12} = -\, 1.16\ 10^{-8}\ \mathrm{ev}.$$

then all the experimental results related to CP violation can be accounted for".

This sentence is part of the conclusion of the Nobel price lecture of J.W. CRONIN (10.12.1980 - Stockholm). What a striking conclusion after 16 years (1964-1980) of very hard and beautiful work of the physics community!

I would like, in the status report I am presenting today, to cast a glance at the parameter $\mathrm{Im}\, M_{12}$, and see with you that J.W. CRONIN was indeed right. In the second part of this report, we shall see what has triggered a revival of activity in the CP problem, since 1981, and where we stand today. In the third part, we shall see which experimental results we can expect in the next 3 years.

1 - INTRODUCTION OF THE PARAMETER $\mathrm{Im}\, M_{12}$: FORMALISM OF THE K SYSTEM

The time evolution of a state $\psi(t)$ of a neutral K system, which can be characterized by time dependent amplitude a(t) and b(t) for the $|K^0\rangle$ and $|\bar{K}^0\rangle$ components

$$\psi(t) = a(t)\ |K^0\rangle + b(t)\ |\bar{K}^0\rangle,$$

is given by the Schrödinger equation

$$i\,\frac{d\psi}{dt} = H\psi.$$

where H, the Hamiltonian describing the decay processes, is not Hermitian because of the decays.

If one writes $H = M - i\Gamma$, then the two matrices M (mass matrix) and Γ (decay matrix) are 2 x 2 HERMITIAN matrices.

The Hermicity of the M and Γ matrices implies :

$$\left| \begin{array}{l} M_{11}, M_{22}, \Gamma_{11}, \Gamma_{22} \quad \text{real} \\ \Gamma_{12} = \Gamma_{21}^{*} \\ M_{12} = M_{21}^{*} \end{array} \right.$$

and so, expressed in terms of their elements, the matrices are :

$$\begin{pmatrix} M_{11} & M_{12} \\ M_{12}^{*} & M_{22} \end{pmatrix} \quad \text{and} \quad \begin{pmatrix} \Gamma_{11} & \Gamma_{12} \\ \Gamma_{12}^{*} & \Gamma_{22} \end{pmatrix}$$

A - Consequences on M_{ij} and Γ_{ij} of symmetry invariance principles

General symmetry principles corresponding to C (particle-antiparticle conjugation), T (time reversal), and P (parity), and to combinations of them, such as CP or CPT, constrain the M and Γ matrix elements, in ways which are fundamental for the formalism of CP.

CPT INVARIANCE

$$M_{11} = M_{22}$$
$$\Gamma_{11} = \Gamma_{22}$$

T INVARIANCE

$$\Gamma_{12}, \Gamma_{21} \text{ real}$$
$$M_{12}, M_{21} \text{ real}$$

CP INVARIANCE

$$\Gamma_{11} = \Gamma_{22} \text{ and } \Gamma_{12}, \Gamma_{21} \text{ real}$$
$$M_{11} = M_{22} \text{ and } M_{12}, M_{21} \text{ real}$$

The above demonstrate that CP violation can be due to CPT or to T violation or to both.

B - The CP eigenstates K_1^0, K_2^0, and definition of the eigenstate of H, K_S^0 K_L^0

With the following conventions :

$$CP|K^0\rangle = - |\bar{K}^0\rangle$$

$$CP|\bar{K}^0\rangle = - |K^0\rangle$$

the two states

$$K_1^0 = \frac{1}{\sqrt{2}} (K^0 + \bar{K}^0)$$

$$K_2^0 = \frac{1}{\sqrt{2}} (K^0 - \bar{K}^0)$$

are eigenvectors of the CP conserving Hamiltonian :

even for K_1^0 $\quad CP|K_1^0\rangle = |K_1^0\rangle$

odd for K_2^0 $\quad CP|K_2^0\rangle = -|K_2^0\rangle$

The discovery, in 1964, of the decay of K_2^0 in $\pi^+\pi^-$ (even under CP, $CP|\pi^+\pi^-\rangle = |\pi^+\pi^-\rangle$) gave evidence that CP was not conserved in K^0 decay. The eigenstates of the weak Hamiltonian H, not CP invariant, were then redefined as K_S and K_L.

The eigenvectors K_S and K_L of the diagonalised matrix $\Gamma + iM$ define physical states with definite mass (m) and lifetime (λ) :

$$\phi(t) = e^{-\lambda t} \phi$$

The Schrödinger equation can be written :

$$(\Gamma+iM)\ \phi = - \frac{d\phi}{dt} = \lambda\phi$$

with eigenvalues

$$\begin{cases} \lambda_S \equiv \gamma_S/2 + im_S \\ \lambda_L \equiv \gamma_L/2 + im_L \end{cases}$$

and eigenvectors

$$\begin{cases} K^0_S = \dfrac{1}{2[(1 + |\epsilon+\delta|^2)]^{1/2}} \left[(1+\epsilon+\delta)|K^0\rangle + (1-\epsilon-\delta)|\bar{K}^0\rangle\right] \\ K^0_L = \dfrac{1}{2[(1 + |\epsilon-\delta|^2)]^{1/2}} \left[(1+\epsilon-\delta)|K^0\rangle - (1-\epsilon+\delta)|\bar{K}^0\rangle\right] \end{cases}$$

ϵ is the CP violation parameter with T non-invariance ;
δ is the CP violation parameter with CPT non-invariance.

$$\epsilon = \frac{-\,\mathrm{Im}\, M_{12} + i\, \mathrm{Im}\, \Gamma_{12}}{i(m_S - m_L) + (\gamma_S - \gamma_L)/2}$$

$$\delta = \frac{1}{2}\,\frac{(\Gamma_{11} - \Gamma_{22}) + i(M_{11} - M_{22})}{i(m_S - m_L) + (\gamma_S - \gamma_L)/2}$$

The non orthogonality of the two eigenvectors K_S and K_L :

$$\langle K^0_S | K^0_L \rangle = 2\ \mathrm{Re}\ \epsilon - 2\ i\ \mathrm{Im}\ \delta$$

can be interpreted as the "impurity" coming from the CP-non-conserving part of the Hamiltonian. The impurity is small (found experimentally to be a few per mill), and the goal, since 1964, has been to find where this CP violation originates : $\mathrm{Im}\, M_{12}$, $\mathrm{Im}\, \Gamma_{12}$, $(\Gamma_{11} - \Gamma_{22})$, $(M_{11} - M_{22})$?

2 - THE PARAMETER ϵ'

The general form of the M and Γ matrix elements is the following :

$$M_{ij} = m_{K^0}\,\delta_{ij} + \langle K^0_i | H_w | K^0_j \rangle + \mathcal{P} \sum_n \frac{\langle K^0_i | H_w | n \rangle \langle n | H_w | K^0_j \rangle}{m_{K^0} - m_n}$$

$\langle K^0_i | H_w | K^0_j \rangle$ are $\Delta S = 2$ transitions

$\langle K^0_i | H_w | n \rangle$ are $|K^0_i\rangle$ transition to virtual state n

$$\Gamma_{ij} = \sum_F \delta(E_F - m_K)\, \langle K^0_i | H_w | F \rangle \langle F | H_w | K^0_j \rangle$$

$\langle K^0_i | H_w | F \rangle$ are $\Delta S = 1$ transition to real final state.

Since CP violation has been found in the $\pi\pi$ channel, we are interested in the contribution of this violation to the imaginary part of Γ_{12}, the so-called direct CP violation.

One projects the K^0 and $\bar{K}^0$ states of the strong interaction onto the $\pi\pi$ isospin base. Because of Bose statistics and because of the pseudoscalar character of K and π, the two allowed values of isospin are I = 0 and 2.

One defines :

$$\langle \pi\pi,\ I=0|T|K^0\rangle = A_0\, e^{i\delta_0}$$

$$\langle \pi\pi,\ I=2|T|K^0\rangle = A_2\, e^{i\delta_2}$$

$$\langle \pi\pi,\ I=0|T|\bar{K}^0\rangle = \bar{A}_0\, e^{i\delta_0}$$

$$\langle \pi\pi,\ I=2|T|\bar{K}^0\rangle = \bar{A}_2\, e^{i\delta_2}$$

when δ_0 and δ_2 are the $\pi\pi$ scattering phase shifts.

CPT invariance implies the following relations :

$$\bar{A}_0 = -A_0^* \qquad \text{if one defines } CPT|K^0\rangle = -|\bar{K}^0\rangle$$
$$\bar{A}_2 = -A_2^*$$

CP and CPT invariance implies :

$$\mathrm{Im}\, A_0 = 0$$
$$\mathrm{Im}\, A_2 = 0 \quad .$$

The experimental amplitudes that one measures are :

$$\eta_{+-} = \frac{\langle \pi^+\pi^-|T|K_L^0\rangle}{\langle \pi^+\pi^-|T|K_S^0\rangle}$$

$$\eta_{00} = \frac{\langle \pi^0\pi^0|T|K_L^0\rangle}{\langle \pi^0\pi^0|T|K_S^0\rangle} \ ,$$

which can be expressed, (using the K_S and K_L definitions and the appropriate Clebsch-Gordon coefficients, and assuming CPT invariance ($\delta = 0$)) as :

$$\eta_{+-} = \frac{\epsilon\,(1 + \omega / \sqrt{2}) + i\,(t_0 + t_2\,\omega / \sqrt{2})}{(1 + \omega / \sqrt{2}) + i\,\epsilon\,(t_0 + t_2\,\omega / \sqrt{2})}$$

$$\eta_{00} = \frac{\epsilon\,(1 - \sqrt{2}\,\omega) + i\,(t_0 - \sqrt{2}\,\omega\,t_2)}{1 - \sqrt{2}\,\omega + i\,\epsilon\,(t_0 - \sqrt{2}\,\omega\,t_2)}\,,$$

where $t_0 = \dfrac{\mathrm{Im}\,A_0}{\mathrm{Re}\,A_0}$, $t_2 = \dfrac{\mathrm{Im}\,A_2}{\mathrm{Re}\,A_2}$, $\omega = \dfrac{\mathrm{Re}\,A_2}{\mathrm{Re}\,A_0}\,e^{i(\delta_2 - \delta_0)}$.

Using $|\omega| \simeq \dfrac{1}{20}$ (given from $K^+ \to \pi^0\pi^0$) and the $\Delta I = 1/2$ rule :

$$\eta_{+-} \simeq \epsilon + i\,t_0 + \frac{i\omega}{\sqrt{2}}\,(t_2 - t_0)$$

$$\eta_{00} \simeq \epsilon + i\,t_0 - i\sqrt{2}\,\omega\,(t_2 - t_0)\,.$$

If there is CP invariance in the decays, the amplitude A_2 and A_0 are real, thus $t_2 = 0$ $t_0 = 0$ and :

$$\boxed{\eta_{+-} = \eta_{00} = \epsilon}$$

Phase convention :

The definition of the parameter ϵ' depends on some phase convention.

1. WU and YANG have defined the K^0, $\bar{K}^0$ phase such that A_0 is real, thus $t_0 = 0$ and :

$$\eta_{+-} = \epsilon + \frac{i}{\sqrt{2}}\,\frac{\mathrm{Im}\,A_2}{A_0}\,e^{i(\delta_2 - \delta_0)}$$

$$\eta_{00} = \epsilon - 2\,\frac{i}{\sqrt{2}}\,\frac{\mathrm{Im}\,A_2}{A_0}\,e^{i(\delta_2 - \delta_0)}$$

With :

$$\boxed{\epsilon' = \frac{i}{\sqrt{2}}\,\frac{\mathrm{Im}\,A_2}{A_0}\,e^{i(\delta_2 - \delta_0)}}$$

we have :

$$\eta_{+-} = \epsilon + \epsilon'$$

$$\eta_{00} = \epsilon - 2\,\epsilon'$$

2. The Kobayashi-Maskawa model introduces another phase convention, in the "quark base" : A_2 is real ($t_2 = 0$), and A_0 has a phase ξ, so one has the relation :

$$\eta_{+-} = \frac{e^{i\pi/4}}{2\sqrt{2}} (\epsilon_m + 2\,\xi) + \epsilon'$$

$$\eta_{00} = \frac{e^{i\pi/4}}{2\sqrt{2}} (\epsilon_m + 2\,\xi) - 2\,\epsilon'$$

$$\epsilon_m = \frac{\mathrm{Im}\, M_{12}}{\mathrm{Re}\, M_{12}} \quad \text{calculated in the "quark base"}$$

and

$$\boxed{\epsilon' = -\frac{i\xi}{\sqrt{2}} \frac{\mathrm{Re}\, A_2}{\mathrm{Re}\, A_0} e^{i(\delta_2 - \delta_0)} = -\frac{i\xi\omega}{\sqrt{2}}}$$

This second definition is used to calculate ϵ' in the Kobayashi-Maskawa model, and we shall see the results later.

In both cases, the phase of ϵ' is given by the $\pi\pi$ phase shift $\phi_{\epsilon'} = \frac{\pi}{2} + (\delta_2 - \delta_0)$.

3 - THE EXPERIMENTAL RESULTS IN 1974 : THE "SUPER WEAK MODEL" OF L. WOLFENSTEIN [5]

An extraordinary experimental programme was launched after 1964 and continued until 1974. All the parameters of CP violation in the K^0 system were determinated, and we give the results quoted by Particle Data group [1] in table 1.

TABLE I

$\Delta_m = m_L - m_S$	$= 0.535 \pm 0.002 \cdot 10^{10}\ s^{-1}$
Γ_S	$= (1.120 \pm 0.003)\ 10^{10}\ s^{-1}$
Asymmetry δ_e	$= (3.33 \pm 0.14)\ 10^{-3}$
δ_μ	$= (3.19 \pm 0.24)\ 10^{-3}$
$\lvert\eta_{+-}\rvert$	$= (2.274 \pm 0.022)\ 10^{-3}$
φ_{+-}	$= (44.6 \pm 1.2)°$
$\lvert\eta_{00}\rvert$	$= (2.33 \pm 0.08)\ 10^{-3}$
φ_{00}	$= (54 \pm 5)°$
$\left\lvert\frac{\eta_{00}}{\eta_{+-}}\right\rvert$	$= 1.015 \pm 0.04$
$\left\lvert\frac{\epsilon'}{\epsilon}\right\rvert$	$= -0.005 \pm 0.014$

* Calculated from :

BANNER et al. [2]	1.03 ± 0.07
HOLDER et al. [3]	1.00 ± 0.06
CHRISTENSON et al. [4]	1.00 ± 0.09

In parallel with the experimental programme, theoretical speculations fluorished. Among many hypotheses, the model proposed by L. WOLFENSTEIN [5] was compatible with the experimental parameters. He proposed the "super weak" model. In this model the CP violation is due to a $\Delta S = 2$ transition.

One writes the weak Hamiltonian in the form :

$$H_w = \alpha H^1_w + \beta H'_{s.w}$$

where H^1_w is the normal weak interaction ($\Delta S = 1$, CP invariant), and $H'_{s.w}$ is $\Delta S = 2$, CP violating.

The amplitude of the violation is of the order of ϵ, and is used to fix the ratio α/β by assuming it is due to the interference term between the first-order "super weak" interaction and the second order "Fermi" interaction.

$$\epsilon \simeq F_{sw}/G^2 = \frac{\beta}{\alpha} \times 10^5$$

$$\frac{\beta}{\alpha} \simeq 10^{-7} .$$

Expressing the formulae for M_{12} and $\Gamma_{i,j}$ in terms of these quantities, one finds :

$$\begin{cases} \text{Im } M_{12} \propto \beta \langle K^0 | H_{sw} | \bar{K}^0 \rangle \\ \text{Re } M_{12} \propto \alpha^2 \\ \text{Im } \Gamma_{12} = 0 \qquad \text{"no direct CP violation". } \epsilon' = 0 \\ \text{Re } \Gamma_{12} \propto \alpha^2 \end{cases}$$

which means :

$$\eta_{+-} = \eta_{00} = \epsilon \qquad \varphi_{+-} = \varphi_{00} = \varphi_2 = 43.7° \pm 0.2° \qquad \epsilon' = 0,$$

which is quite compatible with the data of table I.

Going back to the expression of ϵ :

$$\epsilon = \frac{-\text{Im } M_{12} + i \text{ Im } \Gamma_{12}}{i(m_S - m_L) + (\tau_S - \tau_L)/2} ,$$

one finds :

$$\epsilon_{s.w} = \frac{-\text{Im } M_{12}}{i(m_S - m_L) + (\tau_S - \tau_L)/2} .$$

So, having measured ϵ, $m_S - m_L$, $\gamma_S - \gamma_L$, one can calculate $-\mathrm{Im}\, M_{12} = -1.16 \times 10^{-8}$ ev. This only parameter contains all the information we have on CP violation.

Since no occurence of CP violation has been detected in any other process, we understand Cronin's 1980 statement, with which I started.

4 - THE KOBAYASHI-MASKAWA MODEL : LIMITS ON ϵ'/ϵ CALCULATIONS

The proposition, by Kobayashi and Maskawa in 1973, of a "natural" CP violation in a model employing the gauge group SU(2) x U(1) with three pairs of quarks is remarkable. It has started a new the calculation of the CP-violation parameter.

The weak hadronic current, in this model, is :

$$J_\mu = (\bar{u}, \bar{c}, \bar{t})\, \gamma_\mu\, (1 - \gamma_5)\, U\, (d, s, b)\ ,$$

where U is the famous K - M matrix :

$$U = \begin{pmatrix} U_{ud} & U_{us} & U_{ub} \\ U_{cd} & U^{\delta}_{cs} & U^{\delta}_{cb} \\ U_{td} & U^{\delta}_{ts} & U^{\delta}_{tb} \end{pmatrix}$$

The U_{ij} are functions of 3 angles ("à la Cabibbo") $\theta_1\ \theta_2\ \theta_3$, and the U^{δ}_{ij} are, in addition, functions of "δ", which is interpreted as the CP-violation phase.

If δ is non zero, the U^{δ}_{ij} matrix elements, in coupling $s \to c$, $s \to t$, $b \to c$, $b \to t$, will result in CP violation due to imaginary terms coming from δ. CP violation will not be confined to K system ($s \to c$ and $s \to t$), but can, at least, be expected in association with other flavour particles, B, for instance. These new effects, whether detectable or not, is something which must be considered, but which will not be treated here.

Such an explanation of CP violation is all well and fine, but the next question is can the parameters δ, ϵ, ϵ' be evaluated ? Many detailed papers [6] have been published on this subject.

The two main diagrams, which are necessary to the understanding of these discussions, are shown in figures 1 and 2.

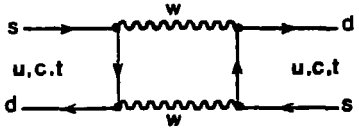

FIG. I

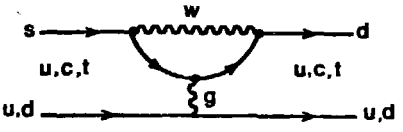

FIG. II

Figure 1, called a "box diagram", is a $\Delta S = 2$ transition, and dominates the M_{12} mass matrix element calculation.

Figure 2, the so-called "Penguin diagram", is a $\Delta S = 1$ transition. It can be used to evaluate Γ_{12} decay matrix element, and to introduce the strong interactions via the gluon exchange.

A detailed calculation of diagrams in figures 1 and 2 is not trivial, but the main point we want to stress is that the calculation, though involving parameters which are not known precisely, will, nevertheless, predict results in a quite large range. We give the main hypotheses and conclusions of some such calculations [6].

1. One still needs more precise values of θ_2, θ_3. The B lifetime and the branching ratio $\Gamma(b \to a) / \Gamma(b \to c)$ are important as input.

2. Obviously, the c and t quark masses are needed to calculate diagrams of the type of figures 1 and 2. The biggest uncertainty is now the t quark mass.

3. QCD calculations are not done following a unique hypothesis. A big factor - which can be as large as a factor 3 - is still questionable.

The conclusions on ϵ and ϵ' are the following :

Using the new phase definition of the K^0 and $\bar{K}^0$ base, which keeps A_0 real, one introduces :

$$\xi = \frac{\mathrm{Im}\, A_0}{A_0}$$

$$\text{or} \quad \underset{\text{quark base}}{(A_0)} \to \exp(-i\,\xi)\underset{\text{quark base}}{(A_0)} = A_0$$

1 - *Result on ϵ*

$$|\epsilon| = 2^{-3/2} \, |\epsilon_m + 2\,\xi|$$

with $$\epsilon_m = \mathrm{Im}\, M_{12} \,/\, \mathrm{Re}\, M_{12} = 2\, s_2\, c_2\, s_3 \sin\delta\, P(\theta_2, \eta)$$

$$P(\theta_2, \eta) = \frac{s_2^2 \,(1 + [\eta/(1-\eta)] \ln \eta) - c_2^2 \,(\eta + [\eta/(1-\eta)] \ln \eta)}{c_2^4\, \eta + s_2^4 - 2\, s_2^2\, c_2^2\, [\eta/(1-\eta)] \ln \eta}$$

where $\eta = \dfrac{m_c^2}{m_t^2}$

$$\xi = f\, s_2\, c_2\, s_3 \sin\delta \, \frac{\ln \eta}{\ln (m_c^2/\mu^2) - s_2^2 \ln \eta}$$

Here, f is the fraction of the effective "Penguin" Hamiltonian contribution to the real decay amplitude A_0 when the phase δ is equal to zero.

Reasonable hypotheses for m_c, m_t, and f gives comparable contributions to ϵ_m and to 2ξ with the opposite sign. But, since these two terms are functions of δ, no definitive conclusion can be drawn for δ and for the value of ϵ.

2 - *Result on $|\epsilon'/\epsilon|$*

In the new base defined earlier, $|\epsilon'/\epsilon|$ can be written :

$$|\epsilon'/\epsilon| = \frac{1}{20} \, |2\xi \,/\, (\epsilon_m + 2\xi)|$$

The cancellation of the factor $2\, s_2\, c_2\, s_3 \sin\delta$ in the ratio of ϵ' to ϵ allows us to predict $|\epsilon'/\epsilon|$.

These results are in the form of limits, and a lower bound on $|\epsilon'/\epsilon|$ has been calculated by F.J. GILMAN and J.S. HAGELIN [7] : $|\epsilon'/\epsilon| > 2/1000$.

As we said, large variations are possible in the determination of $|\epsilon'/\epsilon|$. Some models even predict even a negative value of ϵ'/ϵ.

Using the lower bound of Gilman and Hagelin, one can contrain ϵ'/ϵ to the range :

$$\frac{2}{1000} < \left|\frac{\epsilon'}{\epsilon}\right| < \frac{20}{1000}$$

The conclusion is clear : if we want to contribute to the progress of the CP understanding, we would like to have a measurement of ϵ'/ϵ at a level of precision of $\frac{1}{1000}$.

5 - PRESENT EXPERIMENTAL STATUS OF $|\epsilon'/\epsilon|$ MEASUREMENT

The relations $\eta_{+-} = \epsilon + \epsilon'$

$\eta_{00} = \epsilon - 2\,\epsilon'$

allow us to determine Re ϵ'/ϵ :

$$\frac{|\eta_{00}|^2}{|\eta_{+-}|^2} = 1 - 6\ \mathrm{Re}\ \epsilon'/\epsilon\ , \qquad \text{(if we neglect term in } \omega^2\text{)}.$$

Since the phase of ϵ' is $(48 \pm 8)°$ [8], ϵ and ϵ' are almost collinear. This is why we usually state that we measure ϵ'/ϵ.

Experimentally, one detects the $\pi^+\pi^-$ and $\pi^0\pi^0$ decays of K_L^0 and K_S^0, and then :

$$\epsilon'/\epsilon = \frac{1}{6}\left[1 - \frac{\Gamma(K_L \to 2\,\pi^0)}{\Gamma(K_S \to 2\,\pi^0)}\,\frac{\Gamma(K_S \to \pi^+\pi^-)}{\Gamma(K_L \to \pi^+\pi^-)}\right]$$

The most difficult sample to obtain is $K_L^0 \to \pi^0\pi^0$, for obvious reasons : the small branching ratio (equal to ϵ) ; the detection of π^0 ; and the 3 π^0 background subtraction.

Around 1972, results were obtained on $|\eta_{00}/\eta_{+-}|$ with $\simeq$ 200 $K_L^0 \to \pi^0\pi^0$.

	$\lvert\eta_{00}/\eta_{+-}\rvert$
1972 Banner et al. [2]	1.03 ± 0.07
1972 Holder et al. [3]	1.00 ± 0.06
1979 Christensen et al. [4]	1.00 ± 0.09

These values averaged give $|\epsilon'/\epsilon| = - 0.005 \pm 0.014$.

We have seen that theoretical predictions of $|\epsilon'/\epsilon|$ require the results of more precise measurements. In 1981, a new series of experiments started, and gave results in 1985 based on 2000 to 3000 $K_L^0 \rightarrow \pi^0\pi^0$.

	$\lvert\epsilon'/\epsilon\rvert$	Δ_{stat}	Δ_{syst}
1985 - BNL-YALE [9]	+ 0.0017	± 0.007	± 0.004
1985 - CHICAGO-SACLAY [10]	- 0.0046	± 0.005	± 0.002

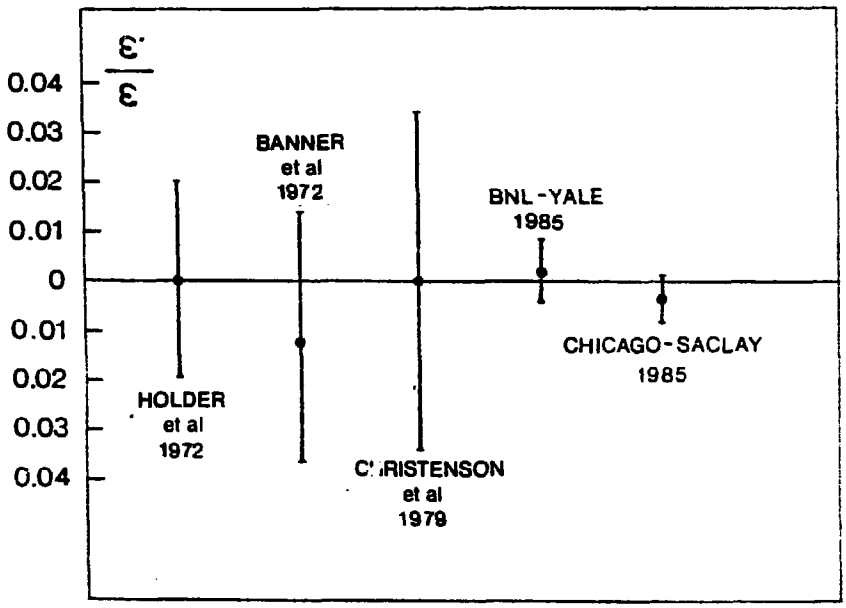

FIG. III

ϵ'/ϵ measurements - statistical errors only

We see in Fig. III the improvement since 1972, but even this effort has not been sufficient.

6 - FUTURE EXPERIMENTS : ϵ'/ϵ WITH A PRECISION OF 1/1000

To answer the challenge of a measurement of ϵ'/ϵ at an accuracy 1/1000 we need :

- Firstly, at least 100 000 events in the most difficult channel : $K_L^o \rightarrow \pi^o\pi^o$; and
- secondly, a knowledge of systematic errors at a level of 10^{-3} or better !

Two experimental groups are now undertaking this work : the Chicago-Fermilab-Princeton-Saclay group [11] and the CERN-Dortmund-Edinburgh-Orsay-Pisa-Siegen group [12]. In what follows, I shall call these the FNAL 2 and CERN experiments respectively.

The first part of the challenge (100 000 $K_L^o \rightarrow \pi^o\pi^o$) can these days be attained, because of improvements in particle flux, in acceptance, and, mainly, in the speed of data recording. If reasonable running time is allocated to both groups, the first goal will be reached.

The second part (reduction of systematic errors) is the key point of the experiments. It so happens that the two groups have chosen different means of obtaining $|\eta_{oo}/\eta_{+-}|^2$, and the different systematics will reinforce the combined result.

One needs to measure a ratio, R, for a given momentum bin, ΔP, in a decay zone, ΔZ, i.e. :

$$R\ (\Delta P, \Delta Z) = \frac{\dfrac{N_L(0)}{N_S(0)}}{\dfrac{N_L(+-)}{N_S(+-)}}$$

This can be done in one of two ways :

$$\frac{N_L(0)}{N_S(0)} * \frac{N_S(+-)}{N_L(+-)} \qquad \text{or} \qquad \frac{N_L(0)}{N_L(+-)} * \frac{N_S(+-)}{N_S(0)}$$

The FNAL 2 experiment is using the double-beam technique, and will run alternatively in neutral and charged mode. One regenerator produces the K^0_S sample in one beam ; the free decay, K_L, being observed in the other beam.

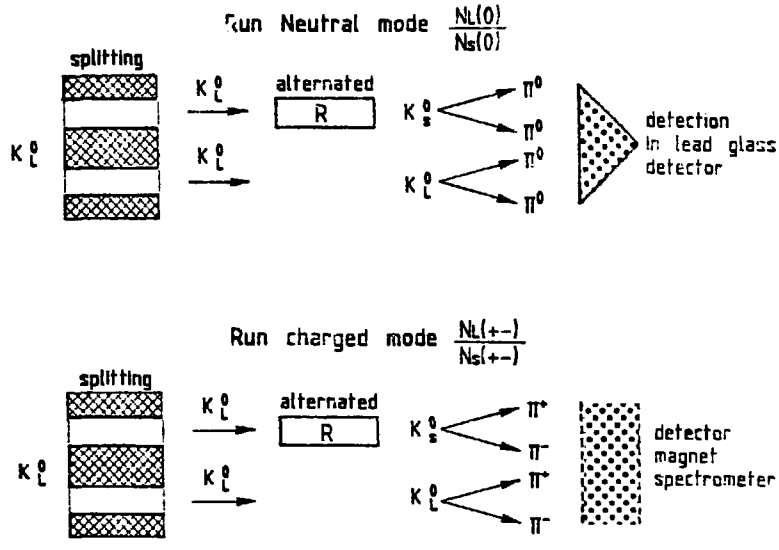

The CERN experiment has chosen not to use a regenerator, but to run with K^0_L, detecting both the charged and neutral modes, and to produce K^0_S in a subsequent run from targets stationed at different positions in order to have a relatively flat K^0_S vertex distribution.

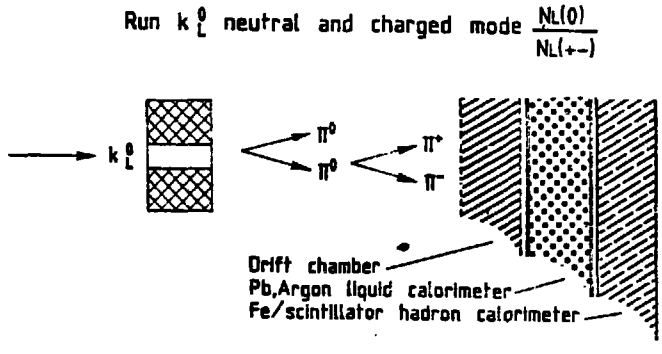

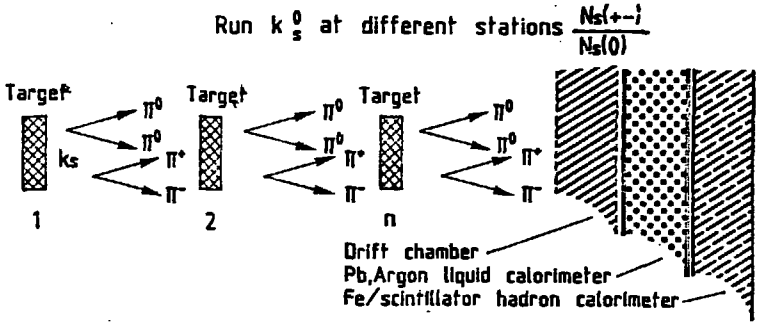

A very detailed comparison of the two experiments is not the purpose of this talk. From this brief description, one sees clearly that the two techniques are sufficiently different that the same systematic effects will not occur with the same emphasis. In both cases, however, the calibration of the calorimeters must be to better than 1 part in 1000.

The present status of these experiments and their future plans are the following :

FNAL 2

10 000 $K^0_L \rightarrow \pi^0\pi^0$ analysed

1986
no results this summer

results December 1986

CERN

25 000 $K^0_L \rightarrow \pi^0\pi^0$ analysed

June 1986

December 1986

Running time

expected 250 000 $K^0_L \rightarrow \pi^0\pi^0$

Running time

expected 100 000 $K^0_L \rightarrow \pi^0\pi^0$

Analysis

↓

March 1987

July 1987

Analysis

↓

You can guess from this schedule when you may expect a result on ϵ'/ϵ at 1/1000 precision ! I think that results from both sides will be given in the summer of 1988. And if these results are not too different, the physics community will really know ϵ'/ϵ to a precision of 10^{-3}.

7 - A NEWCOMER, LEAR

In 1987, the Low-Energy-Antiproton-Ring (LEAR) at CERN will be able to deliver tagged antiprotons at a rate of 10^6 per second.

K^0 and $\bar{K}^0$ production will occur through the reaction :

$$p + \bar{p} \begin{cases} \nearrow K^+\pi^-K^0 \quad (2 \times 10^{-3}) \\ \searrow K^-\pi^+\bar{K}^0 \quad (2 \times 10^{-3}) \end{cases}$$

The detection and identification of K^+ and K^- will fix the strangeness of the K^0. It is unique tool, with which physicists will have the best opportunity for CP studies in the neutral K system.

a) *The CERN/PSCC/86-6 - PSCC/P82 proposal*
(Basle, CERN, CEN-Saclay, DAP Athens, Democrites, ETH, Fribourg, Liverpool, SIN, Stockholm, Thessaloniki collaboration)

This group proposes to measure the interference effects and the asymmetries of different decay amplitudes in the neutral kaon system.

The main point is that the technique is entirely different from the "old classical" studies using K_s or K_L beams, and one expects that the systematic errors will also be of a different sort. Statistics is not the problem in this type of experiments, the problem is non to handle so many events (more than 10^9 events to analyse).

The particular asymmetry

$$A(2\pi) = \frac{\int \Gamma(K^0 \to 2\pi^0) - \Gamma(\bar{K}^0 \to 2\pi^0)}{\int \Gamma(K^0 \to 2\pi^0) + \Gamma(\bar{K}^0 \to 2\pi^0)}$$

$$\simeq 4 \, \mathrm{Re}\, \eta_{00} - 2 \, \mathrm{Re}\, \epsilon$$

should allow a determination of ϵ'/ϵ with $\pm$ 1.5 10^{-3} error.

With data taking expected in the middle of 1988 and with the time necessary to learn about the experiment, results will come late compared to those of FNAL 2 and CERN, expected in 1988. Nevertheless, the difficulty of the latter experiments and the possibility of some discrepancy in their results still make the LEAR measurements useful.

More interesting is the general improvement on all CP parameters we can expect from the Lear experiment, as shown in table 2.

Table 2

The 1σ precision of the parameters including statistical and systematic errors

CP-violation parameters	present precision	10^{13} $\bar{p}$
$\lvert\theta_{+-} - \theta_{00}\rvert$	5°	2° → 1°
$\lvert\epsilon'/\epsilon\rvert$	7×10^{-3}	2×10^{-3}
Δm	4.1×10^{-3}	1.2×10^{-3}
$\lvert\eta_{+-0}\rvert$	$<1.2\times10^{-1}$	$<6\times10^{-4}$
$\lvert\eta_{000}\rvert$	$<10^{-1}$	$<8\times10^{-4}$
Re X	$<2\times10^{-2}$	$<6\times10^{-4}$
Im X	$<2.6\times10^{-2}$	$<7\times10^{-4}$

Such precision may investigate some new ideas on the CP problem.

b - *A proposal for test of time reversal and CPT invariance at LEAR (Zurich, William and Mary College, University of Oxford, University of New Mexico, Ljubjana, Delft, Coimbra University, Birmingham collaboration)*

It is worthwhile to quote the authors of this proposal : "Given CPT invariance, CP violation and T violation are equivalent. However, although the K^0 violation of CP has been known for a long time, no experiment has yet demonstrated an explicit T violation, and the argument advanced for CPT invariance are indirect and not altogether unambiguous".

It is true that no experimental proof of T violation has been found, and that only limits on the electric dipole of the neutron and on the transverse polarization of the muons in K_{μ_3} decay have been given. Nevertheless, as we shall see later, the Bell-Steinberger relation helps by telling us that T violation is consistent with the experimental data on K^0 system.

In the case of this group, it is a direct measure of the T or CPT violation which is proposed.

The measurement of :

- the sum of the K_L decays $\pi^{\pm}e^{\mp}u$, $\pi^{\pm}\mu^{\mp}\nu$ and $\pi^+\pi^-\pi^0$
- the K_S decay to $\pi^+\pi^-$
- the separate $K_{\ell 3}$ decay, $\pi^+e^-\nu$ and $\pi^-e^+\nu$

will determine the real and imaginary part of the parameters ϵ and δ, i.e., the T or CPT contribution to CP violation. An improvement of the limit on the $\Delta S = \Delta Q$ (Im X, Re X) rule will also be possible, through the measurement of $\pi^+e^-\nu$ and $\pi^-e^+\nu$.

All this formalism is correct. If the experiment is possible at the proposal level of precision, then it will be a wonderful way to use the powerful tool provided by Lear : to sample the strangeness of K^0's and to follow their evolution in time. In addition, the group propose a measurement of the difference of the K^+ and K^- lifetimes at a level of 10^{-4}, compared to the present value of 15.10^{-4}.

8 - CPT SYMMETRY

In an analysis of CP asymmetry, Bell and Steinberger [13] have derived a sum rule for the conservation of probability in neutral kaons decays, also called a unitary condition. No assumption of symmetry with respect to T, CP, or CPT are required. The sum rule is :

$$(1 + i \operatorname{tg} \phi_{sw}) (\operatorname{Re} \epsilon - i \operatorname{Im} \Delta) \simeq \sum_f A (K_S^0 \rightarrow f) A (K_L^0 \rightarrow f)$$

where f represents the common decay channels for K_L^0 and K_S^0 : 2π, 3π, $\pi_{e\nu}$, $\pi_{\mu\nu}$...

Such a relation allows us to study the contribution of T (parameter ϵ) and of CPT (parameter Δ) to CP violation.

Successive analyses have been performed, and give results compatible with CPT invariance and T non-invariance. In 1981 for example, J.W. Cronin [14] gave the following results :

where $\tilde{\Delta} = \Delta - a$, $a = \dfrac{A\,(K_L^0 \rightarrow 2\pi \quad I=0)}{A\,(K_1^0 \rightarrow 2\pi \quad I=0)}$; and ϵ and Δ are projected onto axes parallel and perpendicular to tg Φ_{sw} .

$$T \begin{cases} \epsilon_{/\!/} = (2.57 \pm 0.19)\ 10^{-3} \\ \epsilon_{\perp} = (0.14 \pm 0.18)\ 10^{-3} \end{cases}$$

$$CPT \begin{cases} \tilde{\Delta}_{/\!/} = (0.10 \pm 0.14)\ 10^{-3} \\ \tilde{\Delta}_{\perp} = (-0.02 \pm 0.20)\ 10^{-3} \end{cases}$$

Such results show the predominance of the T violation and leave the CPT non-invariance, if any, at a level a factor 10 smaller.

A more recent comment on CPT symmetry has been given by V.V. BARMIN et al. [15] [16].

We will only summarize the conclusions given in this paper :

1. Any CPT violation in the direct channel $\Delta S = 1$, i.e., through the parameter ϵ', is only compatible with experimental data at a 15 % confidence level or less, and has as its most probable cause the measured difference in the phases Φ_{00} and Φ_{+-}.

2. CPT conservation in the $\Delta S = 0$ and $\Delta S = 2$ channels, i.e., through the parameter Δ (or $\tilde{\Delta}$), is inadequately demonstrated. The situation can be improved either by assuming strong CP violation in the 3 π channel, or by assuming $\Delta S = \Delta Q$ rule breaking and CP symmetry in K_{l3} decay, or both. Again, this conclusion is mainly due to the poor measurement of Φ_{00}.

The authors of this paper were complaining in 1984 that they knew of no proposal to measure the phase difference $\Phi_{00} - \Phi_{+-}$.

Since then, two proposals to measure the phase difference to a precision of 1° have been submitted and accepted (in March 1986) : one by the NA 31 collaboration at CERN [17] ; and the other by the E 731 collaboration at FNAL [18]. These two groups will be running in 1987 and 1988 (?) respectively, and, recalling the precision of 1 or 2° in phase measurement of the LEAR proposal, we can expect very precise results on this topic in 1989.

CONCLUSION

The Kobayashi-Maskawa proposition of natural CP violation has provoked a new activity in K^0 experimental physics in 1981. A good and correct answer to the question raised requires very precise, meticulous measurements.

Several experimental groups are active in this task, and, in 1990, a complete new set of CP parameters will be on the market.

Will these new measurements bring discovery, or a better understanding of the CP violation problem ? While surely desirable, it is not certain.

I would like to thank the organizing committee of the KAZIMIERZ Conference for their invitation. Let me also underline the excellent organization of Dr. Z.AJDUK, who made this conference so lively.

To write this talk, the CERN academic training lectures given by A. ZYLBERSTEJN at CERN (1984), was of great help to me.

D. LLYOD OWEN carefully read the manuscript, J. THIOLIERE typed it and H. de LIGNIERES made the drawings. I thank all of them very much.

REFERENCES

[1] Particle Data Group, Phys. Letters 111B (1982) 1

[2] M. BANNER et al., Phys. Rev. Letters 21 (1968) 1103

[3] M. HOLDER et al., Phys. Letters 40B (1972) 141

[4] J.H. CHRISTENSON et al., Phys. Rev. Letters 43 (1979) 1209

[5] L. WOLFENSTEIN, Phys. Rev. Letters 13 (1964) 569

[6] M.K. GAILLARD and B.W. LEE, Phys. Rev. D10 (1974) 897
J. ELLIS et al., Nuclear Phys. B109 (1976) 213
R.D. PECCEI and H. QUINN, Phys. Rev. Letters 38 (1977) 1440
M.A. SCHIFMAN et al., Nuclear Phys. B120 (1977) 316
F.J. GILMAN and M.B. WISE, Phys. Letters 83B (1978) 83
B. GUBERINA and R.D. PECCEI, Nuclear Phys. B163 (1980) 289
F.J. GILMAN and M.B. WISE, Phys. Rev. D20 (1979) 2392

[7] F.J. GILMAN and J.S. HAGELIN, Phys. Letters 126B (1983) 111

[8] T.T. DEVLIN and J.O. DICKEY, Rev. Mod. Phys. 51 (1979) 237

[9] J.K. BLACK et al., Phys. Rev. Letters 54 (1985) 1628

[10] R.H. BERNSTEIN et al., Phys. Rev. Letters 54 (1985) 1631

[11] G. GOLLIN et al., E 731 proposal - FNAL Fev. 83.

[12] D. CUNDY et al., NA 31 proposal - CERN 22/12/83

[13] J.S. BELL and J. STEINBERGER, Proc. Intern. Conf. Elementary Particles, Oxford (1965), p. 195

[14] J.W. CRONIN, Rev. Mod. Phys. 53 (1981) 373

[15] V.V. BARMIN et al., Nuclear Phys. B247 (1984) 293

[16] L. OKUN, Private communication

[17] Addendum to proposal P 174 - CERN/SPSC/86-6 (10 March 1986)

[18] Measurement of the phase difference between η_{00} and η_{+-} - FNAL PAC - March 9th 1986 - presented by G.D. Gollin, Princeton University.

Druck: Kalle Printing G.m.b.H. 4/93/86 300 exp.